공학박사 학위논문

Experiment and Simulation of Load-following Operations of a Lead-cooled Transportable Small Modular Reactor

수송식 납냉각 소형모듈원전의

부하 추종 운전 실험 및 모사 연구

2018년 2월

서울대학교 대학원

에너지시스템공학부

신 용 훈

Experiment and Simulation of Load-following Operations of a Lead-cooled Transportable Small Modular Reactor

지도 교수 황 일 순

이 논문을 공학박사 학위논문으로 제출함

2018 년 1 월

서울대학교 대학원

에너지시스템공학부

신 용 훈

신용훈의 박사 학위논문을 인준함

2018 년 1 월

위 원 장 심 형 진 (인)

부위원장 황 일 순 (인)

위 원 정 호 (인)

위 원 조 형 규 (인)

위 원 김 희 령 (인)

Abstract

Experiment and Simulation of Load-following Operations of a Lead-cooled Transportable Small Modular Reactor

Yong-Hoon Shin

Department of Energy Systems Engineering

The Graduate School

Seoul National University

The nuclear industry of the world faces limited public acceptance for large-scale nuclear power plants. The majority of Korean public tend to be emotional since the outcome of Fukushima accident. In addition to the effects of Fukushima accident, the lack of acceptable management plan for spent nuclear fuel further contributes to this public opposition. In this thesis, , an innovative lead-bismuth eutectic (LBE) cooled small modular reactor (SMR) has been developed as a safe distributed power source that can be operated in hybrid with the renewable electricity sources including solar and wind power. The innovative SMR system features an integral pool-type design achieving enhanced inherent safety by including all the primary reactor components into a single pool while excluding reactor coolant pump. This design innovation leads to an unusual capability for the load-following operation in response to

rapid fluctuations of renewable electricity in an isolated grid system. In addition, the passive safety nature with low-pressure pool-type design provides advantage of the exclusion of loss-of-coolant accident and loss-of-flow accident which is likely happen in most of the current nuclear power plants, even if the likelihood of these accidents are extremely low, from primary piping failure and unexpected pump failure.

Furthermore, the primary coolant, LBE, itself contribute the inherent safety enhancement because it is chemically inert with water and air in contrast with sodium, another liquid metal coolant considered to be the future nuclear system coolant, and a better heat-transfer medium compared to water. LBE also facilitates a long-term burning of nuclear fuel through a hard neutron spectrum that it supports. The hard spectrum leads to the breeding of fissile material from the fertile, and contributes to the criticality that cause sustained over life. In addition, the fast spectrum can help an effective transuranic elements incineration through nuclear conversion as well, which ultimately increases fuel utilization furthermore and minimizes the amount of highly radioactive elements.

For adequate understanding of the integral system behaviors of a LBE-cooled passive system under transients is necessary and furthermore, a predictive tool for passive system behavior is need to be developed. Hence, this study has been conducted in three stages as follows: first, a pool-type integral experimental facility has been devised by hydrodynamic scale reduction from its prototype SMR design and natural circulation experiments has been carried out in both steady state and transients given by external condition changes. Second, a one-dimensional system thermal-hydraulics code is validated two-fold through the experimental results generated from a loop configuration and the results given by the pool-type facility. Third, an analytical model for one-dimensional, time-dependent passive system transient evaluation has been developed. This analytical model has been verified with not only experimental

results made in the second step and but also with one-dimensional system thermal-hydraulics code. Since there is no realization of a LBE-cooled SMR until now, a target reactor URANUS is designed before starting the three-step approach.

The results given by the experimental, numerical, and analytical investigations on the passive LBE-cooled SMR show that passive cooling from natural circulation does not deteriorate the rate of power maneuvering would since the primary side transients are rapidly saturated. In addition, the stability analysis confirms that the reactor core power of URANUS can be regulated within a stable range with respect to the external load demand change. Hence, the maximum achievable power ramp rate under safe, stable condition is related to nuclear fuel integrity, not the passive nature of reactor system. With the analytical simulation model, it is evaluated with an analysis on the step response that the reactor can change its core power rating as fast as 3.5% power per second from 50% of nominal full power to its full power with only considering its thermal-hydraulic and reactor kinetic response.

In addition, as a preliminary study, the dynamics of the secondary side is simulated with the developed analytical reactor dynamics simulation model and the results showed that the heat balance mismatch between the primary and secondary sides during transients can be minimized with feedwater flow control means, a proportional controller with respect to the external load demand in this case. It is concluded that the reactor core power regulation along with feedwater flow rate control is favorable, since the primary side of a passive LBE-cooled SMR is expected to go through slower transients compared to the primary side under given operational condition changes.

Keywords
Lead-bismuth eutectic
Natural circulation
Small modular reactor
Scaling design
Load-following operation

Student Number
2013-21019

Contents

Chapter 1 Introduction 1

1.1 Background 1

1.2 Objective 6

Chapter 2 Literature Review 8

2.1 Lead and LBE-cooled Fast Reactor (LFR) 8

2.2 Passive small modular reactors (SMR) 14

2.3 Experimental studies on LBE natural circulation 18

2.4 Scaling analysis methods for liquid metal experiments 22

Chapter 3 Problem Definition and Research Strategy 26

3.1 Problem definition 26

3.2 Approach 28

3.2.1 SMR reference design definition 30

3.2.2 Experimental setup and tests 30

3.2.3 Numerical validation and modeling 31

3.2.4 Analytical model development and load-following capability assessment 32

Chapter 4 LBE-cooled Passive SMR Design: URANUS 33

4.1 Design goals and requirements 34
4.2 Reactor core design 39
4.2.1 Fuel assembly configurations 39
4.2.2 Fuel rod design 45
4.2.3 Safety control assembly configurations 49
4.2.4 Neutronic analysis 51
4.2.5 Kinetics and reactivity feedback coefficients 56
4.3 Heat transport systems design 62
4.3.1 Primary heat transport system 62
4.3.2 Secondary heat transport system 67
4.3.3 Steady-state thermal-hydraulic analysis 70
4.4 Structure, materials, and components 75
4.4.1 Reactor vessel structure and materials 75
4.4.2 Three-dimensional seismic isolation 77

Chapter 5 Experimental Setup and Test Results 79

5.1 LBE loop natural circulation experiments 80
5.1.1 Experimental setup of LBE loop facility: HELIOS 80
5.1.2 HELIOS experiment procedure and LBE loop natural circulation experimental conditions 89
5.1.3 Experimental results on steady-state LBE loop natural circulation 95
5.2 LBE pool natural circulation experiments 97
5.2.1 Design of LBE pool facility: PILLAR 97
5.2.2 Final design of PILLAR 124
5.2.3 PILLAR experiment procedure and conditions 162

5.2.4 Experiment results and discussion on LBE pool natural circulation 170

Chapter 6 Code Validation and Numerical Analysis 191

6.1 One-dimensional system thermal-hydraulics (STH) code: MARS-LBE 191

6.2 Code validation on thermal-hydraulics with steady-state experimental results 193

6.2.1 Code benchmark with HELIOS loop test results 193

6.2.2 Code benchmark with PILLAR pool test results 210

6.3 Code validation on reactor point kinetics 217

6.4 System thermal-hydraulics modeling on LBE pool transient natural circulation experiments 220

Chapter 7 Load-Following Capability Assessment of Passive LBE-cooled Pool-type SMR 227

7.1 Analytical reactor dynamics simulation model 227

7.1.1 Reactor core model 231

7.1.2 Hot leg and cold leg models 250

7.1.3 Steam generator model 252

7.1.4 Model implementation for numerical simulation 281

7.2 Reactor control model validation 286

7.3 Assessment of fast load-following capability 292

7.3.1 Proportional feedwater control 292
7.3.2 Stability analysis.....300
7.3.3 Planned load-following operation 304
7.3.4 Power recovery from low power to full power.....306
7.3.5 Comparison with a commercial SMR 311

Chapter 8 Conclusions and Future Work..... 314

8.1 Conclusions 314
8.2 Future work..... 316

Nomenclature..... 318

Bibliography 326

초 록 346

List of Tables

Table 4.1 Key design parameters of URANUS 38

Table 4.2 Design parameters of fuel assemblies..... 44

Table 4.3 Design information of fuel rod 48

Table 4.4 Key neutronics parameters of reactor core 55

Table 4.5 Kinetic parameters at beginning of cycle calculated by the deterministic code chain and McCARD 60

Table 4.6 Delayed neutron fractions and precursor decay constants at beginning of cycle calculated by the deterministic code chain and McCARD 61

Table 4.7 Specification of primary and secondary heat transport systems of URANUS 66

Table 4.8 Steady-state system thermal-hydraulic calculation results of URANUS 74

Table 5.1 Thermocouple locations on HELIOS main loop in terms of accumulated length along flow path 88

Table 5.2 Natural circulation test procedure to generate well-defined test results in HELIOS 92

Table 5.3 Test matrix on adiabatic, non-isothermal natural circulation experiments in HELIOS 94

Table 5.4 Adiabatic, non-isothermal, steady-state natural circulation results in HELIOS 96

Table 5.5 PILLAR design requirements and criteria for scaling analysis 101

Table 5.6 Comparison of thermosphysical properties of nuclear fuel, heater rods, and structural materials (Hong and Lee, 2012; Popov and Carbajo, 2000) 117

Table 5.7 PILLAR design specifications for flow area reduction ratio 1:200 122

Table 5.8 Measurement requirements of PILLAR instrumentation system 156

Table 5.9 PILLAR steady-state natural circulation test matrix and case definition 168

Table 5.10 Experimental results on steady-state LBE pool natural circulation in PILLAR 184

Table 6.1 Thermophysical properties of 316 L stainless steel (data retrieved from (Mills et al., 2004; Popov and Carbajo, 2000)) 197

Table 6.2 Correlations used for hydraulic loss coefficient evaluation 198

Table 6.3 MARS-LBE benchmark results for well-defined steady-state experiment results in HELIOS 203

Table 6.4 Node conditions for the original, halved, and trisected models used for sensitivity study 208

Table 7.1 Elements of matrix **A** for linearized state-space formulation 247

Table 7.2 Elements of matrix **B** for linearized state-space formulation 249

Table 7.3 Elements of matrix $Z(\mathbf{x},\mathbf{u})$ 272

Table 7.4 Elements of matrix $F_{\mathbf{x}}(\mathbf{x},\mathbf{u})$ 276

Table 7.5 Elements of matrix $F_{\mathbf{u}}(\mathbf{x},\mathbf{u})$ 280

Table 7.6 Comparison between the developed passive LBE-cooled SMR dynamics model and MARS-LBE 289

List of Figures

Figure 1.1 Material and control limitations in water-cooled reactors for fast and frequent load-following operation 5

Figure 3.1 Thesis research approach 29

Figure 4.1 Radial assembly configuration of active core 42

Figure 4.2 Horizontal view of a single fuel assembly including fuel rods and a central skeletal bar 43

Figure 4.3 Pin-cell model for fuel rod 47

Figure 4.4 Code system used for the neutronic analysis of URANUS core design 53

Figure 4.5 Effective multiplication factor of URANUS core during 20 years of full-power operation 54

Figure 4.6 Schematic diagram of URANUS primary boundary 65

Figure 4.7 Ideal temperature-entropy (T-s) diagram of URANUS..... 69

Figure 4.8 Nodalization of overall heat transport system for steady-state calculation 72

Figure 4.9 Steady-state temperature distributions of fuel centerline, cladding, and coolant bulk at the hottest assembly 73

Figure 4.10 3D seismic base isolation bearing unit, adopted from (Yoo et al., 1999)..... 78

Figure 5.1 (a) System schematic diagram and (b) front-view picture of

HELIOS thermal-hydraulic test loop 83

Figure 5.2 Three-dimensional configuration of HELIOS constituent components and key instrumentation system..... 84

Figure 5.3 (a) Isomeric view (left) and cross-sectional view (right), (b) disassembly view, and (c) photo (white dash) of PILLAR main vessel..... 126

Figure 5.4 Three-dimensional model of PILLAR lower plenum and heater rods assembly in several viewpoints. (a) Isomeric view, (b) cross-sectional view in z-direction, (c) top view, and (d) bottom view..... 130

Figure 5.5 Schematic diagram of PILLAR heater rod..... 131

Figure 5.6 Heater rod and skeletal bar arrangement inside the core region of PILLAR 132

Figure 5.7 Design and axial positions of PILLAR core grid spacers and thermocouple location upon each plate..... 133

Figure 5.8 Three-dimensional model of PILLAR lower vessel and lower barrel assembly in several viewpoints. (a) Isomeric view, (b) cross-sectional view in z-direction, (c) top view, and (d) cross-sectional view in radial direction 136

Figure 5.9 Three-dimensional model of PILLAR dummy rod assembly in several viewpoints. (a) Isomeric view, (b) detail view on the interface with heater rods, and (c) top view..... 137

Figure 5.10 Three-dimensional model of PILLAR middle barrel in several viewpoints. (a) Isomeric view, (b) cross-sectional view

in axial direction, (c) top view, and (d) bolt cover application to middle barrel (left) and middle barrel without the bolt cover (right)..... 139

Figure 5.11 Three-dimensional model of PILLAR upper barrel in several viewpoints. (a) Isomeric view, (b) cross-sectional view in axial direction, (c) top view, and (d) bottom view..... 141

Figure 5.12 Axial position of windows on PILLAR upper barrel and expansion volume for LBE level control with respect to heat exchanger shell side 142

Figure 5.13 Radial position and arrangement of windows on PILLAR upper barrel with respect to heat exchanger and upper vessel 143

Figure 5.14 Three-dimensional model of PILLAR upper vessel in several viewpoints. (a) Isomeric view, (b) cross-sectional view in axial direction, and (c) top (bottom) view 145

Figure 5.15 Three-dimensional model of PILLAR heat exchanger tube side in several viewpoints. (a) Isomeric view, (b) cross-sectional view in axial direction, (c) top view, (d) bottom view, (e) cross-sectional view of lower chamber, and (f) cross-sectional view of upper chambers 148

Figure 5.16 Schematic diagram of lower water chamber and tube arrangements of PILLAR heat exchanger tube side 149

Figure 5.17 Three-dimensional model of PILLAR middle vessel in several viewpoints. (a) Isomeric view, (b) cross-sectional view

in axial direction, and (c) top (bottom) view..... 151

Figure 5.18 Schematic diagram of PILLAR instrumentation system 157

Figure 5.19 Geometrical consideration of thermocouple installation positions on grid spacers 158

Figure 5.20 Axial and radial position of instrumentation probes on the shell side of PILLAR heat exchanger 159

Figure 5.21 Position of instrumentation probes on arbitrary planes A, B, and C in PILLAR heat exchanger on planar cut view 160

Figure 5.22 Position of instrumentation probes on arbitrary planes A, B, and C in PILLAR heat exchanger on axial cut view..... 161

Figure 5.23 Graphical test matrix and case definition on PILLAR transient natural circulation experiments 169

Figure 5.24 PILLAR system integral heat loss evaluation procedure 176

Figure 5.25 Locations of thermocouples for the evaluation of PILLAR system integral heat loss..... 177

Figure 5.26 PILLAR main vessel integral heat loss evaluation test results 178

Figure 5.27 Fitted curve for PILLAR system integral heat loss as a function of temperature difference between surface and ambient temperatures 179

Figure 5.28 PILLAR primary system response to the variation in the amount of heat tracing on the main vessel surface 180

Figure 5.29 PILLAR secondary cooling system (heat exchanger tube side)

response to the variation in the amount of heat tracing on the main vessel surface 181

Figure 5.30 PILLAR transient natural circulation experimental results: instantaneous core power increase (Case No.: T-PINC-210~240/3.5) 187

Figure 5.31 PILLAR transient natural circulation experimental results: instantaneous core power decrease (Case No.: T-PDEC-240~210/3.5) 188

Figure 5.32 PILLAR transient natural circulation experimental results: instantaneous secondary side flow increase (Case No.: T-FINC-240/3.5~4.0) 189

Figure 5.33 PILLAR transient natural circulation experimental results: instantaneous secondary side flow decrease (Case No.: T-FDEC-240/4.0~3.5) 190

Figure 6.1 Nodalization map of HELIOS prepared for MARS-LBE. 196

Figure 6.2 Comparison between measured and calculated mass flow rates as a function of mock-up core power 204

Figure 6.3 Comparison between LBE mass flow rates in HELIOS experiment and MARS-LBE benchmark results..... 205

Figure 6.4 Steady state experiment and benchmark results of HELIOS in cases (a) NC1.0 (9.8 kW power), (b) NC2.0 (15.0 kW power), (c) NC1.0 (27.0 kW power), and (d) NC1.0 (33.6 kW power) 206

Figure 6.5 Comparison of temperature differences between average hot

leg and cold leg temperatures in HELIOS experiment and MARS-LBE benchmark results 207

Figure 6.6 Case study results on the heat exchanger axial node size in (a) the original model with 7 axial nodes, (b) halved model with 14 axial nodes, and (c) trisected model with 21 axial nodes..... 209

Figure 6.7 Nodalization map of PILLAR prepared for MARS-LBE . 212

Figure 6.8 PILLAR heater rod cross-sectional view and equivalent radii for each of constituent material regions 213

Figure 6.9 Comparison between LBE mass flow rates in PILLAR steady-state experiment and MARS-LBE benchmark results 215

Figure 6.10 Comparison of temperature differences between average hot leg and cold leg temperatures in PILLAR steady-state experiment and MARS-LBE benchmark results..... 216

Figure 6.11 Comparison with MARS-LBE modeling results and PILLAR transient natural circulation experimental results: instantaneous core power increase (Case No.: T-PINC-210~240/3.5) 223

Figure 6.12 Comparison with MARS-LBE modeling results and PILLAR transient natural circulation experimental results: instantaneous core power decrease (Case No.: T-PDEC-240~210/3.5) 224

Figure 6.13 Comparison with MARS-LBE modeling results and PILLAR transient natural circulation experimental results: instantaneous secondary side flow rate increase (Case No.: T-

FINC-240/3.5~4.0)..... 225

Figure 6.14 Comparison with MARS-LBE modeling results and PILLAR transient natural circulation experimental results: instantaneous secondary side flow rate decrease (Case No.: T-FDEC-240/4.0~3.5)..... 226

Figure 7.1 Power and steam production regulations in passive SMR by means of control rod movement and feedwater flow control 229

Figure 7.2 Assumptions and approaches for the analytical reactor dynamics simulation model developed in thesis study 230

Figure 7.3 Schematic diagram for core state-space model including both neutronics model and core thermal-hydraulics model 232

Figure 7.4 Schematic diagram for the reactor core model of generic pin-cell model of nuclear fuel..... 240

Figure 7.5 Schematic diagram for steam generator state-space model 255

Figure 7.6 Block chain diagram for reactor state-space model implemented to MATLAB/Simulink environment 285

Figure 7.7 Calculation results comparison on the system transient evaluation model for passive LBE-cooled SMR and MARS-LBE for the power ramp rate of -5%P/min from 100% power output 290

Figure 7.8 Calculation results comparison on the system transient evaluation model for passive LBE-cooled SMR and MARS-LBE for the power ramp rate of +5%P/min from 100% power

output 291

Figure 7.9 Calculation results for the system transients given by a power ramp rate of -10%P/min from 100% power output without feedwater flow rate control 296

Figure 7.10 Calculation results for the system transients given by a power ramp rate of -10%P/min from 100% power output with feedwater flow rate control 297

Figure 7.11 Calculation results for the system transients given by a power ramp rate of -10%P/min from 100% power output with feedwater flow rate control 298

Figure 7.12 Calculation results for the system transients given by a power ramp rate of +10%P/min from 90% power output with feedwater flow rate control 299

Figure 7.13 Root locus for load demand input to core power output . 302

Figure 7.14 Bode diagram for load demand input to core power output 303

Figure 7.15 Comparison of planned load-following operation simulation results between the analytical model developed in this dissertation (line) and MARS-LBE (circle and line) 305

Figure 7.16 Conceptual case on instantaneous power return from low-power condition to nominal full power condition by grid request 309

Figure 7.17 Step response analysis results on reactor core power response and turbine load response with respect to power

recovery request from 50% to 100%..... 310

Figure 7.18 Comparison with a commercial passive load-following concept *NuFollow*™ (excerpted from (Ingersoll et al., 2015)). (a) Required load demand and (b) reactor output and steam bypass by NuScale and URANUS..... 313

Chapter 1 Introduction

1.1 Background

The nuclear industry of the world faces limited public acceptance for large-scale nuclear power plants. The majority of Korean public tend to be emotionally repulsive to nuclear reactors since the outcome of Fukushima accident. In addition to the effects of Fukushima accident, the lack of acceptable management plan for spent nuclear fuel further contributes to this public opposition.

Since Fukushima accident, the paradigm of energy has been changing to expand: the renewable energy sources such as photovoltaic, solar thermal, wind, and so on have been grown and to curtail carbon dioxide. In addition, the resistance to expand power transmission lines results in the deployment of locally distributed power sources will become dominant. This is so-called microgrid which incorporates various types of electricity sources in a small region by increasing electricity utilization with the distributed energy resources (Islam and Gabbar, 2015). Hence, the future energy mix will be likely to be re-established with a high share of renewables.

This energy transition motivates the nuclear industry to develop load-following capacity that supports the microgrid with a significant fraction of renewables. Small modular reactors (SMRs), which are generally defined as

nuclear reactors with power ratings lower than or equal to 300 MWe, receive an increasing attention for continuous and a sustainable nuclear energy utilization. Interests on SMRs are growing and as supporting this, more than 50 SMR designs are under development worldwide (OECD Nuclear Energy Agency, 2016b). Among them, three SMRs including CAREM in Argentina (Marcel et al., 2013), HTR-PM in China (Zhang et al., 2006), and KLT-40s in Russian Federation (Mitenkov and Polunichev, 1997) are under construction and are expected to start their first operations by 2020. In addition, a study on the economics of SMRs states that SMRs that will be built in 2020-2035 could generate up to 21 GWe of the world's electricity based on an optimistic prospect (OECD Nuclear Energy Agency, 2016b).

Not only are the reduced electrical capacity of a single plant, but the enhanced safety and maneuverability of a reactor are required for SMRs to be employed in a microgrid. Fukushima accident suggested that the current active safety systems in nuclear power plants might not be reliably performed during beyond design basis accidents. An outstanding safety can be realized by replacing coolant with lead or lead-bismuth eutectic (LBE) and excluding active components by relying on natural circulation.

Among these promising utilization means, the most competent option is the use as a hybrid power source which incorporates renewable energy sources and SMRs as an integrated power station. Since the electricity generation rate by renewables varies with time in a daily basis and a seasonal basis as well, the installation of energy storage system (ESS) is inevitable. Considering that the market share of renewables will be growing further

worldwide, this innate fluctuation needs to be flattened. In this case, SMR can work like a battery or ESS by changing its electricity generation.

Since the renewables are strongly dependent upon the daily weather of the site, energy storage systems (ESS) should be implemented in a microgrid to compensate for the fluctuation in electricity supply from the sources. Battery-based ESS has been found to be costly and vulnerable to life-shortening under hybrid operation with renewables (Svoboda et al., 2007; Thackeray et al., 2012). SMRs can work as a backup electricity source or the ESS by maneuvering its power output. In this respect, the fast and frequent power maneuvering capability of a nuclear reactor is questioned because most of them are operated under constant and full power conditions or limited power change in a relatively long time span.

Until now, the load-following operation of commercial large-scale nuclear power plants has been developed and sophisticated as seen in French experiences and other practices (Choi et al., 1992; Lokhov, 2011; Ludwig et al., 2011). However, conventional water-cooled reactors are not suitable for the fast and frequent power maneuvering required in the microgrid, which relies a large capacity on the renewables, due to their innate limitations. These can be classified into two categories, material limitations and system control limitation, as summarized in Figure 1.1.

The former includes well-known phenomena in pressurized water reactors such as the pellet-clad interaction (PCI) (Cox, 1990) and stress corrosion cracking (SCC) (IAEA, 2011). A rapid power maneuvering changes the local power and temperature distribution. It leads to pellet fracturing by

which corrosive fission gas such as iodine is no longer able to remain in the pellet structure and contributes to SCC taking place. Furthermore, the pellet goes through a severe deformation called bambooing and the edge of the pellet physically contacts the inner surface of cladding so that PCI can cause cladding failure during fast power ramps. In addition to this, the cladding fatigue failure given by coolant temperature cycle is expected to be present in the cladding.

The latter, the system control limitation, comes from xenon oscillation in principle. Since the reactor power is related to neutron flux, the power maneuvering gives rise to a variation in axial power distribution from the normal operation conditions. Due to the neutron poisoning effect given by xenon, it is required to control its distribution and material balance precisely for a safe and stable operation.

Contrary to the inherent limitations of water-cooled reactors on fast load-following operation and advancement in safety, a passive LBE-cooled SMR can overcome both material failure risks and reactivity non-compliance. In this regard, this thesis mainly focuses on the assessment of fast load-following capability of the system, in terms of passive cooling and stability, with experimental and numerical approaches.

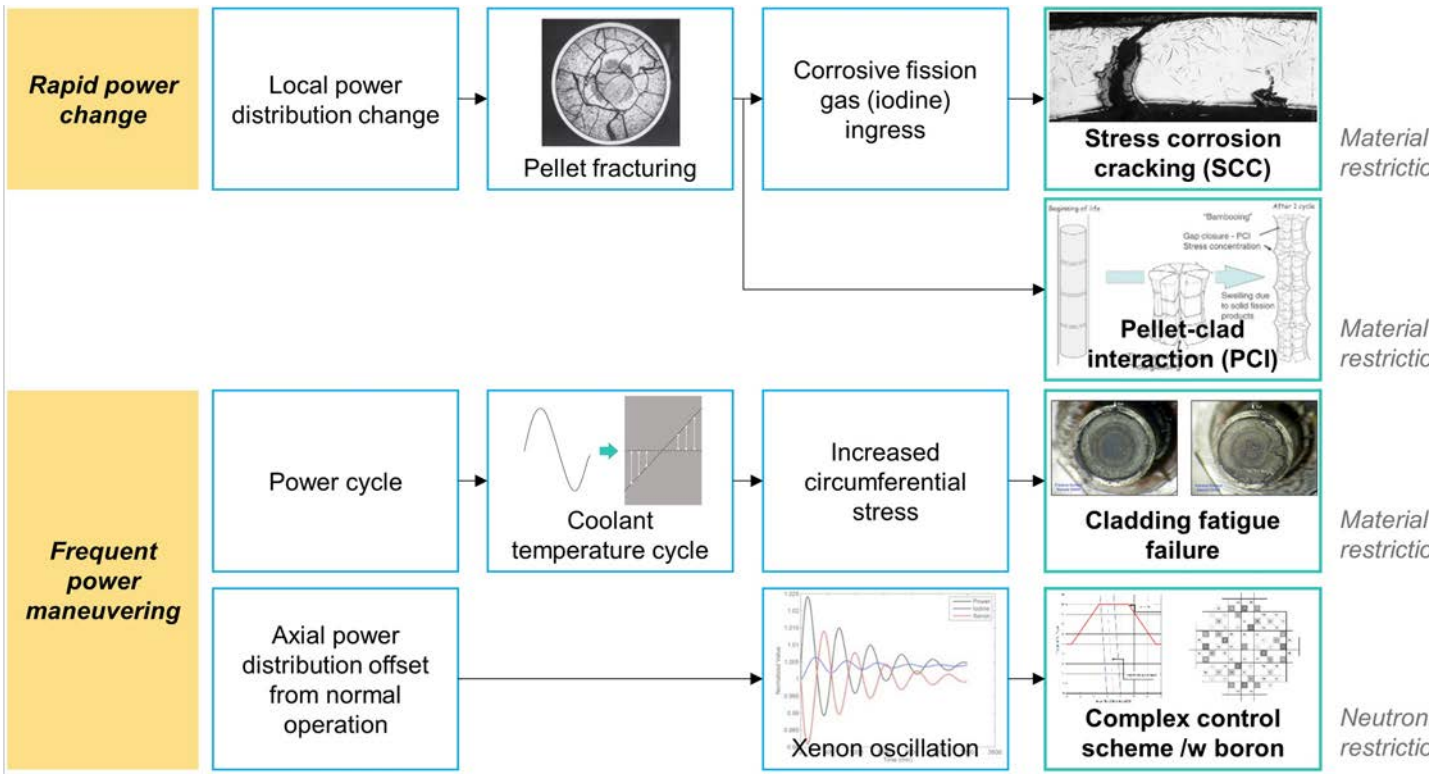

Figure 1.1 Material and control limitations in water-cooled reactors for fast and frequent load-following operation

1.2 Objective

The objective of this thesis study is to evaluate the load-following capability of a passive LBE-cooled pool-type SMR subjected to both safety and stability requirements. To achieve the objective, the thesis study is divided into three separate tasks including experiments, numerical modeling, and analytical studies.

The experimental studies on natural circulation of LBE, both in steady state and transient conditions, are conducted using thermal-hydraulic scaled test loop and pool mockups for a realistic and thorough understanding on the phenomenon. Both steady state and transient test results are utilized for the validation of a numerical system model while the transient results on the system reactions to operational condition maneuvering expected for the load-following operation in an actual passive reactor system are used for the validation of analytical studies.

For the numerical study, a one-dimensional system thermal-hydraulics code named as MARS-LBE that is derived from MARS for a water-cooled reactor is validated for its modeling capability on a passive LBE-cooled reactor. Since water and LBE have significantly different thermophysical properties each other, its thermal-hydraulic simulation results are validated with the steady-state test results produced during the experimental study. Since there is no data from reactor kinetics experiments with lead-cooled systems, the validation in this part is made on the sodium-cooled reactor EBR-II, which are covered extensively by a separate collaboration work.

Finally, the analytical studies resulted in the development of an indigenous analytical formulation which is dedicated to the passive LBE-cooled SMR system, the formulate is used to simulate the system reaction to a variation in external load demand and the stability under that transient. The validity of the simulation results is ensured by the system thermal-hydraulics code that is validated by the numerical model.

Chapter 2 Literature Review

2.1 Lead and LBE-cooled Fast Reactor (LFR)

Lead or lead-alloy cooled fast reactor (LFR) systems are among the six systems selected for joint development by the Generation IV International Forum (GIF) based on their potential to meet the GIF technology goals and have been evaluated as the most promising technology (OECD Nuclear Energy Agency, 2014). The choice of lead and LBE as innovative coolant is motivated by their favorable safety features compared to conventional coolant including water and sodium: chemical inertness that excludes the possibility of heat and pressure load with hydrogen explosion while being compatible with air, carbon dioxide, and water.

The main difference between the heavy liquid metals and other media comes from their significantly higher thermal conductivities (16.6 W/m K for lead at 673 K and 11.8 W/m K for LBE at 573 K) and lower specific heat capacities (~140 J/kg K for lead and ~150 J/kg K for LBE). The former leads to compatible steam generator placement using high heat transfer capability. In addition, their high boiling points (2,021 K for lead, 1,943 K for LBE) enable a system to be free of pressurization and contributes to avoiding the risk of coolant boiling. The kinematic viscosities (0.21E-6 m^2/s for lead at 673 K, 0.18E-6 m^2/s for LBE at 573 K) are considerably smaller than that of air or

water. The higher ratio of inertia force to viscous force leads to good stabilities of coolant flow regime. Small neutron absorption cross-section (0.0060 barn for lead and 0.0015 barn for LBE at 1 MeV), and high atomic mass (207 g/mol for lead and 208 g/mol for LBE), and high retention capability for radionuclides provide additional safety features (OECD Nuclear Energy Agency, 2007).

On the other hand, lead and LBE have some drawbacks in comparison with the conventional coolants as well. One of the issues of lead and LBE is that it is ten times heavier than sodium and water. This presents a challenge to designers of the seismic isolation systems that will be used with these heavy liquid metal reactors. Another drawback connected with LBE, which is not a critical issue to lead, is the accumulated radioactivity, mainly due to the alpha-emitter polonium-210 (^{210}Po), having the half-life of 138 days. ^{210}Po is formed in the process of neutron irradiation on bismuth. Several methods to remove ^{210}Po from lead-polonium compound (PbPo) are introduced such as distillation, hydride stripping, alkaline extraction, rare-earth filtration, and electrodeposition. Lead is considered as a more attractive coolant option than LBE mainly due to its higher availability, lower price and lower amount of induced polonium activity by a factor of 10^4.

LFR systems can have insufficient system lifetime due to the corrosion of structural materials in the primary system. In this regard, FeCrAl and FeCrSi alloys were developed to increase corrosion resistance over lead and LBE in high temperature and strong radiation environments. Austenitic stainless steels experience severe metallic element dissolution while ferritic-martensitic steels suffer from excess oxidation. The studies to improve their

mechanical characteristics were performed by using a FeCrAl or FeCrSi alloy as coating or overlay welding. Thus, FeCrAl or FeCrSi based oxide dispersion strengthened (ODS) steels may solve corrosion and mechanical problems (Hosemann et al., 2008; Kimura et al., 2011; Takaya et al., 2012). In addition, an approach using overlay welding and pilgering techniques to produce corrosion-resistant functionally-graded composite tubes is also under development (Kim et al., 2017; Lee et al., 2016; Short and Ballinger, 2012).

With the efforts to overcome some shortcomings of lead and LBE mentioned above, several LFR concepts have been designed. Among those concepts, GIF has identified three reactor designs as reference systems of LFR in terms of power ratings and the scale of reactor (OECD Nuclear Energy Agency, 2016a). The first one is ELFR which was designed by the European Union to have 600 MWe power rating (Alemberti, 2012). Before the industrial development, a scaled demonstrator called ALFRED was also suggested to demonstrate to achieve safety standards requirements and assess economic competitiveness of the prototypic reactor (Frogheri et al., 2015). A prototype actinide burner, named BREST-OD-300, with the intermediate power rating of 300 MWe was designed by Russian Federation and was designated to be the one of the reference design (Dragunov et al., 2016). SSTAR by the United States is one of the reference designs as well, which has a variable power ranging 10-100 MWe and features a long-life cycle core and the passive cooling of the primary system (Smith et al., 2008). The reactor is distinguished from the use of supercritical carbon dioxide (S-CO_2) Brayton cycle while other two concepts rely on Rankine cycle with superheated steam.

Beyond the GIF reference concepts, several LFR designs have been developed worldwide. A nuclear reactor vendor, Westinghouse, is now developing their own LFR concept while looking at some opportunities in the market and the details are undisclosed at this moment (Westinghouse Global Technology Office, 2017).

Another company, Hydromine, is also developing a compact lead-cooled SMR in cooperation with ENEA, the Italian research center for nuclear and alternative energy (Wallenius et al., 2017). The name of reactor is LFR-AS-200 with 200 MWe power ratings as its name states, while the primary system is arranged in a large single pool.

SEALER is a concept suggested by a Swedish company LeadCold, which targets the deployment in communities and mining sites in the Canadian Arctic (Wallenius et al., 2017). It adopts lead as primary coolant and loads 19.9% enriched uranium oxide fuel. Another feature of this reactor is that it can change its electricity production rate in a range of 3-10 MW while the lifetime of core varies between 10-30 full power years with 90% capacity factor.

G4M also known as Hyperion had been designed in the United States (Zhang et al., 2013). Its single module can produce thermal power of 70 MW, which can be converted to 25 MW per unit. Three applications of the SMR was identified as mining areas, remote communities, and government facilities.

Other than those reactors, a lead-cooled SMR called SVBR-75/100 was designed by Russian Federation (Zrodnikov et al., 2006). With its relatively small power rating within a single module, the reactor can be deployed with several purposes such as renovating old NPP units, supplying heat and

electricity close to urban areas, desalinating seawater in developing countries. SVBR-75/100 features its versatile fuel loading strategy implemented with different types of nuclear fuel based on uranium oxide or mixed oxide (MOX) fuels and nitride or mixed nitride fuels.

Another application of lead and LBE can be found in research activities for accelerator-driven subcritical systems (ADS) that is operated under subcritical conditions by compensating this off-criticality with a high-energy proton accelerator (Satyamurthy and Biswas, 2002). On account of its favorable features, pure lead and/or LBE can be used not only as spallation target for additional neutron generation but also as coolant at the same time. An example of this is EFIT reactor which is a pool-type 100-MWth ADS which uses pure lead as coolant (Cinotti, 2004). Within its design development, some thermal-hydraulic analyses on the system were carried out such as analysis on accidental transients (Bandini et al., 2008a; Bandini et al., 2008b) and pressure drop evaluation for helical tubes in heat exchanger (Castiglia et al., 2012).

Furthermore, SCK-CEN in Belgium has developed MYRRHA which is based on the pool-type ADS concept and utilizes LBE as primary coolant (H. Ait Abderrahim et al., 2011). The design of MYRRHA has progressed and entered into the front end engineering phase (De Bruyn et al., 2014).

China has a plan to develop ADS in three stages by enlarging the magnitudes and incorporating several components in the reactor systems (Wu et al., 2016). In each stage, the magnitudes and proton beam currents of accelerators will be increased so that they support the subcritical cores. As a research facility equipped with a proton accelerator and spallation target,

CLEAR-I is planned to be constructed. After that, a demonstration facility with 100 MWth power ratings, CLEAR-II, will be built. The final stage of Chinese ADS development will be CLEAR-III, a commercial-scale prototype facility having 1,000 MW of thermal power ratings.

2.2 Passive small modular reactors (SMR)

Since the attention to SMR development and its commercialization is increasing, several concepts have been designed with an innovative safety feature by excluding the primary reactor coolant pump in the primary system. An advantage from the exclusion is design simplification that contributes to enabling turnkey-type contracts from vendors by manufacturing whole reactor components in a factory. The other important strength is its enhanced innate safety, which comes from the fact that its passive cooling nature works any conditions as far as temperature difference in coolant along with the height direction is present.

In this respect, a number of SMR concepts that utilizes passive cooling are under development and even under deployment as well. Among them, many of concepts have been designed with a conventional coolant, water. In Argentina, CAREM has been suggested as a passive integral design based on pressurized light water reactor (PWR), which uses light water as coolant and moderator (Marcel et al., 2013). All the primary components are located within the reactor pressure vessel. A notable feature of its reactor system is self-pressurization without adopting a pressurizer, which is achieved by a cold structure in the upper steam dome by means of balance between vapor production and condensation.

NuScale is another PWR-based passive SMR originated from a research done by Oregon State University and the Idaho National Laboratory in the United States (Reyes, 2011; Reyes and Lorenzini, 2010). Thanks to its

integral design, its reactor core is cooled and moderated by the natural circulation of pressurized water, similar to CAREM. NuScale features so-called multi-module concept in a single plant site, which can incorporate up to 12 reactor modules. To enhance the survivability in accident conditions, all the modules are submerged in water inside the reactor building pool so that long-term cooling is viable without any human intervention.

A Russian design, UNITHERM, is also a PWR-based passive SMR which focuses on being used in areas where human access is limited (Alekseev et al., 2014). In this regard, the reactor targets long-term fuel cycle up to 20 years. As water moderates neutrons, it requires a relatively high-enrichment nuclear fuel, about 19.75%, compared to other PWRs while it utilizes CERMET UO_2-ZrO_2 fuel to fulfill its criticality over the target fuel cycle.

Other than PWR-based SMRs, several types of SMRs that exploit light water and heavy water as primary coolant have been presented through common technologies including boiling water reactor (BWR) and pressurized heavy water reactor (PHWR). DMS is a SMR designed by GE-Hitachi and Japan Atomic Power Company and its acronym comes from ‘double MS’, which means modular simplified and medium small (Ikegawa et al., 2010). It utilizes a proven technology based on BWR and features the use of miniaturized, simplified, and standardized equipment while it is constructed in a modular way. A design innovation in this reactor is made through reducing the height of the primary containment vessel about one half (2 m) compared to conventional BWRs (3.7 m). Since its primary flow is given by natural circulation and resultant low flow mass rate, steam and water is separated by only gravity. In

this regard, DMS suggests free surface separation without using steam separators and it contributes to further simplification in reactor component design.

Bahbha Atomic Research Centre, BARC, in India suggested a PHWR-derivative SMR design called AHWR, which stands for the Indian Advanced Heavy Water Reactor (Sinha and Kakodkar, 2006). Since India has an abundant amount of thorium, there have been several domestic studies on the use of thorium-uranium-233 (U-233) fuel cycle. In this purpose, AHWR also aims at the utilization of thorium-based fuel in a large scale. The distinct features of AHWR are reactor system cooling being achieved by light water while neutron moderation is done by heavy water, its geometrical arrangement in terms of using vertical pressure tubes, and the quick replacement of pressure tubes with shop-fabricated coolant channels minimizing effect on other components.

Other than those SMRs using the conventional technologies with light and/or light water, several designs adopting liquid metal coolants have been proposed. It is mainly due to the superiority of heat transfer in liquid metal compared to water, which contributes to enhanced inherent safety with higher temperature distribution in the reactor core and heat flux margin that is expected in low flow rate conditions given by natural circulation. SSTAR, mentioned in Section 2.1 and is one of the reference designs of GIF, is the first SMR concept that relies on natural circulation with lead in the primary side cooling (Smith et al., 2008). Similar to other designs to enhance natural circulation flow rate and reduce hydraulic loss in the core, a large coolant volume fraction is employed.

A Korean design called PASCAR is a LBE-cooled passive SMR with

35 MW of electricity ratings with a single reactor module (Choi et al., 2011a). PASCAR loads metal fuel that is made of uranium and other actinides from spent fuel separated by pyroprocessing. To ensure passive cooling with LBE, the reactor adopts a large flow path and open square lattice between fuel rods allowing cross flow. Its relatively low core power density that finally leads to long-term operation within the given core discharge burnup and low temperature guaranteeing suppressed material degradation.

The Chinese research reactor design based on ADS also introduced in Section 2.1, CLEAR-I can be classified as a passive lead-cooled SMR (Wu et al., 2016). Owing to its low power density along with large expansion coefficient of LBE, passive cooling can be achieved while its safety characteristics are enhanced. In addition, mechanical and chemical damage on structural materials such as corrosion and erosion can be reduced effectively in favor of this low velocity profile.

As a remark, the development of passive SMR is expected to grow further because of its simpler design and better accident tolerance. The up-to-date status of the development can be found further on the IAEA Advanced Reactors Information System (ARIS) website.[1]

[1] The purpose of this remark is some published materials by the IAEA does not recommend to cite their supplement "Advances in Small Modular Reactor Technology Developments (2016)" due to the absence of an official review. The IAEA ARIS website is able to be accessed through: https://aris.iaea.org.

2.3 Experimental studies on LBE natural circulation

Natural circulation enhances the safety of a reactor system through passive cooling and as well as contributes to a simple design by excluding reactor coolant pump from the system. In particular, lead and LBE have an exceptional capability of natural circulation compared to sodium since pressure loss in the core would be reduced by increasing the pitch-to-diameter ratio in fuel bundle (Tuček et al., 2006).

In this regard, the characterization of LBE natural circulation have been made at a large number of laboratories by using loop facilities. An experimental study on LBE natural circulation was performed at TIT in Japan with a water boiling in direct contact with LBE (Takahashi et al., 2005).

Several experiments were carried out in ENEA-Brasimone Research Centre in Italy with NACIE facility for non-isothermal natural circulation given by various heater power ratings and gas-induced circulation by injecting argon bubbles into the loop (Coccoluto et al., 2011; Tarantino et al., 2011). The experiment results were used for the code benchmark of RELAP5/MOD3.3 by implementing the thermophysical properties of LBE.

A large-scale facility TALL at KTH in Sweden was utilized for the characterization of LBE in lead-cooled fast reactors and accelerator-driven systems (Ma et al., 2006; Ma et al., 2007). In KTH studies, various natural circulation phenomena were tested, such as natural circulation capability and stability, start-up from different initial conditions, and accident simulations. Similarly, the experiment results were compared with numerical analyses by

TRAC/AAA and RELAP5 codes.

Experimental studies on the steady-state and transient natural circulation of LBE were also conducted with the HANS facility at BARC in India for a range of core power from 900 W to 5,000 W (Borgohain et al., 2016a). An indigenous code called LeBENC was validated with the test results and the maximum temperature deviation was found to lie within 15% in transient simulations. A new LBE test loop, KTL, was built to investigate natural circulation for a wide temperature range from 200 to 780 °C. The upper limit is significantly higher than the maximum design temperature of most LBE test loops, that is, 550 °C (Borgohain et al., 2016b).

As mentioned above, the thermal-hydraulic behavior of LBE in the one-dimensional loop environments have been studied extensively including those listed. However, when it comes to a pool environment, only limitied studies have been made. The pool behaviors in those systems cannot be approximated one-dimensionally as the main flow is affected by flows in transverse directions to the main flow. Many reactors have hemispherical plenum structures in which the coolant from the downcomer is mixed and redistributed before entering the core. For SMRs that rely on natural circulation as the principal cooling mechanism, the coolant velocity variation in the core is expected to be much greater than those of pump-driven systems. It is because the coolant absorbs different amounts of local power as it flows through subchannels, which in turn generate different buoyancy for flow. Furthermore, if a certain region in the core is restricted for flow or a failure of the steam generator tube causes a void in the core, the perturbations from these three-

dimensional behaviors may propagate to deteriorate the reactor safety.

Understanding of the three-dimensional behaviors in reactor systems is still far beyond the scope of the loop studies. As the first step, many researchers around the world are conducting research into the three-dimensional flow behaviors of LBE under the poo-type reactor configuration.

As aforementioned, in the case of the TALL loop at KTH, the three-dimensional flow simulation region was inserted and converted the original TALL into TALL-3D. An electrical heater was installed outside the three-dimensional flow simulation region of TALL-3D to accelerate the occurrence of thermal stratification in low flow rate conditions to evaluate the effect of the phenomenon on the entire system. In addition, a number of thermocouples are installed in the corresponding area to measure the temperature change over time to measure the data for the verification of three-dimensional CFD codes and the improvement of one-dimensional system analysis code accuracy (Grishchenko et al., 2015; Papukchiev et al., 2015).

At SCK-CEN, the Belgian Nuclear Research Center, a new research reactor is being developed based on fast neutron spectrum to replace their water-cooled research reactor BR-2. For this purpose, MYRRHA is being designed and studied as an LBE-cooled multi-purpose research reactor (H. Ait Abderrahim et al., 2011). To find the effect of the three-dimensional flow inside the MYRRHA reactor pool, E-SCAPE facility, which is a down-scale facility with 1/6 length scale from prototype MYRRHA, is designed. The objectives of the facility is to carry out experiments and tests on the reactor coolant pump since the prototypic reactor uses pumps to circulate the coolant, experiments on

residual heat removal systems after the reactor shutdown, simulation of various accident situations, and data production for the verification of code and one-dimensional system analysis code (Van Tichelen et al., 2015; Van Tichelen et al., 2011).

2.4 Scaling analysis methods for liquid metal experiments

In an engineering point of view, it is unnecessary to make an identical experimental facility with respect to a prototype and thus, a reduction of scale is inevitable. In this regard, several parameters should be selected and designated properly so that the prototype and experimental facility behave equivalently. This procedure is called the scaling design and is started from selecting phenomena of interests and parameters to be conserved.

For decades, several scaling analysis methods have been suggested to apply for real-world experiments. Most of the methods require several considerations on fluid and flow characteristics to determine governing equations according to the conditions of between the prototype and the scale facility. Among them, the scaling methods reviewed for this dissertation are limited to the methods developed for liquid metal fast reactors, as a prototype and a scale facility use LBE as a working fluid.

(Grewal and Gluekler, 1982) suggested a scaling analysis method on natural circulation in SFRs to be tested with water because water and sodium have similar densities utilizing Navier-Stokes equation and several transport equations on heat transfer in the derivation of dimensionless numbers. However, their work did not clearly show how some parameters such as the representative velocity and the representative temperature difference are derived from governing equations, and how a parameter called ‘Euler number’ functions in the scaling analysis. In addition, they simply proposed a possibility in conclusion that an experimental facility with water could simulate thermal-

hydraulic behaviors cast in SFRs if the similarity in main dimensionless numbers is satisfied. (Weinberg et al., 1990) suggested a similar method simulating decay heat removal in SFRs with water like the previous study. In this study, they fixed two main parameters, the representative velocity and representative temperature difference, as core outlet velocity and core inlet-outlet temperature difference, respectively.

Scaling methods on single-phase natural circulation experiments in pool-type SFRs were suggested as well (Eguchi et al., 1997; Takeda et al., 1993). Prototypic reactor in those studies adopted sodium as coolant and the experimental facilities were supposed to be operated with water. It is because water ensures an easy handling due to its visual transparency and material compatibility compared to sodium that is opaque and highly reactive, and above all, it has been studied extensively so that its thermophysical properties are well known. The method features the geometrical similitudes in all directions (horizontal, lateral, and vertical) are equal so that a scale model is to be reduced from a prototype without any distortion in a specific direction. In addition, heat source and heat sink are designated as forms of 'black boxes' which means it is not necessary to conserve geometrical shape between the prototype and model. Internal flow directions in these black boxes are supposed to be unidirectional; in other words, no local flow is available. Furthermore, this study covered the role of Euler number in scaling analysis and the necessity of its conservation, which were not fully shown by former studies, so that previous studies can be supplemented. This methods was also applied to the design of E-SCAPE, a down-scale facility for the MYRRHA reactor developed by SCK-CEN, and

both the prototypic reactor and the scale facility utilize LBE as primary coolant (Van Tichelen et al., 2015).

There was a study on the scaling of pool-type passive LFR to be simulated by water (Chen, 2015). The author suggested not only the scaling analysis method itself but also the methodology to evaluate natural circulation stability in the water model. However, a test facility utilizing this method requires water temperature to be higher than its normal boiling point in a specific condition because many of thermophysical properties of LBE are quite exotic compared to those of water. In this case, the whole facility must include pressurizing means and be designed to ensure high operating pressure.

A scaling analysis method on natural circulation by single-phase and two-phase flows through area-average one-dimensional formulations was studied (Ishii and Kataoka, 1984; Ishii et al., 1998). The nondimensionalization of conservation equations in this method is done by utilizing the steady-state solution of the equations as the representative velocity and representative temperature difference. This method features scaling ratio in length direction (flow traversing direction; z-direction) can be chosen independently and similarity in transient conditions is also conserved because heat transfer between solid heat sources and fluid is also included in governing equations. On the other hand, this method has a limitation in simulating the local phenomena given in the prototype having a large flow area in the scale facility, as it utilizes area-averaged parameters for the set of one-dimensional equations. In this process, such behaviors in traversing directions, perpendicular to the z-direction, are no longer viable. In addition, this method was derived for the

natural circulation of water in single-phase and two-phase conditions. Still, it is applicable to a liquid metal as well, if its thermophysical properties does not vary with temperature.

Chapter 3 Problem Definition and Research Strategy

3.1 Problem definition

As aforementioned in Section 1.2, the objective of this dissertation is to evaluate the load-following capability of URANUS, a passive LBE-cooled pool-type SMR. Since the naturally cooled system is operated without an external momentum source like a reactor coolant pump, primary mass flow rate can be determined by core power and resultant temperature distribution. In this respect, the natural circulation dynamics gives rise to a delayed system reaction. During a system maneuvering in some conditions, its stability might be lost. Therefore, the load-following capability is determined by the stability limits. To achieve the objective, three specific research questions are risen:

1) Question 1: How does a pool-type passive LBE-cooled system react to changes in external operating condition?

2) Question 2: How is the transient integral behaviors of pool-type passive fast reactor system evaluated?

3) Question 3: What is the condition under which a passive LBE-cooled system safely controlled and regulated to follow varying load demand?

To settle the first question, experimental studies on the natural circulation of LBE were conducted with two types of experimental facilities including HELIOS loop and PILLAR pool. Experimental results are given in Chapter 4. Utilizing a loop-type full-height scale facility, several steady-state natural circulation results were generated. After that, a pool-type thermal-hydraulic integral test facility scaled from URANUS was designed and several experiments was conducted using the facility.

The second question was resolved by using the numerical code called MARS-LBE. To do so, the experimental data were utilized in the validation preceded to the numerical modeling. It was concluded that the code calculation showed a good agreement with experimental results and the numerical tool would be able to be used for the design and safety analysis purposes for passive LBE-cooled systems.

Lastly, the third question was cleared by developing an analytical model. The model is dedicated to the passive LBE-cooled system and simulates the system reaction to a variation in external load demand and the stability under that transient. With the model, the passive LBE-cooled SMR can be operated in load-following operation with stable and rapid change of power.

3.2 Approach

The thesis study is prepared with three approaches including experiments, numerical modeling, and analytical simulation. The experimental study deals with steady-state and transient natural circulation in two different geometrical configurations, loop and pool. For the steady-state tests, core power is an independent variable so that sets of natural circulation experiments can be performed. On the other hand, the transient tests are conducted by external operation condition changes in primary side power and heat sink flow rate, which represent the operational condition maneuvering in a reactor system. As a tool for the design and safety analysis of passive LBE-cooled reactor systems, a one-dimensional system thermal-hydraulics code, originally developed for the analyses of water-cooled reactors, was validated. For control design and evaluation purposes, this dissertation seeks to develop an analytical model. With the developed model, the stability of transients given in the passive LBE-cooled SMR in response to load demand and its achievable operation range were evaluated. The research flow and relation between the approaches of this dissertation are depicted in Figure 3.1.

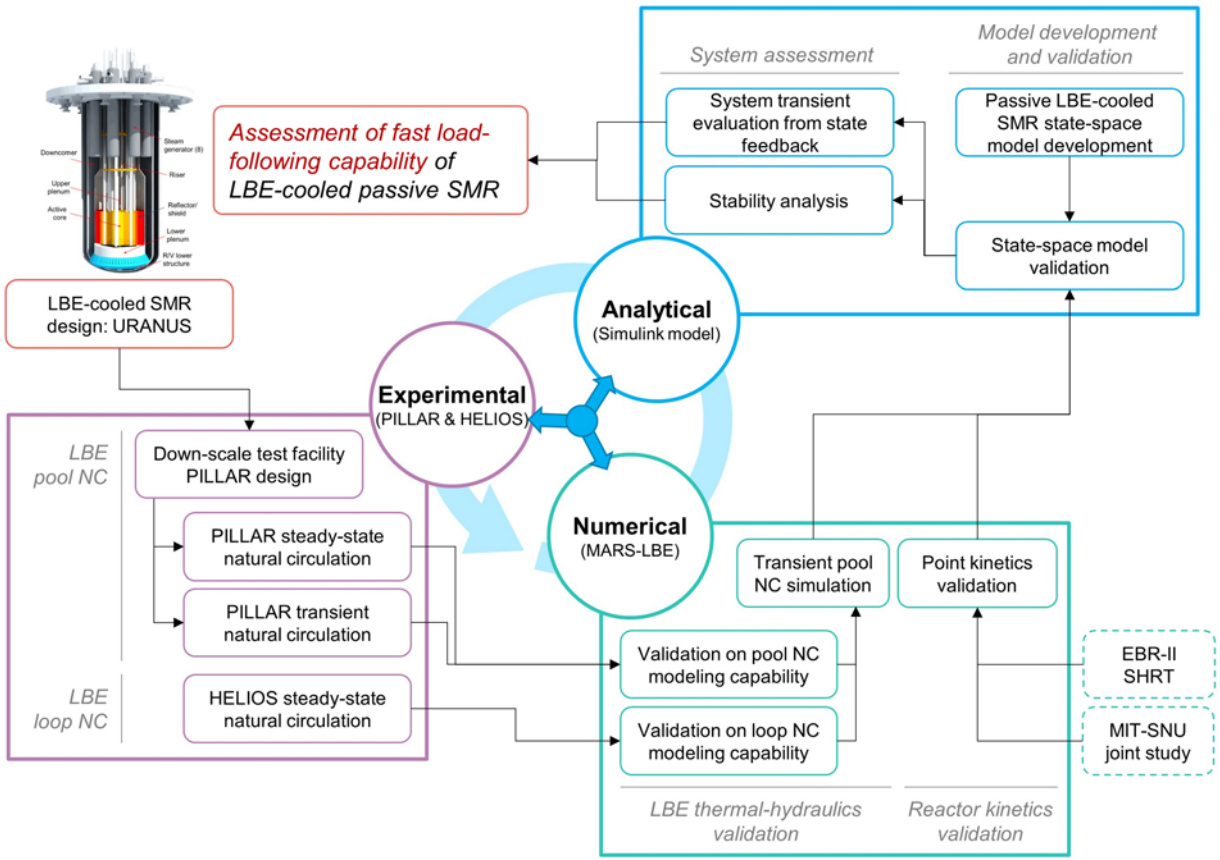

Figure 3.1 Thesis research approach

3.2.1 SMR reference design definition

Until now, no pool-type SMR that utilizes lead or LBE as primary coolant is built or operated. In this regard, a target conceptual design is required and the dissertation begins with the design of a passive LBE-cooled SMR. The activity includes the definition of SMR design criteria and requirements, neutronic core design which enables a long fuel cycle under safety parameters are controlled, system thermal-hydraulics analysis for a normal full-power condition, and conceptualization on the requirements of structural components. The establishment of this physical model is described in detail in Chapter 4

3.2.2 Experimental setup and tests

System integral behaviors given by external condition change in a passive LBE-cooled SMR is studied with experimental campaigns. A thorough understanding on natural circulation is essential since the primary system of the reactor can only be cooled by natural convection.

The experimental campaigns proceed in twofold: firstly, experimental investigation was conducted in a simple geometrical configuration, loop. Several steady-state test results were gathered by changing heat source conditions controlling electrical heaters. Secondly, experiments that are more realistic were carried out with a pool-type test facility. By utilizing the physical model, a pool-type integral test facility dedicated to the evaluation of system

behaviors of the prototypic reactor is designed by scaling analysis. The experimental studies are covered in Chapter 5.

3.2.3 Numerical validation and modeling

As a tool for the design and safety analysis of passive LBE-cooled reactor systems, a one-dimensional system thermal-hydraulics code, originally developed for the analyses of water-cooled reactors, was validated. For a reactor analysis, the code must be validated in two physical aspects: thermal-hydraulics and reactor kinetics. The test results made by two different types of geometrical configuration were utilized for the validation of thermal-hydraulics capability of the code. The code was suitably modified to implement the thermophysical characteristics of LBE. With the steady-state test results in loop and pool configurations, the code was confirmed that it can be used for the analysis of LBE coolant environments. The validated code was utilized for the modeling of transient tests in LBE natural circulation.

The other part, the reactor kinetics, was validated by other studies outside of this dissertation because there have been no experiments on the reactor kinetics of lead-cooled systems. Hence, as liquid metal cooled fast reactors are expected to have similar neutronic behaviors due to its fast neutron spectra, the validation of the code was regarded to be done by sodium-cooled fast reactor experiments. The validation of numerical model is elaborated in Chapter 6.

3.2.4 Analytical model development and load-following capability assessment

When the external load demand differs from a specific condition, the core power should follow it in a load-following operation mode. To do so, the position of control rods are maneuvered to reduce the discrepancy between the core power and load demand. For the assessment of fast load-following capability of a passive LBE-cooled SMR, this dynamic behavior must be included and is not able to be solved in the validated system codes in standalone.

For control design and evaluation purposes, this dissertation seeks to develop an analytical model, which implements the control rod movements and is capable of stability analysis and system behavior simulation at the same time. With the developed model, the stability of transients given in the passive LBE-cooled SMR in response to load demand and its achievable operation range were evaluated. The details in development of analytical model and assessment of load-following capability of the passive LBE-cooled SMR are illustrated in Chapter 7.

Chapter 4 LBE-cooled Passive SMR Design: URANUS[2]

This chapter first conceptualizes a passive LBE-cooled SMR, named as Ubiquitous, Rugged, Accident-forgiving, Nonproliferating, and Ultra-lasting Sustainer (URANUS), with a thermal power rating of 100 MW, for the target conceptual design on the assessment of fast load-following capability. The reactor does not require any fuel refueling nor assembly reconfiguration such as shuffling during its single fuel cycle as long as 20 years. This reactor is a pool-type fast reactor with an array of heterogeneous hexagonal core (Choi et al., 2011b). The coolant is chemically inert and has good neutron characteristics and a high boiling point. To avoid the unexpected common failures of active safety systems, the primary cooling system is operated without reactor coolant pumps. Material corrosion is limited by using corrosion-resistant materials in combination with an oxygen control technique (Ballinger and Lim, 2004; Fazio et al., 2001; Hwang et al., 2000; Li, 2008; Müller et al., 2000; Sekimoto and Su'ud, 1995; Takahashi et al., 2008). The entire reactor containment and its heat transport systems are seismically isolated from the ground through three-dimensional isolators.

---

[2] This chapter has been written based on the following journal paper: Yong-Hoon Shin et al., "Advanced passive design of small modular reactor cooled by heavy liquid metal natural circulation," Progress in Nuclear Energy, 83, 433-442, 2015.

4.1 Design goals and requirements

URANUS is designed to fulfill the philosophies that GIF suggests as described in Section 2.1. Table 4.1 shows the key design parameters of URANUS. These design parameters were estimated based on four design goals for ensuring technical, operational, and economic performances:

1) The reactor module is required to produce 100 MW_{th};
2) The length of one cycle is 20 effective full power years (EFPYs) without fuel refueling or assembly reconfiguration;
3) Geometrical configurations permit full heat removal by only coolant natural circulation by reducing pressure loss; and
4) The diameters of active core and reactor vessel are smaller than 2 m and 4.5 m, respectively, for ensuring land-transportable sizes.

To ensure nonproliferation and nuclear security, several Generation-IV concepts pursue no on-site refueling strategy and adopt cradle-to-grave fuel services, as illustrated in Travelling Wave Reactor that is being designed by Terrapower, LLC (Hejzlar et al., 2013). Since this approach may lead to increase in the frequency and difficulty of fuel transportation from a reactor site to a vendor plant, URANUS aim at a long-burning fuel cycle.

Design constraints were selected for safe and secure operation with sufficient margins without thermal, radiation, material, and structural failures

(Choi et al., 2011a; Nam et al., 2007). The thermal design constraints are:

1) Fuel centerline temperature at the hottest rod should be limited to be lower than the melting temperature of UO_2 fuel, 2,865 °C, with sufficient margin during all operating conditions even in design basis accidents;

2) Peak cladding temperature must not exceed the melting point of HT-9 or T-91 cladding overlaid with Al containing ferrite steels, 1,500 °C, with sufficient safety margin;

3) Inherent negative reactivity feedback has to be secured with sufficient safety margins under all operating conditions to prevent fuels from melting down (Choi et al., 2011a);

4) Reactivity swing has to be less than $1 without burnable poison rods to minimize positive reactivity insertions in the case of control assembly withdrawal without scram (Choi et al., 2011a); and

5) Decay heat can be removed passively on the outermost surface of reactor vessel which uses air cooling in accident conditions (Choi et al., 2011a).

The radiation design constraints are:

1) Peak discharge fuel burnup is required to be as large as possible, but is limited not to exceed an experimentally verified value, 100,000

MWd/MTU (Astegiano et al., 2004); and

2) Fast neutron fluence is limited not to exceed an experimentally verified value to avoid material embrittlement caused by radiation damage and to ensure fuel cladding integrity (Nam et al., 2007). HT-9 or T-91 were observed to has less than 2% swelling up to 200 dpa at around 400-420 °C, higher irradiation resistance than that of austenitic stainless steels (Garner et al., 2000; Klueh and Nelson, 2007).

The material design constraints are:

1) Outlet coolant temperature limit is 450 °C where corrosive reactions between LBE coolant and structural materials are well controlled for long-term full power operation by employing qualified materials and dissolved oxygen controls (Li, 2008);

2) Clad collapse limit from internal fission gas pressure is constrained by American Society of Mechanical Engineers (ASME) Section 3 (Nam et al., 2007);

3) Cumulative fatigue from fuel-clad mechanical interactions and flow-induced vibrations is constrained by ASME Section 3 (Nam et al., 2007); and

4) Total creep strain including both thermal- and irradiation-enhanced creep has to be maintained below creep rupture strain, conservatively set as 1% (Nam et al., 2007).

The structural design constraints are:

1) Radial power peaking factor is required to stay low enough, lower than 1.5, to reduce thermal stress on structures from temperature difference and to secure high margins on fuel melting (Choi et al., 2011a);

2) Reliable seismic isolation has to endure an earthquake of 0.5g zero period acceleration (ZPA) for the Safe Shutdown Earthquakes (SSE) (Yoo et al., 2000); and

3) Containment built underground is needed to assure robust features in support of air defense, explosion proof, and protection from external sabotage actions.

Table 4.1 Key design parameters of URANUS

Design parameter	Value or characteristic
Thermal power	100 MWt
Refueling interval	20 years
Plant design lifetime	60 years
Primary coolant	Lead-bismuth eutectic
Primary heat transport system	Compact pool type
Core configuration	Open hexagonal array
Primary normal cooling mode	Fully natural circulation
Normal decay heat removal	Coolant natural circulation in the primary system combined with water/steam forced circulation in the secondary system
Abnormal decay heat removal	Reactor vessel auxiliary cooling by air
Fuel	UO_2
Cladding	HT-9 or T-91 overlaid with Al containing ferrite steels in functionally graded composite
Steam generators	8 modules of straight shell-tube type
Secondary water/steam cycle	Rankine cycle with superheated steam
Seismic design	Three-dimensional seismic isolators

4.2 Reactor core design

In order to enhance its inherent safety, the reactor coolant pump was excluded from the system so that it resorts natural circulation in both normal and abnormal conditions for a cooling mechanism. Considering the maximization of coolant flow rate, it is required to reduce pressure loss along flow paths and it leads to the enlarged pitch-to-diameter ratio; the wide path of coolant flow reduces pressure loss in the core region. In addition, the core configuration decreases volume power density and discharge burnup compared to conventional fast reactors, and extensively reduces peak excess reactivity and reactivity swing.

4.2.1 Fuel assembly configurations

The reactor core consists of two enrichment zones of fuel assemblies, the three types of reactivity control and shutdown assemblies, and a surrounding LBE reflector zone as shown in Figure 4.1. There are 108 fuel assemblies, 6 primary control assemblies, 6 secondary shutdown assemblies, and 1 ultimate shutdown assembly. The liquid LBE reflectors in which the fluid has almost no flow velocity surround the fuel zones for neutron economy by reflection.

The enrichment of inner core zone is 9.55% while that of outer zone is 17.09%. A large difference in enrichment between inner and outer regions was adopted for three reasons: first, this enrichment zoning is intended to flatten

power distribution to reduce radial power peaking without assembly reconfiguration, providing adequate safety margin and mitigating the effects of thermal gradient. Second, it also helps increase internal breeding by loading enough fertile materials at the center region of core, which in turn loading lower fissile materials on high flux region. Third, it contributes to maintain a radial peaking factor lower than 1.5 from the beginning of cycle (BOC) to the end of cycle (EOC).

The total amount of uranium loaded is nearly 17.8 metric tons. The reactivity swing, which is defined as the difference of maximum and minimum reactivity values over a single fuel loading cycle, is lower than $1. This small reactivity swing reduces the control rod worth and the positive reactivity insertion of a control rod ejection accident (Choi et al., 2011a). The refueling interval could be extended beyond 20 years with material improvements. The determination of refueling interval and plant design lifetime considers cladding corrosion, creep, fatigue and radiation embrittlement (Nam et al., 2007). The specific power density is reduced to achieve a long fuel cycle with a small reactivity swing (Blue et al., 2005; Hill et al., 1999).

A fuel assembly consists of 60 fuel pins and 1 central skeletal bar in a hexagonal lattice with grid plates, as shown in Figure 4.2. The pitch to diameter ratio is 1.35 and the assembly pitch is 166.25 mm. The wide coolant paths between the rods significantly enhance natural circulation by reducing pressure drop, but simultaneously deteriorate neutron economy due to a low fuel volume fraction, which requires more fissile materials to be loaded. Furthermore, the low fuel volume fraction harms breeding performance by softening neutron

spectrum and increasing neutron leakage. In spite of this, it is still sufficient to achieve both neutronics and thermal-hydraulic design goals.

The specifications of fuel assemblies are summarized in Table 4.2. The active core height is 1,800 mm and the active core equivalent diameter is 1,900 mm. The upper fission gas plenum length is 1,300 mm accommodating fission gas released; both low and upper plugs length is 300 mm. Total loaded enriched uranium is 17,812 kg including 6,412 kg for inner core and 11,399 kg for outer core. The total weight of coolant and internal structure including nuclear fuels is less than 750 metric tons. The peak fuel centerline temperature during the normal operation is approximately 760 ^{o}C assuring sufficient margin to the fuel melting point.

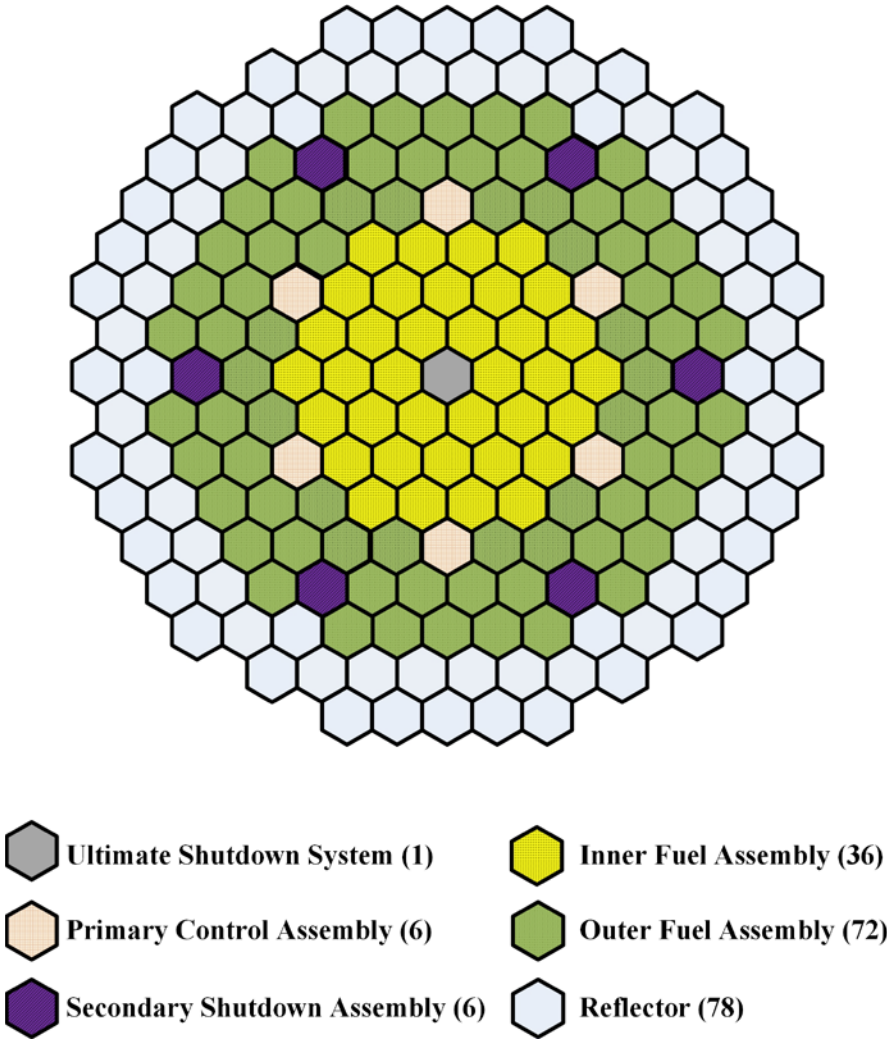

Figure 4.1 Radial assembly configuration of active core

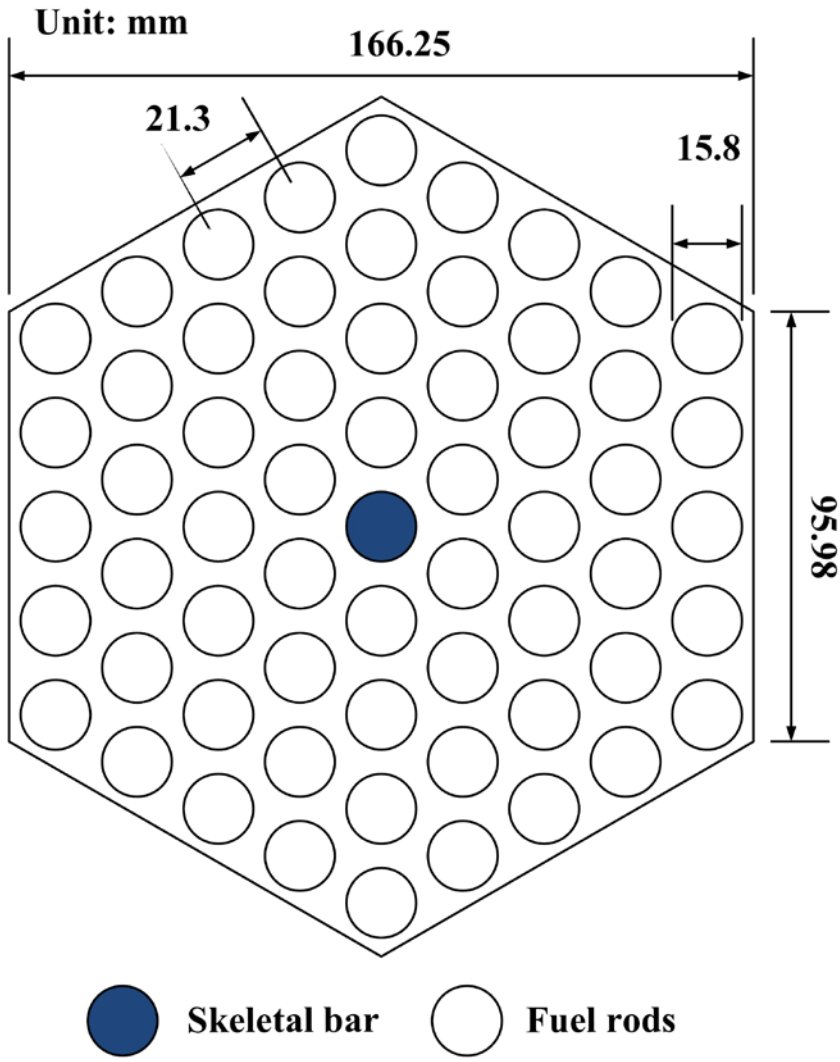

Figure 4.2 Horizontal view of a single fuel assembly including fuel rods and a central skeletal bar

Table 4.2 Design parameters of fuel assemblies

Design parameter	Value
Number of pins per one assembly	61 including 1 skeletal bar
Enrichment	9.55 (wt%) in the inner core
	17.09 (wt%) in the outer core
Pin pitch-to-diameter ratio	1.35
Fuel pin pitch	21.3 (mm)
Fuel pin diameter	15.8 (mm)
Active core height	1,800 (mm)
Equivalent core diameter	1,900 (mm)
Fission gas plenum height	1,300 (mm)
Lower plenum height	300 (mm)

4.2.2 Fuel rod design

Figure 4.3 shows the one-twelfth pin-cell model of a fuel rod. The length of the fuel rod is 3,400 mm including the lower plug, the lower plenum, the UO_2 fuel slug, the upper gas plenum, and the upper plug. Among them, the length of the active core is 1,800 mm as indicated in Table 4.3. The upper fission gas plenum is 1,300 mm long, and the length ratio of the fission gas plenum to the active core is 0.72. This ratio is smaller than the conventional ratio of 2.0 because the low outlet temperature, about 450 °C, limits the ingress of fission gas pressure. The diameter of UO_2 fuel is 14.6 mm and the diameter of fuel rod including cladding is 15.8 mm. This fuel rod has a large fuel diameter for improving natural circulation capability by enlarging coolant flow paths and for loading nuclear materials as much as possible at the same time.

It is known that the oxide thickness of the FeCrAl ferrite steels as a form of Al_2O_3 at 450 °C and 600 °C for 20 years is predicted to be only about 0.5 and 2.5 μm, respectively, so that the alloy can be used for the cladding materials in high temperature LBE environments (Lim et al., 2010). However, Al-containing ferrite steels show significant radiation embrittlement as a result of Al segregation to grain boundaries and Cr-rich α' phase formation at the temperature range of 300-500 °C (Dvoriashin et al., 2007). To achieve appropriate corrosion resistance while keeping desirable mechanical properties, the hybrid fuel cladding tube, HT-9 or T-91 overlaid with Al-containing ferrite steels, was selected (Hwang and Lim, 2010). The thickness of Al-containing ferrite steels is 0.5 mm, forming a thin protective Al oxide layer. This hybrid

approach has been pursued by the MIT based on standard commercial practice with Si-containing alloys (Ballinger and Lim, 2004). A gap is introduced to accommodate fission gas, which is about 0.1 mm thickness between the inner cladding wall and the outer surface of UO_2 rod.

Tag gas capsules are loaded in the fission gas plenum in order to find the location of a failed fuel pin easily. This capsule contains an isotopic blend of inert gases that is unique to that assembly. During the final fabrication, this capsule is punctured into the fission gas plenum and it escapes into the primary coolant in the cladding failure.

Honeycomb-type grid spacers hold each of fuel rods and maintain the hexagonal lattice. Unlike wire wraps, grid spacers have advantages for better structural strength with reduced steel volume, which allows the potential increases of fuel volume and coolant flow area. Furthermore, the use of grid spacers allows the hot channel factor to be lowered by lateral heat conduction and convection.

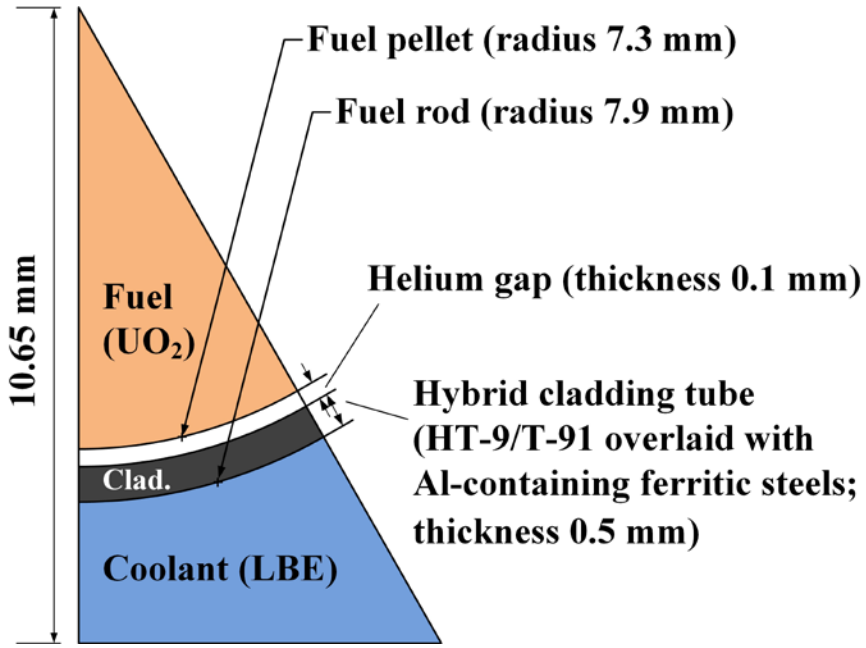

Figure 4.3 Pin-cell model for fuel rod

Table 4.3 Design information of fuel rod

Parameter	Value
Fuel type	UO_2
Enrichment	9.35 (wt%) in the inner core
	17.75 (wt%) in the outer core
UO_2 fuel pellet diameter	14.6 (mm)
Initial gap thickness	0.10 (mm)
Cladding thickness	0.50 (mm)
Cladding material	Al-containing ferrite steels

4.2.3 Safety control assembly configurations

As aforementioned in Section 4.2.1, three independent sets of control systems are employed: the primary control assemblies, secondary shutdown assemblies, and ultimate shutdown system. Both primary and secondary control assemblies are inserted to the active core from the top of the core with the drive mechanisms located at the top of the vessel closure head. The ultimate shutdown system is located at the bottom of reactor vessel. The control and shutdown assemblies consist of a closely packed absorber bundle of natural boron carbide pellets within a duct. The natural boron contains 19.9 at.% of ^{10}B which is a strong neutron absorber.

The primary control system is composed of six assemblies located right outside of inner core assemblies as shown in Figure 4.1. A stepping motor with electro-magnetic holding operates the primary control assemblies. With maneuvering primary control assemblies, reactivity control during normal operation and normal shutdown are achieved. The primary control system is required to shut down the reactor to cold standby conditions from any operation conditions including full-power operation, unprotected transient overpower, and unprotected loss of heat sink conditions. It has sufficient reactivity worth even if one assembly having the largest reactivity worth is not inserted and is able to compensate for the reactivity loss from the fuel burnup and uncertainties in uranium enrichment.

The secondary shutdown system is also consisted of six assemblies located slightly outside compared to the primary control system. The secondary

shutdown system magnetically grasped during the normal condition is passively inserted by gravity when the primary control system is not operated properly and the temperature of holding magnet reaches its Curie point. Similar to the primary system, this secondary shutdown system can shut down the reactor without the insertion of assembly having the highest reactivity worth. The secondary shutdown system is capable of shutting down the reactor at the full power operation condition when the primary control assemblies are suddenly withdrawn.

The ultimate shutdown system is located at the center of the active core. This system works passively without an external trigger signal and a power source. It consists of boron stainless steel balls and is inserted into the core by buoyancy force under the event of core overheating and melting of its fusible stopper. Because it is located at the bottom of reactor vessel, its temperature change is delayed by one primary coolant cycle. Hence, it is an engineering redundancy for the failures of both primary and secondary shutdown systems.

4.2.4 Neutronic analysis

The neutronics analysis of the reactor core was performed by solving nodal diffusion theory methods for a hexagonal geometry option in REBUS-3, a multi-group fuel cycle analysis code (Toppel, 1983). This code can calculate the flux solutions of homogenized nodes or mesh cells using the DIF3D module without thermal-hydraulic feedback effects (Lawrence, 1983). All calculations used a 24 energy-group structure and a TRU burnup chain from Th-232 to Cm-245. Some important long-lived fission products (LLFPs) such as Tc-99, I-129, Sr-90, and Cs-137 were independently treated, while other fission products were not individually considered by classifying them into 4 lumped fission products (LFPs) groups (Hwang et al., 2000).

A cross section library with 80 groups for neutrons and 24 groups for gamma rays based on JEFF3.0, ENDF/B-VI.8, and JENDL3.3 were used as an input of TRANSX-2 producing transport tables in binary cross sections (MacFarlane, 1992). The final cross section for REBUS-3 was weighted by a regional neutron flux calculated by a discrete-ordinates transport code, DANTSYS (Alcouffe et al., 1995). The calculation chain showing data flows and methods used in the codes is described in Figure 4.4.

As can be seen in Figure 4.5, the excess reactivity at BOC is 224 pcm. The excess reactivity continuously decreases down to 135 pcm at the 13^{th} effective full power year (EFPY) and then increases again at EOC. At the initial stage, the breeding ratio is small because the fissile to fertile ratio is relatively large. In addition, the high neutron flux in the outer zone causes high neutron

leakage. After that, the breeding ratio increases as because the fissile to fertile ratio decreases and the neutron flux in the inner zone increases. As listed in Table 4.4, the reactivity swing during 20 years operation is 88.6 pcm, being lower than $1 and satisfying the design parameters listed in Section 4.1.

The average core power density is 19.42 MW/m^3 due to large coolant volume for natural circulation. The average linear heat generation rate is 8.57 kW/m and it is relatively small because the diameter of fuel rods is large, 15.8 mm. The large fuel diameter significantly decreases the ratio of surface area to fuel loading, improving natural circulation capability. The power density is limited to satisfy the outlet coolant temperature. Because of passive natural circulation, the flow rate of LBE coolant is comparatively low, resulting in the small volume density than those of conventional fast reactors. Peak discharge burnup, 40.98 MWd/kg, is smaller than the limit.

Internal conversion continuously increases during 20 years operation. The average conversion ratio is 0.7227, which means that the core internal breeding is properly suppressed in terms of waste management and proliferation resistance while the long-term operation is achieved. Maximum fast fluences, defined as the number of irradiated neutrons over 100 keV on the unit area, for inner and outer core are respectively 1.37E+23 neutrons/cm^2 and 1.54E+23 neutrons/cm^2. In other words, the radiation damage of inner core is 68.7 dpa, and that of outer core is 76.9 dpa.

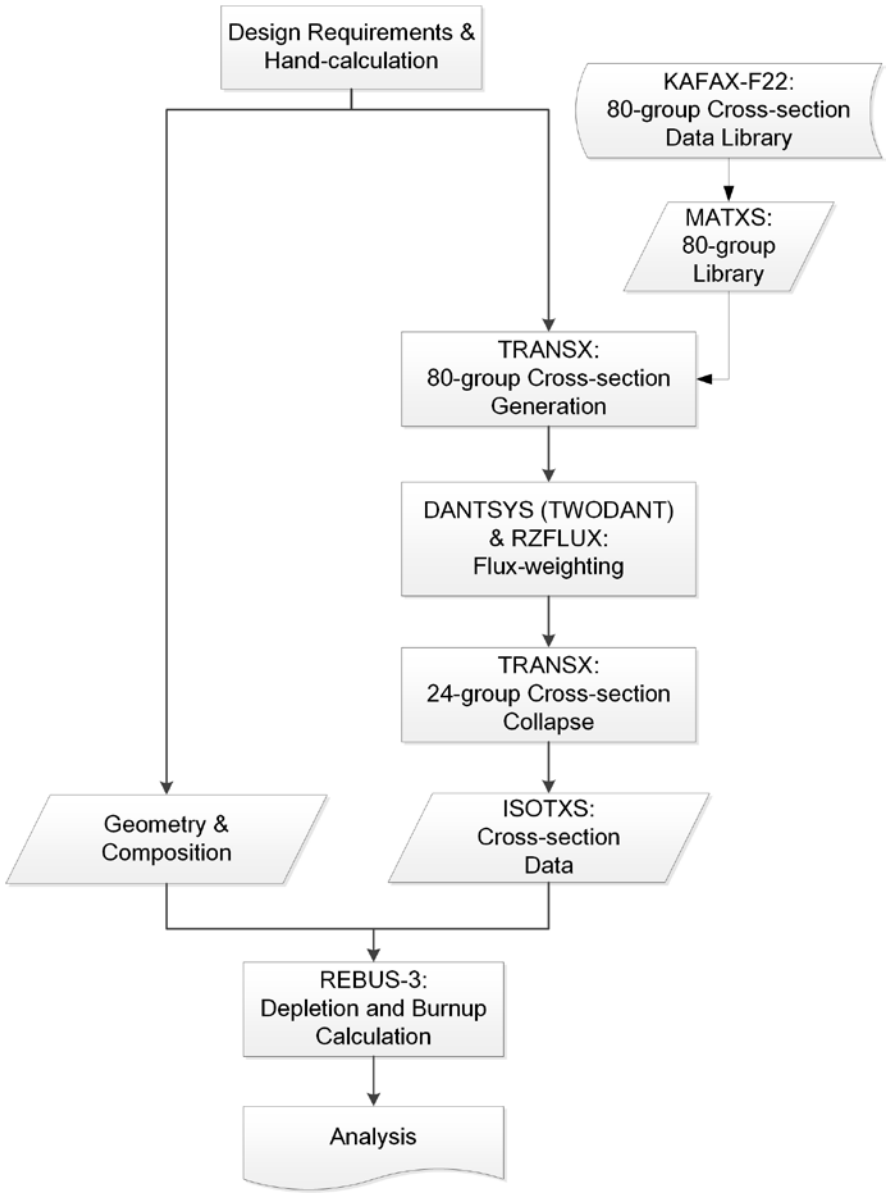

Figure 4.4 Code system used for the neutronic analysis of URANUS core design

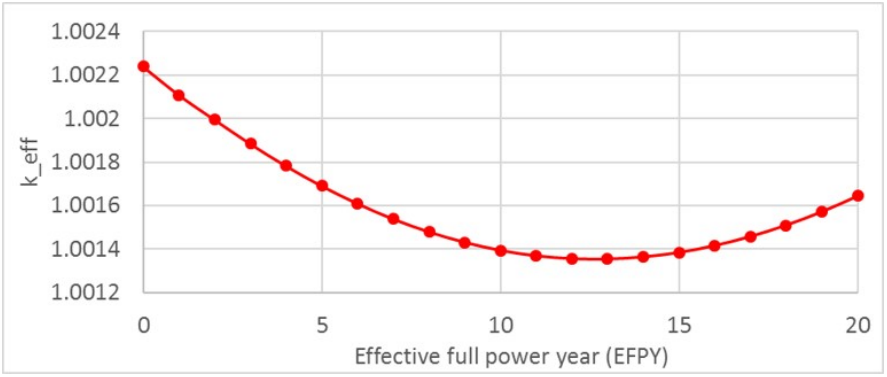

Figure 4.5 Effective multiplication factor of URANUS core during 20 years of full-power operation

Table 4.4 Key neutronics parameters of reactor core

Parameter	Value
Reactivity swing	88.6 pcm
Average effective multiplication factor	1.0016
Excess reactivity at the beginning of cycle	224 pcm
Minimum excess reactivity during cycle	135 pcm (13^{th} effective full power year)
Peak fuel discharge burnup	40.98 (MWd/kg)
Fast neutron fluence	68.7 (dpa) in the inner core
	76.9 (dpa) in the outer core

4.2.5 Kinetics and reactivity feedback coefficients

For the safety analysis and control rod design for normal operation of a nuclear reactor, the values of several kinetic parameters and reactivity feedback coefficients are required. In this section, those values are to be evaluated for BOC using two different code schemes, including the deterministic code system (Alcouffe et al., 1995; MacFarlane, 1992; Toppel, 1983) that has been utilized for the core design and burnup calculation of URANUS as discussed in Section 4.2.4, and a Monte Carlo neutron-photon transport simulation code. For the Monte Carlo analysis, a versatile tool called McCARD (Shim et al., 2012) is used, which features whole-core neutronics calculations, the evaluation of few-group constants, uncertainty propagation calculations, and burnup analysis by incorporating ORIGEN2-type (Croff, 1983) depletion equation solver.

For the analysis of URANUS core, the kinetic parameters to be used include Doppler coefficient, fuel axial expansion coefficient, core radial expansion coefficient, and coolant density coefficient, which are widely used for the fast reactor analyses. Because of the high boiling point of LBE coolant, the coolant void effect is not considered. Although the fuel axial expansion coefficient and the core radial expansion coefficient are usually defined by dimensional change, it is derived with respect to temperature change by converting the dimensional change with linear length expansion relations. Those parameters, denoted by α, are determined as reactivity change $\delta\rho$ given by the temperature change δT of a specific component x, as in Eqn. (4.1):

$$\alpha_x = \frac{\delta\rho}{\delta T_x}, \tag{4.1}$$

where the reactivity change $\delta\rho$ is defined with change in reciprocal effective multiplication factors, $1/k_{eff}$, for two temperature states 1 and 2, respectively, as in Eqn. (4.2):

$$\delta\rho = \frac{1}{k_1} - \frac{1}{k_2}. \tag{4.2}$$

In this case, the subscript 1 means a base design that is determined in Section 4.2.4 while the latter, the subscript 2, refers to a new state that the temperature of a specific component is changed. The multiplication factors in the above equation are evaluated by means of the deterministic code chain and McCARD. The specific components are D for the Doppler coefficient, *l* for the fuel axial coefficient, *R* for the core radial coefficient, and *LBE* for the coolant density coefficient, respectively.

Table 4.5 contains important kinetic parameters at BOC calculated by the deterministic code chain and McCARD including the Doppler coefficient, the fuel axial expansion coefficient, the core radial expansion coefficient, and the coolant density coefficient. For the McCARD calculation for effective multiplication factors, 500,000 particles were used for each cycle under 50 inactive and 100 active cycles while utilizing ENDF/B-VII.1 nuclear cross section library. Two methods show slight different calculation results because it is affected by the use of neutron cross section library. Still, all the coefficients

are negative, which in turn are the reactor core is inherently safe under those temperature-induced reactivity insertion conditions.

The Doppler coefficient produces the largest negative feedback effect when fuel temperature increases. Having a softer neutron spectrum than that of a conventional metal-fueled fast reactor, more neutrons can be captured in the resonance peaks. In addition, a temperature rise results in the axial expansion of fuel rod and the radial expansion of fuel assembly. These expansions reduces the density of fissile materials in the active core, producing negative feedback. At the same time, these expansions can decrease neutron leakage and produce positive feedback (Chang et al., 2005). Since the first effect is stronger, the net effects of axial and radial expansions are negative feedback. The coolant density coefficient is also negative since neutron leakage increases when coolant density decreases.

The effective delayed neutron fraction, β_{eff}, which determines the kinetic response of a reactor core, is also calculated by two methods similar to the evaluation of kinetic parameters. However, the effective delayed neutron fraction is required to be calculated by adjoint flux weighting (Waltar and Reynolds, 1980). While McCARD processes this weighting internally and automatically, it is required for the deterministic method to perform the similar calculation by hand. In addition, McCARD is also capable of the evaluation of point kinetics parameters including the j-th group delayed neutron fractions, β_j, precursor decay constants, λ_j , and neutron generation time, Λ, defined in six-group point kinetics equations.

Table 4.6 summarizes the effective and group delayed neutron

fractions, prompt neutron generation time, and group precursor decay constants at BOC from a literature (Waltar and Reynolds, 1980) and calculated by McCARD. The computational conditions were the same with that of the kinetic parameter evaluation for the base case. Those two results show slightly different but similar values since the values are dependent upon the composition and geometrical distribution of nuclear materials in the core. Nevertheless, the effective delayed neutron fraction is similar to that of ^{235}U, about 680 pcm, because this reactor uses enriched uranium fuels (Waltar and Reynolds, 1980). McCARD evaluates the prompt neutron generation time of URANUS is slightly greater than that of typical fast spectrum reactors, about 4.00E-07 s (Waltar and Reynolds, 1980). Considering this, the reactor transients of URANUS driven by reactivity change are expected to be slower than typical fast reactors.

Table 4.5 Kinetic parameters at beginning of cycle calculated by the deterministic code chain and McCARD

Parameter	Deterministic code chain*	McCARD
Doppler coefficient (α_D)	-0.8735 (pcm/K)	-0.5766 (pcm/K)
Fuel axial expansion coefficient (α_l)	-0.2404 (pcm/K)	-0.2287 (pcm/K)
Core radial expansion coefficient (α_R)	-0.3105 (pcm/K)	-0.4638 (pcm/K)
Coolant density coefficient (α_{LBE})	-0.2874 (pcm/K)	-0.4906 (pcm/K)

* ** Deterministic code chain refers to the calculation system used for the reactor core analysis for URANUS, as defined in Section 4.2.4.*

Table 4.6 Delayed neutron fractions and precursor decay constants at beginning of cycle calculated by the deterministic code chain and McCARD

Parameter	Literature (Waltar and Reynolds, 1980)	McCARD
Effective delayed neutron fraction (β_{eff})*	676.0 pcm	709.4 pcm
Group delayed neutron fraction	β_1 2.184E-04	2.242E-04
	β_2 1.477E-03	1.157E-03
	β_3 1.331E-03	1.147E-03
	β_4 2.673E-03	2.723E-03
	β_5 7.801E-04	1.318E-03
	β_6 2.808E-04	5.257E-04
Neutron generation time (Λ)	4.000E-07 s	5.387E-07 s
Group precursor decay constant	λ_1 1.343E-02 s^{-1}	1.337E-02 s^{-1}
	λ_2 3.069E-02 s^{-1}	3.256E-02 s^{-1}
	λ_3 1.170E-01 s^{-1}	1.211E-01 s^{-1}
	λ_4 3.033E-01 s^{-1}	3.054E-01 s^{-1}
	λ_5 8.637E-01 s^{-1}	8.566E-01 s^{-1}
	λ_6 2.926E+00 s^{-1}	2.878E+00 s^{-1}

** Calculated for URANUS based on the data from (Waltar and Reynolds, 1980).*

4.3 Heat transport systems design

As illustrated in Figure 4.6, the primary system and the steam generator modules are encapsulated within the reactor vessel. Since no pump is included in the primary system, it is cooled by LBE natural circulation in both normal operation and accidental conditions. In the heat transport systems design, the balance of plant (BOP) design is out of consideration in this dissertation because the reactor module is postulated to utilize the most reliable BOP design used in commercial power plants when it is deployed.

4.3.1 Primary heat transport system

The primary heat transport system is located in a double-walled pool-type reactor vessel. The double-walled vessel provides enhanced resistance against the loss of coolant accidents. The reactor vessel is determined to assure its structural integrity under accidental overpressure as well as seismic loads. The pressure of primary system depends on the static pressure of LBE coolant because the primary system does not need a pressurizing mean due to the high boiling point of LBE.

The design parameters of both primary and secondary heat transport systems are summarized in Table 4.7. In the primary system, LBE coolant flows through the reactor system by natural circulation. First, the coolant heated in the core moves upward through the riser region. After that, the coolant flows

outward through the inner barrel windows at the top and passes the steam generator shell. Then, coolant flows downward in the downcomer and gathers at the lower plenum to enter into the active core again by gravity. The temperature difference and vertical distance between the heat source – reactor core – and the heat sink –steam generators – can lead a significant driving force for natural circulation as buoyancy (Choi et al., 2011a).

The core inlet coolant temperature is targeted to around 300 °C which is high enough for maintaining the liquid phase of LBE. The average core outlet coolant temperature is lower than 450 °C, which is low enough for ensuring a slow corrosion rate during the design lifetime of 20 years for fuel-cladding materials and 60 years for the overall system components (Fazio et al., 2001).

Every single assembly is designed to be ductless so that cross-flow among assemblies is allowed to take advantage of a heat transfer mechanism of turbulent mixing. The ductless channels also enhance the inherent safety in postulated accident situations regarding local blockage (Choi et al., 2011a). A large flow area improves natural circulation with reduced pressure drop and produces pressure loss as low as 5 kPa inside the core so that natural circulation performance of primary cooling system is guaranteed and improved (Cho et al., 2011).

If an accident breaks out and the reactivity shutdown systems actuates by the reactor protection system, and residual heat including decay heat can be removed by two passive means such as coolant natural circulation and the reactor vessel auxiliary cooling system (RVACS). RVACS is a passive emergency residual heat removal system using natural circulation of air in an

event of system overheating. The outer surface of the guard vessel is cooled by environmental air, which comes along the cavity to remove the decay heat.

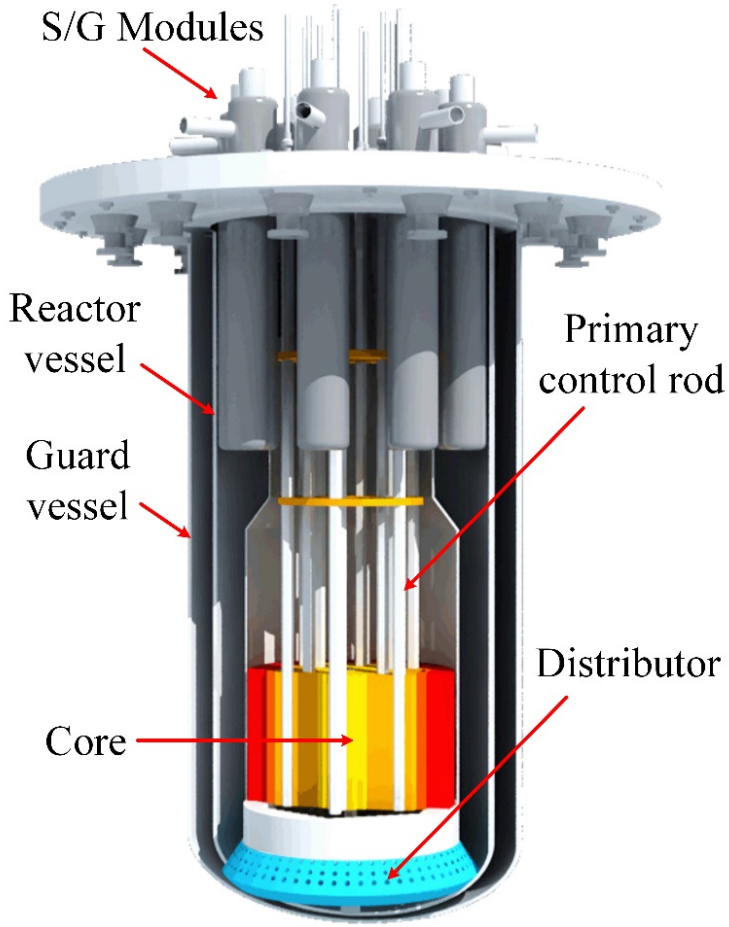

Figure 4.6 Schematic diagram of URANUS primary boundary

Table 4.7 Specification of primary and secondary heat transport systems of URANUS

Design parameter	Value or characteristic
Primary side	
Inner diameter of cylindrical shell	3741 (mm)
Wall thickness of cylindrical shell	50.0 (mm)
Total height, inside	9860 (mm)
Design pressure/temperature	1.0 (MPa) / 700 (°C)
Reactor operating pressure	0.1 (MPa)
Total weight with LBE and internal structure	758 (ton)
Secondary side	
Type	Straight shell-tube
Number of modules	8
Mode of operation	Secondary coolant inside tubes
Material	Functionally Graded Tube (Alloy 690 TT in the water/steam side, Al-containing ferrite steel in the LBE side)
Operating pressure	8.0 (MPa)
Feedwater temperature	252.0 (°C)
Steam outlet temperature	356.0 (°C)
Steam thermal state	Superheated
Steam flow rate	52.68 (kg/s)

4.3.2 Secondary heat transport system

In the secondary system, eight modules of once-through shell-and-tube type steam generators are installed and the tubes are made of functionally graded duplex tubes, Alloy 690TT (Ni-30Cr-10Fe) for the secondary water/steam side and Al-containing ferrite steels for the primary LBE side. The details of secondary heat transport system are elaborated in Table 4.7. The pressurized water at 80 bar is pumped into the steam generators where the water flows downward in the central feedwater pipe and then upward in the tube side while it is heated by the primary coolant flow from the shell side. The downward U-shape flow path of the secondary coolant provides driving force for prolonged natural circulation in the event of the secondary pump failure. The steam flow from the steam generators is collected in steam headers and sent through main steam lines to turbine generators with the flow rate of about 190 metric tons per hour. The main steam lines penetrate two containment vessels heads through double isolation valves that automatically shut in the event of steam generator tube rupture or main steam line break. Feedwater temperature is about 250 °C, while final steam temperature from the steam generators is approximately 360 °C, which ensures superheated state.

Since the detail design of BOP has not been made, the thermal efficiency of the single module of URANUS is only able to be evaluated by assuming ideal Rankine cycle with a single-step turbine generator and a condenser. By using the fluid conditions, the temperature-entropy diagram can be drawn as Figure 4.7 and the thermal efficiency can be estimated to be 39.7% .

In this evaluation, specific assumptions on the condenser is applied; the pressure in the component is given to be 0.005 bar. Considering that the thermal efficiencies of most liquid metal cooled fast reactors lie in a range of 35-45%, the evaluation is reasonable and the additional optimization can be followed after the specific design of BOP is made.

Since LBE has virtually no chemical activities with water or air, steam generator tube rupture accidents can be well managed with the containment. The interaction between LBE and pressurized water was already tested and this experiment confirmed the chemical inertness of LBE coolant (Ciampichetti et al., 2008).

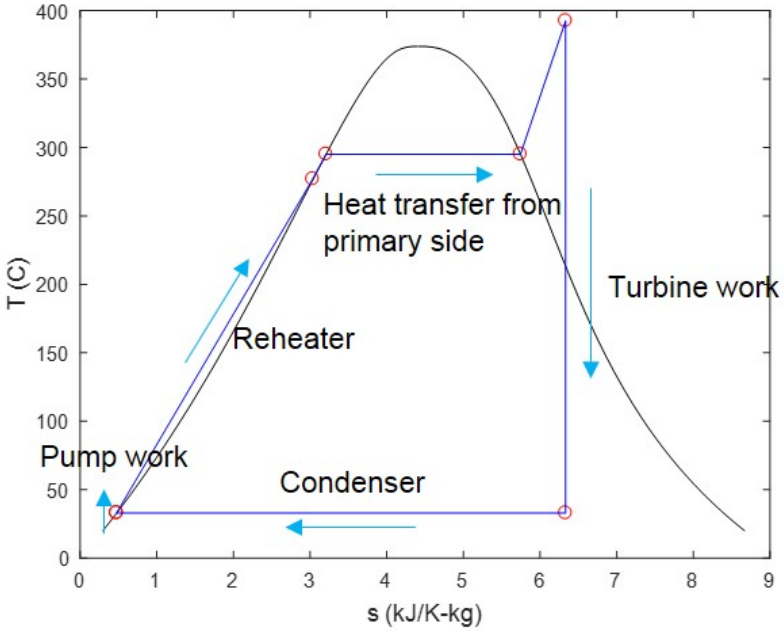

Figure 4.7 Ideal temperature-entropy (T-s) diagram of URANUS

4.3.3 Steady-state thermal-hydraulic analysis

For the thermal-hydraulic analysis under steady-state conditions of URANUS, a system thermal-hydraulics simulation code, named as Multi-dimensional Analysis Reactor System (MARS), was used (KAERI, 2006). A detailed description and code modification is elaborated in Chapter 6.1 with code validation through benchmarking. Figure 4.8 shows a nodalization map of the heat generation and removal systems. To calculate the core region more precisely than other parts, this region, indicated as P100 in Figure 4.8, is divided into 9 sections in the flow direction.

Two variables govern the natural circulation capability of the primary system. The first variable is the pressure loss induced by the hydraulic resistance in the primary system (Idelchik, 1986) while the second one is the thermal center difference defined as height difference between the center of reactor core and the center of steam generators in axial direction. Under the normal condition, the pressure loss and the buoyancy force are balanced as about 10.1 kPa, and thermal center difference is about 4.91 meters. The enhancement of natural circulation requires that hydraulic resistance should be lowered and that thermal center distance is needed to increase.

The temperature distributions of fuel centerline, cladding, and coolants in the hottest fuel assembly under the steady-state conditions is evaluated as shown in Figure 4.9. The peak fuel centerline temperature is near 756 °C having a sufficient margin to the melting point. LBE coolant with the temperature of around 300 °C enters from the inlet plenum and traverses

upward through the core to heat exchanger with the average temperature of 440 °C in the core outlet, as the results of the thermal-hydraulic calculation are summarized in Table 4.8. This temperature increase under the normal condition is within the acceptable range for reducing the corrosion of structural materials and the integrity of fuel rods. The temperature of the cladding at the hottest assembly is maintained below 550 °C.

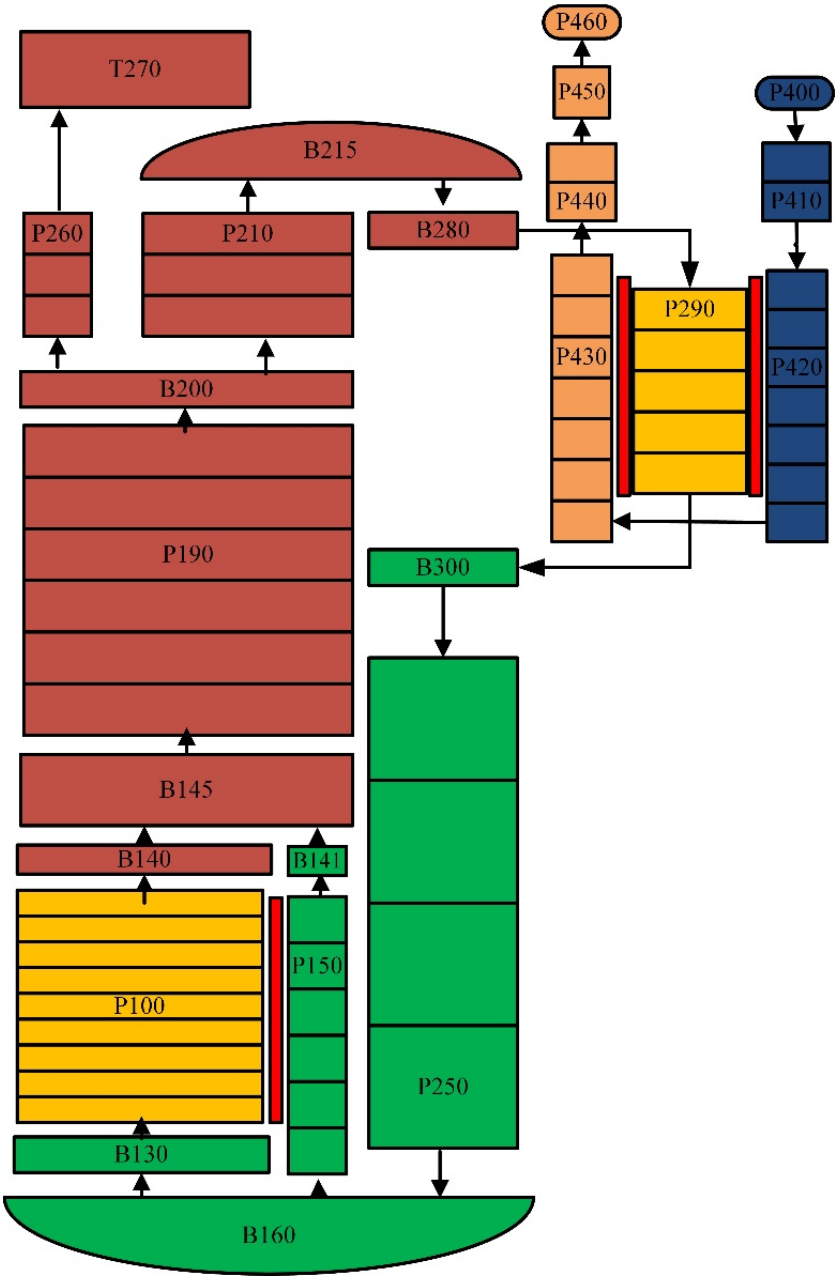

Figure 4.8 Nodalization of overall heat transport system for steady-state calculation

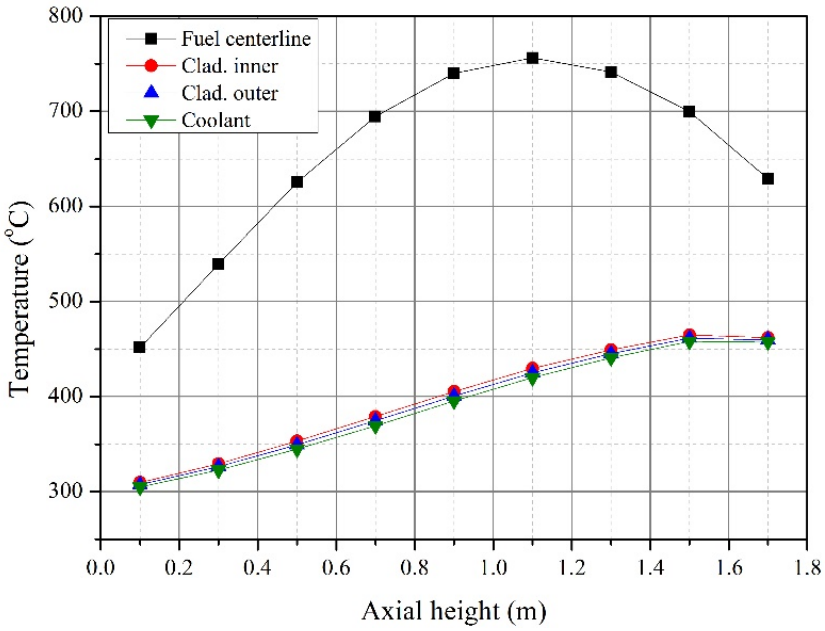

Figure 4.9 Steady-state temperature distributions of fuel centerline, cladding, and coolant bulk at the hottest assembly

Table 4.8 Steady-state system thermal-hydraulic calculation results of URANUS

Parameter	Value
Reactor coolant mass flow rate	4,886 (kg/s)
Core coolant inlet temperature	304.95 (°C)
Core coolant outlet temperature	440.76 (°C)
Peak fuel centerline temperature	756.25 (°C)
Peak cladding temperature	464.96 (°C)

4.4 Structure, materials, and components

The simple primary system design has been adopted to reduce capital cost and fabrication and construction times as well as enhance the quality of components. All reactor internals are replicable and replaceable; enough space is available for in-service inspection. The whole reactor module is separated from land by a three-dimensional isolation system. The double-walled vessels are to reduce the probability of the event of coolant leak and to exclude the outbreak of loss of coolant accident. In order to ensure the integrity of both inner reactor vessel and outer guard vessel, the following design features are applied to the pool-type system:

1) there are no attachments or penetrations in the shells and bottom head of both the reactor vessel and the guard vessel;
2) the vessels have the simple geometries of circular cylinders; and
3) the core support structure is attached to the bottom head of the reactor vessel.

4.4.1 Reactor vessel structure and materials

The double-walled vessels, made of austenitic stainless steels, is about 9.9 m in height and 3.6 m in diameter. The thickness of both vessels is 5 cm. The reactor

vessel and its cover constitute the primary coolant boundary that envelopes and supports the core, reactor internals, coolant, control assemblies, shutdown assemblies, a barrel, steam generators and other components, as shown in Figure 4.6. The reactor vessel hangs from a support ledge, and the head is bolted to this structure with a leak-tight gasket. The core is located on the top of a core support structure hung from the reactor vessel. Assemblies are slotted into positioning holes in the core support structure (Waltar and Reynolds, 1980). The reactor vessel is designed to accommodate high static loads at design temperatures and to minimize the dead load deflections of the reactor cover. It is also important to ensure the uniform radial thermal expansion of the reactor vessel about the vertical center of the entire reactor structure.

The guard vessel provides the secondary containment for the primary LBE coolant in the unlikely event that the reactor vessel has a leak. The gap between the two vessels are decided as wide enough to accommodate electric heating elements for the LBE melting during the initial start-up and the in-service inspection sensors and narrow enough to limit the coolant leak from the reactor vessel down to the acceptable level. The coolant level should be high enough to allow convective cooling from the core to the steam generators. The outer surface of the guard vessel is passively cooled by the RVACS system during accident conditions.

The cover gas control system located above the reactor module controls the oxygen concentration in LBE for the corrosion control. In addition, this system removes toxic gases including Po gas from the primary containment space (Hwang et al., 2008a; Hwang et al., 2008b; Nam et al., 2008).

4.4.2 Three-dimensional seismic isolation

Since LBE is a dense and heavy material, the major challenge in system structural design is to survive a seismic event and provide adequate safe shutdown after earthquake events. The reactor module employs a passive type of seismic isolators in order to achieve this goal (Yoo et al., 2000). The seismic design is based on the earthquake of 0.5g zero-period acceleration for the safe shutdown earthquake. Three-dimensional (3D) isolators are designed to reduce seismic acceleration responses in both vertical and horizontal directions, whereas two-dimensional isolators only work in the horizontal direction. A preliminary design is to float the entire reactor building from land with a 3D seismic isolation system. Figure 4.10 shows the isolation system that combines two-dimensional isolators using horizontal laminated rubber bearing (LRB) with a vertical isolation device, which uses a series of disc (Belleville) springs to provide seismic isolation in all three dimensions.

This system will ensure that the rigid body motion of the reactor building during the earthquake will not affect the reactor building. The space between the intermediate and upper reactor mats is used for the installation, inspection, and maintenance of the isolators. The application of 3D isolators results in the reduction of the horizontal floor acceleration by the reactor vessel, the reactor internals, and other components within the reactor system. Thus, the thickness of reactor vessel cover can be reduced and the relative motions between the control assemblies and the fuel assemblies can be minimized.

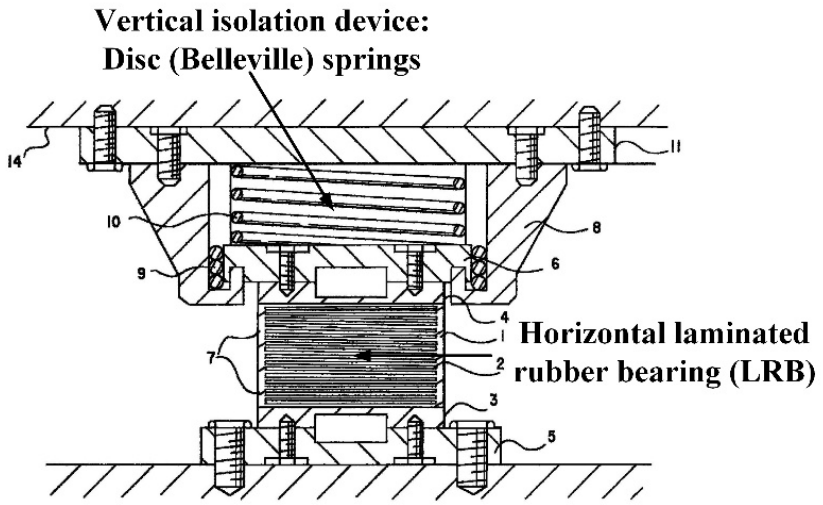

Figure 4.10 3D seismic base isolation bearing unit, adopted from (Yoo et al., 1999)

Chapter 5 Experimental Setup and Test Results

In this chapter, the integral behaviors of passive LBE-cooled systems are investigated experimentally: firstly, the natural circulation tests of LBE in loop configuration is conducted. As a test bed, HELIOS loop is utilized. By changing core power ratings, several sets of natural circulation cases in steady state are produced. In addition to the experimental data generation, system operation practices are also achieved in a rather simple geometry.

Secondly, a pool-type down-scale research facility PILLAR is designed and constructed from a specific reactor concept, URANUS, as designed in Chapter 4. Similar to the HELIOS case, several steady-state natural circulation test results are brought out. Furthermore, since the power level change leads to the variation of natural circulation mass flow rate and temperature distribution in a passive LBE-cooled system, the transient tests are carried out by giving instantaneous changes in the core power rating. In addition to the core power maneuvering, the secondary side condition in terms of mass flow rate is designated to another independent variable to see the effect of heat sink condition change on the primary natural circulation flow and heat transfer rate.

5.1 LBE loop natural circulation experiments[3]

5.1.1 Experimental setup of LBE loop facility: HELIOS

5.1.1.1 Facility descriptions

HELIOS is an integral test facility at SNU (Jeong, 2006) which was originally designed and built to validate the operation capability and safety characteristics of a prototypic LBE-cooled dedicated burner (high-level nuclear waste transmutation reactor), PEACER-300 (Hwang et al., 2000). Scaling ratios for thermal power and height were selected to be 5000:1 and 1:1 on its design, respectively, so that its maximum core power given by electrical heater rods is 60.0 kW and the total height of the facility is about 12 m. In addition to the height conservation, total pressure loss coefficient is conserved to have similar hydraulic loss aspects in natural circulation (Jeong, 2006). With the thermal power reduction and height conservation, flow area reduction is inevitable and therefore friction loss coefficients are dramatically affected by hydraulic diameter change. To accomplish total pressure loss coefficient conservation, some hydrodynamic components in which form loss occurs, such as gate valves,

[3] This section has been written based on the following journal paper: Yong-Hoon Shin et al., "Experimental studies and computational benchmark on heavy liquid metal natural circulation in a full height-scale test loop for small modular reactors," Nuclear Engineering and design, 316, 26-37, 2017.

are installed.

The loop is capable of not only thermal-hydraulic experiments but also materials corrosion tests in LBE flow conditions (Jeong et al., 2006; Lim et al., 2007). Especially, its conservation of height enables it to be used for the investigation of natural circulation capability in SMRs without reactor coolant pumps because its thermal center difference, defined by the distance between the center of heat source (mock-up core) and that of heat sink (heat exchanger) in height direction, is about 7.4 m. Hence, natural circulation experimental data produced with HELIOS can be utilized for the validation of safe operation under natural circulation in the new LBE-cooled SMR concepts as well as in the prototypic reactor. The schematic diagram and picture of the loop are depicted as Figure 5.1.

In HELIOS, two main fluid systems simulate the primary and secondary sides of the prototypic reactor; each system adopts working fluids as LBE and a single-phase, high flashing-point heat transfer oil (Dowtherm© RP), respectively. In virtue of the thermal oil's high boiling point (360 °C) at atmospheric pressure, the secondary side can be operated without any pressurization means.

The primary loop is arranged with mock-up core, expansion tank, mechanical pump, heat exchanger (shell side), and other hydrodynamic elements such as tee-junctions, gate valves, elbows and straight piping with 49.5 mm inner diameter (ANSI SCH 80 2'' pipe) connecting between components. Each component is fabricated from 316L stainless steel. By accepting widely used terminologies on hot leg and cold leg in a nuclear power

plant system, some parts of the primary loop are referred to as hot leg and cold leg. The hot leg is designated as a flow path from mock-up core outlet to heat exchanger inlet; in contrast, the cold leg is assigned to a path from heat exchanger outlet to mockup core inlet. The detailed design and exact dimensions of the components can be found in a report published by the OECD Nuclear Energy Agency (OECD Nuclear Energy Agency, 2012).

For thermal-hydraulic experiments, HELIOS can be operated in two modes, either forced circulation or natural circulation, by selecting flow paths between the heat exchanger and the mockup core; one is connected to the mechanical pump and the other one bypasses it, as shown in Figure 5.1. In natural circulation tests, the pump was bypassed to throughout this thesis study.

Due to a large surface area of the system compared to its volume, the outer surface of HELIOS components is enclosed by local surface heaters and thermal insulation to compensate heat loss to the environment. Hence, these local heaters are actively regulated during most of natural circulation operations as well as in pre-test stages when LBE is being filled up to the top of loop after increasing system temperature above the LBE melting.

The total inventory of LBE is stored in a LBE storage tank located below the loop when the system is not in operation. LBE is melted by heaters on the surface of the tank and is purged with the mixture gas of 4% hydrogen and argon balance to remove dissolved oxygen until operation condition is established.

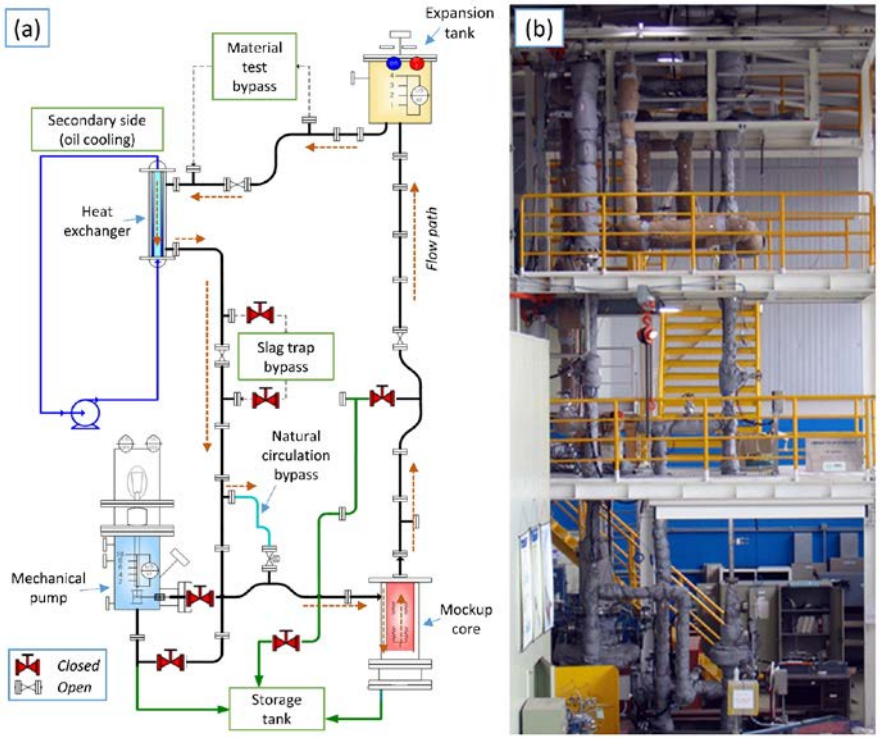

Figure 5.1 (a) System schematic diagram and (b) front-view picture of HELIOS thermal-hydraulic test loop

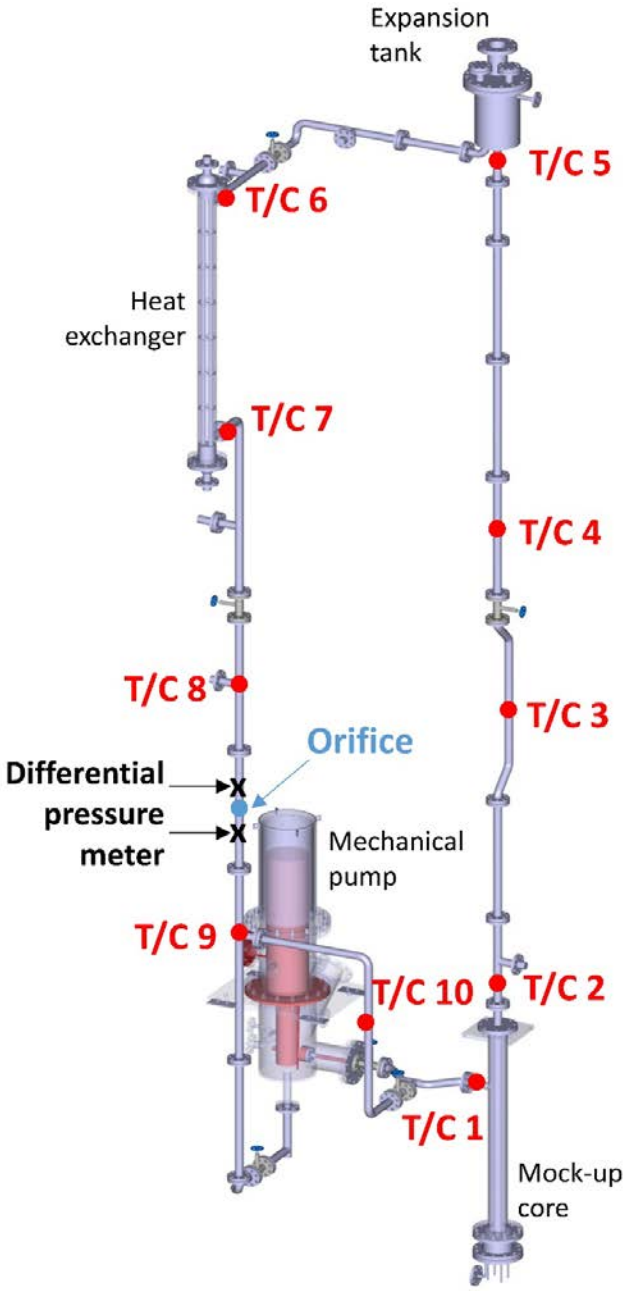

Figure 5.2 Three-dimensional configuration of HELIOS constituent components and key instrumentation system

5.1.1.2 Instrumentation system and uncertainty analysis

In natural circulation experimental campaigns, two thermal-hydraulic parameters of a working fluid are of primary interest: temperature and mass flow rate. For the temperature measurements, Type K thermocouples, which are broadly used in industry and experimental facilities and can be applied to wide temperature range with relatively small error, were selected and installed through the piping for fluid temperature measurement both in primary and secondary fluids in HELIOS. Among various methods to measure mass flow rate of a fluid, pressure drop measurement was used to obtain LBE mass flow rate. For the measurements of secondary side oil flow rate, a turbine flowmeter was used.

The uncertainties in measurements were estimated in terms of the combined standard uncertainty which is the root-mean-square of the systematic standard uncertainty and random standard uncertainty of the mean according to the Performance Test Code (PTC) written by the American Society of Mechanical Engineers (ASME, 2005). For the calculation of systematic standard uncertainty, annually performed calibration data and sensor specification sheets given by manufacturer were used. Expanded uncertainty is reported with a 95% confidence level.

The locations of each Type K thermocouples are depicted as Figure 5.2 and are designated in terms of accumulated length, which is defined by the path length measured from the mock-up core inlet to a certain point, as listed in Table 5.1. The secondary fluid temperatures are measured from the oil inlet and

outlet. The total systematic error of the thermocouples was reported as about ±1.0 K in a temperature range from 200 to 1000 °C by the manufacturer. The maximum expanded uncertainty of measurement by thermocouples in HELIOS was estimated to be ±2.2 K.

In order to make use of increased pressure loss on LBE mass flow rate measurement, an orifice is located in the middle of cold leg and a differential pressure transducer (Rosemount 3051 CD3A) with capillary probes measures the pressure drop over the orifice. The locations of differential pressure measurement are also shown in Figure 5.2. It shows total systematic error in terms of differential pressure as ±0.065% in the full range of 0.8 bar and the maximum expanded uncertainty of measurement by the transducer was estimated to be ±176.8 Pa. The orifice produces pressure loss with sudden area change. The necessity of orifice is due to the fact that the flow rate of natural convection is relatively low compared to that of forced circulation. The pressure drop is proportional to the square of mass flow rate. With the orifice, the small pressure loss can be accurately measured. The conversion equation from measured differential pressure to mass flow rate was produced by calibration test and formulated into a correlation in a previous study (Cho et al., 2011). The error in flow rate measurement has been derived from the correlation and the maximum expanded uncertainty was computed to be ±0.096 kg/s.

A turbine flowmeter (EKFM Industry KT-100-F-F) has been used to measure the secondary side oil flow rate. Its accuracy was given to be ±0.5% of full scale and it is estimated that its maximum expanded uncertainty is ±0.40 L/min. As the flowmeter directly measures volumetric flow rate instead of mass

flow rate, it is required to multiply the oil density at the measurement temperature to obtain mass flow rates. Considering this, the maximum expanded uncertainty of oil mass flow rate measurement was estimated to be ±0.0065 kg/s.

Table 5.1 Thermocouple locations on HELIOS main loop in terms of accumulated length along flow path

T/C No.	Description/position	Accumulated length along flow path (m)
T/C 1	Mock-up core inlet	0.00
T/C 2	Mock-up core outlet	3.72
T/C 3	Hot leg (1)	6.54
T/C 4	Hot leg (2)	9.47
T/C 5	Expansion tank inlet	10.88
T/C 6	Heat exchanger inlet	14.32
T/C 7	Heat exchanger outlet	16.52
T/C 8	Cold leg (1)	19.23
T/C 9	Cold leg (2)	21.42
T/C 10	Cold leg (3); in natural circulation bypass	22.65

5.1.2 HELIOS experiment procedure and LBE loop natural circulation experimental conditions

Non-isothermal LBE natural circulation experiments were performed in HELIOS facility. Well-defined steady-state, adiabatic experiments were conducted and the results were used for the code benchmark of MARS-LBE while some of the results were utilized in an international benchmark program called LACANES (OECD Nuclear Energy Agency, 2012). In order to generate the adiabatic conditions, heat loss through the loop surface was compensated by the local surface heaters.

5.1.2.1 Experiment procedure

HELIOS has to be properly configured to perform natural circulation experiments with the mechanical pump bypassed. To prepare for a steady-state test campaign, the main loop of HELIOS should be filled with LBE, which normally stored in the storage tank when not operated. In the meantime, the local surface heaters on the main loop are activated to maintain temperature at any point over 200-250 °C. After the preheating condition is satisfied, LBE is transferred from the storage tank to the main loop by pressure exerted by the injection of high-purity argon gas or the mixture gas of 4% hydrogen with argon balance. The main loop and the storage tank are isolated after about 1.9 tons of LBE being transferred.

When a hot standby condition is stabilized, all local surface heaters are turned off, and main heater rods in the mock-up core are activated to a specific power rating while the secondary side oil pump is set to a specific flow rate. With these manipulations, natural circulation flow is generated by energy displacements from heat source to heat sink and temperature distribution is also changed until the system reaches first steady state.

Considering the generation of well-defined experimental data for code benchmark, any uncertainties which can affect simulation results must be minimized. In HELIOS, there is no instrumentation system for measuring heat loss, so the uncertainties given by heat loss are inevitable. Furthermore, strictly speaking, ideal adiabatic conditions would not be achievable by nature. Nevertheless, a nearly adiabatic condition can be achieved by compensating heat dissipation to the environment with the surface heaters.

In this regard, heat compensation is made in several steps as follows: firstly, the amount of heat loss over each section defined by a region between two adjacent thermocouples, for example, T/C 1 – T/C 2, T/C 2 – T/C 3, and so on, is estimated from temperature distribution along the main loop with measured mass flow rate at a given state and heat capacity of LBE at a given temperature. Secondly, electric power ratings equivalent to the estimated heat loss over sections are supplied to local surface heaters. Followed by heat addition to the system, temperature transients are expected to take place. The local surface heaters are tuned by trial-and-error until individual temperature measurements in the hot leg and cold leg are respectively in close ranges each other, and the mock-up core power rating and the heat withdrawn by the

secondary side oil are in balance. The total experimental procedures for generating well-defined experiment results are summarized in Table 5.2.

Table 5.2 Natural circulation test procedure to generate well-defined test results in HELIOS

No.	Procedure	Detail	
1	LBE filling to main loop	1.1.	Local surface heaters are turned on to make main loop temperature 200-250 °C.
		1.2.	LBE is transferred to the main loop by Ar (+4% H_2) gas pressure.
		1.3.	Main loop and LBE storage tank are isolated.
2	Natural circulation test start	2.1.	Local surface heaters are turned off and main heater is activated to a given power.
		2.2.	Secondary side flow is generated by oil side pump.
3	First natural circulation steady state with heat loss	3.1.	First equilibrium is reached after temperature and mass flow transients with local surface heater off.
4	Heat compensation to reach adiabatic condition	4.1.	Local surface heaters are turned to compensate heat loss considering temperature drop, mass flow rate, and heat capacity.
		4.2.	System temperature distribution is tuned by trial and error.
5	Final adiabatic steady state with heat compensation	5.1.	Cold leg and hot leg temperatures are close in specific ranges, respectively
		5.2.	Primary and secondary loops are in energy balance.

5.1.2.2 Experiment conditions and test matrix

In non-isothermal natural circulation experiments, the amounts of heat given to and withdrawn from a system are important because natural circulation flow is made by energy transfer in principle. In this context, experimental activities done in HELIOS were classified primarily with the total mock-up core power ratings. Following the experimental procedure, a final steady-state, adiabatic condition can be made after heat compensation on the main loop is achieved and heat balance between the mock-up core power rating and heat transferred to the secondary side oil become consistent. In this study, only those results are utilized for the system code benchmark, even though there had been temperature transients and some fine-tuning processes before reaching the final states.

For the experimental conditions on natural circulation, four different total mock-up core power ratings were selected: 9.8, 15.0, 27.0, and 33.6 kW. Each power rating condition was directly chosen as test numbers from NC1.0 to NC4.0. Other than heat source information, the main LBE loop and secondary side oil conditions in final steady states are listed and illustrated in Table 5.3. In NC1.0 and NC2.0 cases, all four electrical heater rods in the mock-up core were in active, while only three rods were activated in the cases NC3.0 and NC4.0.

Table 5.3 Test matrix on adiabatic, non-isothermal natural circulation experiments in HELIOS

ID	Total mock-up core power (kW)	No. of active heater rods	Avg. oil inlet temperature (°C)	Avg. oil mass flow rate (kg/s)	Total experimental time (hr)
NC1.0	9.8	4	99.65	0.374	80
NC2.0	15.0	4	122.63	0.374	70
NC3.0	27.0	3	155.03	0.382	72
NC4.0	33.6	3	167.60	0.390	48

5.1.3 Experimental results on steady-state LBE loop natural circulation

Non-isothermal natural circulation experiments were performed with four different core power ratings. There was no heat compensation in the beginning of each test case and the system finally reached adiabatic steady state by the trial-and-error approach as described in previous sections. Owing to ambient temperature fluctuation within a day, the whole system reacted to it and temperature distribution along the main loop had periodical change. In other words, a strict 'steady' state could not be achieved due to the temperature change. To overcome this, the system had been maintained and observed without any intervention or manipulation in the last 24 hours out of full test history after reaching adiabatic wall boundary conditions.

The well-defined experimental data were generated from the measurements given in 6-7 hours in which the system showed rather moderate temperature fluctuation out of the 24-hour observation. In those steady state conditions, the individual temperature measurements in the hot leg and cold leg lied in 5-7 °C variation, respectively. In Table 5.4, the experimental data are summarized. The average hot leg temperature is a mean of temperatures measured by T/C-2, 3, 4, 5, and T/C-6, and the average cold leg temperature is defined by averaging measurements from T/C-7, 8, 9, 10, and T/C-1. Also, the average temperature difference means the difference between two average temperatures. Temperature distributions along the loop measured in the experiment cases are described with the code benchmark results in Section 6.2.1.

Table 5.4 Adiabatic, non-isothermal, steady-state natural circulation results in HELIOS

No.	Main loop (LBE side)					Secondary loop (oil side)		
	Total core power (kW)	Hot leg temperature (°C)	Cold leg temperature (°C)	Temperature difference (°C)	LBE mass flow rate (kg/s)	Oil inlet temperature (°C)	Oil outlet temperature (°C)	Oil mass flow rate (kg/s)
NC1.0	9.8	273.84	237.32	36.52	1.80	99.65	114.00	0.374
NC2.0	15.0	315.84	266.83	49.01	2.09	122.63	144.33	0.374
NC3.0	27.0	367.63	300.85	66.78	2.74	155.03	187.52	0.382
NC4.0	33.6	394.43	315.31	79.12	2.83	167.60	204.18	0.390

Note: all of the values given above are average values from measurements in each case.

5.2 LBE pool natural circulation experiments

In contrast with pump-driven systems, the mass flow rate of primary coolant varies with core power rating in passive systems like URANUS. In this situation, a question may arise that the system could be maneuvered properly in power transients because reactor power output changes as control rod moves. In order to investigate the fast load-following capability of a passive pool-type LBE system, a pool-type integral experimental facility was designed and constructed by using thermal-hydraulic scaling analysis. The name of facility is PILLAR, which stands for Pool-type Integral Leading test facility for Lead-Alloy-cooled small modular Reactor. PILLAR features the conservation of height as same as the prototypic reactor URANUS while its radial diameter is reduced with a factor of about 1/14. In this section, a detailed design procedure using thermal-hydraulic scaling method, the area-average method, experimental setup and procedure, and experimental results are elaborated.

5.2.1 Design of LBE pool facility: PILLAR

This section deals with the scaling analysis, design, and specifications of PILLAR. Since there have been many studies on design procedures with scaling analysis, the selection of proper design requires a literature survey. After a suitable method is chosen, some mathematical formulations are to be constructed. Finally, a detail design is achieved in terms of several important

parameters to be conserved.

5.2.1.1 Design requirements and consideration for PILLAR

As reviewed in Chapter 2.4, several scaling analysis methods for the experiment of natural circulation of liquid metal cooled reactors have been suggested and hence, it is required to apply a suitable method to observe the phenomena of interest. The scaling method for PILLAR was determined by considering experimental requirements, budgetary consideration, and physical limitations.

Firstly, the length scale is designated to be unity, in other words, to have same height scale in the prototype and model. It is because the most important behavior to be validated is LBE natural circulation, as it is strongly dependent upon buoyancy force given by height difference. Therefore, the conservation of height and the height difference of heat source and heat sink would be the easiest way not to distort the behavior. Throughout this, the scale model can simulate the natural circulation capability of prototypic reactor without a distortion in the length scale.

Secondly, In this regard, the flow area of downscale facility must be decreased in terms of volume reduction. However, if flow area is too narrow, then it might lead to an unrealistic simulation with a loop configuration. Furthermore, buying new LBE was restricted with a budgetary limit and about 4 metric tons of the retained liquid metal used for HELIOS were to be used.

Thus, the reduction ratio of flow area where volume reduction occurs is able to be chosen to an extent that it can utilize the retained amount of LBE.

Additionally, mean velocity at the core outlet, which is the reference velocity on the scaling analysis, needs to be greater than 10 cm/s so that flow measurement is viable and the thickness of each physical component should be designated with the consideration of design pressure with 20 bar. The requirements and consideration done before the selection of scaling analysis method is summarized in Table 5.5.

Scaling analysis method is decided regarding the limitations and requirements given above. First, the scaling methods suggested by (Grewal and Gluekler, 1982) and (Weinberg et al., 1990) were excluded due to their lack of actual application and insufficient explanations in nondimensionalization. The methods for the geometrical scaling in all directions (Eguchi et al., 1997; Takeda et al., 1993), which were validated through their own SFR facility described in their work and the E-SCAPE facility in the SCK-CEN (Van Tichelen et al., 2015), were ruled out as all the scaling ratios in width, length, and height to be the same and the height scale criterion designated to be unity cannot be met. The method suggested by (Chen, 2015) is not available because it is about the experiments with water replacing LBE.

Hence, the scaling ratios in longitudinal directions (x- and y-directions) need to be differentiated from the height scale (z-direction) to meet the height scale requirements and it leads to the choice of area-average method (Ishii and Kataoka, 1984; Ishii et al., 1998) being the most proper one. As aforementioned, this method can be applicable to liquid metal environments since it had been

applied to the design of HELIOS and STELLA-1 (Hong and Lee, 2012; Jeong, 2006). A shortcoming to this method is that it is impossible to simulate some local phenomena because governing equations are constructed through the area averaging. Therefore, in the design utilizing the area-average method, the local phenomena is limited to that of the facility, not to that of the prototypic reactor.

Table 5.5 PILLAR design requirements and criteria for scaling analysis

Criteria	Facility limitations/requirements
Length scale	1:1
Flow area scale	Limited by the total amount of LBE (< 1/100)
Total LBE mass	< 4.0 ton
Core outlet flow velocity	> 10 cm/s
Design pressure	20 bar (2.0 MPa)

5.2.1.2 Nondimensionalization of governing equations in area-average scaling method

In this section, the governing equations are expressed in nondimensionalized forms by following the area-average method. To do so, the following assumptions are applied:

1) The working fluid is incompressible as its density does not vary with applied pressure or it exists in a system that pressure upon it does not change largely. In addition, the fluid density change is almost linear in a given temperature range so that the buoyancy term in momentum conservation equation is treated by the Boussinesq approximation;
2) The thermophysical properties of working fluid does not change by temperature and is the same in any flow direction, in other words, isotropic; and
3) Heat generated in the solid heat source only conducts in the perpendicular direction to the main flow direction, the transverse direction, and axial heat conduction in the working fluid is neglected.

The area-average method utilizes five equations on mass conservation, momentum conservation, energy conservation in solid and fluid, and boundary condition between fluid and solid media. Furthermore, the Boussinesq approximation is applied to the momentum change term by buoyancy in the

momentum conservation equation and the pressure loss term only consists of momentum loss by friction and form loss. Each term in mass and momentum conservation equations is integrated over flow area and the other equations are given in differential form, as shown in from Eqn. (5.1) to Eqn. (5.5). When it comes to a velocity term (u_i) is included, the term is expressed with the reference velocity (u_r) with Eqn. (5.1). The meaning and use of each of parameters hereafter are defined in Nomenclature.

$$u_i = \frac{a_0}{a_i} u_r \tag{5.1}$$

$$\rho \frac{du_r}{dt} \sum_i \frac{a_0}{a_i} l_i = \rho g \beta \Delta T_0 l_h - \frac{\rho {u_r}^2}{2} \sum_i \left(\frac{l}{d} f + K \right)_i \left(\frac{a_0}{a_i} \right)^2 \tag{5.2}$$

$$\rho C_p \left(\frac{\partial T}{\partial t} + u \frac{\partial T}{\partial z} \right)_i = \frac{4h_i}{d_i} (T_s - T)_i \tag{5.3}$$

$$\left(\rho_s C_{ps} \frac{\partial T_s}{\partial t} \right)_i + \left(k_s \nabla^2 T_s \right)_i - \dot{q}_{si} = 0 \tag{5.4}$$

$$-k_{si} \frac{\partial T_{si}}{\partial y} = h_i (T_s - T)_i \tag{5.5}$$

The following Eqns. (5.7) to (5.11) are in nondimensional forms by defining dimensionless parameter as shown in Eqn. (5.6). In these formulations, each term can be more simplified by designating a specific component in the system as a reference, expressed with the subscript *r*; in this dissertation, the values from the core, which works as heat sources in the prototype and the scale facility, are appointed as reference constants with the subscript 0. In this situation, the

nondimensional area A_r is given by $A_r = a_r/a_0$ and each formula can be simplified further with $A_r = 1$ as a_r and a_0 are to be the same.

$$\begin{array}{llll} U_i = u_i / u_0 & U_r = u_r / u_0 & & \\ L_i = l_i / l_0 & L_h = l_h / l_0 & Y = y/\delta & Z = z / l_0 \\ \tau = tu_0 / l_0 & \theta = \Delta T / \Delta T_0 & & \\ A_i = a_i / a_0 & \nabla^{*2} = \delta^2 \nabla^2 & & \end{array} \tag{5.6}$$

$$U_i = \frac{U_r}{A_i} \tag{5.7}$$

$$\frac{dU_r}{d\tau}\sum_i \frac{L_i}{A_i} = \mathrm{Ri}(\theta_h - \theta_c)L_h - \frac{U_r^{\,2}}{2}\sum_i F_i \frac{1}{A_i^{\,2}} \tag{5.8}$$

$$\frac{\partial \theta_i}{\partial \tau} + \frac{U_r}{A_i}\frac{\partial \theta_i}{\partial Z} = \mathrm{St}_i(\theta_{si} - \theta_i) \tag{5.9}$$

$$\frac{\partial \theta_{si}}{\partial \tau} + \mathrm{Ti}_i \nabla_i^{*2}\theta_{si} - Q_{si} = 0 \tag{5.10}$$

$$\frac{\partial \theta_{si}}{\partial Y_i} = \mathrm{Bi}_i(\theta_{si} - \theta_i) \tag{5.11}$$

Additionally, the hydraulic diameter d_i is related to the flow area a_i and the wetted perimeter ξ_i given as Eqn. (5.12). In addition, the conduction depth δ_i can be defined as the transverse direction area of the solid heat source a_{si} and the wetted perimeter ξ_i as shown in Eqn. (5.13).

$$d_i = \frac{4a_i}{\xi_i} \tag{5.12}$$

$$\delta_i \equiv \frac{a_{si}}{\xi_i} \tag{5.13}$$

The names, physical meanings, and formulae of each of nondimensional parameters shown in the nondimensional equations above are

as follows:

Richardson number	$\mathrm{Ri} \equiv \frac{g\beta\Delta T_0 l_0}{u_0^{\,2}}$	Buoyancy to inertia ratio	(5.14)
Friction number	$F_i \equiv \left(\frac{l}{d} f + K\right)_i$	Friction to inertia ratio	(5.15)
(Modified) Stanton number	$\mathrm{St}_i \equiv \left(\frac{4hl_0}{\rho C_p u_0 d}\right)_i$	Ratio of convective heat transfer from the solid heat source wall to the fluid to convective heat transfer in the flow direction	(5.16)
Time ratio number	$\mathrm{Ti}_i \equiv \left(\frac{\alpha_s}{\delta^2}\frac{l_0}{u_0}\right)_i$	Transport time to conduction time ratio	(5.17)
Biot number	$\mathrm{Bi}_i \equiv \left(\frac{h\delta}{k_s}\right)_i$	Ratio of convective heat transfer from solid heat source wall to the fluid to thermal conductivity in solid heat source	(5.18)
Heat source number	$Q_{si} \equiv \left(\frac{\dot{q}_s l_0}{\rho_s C_{ps} u_0 \Delta T_0}\right)_i$	Ratio of heat source output to energy transfer rate in the flow direction	(5.19)

Accordingly, to obtain the reference temperature difference, ΔT_0, heat generation in the solid heat source and heat transferred to the fluid between the core inlet and outlet are considered as shown in (5.20).

$$\begin{aligned} &\dot{q}_{s0} a_{s0} l_0 = \dot{m} C_p \Delta T_0 = (\rho u_0 a_0) C_p \Delta T_0 \\ &\Rightarrow \Delta T_0 = \frac{\dot{q}_{s0} l_0}{\rho C_p u_0} \frac{a_{s0}}{a_0} \end{aligned} \tag{5.20}$$

Utilizing the reference temperature difference, the core outlet velocity is derived by Eqn. (5.2) at a steady state as in Eqn. (5.21) with vanishing the temporal change term.

$$\rho \frac{du_0}{dt} \sum_i \frac{l_i}{A_i} = 0 = \rho g \beta \Delta T_0 l_h - \frac{\rho u_0^{\,2}}{2} \sum_i \left(\frac{F_i}{A_i} \right)^2$$
$$\Rightarrow 0 = g\beta \frac{\dot{q}_{s0} l_0}{\rho C_p u_0} \frac{a_{s0}}{a_0} l_h - \frac{u_0^{\,2}}{2} \sum_i \left(\frac{F_i}{A_i} \right)^2 \qquad (5.21)$$
$$\Rightarrow u_0 = \left[\beta \frac{\dot{q}_{s0} l_0}{\rho C_p u_0} \frac{a_{s0}}{a_0} l_h \Big/ \frac{1}{2g} \sum_i \left(\frac{F_i}{A_i} \right)^2 \right]^{1/3}$$

5.2.1.3 Similarity requirements in area-average method

In order to make the prototype and model behave in physical equivalence, each term in governing equations must satisfy a criterion given as Eqn. (5.22) with a specific parameter or term expressed by ψ:

$$\psi_R \equiv \frac{\psi_{\text{model}}}{\psi_{\text{prototype}}} = 1. \qquad (5.22)$$

However, not all the ratios of dimensionless numbers can be designated unity and therefore the similitudes of the dimensionless numbers derived from ~~~ should be conserved in which distortion in physical phenomena is minimized as achieved as possible.

Above all, the geometrical similarity is considered. It is the most

fundamental criteria in scaling analysis and defined as dimensionless area ratio given as Eqn. (5.23) and dimensionless length ratio as (5.24) in this method.

$$A_{iR} = \frac{A_{im}}{A_{ip}} = \frac{\left(a_i / a_0\right)_m}{\left(a_i / a_0\right)_p} = 1 \tag{5.23}$$

$$L_{iR} = \frac{\left(l_i / l_0\right)_m}{\left(l_i / l_0\right)_p} = 1 \qquad \left(L_{hR} = \frac{\left(l_h / l_0\right)_m}{\left(l_h / l_0\right)_p} = 1 \right) \tag{5.24}$$

The ideal condition would be the prototype and model are in the geometrical similarity, but it is technically not achievable in most of engineering cases. Hence, in this downscale model, the core, which drives overall behaviors of the system as a heat source, is forced to be in a geometrical similarity while slight geometrical distortions on other components are tolerated. Furthermore, dimensionless length ratio, which include the height difference between the heat source and heat sink, is strictly conserved as unity.

From dynamic similarity, the following Eqn. (5.25) is established:

$$\left(\sum_i F_i / A_i^2 \right)_R = 1. \tag{5.25}$$

If dimensionless areas A_i for all the components are the same between the prototype and the scale model, then this criterion falls in the ratio of gross sum of Friction numbers being unity ($(\sum_i F_i)_R = 1$). In other words, system dynamic behaviors are conserved if the ratios of dimensionless areas in the prototype

and the scale model vary within the kinematic similarity being conserved. Pressure drop criteria are difficult to be matched because total pressure loss in most of downscale models tends to decrease greater than that is needed. Considering the kinematic similarity and the nondimensional area at the same time, the criteria can be met by adding some parts arising pressure drop such as an orifice. As stated, the kinematic similarity criteria can also contribute to mitigate the effect of geometrical similarity distortion.

Successively, the similarity requirements of six nondimensional numbers are considered. As the friction number was already considered by kinematic similarity, the other five nondimensional numbers are covered. In other words, the kinematic similarity which contains the friction number and nondimensional area must be conserved independent of the conservation of other parameters. In order to simplify the equations further, some selected thermophysical properties in both prototype and model are almost the same as shown in Eqn. (5.26).

$$\rho_R = C_{pR} = \beta_R \approx 1 \tag{5.26}$$

Applying this, Eqns. (5.27) to (5.31) are derived from each of nondimensional parameters. If the paramters below become unity then phenomena parametrized by each of terms are conserved in the prototype and the model.

$$\mathrm{Ri}_R = \frac{\Delta T_{0R} l_{0R}}{{u_{0R}}^2} = 1 \tag{5.27}$$

$$\mathrm{St}_{iR} = \frac{h_{iR} l_{0R}}{u_{0R} d_{iR}} = 1 \tag{5.28}$$

$$\mathrm{Bi}_{R} = \frac{h_{iR} \delta_{iR}}{k_{siR}} = 1 \tag{5.29}$$

$$\mathrm{Ti}_{iR} = \frac{\alpha_{s_R} l_{0R}}{{\delta_{iR}}^2 u_{0R}} = 1 \tag{5.30}$$

$$Q_{s0R} = \frac{\dot{q}_{s0R} l_{0R}}{\left(\rho_s C_{ps}\right)_R u_{0R} \Delta T_{0R}} = 1 \tag{5.31}$$

From the heat conservation equation in Eqn. (5.20), the requirements for the thermal output in the prototype and the model can be derived as shown in Eqn. (5.32). This equation suggests that when the ratio of the thermophysical properties of the heat source changes, the flow area scale and the cross-sectional area scale of the solid heat source varies with the heat capacity ratio per unit volume. If the ratio of the heat capacity per unit volume is large, the solid heat source area will be reduced more than the flow area, and in the opposite case, the flow area must be reduced more than the solid heat source area.

$$\begin{aligned} & u_{0R} a_{0R} \Delta T_{0R} = \dot{q}_{s0R} a_{s0R} l_{0R} \\ & \Rightarrow a_{0R} = \dot{q}_{s0R} \frac{l_{0R}}{u_{0R} \Delta T_{0R}} a_{s0R} = \left(\rho_s C_{ps}\right)_R a_{s0R} \end{aligned} \tag{5.32}$$

Meanwhile, the velocity requirement can be independently designated from the similarity in Richardson number given in (5.33):

$$\mathrm{Ri}_{R} = \frac{\Delta T_{0R} l_R}{{u_{0R}}^2} = 1 \Rightarrow u_{0R} = {\Delta T_{0R}}^{1/2} {l_{0R}}^{1/2}. \tag{5.33}$$

Consecutively, Eqns. (5.34) to (5.36) shows the requirements on conduction thickness, the ratio of convective heat transfer coefficients, and hydraulic diameter from the Time ratio number, Biot number, and (Modified) Stanton number. The velocity ratio and thermal conduction thickness are further substituted as obtained in Eqn. (5.33) and (5.34). Through this process, the three parameters are specified as functions of the ratios of thermophysical properties (ρ_s, C_{ps}, k_s, α_s), length scale ratio, or the ratio of temperature difference.

$$\begin{aligned} &\mathrm{Ti}_{iR} = \frac{\alpha_{sR} l_{0R}}{\delta_{iR}^{\ 2} u_{0R}} = 1 \\ &\Rightarrow\ \delta_{iR} = \left(\frac{\alpha_{sR} l_{0R}}{u_{0R}} \right)^{1/2} = \alpha_{sR}^{\ 1/2} l_{0R}^{\ 1/4} \Delta T_{0R}^{\ -1/4} \end{aligned} \tag{5.34}$$

$$\begin{aligned} &\mathrm{Bi}_{iR} = \frac{h_{iR} \delta_{iR}}{k_{siR}} = 1 \\ &\Rightarrow\ h_{iR} = \frac{k_{siR}}{\delta_{iR}} = \left(k_s \rho_s C_{ps} \right)_{iR}^{1/2} l_{0R}^{\ -1/4} \Delta T_{0R}^{\ 1/4} \end{aligned} \tag{5.35}$$

$$\begin{aligned} &\mathrm{St}_{iR} = \frac{h_{iR} l_{0R}}{u_{0R} d_{iR}} = 1 \\ &\Rightarrow\ d_{iR} = \frac{h_{iR} l_{0R}}{u_{0R}} = h_{iR} l_{0R}^{\ 1/2} \Delta T_{0R}^{\ -1/2} \\ &\qquad = \left(k_s \rho_s C_{ps} \right)_{iR}^{1/2} l_{0R}^{\ 1/4} \Delta T_{0R}^{\ -1/4} \end{aligned} \tag{5.36}$$

The equations above are derived for a case that all of each nondimensional parameter are unity, in other words. In this situation, if the similarities of Time ratio number, Biot number, and heat source number are conserved, then that of (modified) Stanton number is automatically obtained, as shown in Eqn. (5.37), by utilizing the hydraulic diameter and the thermal conduction thickness ratios

given in Eqn. (5.12) and (5.13), respectively, and flow area scale and solid heat source area scale as designated by Eqn. (5.33).

$$\begin{aligned}
\mathrm{St}_{iR} &= \frac{h_{iR} l_{0R}}{u_{0R} d_{iR}} = \frac{\alpha_{sR} l_{0R}}{\delta_{iR}{}^2 u_{0R}} \frac{h_{iR} \delta_{iR}}{k_{siR}} \frac{\delta_{iR}{}^2 k_{siR}}{\alpha_{sR} d_{iR} \delta_{iR}} \\
&= \mathrm{Ti}_i \mathrm{Bi}_i \left(\rho_s C_{ps}\right)_R \frac{\delta_{iR}}{d_{iR}} \\
&= \mathrm{Ti}_i \mathrm{Bi}_i \left(\rho_s C_{ps}\right)_R \frac{\alpha_{s0R} / \xi_{0R}}{a_{0R} / \xi_{0R}} \\
&= \mathrm{Ti}_i \mathrm{Bi}_i \frac{\left(\rho_s C_{ps}\right)_R \alpha_{s0R}}{a_{0R}} \\
&= \mathrm{Ti}_i \mathrm{Bi}_i = 1
\end{aligned} \tag{5.37}$$

However, as shown in Eqn. (5.35) for Biot number, the similarity in Biot number is hard to be met between the prototype and the model because it includes convective heat transfer coefficient (Ishii and Kataoka, 1984), which is generally given by the Nusselt number (Nu) in Eqn. (5.38):

$$\mathrm{Nu} = \frac{hd}{k} \Rightarrow h = \frac{\mathrm{Nu} \cdot k}{d}. \tag{5.38}$$

Furthermore, Nu is given as a function of Reynolds number (Re) and Prandtl number (Pr) and is dependent upon the characteristics of fluid, heat transfer condition, flow regime, etc. For LBE in turbulent flow regime, Seban-Shimazaki correlation shown in Eqn. (5.39) is widely used (Seban and Shimazaki, 1949). Hereafter, the fluid is assumed to be turbulent for all time in an engineering point of view, since most of LBE flow has large Re enough to

be turbulent and it will not be laminar in both the prototypic reactor and the scale model.

$$\begin{aligned} \mathrm{Nu} &= f(\mathrm{Re},\mathrm{Pr}) = 5.0 + 0.025\left(\mathrm{RePr}\right)^{0.8} \\ &= 5.0 + 0.025\mathrm{Pe}^{0.8} \end{aligned} \tag{5.39}$$

As the prototype and the scale model utilizes the same working fluid, Pr is almost the same and Nu strongly depends on Re. Furthermore, Re is a function of flow velocity and hydraulic diameter; it is limited to designate the value of convective heat transfer coefficients in the prototype and the scale model with the Biot number and (modified) Stanton number being conserved at the same time. Hence, it is inevitable to have a distortion from the Biot number and (modified) Stanton number and it leads to an impact in terms of the distortion in hydraulic diameter and convective heat transfer coefficient.

Finally, volumetric power density can be derived as shown in Eqn. (5.40) from Eqn. (5.31). Utilizing this and Eqn. (5.20) on heat conservation, the requirement on heat source power is obtained as in Eqn. (5.41). Applying this formula, it can be seen that the ratio of core power outputs is given as a function of the flow area scale, the length scale, and the reduction of the temperature differences as shown in Eqn. (5.40).

$$\begin{aligned} & Q_{s0R} = \frac{\dot{q}_{s0R} l_{0R}}{\rho_{sR} C_{psR} u_{0R} \Delta T_{0R}} = 1 \\ & \Rightarrow \ \dot{q}_{s0R} = \frac{u_{0R} \Delta T_{0R}}{l_{0R}} \left(\rho_s C_{ps}\right)_R = \left(\rho_s C_{ps}\right)_R l_{0R}{}^{-1/2} \Delta T_{0R}{}^{3/2} \end{aligned} \tag{5.40}$$

$$
\begin{aligned}
& P_0 = \dot{q}_{s0} a_{s0} l_0 \\
\Rightarrow\ & P_{0R} = \dot{q}_{s0R} l_{0R} a_{s0R} = \left(\rho_s C_{ps}\right)_R \Delta T_{0R}{}^{3/2} l_{0R}{}^{1/2} a_{s0R} \\
& \quad = a_{0R} l_{0R}{}^{1/2} \Delta T_{0R}{}^{3/2}
\end{aligned}
\tag{5.41}
$$

As explained that the similarity distortion in Biot number and the (modified) Stanton number is inevitable, the similarity of nondimensional numbers parametrizing heat transfer should be conserved by securing the similarity of the Time ratio number and the heat source number. Both nuclear fuel rods in the prototypic reactor and heater rods in the scale facility are produced and operated in cylindrical forms and determined as an appropriated numbers, which can contribute to the similarity of the two nondimensional numbers. Since both the diameter ratio and the thermal conduction thickness ratio are in length dimensions, the diameter ratio between nuclear fuel rods and heater rods can be determined by Eqn. (5.42) from the similairity of the Time ratio number in Eqn. (5.34).

$$
d_{rod,R} = \delta_{0R} = \alpha_{sR}{}^{1/2} l_{0R}{}^{1/4} \Delta T_{0R}{}^{-1/4} \tag{5.42}
$$

From Eqn. (5.32), the relationship between the number of fuel rods and the number of heater rods can be derived as shown in the following Eqn. (5.43):

$$
\begin{aligned}
a_{s0R} &= \frac{a_{0R}}{\left(\rho_s C_{ps}\right)_R} \\
&= \frac{N_{rod,m}}{N_{rod,p}} \frac{\left(\pi/4\right) d_{rod,m}{}^2}{\left(\pi/4\right) d_{rod,p}{}^2} = N_{rod,R} d_{rod,R}{}^2 \\
N_{rod,R} &= \frac{a_{0R}}{\delta_{0R}{}^2 \left(\rho_s C_{ps}\right)_R} = \left(\frac{\Delta T_{0R}{}^{1/4}}{\alpha_{sR}{}^{1/2} l_{0R}{}^{1/4}} \right)^2 \frac{a_{0R}}{\left(\rho_s C_{ps}\right)_{0R}} \\
&= k_{sR}{}^{-1} l_{0R}{}^{-1/2} \Delta T_{0R}{}^{1/2} a_{0R}
\end{aligned}
\quad . \qquad (5.43)
$$

5.2.1.4 Comparison of thermophysical properties of solids

The similarity requirements derived in the former Chapter 5.2.1.3 are shown to be expressed by the ratios of thermophysical properties between the prototype and the scale model. Therefore, it is necessary to compare the solid properties to be used in the prototype and scale model. In the case of the prototype, the solid materials include structural materials and nuclear fuel, while those are comprised of structural materials and the heater rods in the core, which simulate the nuclear fuel. In particular, to maintain the similarity between the time ratio number and the heat source number, it is necessary to confirm the difference in properties between the heater rod and the fuel because the heat source characteristics in the prototype and the scale model must be matched. The physical properties required for the scaling analysis are density (ρ_s), thermal conductivity (k_s), and isobaric heat capacity (C_{ps}). In addition to these properties, the thermal diffusivity (α_s) and the isobaric heat capacity per unit volume ($\rho_s C_{ps}$), which can be calculated as a function of these three properties are identified.

The nuclear fuel adopted for the prototypic reactor is UO_2, as indicated throughout Chapter 4. In reality, its thermophysical properties are affected by neutron irradiation and temperature distribution (Popov and Carbajo, 2000). In this study, it is assumed that it is a fresh fuel, which has not gone through neutron irradiation, and has a small porosity so that its actual density is given in 95% of theoretical density.

Meanwhile, there are various suppliers who produce diverse types of heater rods that simulate the nuclear fuel. In other words, the physical properties would be affected by the selection of the heater rods. Therefore, it was suggested to determine the material properties based on a specific design specification in the scaling analysis and design.

Although there are many candidate structural materials to be used for the scale facility, only selected materials are to be covered in this study (Hong and Lee, 2012). It can be seen from Table 5.6, which summarizes the thermophysical properties of those materials, that some of the metal candidates (stainless steel Type 304 and 316L, nichrome) have similar properties each other so that the structural materials of the prototype and the scale facility are approximated to have almost the same properties. They are also evaluated to have higher thermal conductivity, heat capacity, and thermal diffusivity compared to UO_2 fuel.

The heater rods are comprised of sheath, thermal insulation, heating element, and core constituting the radial center of each rod. Among these elements, the use of ceramic materials such as thermal insulation and the radial core make the heater rods have more similar heat transfer characteristics to UO_2

than metal. However, since the difference in properties is not negligible, it must be considered in the design.

Table 5.6 Comparison of thermosphysical properties of nuclear fuel, heater rods, and structural materials (Hong and Lee, 2012; Popov and Carbajo, 2000)

Material	Property (unit)	Temperature (K)			
		300	400	600	800
SS ANSI 304 (Hong and Lee, 2012)	ρ_s* (kg/m^3)	7900	-	-	-
	C_{ps} (J/kg K)	-	515	557	582
	k_s (W/m K)	-	16.6	19.8	22.6
	$\rho_s C_{ps}$ (J/m^3 K)	-	4.07E+06	4.40E+06	4.60E+06
	α_s (m^2/s)	-	4.08E-06	4.50E-06	4.92E-06
SS ANSI 316L (Hong and Lee, 2012)	ρ_s* (kg/m^3)	8238	-	-	-
	C_{ps} (J/kg K)	-	504	550	576
	k_s (W/m K)	-	15.2	18.3	21.3
	$\rho_s C_{ps}$ (J/m^3 K)	-	4.15E+06	4.53E+06	4.75E+06
	α_s (m2/s)	-	3.66E-06	4.04E-06	4.49E-06
Nichrome (Hong and Lee, 2012)	ρ_s* (kg/m^3)	8400			
	C_{ps} (J/kg K)	-	480	525	545
	k_s (W/m K)	-	14	16	21
	$\rho_s C_{ps}$ (J/m^3 K)	-	4.03E+06	4.41E+06	4.58E+06
	α_s (m^2/s)	-	3.47E-06	3.63E-06	4.59E-06

* *Density at 300 K is used as a reference in calculation of thermal diffusivity and isothermal heat capacity per unit volume.*
*** The physical properties of the heater rods are obtained through individual contact with the manufacturer. Thermal conductivity, thermal capacity per unit volume, thermal diffusivity coefficient are calculated from an arbitrary design and only the physical properties at 800K, operating condition, are considered.*

Table 5.6 Comparison of thermosphysical properties of nuclear fuel, heater rods, and structural materials (Hong and Lee, 2012; Popov and Carbajo, 2000) (contd.)

Material	Property (unit)	Temperature (K)			
		300	400	600	800
Heater rod**	ρ_s* (kg/m^3)	-	-	-	-
	C_{ps} (J/kg K)	-	-	-	-
	k_s (W/m K)	-	-	-	4.70
	$\rho_s C_{ps}$ (J/m^3 K)	-	-	-	3.82E+06
	α_s (m^2/s)	-	-	-	1.23E-06
UO_2 (Popov and Carbajo, 2000)	ρ_s* (kg/m^3)	10413	-	-	-
	C_{ps} (J/kg K)	-	264.3	293.0	305.8
	k_s (W/m K)	-	6.58	5.14	4.17
	$\rho_s C_{ps}$ (J/m^3 K)	-	2.75E+06	3.05E+06	3.18E+06
	α_s (m^2/s)	-	2.39E-06	1.68E-06	1.31E-06

** Density at 300 K is used as a reference in calculation of thermal diffusivity and isothermal heat capacity per unit volume.*
*** The physical properties of the heater rods are obtained through individual contact with the manufacturer. Thermal conductivity, thermal capacity per unit volume, thermal diffusivity coefficient are calculated from an arbitrary design and only the physical properties at 800K, operating condition, are considered.*

5.2.1.5 PILLAR scale design using thermal-hydraulic similarity

This section describes the detail design of PILLAR by using the area-average scaling analysis method. Parameters related to the core power and thermal conditions are designated to be key parameters to the scale design among many parameters, in order to conserve the heat transfer characteristics between the prototype and the scale model as much as possible. Therefore, the thermophysical properties of the fuel rods and electrical heater rods are conserved as similar as possible between the prototype and the model. Other requirements are considered afterwards, independently.

The PILLAR scale design was determined as follows: firstly, the length ratio is chosen to be unity as in the basic design criteria. In addition, the similarities of the Time ratio number and the Biot number is not strictly conserved because it is difficult to be matched between the systems. In this case, most of parameters are rearranged as shown in Eqn. (5.44), but there is no need to have similarity in the parameters that are derived from the Time ratio number as described by Eqn. (5.45):

$$l_{0R}=1 \Rightarrow \begin{cases} \dot{q}_{s0R}=\left(\rho_s C_{ps}\right)_R \Delta T_{0R}{}^{3/2} \\ P_{0R}=a_{0R}\Delta T_{0R}{}^{3/2} \\ N_{rod,R}=k_{sR}{}^{-1}\Delta T_{0R}{}^{1/2}a_{0R} \\ a_{s0R}=N_{rod,R}\alpha_{sR}\Delta T_{0R}{}^{-1/2} \end{cases}, \text{ and} \tag{5.44}$$

$$d_{rod,R}=\alpha_{sR}{}^{1/2}\Delta T_{0R}{}^{-1/4} \text{ (not necessarily be conserved).} \tag{5.45}$$

Secondly, power density ratio and the diameter ratio between nuclear fuel rods and heater rods are designated to be unity so as to match the thermal characteristics of two rods:

$$\begin{aligned} &\dot{q}_{s0R} = \left(\rho_s C_{ps}\right)_R \Delta T_{0R}{}^{3/2} = 1 \\ &\Rightarrow\ \Delta T_{0R} = \left(\rho_s C_{ps}\right)_R^{-2/3} \Rightarrow \begin{cases} P_{0R} = a_{s0R} = \left(\rho_s C_{ps}\right)_R^{-1} a_{0R} \\ N_{rod,R} = k_{sR}{}^{-1}\left(\rho_s C_{ps}\right)_R^{-1/3} a_{0R} \end{cases} . \\ &d_{rod,R} \equiv 1 \end{aligned} \qquad (5.46)$$

Thirdly, for the flow area ratio, it is decided to use an appropriate value (1/200) so that the amount of LBE does not exceed the retaining amount according to the basic requirement. Additional conditions on physical properties, $(\rho_s C_{ps})_R = 1.200$ and $k_{sR} = 1.129$ by referring to Table 5.6, are applied to derive the conditions given in (5.47):

$$\left.\begin{array}{c} l_{0R} = 1 \\ \dot{q}_{s0R} = 1 \\ \Delta T_{0R} = \left(\rho_s C_{ps}\right)_R^{-2/3} \\ P_{0R} = a_{s0R} = \left(\rho_s C_{ps}\right)_R^{-1} a_{0R} \\ N_{rod,R} = k_{sR}{}^{-1}\left(\rho_s C_{ps}\right)_R^{-1/3} a_{0R} \\ d_{rod,R} \equiv 1 \end{array}\right\} \xrightarrow[a_{0R}=1/200,\ k_{sR}=1.129]{\left(\rho_s C_{ps}\right)_R=1.200} \begin{cases} \Delta T_{0R} = 0.8855 \\ P_{0R} = 0.004167 \\ N_{rod,R} = 0.004168 \end{cases} . \qquad (5.47)$$

Finally, using the above relations leads to the establishment of requirements on the PILLAR core power output and number of heater rods as

seen in (5.48). Table 5.7 shows the final design values with this four-step approach.

$$\begin{aligned} P_{0R} = 0.004167 &\xrightarrow{P_{0p}=100000\text{kW}} P_{0m} = 417\text{kW} \\ N_{rod,R} = 0.004168 &\xrightarrow{N_{rod,p}=6480} N_{rod,m} = 27 \end{aligned} \tag{5.48}$$

Table 5.7 PILLAR design specifications for flow area reduction ratio 1:200

Specification	Unit	Prototype (URANUS); p	Scale model (PILLAR); m	Scale; m/p
Core power	kW	100000	417	0.00417
Total amount of LBE	ton	470	2.51	0.00534
Core inlet/outlet temperature difference	°C	153	135	0.886
Core inlet (heat exchanger outlet) temperature	°C	304	304	-
Core outlet (heat exchanger inlet) temperature	°C	457	440	-
Total amount of fuel rod/heater rod	-	6480	27	0.00417
Outer diameter of fuel rod/heater rod	m	0.0158	0.0158	1.00
Total heat transfer area	m^2	578.97	2.41	0.00417
Power given by a single fuel rod/heater rod	kW	15.43	15.43	1.00
Linear power given by a single fuel rod/heater rod	kW/m	8.57	8.57	1.00
Heat flux given by a single fuel rod/heater rod	W/m^2	1.73E+05	1.73E+05	1.00
Core volumetric power density	W/m^3	4.37E+07	4.37E+07	1.00

Table 5.7 PILLAR design specifications for flow area reduction ratio 1:200 (contd.)

Specification	Unit	Prototype (URANUS); p	Scale model (PILLAR); m	Scale; m/p
Effective thermal conductivity of fuel rod/heater rod	W/mK	4.17	4.70	1.13
Effective thermal diffusivity of fuel rod/heater rod	m^2/s	1.31E-06	1.23E-06	0.941
Volumetric heat capacity of fuel rod/heater rod	J/m^3K	3.18E+06	3.82E+06	1.20
LBE average velocity at core outlet	m/s	0.3123	0.2631	0.940
LBE mass flow rate	kg/s	4546.0	21.37	0.00468
Total pressure loss of system	Pa	9743.5	8456.5	0.886

5.2.2 Final design of PILLAR

As described in the previous sections, PILLAR had been designed to be a pool-type experimental facility conserving the axial height of each component while reducing the flow area with a reduction ratio of 1:200 through comprehensive reviews on the scaling analysis methods. In order not to distort the LBE behaviors in the prototype as much as possible, PILLAR was designed to have the pool configuration as well. Considering the geometrical size of the facility, it forms a dual piping structure of outside reactor vessel with inner barrels.

Even if the scale facility has a design of reduction in the flow area, it is inevitable to have a slight distortion to some extent. Originally, the steam generator in URANUS consists of eight independent modules in total; but in PILLAR, it has one single heat exchanger that is comprised of 3 vertically downward feedwater pipes, a chamber, and 21 vertically upward tubes. In addition, the LBE reflector region, which is made up of stagnant LBE so that the coolant itself can be used as a neutron reflector in the actual reactor core, is not considered since it has no importance in the thermal-hydraulic point of view. Furthermore, all components were configured with piping with an ANSI standard profile, i.e. SCH 40, by taking into account the fabrication. As discussed, the area-average method regards each of hydrodynamic regions as the composition of length, (hydraulic) diameter, and flow area. Therefore, if the flow area distortion of components is not large with proper flow areas, the distortion of the entire system's behaviors given by the partial configuration adjustment will not be significant.

In this section, the specifications of components comprising the thermal-hydraulic system of PILLAR are described in the following subsections. Figure 5.3 shows the final design of the facility with an isomeric view, a disassembly view and an actual photograph; the name of each part is also denoted in the isomeric view or in the disassembly view. For a consistency, components that consist of internal structure are designated to be barrels while those that comprise of outer structure are named as vessels.

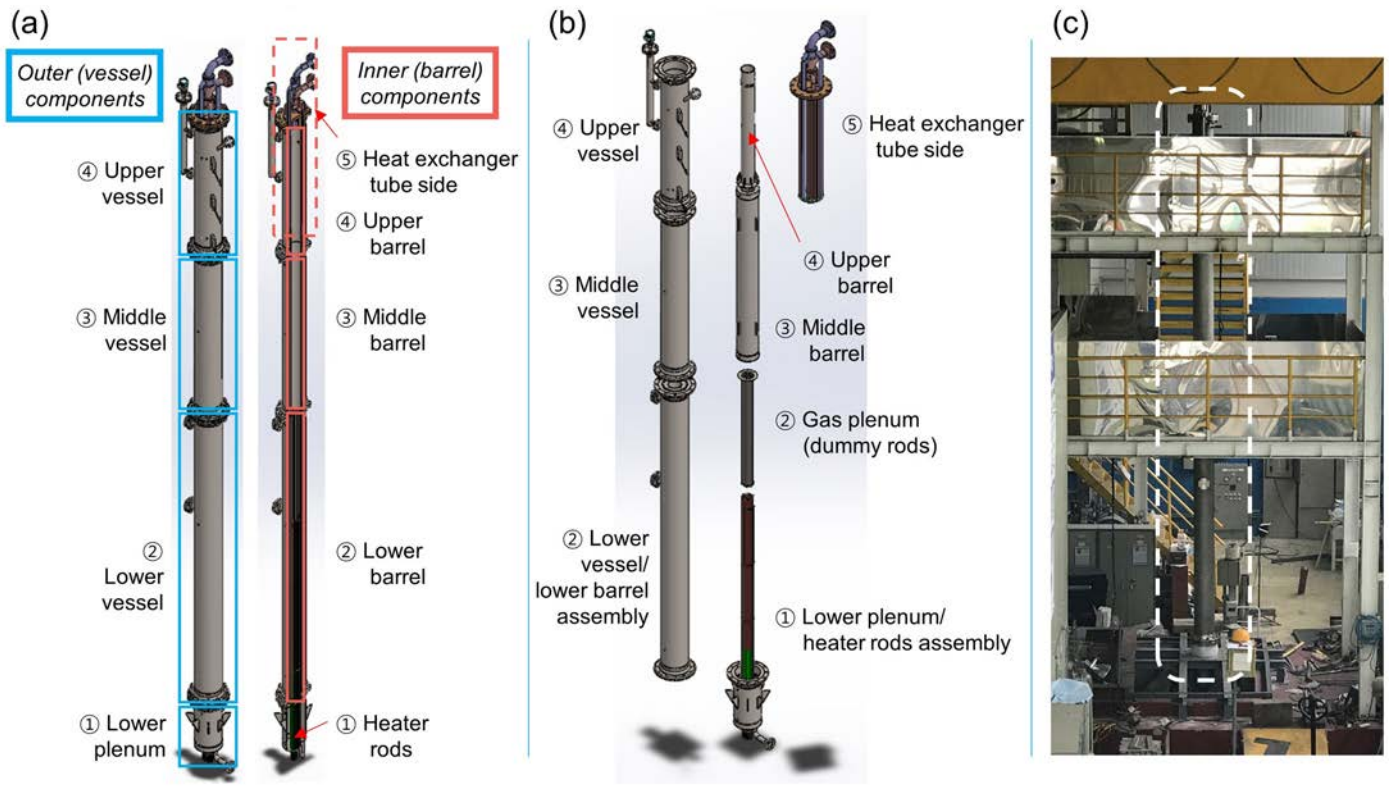

Figure 5.3 (a) Isomeric view (left) and cross-sectional view (right), (b) disassembly view, and (c) photo (white dash) of PILLAR main vessel

5.2.2.1 Lower plenum and heater rods assembly

As indicated in Figure 5.3 (b) the disassembly view of the PILLAR main vessel, the lower plenum and heater rods are combined together as an assembly. Hereafter, all the names of other components are provided by the dissembly view. It consists of the lowest part of the PILLAR main vessel. In the prototypic reactor, the lower plenum is the lowest part of the reactor vessel, which is the region through which LBE came from the downcomer passes before going into the core. It is a large pool and the flow direction changes according to the position, resulting in a local velocity field distribution. The same applies to the lower plenum of PILLAR, while the difference is that the extension of the heater rods penetrates through this region. Figure 5.4 shows the three-dimensional model of the lower plenum and heater rods assembly in several points of views including isomeric, cross-sectional, top, and bottom views.

Unlike nuclear fuel, since the heater rods installed in PILLAR cannot generate heat spontaneously with nuclear reaction, they must have electrical connections at least on one point, such as the top, bottom, or any points on their sides, to provide electrical power. Such connections eventually require multiple power cables, which cannot maintain integrity in high-temperature, about 300 °C, and liquid metal environments. Therefore, a part of the heater rod is extended to the lower end of the vessel to support the rod in the vertical direction while supplying electric power as shown in Figure 5.5. The heating part is as long as 1,800 mm while the non-heating part that is elongated from the end of heating part is about 1,200 mm. At the top of a heater rod, another

non-heating element called end pin is included as a finishing material. In this regard, this extension of non-heating element led to the connection of two elements as a single assembled component joined by welding at each of joints where the heater rods and the vessel meet. This connection is described in the inset (d) in Figure 5.4.

As determined in the final design stage, 27 heater rods were installed in the facility as shown in Figure 5.6. Since the similarity in geometrical arrangement of fuel or heater rods was to be conserved, the heater rods were arranged in a triangular lattice structure while the distance between heater rods was the same with the prototypic reactor as well. They consist of two different voltage ratings, namely with 380 V (rod numbers 7-27 in Figure 5.6) and 460 V (rod numbers 1-6 in Figure 5.6), with the same power rating, 15.5 kW, so that they can be operated under the electrical circumstances of the site where PILLAR is located. Furthermore, the heater rods with voltage rating with 380 V are divided into two groups due to a similar reason on the electrical situations. One group consists of the heater rods Nos. 9, 10, 13, 14, 17, and 18 while the other heater rods with 380 V voltage rating are grouped and controlled as a whole.

In order to prevent the shaking of the rods possibly given by LBE flow, three grid spacers are installed in the axial direction. The design and axial positions of those grids spacers are depicted in Figure 5.7. They were manufactured by electro-discharge machining and wire cutting techniques from a stainless steel plate with 10 mm thickness. Three additional skeletal bars provide a sturdy support among the spacers while the ring on the spacers do not

touch or grab the rods since their inner diameter are slightly larger than the outer diameter of heater rods. In addition, several thermocouples are mounted on the grid plates to measure temperature distribution inside the core region. The detailed information on the temperature measurement is summarized in Section 5.2.2.8.

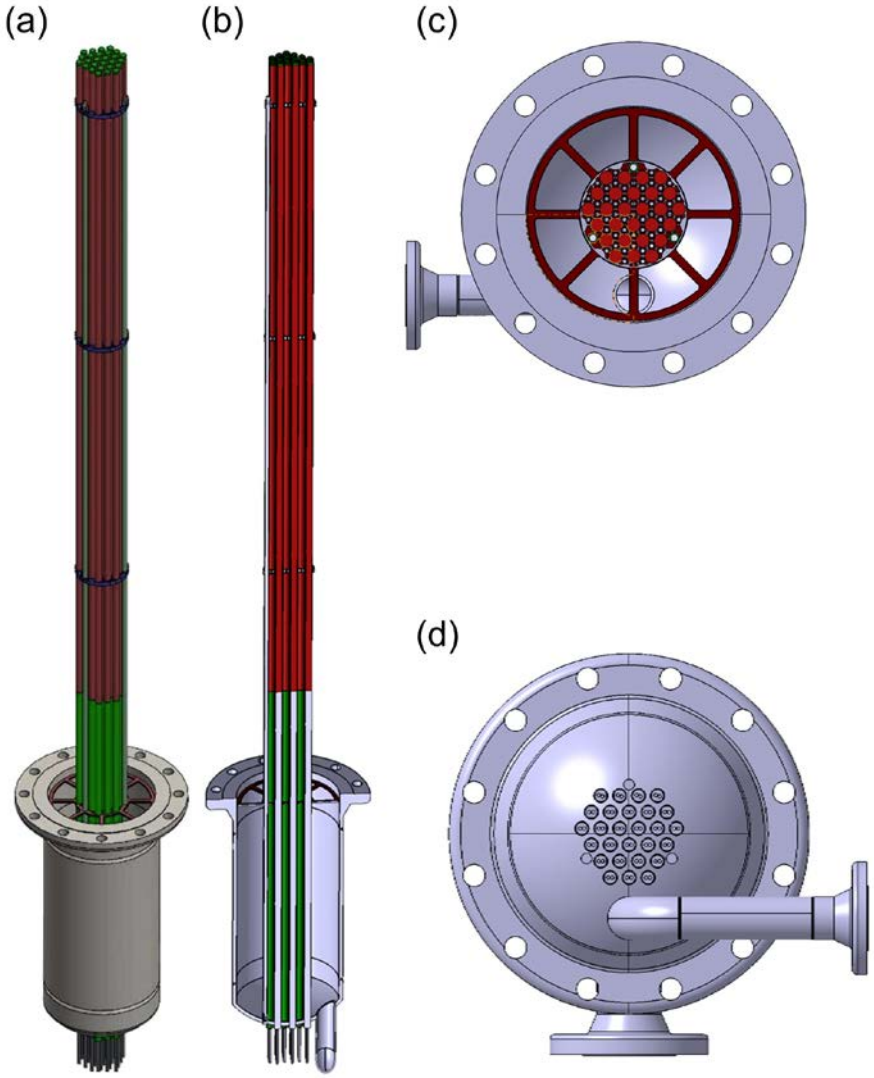

Figure 5.4 Three-dimensional model of PILLAR lower plenum and heater rods assembly in several viewpoints. (a) Isomeric view, (b) cross-sectional view in z-direction, (c) top view, and (d) bottom view

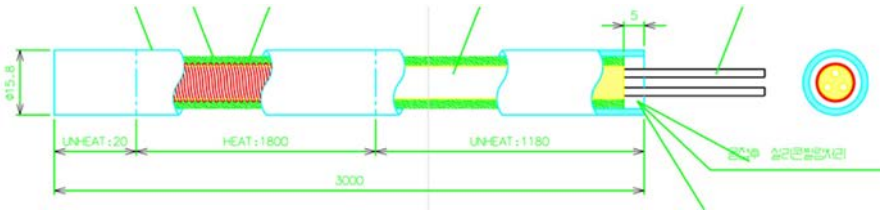

Figure 5.5 Schematic diagram of PILLAR heater rod

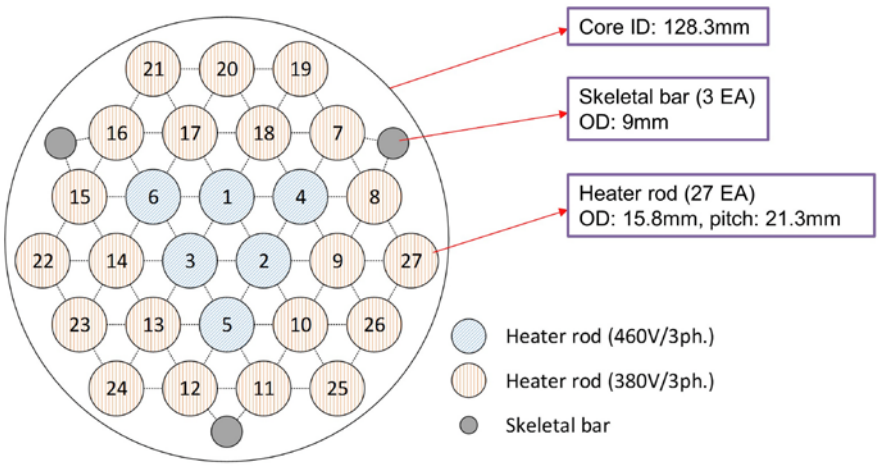

Figure 5.6 Heater rod and skeletal bar arrangement inside the core region of PILLAR

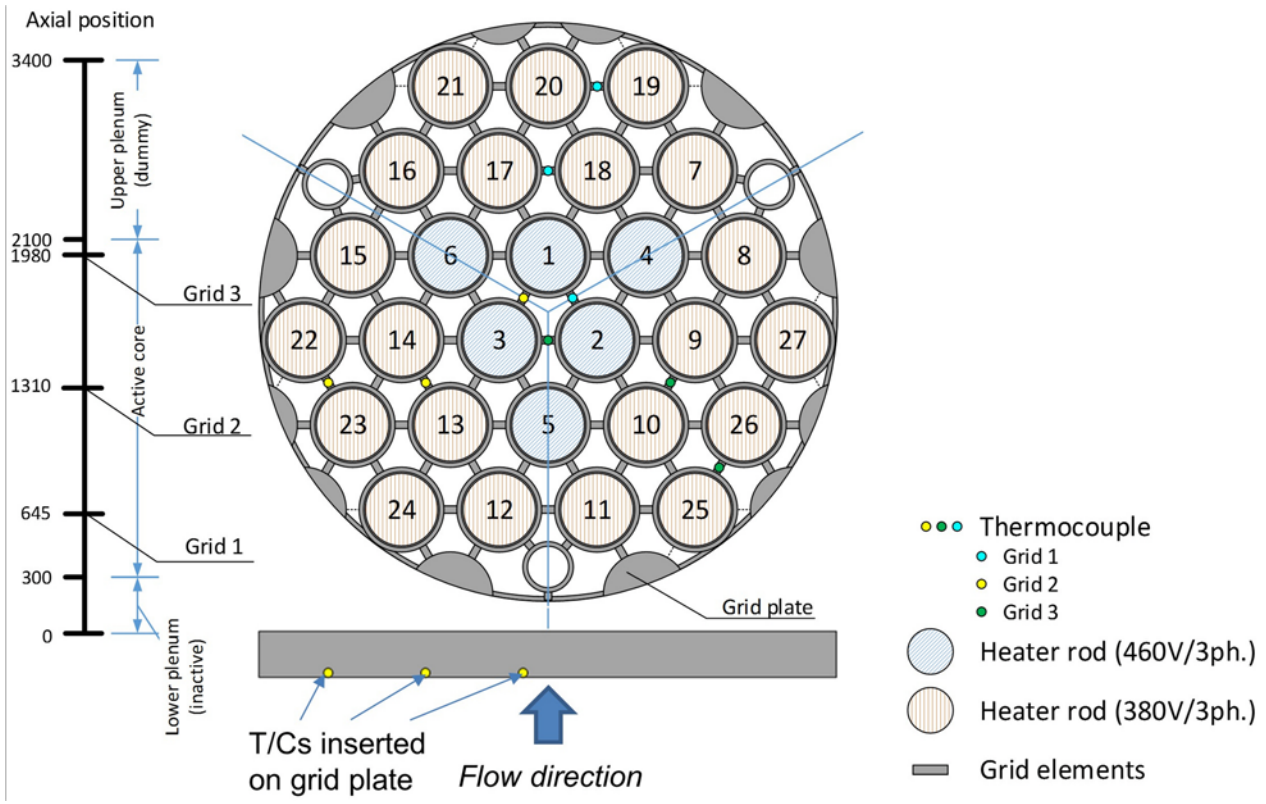

Figure 5.7 Design and axial positions of PILLAR core grid spacers and thermocouple location upon each plate

5.2.2.2 Lower vessel and lower barrel assembly

Since the design of PILLAR is a shell-in-shell configuration, it is difficult to keep an external shell and an internal piping on the concentric axis and to maintain the latter from shaking or moving. Therefore, the lower vessel and lower barrel assembly was designed to include several regions such as lower plenum, core, gas plenum and a lower part of downcomer by constructing concentric configurations. Figure 5.8 shows the three-dimensional model of the lower vessel and lower barrel assembly in various viewpoints with isomeric, cross-sectional, and top views.

In the prototypic reactor, the nuclear fuel rod lies within three regions, the lower plenum, core, and gas plenum. As shown in the previous section, the non-heating element of heater rod supports the rod itself with extrusion through the lower vessel that simulates the lower plenum region. On the other hand, the remaining upper part, gas plenum, needs to have the extension from each of heater rods to conserve the similarity within the region. To do so, another assembly consist of non-heating dummy rods are installed to mimic flow configuration inside the gas plenum as depicted in Figure 5.9. The dummy rods are placed on the top of the assembly and right above the heater rods through the upper plenum region. Since the gas plenum is thought to be an extension of fuel rods, the arrangement of dummy rods are identical to that of heater rods as also shown in the inset (c) in Figure 5.9.

Contrary to URANUS, there are no neutron reflector and/or shielding region in PILLAR, which are placed in the outside of the core in radial direction.

It is expected that LBE flow rate is extremely low in the reflector region while no LBE flow exists inside the shielding region. In this consideration, those parts were excluded in the experimental setup. However, those non-flow region still needs to exist physically for the conservation of geometrical similarity between the prototype and scale facility. Therefore, to eliminate those parts while avoiding geometrical distortion, two inner barrels were included as in a concentric, double-wall structure without filling inside between the barrels. In addition, since the double piping naturally creates an empty space, heat transfer can be effectively suppressed, which contributes to prevent unnecessary heat transfer in the radial direction, leading to a reduction of heat loss through the internal walls.

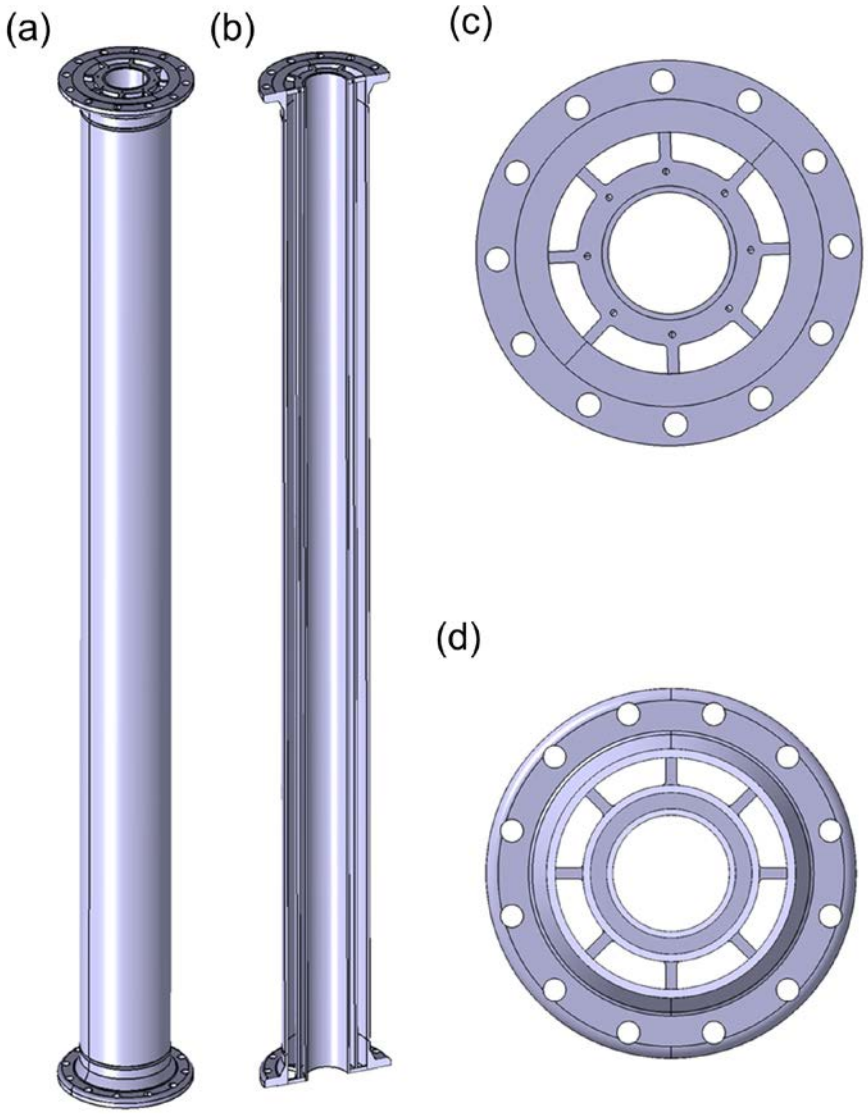

Figure 5.8 Three-dimensional model of PILLAR lower vessel and lower barrel assembly in several viewpoints. (a) Isomeric view, (b) cross-sectional view in z-direction, (c) top view, and (d) cross-sectional view in radial direction

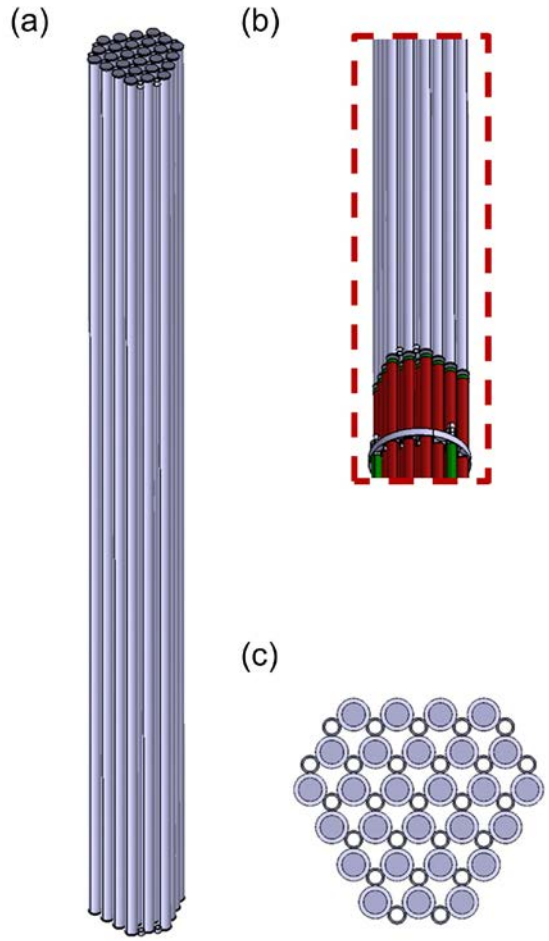

Figure 5.9 Three-dimensional model of PILLAR dummy rod assembly in several viewpoints. (a) Isomeric view, (b) detail view on the interface with heater rods, and (c) top view

5.2.2.3 Middle barrel

The middle barrel is a component dividing two flow regions, the upper part of downcomer and the lower part of riser, which refers to the downstream region of gas plenum and the upstream of heat exchanger, as shown in Figure 5.10. Similar to the lower barrel, the middle barrel also adopts double-wall structure in radial direction. The inset (c) of Figure 5.10 describes eight fins on the surface of the barrel in the radial direction, which provide a firm position to the middle barrel on the concentric axis and out of eccentricity with the outermost shell, the middle vessel. To minimize the unnecessary flow resistance given by flanges and bolts, two bolt covers that surrounds the flanges at both ends of the barrel are provided, as depicted in the inset (d) of Figure 5.10.

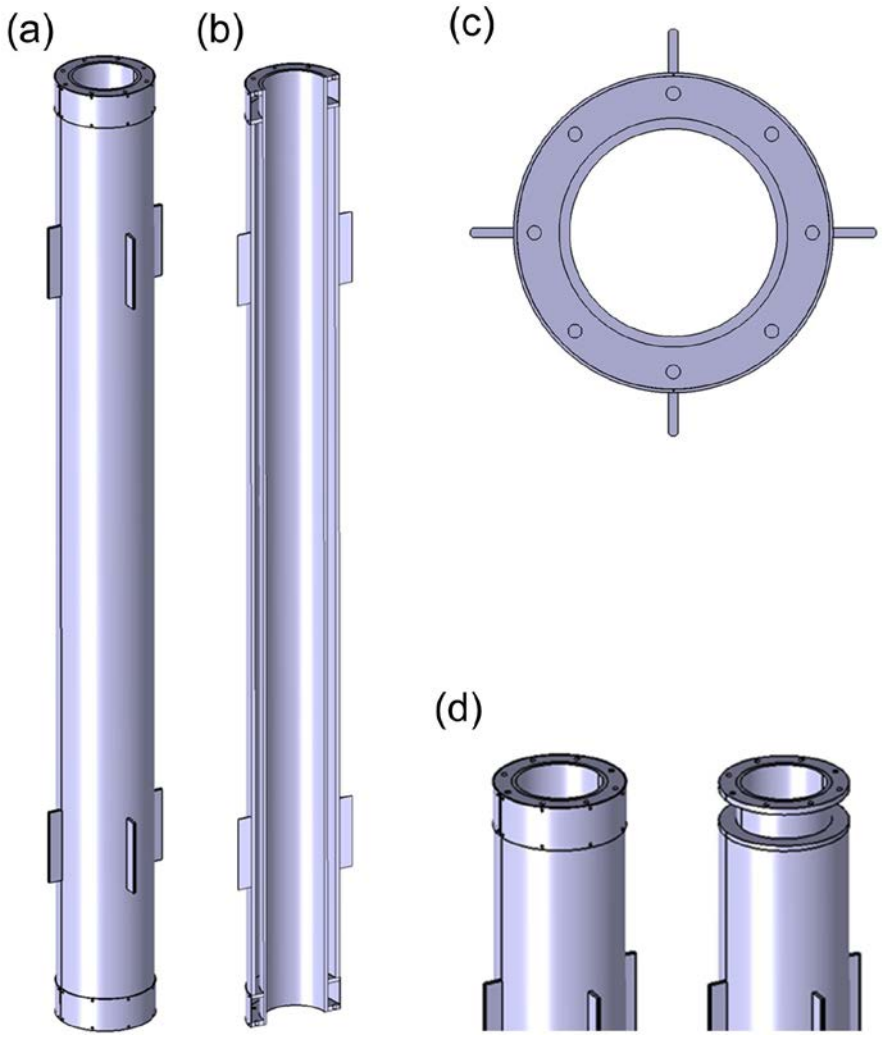

Figure 5.10 Three-dimensional model of PILLAR middle barrel in several viewpoints. (a) Isomeric view, (b) cross-sectional view in axial direction, (c) top view, and (d) bolt cover application to middle barrel (left) and middle barrel without the bolt cover (right)

5.2.2.4 Upper barrel

Figure 5.11 shows the upper barrel that is a component dividing two flow regions, the shell side of heat exchanger and the upper part of riser, similar to the middle barrel. The most distinct feature compared to the middle barrel is that it does not have the double-walled structure to radial direction so that the shell side of heat exchanger have an enough flow area. As shown in Figure 5.12, it also has three windows through which LBE can flow to the shell side while it is connected with the middle barrel with a flange on the bottom. In order to have a margin for the LBE level control, it is elongated for about 300 mm above the windows. In actual experimental situations, an additional piping attached to the upper vessel that has a waveguide radar level sensor controls the free surface level of LBE. Figure 5.13 shows the radial arrangement of those windows. The positions of windows were intended to have an effective heat transfer from LBE to pressurized water through large heat transfer area with several tubes. Detailed descriptions on the heat exchanger and upper vessel are provided in the next chapter.

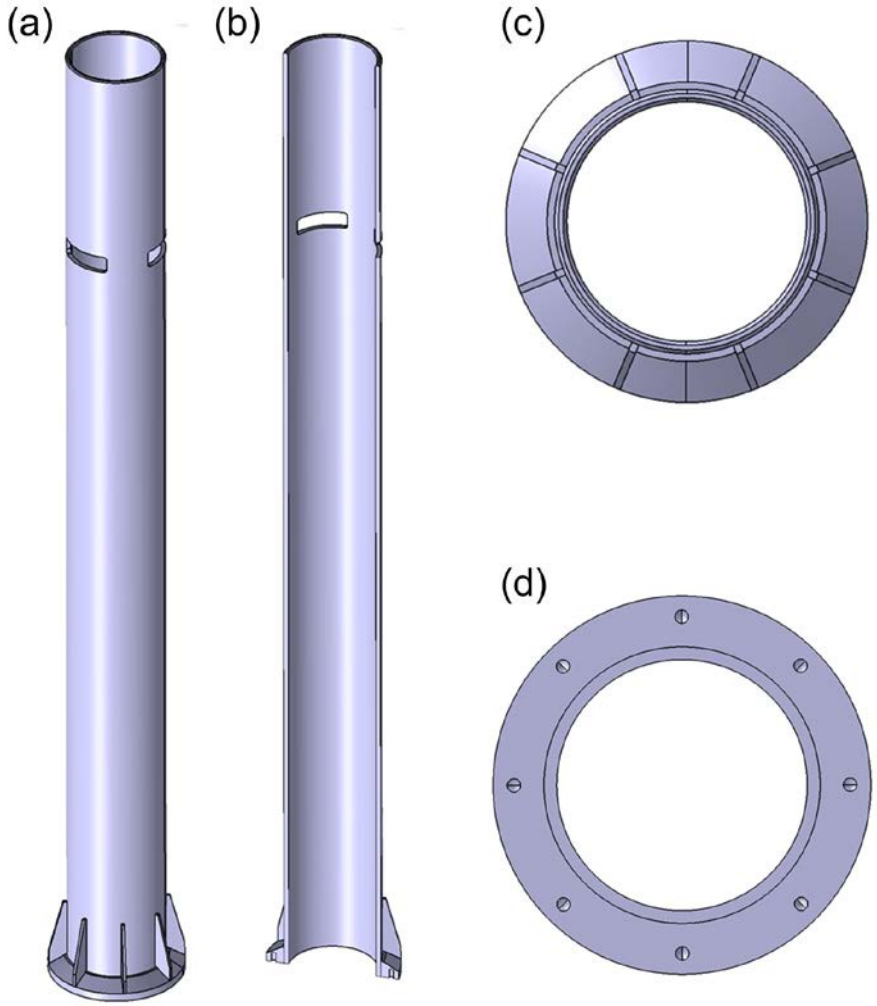

Figure 5.11 Three-dimensional model of PILLAR upper barrel in several viewpoints. (a) Isomeric view, (b) cross-sectional view in axial direction, (c) top view, and (d) bottom view

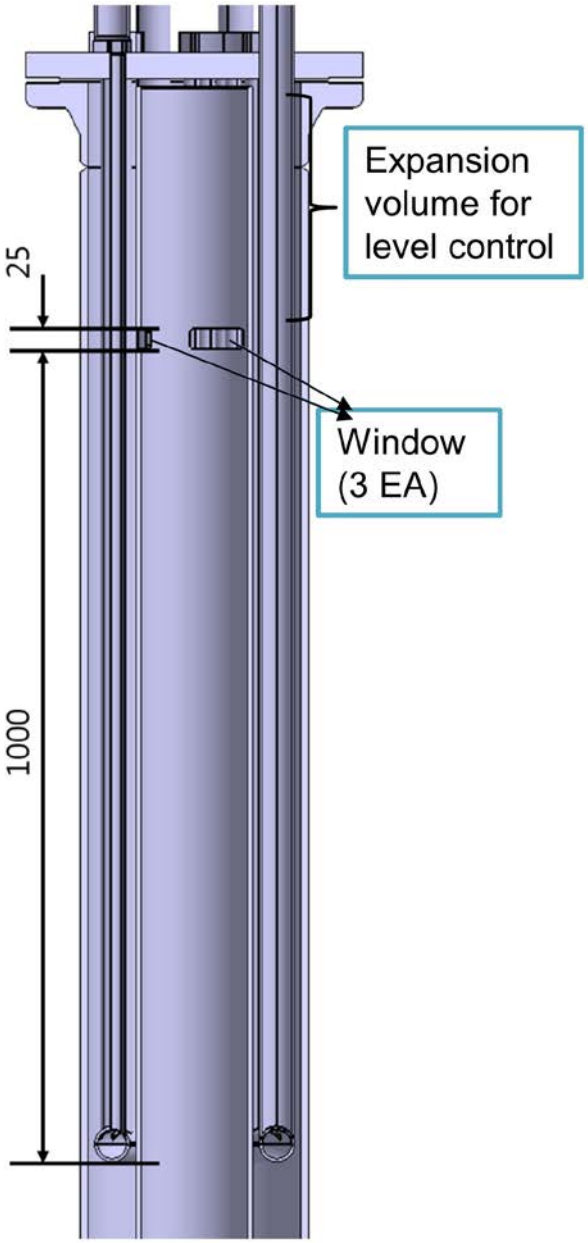

Figure 5.12 Axial position of windows on PILLAR upper barrel and expansion volume for LBE level control with respect to heat exchanger shell side

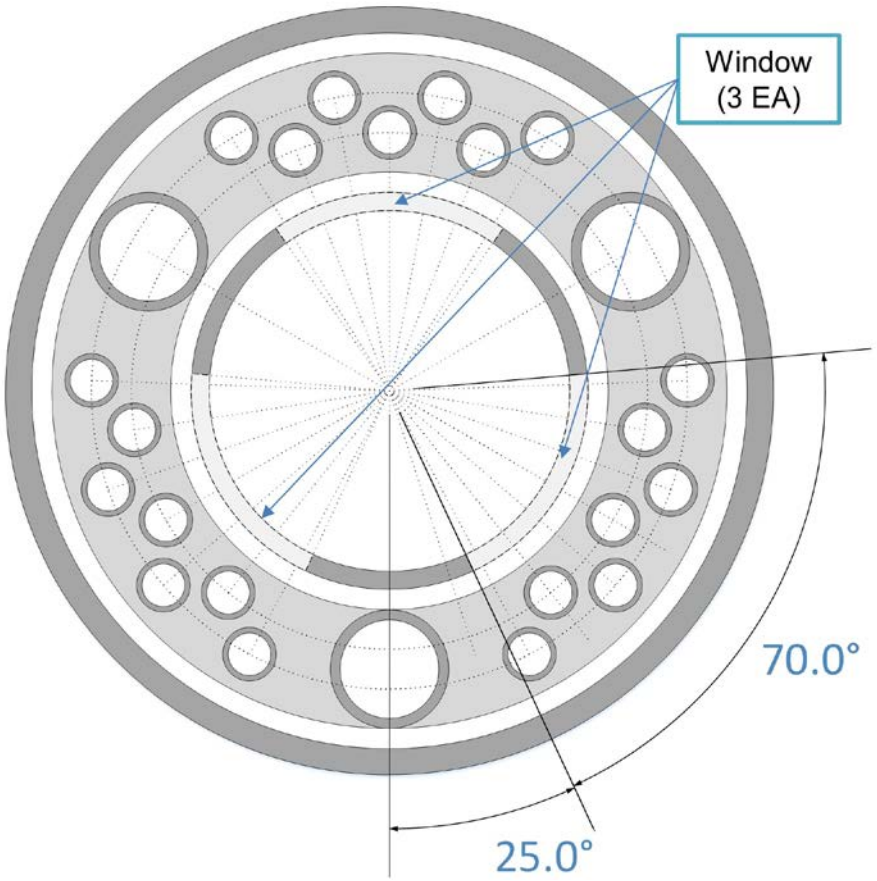

Figure 5.13 Radial position and arrangement of windows on PILLAR upper barrel with respect to heat exchanger and upper vessel

5.2.2.5 Upper vessel

The upper vessel is the outermost shell consisting of the heat exchanger shell side as depicted in Figure 5.14. The heat exchanger tube side is connected with the upper vessel on the top with a flange so that pressure boundary is established while the bottom end is joined with the middle vessel. With the same region for the level control as in the case of upper barrel, this component was elongated about 300 mm. Several instrumental probes are installed through the wall of upper vessel to measure LBE temperature and flow velocity within the shell side of heat exchanger.

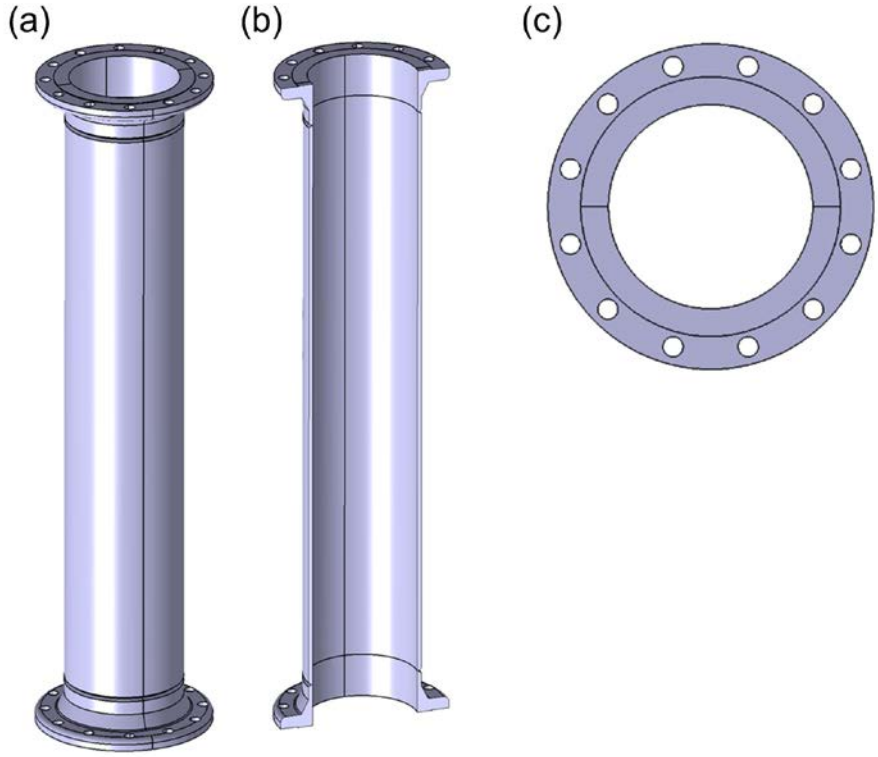

Figure 5.14 Three-dimensional model of PILLAR upper vessel in several viewpoints. (a) Isomeric view, (b) cross-sectional view in axial direction, and (c) top (bottom) view

5.2.2.6 Heat exchanger tube side

The tube side of heat exchanger shown in Figure 5.15 is a key component of PILLAR main vessel, which works as a heat sink that drives LBE natural circulation flow in non-isothermal conditions. It is located inside of the upper vessel within which the shell side of heat exchanger is established with LBE flow and power generated from the core region is transferred to water. As aforementioned, the connection with the upper vessel forms the pressure boundary of PILLAR main vessel and it makes this region to work as a level control system as well. Thus, it is also required that all of the attached tubes were elongated about 300 mm.

The tube side of heat exchanger consists of several tubes for heat transfer from LBE, a top flange, and water chambers connected to the tubes as depicted in the insets (a) and (b) of Figure 5.15. The tubes are categorized by their diameters, which include three downward tubes with a standard dimension with ANSI SCH 40 1-1/4" and 21 upward tubes having 19.05 mm of outer diameter, defined by the direction of water inside those tubes. These tubes are arranged in azimuthal symmetry of 120˚ to prevent distortion that may arise by local flow distribution. A schematic diagram, Figure 5.16, shows the arrangement of those tubes and connection between the lower water chamber. As described in Section 5.2.2.4, the three windows on the upper barrel are arranged so that they ensure an efficient heat transfer at a large area of heat transfer for LBE to face the 21 upward tubes.

Since the cooling of primary side of PILLAR main vessel was

intended to be done with slightly pressurized water, about 8-10 bars, through forced convection given by a centrifugal pump, all the tubes were selected to be withstand that pressure and a pressure test under 25 bars were conducted to confirm the integrity of welding. In a working condition, water enters into the inlet pipe then divided into three downward tubes. After flowing along with those tubes, it is distributed in a lower torus-type chamber, which has the same diameter with the downward tubes as shown in the inset (e) of Figure 5.15, and then flows through the upward tubes. All of water flow is gathered in three upper water chambers connected to seven tubes each as described in the inset (f) of Figure 5.15. Those three-way flows are finally merged in the water outlet and pumped to the ultimate heat sink in the secondary side, the cooling tower.

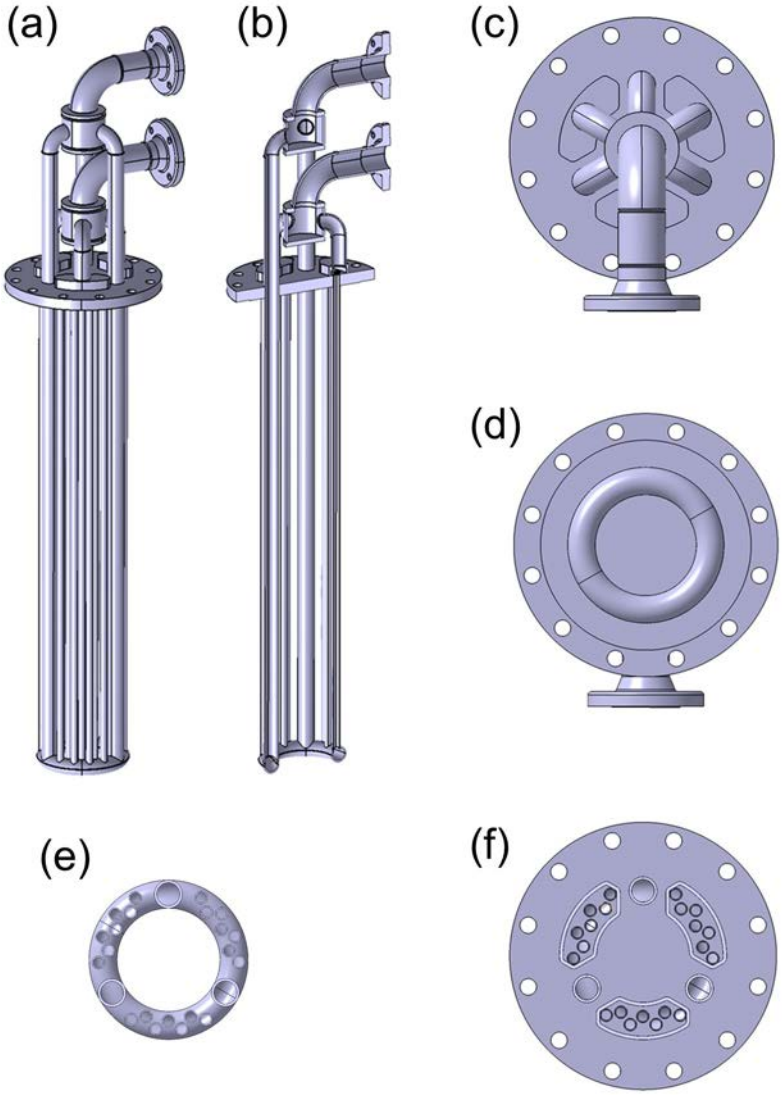

Figure 5.15 Three-dimensional model of PILLAR heat exchanger tube side in several viewpoints. (a) Isomeric view, (b) cross-sectional view in axial direction, (c) top view, (d) bottom view, (e) cross-sectional view of lower chamber, and (f) cross-sectional view of upper chambers

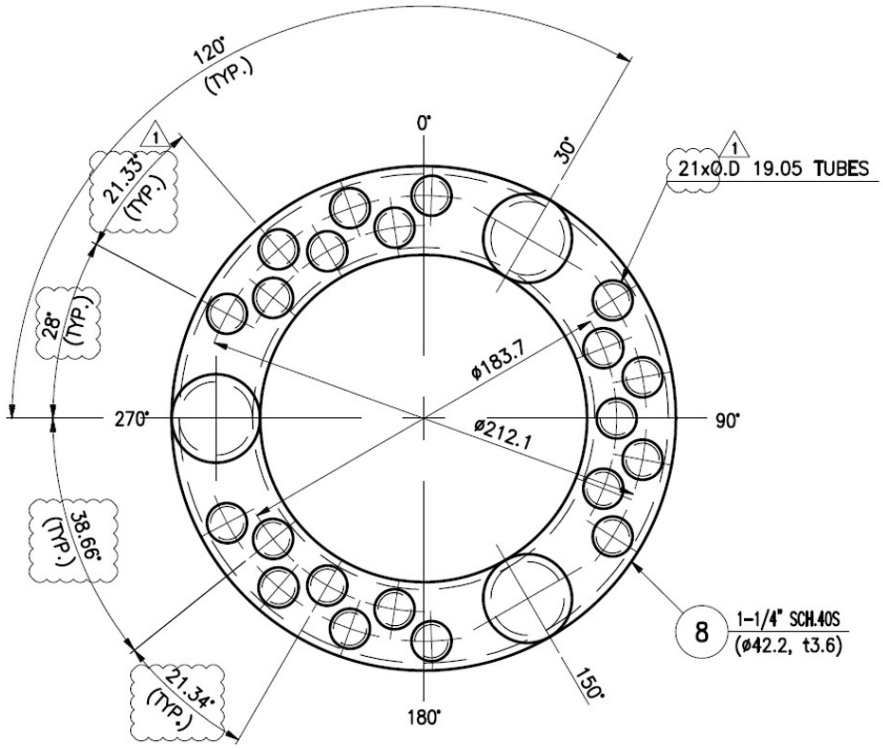

Figure 5.16 Schematic diagram of lower water chamber and tube arrangements of PILLAR heat exchanger tube side

5.2.2.7 Middle vessel

As discussed in Section 5.2.2.2, the downcomer region of PILLAR is divided into two parts, the lower vessel and middle vessel. Figure 5.17 shows the three-dimensional model of the middle vessel in numerous points of view with isomeric, cross-sectional, and top (bottom) views. Through the outer wall of the vessel, several instrumentation probes are installed to measure LBE cold leg temperature in the downcomer.

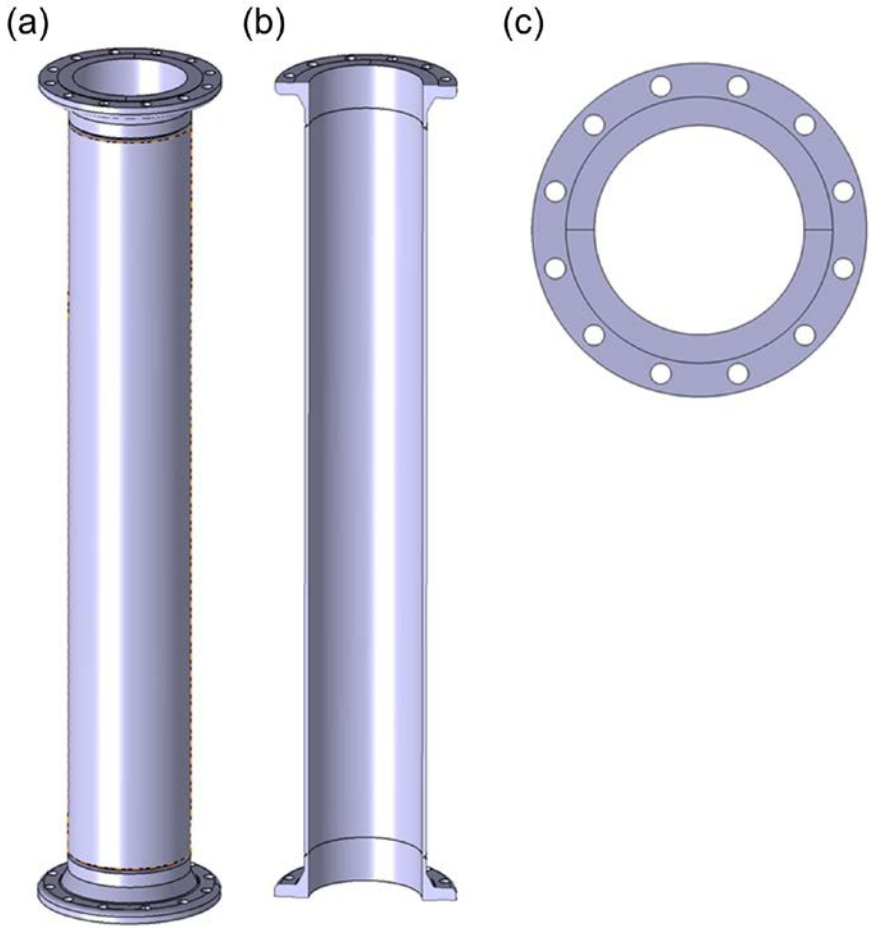

Figure 5.17 Three-dimensional model of PILLAR middle vessel in several viewpoints. (a) Isomeric view, (b) cross-sectional view in axial direction, and (c) top (bottom) view

5.2.2.8 Instrumentation system of PILLAR

PILLAR is designed in the shell-in-shell configuration unlike general loop-type experimental facilities so that there are additional characteristics to be considered for installation and operation of sensors. For example, in the case of downcomer, it is possible to measure the flow by inserting a probe (radially) through or by putting on the sensor the outermost shell, but it is not possible for innermost regions, such as core, upper plenum, and riser. In addition, too many penetrations are not favorable on the viewpoint of assembly and operation because the probes installed through those penetrations interfere with the structure.

For material compatibility, it is not easy to select the material of the lead wire connected to the probes, since LBE temperature is high and chemically reacts with a number of metals. Therefore, it is important to reduce the number of sensors inside the inner shell as much as possible, and to arrange the sensors so that the measurements can be performed only with the limited number of probes. In accordance with this principle, the number of sensors included in the inner shell was determined to be nine Type K thermocouples inside the core region and the remaining sensors are located other than the inner shell region.

Since the heater rods and heat exchanger tubes are installed symmetrically, if the proper position is selected, the flow characteristics can be indirectly grasped without installing sensors to most of parts. Focusing on the measurement of the core and heat exchanger shell side, the instrumentation

system of PILLAR is elaborated. Table 5.8 summarizes the requirements applied to the selection of instrumentation probes and the role of each of sensors. The remaining instrumentation system is not introduced in detail but illustrated on the schematic diagram of the instrumentation system, as shown in Figure 5.18.

As mentioned earlier, the sensors to be included in the internal piping are limited to the core region. This is because the core receives the power from the heater rods, so that the temperature change of the LBE is expected to be the largest. In addition, this region is more important in the thermal-hydraulic point of view as it simulates the actual core in the prototypic reactor. However, there are also limitations in the core region since there are many heater rods that reduces free volume. If the probes are excessively inserted, it may go through some unexpected results by the flow interference from the probes.

To do so, thermocouples were installed, which can easily measure the temperature field inside the core region while their physical dimensions are small enough. However, there is a remaining problem to this configuration because the lead wire connected to the thermocouple is also in contact with the high temperature LBE. Hence, all the thermocouples in the core region were designated to be installed on the three grid spacers, illustrated in Section 5.2.2.1, so that they could remain their positions without disturbing the flow.

Figure 5.7 shows the installation plan and the position of each thermocouple accompanied by the arrangement of the heater rods. The thermocouples were placed on thin plates that connects the support rings in the grid spacers in order not to disturb the flow as much as possible. In addition,

the probes were installed at the bottom of the grid spacers because the flow direction is from bottom to top. Each of grid plates have tiny grooves to accommodate the tips of thermocouples and to prevent them from leaving their positions.

Figure 5.19 illustrates the positioning rationale of the thermocouples. It was done by dividing the region of interest into three zones, depicted by Zones 1, 2, and 3, in the radial direction, and by placing the thermocouples that represent the zone at the center of each zone. Since the arrangements of heater rods have a symmetry in azimuthal direction by 120°, temperature is measured at nearly constant intervals in the radial direction if three thermocouples are placed on each of the grid spacers.

The shell side of PILLAR heat exchanger is located between the inner shell and the external piping through which the flow region is easy to access. In this region, fluid temperature, the outer wall temperature of the heat exchanger tubes, and the LBE flow rate in terms of flow speed are measured. In the case of the LBE temperature measurement, relatively thick thermocouples are installed through the wall to measure it at several positions similar to the core region. The flow rate, in other words, flow speed of LBE is measured with Pitot tubes, which is actually measured by measuring the differential pressure at the locations where the tips of Pitot tubes are located, since the flow velocity is able to be converted from the local pressure measurements. In this case, the pitot tube is also inserted through the outermost pipe, and since it has a curvature perpendicular to the flow direction at the tip portion of the pitot tube, small ducts are attached to a part of the outermost pipe

and each pitot tube is inserted through the ducts. The outer surface temperature of the tube is measured with thin thermocouples that are used in the core region by welding them to the tube surface.

As in the case of the core region, the probes are installed by the azimuthal symmetry. In this regard, only a small part was targeted to have the penetrations so that those would not affect the assembly and/or disassembly process. The axial and radial positions of each of probes are shown in Figure 5.20. Three planes A, B, and C in the axial direction and planes 1, 2, and 3 in the azimuthal direction were arbitrarily chosen to impose different positions. Most of the probes are located on the lines made by those planes and the location is labeled first in the azimuthal direction and then in the axial direction. As depicted in Figure 5.21 and Figure 5.22, three Pitot tubes are on the 1-A, 1-B and 1-C lines while six thermocouples for LBE temperature measurement are on the 2-A, 2-B, 2-C, 3-A, 3-B, and 3-C lines. The number of thermocouples used to measure the temperature outside the tube varies depending on the size of the heat exchanger tube. For the surface temperature measurement on upward pipes, the 1-A and 1-B lines are used while two thermocouples each were installed on the surface of downward tube on plane A and plane B.

Table 5.8 Measurement requirements of PILLAR instrumentation system

System	Type	Parameter to be measured	Precision requirement
Primary system	Type K thermocouple	LBE temperature, environmental temperature	±1 K
	Differential pressure transducer with pitot tube	Local LBE flow velocity/dynamic pressure	±2%
	Pressure transducer	Pressure of pressure boundary above LBE free surface	0.25% (full range)
	Level sensor	LBE free surface level	±2 mm
Secondary system	Type K thermocouple	Water temperature	±1 K
	Electromagnetic flowmeter	Water volumetric flow rate	0.5% (full range)
	Pressure transducer	Water pressure	0.25% (full range)
Auxiliary system	Type K thermocouple	LBE temperature	±1 K
	Pressure transducer	Pressure of pressure boundary in LBE storage tank	0.25% (full range)
	Load cell	LBE mass in LBE storage tank	±10 kg

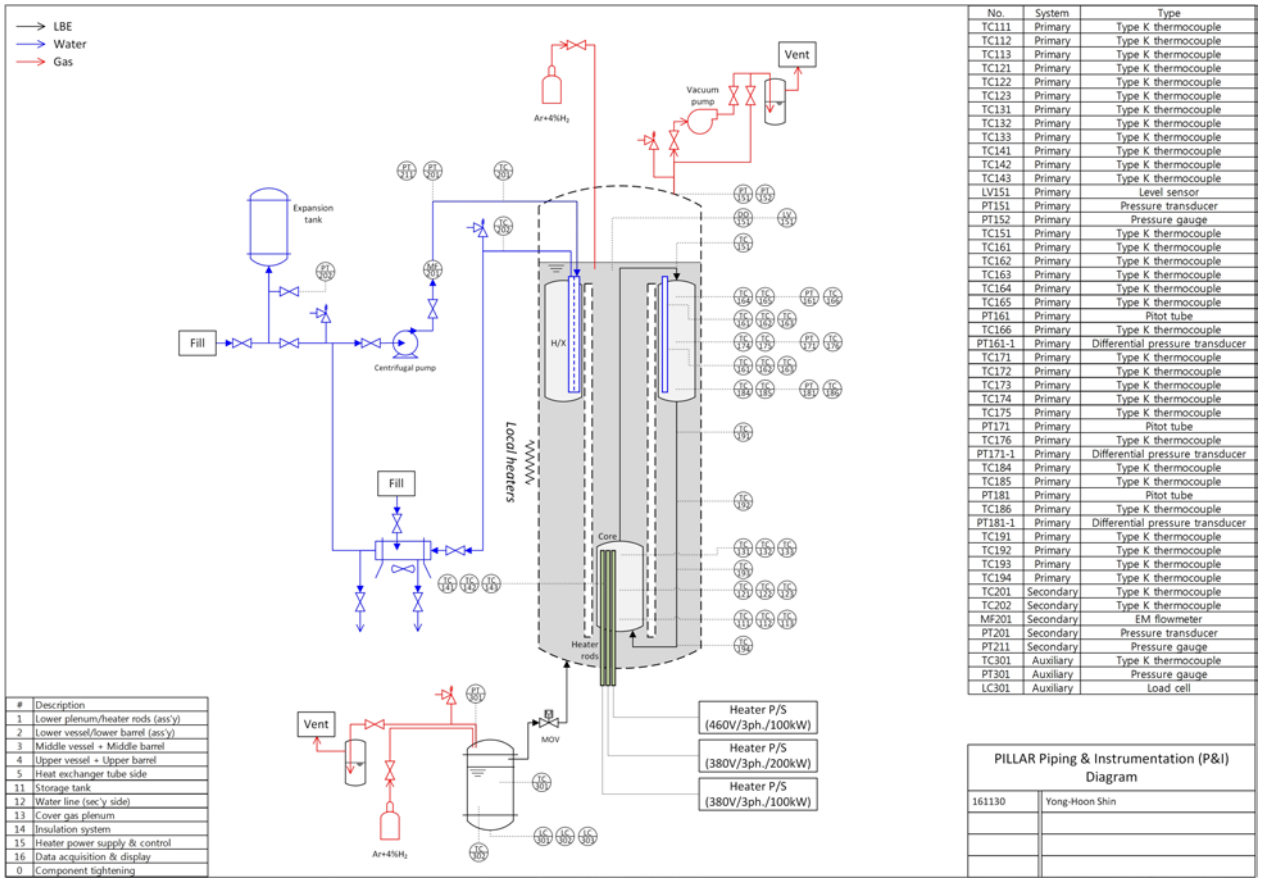

#	Description
1	Lower plenum/heater rods (ass'y)
2	Lower vessel/lower barrel (ass'y)
3	Middle vessel + Middle barrel
4	Upper vessel + Upper barrel
5	Heat exchanger tube side
11	Storage tank
12	Water line (sec'y side)
13	Cover gas plenum
14	Insulation system
15	Heater power supply & control
16	Data acquisition & display
0	Component tightening

No.	System	Type
TC111	Primary	Type K thermocouple
TC112	Primary	Type K thermocouple
TC113	Primary	Type K thermocouple
TC121	Primary	Type K thermocouple
TC122	Primary	Type K thermocouple
TC123	Primary	Type K thermocouple
TC131	Primary	Type K thermocouple
TC132	Primary	Type K thermocouple
TC133	Primary	Type K thermocouple
TC141	Primary	Type K thermocouple
TC142	Primary	Type K thermocouple
TC143	Primary	Type K thermocouple
LV151	Primary	Level sensor
PT151	Primary	Pressure transducer
PT152	Primary	Pressure gauge
TC151	Primary	Type K thermocouple
TC161	Primary	Type K thermocouple
TC162	Primary	Type K thermocouple
TC163	Primary	Type K thermocouple
TC164	Primary	Type K thermocouple
TC165	Primary	Type K thermocouple
PT161	Primary	Pitot tube
TC166	Primary	Type K thermocouple
PT161-1	Primary	Differential pressure transducer
TC171	Primary	Type K thermocouple
TC172	Primary	Type K thermocouple
TC173	Primary	Type K thermocouple
TC174	Primary	Type K thermocouple
TC175	Primary	Type K thermocouple
PT171	Primary	Pitot tube
TC176	Primary	Type K thermocouple
PT171-1	Primary	Differential pressure transducer
TC184	Primary	Type K thermocouple
TC185	Primary	Type K thermocouple
PT181	Primary	Pitot tube
TC186	Primary	Type K thermocouple
PT181-1	Primary	Differential pressure transducer
TC191	Primary	Type K thermocouple
TC192	Primary	Type K thermocouple
TC193	Primary	Type K thermocouple
TC194	Primary	Type K thermocouple
TC201	Secondary	Type K thermocouple
TC202	Secondary	Type K thermocouple
MF201	Secondary	EM flowmeter
PT201	Secondary	Pressure transducer
PT211	Secondary	Pressure gauge
TC301	Auxiliary	Type K thermocouple
PT301	Auxiliary	Pressure gauge
LC301	Auxiliary	Load cell

PILLAR Piping & Instrumentation (P&I) Diagram	
161130	Yong-Hoon Shin

Figure 5.18 Schematic diagram of PILLAR instrumentation system

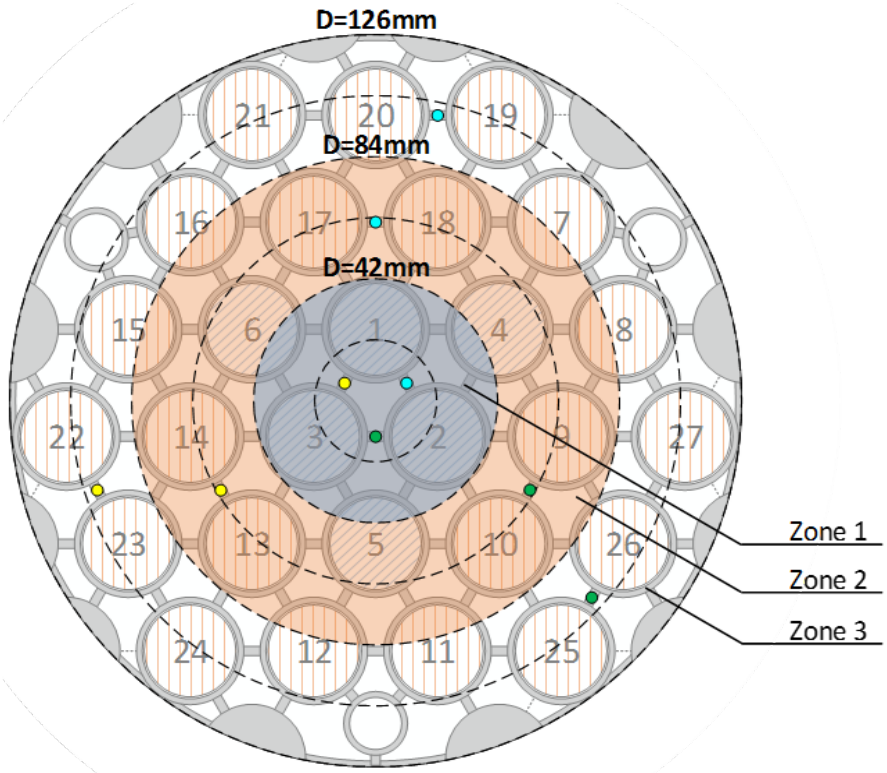

Figure 5.19 Geometrical consideration of thermocouple installation positions on grid spacers

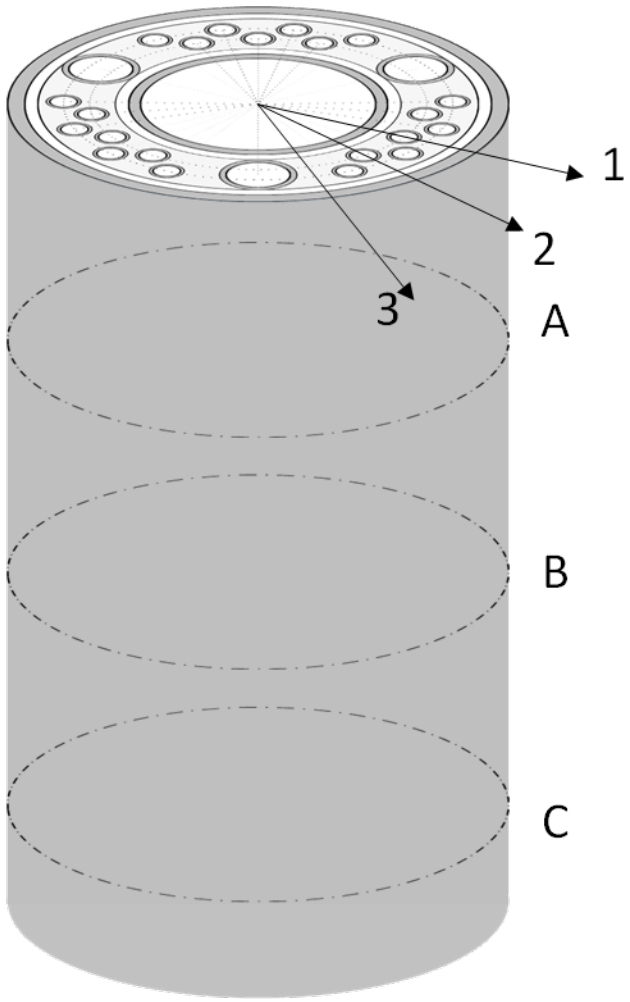

Figure 5.20 Axial and radial position of instrumentation probes on the shell side of PILLAR heat exchanger

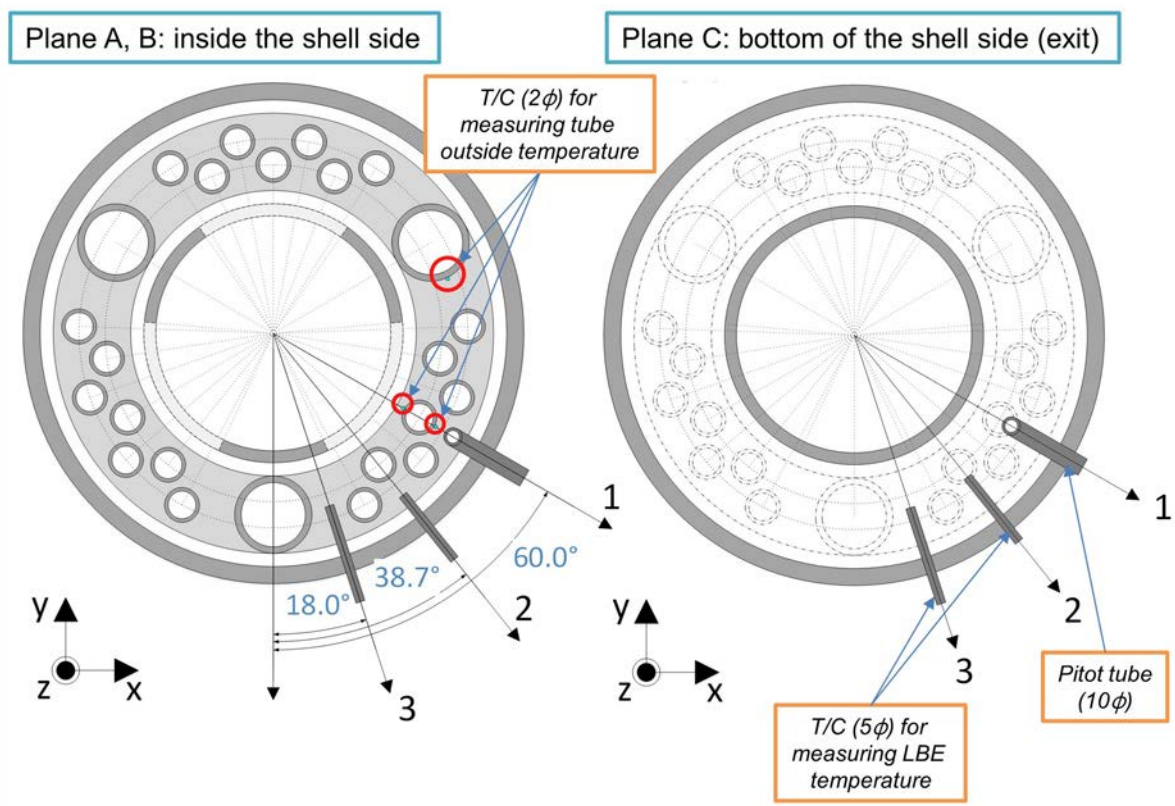

Figure 5.21 Position of instrumentation probes on arbitrary planes A, B, and C in PILLAR heat exchanger on planar cut view

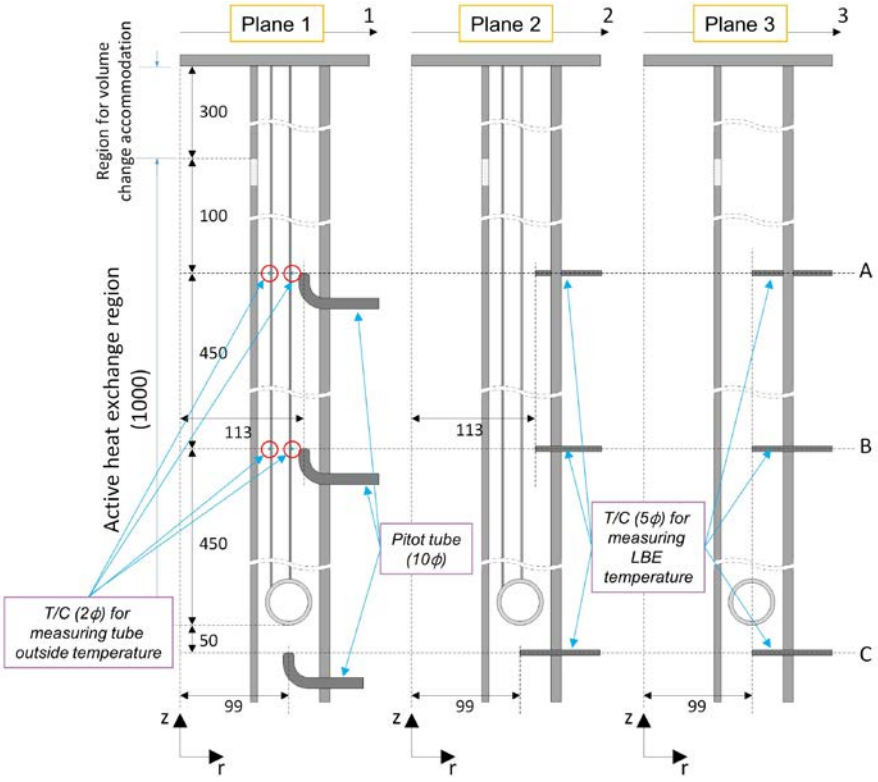

Figure 5.22 Position of instrumentation probes on arbitrary planes A, B, and C in PILLAR heat exchanger on axial cut view

5.2.3 PILLAR experiment procedure and conditions

Both steady state and transient LBE natural circulation experiments were carried out using PILLAR LBE pool integral test facility. Prior to those tests, a pre-conditioning for the new facility and preliminary tests to assess the heat loss of facility was performed. Several sets of the steady-state experiment results were generated for the code benchmark of MARS-LBE by varying the core power rating while trying to keep secondary side conditions as same as possible for all of the sets. The transient experiments were conducted by changing the operation conditions in terms of instantaneous maneuvering in the electrical power supplied to core heater rods and the secondary side pump speed.

5.2.3.1 Pre-conditioning of the facility

As all the components consisting of PILLAR was newly constructed, the conditioning of facility proceeded first. The empty LBE storage was filled with LBE ingots, at least 60% volume of the vessel, as its volume is about 0.5 m^3 and the necessary amount of LBE when running a test is about 0.3 m^3. LBE was prepared with a form of ingot and transferred through an opening, which is usually blocked by a blind flange in normal operation. After that, the heating jackets attached on the surface of the tank were activated to melt the LBE.

The second step for the conditioning was purging hydrogen gas, 4% hydrogen with argon balance, to reduce the amount of oxygen. Even if LBE is

not reactive with oxygen, the surface of LBE ingot might be oxygenated before putting into the storage tank. For a better efficiency, H_2 gas was supplied both on the top of LBE free level and under the level through a submerged feeding line. Since the oxygen content in LBE may change the surface condition of contacting steel, this hydrogen purging can be re-performed between each test campaign when LBE is not on the main vessel to maintain the chemical condition of LBE with respect to oxygen.

The last step is a trial run for the heat exchanger tube side. A centrifugal pump and a glove is two main components comprising the secondary water cooling loop, which controls flow speed and pressure to the fluid, about 6-8 bar. The pump cannot sustain pressure head in a large flow rate if the glove valve is fully opened. Hence, to operate the pump in a desired flow rate range, the openness of glove valve must be controlled. In order to minimize the control effort, only controlling the speed of pump was chosen and the glove valve was to be kept at the same openness by designating it through a trial run. Checking the flow rate and pressure at the same time in the trial run, a conversion curve for inverter frequency, which governs the flow speed, versus flow rate was secured and used for the experimental campaigns.

5.2.3.2 Experimental procedure

A test campaign can proceed when all the LBE in the storage tank is liquefied. The procedure is similar to the first paragraph as described in Section 5.2.3.1.

After LBE is melted, the heating jackets not only on the surface of main vessel and the transfer line between the main vessel and the tank are turned on to make temperature to be higher than 200 ˚C, as in the HELIOS operation procedure. Filling up LBE into the main vessel is the same with the HELIOS as well by exerting gas pressure to the LBE storage tank so that LBE free surface is pushed.

By checking the signals from the sensors, the amount of LBE needed for a test run is finely tuned by trial and error. Especially, the free surface level on the main vessel is of importance in this procedure, while in the HELIOS case it was designated to be higher than the lowest point of expansion vessel. The difference comes from the fact that the level of LBE determines the heat transfer length in the heat exchanger and it must be in a conceivable range expected at the design stage to conduct a precisely controlled experiment. To do so, the final level of LBE is decided by using the signal from the guided wave level sensor (LV151) located in the leveling pipe attached to the shell side of heat exchanger. After the fine tuning is done, the motor-operated valve is closed so that the main vessel and the storage tank are isolated.

Since PILLAR uses pressurized water for the cooling of system, LBE might freeze or water might boil in a certain condition. If LBE is transferred to the main vessel when water is filled in the tube side, the former can happen and the level control no longer is achievable until LBE melts by getting heat from the surface jacket heater. As aforementioned, the LBE level control at the test preparation is of prime importance, so water filling to the secondary side is designated to be preceded by the LBE filling process. In this regard, the freezing of LBE and boiling of water is not avoidable when water is filling up the heat

exchanger tube. For the reliable operation of the centrifugal pump, it is required to fill up the whole system without a cavity. To do so, boiled water needs to be released by opening the valve at the top of the secondary side while water is being purged so that water fills the piping. In this moment, LBE freezing is inevitable. After water fills the whole loop, the secondary side is pressurized and water temperature rises while LBE melts by heat supplied from the heating jacket.

When both LBE is in liquid state and the secondary side is full of pressurized water, a test session can be started by controlling the electrical power supplied to the heater rods in the core region. A certain amount of heat can be supplied to the core and it determines LBE natural circulation flow rate and temperature difference between heat sink and heat source. Before started, all the heating jackets that heat up the surface of main vessel needs to be turned off because during the test campaigns, heat loss to the environment will not be considered, which will be described in Section 5.2.4.1. At the same time, the centrifugal pump for the secondary side is activated by controlling the frequency of inverter as measured and pre-determined by the process delineated in the last section.

These manipulations generate LBE natural circulation flow and temperature distribution through energy transport until the system reaches a new steady state. For a steady state experiment, no other manipulation is made for a few hours so that a set of steady-state experimental data is collected and its quality, in terms of standard deviation when each of parameters are averaged, is maximized. On the other hand, for a transient experiment, any parameter of

interest should be manipulated so that the system reacts to the condition change. In this regard, the transient test begins only after a 'steady state' is maintained over at least two hours so that any interference on reaching the steady state is suppressed as much as possible. When a transient session is started by maneuvering the system, this principle still holds: for two hours, no manipulation is allowed so that the system transients are not interrupted or interfered by the manipulation.

5.2.3.3 Experiment conditions and test matrices

As in the HELIOS experiments, the steady state experiments conducted in PILLAR were defined with the core power ratings. Final steady-state conditions were reached after some manipulations on the system following the experimental procedure. For natural circulation experiments, there are only the limited number of variables to be controlled as the phenomenon is dependent upon the inherent nature of a system such as height difference between heat source and heat sink, the buoyancy of a working fluid given by density difference, and hydraulic resistance, which is affected by the geometrical arrangements of the system. Hence, test conditions that can be controlled directly by maneuvering the facility would only be the electrical power supplied to the core, water flow rate and inlet temperature of the heat exchanger tube side.

For the steady-state natural circulation experiments, seven sets of tests

were performed in terms of different core power ratings: 249, 253, 284, 293, 302, 306, and 315 kW, classified in an ascending order. These conditions were directly designated as test numbers as S-01 to S-07, where the leading 'S' means the test is for steady state and following numbers indicate each case. Besides, the secondary side conditions including water inlet temperature, water mass flow rate, and pressure exerted on it were to made nearly constant to reduce potential uncertainties from boundary condition change so that these results can be utilized for the code validation. Table 5.9 gives the test matrix and the definition of each case.

Unlike the steady state experiments in which the final state is determined distinctively, transient tests needs to be defined by two states, namely, the first state when not manipulated and the final state after the system saturates. Considering the tests are performed by controlling the core power and the secondary side flow rate, the conditions are to be written as in a form of T-VPPP-P1~P2/F1~F2: the leading letter, T, indicates this case is for a transient test. The following V describes which parameter is manipulated and: the letter V is designated to be P for a power transient, while it is F for a secondary side flow transient. PPP is for a condition change such that INC for increasing and DEC for decreasing. The last part consists of the two states given by P1 and F1 as the first condition and P2 and F2 as the final condition. Hence, when just one parameter is manipulated, then it can be expressed like P1/F1~F2 or P1~P2/F1. The power indicators P1 and P2 are given in kW while the flow indicators F1 and F2 are in kg/s. Figure 5.23 shows the definition of each case and test matrix graphically.

Table 5.9 PILLAR steady-state natural circulation test matrix and case definition

Test ID	Core power (kW)	Avg. water inlet temperature (°C)	Avg. water mass flow rate (kg/s)	Avg. water pressure (bar)
S-01	249	102.5	3.30	6.20
S-02	253	100.1	3.26	6.39
S-03	284	102.2	3.31	6.17
S-04	293	102.3	3.32	6.07
S-05	302	102.6	3.31	6.13
S-06	306	101.2	3.23	6.33
S-07	315	102.5	3.32	6.08

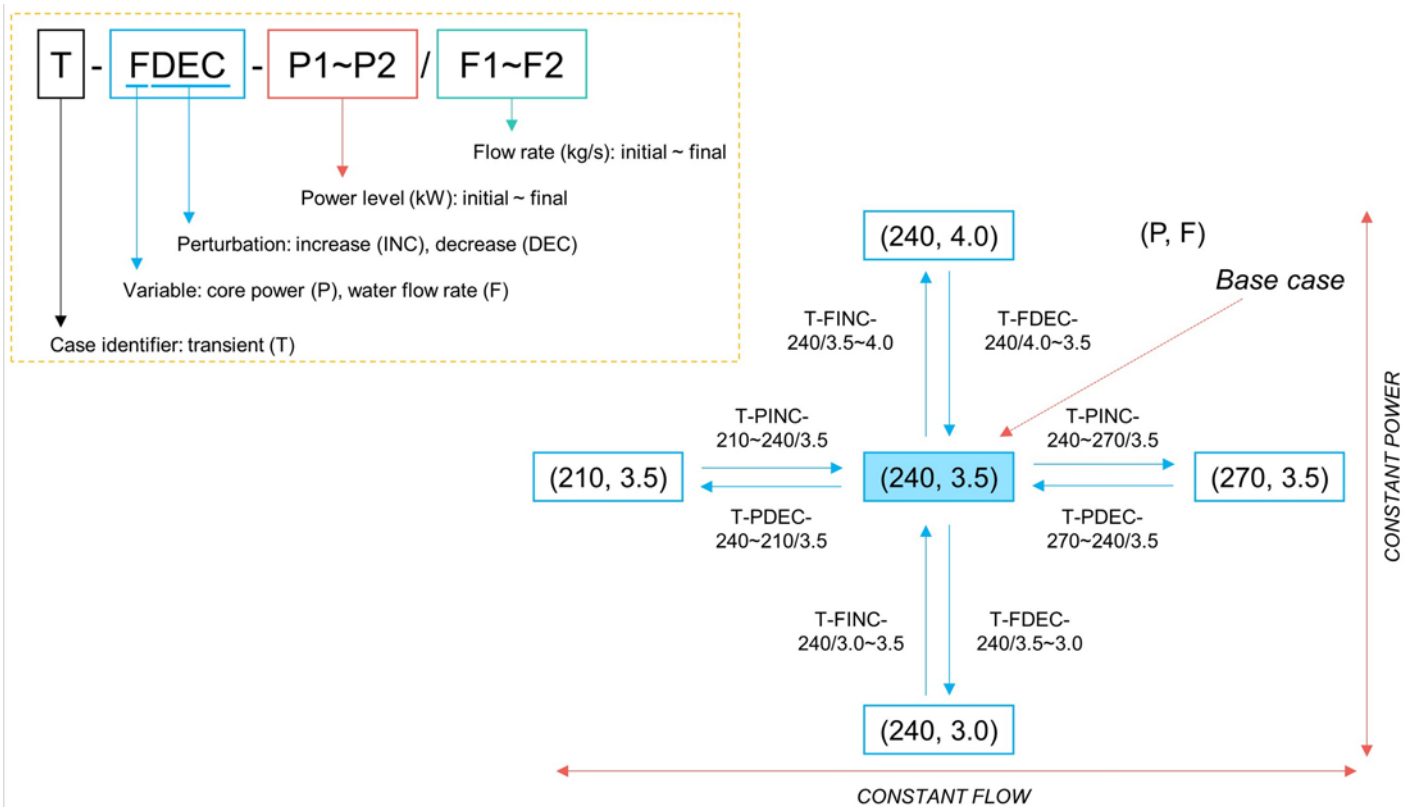

Figure 5.23 Graphical test matrix and case definition on PILLAR transient natural circulation experiments

5.2.4 Experiment results and discussion on LBE pool natural circulation

5.2.4.1 System heat loss evaluation

Prior to starting experiments with the installed PILLAR facility, a trial run and preliminary experiments were conducted to grasp the characteristics of the system. The most important point in the preliminary experiments is to evaluate heat loss, which is crucial in thermal hydraulic experiments, especially in natural circulation in which the behavior of the system depends on the thermal equilibrium between heat source and heat sink. Heat loss to the environment is inherent in the real world; hence, there is no way to prevent. However, if the amount of heat loss is measured, it can be controlled with a corresponding action by compensating for the amount. Therefore, this procedure must precede the actual experimental campaign to increase the reliability of the experimental data.

For this purpose, the heating jacket, a device which incorporates external surface heater to heat up the surface and thermal insulation to prevent heat loss, was operated without filling LBE to the PILLAR main vessel. After the temperature of the whole system was raised, measurements were taken over a few hours. The heating jacket is connected to a proportional-integral-differential (PID) controller to control the heater output so that the system temperature fluctuation can be minimized. In order not to make any uncertainties, the secondary side (H/X tube side) is not filled up with water

during the evaluation procedure because water may contribute to the removal of extra heat further from the system. The above measurements were sustained and repeated for about 2-3 hours to minimize the variation with time.

Through this procedure, the amount of change in the heater output over time can be inversely calculated based on the integrated average of the measurement span. Hence, utilizing the sum of time average of the electric power delivered to each of the heating jackets, which are denoted by subscript i, during the time span from t_0 to $t_0 + \Delta t$, the total amount of heat loss of the system, Q_{loss}, can be defined as in the following Eqn. (5.49). The overall procedure is described in Figure 5.24.

$$Q_{loss} \equiv \sum_i \frac{1}{\Delta t} \int_{t_0}^{t_o + \Delta t} Q_i dt \tag{5.49}$$

In a strict manner, the adiabatic condition cannot be met due to the (laminar) natural convection by surrounding air. When a particular object lying in the air is at a higher temperature than its surroundings, heat loss occurs primarily through natural convection with a slow rate of heat transfer. It is known that this relationship can be expressed as a product of dimensionless numbers, Nusselt number (Nu) and Rayleigh number (Ra) (Lienhard, 1973):

$$\frac{\mathrm{Nu}}{\mathrm{Ra}^{1/4}} = const. \tag{5.50}$$

Each of these parameters have proportional relationships with the convective

heat transfer coefficient and the temperature difference between the fluid surrounding the object, the air in this case, and the wall surface, as shown in Eqn. (5.51):

$$\mathrm{Nu} = \frac{hL}{k},\ \mathrm{Ra} = \frac{g\beta\Delta T\rho^2 C_p L^3}{\mu k} \Rightarrow h \propto \mathrm{Nu},\ \Delta T \propto \mathrm{Ra}\,. \qquad (5.51)$$

With a further manipulation, Eqn. (5.51) can be cast with Q_{loss} and an arbitrary constant c_1 as given in Eqn. (5.52):

$$\begin{aligned} &Q_{loss} = hA\left(T_{surf} - T_\infty\right) = hA\Delta T \\ &Q_{loss} \propto \mathrm{Nu}\Delta T \Leftrightarrow \propto \mathrm{Ra}^{1/4}\Delta T \Leftrightarrow \propto \Delta T^{5/4}\,. \qquad (5.52) \\ &\Rightarrow Q_{loss} = c_1\Delta T^{5/4} \end{aligned}$$

In other words, by knowing the time average of the power variation and the temperature difference between the surrounding air and the system surface, the constant c_1 can be obtained, and it is possible to evaluate the integral heat loss with respect to the change of the system temperature. To do this, the air bulk temperature and the surface temperature of the main vessel of PILLAR should be measured and it was done by installing several thermocouples. The system integral heat loss would be generated through the outside of the heating jacket now that there is no need to remove the heating jacket during the experiment. Therefore, the surface temperature was designated as the surface temperature of the heating jacket measured at a specific point.

In order to select a representative system temperature, the

thermocouples were installed at the center of the device in the axial direction. Three thermocouples were installed, one for measuring the surface temperature and the other for the ambient temperature with a radial offset to allow the measurement of temperature change slightly away from the main vessel surface. The locations of the thermocouple tip was set at the same level with the tip of a thermocouple that measures the internal temperature of the main vessel so that the temperature gradient can be determined qualitatively. The established set of thermocouples for heat loss evaluation is shown in Figure 5.25.

The heat loss evaluation was made using three averages and each utilizes about 2-3 hours of data to reduce the error. The temperature variation and time-average interval in the evaluation are shown in Figure 5.26. One average point that is not visible in the figure is from the data that was measured when the heating jacket was first installed and its first run was conducted. The data were fitted in the form given by Eqn. (5.52); each black dot represents the time-averaged system total heat loss and the red curve in Figure 5.27 presents the fitting, where the function of the fitted curve and R^2 value are given by:

$$\begin{aligned} Q_{loss} &= c_1 \Delta T^{5/4} = 0.09674 \Delta T^{5/4} \\ R^2 &= 0.98815 \end{aligned} . \qquad (5.53)$$

As a result, the heat loss is about 4 kW even when the difference between the outer surface temperature of the heating jacket and the ambient temperature is about 20 ˚C. Considering that the actual experiment campaigns in the following sections were carried out with over 200 kW of core power

ratings, this amount is relatively negligible. In order to make sure of the effect of heat loss and power compensation, a test was conducted by filling the PILLAR main vessel with LBE and providing 250 kW core power for more than 70 hours. Contrary to the heat loss evaluation given earlier, the heat exchanger tube side was active by pumping water into the secondary side to remove the heat from the system. Meanwhile, the PID controller to the heating jackets was allowed to supply electrical power automatically through the temperature measurements. The obtained results are described in Figure 5.28 and Figure 5.29.

In the experiment in approximately 70 hours, after the steady state natural circulation was achieved, a relatively large amount of electrical power was supplied to the external heat tracing over the first 30 hours. It was gradually decreased from 30 hours and about 35 hours from the beginning, about 1/3 to the initial amount was maintained for about 20 hours. From about 55 hours, most PID controllers were turned to be inactive and only one PID controller was active. The amount of heat supplied to the entire system through the heating jackets had changed, but when the temperature variation of the system was observed, it was rather influenced by the fluctuation of the ambient air temperature, as seen in the lower inset of Figure 5.28. As can be seen in Figure 5.29, the amount of heat provided by the primary core is removed in a small error range, regardless of the amount of heat supplied to the heating jacket. Therefore, it is estimated that the heat given by the heating jacket does not have a great influence on the change of the overall system temperature in high core power rating conditions, as previously confirmed that the PILLAR main vessel

has negligible heat loss.

In HELIOS case, about 1/3 of the core output is released to the ambient air when the external surface heater is not operated since the flow traversing length is more than 20 m and the loop has a relatively large surface area compared to its volume. On the other hand, the heat loss of PILLAR can be effectively suppressed mainly due to its three distinct features: firstly, it has small surface area over its volume. Secondly, the components including core, upper plenum, and riser are enclosed by the external components. Lastly, it adopts an improved insulation with its thickness being twice as thick as that of HELIOS (PILLAR: 5cm, HELIOS: 2cm).

The actual test showed that even if the core power rating of 250 kW or more was applied, the difference between the outer surface temperature of the heating jacket and the ambient air temperature was 20 ˚C. Therefore, it was concluded that the heat loss of the entire system is negligible that it will not affect the experimental results. In the experimental conditions, the heating jacket controller is set at a relatively low temperature so that only a small amount of heat loss is compensated.

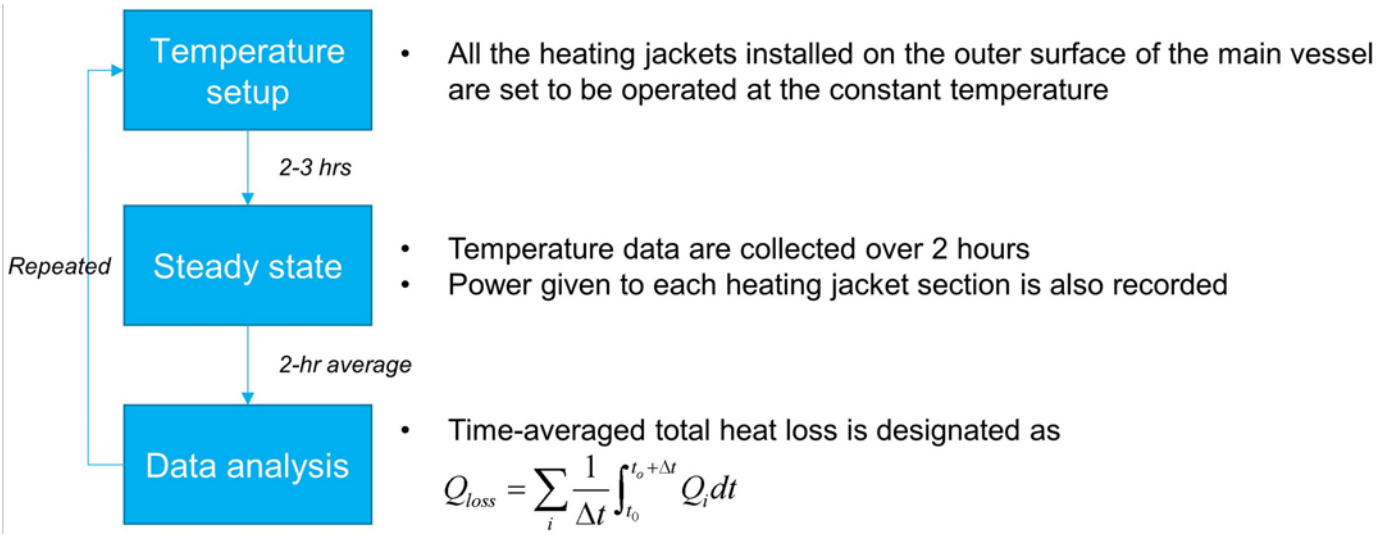

Figure 5.24 PILLAR system integral heat loss evaluation procedure

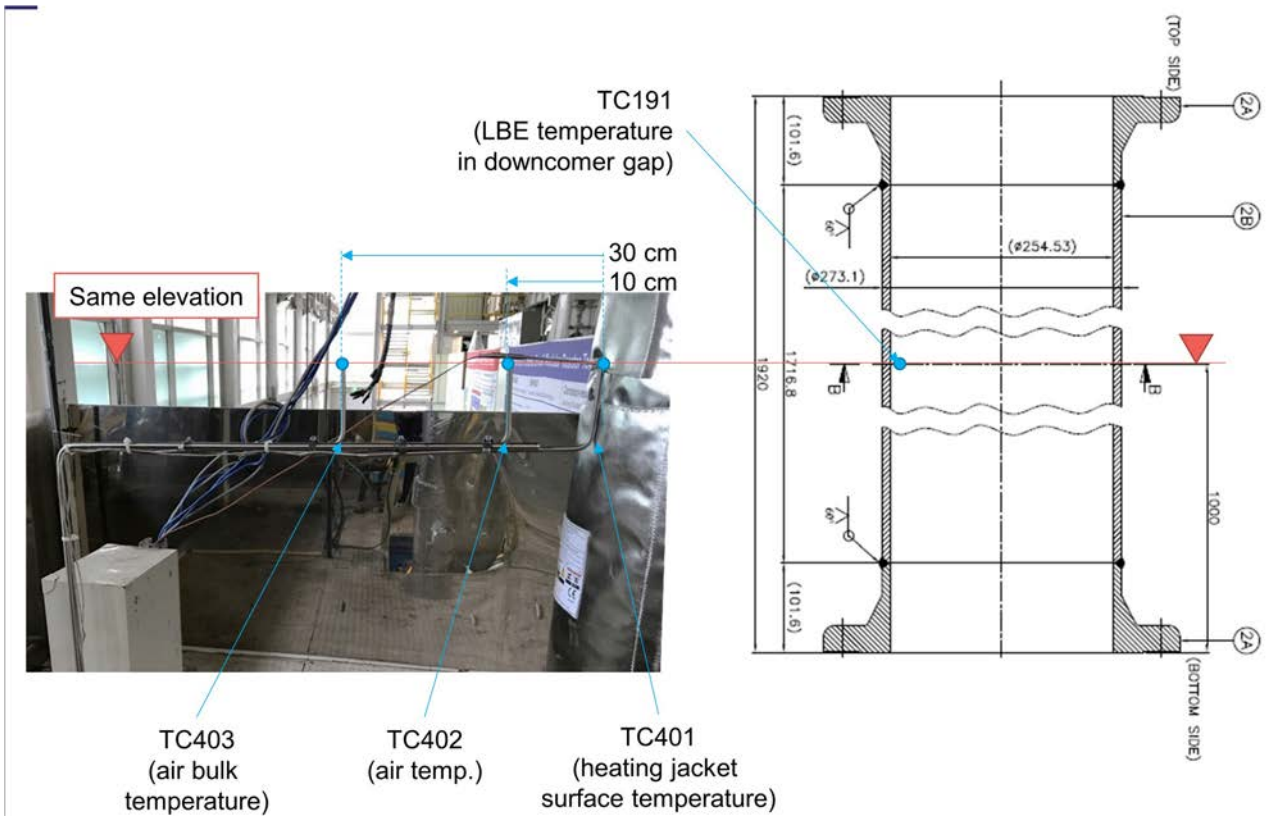

Figure 5.25 Locations of thermocouples for the evaluation of PILLAR system integral heat loss

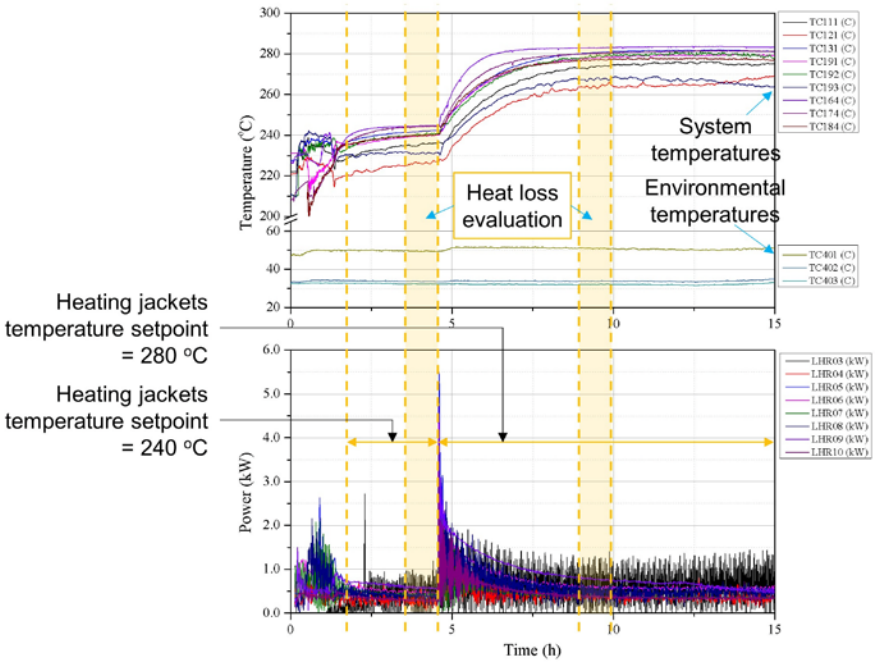

Figure 5.26 PILLAR main vessel integral heat loss evaluation test results

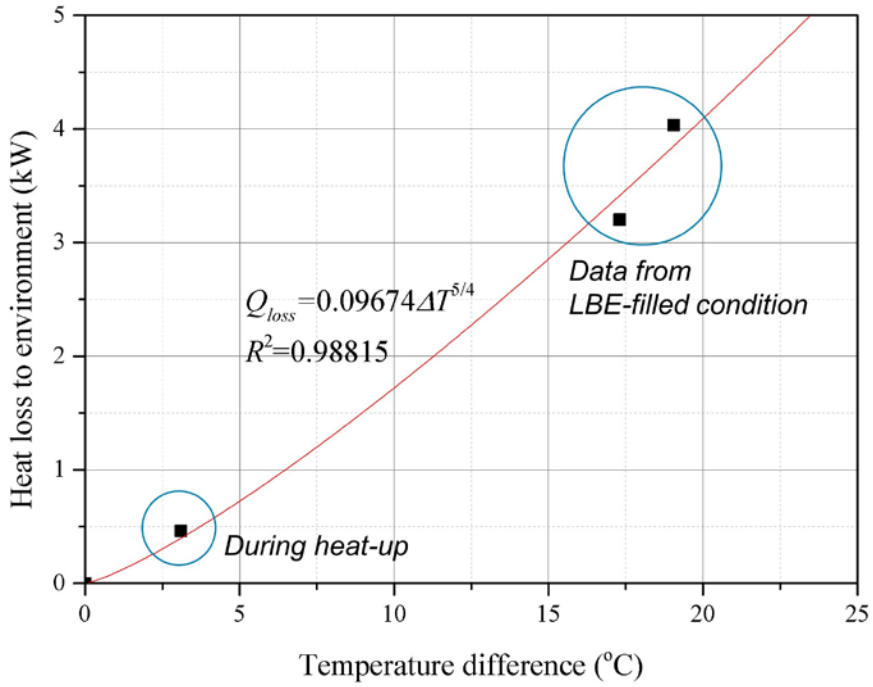

Figure 5.27 Fitted curve for PILLAR system integral heat loss as a function of temperature difference between surface and ambient temperatures

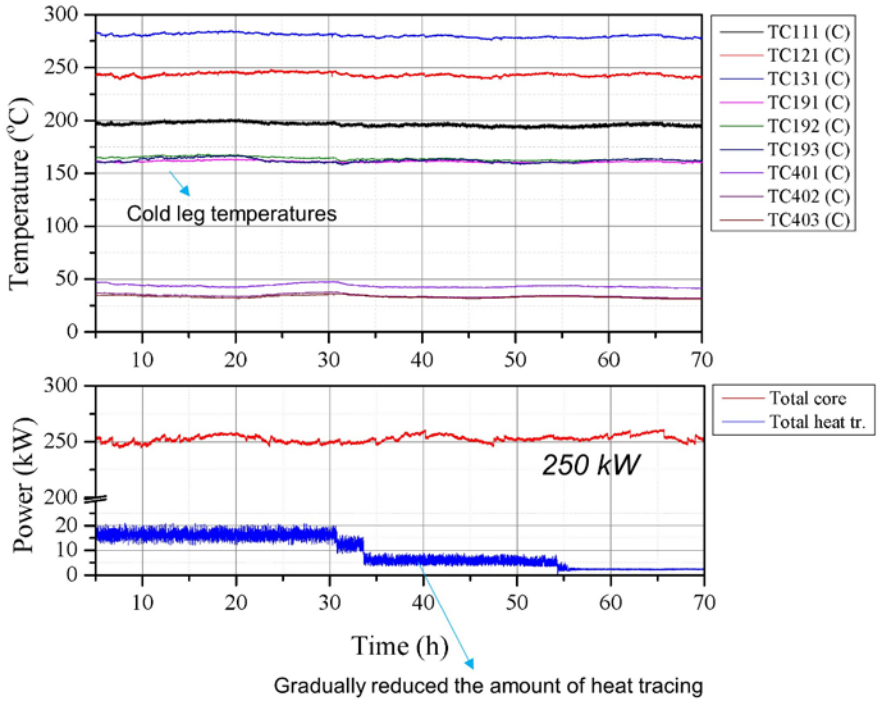

Figure 5.28 PILLAR primary system response to the variation in the amount of heat tracing on the main vessel surface

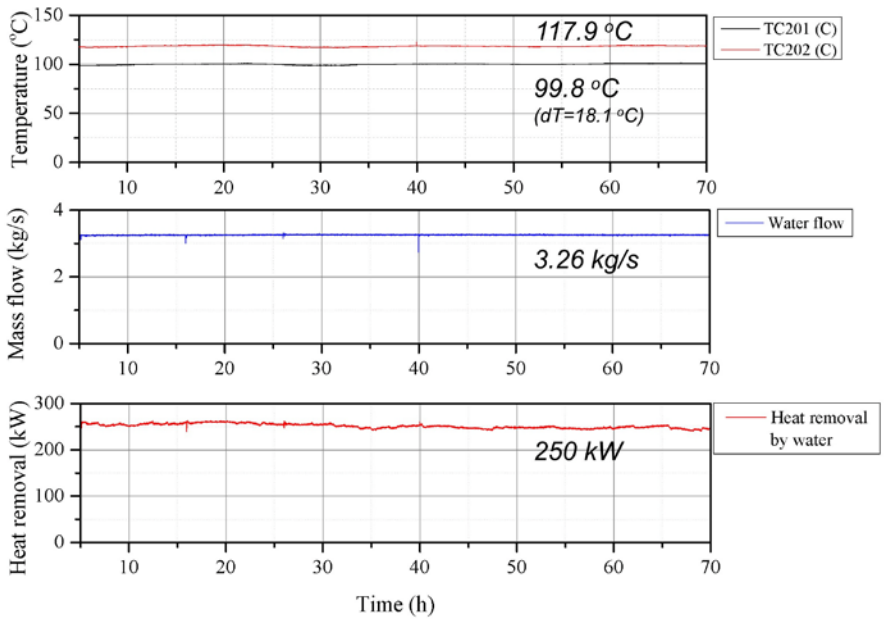

Figure 5.29 PILLAR secondary cooling system (heat exchanger tube side) response to the variation in the amount of heat tracing on the main vessel surface

5.2.4.2 Experimental results and discussion on steady-state LBE pool natural circulation

As defined in Table 5.9, seven LBE steady-state natural circulation experiments were carried out in the pool configuration with PILLAR. Since the main vessel showed negligible heat loss to the environment, no heat compensation was made. Similar to the HELIOS cases, there were slight temperature fluctuations within a day due to the daily temperature change and the system was maintained at least for two hours to minimize the error by following the principle described in Section 5.2.3.2.

Table 5.10 summarizes the steady-state experimental results from S-01 to S-07 cases in terms of temperatures, mass flow rates and pressure in both primary and secondary sides. In all cases, heat balances between primary and secondary side were calculated to be matched within 5% ranges. Considering that there was no heat compensation through the outermost wall of the main vessel, it can be also made certain that the system is equipped with enough insulation so that it loses a negligible amount of heat to the environment.

It is notable that the cold leg temperatures were relatively low compared to the prototypic reactor, about 300 °C. This low cold leg temperature comes from the cooling capability of the heat exchanger; in other words, it is due to a large overall heat transfer coefficient in the heat exchanger. Since temperature difference between heat exchanger and primary coolant is determined by the overall heat transfer coefficient, the secondary side conditions work as boundary conditions in natural circulation. Moreover, at the

same power removal rate, the temperature difference would decrease if the overall heat transfer coefficient increases, vice versa. To elevate the primary side temperature, the secondary water can be heated so that the secondary side inlet temperature would rise, but this approach is limited the pressure exerted upon water and the thickness of each tube in the heat exchanger. Thus, low-power operation is not viable in PILLAR because of the design and cooling capability of heat exchanger. Regarding the experience and the experimental results, the lowest core power would be 200 kW since the cold leg temperature would be about 150 ℃ in this condition. It is recommended to have slight temperature margin between operation condition and LBE freezing condition, 125 ℃, because the system needs to be maneuverable in an exceptional condition during experiments.

Table 5.10 Experimental results on steady-state LBE pool natural circulation in PILLAR

ID	Primary (LBE) side					Secondary (water) side			
	Total core power (kW)	Hot leg temperature (°C)	Cold leg temperature (°C)	Temperature difference (°C)	LBE mass flow rate (kg/s)	Inlet tempe-rature (°C)	Outlet tempe-rature (°C)	Water mass flow rate (kg/s)	Pressure (bar)
S-01	249	163.46	252.53	89.07	18.55	102.5	119.8	3.30	6.20
S-02	253	161.54	251.17	89.63	18.67	100.1	118.2	3.26	6.39
S-03	284	170.74	268.56	97.83	19.25	102.2	122.0	3.31	6.17
S-04	293	172.48	272.74	100.3	19.49	102.3	122.7	3.32	6.07
S-05	302	173.89	276.50	102.6	19.63	102.6	123.6	3.31	6.13
S-06	306	170.60	274.44	103.8	19.70	101.2	122.7	3.23	6.33
S-07	315	176.30	282.82	106.5	19.85	102.5	124.4	3.32	6.08

Note: all of the values given above are average values from measurements in each case.

5.2.4.3 Experimental results and discussion on transient LBE pool natural circulation

Among several experimental sets conducted as defined in the graphical test matrix shown in Figure 5.23, only four cases, T-PINC-210~240/3.5, T-PDEC-240~210/3.5, T-FINC-240/3.5~4.0, and T-FDEC-240/4.0~3.5, are to be presented in this session. It is because each type of tests showed similar aspects in system reactions and therefore, including all the results would be redundant. Each of cases are shown in Figure 5.30 to Figure 5.33, respectively.

For the core power transients tested in T-PINC-210~240/3.5, T-PDEC-240~210/3.5 cases, depicted as Figure 5.30 and Figure 5.31, correspondingly, mass flow rate given by natural circulation saturated within 3 minutes after the core power rating was changed when 12.5% of core power varied from initial conditions. Considering the time needed to be saturated, the primary side tend to saturate to a new steady state faster than secondary side. In addition, water enthalpy at the outlet of secondary side varied so that heat balance to be matched; and it contributed to the much slower saturation. In this condition, heat balance mismatch over the heat exchanger happens until outlet enthalpy increases when a proper control on the secondary side conditions are not given.

As shown in the cases of T-FINC-240/3.5~4.0 and T-FDEC-240/4.0~3.5 with Figure 5.32 and Figure 5.33, respectively, slight overcooling and undercooling were drawn by secondary side flow rate changes while a negligible amount of change happens in core inlet temperature, which is the same with heat exchanger outlet temperature. Since the instantaneous mismatch

in heat balance between the primary and secondary side, the outlet enthalpy also varied similar to the investigation in the power transients so that heat balance were to be matched.

The experimental results with the transient tests can be compared with the actual reactor. Considering that PILLAR does not load nuclear fuel rods but electrical heaters instead, a conceivable difference between the facility and the reactor is the existence of reactivity feedback. For a rapid power transient, it can be achieved in the actual reactor core as well due to a rapid power change expected in the reactor with a steep reactivity insertion. Hence, the power transient tests conducted with PILLAR can be thought to be realistic. Furthermore, the overcooling and/or undercooling expected in the instantaneous change of secondary side flow rate will lead to core inlet temperature change and finally, the reactor core would get a slight amount of reactivity insertion. Meanwhile, similar to the test results, the secondary side of the actual reactor would require more time to be saturated in comparison with the primary side. Overall, the experimental sessions carried out by PILLAR are thought to be represent the behaviors expected in actual passive LBE-cooled systems.

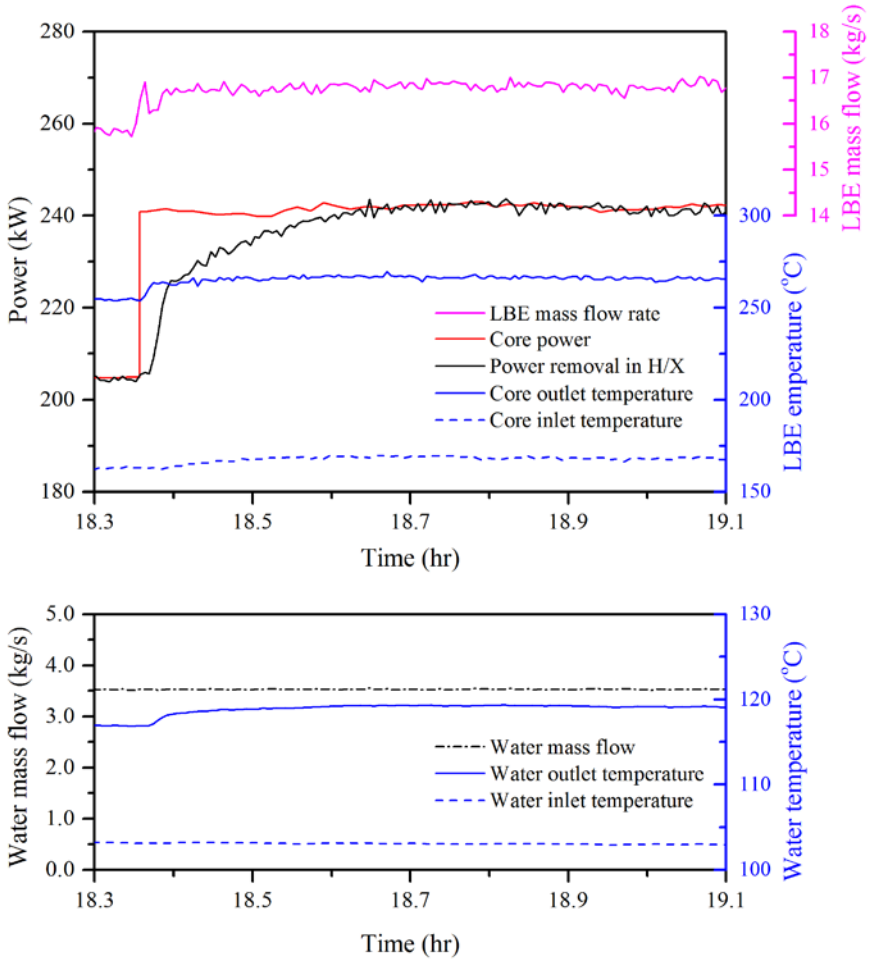

Figure 5.30 PILLAR transient natural circulation experimental results: instantaneous core power increase (Case No.: T-PINC-210~240/3.5)

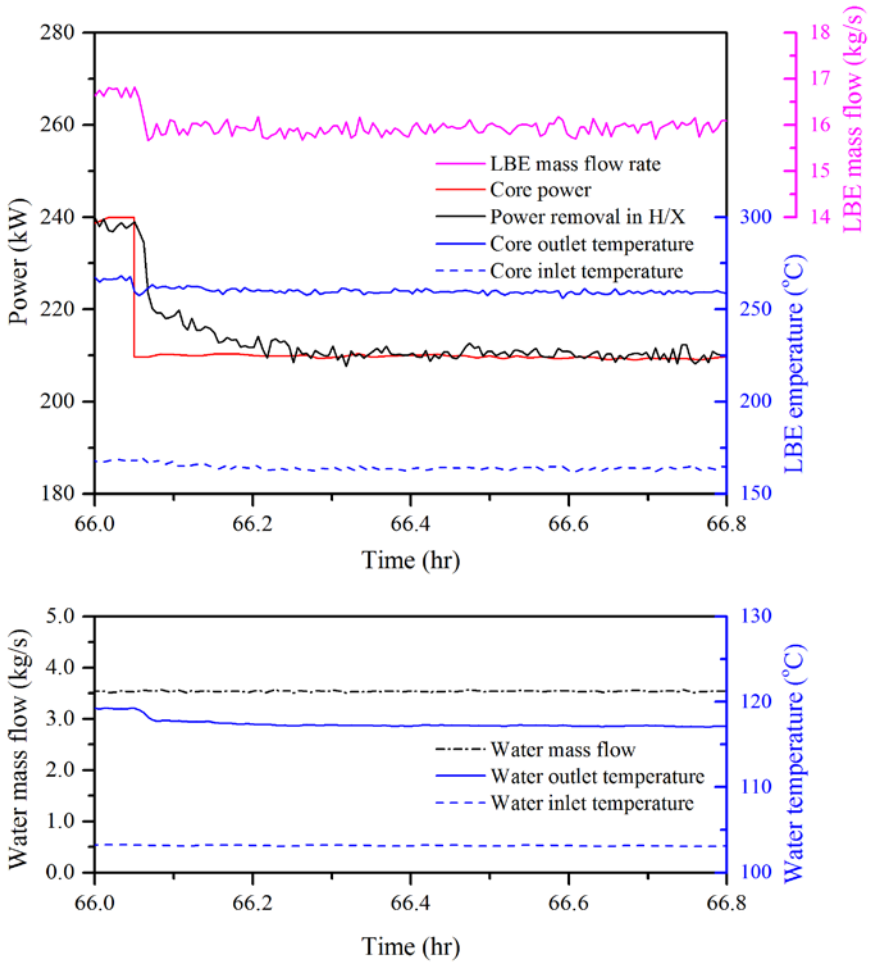

Figure 5.31 PILLAR transient natural circulation experimental results: instantaneous core power decrease (Case No.: T-PDEC-240~210/3.5)

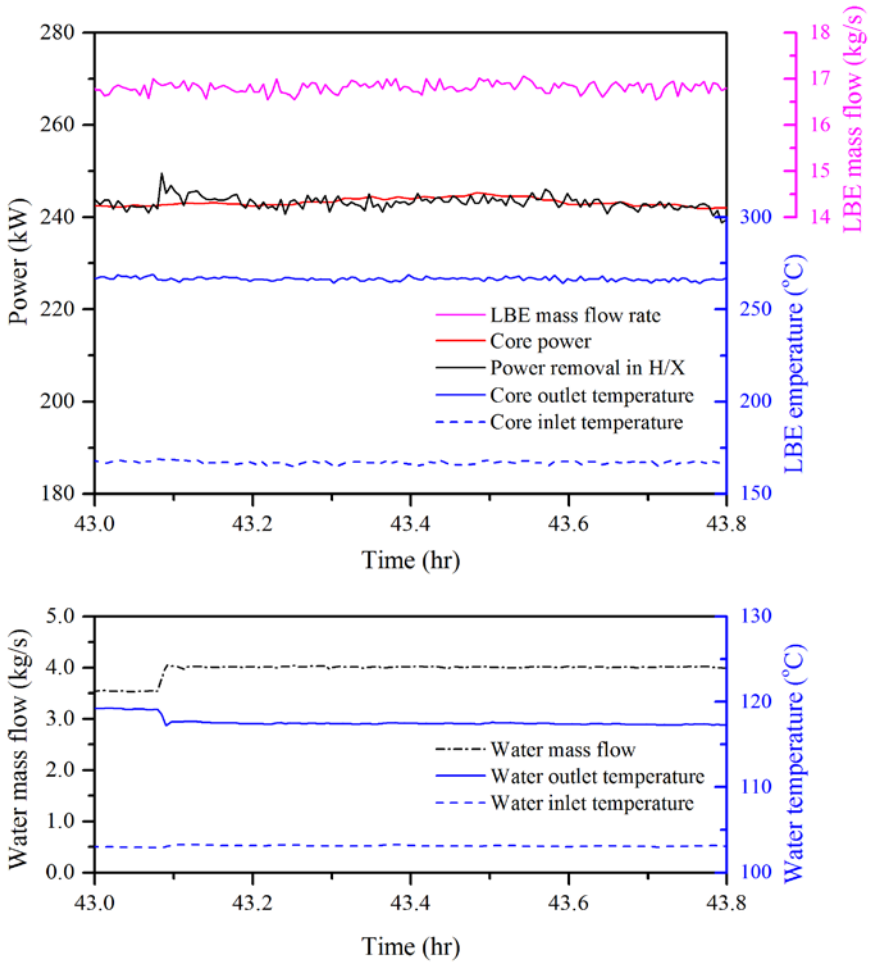

Figure 5.32 PILLAR transient natural circulation experimental results: instantaneous secondary side flow increase (Case No.: T-FINC-240/3.5~4.0)

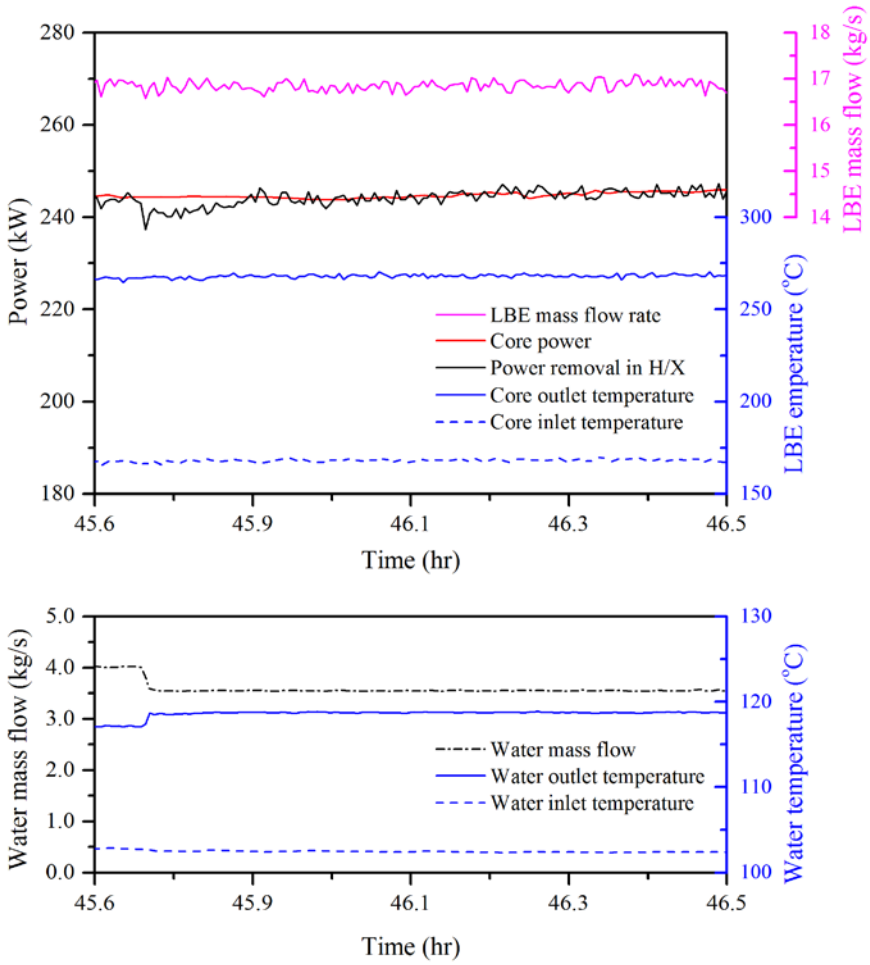

Figure 5.33 PILLAR transient natural circulation experimental results: instantaneous secondary side flow decrease (Case No.: T-FDEC-240/4.0~3.5)

Chapter 6 Code Validation and Numerical Analysis

6.1 One-dimensional system thermal-hydraulics (STH) code: MARS-LBE[4]

MARS is a system safety analysis code based on best-estimate modeling developed by KAERI (Korea Atomic Energy Research Institute) by integrating RELAP5/MOD3 and COBRA-TF which are widely used codes in the thermal-hydraulic analyses for LWR; the integrated code is capable of one-dimensional thermal-hydraulic system analysis and multi-dimensional subchannel analysis where its backbone codes are applicable, respectively (KAERI, 2006). RELAP5 is established on one-dimensional, two-fluid flow model using two-fluid, six-equation formulation given by mass, momentum, and energy conservation of water and steam with several relations on phase transition between two fluids (Carlson et al., 1990). COBRA-TF is a three-field, three-dimensional analysis code and two-phase flow with reflood heat structure

[4] This section has been written based on the following journal paper: Yong-Hoon Shin et al., "Experimental studies and computational benchmark on heavy liquid metal natural circulation in a full height-scale test loop for small modular reactors," Nuclear Engineering and design, 316, 26-37, 2017.

model can be treated with flexible noding schemes (Thurgood et al., 1983). These two codes are coupled implicitly by using dynamic link library techniques in MARS code structure. The code is also capable of other reactor safety calculations such as point kinetics modeling.

MARS has been updated by implementing various fluid properties for instance sodium (Na), helium (He), and carbon dioxide (CO_2) to cope with growing interests on the generation-IV reactor system analysis. In this respect, a group of researchers in SNU has improved the code by modifying some calculation schemes in convective heat transfer suitable for heavy liquid metal and updating LBE thermophysical property table (OECD Nuclear Energy Agency, 2007). The updated code is called MARS-LBE 3.11, which has been originated from MARS 3.1 release.

6.2 Code validation on thermal-hydraulics with steady-state experimental results

6.2.1 Code benchmark with HELIOS loop test results

6.2.1.1 System nodalization and input preparation on HELIOS

For computational modeling, nodalization needs to be preceded by interpreting the system into several calculation nodes with respect to the scope of calculation and the capability of computational code. In this respect, In the input file for MARS-LBE, HELIOS hydrodynamic components are described with several one-dimensional components such as pipes, junctions, time-dependent volumes, and time-dependent junctions to impose unsteady boundary conditions with about 170 hydrodynamic cells, as depicted in Figure 6.1. Considering that the natural circulation experiments were carried out in a loop configuration, one-dimensional calculation schemes used in MARS were sufficient to analyze the global phenomena. In addition, heat structure models are included where heat transfer occurs among solid bodies like heater rods and heat exchanger, and the themophysical properties of constituent material, 316L stainless steel, are provided as listed in Table 6.1 (Mills et al., 2004).

In MARS-LBE, convective heat transfer is treated in a subroutine by calculating convective heat transfer coefficient from Nu, which is generally given by a function of Re (Re = $\rho v_0 d_h/\mu$) and Pr (Pr = $\mu C_p/k$) (or a product of two nondimensional parameters, Pe = $\rho C_p v_0 d_h/k$) of a fluid in a calculation cell.

As convective heat transfer aspects varies considerably with the thermophysical property of a fluid, in other words, the magnitude of Pr, correlations used for Nu is properly chosen accordingly. Seban-Shimazaki correlation (Seban and Shimazaki, 1949) is applied to any heat transfer conditions for LBE:

$$\mathrm{Nu}_{LBE} = 5.0 + 0.025(\mathrm{Re}\,\mathrm{Pr})^{0.8} = 5.0 + 0.025\mathrm{Pe}^{0.8}. \qquad (6.1)$$

Sieder-Tate correlation (Sieder and Tate, 1936) is used for the secondary oil:

$$\mathrm{Nu}_{oil} = 0.027\,\mathrm{Re}^{0.8}\,\mathrm{Pr}^{0.33}\left(\frac{\mu}{\mu_w}\right)^{0.14}, \qquad (6.2)$$

as suggested by the thermal fluid manufacturer (Dow Chemical Company, 1996).

MARS-LBE predicts pressure loss in a component due to friction and flow condition change by following relation:

$$\Delta p_i = \sum_i \frac{\rho_i v_i^2}{2}\left(f\frac{l}{d_h} + K\right)_i \qquad (6.3)$$

In case of the friction loss coefficient ($f(l/d_h)_i$), a user is asked to specify pipe roughness (ε) and an internal subroutine in the code calculates its value in a component. However, form loss coefficient (K_i) should be explicitly provided except the case of using internal sudden area change model. In previous activities (Cho et al., 2011; OECD Nuclear Energy Agency, 2012), all of the

hydraulic loss coefficients in HELIOS were investigated. As a result, the best-practice guidelines for the prediction of the coefficients were suggested. The correlations used in this study are summarized in Table 6.2. Pipe roughness is designated to be 2.53 μm as measured.

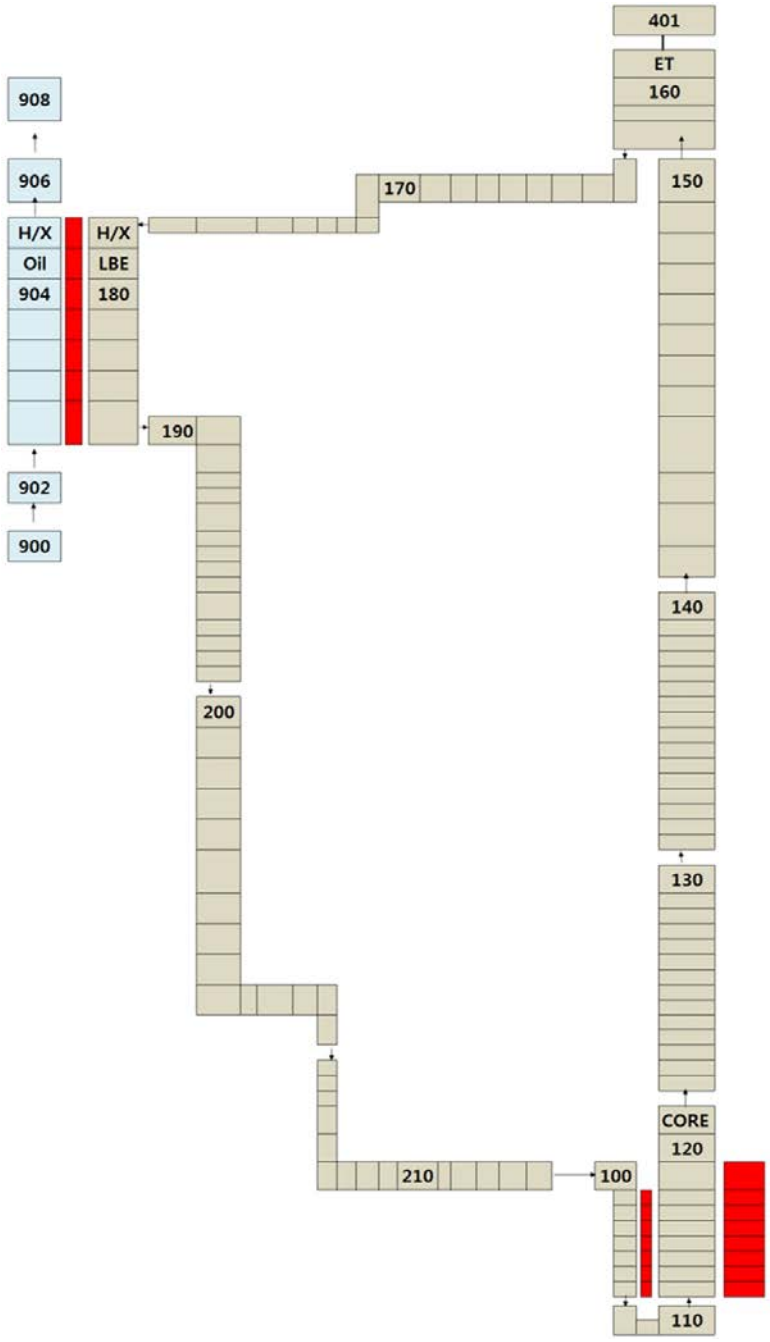

Figure 6.1 Nodalization map of HELIOS prepared for MARS-LBE

Table 6.1 Thermophysical properties of 316 L stainless steel (data retrieved from (Mills et al., 2004; Popov and Carbajo, 2000))

Temperature (°C)	Thermal conductivity (W/m K)	Volumetric heat capacity (10^6 J/m^3 K)
20	14.2	3.78
94	15.3	3.93
205	17.1	4.09
316	18.8	4.21
427	20.5	4.31
538	22.1	4.41
649	23.6	4.50
760	25.1	4.58
871	26.6	4.66
1205	30.7	4.90

Table 6.2 Correlations used for hydraulic loss coefficient evaluation

Hydraulic loss model	Correlation		Note
Wall Friction (Popov and Carbajo, 2000; Zigrang and Sylvester, 1985)	$f = \frac{64}{\mathrm{Re}}$	$0 \le \mathrm{Re} \le 2200$ (Laminar)	Calculated by a subroutine in MARS-LBE, $f_{L,3000}$: value at Re = 2200, $f_{T,3000}$: value at Re = 3000
	$f = \left(3.75 - \frac{8250}{\mathrm{Re}}\right)(f_{T,3000} - f_{L,2200}) + f_{L,2200}$	$2200 < \mathrm{Re} < 3000$ (Transition)	
	$\frac{1}{\sqrt{f}} = -2\log_{10}\left\{\frac{\varepsilon}{3.7d_h} + \frac{2.51}{\mathrm{Re}}\left[1.14 - 2\log_{10}\left(\frac{\varepsilon}{d_h} + \frac{21.25}{\mathrm{Re}^{0.9}}\right)\right]\right\}$	$\mathrm{Re} \ge 3000$ (Turbulent)	
Sudden area change (Trapp and Ransom, 1977)	$K = \left(1 - \frac{A_1}{A_2}\right)^2$	Sudden expansion	Calculated by a subroutine in MARS-LBE
	$K = \left(1 - \frac{A_2}{A_c}\right)^2,\ \frac{A_c}{A_2} = 0.62 + 0.38\left(\frac{A_2}{A_1}\right)^3$	Sudden contraction	
Mock-up core grid spacer (Cho et al., 2011; Rehme, 1973)	$K = C_v\left(\frac{A_s}{A_v}\right)^2,\ C_v = -7.65\log_{10}\mathrm{Re} + 49.0$		Modified drag coefficient suitable for HELIOS core grids
Elbow (Nippert, 1929)	$K = K_{\mathrm{Re}}K_{\mathrm{loc}} + K_{\mathrm{fr}}$		
Orifice (Idelchik, 1953)	$K = \left(1 + 0.707\sqrt{1 - \frac{A_{or}}{A_1}} - \frac{A_{or}}{A_1}\right)^2\left(\frac{A_1}{A_{or}}\right)^2$		$\mathrm{Re} > 10^5$

6.2.1.2 Code benchmark results for HELIOS natural circulation tests

Using the well-defined experimental data generated with HELIOS, MARS-LBE code was benchmarked. The purpose of this benchmark is to validate the capability of MARS-LBE code in a given non-isothermal natural circulation condition by making the code to estimate LBE mass flow rate and LBE temperature distribution in a system. In this respect, boundary conditions such as the mock-up core power rating, secondary side inlet temperature and mass flow rate were designated explicitly as forms of the time-dependent volumes and junctions, heat structures, and property tables in the model.

The code benchmark results for the cases from NC1.0 to NC4.0 are summarized in Table 6.3. Oil side conditions including mass flow rate and inlet temperature are not specified in the table because these parameters were assigned to the boundary conditions since the same values were used in the benchmark. Considering that the measured and calculated temperatures of oil side outlet are within a few degrees deviation, it can be concluded indirectly that the experiments from NC1.0 to NC4.0 were performed in sufficiently adiabatic wall boundary conditions.

The measured LBE mass flow rates and calculated results by MARS-LBE for all cases are compared in Figure 6.2, as a function of mock-up core power rating. The benchmark results show good agreement with measurement within maximum 7% discrepancies as also shown in Figure 6.3. As described, the parameters of interest in natural circulation estimation, mass flow rate and

temperature difference of LBE, show good agreement between experiment and code benchmark results.

Comparisons between experiment and calculation results on LBE temperature distribution and the secondary side temperature distribution for each case are shown in Figure 6.4 (a)-(d). The absolute LBE temperatures along the main loop are benchmarked closely within 1% ranges except the NC1.0 case, as shown in Figure 6.4 (a). In that case, the code benchmark shows about 25 °C temperature underestimation. However, as depicted in Figure 6.5, the temperature differences between measurement and calculation are in a close range, within 7%.

To find the cause of this discrepancy in absolute temperature distribution, the nodalization on the heat exchanger is investigated first with a sensitivity study. In a modeling of a heat exchanger, it is required that the size of calculation nodes should be moderate and fine enough to simulate heat transfer properly within a node since both convective and conductive heat transfer are present and the working fluids flow in the opposite direction. For the sensitivity study, two more numerical cases for each of natural circulation experiments from NC1.0 to NC4.0 are prepared, with the increased number of calculation nodes.

To increase the number of axial nodes, the size of a node is halved and trisected, respectively, which means the total number of calculation nodes in the heat exchanger is doubled and tripled. A comparison on the three models for the sensitivity study is summarized in Table 6.4 in terms of the number of axial nodes and node length-to-diameter ratio (l_i/d_h) defined by the ratio

between node length and hydraulic diameter of a unit node. The sensitivity models were selected in the range of l_i/d_h values being greater than unity below which a calculation model can suffer from numerical instability. The trisected model satisfies this limitation with the ratio being 1.358.

The nodalization of each model is graphically shown in the left hand side of Figure 6.6 (a)-(c): (a) the original, (b) the halved, and (c) the trisected models, respectively. For the sensitivity study, absolute LBE temperature distribution in the heat exchanger is chosen because it is an important parameter of interest in natural circulation as aforementioned. Along with numerical nodalization, the right hand side of Figure 6.6 shows LBE temperature calculation results for each case. The LBE temperatures are reported at the center of each axial node. As a result, all 12 cases including original, halved, and trisected cases for each natural circulation experiment from NC1.0 to NC4.0 shows well-agreed calculation results within 1 °C variation in absolute temperature. It turns out that nodal condition in the original model with seven axial nodes is already sufficient to simulate heat transfer in the heat exchanger properly. In addition, the numerical discrepancy given in the NC1.0 case would not be affected by the node size in the original model.

Another potential cause of this discrepancy can be the correlations that we used for convective heat transfer coefficients because the final temperature distribution over a heat structure model depends on the values of those coefficients in MARS-LBE calculation scheme. If one of the correlations for LBE and secondary oil (or both) is not applicable in terms of flow regime and temperature condition, then it misleads calculation results by nature. Eqn. (6.1)

is recommended to be applicable to a Re range in $0<Re<5\times10^6$, while LBE flow regime in the NC1.0 lies in Re~25,000. Meanwhile, Eqn. (6.2) is suitable for using in sufficiently high turbulent regime (Re>10,000) but oil was under low turbulent regime (Re~6,000). However, this potential cause cannot be confirmed or evaluated due to the absence of heat transfer measurement system in the heat exchanger.

Table 6.3 MARS-LBE benchmark results for well-defined steady-state experiment results in HELIOS

No.	Main loop (LBE side)					Secondary loop (oil side)
	Total core power (kW)	Hot leg temperature (°C)	Cold leg temperature (°C)	Temperature difference (°C)	LBE mass flow rate (kg/s)	Oil outlet temperature (°C)
NC1.0	9.8	247.11	212.64	34.47	1.90	113.43
NC2.0	15.0	314.39	268.74	45.64	2.23	143.09
NC3.0	27.0	369.60	302.43	67.18	2.76	189.10
NC4.0	33.6	397.47	318.00	79.48	2.90	208.03

Note: all of the values given above are average values from measurements in each case.

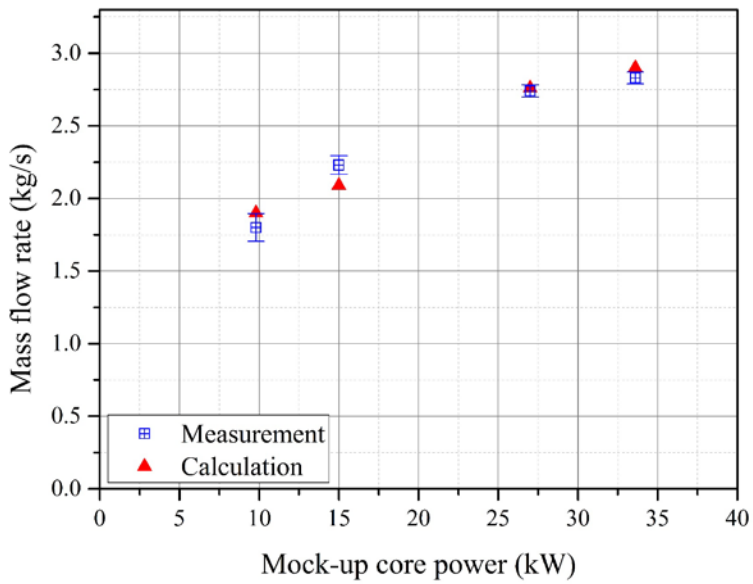

Figure 6.2 Comparison between measured and calculated mass flow rates as a function of mock-up core power

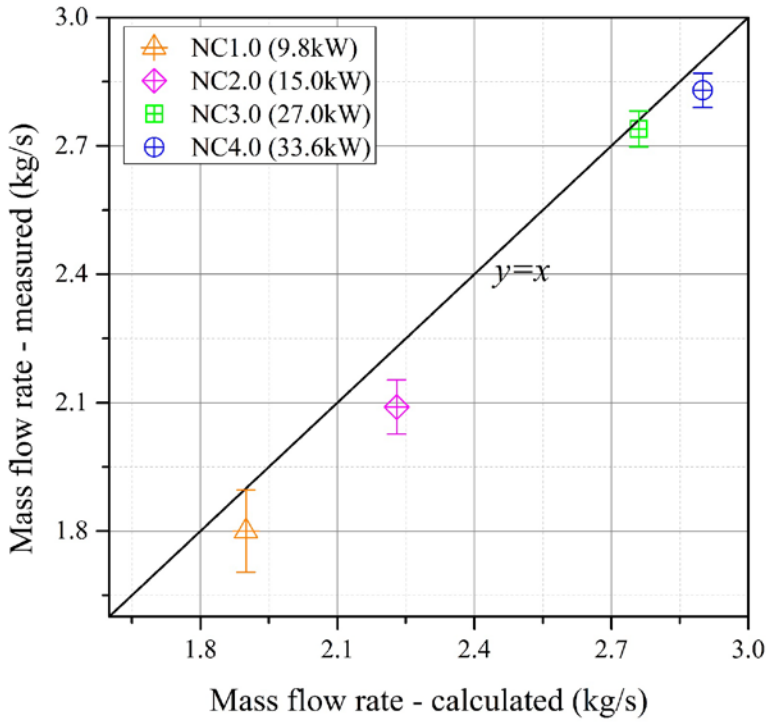

Figure 6.3 Comparison between LBE mass flow rates in HELIOS experiment and MARS-LBE benchmark results

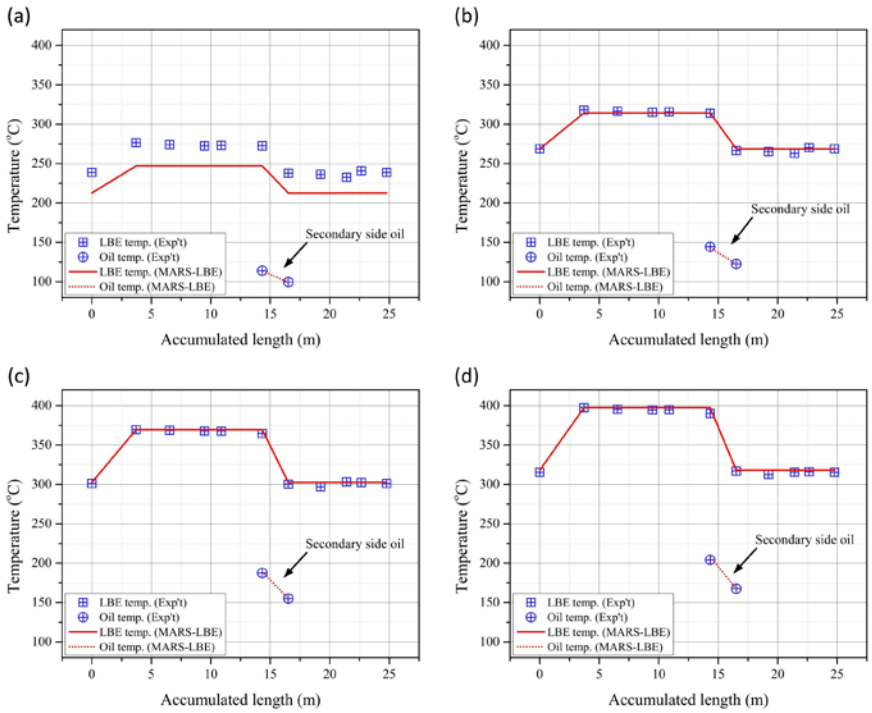

Figure 6.4 Steady state experiment and benchmark results of HELIOS in cases (a) NC1.0 (9.8 kW power), (b) NC2.0 (15.0 kW power), (c) NC1.0 (27.0 kW power), and (d) NC1.0 (33.6 kW power)

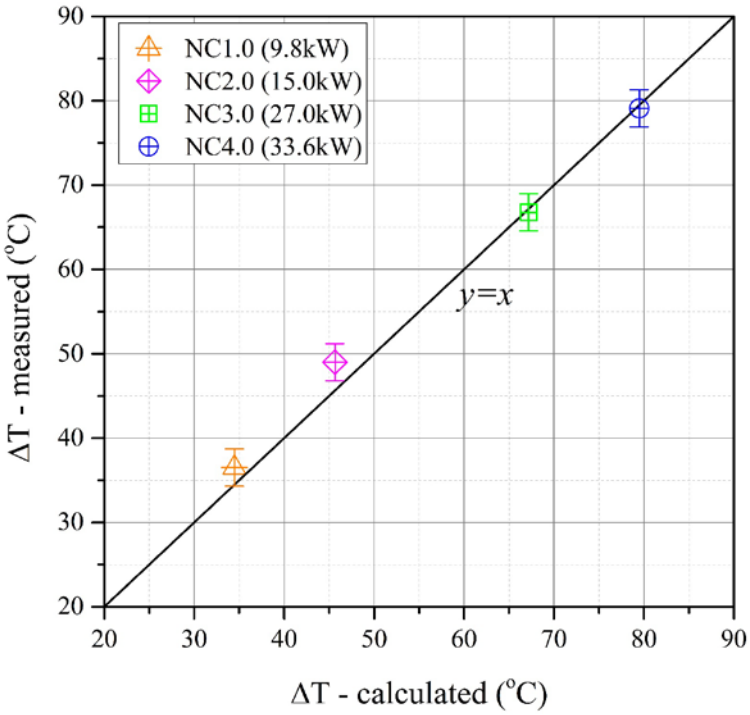

Figure 6.5 Comparison of temperature differences between average hot leg and cold leg temperatures in HELIOS experiment and MARS-LBE benchmark results

Table 6.4 Node conditions for the original, halved, and trisected models used for sensitivity study

Model description	No. of axial nodes	Node length-to-diameter ratio (l_i/d_h)
Original model	7	4.074
Halved	14	2.037
Trisected	21	1.358

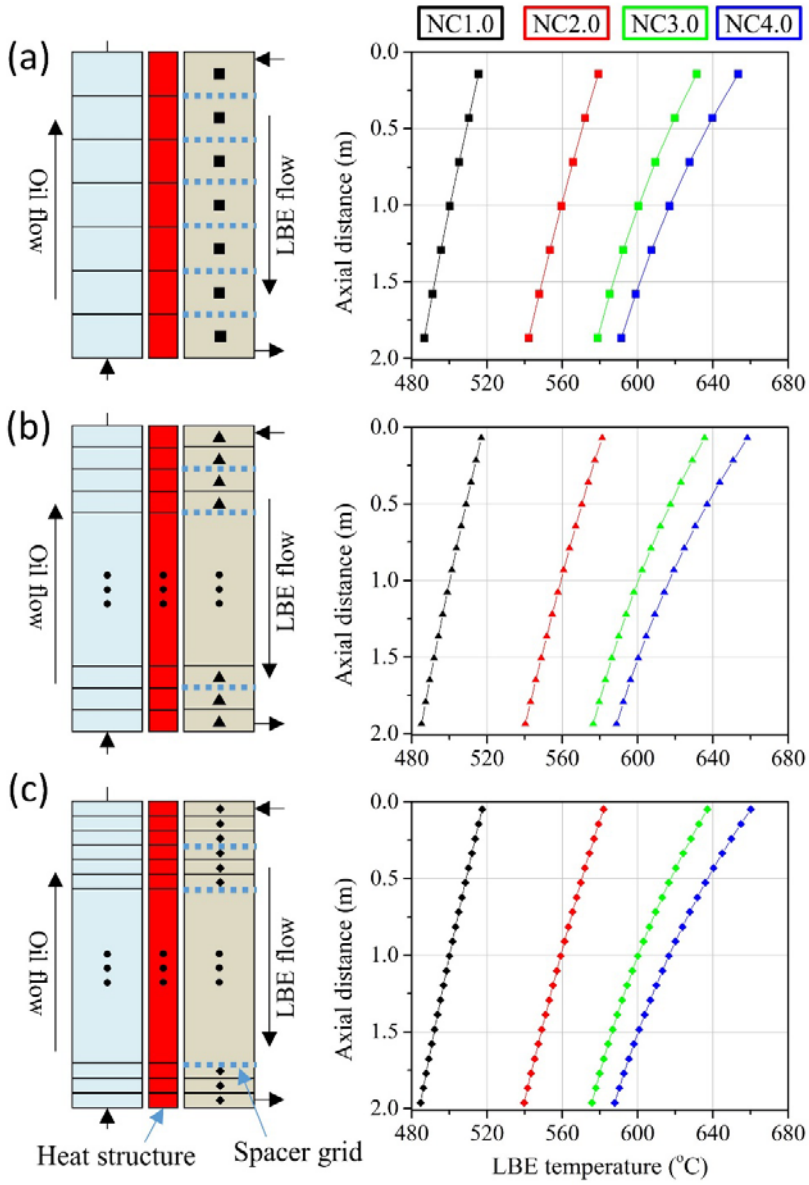

Figure 6.6 Case study results on the heat exchanger axial node size in (a) the original model with 7 axial nodes, (b) halved model with 14 axial nodes, and (c) trisected model with 21 axial nodes

6.2.2 Code benchmark with PILLAR pool test results

6.2.2.1 System nodalization and input preparation on PILLAR

Similar to the HELIOS case, PILLAR is nodalized into several one-dimensional components with about 210 hydrodynamic cells as shown in Figure 6.7. Most of parts are arranged with pipes or annuli, and junctions while the use of the one-dimensional pipe forces to simulate the flow inside the core and upper plenum being averaged over whole flow area.

Several heat structures are designated such as the heater rods, heat exchanger tubes, and the inner shells between downcomer and riser or core regions. Since the themophysical properties of each of heat structures are required to be provided, those of 316L stainless steel for the component wall and heat exchanger tubes are the same with the HELIOS case, as described in Table 6.1. However, the heater rods are comprised of dissimilar materials, as mentioned in Section 5.2.1.4. Furthermore, as depicted in Figure 6.8, there are several lead pins to connect the heating element to electrical lead. For a precise simulation on the effect of thermal inertia, all of the regions are to be included in the modeling while those are interpreted to have equivalent radii by neglecting the lead pins inside the magnesia (MgO) bobbin. The radius of each region is also shown in Figure 6.8 and the thermophysical properties are utilized from Table 5.6.

Differ from the HELIOS case, the convective heat transfer coefficient on water is designated to be the Dittus-Boelter relation (Dittus and Boelter,

1930), a widely used correlation for single- and two-phase water flow in a circular duct, is adopted:

$$\mathrm{Nu}_{water} = 0.023\,\mathrm{Re}^{0.8}\,\mathrm{Pr}^{0.4}, \tag{6.4}$$

where the power of Pr is determined by the state of heat transfer to fluid. In this benchmark, it is given as 0.4 because water is heated so that the primary side LBE is cooled. On the other hand, a value with 0.3 can be used when the fluid is cooled when it flows inside a duct.

For the estimation of hydraulic loss, most of correlations used for HELIOS were taken into account for the PILLAR benchmark. In this respect, the same friction loss correlation is exploited. The roughness of component wall is designated to be 1.0 μm as suggested by manufacturer.

In addition to the system nodalization, the boundary conditions are given by the core power rating exerted to the core through the heat structure for heater rods, and the secondary feedwater conditions including mass flow rate, inlet temperature, and pressure. As the insulation of the system is sufficient to be adiabatic, no heat loss to the environment is modeled.

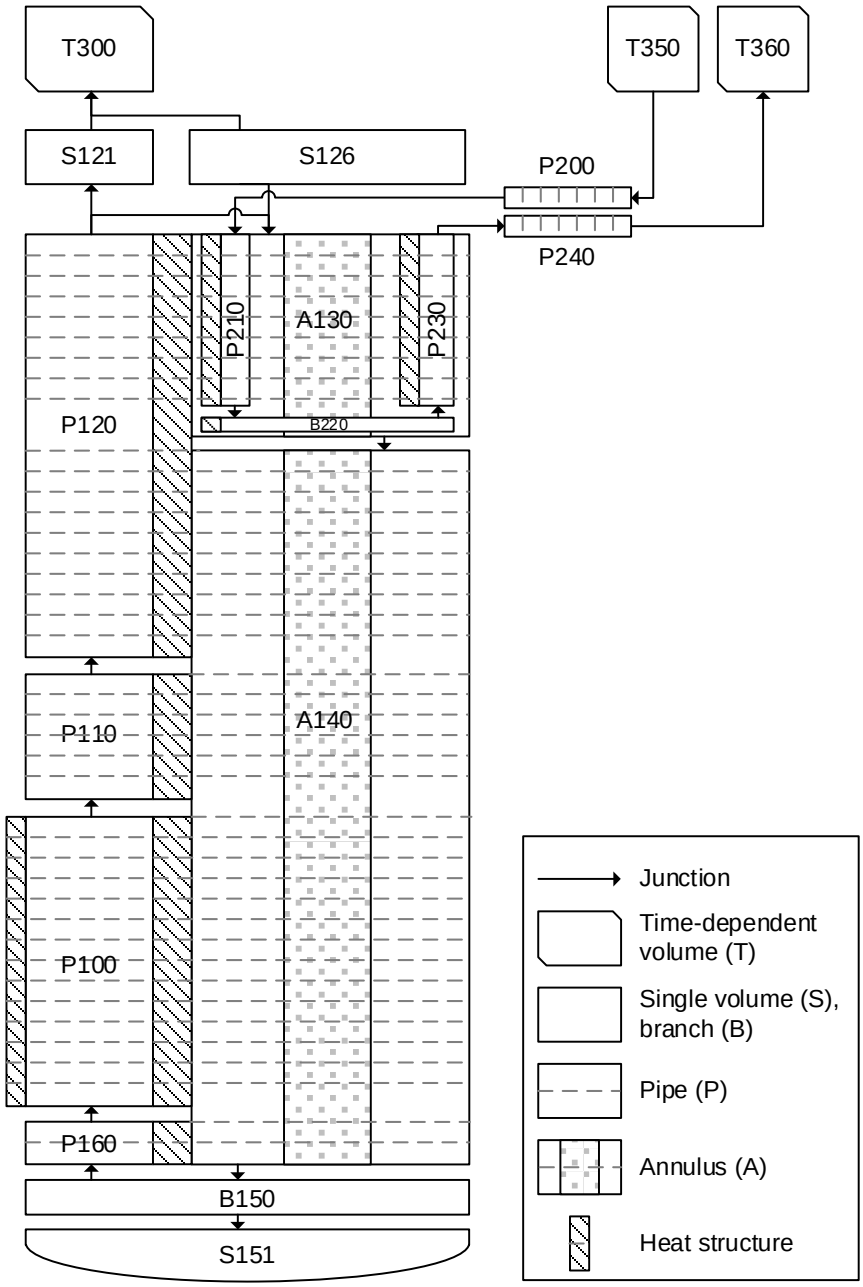

Figure 6.7 Nodalization map of PILLAR prepared for MARS-LBE

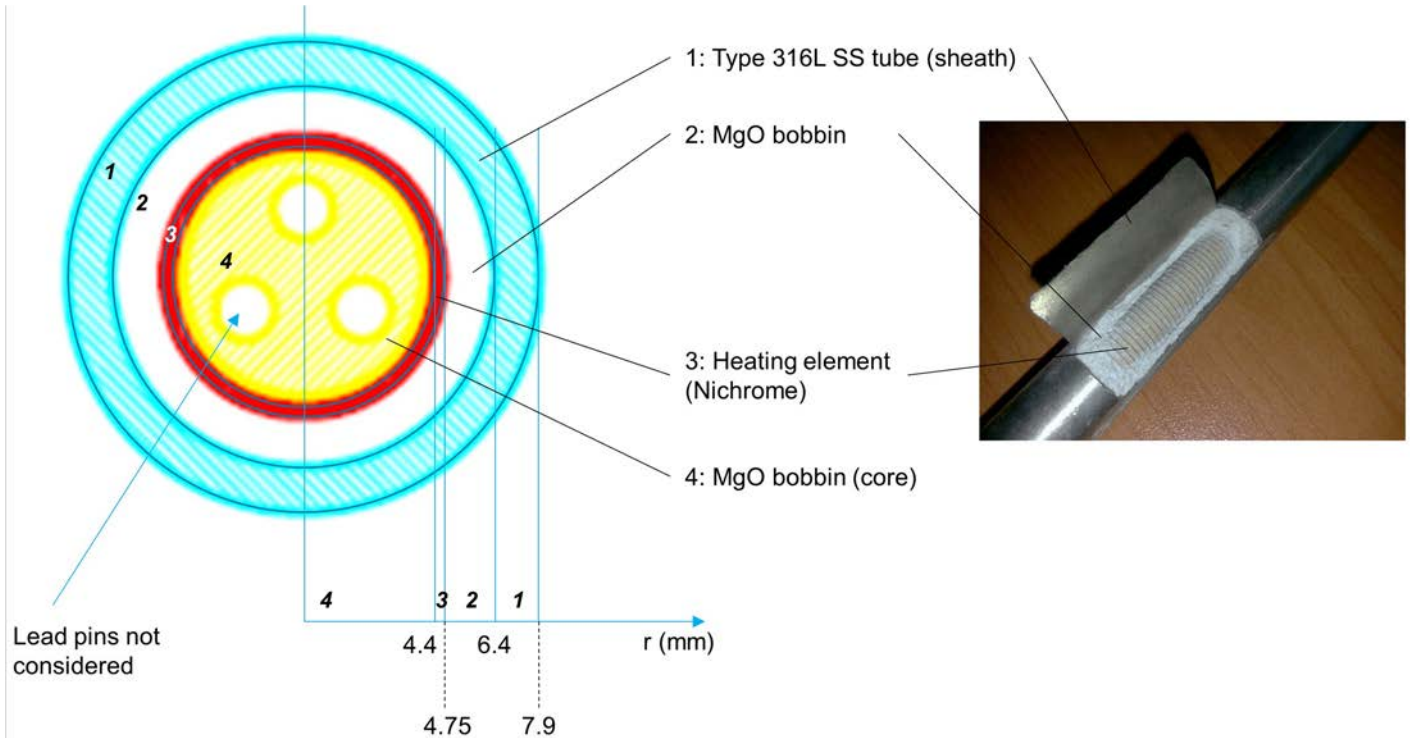

Figure 6.8 PILLAR heater rod cross-sectional view and equivalent radii for each of constituent material regions

6.2.2.2 Code benchmark results for PILLAR natural circulation tests

In this section, the benchmark results of MARS-LBE for LBE natural circulation in pool configuration is described. Through this benchmark, the capability of MARS-LBE on system integral natural circulation behaviors can be validated. The code is made to estimate LBE mass flow rate and temperature difference between the core outlet and inlet within the steady-state natural circulation experimental cases as defined in Section 5.2.4.2. Similar to the benchmark process for HELIOS, boundary conditions such as the core electrical power rating, secondary side conditions including water inlet temperature, mass flow rate, and system pressure were designated with the time-dependent volumes and junctions, and heat structures in the code input file.

Figure 6.9 compares the measured and calculated mass flow rates for all steady-state experimental cases while Figure 6.10 shows the temperature differences between the core inlet and outlet. The benchmark results show that MARS-LBE has a capability on the simulation of LBE natural circulation in pool geometry. As seen in the figures, the measurements and code calculation results lie within maximum ±3% deviations in LBE mass flow rate and the temperature difference, respectively. However, it cannot be confirmed that the code is also capable of simulating some local effects, since the purpose of this benchmark is limited to the integral behavior, mostly on measuring natural circulation flow rate and temperature difference.

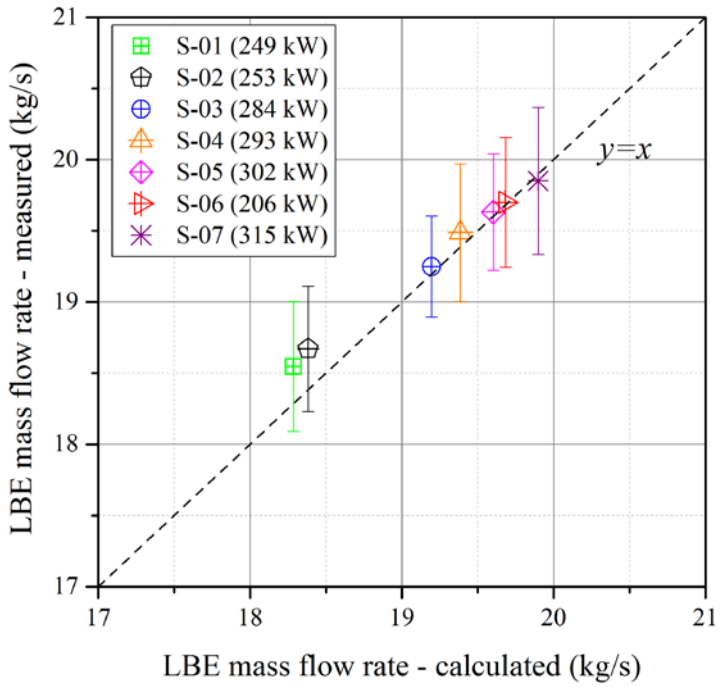

Figure 6.9 Comparison between LBE mass flow rates in PILLAR steady-state experiment and MARS-LBE benchmark results

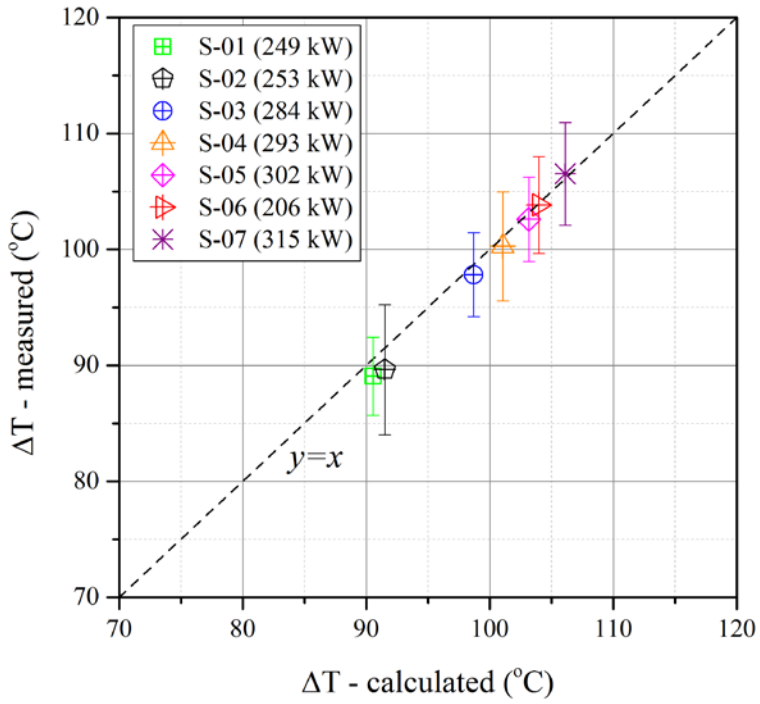

Figure 6.10 Comparison of temperature differences between average hot leg and cold leg temperatures in PILLAR steady-state experiment and MARS-LBE benchmark results

6.3 Code validation on reactor point kinetics

Most of calculation capabilities of MARS-LBE are the same with the original code MARS and one of its variants MARS-LMR, which is prepared for the simulation of liquid metal cooled reactors (KAERI, 2007). The one-dimensional calculation module of MARS can be divided into three main modules including thermal-hydraulics model, reactor kinetics model, and heat structure model. Each of models are related to each other by passing several parameters. Thermal-hydraulics model and heat structure model calculate moderator (coolant) density and fuel temperature, respectively, and the values of those parameters are transferred to the reactor kinetics model. Meanwhile, reactor kinetics model calculates thermal power and passes it to heat structure model. In addition, reactor kinetics model utilizes point kinetics equations for the estimation of neutronic behaviors.

With the validation through the benchmark with LBE natural circulation experimental results as given in Section 6.2, the capability on thermal-hydraulic analysis for LBE systems was ensured. In addition, reactor kinetics module should be validated for the safety analysis of a fast reactor system as well, since MARS was developed for thermal reactors, especially water reactors. However, there has been no experiments for the reactor kinetics of LBE systems so far. Thus, the code cannot be validated in a near term using the experimental data dedicated to LFR.

On the other hand, reactor-scale experiments were conducted with EBR-II (Lehto et al., 1988) in which utilized sodium as primary coolant. As

liquid sodium has more similar thermophysical properties with LBE compared to water and SFR provides fast neutron spectrum, the experimental data have been used for the validation of reactor kinetics module in MARS and MARS-LMR as well. In this respect, the validity of neutron kinetics module in MARS-LBE can be regarded to be confirmed because the backbone code was validated with the sodium experience. This section describes some of the validation work done by other studies.

The International Atomic Energy Agency (IAEA) launched an international benchmark program on the Shutdown Heat Removal Test (SHRT) conducted in EBR-II (Briggs et al., 2015; Briggs et al., 2013). This program designated two different experiments as benchmark targets, SHRT-17 and SHRT-45R, which are loss-of-flow tests with and without scram, respectively. With two experimental results, three main tasks were imposed as system analyses on two test sets and neutronic analysis only on the SHRT-45R test (Sumner and Wei, 2012).

For the former case, SHRT-17, a performance test of MARS was conducted (Choi and Ha, 2016a). The study showed that the calculation results from MARS-LMR and experimental results in transient were in good agreement in overall except the prediction of flow and temperature in a non-fueled subassembly. Another study that dealt with the latter experimental case, SHRT-45R, showed that neutronic and thermal-hydraulic behaviors predicted by MARS-LMR and the measurements were well agreed each other (Choi and Ha, 2016b). Once again, the code had a deviation in the calculation of flow and temperature in the non-fueled subassembly similar to the case of SHRT-17. As

an independent work to the IAEA benchmark program, a code-to-code validation between RELAP-5 and MARS was conducted, by comparing the simulation results on the SHRT-17 data (Shirvan and Ballinger, 2017). The comparison showed consistency in the calculation results from two codes. Considering those activities were reported to be in good agreements with the SFR experiments on simulating reactivity feedback, the reactor kinetics module in MARS-LBE can be concluded to be capable of the prediction of system behaviors under reactivity feedback and sufficient to use the point kinetics equations when it comes to modeling fast neutron reactors.

6.4 System thermal-hydraulics modeling on LBE pool transient natural circulation experiments

As described in Section 6.2, it is identified that the code is capable of the simulation and assessment of thermal-hydraulic behaviors in LBE-cooled systems, especially on natural circulation when it reaches a steady state. However, the validation does not ensure whether MARS-LBE still have the validity on the calculation of time-dependent variation of system parameters. Hence, in this section, the capability of MARS-LBE in transient simulations is verified by comparing the measurements from several sets of transient test results conducted with PILLAR, as described in Section 5.2.4.3.

In order to simulate transient system behaviors with MARS-LBE, several parameters need to be maneuvered within running a problem as simulation time proceeds. MARS-LBE is capable of simulating such cases with a time-dependent component and a control system component (KAERI, 2006). In general, the former directly deals with a specific parameter in the hydrodynamic system by changing its value such as temperature, pressure, mass flow rate, heat flux, and so on. Thus, this model modifies several boundary conditions of the system to make the transient. Several components can also be used as the model described above so that it is a time-dependent component by giving a table that includes temporal change of a given parameter. The latter gives a logical relation as if it is a specific signal to the system. When a system parameter to reach some pre-defined conditions, the control system component can work as a triggering action to a specific component. If this action is defined

by several parameters satisfying each of conditions, then it is required to be constructed with Boolean operations. Due to its versatility, it can be adopted for opening or closing a valve, releasing over-pressure, initiating a certain system transient, and so on.

In this simulation activity, the former elements, time-dependent components, were utilized to impose varying boundary conditions. The conditions were prepared based on the experimental conditions on the core power ratings and secondary side mass flow rates. Other than the component used, those transient results were made from each of steady-state results simulated for the initial conditions. By using the restart option supported by MARS-LBE, it was able to run the transients by initializing system conditions with pre-calculated output data.

Four figures, from Figure 6.11 to Figure 6.14, compare the transient tests conducted with PILLAR and simulation with MARS-LBE. For a better comparison, the test results described in Section 5.2.4.3 with figures from Figure 5.30 to Figure 5.33 are overlapped with the simulation results. The MARS-LBE simulation results, expressed with lines and square marks, and the test results, drawn with bold lines, agree well in all cases including the instantaneous core power and secondary flow rate changes. Some specific behaviors notable in the experiments, such as the time delay for tube side heat transfer saturation, the water outlet temperature variation due to enthalpy change, and the instantaneous tube side heat transfer jump or drop from flow rate changes, are also able to be found in the simulation results. In conclusion, with the benchmarks given in this section, MARS-LBE is capable of simulating

transients in LBE-cooled passive pool-type systems.

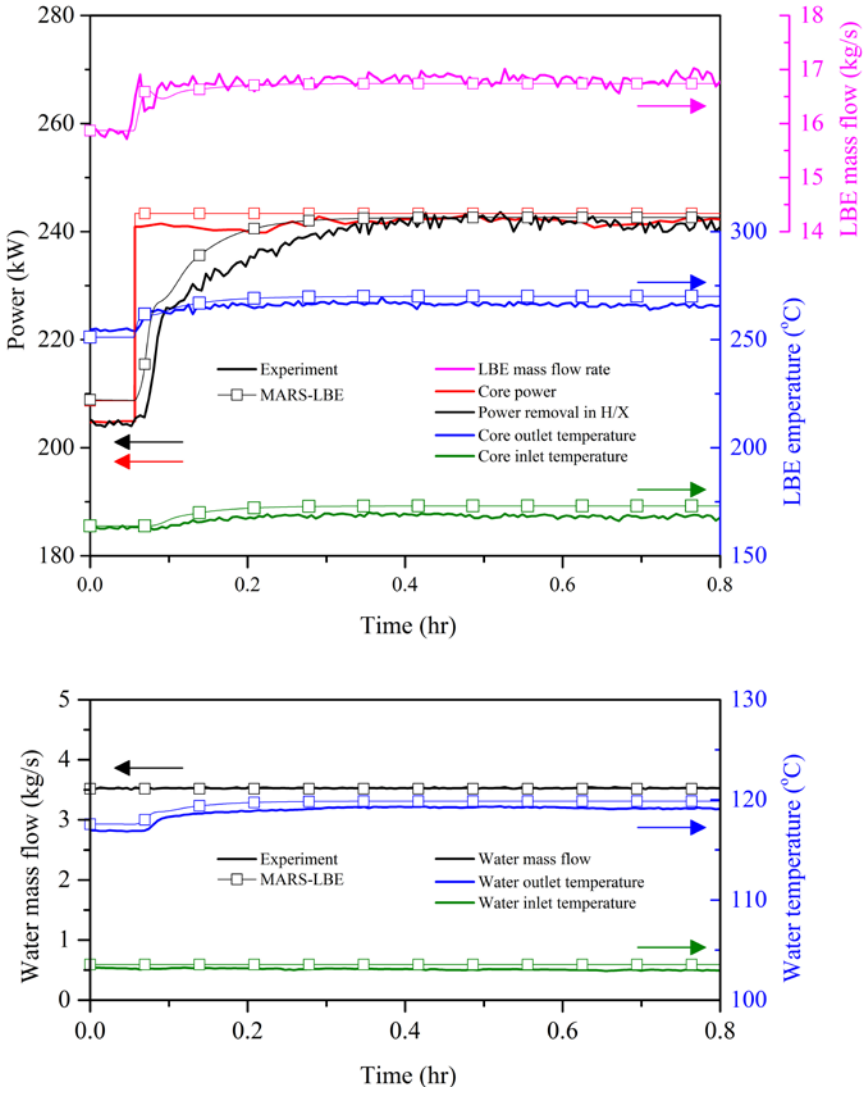

Figure 6.11 Comparison with MARS-LBE modeling results and PILLAR transient natural circulation experimental results: instantaneous core power increase (Case No.: T-PINC-210~240/3.5)

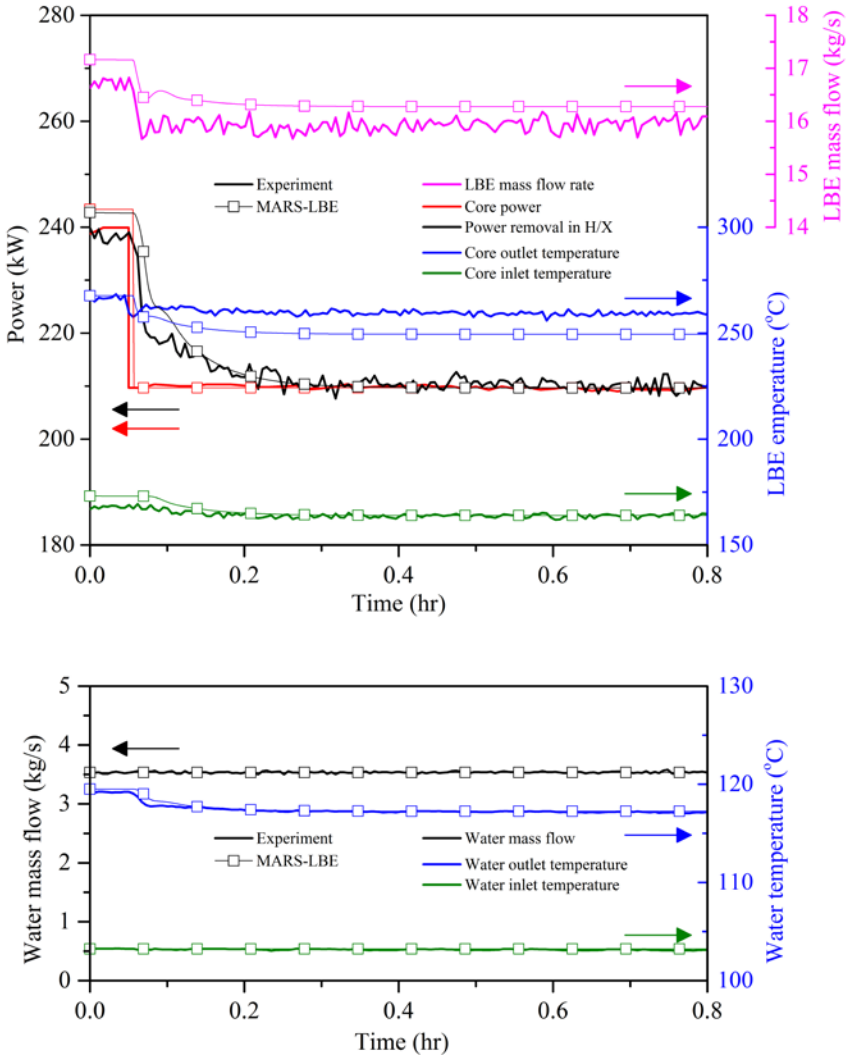

Figure 6.12 Comparison with MARS-LBE modeling results and PILLAR transient natural circulation experimental results: instantaneous core power decrease (Case No.: T-PDEC-240~210/3.5)

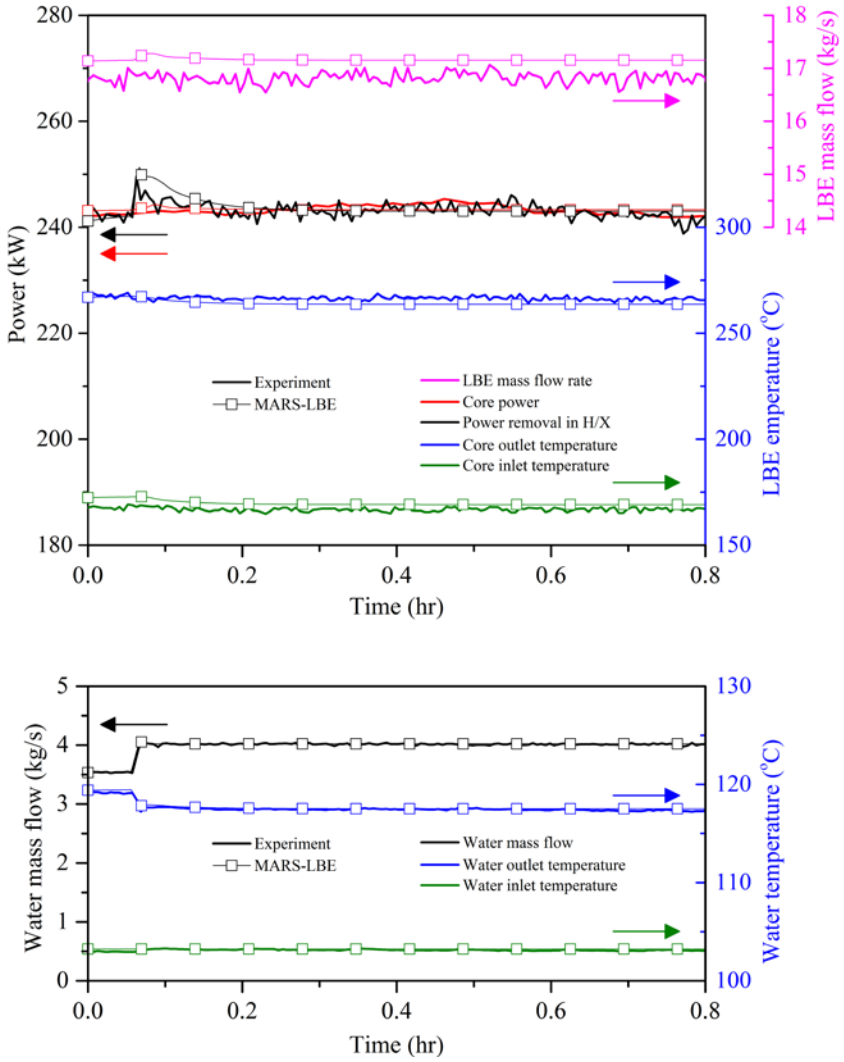

Figure 6.13 Comparison with MARS-LBE modeling results and PILLAR transient natural circulation experimental results: instantaneous secondary side flow rate increase (Case No.: T-FINC-240/3.5~4.0)

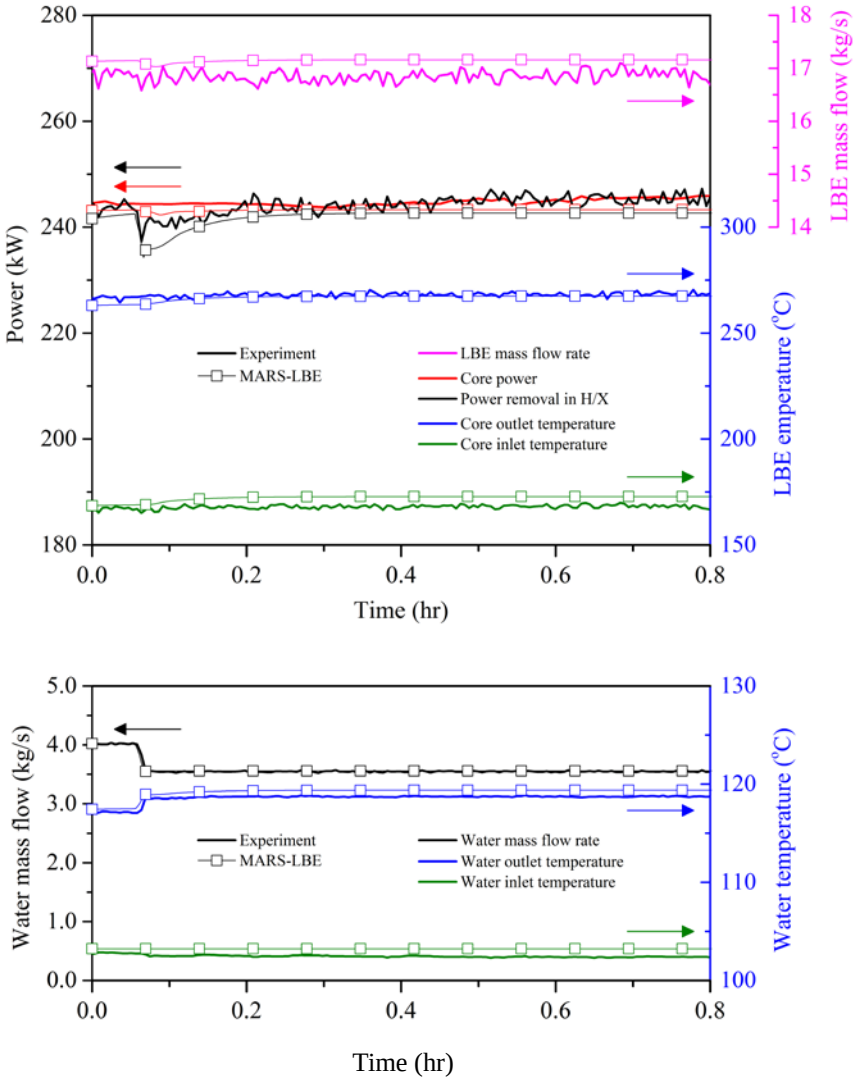

Figure 6.14 Comparison with MARS-LBE modeling results and PILLAR transient natural circulation experimental results: instantaneous secondary side flow rate decrease (Case No.: T-FDEC-240/4.0~3.5)

Chapter 7 Load-Following Capability Assessment of Passive LBE-cooled Pool-type SMR

7.1 Analytical reactor dynamics simulation model

The core power of a passive nuclear system can only be maneuvered by means of control rod movements because there is no reactor coolant pump that can induce the change of temperature condition resulted from flow rate variation so that reactivity feedback comes into action. Considering the maneuverability of the secondary side, another control mechanism can be thought as feedwater flow rate regulation. Reactor power is regulated by the position of control rod while steam production rate is regulated by the amount of feedwater supply and resultant heat removal from the steam generator modules.

In this section, an analytical reactor dynamics simulation model is presented for the purpose of reactor dynamics simulation dedicated to the passive LBE-cooled SMR. The load-following capability of a reactor is assessed and/or evaluated by a simulation considering its dynamic behaviors during maneuvering. Figure 7.1 depicts reactor power and steam production regulations in a passive SMR with control rod movement and feedwater flow control as a schematic diagram. In this formulation, an error signal defined by the discrepancy between a new target state and current state drives the temporal change and the dynamic response of the system. As a simulation target of this

model, URANUS is designated since it is a pool-type passive LBE-cooled SMR, which corresponds to the modeling purpose.

The model is formulated with a lumped parameter approach that nodalizes the whole system into several lumps in which thermophysical properties in a single lump are constant and coolant mass remains constant with respect to coolant temperature change. In this respect, the system of interest, a passive, pool-type, LBE-cooled SMR, is divided into sub-models, reactor core, steam generator, hot leg, and cold leg. As shown in Figure 7.2, a number of assumptions are established for this model, which are discussed in detail through the following sections. The resultant formulations are established in a state-space model that describes time-dependent change of given states in a system. This passive SMR simulation model works along with MATLAB/Simulink R2017a environments that enables relatively short simulation time with high-fidelity solvers and user-friendly graphical interfaces (Mathworks, 2017).

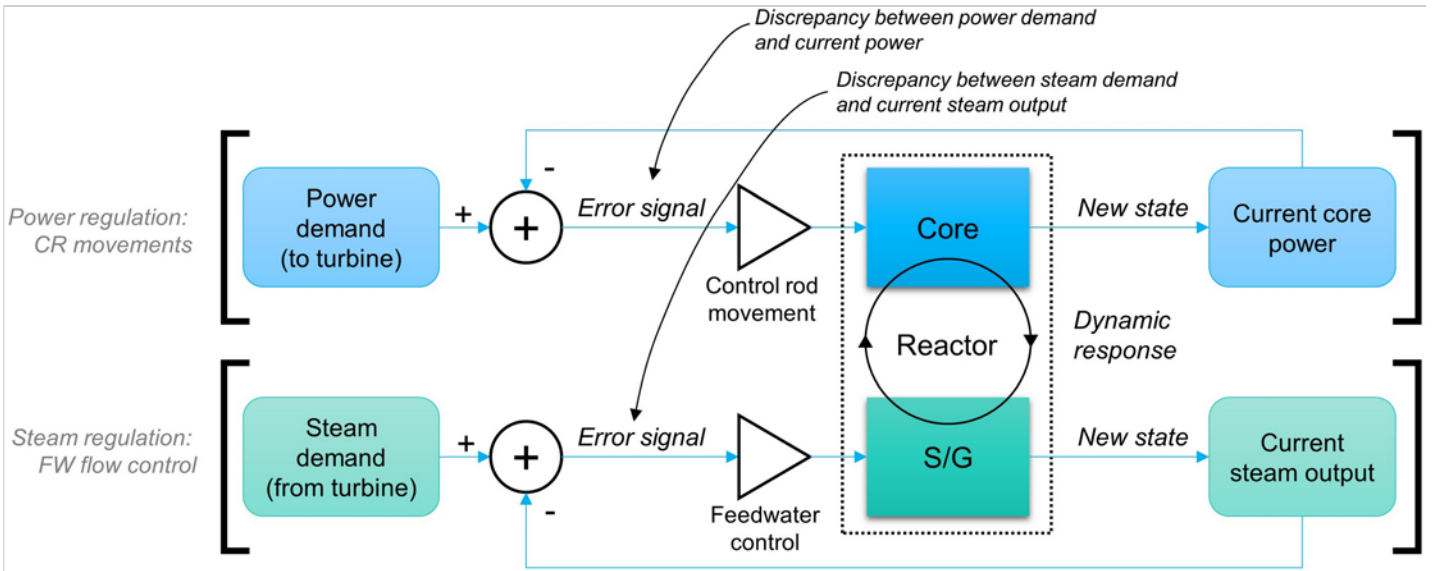

Figure 7.1 Power and steam production regulations in passive SMR by means of control rod movement and feedwater flow control

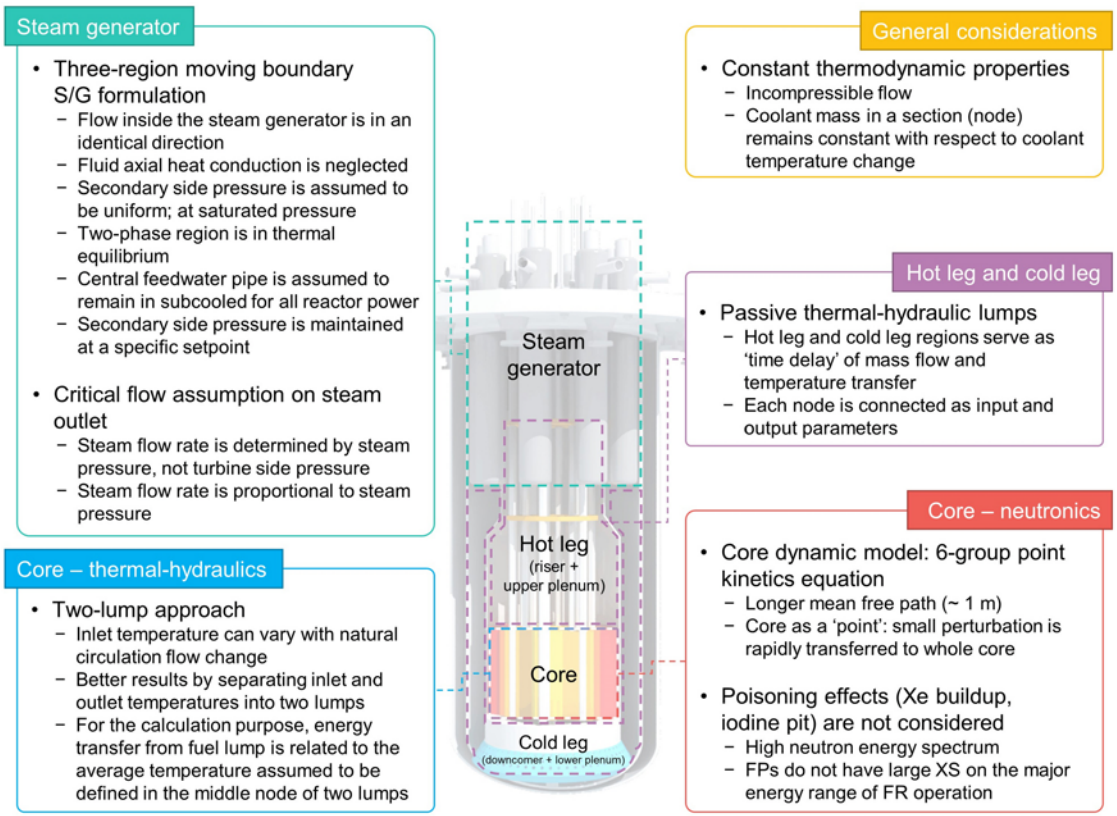

Figure 7.2 Assumptions and approaches for the analytical reactor dynamics simulation model developed in thesis study

7.1.1 Reactor core model

The nonlinear nature of reactor dynamics starts from the reactor core since neutron kinetics is affected by both neutronic and thermal-hydraulic aspects. Considering this, the reactor core model can be comprised of mainly two sub-models: neutronics model that deals with reactivity insertion and feedback and thermal-hydraulics model that is for heat transfer and resultant temperature and mass flow conditions. Within the reactor core model, two sub-models are coupled together by means of reactivity change. Figure 7.3 describes the schematic structure of the reactor core model. The details of each section are elaborated in the following sections.

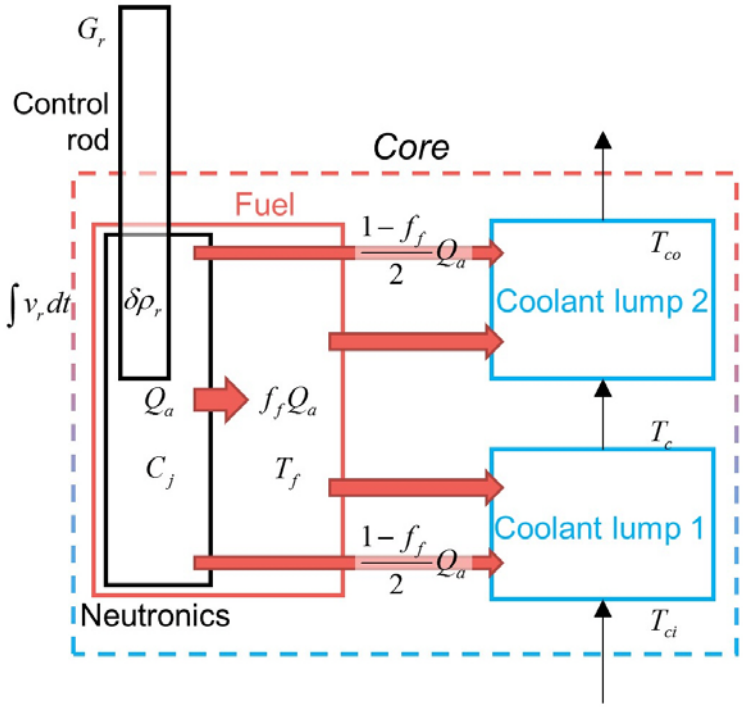

Figure 7.3 Schematic diagram for core state-space model including both neutronics model and core thermal-hydraulics model

7.1.1.1 Neutronics model

For the neutronics model, the point kinetics model is adopted, which utilizes six-group relations and is commonly used among nuclear reactor analyses. The reactor core is treated like a point that has no directional dependence and this assumption is more reasonable for a fast reactor than a thermal reactor due to a longer neutron mean free path in fast neutron spectrum. It is because a small perturbation is rapidly transferred to the entire region in the reactor core by the higher energy spectrum of neutrons (Waltar and Reynolds, 1980). Furthermore, there is no need to consider neutron poisoning effects such as xenon buildup and iodine pit, which exert large negative reactivity insertions, as well. Fission products do not have large neutron absorption cross section on the major energy range of fast reactor operation (Waltar and Reynolds, 1980).

The point kinetics equation used for this model can be formulated with a set of six-group point kinetics equations in terms of the neutron and reactivity balance and delayed neutron precursor densities as shown in Eqns. (7.1) and (7.2):

$$\frac{dn(t)}{dt} = \frac{\rho(t) - \beta_{eff}}{\Lambda} n(t) + \sum_j \lambda_j C_j(t) \quad \text{and} \tag{7.1}$$

$$\frac{dC_j(t)}{dt} = \frac{\beta_j}{\Lambda} n(t) - \lambda_j C_j(t)\,, \tag{7.2}$$

where the effective delayed neutron fraction β_{eff} is expressed with j-th group delayed neutron fractions β_j and precursor decay constants λ_j such that

$\beta_{eff} = \sum_{j=1}^{6} \beta_j$, $\frac{\beta}{\lambda} = \sum_{j=1}^{6} \left(\frac{\beta_j}{\lambda_j} \right)$. Since the temporal terms vanish at the initial condition, t = 0, the following relation can be derived from Eqn. (7.1): $\frac{\beta_j}{\Lambda} n_0 = \lambda_j C_{j0}$. Hence, the equations can be further recast in normalized forms as in Eqns. (7.3) and (7.4):

$$\begin{aligned} \frac{d}{dt} n_r &= \frac{\rho - \beta_{eff}}{\Lambda} n_r + \frac{1}{n_0} \sum_j \lambda_j C_{j0} C_{jr} \\ &= \frac{\rho - \beta_{eff}}{\Lambda} n_r + \sum_j \frac{\beta_j}{\Lambda} C_{jr} \end{aligned}, \tag{7.3}$$

$$\frac{d}{dt} C_{jr} = \frac{\beta_j}{\Lambda} \frac{n_0}{C_{j0}} n_r - \lambda_j C_{jr} = \lambda_j n_r - \lambda_j C_{jr} . \tag{7.4}$$

Since the simulation target is URANUS, the values of kinetic parameters to be used in the model shown in the equations above are also designated to be those calculated in the design stage, as discussed in Section 4.2.

Since the reactor core reacts to total reactivity change as described by the point kinetics equation, the total reactivity change at a specific time, $\delta\rho$, can be given by the sum of reactivity changes induced from control rod movements and several reactivity feedback mechanisms with respect to the temperature change of components as shown in Eqn. (7.5):

$$\delta\rho = \delta\rho_{rod} + \alpha_f \left(T_f - T_{f0} \right) + \alpha_c \left(T_c - T_{c0} \right) . \tag{7.5}$$

In the above equation, the fuel temperature coefficient, α_f, is defined as

$\alpha_f = \alpha_D + \alpha_l$ while the coolant temperature coefficient, α_c, is given by $\alpha_c = \alpha_{LBE} + \alpha_R$ so that the equations can be formulated with fuel and coolant temperature changes within the fuel and coolant lumps depicted in Figure 7.3.

In addition, the rate of external reactivity insertion depends on the rate of rod insertion, i.e. control rod speed, and the reactivity worth of control rods. In general, the reactivity worth of control rods is not the same along the axial direction; in other words, it has an axial profile for more effective and stable regulation of core power. However, this model assumes it constant over the position of control rods. In this regard, the rate of external reactivity insertion is defined as in Eqn. (7.6) with control rod speed and reactivity worth per unit length (Edwards et al., 1990):

$$\frac{d}{dt}\delta\rho_{rod} = G_{rod} v_{rod}\,, \tag{7.6}$$

where the value of reactivity worth per unit length is calculated from a similar design of LBE-cooled passive SMR such that G_{rod} = 4.214E-2 (dk/k)/m (Choi et al., 2011a).

7.1.1.2 Core thermal-hydraulics model

Typically, most of thermal-hydraulic analysis utilizes three transport equations for mass conservation, momentum conservation, and energy balance. In a numerical point of view, the formulations need to be recast since the original

forms are not easy to handle. Hence, the purpose of calculation and the physical aspect of analysis such as the scale of phenomena should be considered. In this regard, the core thermal-hydraulics model and other models for the passive SMR dynamics simulation model developed for this thesis study are defined within the lumped parameter approach so that the model is capable of calculating the transient response of the system.

The core thermal-hydraulics model consists of three lumps that are fuel lump and two coolant lumps. The former treats all the nuclear fuel as a single lump. It is assumed that axial heat transfer in the fuel lump is negligible while core power generated in the fuel lump is transferred to coolant lumps in radial direction. The coolant region is divided into lower and upper coolant lumps, which is called Mann's model named after its developer (Kerlin et al., 1976; Kerlin, 1978). Since core inlet temperature can vary with natural circulation flow change and resultant temperature distribution change in the passive SMR, the most important purpose of this division is to simulate inlet and outlet temperatures independently. The coolant lumps are assumed that fluid flow within each of the lumps are well-mixed, in other words, thermophysical properties in each of the lumps are constant. In addition, this Mann's model features that heat transfer from the fuel lump to coolant is driven by the temperature difference between fuel lump temperature and average coolant temperature, which is defined by the mean value of two coolant lump temperatures.

Applying energy balance relations within and between those lumps, the governing equations of the model can be obtained. In this core thermal-

hydraulics model, heat conduction equation is mainly utilized to relate the fuel lump and coolant lumps accounting for energy balance. As reactor power is proportional to neutron flux or population in the core, it can be expressed with the normalized neutron population and proportional coefficient at the full-power operation condition, as shown in Eqn. (7.7):

$$Q_a(t) = Q_{a0} n_r(t) \quad \cdots \quad Q_{ar}(t) = \frac{Q_{a0} n_r(t)}{Q_{a0}} = n_r(t) \,. \tag{7.7}$$

Heat transfer from fuel to coolant is parametrized by the temperature difference between fuel lump and coolant average temperature, which is defined at the center of each coolant lump. Considering the overall heat transfer coefficient defined by Eqn. (7.8) within a generic pin-cell of nuclear fuel as shown in Figure 7.4, the rate of heat transfer from fuel to coolant is given by Eqn. (7.9):

$$\begin{aligned} \Omega_f = 2\pi N_{rod} H_{rod} \Bigg[& \frac{1}{2k_f} + \frac{1}{r_f h_g} \\ & + \frac{1}{k_{clad}} \ln\left(\frac{r_f + t_g + t_{clad}}{r_f + t_g} \right) + \frac{1}{r_{rod} h_c} \Bigg]^{-1}, \end{aligned} \tag{7.8}$$

$$Q_c(t) = \Omega_f \left(T_f(t) - T_c(t) \right). \tag{7.9}$$

From Eqn. (7.9), the differential form of heat transfer relation can be given as Eqn. (7.10), by assuming that reactor power generated by nuclear reaction is transferred to the fuel lump with a fraction of f_f while the remaining fraction of $(1 - f_f)$ directly heats the coolant:

$$
\begin{aligned}
& f_f Q_a(t) = \left(M_f C_{pf}\right)\frac{d}{dt}T_f + Q_c(t) \\
& \Rightarrow \frac{dT_f}{dt} = \frac{f_f}{\mu_f}Q_{0a}n_r - \frac{\Omega_f}{\mu_f}T_f + \frac{\Omega_f}{\mu_f}T_c
\end{aligned}, \qquad (7.10)
$$

where the total heat capacity of fuel μ_f is given by $\mu_f = M_f C_{pf}$ and the power fraction transferred to the fuel lump f_f is $f_f = 0.98$ (Edwards et al., 1990). It is due to the assumption that coolant mass remains constant to coolant temperature change.

When it comes to heat removal in the two coolant lumps, denoted by node 1 and 2 for lower and upper lumps, respectively, energy balance equation can be formulated as shown in Eqns. (7.11) and (7.12):

$$
\begin{aligned}
& \left(\frac{M_{c,core}}{2}C_{pc}\right)\frac{d}{dt}T_{co} + \dot{m}_p C_{pc}\left(T_{co} - T_c\right) \\
& \qquad = \frac{1}{2}\left[\left(1 - f_f\right)Q_a(t) + Q_c(t)\right] \\
& \Rightarrow \frac{d}{dt}T_{co} = \frac{\left(1 - f_f\right)Q_{0a}}{\mu_{c,core}}n_r + \frac{\Omega_f}{\mu_{c,core}}T_f \\
& \qquad - \frac{\Omega_f}{\mu_{c,core}}T_c + \frac{2C_{pc}}{\mu_{c,core}}\dot{m}_p T_c - \frac{2C_{pc}}{\mu_{c,core}}\dot{m}_p T_{co}
\end{aligned}, \qquad (7.11)
$$

$$
\begin{aligned}
& \left(\frac{M_{c,core}}{2}C_{pc}\frac{d}{dt}\right)T_c + \dot{m}C_{pc}\left(T_c - T_{ci}\right) \\
& \qquad = \frac{1}{2}\left[\left(1 - f_f\right)Q_a(t) + Q_c(t)\right] \\
& \Rightarrow \frac{d}{dt}T_c = \frac{\left(1 - f_f\right)P_{0a}}{\mu_{c,core}}n_r + \frac{\Omega_f}{\mu_{c,core}}T_f - \frac{\Omega_f}{\mu_{c,core}}T_c \\
& \qquad - \frac{2C_{pc}}{\mu_{c,core}}\dot{m}_p T_c + \frac{2C_{pc}}{\mu_{c,core}}\dot{m}_p T_{ci}
\end{aligned}, \qquad (7.12)
$$

where the total heat capacity of coolant within the core region $\mu_{c,core}$ is defined similarly to that of fuel above, such that $\mu_{c,core} = M_{c,core} C_{pc}$. It is noticed that the coolant is directly heated by reactor power generated from nuclear reaction with a fraction of (1 - f_f), as aforementioned.

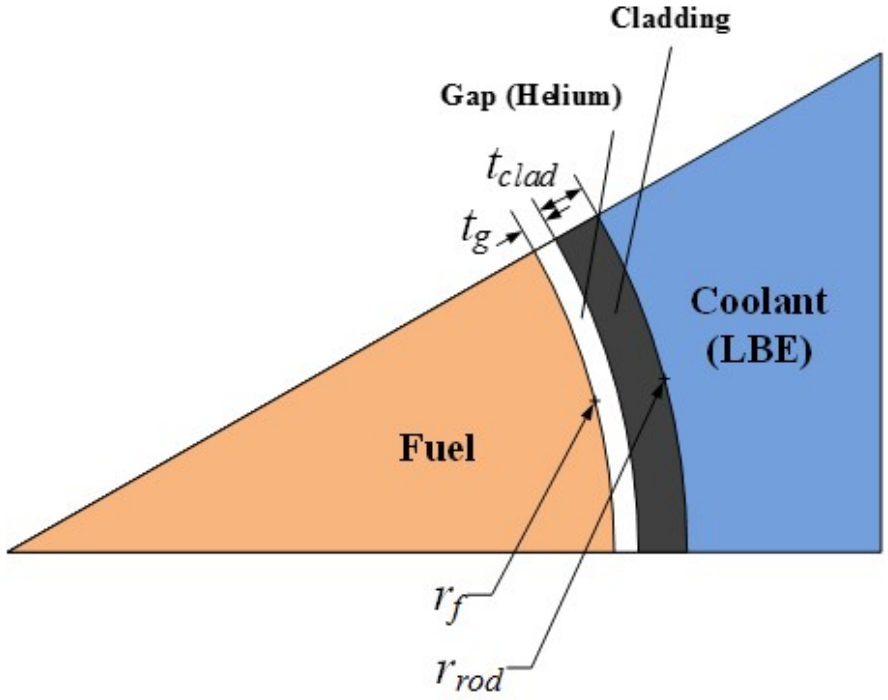

Figure 7.4 Schematic diagram for the reactor core model of generic pin-cell model of nuclear fuel

7.1.1.3 Coolant mass flow rate

In a passive system, coolant mass flow rate given by natural circulation is determined from a balance between buoyancy and hydrodynamic resistance. The buoyancy force is a resultant driving force from the coolant density change caused by coolant temperature gradient along the direction of gravitational force and height difference between the positions where temperature varies. In this regard, the core and steam generator, the heat source and heat sink in a passive SMR, respectively, are the main contributors that generate natural circulation flow. Since the height difference would not remarkably change in most of operating conditions, the temperature difference is a key value that determines natural circulation flow and it can only be regulated by the core power rating. Hence, the mass flow rate varies during load-following operation accompanied by time-dependent power rating change. Meanwhile, the hydrodynamic resistance is dependent upon the configurations and geometries of flow paths, flow speed, flow characteristics, surface conditions, and so on. In general, it is able to be classified with two main categories including friction loss and form loss. In addition, those loss terms are usually nonlinear, which lead to the computation and evaluation of their effects being required to solve it in iterative ways.

In contrast to pump-driven systems, the coolant flow rate is no longer able to be given with a constant value. Due to the existence of the latter, the hydrodynamic resistance, natural circulation flow rate cannot be evaluated with a simple method. The evaluation may need additional computational schemes

with iterations. However, considering the advantage of the lumped parameter approach used in this analytical reactor dynamics simulation model, it is not desirable to implement high-fidelity computational routines for the natural circulation flow rate calculation. In this respect, a simple nonlinear model is applied so that the flow rate is determined independent of other states.

The formulation to evaluate the natural circulation flow rate begins with momentum balance along the flow paths as shown in Eqn. (7.13):

$$\left(\sum_k \frac{L_k}{A_k} \right) \frac{d\dot{m}_p}{dt} = \Delta p_B - \sum_k \Delta p_{loss,k} \ . \tag{7.13}$$

It is noted that the buoyancy head and total pressure drop along the flow paths must be equal to each other in steady-state conditions due to the temporal change of mass flow rate is neglected. To proceed further, a linear relation so-called the Boussinesq approximation, which assumes the fluid density change is linearly given with respect to temperature change, is applied the bouyancy term. As discussed, the sum of pressure drop is usually a nonlinear function of mass flow rate. In this model, an additional assumption is implemented, which describes the total pressure loss is given in a form of Eqn. (7.14) below:

$$\sum_k \Delta p_{loss,k} = C_R \frac{\dot{m}_p^{\ 2}}{2\rho_c}, \tag{7.14}$$

where C_R is the hydraulic resistance coefficient defined by $C_R = R(\dot{m}_p)^{-n}$

(Todreas and Kazimi, 2001). In this relation, *R* is a proportionality constant that can be distinctively determined with the nominal operation condition of the system such that:

$$\sum_k \Delta p_{loss,k} = \frac{R}{2\rho_c}\dot{m}^{2-n} \;\Rightarrow\; R = \frac{2{\rho_c}^2 g\beta\Delta H}{{\dot{m}_0}^{2-n}}\left(T_{co,0} - T_{ci,0}\right). \qquad (7.15)$$

The power *n* is dependent upon flow characteristics. For highly turbulent flow, *n* = 0.2 is to be utilized. Since most of LBE flow expected in URANUS is in turbulent flow regime, this value is used. Accounting for Eqns. (7.14) and (7.15), the momentum balance equation can be further developed as shown in Eqn. (7.16). Since the term $\sum_k \frac{L_k}{A_k}$ is evidently predetermined by the system configurations, it can be given by a constant, c_m.

$$\begin{aligned} &\left(\sum_k \frac{L_k}{A_k}\right)\frac{d\dot{m}_p}{dt} = \rho_c g\beta\Delta H\left(T_{co}(t) - T_{ci}(t)\right) - \frac{R}{2\rho_c}\left\{\dot{m}_p(t)\right\}^{2-n} \\ &\Rightarrow\; \frac{d\dot{m}_p}{dt} = \frac{\rho_c g\beta\Delta H}{c_m}\left(T_{co}(t) - T_{ci}(t)\right) - \frac{1}{c_m}\frac{R}{2\rho_c}\left\{\dot{m}_p(t)\right\}^{2-n} \end{aligned}. \qquad (7.16)$$

For the evaluation of mass flow rate due to natural circulation, the resultant relation above is utilized. It is notable that the dependence of the mass flow rate to the core power is recast with the temperature difference.

7.1.1.4 State-space formulation by linearization

For the establishment of a reactor control model, it is desirable to utilize linearized formulations by designating a state parameter, $\psi(t)$, with an initial value term, ψ_0, and the deviation term, $\delta\psi$, such that $\psi(t) = \psi_0 + \delta\psi$. After replacing all the state parameters with the notation given above and rearranging them with several 1st order terms and 2nd order terms, it can be achieved by leaving only the 1st order terms while neglecting the 2nd order terms, since those terms have negligible impacts (Khalil, 1996).

In this point of view, all the equations established for the reactor core model are to be linearized. First of all, Eqns. (7.17) and (7.18) are rearranged from Eqns. (7.3) and (7.4) with the fact that the initial reactivity is given as $\rho_0 = 0$ and the total reactivity deviation from the initial state is expressed with $\delta\rho = \delta\rho_{rod} + \alpha_f \delta T_f + \frac{\alpha_c}{2}\delta T_{co} + \frac{\alpha_c}{2}\delta T_{ci}$:

$$\frac{d}{dt}\delta n_r = -\frac{\beta_{eff}}{\Lambda}\delta n_r + \sum_j \frac{\beta_j}{\Lambda}\delta C_{ir} + \frac{n_{r0}}{\Lambda}\delta\rho_{rod} + \frac{n_{r0}}{\Lambda}\alpha_f \delta T_f + \frac{n_{r0}}{\Lambda}\frac{\alpha_c}{2}\delta T_{co} + \frac{n_{r0}}{\Lambda}\frac{\alpha_c}{2}\delta T_{ci}, \tag{7.17}$$

$$\frac{d}{dt}\left(\delta C_{jr}\right) = \lambda_j \delta n_r - \lambda_j \delta C_{jr}. \tag{7.18}$$

The time-dependent change of fuel temperature, Eqn. (7.10), can be recast as in Eqn. (7.19):

$$\frac{d}{dt}\delta T_f = \frac{f_f Q_{0a}}{\mu_f}\delta n_r - \frac{\Omega_f}{\mu_f}\delta T_f + \frac{\Omega_f}{\mu_f}\delta T_c . \tag{7.19}$$

The energy balance equations for the lower and upper coolant lumps, Eqns (7.11) and (7.12), are rearranged to be Eqns. (7.20) and (7.21), respectively:

$$\begin{aligned}\frac{d}{dt}\delta T_{co} = {} & \frac{\left(1-f_f\right)Q_{0a}}{\mu_{c,core}}\delta n_r + \frac{\Omega_f}{\mu_{c,core}}\delta T_f - \frac{2\dot{m}_{p0}C_{pc}}{\mu_{c,core}}\delta T_{co} \\ & - \frac{\Omega_f - 2\dot{m}_{p0}C_{pc}}{\mu_{c,core}}\delta T_c - \frac{2C_{pc}}{\mu_{c,core}}\left(T_{co,0} - T_{c0}\right)\delta\dot{m}_p\end{aligned}, \tag{7.20}$$

$$\begin{aligned}\frac{d}{dt}\delta T_c = {} & \frac{\left(1-f_f\right)Q_{0a}}{\mu_{c,core}}\delta n_r + \frac{\Omega_f}{\mu_{c,core}}\delta T_f - \frac{\Omega_f + 2\dot{m}_{p0}C_{pc}}{\mu_{c,core}}\delta T_c \\ & + \frac{2C_{pc}\dot{m}_{p0}}{\mu_{c,core}}\delta T_{ci} - \frac{2C_{pc}}{\mu_{c,core}}\left(T_{c0} - T_{ci,0}\right)\delta\dot{m}_p\end{aligned}. \tag{7.21}$$

The simplified equation for natural circulation mass flow rate, Eqn. (7.16), has a nonlinear term with the power of (2 - *n*), where *n* is determined by coolant flow regime. Eqn. (7.22) shows its binary series expansion and there are resultant higher order terms with respect to $\delta\dot{m}$:

$$\begin{aligned}\left(\dot{m}_{p0} + \delta\dot{m}\right)^{2-n} = {} & \dot{m}_{p0}{}^{2-n} + (2-n)\dot{m}_{p0}{}^{1-n}\delta\dot{m} \\ & + \frac{(2-n)(1-n)}{2}\dot{m}_{p0}{}^{-n}\left(\delta\dot{m}\right)^2 + O\left(\left(\delta\dot{m}\right)^3\right)\end{aligned}. \tag{7.22}$$

Since this linearization process is to neglect the higher order terms above 2nd order, Eqn. (7.16) finally falls into Eqn. (7.23):

$$\frac{d}{dt}\left(\delta \dot{m}_p\right) = \frac{\rho g \beta \Delta H}{c_m}\delta T_{co} - \frac{\rho_c g \beta \Delta H}{c_m}\delta T_{ci} - \frac{R}{2 c_m \rho_c}(2-n)\dot{m}_{p0}^{\,1-n}\delta \dot{m}_p \quad . \tag{7.23}$$

The linearized equations can be used for state-space representation as forms of vector and matrix notations. In general, the temporal change of state vector **x** which represents the states in the system can be expressed with the input vector **u** and coefficient matrices **A** and **B** having appropriate dimensions as in the following relation, Eqn. (7.24):

$$\dot{\mathbf{x}} = \mathbf{A}\mathbf{x} + \mathbf{B}\mathbf{u} \, . \tag{7.24}$$

The resultant state vector x and input vector u is given by Eqns. (7.25) and (7.26), respectively:

$$\mathbf{x} = \left[\delta n_r \quad \delta C_{1r} \quad \delta C_{2r} \quad \delta C_{3r} \quad \delta C_{4r} \quad \delta C_{5r} \quad \delta C_{6r} \quad \delta T_f \quad \delta T_{co} \quad \delta T_c \quad \delta \dot{m}_p \quad \delta \rho_{rod}\right]^T , \text{ and} \tag{7.25}$$

$$\mathbf{u} = \left[\delta T_{cl} \quad \delta \dot{m}_p \quad v_{rod}\right]^T , \tag{7.26}$$

while the elements of coefficient matrices **A** and **B** are summarized in Table 7.1 and Table 7.2. Since those matrices are sparse matrices, non-zero elements are only presented otherwise noted. $a_{i,j}$ and $b_{i,j}$ are the elements of **A** and **B** on the i-th row and the j-th column, respectively.

Table 7.1 Elements of matrix **A** for linearized state-space formulation

Index	Elements	Index	Elements
$a_{1,1}$	$\frac{-\beta_{eff}}{\Lambda}$	$a_{4,4}$	$-\lambda_3$
$a_{1,2}$	$\frac{\beta_1}{\Lambda}$	$a_{5,1}$	λ_4
$a_{1,3}$	$\frac{\beta_2}{\Lambda}$	$a_{5,5}$	$-\lambda_4$
$a_{1,4}$	$\frac{\beta_3}{\Lambda}$	$a_{6,1}$	λ_5
$a_{1,5}$	$\frac{\beta_4}{\Lambda}$	$a_{6,6}$	$-\lambda_5$
$a_{1,6}$	$\frac{\beta_5}{\Lambda}$	$a_{7,1}$	λ_6
$a_{1,7}$	$\frac{\beta_6}{\Lambda}$	$a_{7,7}$	$-\lambda_6$
$a_{1,8}$	$\frac{n_{r0}\alpha_f}{\Lambda}$	$a_{8,1}$	$\frac{f_f Q_{0a}}{\mu_f}$
$a_{1,9}$	$\frac{n_{r0}\alpha_c}{2\Lambda}$	$a_{8,8}$	$\frac{-\Omega_f}{\mu_f}$
$a_{1,12}$	$\frac{n_{r0}}{\Lambda}$	$a_{8,10}$	$\frac{\Omega_f}{\mu_f}$
$a_{2,1}$	λ_1	$a_{9,1}$	$\frac{\left(1-f_f\right)Q_{0a}}{\mu_{c,core}}$
$a_{2,2}$	$-\lambda_1$	$a_{9,8}$	$\frac{\Omega_f}{\mu_{c,core}}$
$a_{3,1}$	λ_2	$a_{9,9}$	$\frac{-2\dot{m}_{p0}C_{pc}}{\mu_{c,core}}$
$a_{3,3}$	$-\lambda_2$	$a_{9,10}$	$\frac{-\Omega_f+2\dot{m}_{p0}C_{pc}}{\mu_{c,core}}$
$a_{4,1}$	λ_3	$a_{9,11}$	$\frac{-2C_{pc}\left(T_{co,0}-T_{c0}\right)}{\mu_{c,core}}$

Table 7.1 Elements of matrix **A** for linearized state-space formulation (contd.)

Index	Elements
$a_{10,1}$	$\frac{\left(1-f_f\right)Q_{0a}}{\mu_{c,core}}$
$a_{10,8}$	$\frac{\Omega_f}{\mu_{c,core}}$
$a_{10,10}$	$\frac{-\Omega_f - 2\dot{m}_{p0}C_{pc}}{\mu_{c,core}}$
$a_{10,11}$	$\frac{-2C_{pc}\left(T_{c0}-T_{ci,0}\right)}{\mu_{c,core}}$
$a_{11,9}$	$\frac{\rho_c g \beta \Delta H}{c_m}$
$a_{11,11}$	$\frac{-(2-n)R\dot{m}_{p0}^{\,1-n}}{2c_m\rho_c}$

Table 7.2 Elements of matrix **B** for linearized state-space formulation

Index	Elements
$b_{1,1}$	$\frac{n_{r0}\alpha_c}{2\Lambda}$
$b_{10,1}$	$\frac{2\dot{m}_{p0}C_{pc}}{\mu_{c,core}}$
$b_{11,1}$	$\frac{-\rho_c g \beta \Delta H}{c_m}$
$b_{12,3}$	G_r

7.1.2 Hot leg and cold leg models

7.1.2.1 Thermal-hydraulic models for hot leg and cold leg

The hot leg and cold leg are physical upstream and downstream components of the core and steam generator, vice versa, as shown in Figure 7.2. Compared to those heat source and sink, there is no heat generation nor heat removal in the hot leg and cold leg and these regions are rather passive components that propagate the change of thermophysical states from a component to the other. Similar to the formulations established for the core thermal-hydraulics sub-model in the reactor core model described in Section 7.1.1.2, energy balance equations can be derived as shown in Eqns. (7.27) and (7.28) for the hot leg and cold leg, respectively:

$$\begin{aligned} &\mu_{c,hl}\frac{d}{dt}T_{hl} = \dot{m}_p C_{pc}\left(T_{co} - T_{hl}\right) \\ &\Rightarrow \frac{dT_{hl}}{dt} = \frac{C_{pc}}{\mu_{c,hl}}\dot{m}_p T_{co} - \frac{C_{pc}}{\mu_{c,hl}}\dot{m}_p T_{hl} \end{aligned}, \tag{7.27}$$

$$\begin{aligned} &\mu_{c,cl}\frac{d}{dt}T_{cl} = \dot{m}_p C_{pc}\left(T_{p1} - T_{cl}\right) \\ &\Rightarrow \frac{dT_{cl}}{dt} = \frac{C_{pc}}{\mu_{c,cl}}\dot{m}_p T_{p1} - \frac{C_{pc}}{\mu_{c,cl}}\dot{m}_p T_{cl} \end{aligned}. \tag{7.28}$$

In the above equations, the total heat capacity of coolant in the hot leg $\mu_{c,hl}$ is given as $M_{c,hl}C_{pc} = \mu_{c,hl}$ while that of coolant in the cold leg $\mu_{c,cl}$ is expressed as $M_{c,cl}C_{pc} = \mu_{c,cl}$, similar to the case in the core thermal-hydraulics sub-model.

Physically, those hot leg and cold leg lumps serve as the time delay of mass flow and temperature transfer. However, this time delay is not constant because the mass flow rate term also depends on the core power rating. With the coolant mass flow rate model implemented in Section 7.1.1.3, the time delay would be influenced.

7.1.2.2 State-space formulation by linearization

In a similar way with the linearization process conducted in Section 7.1.1.4, the hot leg and cold leg models are to be linearized. First, from the energy balance equations for the hot leg as in Eqns. (7.27), the state vector x is given by $\mathbf{x} = \left[\delta T_{hl}\right]$ while the input vector u is designated to be $\mathbf{u} = \left[\delta T_{co} \quad \delta \dot{m}_p\right]^T$. With the same representation shown in Eqn. (7.24), the coefficient matrices **A** and **B** for the hot leg model are:

$$\mathbf{A} = \left[-\frac{\dot{m}_{p0} C_{pc}}{\mu_{c,hl}}\right], \tag{7.29}$$

$$\mathbf{B} = \left[\frac{\dot{m}_{p0} C_{pc}}{\mu_{c,hl}} \quad \frac{C_{pc}\left(T_{co,0} - T_{hl,0}\right)}{\mu_{c,hl}}\right], \tag{7.30}$$

The same approach can be applied to the energy balance equation for the cold leg model, Eqn. (7.28), in which the state vector **x** and input vector **u** are given

by $\mathbf{x} = \left[\delta T_{cl} \right]$ and $\mathbf{u} = \left[\delta T_{po} \quad \delta \dot{m}_p \right]^T$, respectively. The coefficient matrices **A** and **B** for the cold leg model are described in Eqns. (7.31) and (7.32):

$$\mathbf{A} = \left[-\frac{\dot{m}_{p0} C_{pc}}{\mu_{c,cl}} \right], \tag{7.31}$$

$$\mathbf{B} = \left[\frac{\dot{m}_{p0} C_{pc}}{\mu_{c,cl}} \quad \frac{C_{pc} \left(T_{po,0} - T_{cl,0} \right)}{\mu_{c,cl}} \right]. \tag{7.32}$$

7.1.3 Steam generator model

URANUS has eight identical steam generator modules. Each steam generator is a once-through, shell-and-tube type heat exchanger where LBE flows through the shell side while water remove the reactor power with phase transition into superheated steam inside the tube side. Inside the tube side of steam generators, subcooled water comes along central downward feedwater pipes and then distributed in the lower chamber. After that, the fluid flows along the tubes in which most of heat transfer takes place so that counter-current flow with respect to the primary coolant flow is established. As discussed in Section 4.3.2, superheated steam is produced and flows out from the steam generator outlet.

For simplicity, the steam generator model for the reactor dynamics simulation model treats all the modules as a single region by applying the lumped parameter, moving boundary approach (He et al., 1995; Pettit et al.,

1998; Rasmussen and Alleyne, 2006; Willatzen et al., 1998), which utilizes lumped parameter models for each of calculation nodes in a dynamic simulation. This approach is mainly prepared for the prediction of point or position where phase transition occurs in a heat exchanger.

Figure 7.5 shows a simplified moving boundary diagram for steam generator. Since subcooled water transforms into superheated steam as flowing through the tube side, three regions fluid regions such as subcooled, two-phase, and superheated regions are need to be defined. The moving boundaries are designated between those regions. It is assumed that this division into three regions are applied only to the tube bundles, not to the central feedwater pipes as most of heat transfer occurs through the tube bundles, about 95% of total power removal. However, for a consistency of heat transfer relations, the moving boundaries also adopted for the central feedwater pipe region and the tube wall regions comprising of not only the tube bundles but also the feedwater pipes even though there is no phase transition at all. In addition, the lower chamber connecting the central feedwater pipe and tube bundles are not modelled for a simplicity.

Based on the lumped regions as defined and shown in Figure 7.5, the formulations of steam generator model are derived from the partial differential equations, especially on mass conservation and energy balance. By integrating both sides of the equations in terms of flow area, simplified mass conservation equation and energy balance equation can be drawn as shown in Eqns. (7.33) and (7.34), respectively:

$$A_s \frac{\partial \rho}{\partial t} + \frac{\partial \dot{m}_s}{\partial z} = 0\,, \tag{7.33}$$

$$A_s \frac{\partial \left(\rho h - P_s\right)}{\partial t} + \frac{\partial \left(\dot{m}_s h\right)}{\partial z} = \pi d_s h_s N_{tube} \left(T_t - T_s\right). \tag{7.34}$$

As the steam generators have a number of tube bundles, the heat transfer areas between the fluid and the tube surface would proportionally increase. The equations above are further modified by applying an integration rule known as Leibniz's rule as defined in Eqn. (7.35):

$$\begin{aligned} &\int_{a(t)}^{b(t)} \frac{\partial f(z,t)}{\partial t} dz \\ &= \frac{d}{dt}\int_{a(t)}^{b(t)} f(z,t)dz - f(b(t),t)\frac{db(t)}{dt} + f(a(t),t)\frac{da(t)}{dt} \end{aligned}. \tag{7.35}$$

In the following sections, several equations will be described for all the fluid regions by means of Eqn. (7.33) and (7.34), which are suitably recast by the rule given as Eqn. (7.35). The number of equations are dependent upon the number of fluid regions defined moving boundaries that divide the different states of fluids. Since the control volumes are directly related to those moving boundaries, most of sets of equations in each of the fluid regions are given in an almost identical way. However, the formulations in two-phase region should differ from those of other single-phase regions due to additional relations for the mean parameters, such as mean void fraction, being required. It is noted that the derivation and definition of each of those mean parameters are extensively summarized in (Pettit et al., 1998; Rasmussen and Alleyne, 2006) and this thesis will utilize the final forms.

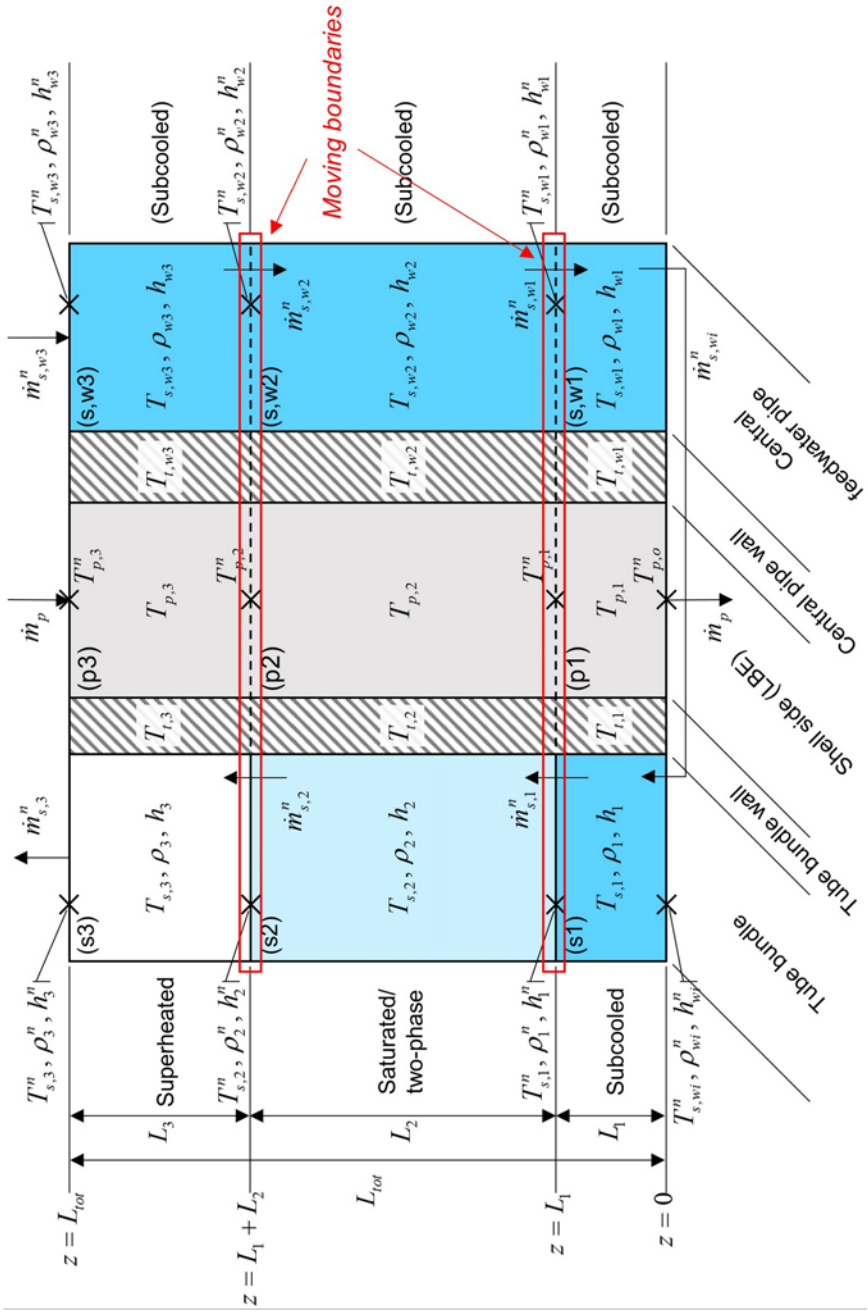

Figure 7.5 Schematic diagram for steam generator state-space model

7.1.3.1 Single phase regions

As shown in Figure 7.5, there are several lumped regions that are filled with single phase fluids, including subcooled water and superheated steam: for example, Regions s1, sw1, sw2, sw3 are for subcooled water while Region s3 is for superheated steam. In those parts, the mean values of fluid density, enthalpy, and volumetric enthalpy, which is defined by the two former parameters, are defined as in Eqns. (7.36) - (7.38), respectively, within the regions between $z = a$ and $z = b$ in which the averaging takes place:

$$\rho_j = \frac{1}{b-a}\int_a^b \rho(z,t)dz = \rho(P_s, h_j)\,, \tag{7.36}$$

$$h_j = \frac{1}{b-a}\int_a^b h(z,t)dz = \frac{h_{j-1}^n + h_j^n}{2}\,, \tag{7.37}$$

$$\rho_j h_j = \frac{1}{b-a}\int_a^b \rho(z,t)h(z,t)dz\,. \tag{7.38}$$

By integrating both sides of Eqns. (7.33) and (7.34) over $z = z_{j-1}$ and $z = z_j$, the following relations, Eqns. (7.39) and (7.40), respectively, can be accounted for the single phase regions:

$$\begin{aligned}
&\int_{z_{j-1}}^{z_j} A_s \frac{\partial \rho}{\partial t}dz + \int_{z_{j-1}}^{z_j} \frac{\partial \dot{m}_s}{\partial z}dz = 0 \\
&\Rightarrow \dot{m}_{s,j-1}^n - \dot{m}_{s,j}^n = A_s L_j \frac{d\rho_j}{dt} + A_s \rho_j \frac{dL_j}{dt} \\
&\qquad\qquad - A_s \rho_j^n \frac{dz_j}{dt} + A_s \rho_{j-1}^n \frac{dz_{j-1}}{dt}
\end{aligned}\,, \tag{7.39}$$

$$
\begin{aligned}
&\int_{z_{j-1}}^{z_j} A_s \frac{\partial\left(\rho h - P_s\right)}{\partial t} dz + \int_{z_{j-1}}^{z_j} \frac{\partial\left(\dot{m}_s h\right)}{\partial z} dz \\
&\quad = \int_{z_{j-1}}^{z_j} \pi d_s h_s N_{tube}\left(T_t - T_s\right) dz \\
&\Rightarrow \pi d_s L_j N_{tube} h_{s,j}\left(T_{t,j} - T_{s,j}\right) + h_{j-1}^n \dot{m}_{s,j-1}^n - h_j^n \dot{m}_{s,j}^n \\
&\quad = -A_s \rho_j^n h_j^n \frac{dz_j}{dt} + A_s \rho_{j-1}^n h_{j-1}^n \frac{dz_{j-1}}{dt} + A_s \rho_j h_j \frac{d\left(z_j - z_{j-1}\right)}{dt} \\
&\qquad - A_s (z_j - z_{j-1}) \frac{dP_s}{dt} + A_s (z_j - z_{j-1}) \frac{d\left(\rho_j h_j\right)}{dt}
\end{aligned}
\qquad (7.40)
$$

For a remark, the direction of integration in the equations above are defined from a direction from bottom to top, the opposite direction to the direction of gravitational force, based on Regions s1 and s3. In the case of the central feedwater pipe regions, including Regions sw1, sw2, and sw3, the direction should be flipped, from top to bottom. In addition, since the equations above uses several thermophysical parameters that are defined on the boundaries and are averaged in the lumped regions at the same time, a careful formulation is required. The parameters with superscript *n* deal with those defined on the boundaries.

From the intermediate forms of mass and energy balance equations as described in Eqns. (7.39) and (7.40), the formulations for each of single phase regions can be further arranged. In the derivation hereafter, several partial derivatives for parameter change with respect to other parameters are utilized, which can be determined by using the so-called steam table, a property table for water and steam. The details on the derivation of those partial derivatives are extensively studied by previous studies (Pettit et al., 1998; Rasmussen and

Alleyne, 2006). Firstly, the final forms for the subcooled region in the tube bundles, Region s1, is given by Eqns. (7.41) and (7.42):

$$\begin{aligned}
&\dot{m}_{s,wi}^{n} - \dot{m}_{s,1}^{n} \\
&= A_{st}\left(\rho_1 - \rho_f\right)\frac{dL_1}{dt} + A_{st}L_1\left(\left.\frac{\partial\rho_1}{\partial P_s}\right|_{h_1} + \frac{1}{2}\left.\frac{\partial\rho_1}{\partial h_1}\right|_{P_s}\frac{\partial h_f}{\partial P_s}\right)\frac{dP_s}{dt}, \\
&\quad + \frac{1}{2}A_{st}L_1\left.\frac{\partial\rho_1}{\partial h_1}\right|_{P_s}\frac{dh_{wi}^{n}}{dt}
\end{aligned} \tag{7.41}$$

$$\begin{aligned}
&h_{s,1}A_{ti,1}\left(T_{t,1} - T_{s,1}\right) + h_{wi}^{n}\dot{m}_{s,wi}^{n} - h_f\dot{m}_{s,1}^{n} \\
&= A_{st}\left(\rho_1 h_1 - \rho_f h_f\right)\frac{dL_1}{dt} \\
&\quad + A_{st}L_1\left[\frac{\rho_1}{2}\frac{\partial h_f}{\partial P_s} + h_1\left(\left.\frac{\partial\rho_1}{\partial P_s}\right|_{h_1} + \frac{1}{2}\left.\frac{\partial\rho_1}{\partial h_1}\right|_{P_s}\frac{\partial h_f}{\partial P_s}\right) - 1\right]\frac{dP_s}{dt}\cdot \\
&\quad + \frac{A_{st}L_1}{2}\left(\rho_1 + h_1\left.\frac{\partial\rho_1}{\partial h_1}\right|_{P_s}\right)\frac{dh_{wi}^{n}}{dt}
\end{aligned} \tag{7.42}$$

Analogously, for the superheated region in tube bundles, Region s3, two following equations are formulated:

$$\begin{aligned}
&\dot{m}_{s,2}^{n} - \dot{m}_{s,3}^{n} \\
&= A_{st}\left(\rho_g - \rho_3\right)\frac{d_1(L_1 + L_2)}{dt} \\
&\quad + A_{st}L_3\left(\left.\frac{\partial\rho_3}{\partial P_s}\right|_{h_3} + \frac{1}{2}\left.\frac{\partial\rho_3}{\partial h_3}\right|_{P_s}\frac{\partial h_g}{\partial P_s}\right)\frac{dP_s}{dt} + \frac{1}{2}A_{st}L_3\left.\frac{\partial\rho_3}{\partial h_3}\right|_{P_s}\frac{dh_3^{n}}{dt}
\end{aligned}, \tag{7.43}$$

$$
\begin{aligned}
&h_{s,3}A_{ti,3}\left(T_{t,3}-T_{s,3}\right)+h_g\dot{m}^n_{s,2}-h^n_3\dot{m}^n_{s,3}\\
&=A_{st}\left(\rho_g h_g-\rho_3 h_3\right)\frac{d\left(L_1+L_2\right)}{dt}\\
&\quad+A_{st}L_3\left[\frac{\rho_3}{2}\frac{\partial h_g}{\partial P_s}+h_3\left(\left.\frac{\partial\rho_3}{\partial P_s}\right|_{h_3}+\frac{1}{2}\left.\frac{\partial\rho_3}{\partial h_3}\right|_{P_s}\frac{\partial h_g}{\partial P_s}\right)-1\right]\frac{dP_s}{dt}\\
&\quad+\frac{A_{st}L_3}{2}\left(\rho_3+h_3\left.\frac{\partial\rho_3}{\partial h_3}\right|_{P_s}\right)\frac{dh^n_3}{dt}
\end{aligned}
\qquad (7.44)
$$

Region sw3, a subcooled region defined in the central feedwater pipes is directly connected to water inlet. The final formulations are:

$$
\begin{aligned}
&\dot{m}^n_{s,w1}-\dot{m}^n_{s,wi}\\
&=A_{sw}\left(\rho_{w1}-\rho^n_{w1}\right)\frac{dL_1}{dt}+A_{sw}L_1\left.\frac{\partial\rho_{w1}}{\partial P_s}\right|_{h_{w1}}\frac{dP_s}{dt}\\
&\quad+\frac{A_{sw}L_1}{2}\left.\frac{\partial\rho_{w1}}{\partial h_{w1}}\right|_{P_s}\frac{dh^n_{wi}}{dt}+\frac{A_{sw}L_1}{2}\left.\frac{\partial\rho_{w1}}{\partial h_{w1}}\right|_{P_s}\frac{dh^n_{w1}}{dt}
\end{aligned}
\qquad (7.45)
$$

$$
\begin{aligned}
&h_{s,w1}A_{twi,1}\left(T_{t,w1}-T_{s,w1}\right)+h^n_{w1}\dot{m}^n_{s,w1}-h^n_{wi}\dot{m}^n_{s,wi}\\
&=A_{sw}\left(\rho_{w1}h_{w1}-\rho^n_{w1}h^n_{w1}\right)\frac{dL_1}{dt}+A_{sw}L_1\left(h_{w1}\left.\frac{\partial\rho_{w1}}{\partial P_s}\right|_{h_{w1}}-1\right)\frac{dP_s}{dt}\\
&\quad+\frac{A_{sw}L_1}{2}\left(\rho_{w1}+h_{w1}\left.\frac{\partial\rho_{w1}}{\partial h_{w1}}\right|_{P_s}\right)\frac{dh^n_{wi}}{dt}\\
&\quad+\frac{A_{sw}L_1}{2}\left(\rho_{w1}+h_{w1}\left.\frac{\partial\rho_{w1}}{\partial h_{w1}}\right|_{P_s}\right)\frac{dh^n_{w1}}{dt}
\end{aligned}
\qquad (7.46)
$$

Region sw2 is also another subcooled region in the central feedwater pipes and the formulations for this region are given by the following Eqns. (7.47) and

(7.48):

$$
\begin{aligned}
&\dot{m}_{s,w2}^{n}-\dot{m}_{s,w1}^{n}\\
&=A_{sw}\left(\rho_{w1}^{n}-\rho_{w2}^{n}\right)\frac{dL_1}{dt}+A_{sw}\left(\rho_{w2}-\rho_{w2}^{n}\right)\frac{dL_2}{dt}\\
&\quad+A_{sw}L_2\left.\frac{\partial\rho_{w2}}{\partial P_s}\right|_{h_{w2}}\frac{dP_s}{dt}+\frac{A_{sw}L_2}{2}\left.\frac{\partial\rho_{w2}}{\partial h_{w2}}\right|_{P_s}\frac{dh_{w1}^{n}}{dt}\,,\\
&\quad+\frac{A_{sw}L_2}{2}\left.\frac{\partial\rho_{w2}}{\partial h_{w2}}\right|_{P_s}\frac{dh_{w2}^{n}}{dt}
\end{aligned}
\tag{7.47}
$$

$$
\begin{aligned}
&h_{s,w2}A_{twi,2}\left(T_{t,w2}-T_{s,w2}\right)+h_{w2}^{n}\dot{m}_{s,w2}^{n}-h_{w1}^{n}\dot{m}_{s,w1}^{n}\\
&=A_{sw}\left(\rho_{w1}^{n}h_{w1}^{n}-\rho_{w2}^{n}h_{w2}^{n}\right)\frac{dL_1}{dt}+A_{sw}\left(\rho_{w2}h_{w2}-\rho_{w2}^{n}h_{w2}^{n}\right)\frac{dL_2}{dt}\\
&\quad+A_{sw}L_2\left(h_{w2}\left.\frac{\partial\rho_{w2}}{\partial P_s}\right|_{h_{w2}}-1\right)\frac{dP_s}{dt}\\
&\quad+\frac{A_{sw}L_2}{2}\left(\rho_{w2}+h_{w2}\left.\frac{\partial\rho_{w2}}{\partial h_{w2}}\right|_{P_s}\right)\frac{dh_{w1}^{n}}{dt}\\
&\quad+\frac{A_{sw}L_2}{2}\left(\rho_{w2}+h_{w2}\left.\frac{\partial\rho_{w2}}{\partial h_{w2}}\right|_{P_s}\right)\frac{dh_{w2}^{n}}{dt}
\end{aligned}
\tag{7.48}
$$

The other subcooled region in the central feedwater pipes is Region sw3, which is assumed to connect the feedwater pipes and tube bundles directly. Eqns. (7.49) and (7.50) describe mass and energy balances within the region:

$$
\begin{aligned}
&\dot{m}_{s,w3}^{n} - \dot{m}_{s,w2}^{n} \\
&= A_{sw}\left(\rho_{w2}^{n} - \rho_{w3}\right)\frac{dL_1}{dt} + A_{sw}\left(\rho_{w2}^{n} - \rho_{w3}\right)\frac{dL_2}{dt} \\
&\quad + A_{sw}L_3\left.\frac{\partial \rho_{w3}}{\partial P_s}\right|_{h_{w3}}\frac{dP_s}{dt} + \frac{1}{2}A_{sw}L_3\left.\frac{\partial \rho_{w3}}{\partial h_{w3}}\right|_{P_s}\frac{dh_{w2}^{n}}{dt}, \\
&\quad + \frac{1}{2}A_{sw}L_3\left.\frac{\partial \rho_{w3}}{\partial h_{w3}}\right|_{P_s}\frac{dh_{w3}^{n}}{dt}
\end{aligned}
\tag{7.49}
$$

$$
\begin{aligned}
&h_{s,w3}A_{twi,3}\left(T_{t,w3} - T_{s,w3}\right) + h_{w3}^{n}\dot{m}_{s,w3}^{n} - h_{w2}^{n}\dot{m}_{s,w2}^{n} \\
&= A_{sw}\left(\rho_{w2}^{n}h_{w2}^{n} - \rho_{w3}h_{w3}\right)\frac{dL_1}{dt} + A_{sw}\left(\rho_{w2}^{n}h_{w2}^{n} - \rho_{w3}h_{w3}\right)\frac{dL_2}{dt} \\
&\quad + A_{sw}L_3\left(h_{w3}\left.\frac{\partial \rho_{w3}}{\partial P_s}\right|_{h_{w3}} - 1\right)\frac{dP_s}{dt} \\
&\quad + \frac{A_{sw}L_3}{2}\left(\rho_{w3} + h_{w3}\left.\frac{\partial \rho_{w3}}{\partial h_{w3}}\right|_{P_s}\right)\frac{dh_{w2}^{n}}{dt} \\
&\quad + \frac{A_{sw}L_3}{2}\left(\rho_{w3} + h_{w3}\left.\frac{\partial \rho_{w3}}{\partial h_{w3}}\right|_{P_s}\right)\frac{dh_{w3}^{n}}{dt}
\end{aligned}
\tag{7.50}
$$

7.1.3.2 Two-phase region

Contrary to the single phase regions described in Section 7.1.3.1, the two-phase region, Region s2, is where phase transition take places. Hence, it is assumed that the thermophysical properties of the working fluid at both ends, the inlet and outlet, are saturated; saturated water at its inlet whilst saturated steam at its outlet. Furthermore, the mean thermophysical properties within the region is defined in terms of the mean void fraction, the volume ratio of vapor to liquid (Rasmussen and Alleyne, 2006; Willatzen et al., 1998). For this assumption

being plausible, it is required that its mean void fraction does not so much change during operation and several experimental results show that this assumption is valid (Wedekind et al., 1978). In this respect, the mean values of fluid density, enthalpy, and volumetric enthalpy are defined in terms of the mean void fraction, γ, of the region and saturated properties as shown in Eqns. (7.51) - (7.53) (Willatzen et al., 1998):

$$\overline{\rho}_2 = \gamma\rho_g + (1-\gamma)\rho_f\,, \tag{7.51}$$

$$\overline{h}_2 = \gamma h_g + (1-\gamma)h_f\,, \tag{7.52}$$

$$\overline{\rho}_2\overline{h}_2 = \gamma\rho_g h_g + (1-\gamma)\rho_f h_f\,. \tag{7.53}$$

For the calculation of the mean void fraction, a correlation given in terms of the ratio of the density of saturated vapor to that of saturated liquid (Jensen and Tummescheit, 2002):

$$\gamma = 1 - \frac{1 + \left(\rho_g/\rho_f\right)^{2/3}\left[(2/3)\ln\left(\rho_g/\rho_f\right) - 1\right]}{\left[\left(\rho_g/\rho_f\right)^{2/3} - 1\right]^2}. \tag{7.54}$$

In analogy with the formulations for the single phase regions, the intermediate forms as described in Eqns. (7.39) and (7.40) are rearranged with the above relations as shown in Eqns. (7.55) and (7.56):

$$
\begin{aligned}
&\dot{m}_{s,1}^{n} - \dot{m}_{s,2}^{n} \\
&= A_{st}\left(\rho_f - \rho_g\right)\frac{dL_1}{dt} + A_{st}\left(1-\gamma\right)\left(\rho_f - \rho_g\right)\frac{dL_2}{dt}, \\
&\quad + A_{st}L_2\left[\gamma\frac{\partial\rho_g}{\partial P_s} + \left(1-\gamma\right)\frac{\partial\rho_f}{\partial P_s}\right]\frac{dP_s}{dt}
\end{aligned}
\tag{7.55}
$$

$$
\begin{aligned}
&h_{s,2}A_{ti,2}\left(T_{t,2} - T_{s,2}\right) + h_f\dot{m}_{s,1}^{n} - h_g\dot{m}_{s,2}^{n} \\
&= A_{st}\left(\rho_f h_f - \rho_g h_g\right)\frac{dL_1}{dt} + A_{st}\left(1-\gamma\right)\left(\rho_f h_f - \rho_g h_g\right)\frac{dL_2}{dt}. \\
&\quad + A_{st}L_2\left[\gamma\frac{\partial(\rho_g h_g)}{\partial P_s} + \left(1-\gamma\right)\frac{\partial(\rho_f h_f)}{\partial P_s} - 1\right]\frac{dP_s}{dt}
\end{aligned}
\tag{7.56}
$$

7.1.3.3 Energy balance equations in constituent walls

As the wall regions including tube bundles and central feedwater pipes work as conductive thermal resistance and there are no fluid flows inside, only energy balance equation is utilized. For this model, the temperature of a wall region, which is defined by the moving boundaries for the two-phase region in the tube bundles, is defined at the center of each lump. In addition, it is assumed that there is no axial conduction among those wall regions. The energy conservation equations for the tube bundles and central feedwater pipes are given as Eqns. (7.57) and (7.58), respectively:

$$
\rho_t C_{pt} A_t \frac{\partial T_t}{\partial t} = -\pi d_p N_{st} h_p\left(T_t - T_p\right) - \pi d_s N_{st} h_s\left(T_t - T_s\right), \tag{7.57}
$$

$$\rho_t C_{pt} A_{tw} \frac{\partial T_{t,w}}{\partial t} = -\pi d_{pw} N_{sw} h_p \left(T_{t,w} - T_p \right) - \pi d_s N_{sw} h_s \left(T_{t,w} - T_{s,w} \right) . \quad (7.58)$$

The above equations require the convective heat transfer coefficients of primary and secondary coolants. For the primary coolant, the Seban-Shimazaki correlation (Seban and Shimazaki, 1949), which already given in Eqn. (6.1), is applied while a widely used correlation for single phase water flows, the Dittus-Boelter correlation (Dittus and Boelter, 1930), is used. Since the two-phase region is also treated as if it is another single-phase flow by means of mean void fraction, the same correlation is utilized to the region.

Considering the boundary conditions given by the fluid regions surrounding those wall regions, the equations above can be further recast. The energy balance equations for the tube bundle wall regions, Region t1, t2, and t3 can indeed be formulated with Eqns. (7.59) - (7.61):

$$\rho_t C_{pt} A_t L_1 \frac{dT_{t,1}}{dt} + \rho_t C_{pt} A_t \left(T_{t,1} - T_{t,2} \right) \frac{dL_1}{dt} = -h_{p,1} A_{to,1} \left(T_{t,1} - T_{p,1} \right) - h_{s,1} A_{ti,1} \left(T_{t,1} - T_{s,1} \right) , \quad (7.59)$$

$$\rho_t C_{pt} A_t L_2 \frac{dT_{t,2}}{dt} = -h_{p,2} A_{to,2} \left(T_{t,2} - T_{p,2} \right) - h_{s,2} A_{ti,2} \left(T_{t,2} - T_{s,2} \right) , \text{ and} \quad (7.60)$$

$$\rho_t C_{pt} A_t L_3 \frac{dT_{t,3}}{dt} + \rho_t C_{pt} A_t \left(T_{t,2} - T_{t,3} \right) \frac{dL_1}{dt} + \rho_t C_{pt} A_t \left(T_{t,2} - T_{t,3} \right) \frac{dL_2}{dt} = -h_{p,3} A_{to,3} \left(T_{t,3} - T_{p,3} \right) - h_{s,3} A_{ti,3} \left(T_{t,3} - T_{s,3} \right) , \quad (7.61)$$

where heat transfer areas between a fluid region and the wall region, including $A_{ti,j}$, $A_{to,j}$, $A_{twi,j}$, and $A_{two,j}$, are respectively defined by $A_{ti,j} = \pi d_s N_{st} L_j$, $A_{to,j} = \pi d_p N_{st} L_j$, $A_{twi,j} = \pi d_{sw} N_{sw} L_j$, and $A_{two,j} = \pi d_{pw} N_{sw} L_j$. Similarly, the central feedwater pipe wall regions, Region tw1, tw2, and tw3 have the following energy balance described with Eqns. (7.62) - (7.64):

$$\begin{aligned} &\rho_t C_{pt} A_{tw} L_1 \frac{dT_{t,w1}}{dt} + \rho_t C_{pt} A_{tw} \left(T_{t,w1} - T_{t,w2}\right) \frac{dL_1}{dt} \\ &= -h_{p,1} A_{two,1} \left(T_{t,w1} - T_{p,1}\right) - h_{s,w1} A_{twi,1} \left(T_{t,w1} - T_{s,w1}\right) \end{aligned} \quad , \tag{7.62}$$

$$\begin{aligned} &\rho_t C_{pt} A_{tw} L_2 \frac{dT_{t,w2}}{dt} \\ &= -h_{p,2} A_{two,2} \left(T_{t,w2} - T_{p,2}\right) - h_{s,w2} A_{twi,2} \left(T_{t,w2} - T_{s,w2}\right) \end{aligned} \quad \text{, and} \tag{7.63}$$

$$\begin{aligned} &\rho_t C_{pt} A_{tw} L_3 \frac{dT_{t,w3}}{dt} + \rho_t C_{pt} A_{tw} \left(T_{t,w2} - T_{t,w3}\right) \frac{dL_1}{dt} \\ &+ \rho_t C_{pt} A_{tw} \left(T_{t,w2} - T_{t,w3}\right) \frac{dL_2}{dt} \\ &= -h_{p,3} A_{two,3} \left(T_{t,w3} - T_{p,3}\right) - h_{s,w3} A_{twi,3} \left(T_{t,w3} - T_{s,w3}\right) \end{aligned} \quad . \tag{7.64}$$

7.1.3.4 Shell side regions

The primary side of a steam generator consists of the shell side. In analogy with other regions, the shell side regions are also divided into three regions according to the moving boundaries given in the tube bundles, which are Region p1, p2 and p3 as depicted in Figure 7.5. Since the phase transition of primary coolant never takes place in URANUS in most of operating and accidental conditions and the mass flow rate relation given in Section 7.1.1.3 accounts for hydraulic

loss for all components, only the energy balance equations are required to describe physical behaviors in the shell side regions. In addition, those regions are related to both the central feedwater pipe regions and the tube bundle regions. Hence, the balance equations are drawn as shown in Eqn. (7.65) by adding those two contributions:

$$\begin{aligned}\rho_c C_{pc} A_p \frac{\partial T_p}{\partial t} = &-\dot{m}_p C_{pc} \frac{\partial T_p}{\partial z} - \pi d_p h_p N_{st} \left(T_p - T_t\right) \\ &- \pi d_{pw} h_p N_{sw} \left(T_p - T_{t,w}\right)\end{aligned} \tag{7.65}$$

By integrating both sides within each of the regions, the above equation can be rearranged as the following equations, Eqns. (7.66), (7.67), and (7.68), for Region p1, p2, and p3, respectively:

$$\begin{aligned}&\rho_c C_{pc} A_p L_1 \frac{dT_{p,1}}{dt} + \rho_c C_{pc} A_p \left(T_{p,1} - T_{p,2}\right) \frac{dL_1}{dt} \\ &= \dot{m}_p C_{pc} \left(T_{p,2} - T_{p,1}\right) - h_{p,1} A_{to,1} \left(T_{p,1} - T_{t,1}\right) \\ &\quad - h_{p,1} A_{two,1} \left(T_{p,1} - T_{t,w1}\right)\end{aligned} \quad , \tag{7.66}$$

$$\begin{aligned}&\rho_c C_{pc} A_p L_2 \frac{dT_{p,2}}{dt} \\ &= \dot{m}_p C_{pc} \left(T_{p,3} - T_{p,2}\right) - h_{p,2} A_{to,2} \left(T_{p,2} - T_{t,2}\right), \\ &\quad - h_{p,2} A_{two,2} \left(T_{p,2} - T_{t,w2}\right)\end{aligned} \tag{7.67}$$

$$\begin{aligned}&\rho_c C_{pc} A_p L_3 \frac{dT_{p,3}}{dt} + \rho_c C_{pc} A_p \left(T_{p,2} - T_{p,3}\right) \frac{dL_1}{dt} \\ &\quad + \rho_c C_{pc} A_p \left(T_{p,2} - T_{p,3}\right) \frac{dL_2}{dt} \\ &= \dot{m}_p C_{pc} \left(T_{p,in} - T_{p,3}\right) - h_{p,3} A_{to,3} \left(T_{p,3} - T_{t,3}\right) \\ &\quad - h_{p,3} A_{two,3} \left(T_{p,3} - T_{t,w3}\right)\end{aligned} \quad , \tag{7.68}$$

7.1.3.5 State-space formulation for steam generator

With the same point of view, the steam generator model has several nonlinear equations and it is appropriate to utilize the linearized forms of those equations for control purposes. Contrary to the case of the reactor core model, the formulations for this model is highly nonlinear. In detail, several number of equations are not easily arranged as a linear summation of temporal term of a state and other terms that are related to the other states so that the state vector is established with the final linear relation, Eqn. (7.24), since the state vector is not linear independent. In this regard, the simple derivation, which is conducted by dividing a state into the initial value and deviation, does not work for the linearization process on constructing state-space formulation of the steam generator model.

In order to overcome this problem, a linear algebraic approach is to be used (Khalil, 1996). A detailed derivation can be found in a previous study (Rasmussen and Alleyne, 2006). This approach begins with the state-space formulation, which is not yet linearized, is given as a form shown in Eqn. (7.69):

$$Z(\mathbf{x},\mathbf{u})\dot{\mathbf{x}} = f(\mathbf{x},\mathbf{u}), \tag{7.69}$$

where $\mathbf{x}$ is the state vector, $\mathbf{u}$ is the input vector, the matrices $Z(\mathbf{x},\mathbf{u})$ and $f(\mathbf{x},\mathbf{u})$ is given by arranging the system of differential equations with vector-matrix formats, respectively, which are derived from the equations for the steam

generator model. If the matrix $Z(\mathbf{x},\mathbf{u})$ is assumed to be invertible, Eqn. (7.69) can be rearranged by adopting a new matrix form $g(\mathbf{x},\mathbf{u})$:

$$\dot{\mathbf{x}} = Z^{-1}(\mathbf{x},\mathbf{u})\, f(\mathbf{x},\mathbf{u}) \equiv g(\mathbf{x},\mathbf{u}) . \tag{7.70}$$

By using the perturbation notation, $\delta\dot{\mathbf{x}} = \mathbf{x} - \mathbf{x}_0$, one would finally get:

$$\delta\dot{\mathbf{x}} = \left[\left.\frac{\partial g}{\partial \mathbf{x}}\right|_{\mathbf{x}_0,\mathbf{u}_0}\right]\delta\mathbf{x} + \left[\left.\frac{\partial g}{\partial \mathbf{u}}\right|_{\mathbf{x}_0,\mathbf{u}_0}\right]\delta\mathbf{u} . \tag{7.71}$$

Then, the matrix differentiation terms in Eqn. (7.71) are expressed as follows:

$$\begin{aligned}\left[\left.\frac{\partial g}{\partial \mathbf{x}}\right|_{\mathbf{x}_0,\mathbf{u}_0}\right] &= \left[Z\big|_{\mathbf{x}_0,\mathbf{u}_0}\right]^{-1}\left[\left.\frac{\partial f}{\partial \mathbf{x}}\right|_{\mathbf{x}_0,\mathbf{u}_0}\right] \\ &\quad - \left[Z\big|_{\mathbf{x}_0,\mathbf{u}_0}\right]^{-2}\left[\left.\frac{\partial Z}{\partial \mathbf{x}}\right|_{\mathbf{x}_0,\mathbf{u}_0}\right]^{-1}\cancel{\left[f_{\mathbf{x}_0,\mathbf{u}_0}\right]} \\ &= \left[Z\big|_{\mathbf{x}_0,\mathbf{u}_0}\right]^{-1}\left[\left.\frac{\partial f}{\partial \mathbf{x}}\right|_{\mathbf{x}_0,\mathbf{u}_0}\right]\end{aligned} \tag{7.72}$$

$$\begin{aligned}\left[\left.\frac{\partial g}{\partial \mathbf{u}}\right|_{\mathbf{x}_0,\mathbf{u}_0}\right] &= \left[Z\big|_{\mathbf{x}_0,\mathbf{u}_0}\right]^{-1}\left[\left.\frac{\partial f}{\partial \mathbf{u}}\right|_{\mathbf{x}_0,\mathbf{u}_0}\right] \\ &\quad - \left[Z\big|_{\mathbf{x}_0,\mathbf{u}_0}\right]^{-2}\left[\left.\frac{\partial Z}{\partial \mathbf{u}}\right|_{\mathbf{x}_0,\mathbf{u}_0}\right]^{-1}\cancel{\left[f_{\mathbf{x}_0,\mathbf{u}_0}\right]} \\ &= \left[Z\big|_{\mathbf{x}_0,\mathbf{u}_0}\right]^{-1}\left[\left.\frac{\partial f}{\partial \mathbf{u}}\right|_{\mathbf{x}_0,\mathbf{u}_0}\right]\end{aligned} \tag{7.73}$$

With the coefficient matrices for the initial values $\mathbf{x}_0$ and $\mathbf{u}_0$, the final linearized form can be drawn as in Eqn. (7.74):

$$\begin{aligned}\dot{\mathbf{x}} &= \left[Z\big|_{\mathbf{x}_0,\mathbf{u}_0} \right]^{-1} \left[\frac{\partial f}{\partial \mathbf{x}}\bigg|_{\mathbf{x}_0,\mathbf{u}_0} \right] \delta\mathbf{x} + \left[Z\big|_{\mathbf{x}_0,\mathbf{u}_0} \right]^{-1} \left[\frac{\partial f}{\partial \mathbf{u}}\bigg|_{\mathbf{x}_0,\mathbf{u}_0} \right] \delta\mathbf{u} \\ &= \left[Z\big|_{\mathbf{x}_0,\mathbf{u}_0} \right]^{-1} F_{\mathbf{x}} \delta\mathbf{x} + \left[Z\big|_{\mathbf{x}_0,\mathbf{u}_0} \right]^{-1} F_{\mathbf{u}} \delta\mathbf{u}\end{aligned}, \qquad (7.74)$$

where the coefficients $F_{\mathbf{x}}$ and $F_{\mathbf{u}}$ are designated to be $F_{\mathbf{x}} = \left[\frac{\partial f}{\partial \mathbf{x}}\bigg|_{\mathbf{x}_0,\mathbf{u}_0} \right]$ and $F_{\mathbf{u}} = \left[\frac{\partial f}{\partial \mathbf{u}}\bigg|_{\mathbf{x}_0,\mathbf{u}_0} \right]$, respectively. In conclusion, the linearization process is about the estimation of the coefficients $F_{\mathbf{x}}$ and $F_{\mathbf{u}}$. The resulting equation above, Eqn. (7.74), is equivalent to the linearized state-space formulation given in Eqn. (7.24) if $\left[Z\big|_{\mathbf{x}_0,\mathbf{u}_0} \right]^{-1} F_{\mathbf{x}}$ and $\left[Z\big|_{\mathbf{x}_0,\mathbf{u}_0} \right]^{-1} F_{\mathbf{u}}$ are designated as $\left[Z\big|_{\mathbf{x}_0,\mathbf{u}_0} \right]^{-1} F_{\mathbf{x}} = \mathbf{A}$ and $\left[Z\big|_{\mathbf{x}_0,\mathbf{u}_0} \right]^{-1} F_{\mathbf{u}} = \mathbf{B}$, respectively.

The resultant 21 differential equations for the steam generator model are required to be rearranged, since they are only expressed with 16 terms related to the temporal changes of states. To do so, Eqns. (7.41), (7.43), (7.45), (7.47), (7.49), and (7.55), which describes mass conservation within the regions, are summed to reduce the number of the differential relations. Meanwhile, the mass flow rate terms given in Eqns. (7.42), (7.44), (7.46), (7.48), (7.50), and (7.56), which represent energy balance within the regions, are replaced with several proper combination of the mass conservation equations above. The derivation of each of relations are quite tedious and is not elaborated in this

section. After this reduction of intermediate terms, the formulation of the linearized state-space model begins with collecting all the states in the steam generator model, the state vector **x** and the input vector **u** are firstly given by Eqns. (7.75) and (7.76), respectively:

$$\mathbf{x} = \begin{bmatrix} L_1 & L_2 & P_s & h_3^n & h_{wi}^n & h_{w1}^n & h_{w2}^n & T_{p,1} \\ T_{p,2} & T_{p,3} & T_{t,1} & T_{t,2} & T_{t,3} & T_{t,w1} & T_{t,w2} & T_{t,w3} \end{bmatrix}^T, \text{ and} \tag{7.75}$$

$$\mathbf{u} = \begin{bmatrix} \dot{m}_{s,w3}^n & \dot{m}_{s,wi}^n & \dot{m}_{s,3}^n & h_{w3}^n & T_{p,in} & \dot{m}_p \end{bmatrix}^T. \tag{7.76}$$

In addition, The matrix $Z(\mathbf{x},\mathbf{u})$ is given by arranging the system of differential equations with vector-matrix format. All of the entries are given in Table 7.3, where $z_{i,j}$ is the i-th row, j-th column entry of $Z(\mathbf{x},\mathbf{u})$. On the right hand side of Eqn. (7.69), $f(\mathbf{x},\mathbf{u})$ is given by the following Eqn. (7.77):

$$f(\mathbf{x},\mathbf{u})=\begin{bmatrix}
h_{s,1}A_{ti,1}\left(T_{t,1}-T_{s,1}\right)+\left(h_{wi}^{n}-h_{f}\right)\dot{m}_{s,wi}^{n}\\
h_{s,2}A_{ti,2}\left(T_{t,2}-T_{s,2}\right)+h_{l}\dot{m}_{s,wi}^{n}-h_{g}\dot{m}_{s,3}^{n}\\
h_{s,3}A_{ti,3}\left(T_{t,3}-T_{s,3}\right)+\left(h_{g}-h_{3}^{n}\right)\dot{m}_{s,3}^{n}\\
h_{s,w1}A_{twi,1}\left(T_{t,w1}-T_{s,w1}\right)+\left(h_{w1}^{n}-h_{wi}^{n}\right)\dot{m}_{s,wi}^{n}\\
h_{s,w2}A_{twi,2}\left(T_{t,w2}-T_{s,w2}\right)+h_{w2}^{n}\dot{m}_{s,w3}^{n}-h_{w1}^{n}\dot{m}_{s,wi}^{n}\\
h_{s,w3}A_{twi,3}\left(T_{t,w3}-T_{s,w3}\right)+\left(h_{w3}^{n}-h_{w2}^{n}\right)\dot{m}_{s,w3}^{n}\\
\dot{m}_{s,w3}^{n}-\dot{m}_{s,3}^{n}\\
\dot{m}_{p}C_{pc}\left(T_{p,2}-T_{p,1}\right)-h_{p,1}A_{to,1}\left(T_{p,1}-T_{t,1}\right)-h_{p,1}A_{two,1}\left(T_{p,1}-T_{t,w1}\right)\\
\dot{m}_{p}C_{pc}\left(T_{p,3}-T_{p,2}\right)-h_{p,2}A_{to,2}\left(T_{p,2}-T_{t,2}\right)-h_{p,2}A_{two,2}\left(T_{p,2}-T_{t,w2}\right)\\
\dot{m}_{p}C_{pc}\left(T_{p,in}-T_{p,3}\right)-h_{p,3}A_{to,3}\left(T_{p,3}-T_{t,3}\right)-h_{p,3}A_{two,3}\left(T_{p,3}-T_{t,w3}\right)\\
-h_{p,1}A_{to,1}\left(T_{t,1}-T_{p,1}\right)-h_{s,2}A_{ti,1}\left(T_{t,1}-T_{s,1}\right)\\
-h_{p,2}A_{to,2}\left(T_{t,2}-T_{p,2}\right)-h_{s,2}A_{ti,2}\left(T_{t,2}-T_{s,2}\right)\\
-h_{p,3}A_{to,3}\left(T_{t,3}-T_{p,3}\right)-h_{s,3}A_{ti,3}\left(T_{t,3}-T_{s,3}\right)\\
-h_{p,1}A_{two,1}\left(T_{t,w1}-T_{p,1}\right)-h_{s,w1}A_{twi,1}\left(T_{t,w1}-T_{s,w1}\right)\\
-h_{p,2}A_{two,2}\left(T_{t,w2}-T_{p,2}\right)-h_{s,w2}A_{twi,2}\left(T_{t,w2}-T_{s,w2}\right)\\
-h_{p,3}A_{two,3}\left(T_{t,w3}-T_{p,3}\right)-h_{s,w3}A_{twi,3}\left(T_{t,w3}-T_{s,w3}\right)
\end{bmatrix}. \tag{7.77}$$

In order to derive the final linearized form as shown in Eqn. (7.74), the coefficients $F_{\mathbf{x}}$ and $F_{\mathbf{u}}$ are need to be addressed. By estimating partial derivatives, all the elements of $F_{\mathbf{x}}$ and $F_{\mathbf{u}}$ are respectively summarized in Table 7.4 and Table 7.5, where $f_{\mathbf{x},(i,j)}$ is i-th row, j-th column entry of $F_{\mathbf{x}}$ while $f_{\mathbf{u},(i,j)}$ is that of $F_{\mathbf{u}}$. Upon the derivation, several partial derivatives are also presented. It is noted that four partial derivatives, $\frac{\partial h_{wi}^{n}}{\partial P_{s}}$, $\frac{\partial h_{w1}^{n}}{\partial P_{s}}$, $\frac{\partial h_{w2}^{n}}{\partial P_{s}}$, and $\frac{\partial h_{w3}^{n}}{\partial P_{s}}$ are neglected since the rates of enthalpy change with respect to saturated pressure would not be significant compared to other terms. The final form can be established by matrix inversion of $Z(\mathbf{x},\mathbf{u})$ in the calculation process.

Table 7.3 Elements of matrix $Z(\mathbf{x},\mathbf{u})$

Index	Element
$z_{1,1}$	$A_{st}\rho_1\left(h_1-h_f\right)$
$z_{1,3}$	$A_{st}L_1\left[\frac{\rho_1}{2}\frac{\partial h_f}{\partial P_s}+\left(h_1-h_f\right)\left(\left.\frac{\partial\rho_1}{\partial P_s}\right\|_{h_1}+\frac{1}{2}\left.\frac{\partial\rho_1}{\partial h_1}\right\|_{P_s}\frac{\partial h_f}{\partial P_s}\right)-1\right]$
$z_{1,5}$	$\frac{1}{2}A_{st}L_1\left[\rho_1+\left(h_1-h_f\right)\left.\frac{\partial\rho_1}{\partial h_1}\right\|_{P_s}\right]$
$z_{2,1}$	$A_{st}\left(\rho_1 h_f-\rho_3 h_g\right)$
$z_{2,2}$	$A_{st}\left[(1-\gamma)\left(\rho_f h_f-\rho_g h_g\right)+\left(\rho_g-\rho_3\right)h_g\right]$
$z_{2,3}$	$A_{st}\left[h_f L_1\left(\left.\frac{\partial\rho_1}{\partial P_s}\right\|_{h_1}+\frac{1}{2}\left.\frac{\partial\rho_1}{\partial h_1}\right\|_{P_s}\frac{\partial h_f}{\partial P_s}\right)+L_2\left[\gamma\frac{\partial(\rho_g h_g)}{\partial P_s}+(1-\gamma)\frac{\partial(\rho_f h_f)}{\partial P_s}-1\right]\right.$ $\left.+h_g L_3\left(\left.\frac{\partial\rho_3}{\partial P_s}\right\|_{h_3}+\frac{1}{2}\left.\frac{\partial\rho_3}{\partial h_3}\right\|_{P_s}\frac{\partial h_g}{\partial P_s}\right)\right]$
$z_{2,4}$	$\frac{1}{2}A_{st}L_3 h_g\left.\frac{\partial\rho_3}{\partial h_3}\right\|_{P_s}$
$z_{2,5}$	$\frac{1}{2}A_{st}L_1 h_f\left.\frac{\partial\rho_1}{\partial h_1}\right\|_{P_s}$
$z_{3,1}$	$A_{st}\rho_3\left(h_g-h_3\right)$
$z_{3,2}$	$A_{st}\rho_3\left(h_g-h_3\right)$
$z_{3,3}$	$A_{st}L_3\left[\frac{\rho_3}{2}\frac{\partial h_g}{\partial P_s}+\left(h_3-h_g\right)\left(\left.\frac{\partial\rho_3}{\partial P_s}\right\|_{h_3}+\frac{1}{2}\left.\frac{\partial\rho_3}{\partial h_3}\right\|_{P_s}\frac{\partial h_g}{\partial P_s}\right)-1\right]$
$z_{3,4}$	$\frac{1}{2}A_{st}L_3\left[\rho_3+\left(h_3-h_g\right)\left.\frac{\partial\rho_3}{\partial h_3}\right\|_{P_s}\right]$
$z_{4,1}$	$A_{sw}\rho_{w1}\left(h_{w1}-h_{w1}^n\right)$
$z_{4,3}$	$A_{sw}L_1\left(\left(h_{w1}-h_{w1}^n\right)\left.\frac{\partial\rho_{w1}}{\partial P_s}\right\|_{h_{w1}}-1\right)$

Table 7.3 Elements of matrix $Z(\mathbf{x},\mathbf{u})$ (contd.)

Index	Element
$z_{4,5}$	$\frac{A_{sw}L_1}{2}\left(\rho_{w1}+\left(h_{w1}-h_{w1}^n\right)\left.\frac{\partial\rho_{w1}}{\partial h_{w1}}\right\|_{P_s}\right)$
$z_{4,6}$	$\frac{A_{sw}L_1}{2}\left(\rho_{w1}+\left(h_{w1}-h_{w1}^n\right)\left.\frac{\partial\rho_{w1}}{\partial h_{w1}}\right\|_{P_s}\right)$
$z_{5,1}$	$A_{sw}\left(\rho_{w1}h_{w1}^n-\rho_{w3}h_{w2}^n\right)$
$z_{5,2}$	$A_{sw}\left(\rho_{w2}h_{w2}-\rho_{w3}h_{w2}^n\right)$
$z_{5,3}$	$A_{sw}\left[L_1 h_{w1}^n\left.\frac{\partial\rho_{w1}}{\partial P_s}\right\|_{h_{w1}}+L_2\left(h_{w2}\left.\frac{\partial\rho_{w2}}{\partial P_s}\right\|_{h_{w2}}-1\right)+L_3 h_{w2}^n\left.\frac{\partial\rho_{w3}}{\partial P_s}\right\|_{h_{w3}}\right]$
$z_{5,5}$	$\frac{A_{sw}L_1}{2}h_{w1}^n\left.\frac{\partial\rho_{w1}}{\partial h_{w1}}\right\|_{P_s}$
$z_{5,6}$	$\frac{A_{sw}}{2}\left[L_1 h_{w1}^n\left.\frac{\partial\rho_{w1}}{\partial h_{w1}}\right\|_{P_s}+L_2\left(\rho_{w2}+h_{w2}\left.\frac{\partial\rho_{w2}}{\partial h_{w2}}\right\|_{P_s}\right)\right]$
$z_{5,7}$	$\frac{A_{sw}}{2}\left[L_2\left(\rho_{w2}+h_{w2}\left.\frac{\partial\rho_{w2}}{\partial h_{w2}}\right\|_{P_s}\right)+L_3 h_{w2}^n\left.\frac{\partial\rho_{w3}}{\partial h_{w3}}\right\|_{P_s}\right]$
$z_{6,1}$	$A_{sw}\rho_{w3}\left(h_{w2}^n-h_{w3}\right)$
$z_{6,2}$	$A_{sw}\rho_{w3}\left(h_{w2}^n-h_{w3}\right)$
$z_{6,3}$	$A_{sw}L_3\left(\left(h_{w3}-h_{w2}^n\right)\left.\frac{\partial\rho_{w3}}{\partial P_s}\right\|_{h_{w3}}-1\right)$
$z_{6,7}$	$\frac{1}{2}A_{sw}L_3\left(\rho_{w3}+\left(h_{w3}-h_{w2}^n\right)\left.\frac{\partial\rho_{w3}}{\partial h_{w3}}\right\|_{P_s}\right)$
$z_{7,1}$	$A_{st}\left(\rho_1-\rho_3\right)+A_{sw}\left(\rho_{w1}-\rho_{w3}\right)$
$z_{7,2}$	$A_{st}\left[(1-\gamma)\left(\rho_f-\rho_g\right)+\left(\rho_g-\rho_3\right)\right]+A_{sw}\left(\rho_{w2}-\rho_{w3}\right)$

Table 7.3 Elements of matrix $Z(\mathbf{x},\mathbf{u})$ (contd.)

Index	Element
$z_{7,3}$	$A_{st}\left[L_1\left(\left.\frac{\partial\rho_1}{\partial P_s}\right\|_{h_1}+\frac{1}{2}\left.\frac{\partial\rho_1}{\partial h_1}\right\|_{P_s}\frac{\partial h_f}{\partial P_s}\right)+L_2\left(\gamma\frac{\partial\rho_g}{\partial P_s}+(1-\gamma)\frac{\partial\rho_f}{\partial P_s}\right)\right.$ $\left.+L_3\left(\left.\frac{\partial\rho_3}{\partial P_s}\right\|_{h_3}+\frac{1}{2}\left.\frac{\partial\rho_3}{\partial h_3}\right\|_{P_s}\frac{\partial h_g}{\partial P_s}\right)\right]$ $+A_{sw}\left[L_1\left.\frac{\partial\rho_{w1}}{\partial P_s}\right\|_{h_{w1}}+L_2\left.\frac{\partial\rho_{w2}}{\partial P_s}\right\|_{h_{w2}}+L_3\left.\frac{\partial\rho_{w3}}{\partial P_s}\right\|_{h_{w3}}\right]$
$z_{7,4}$	$\frac{A_{st}}{2}L_3\left.\frac{\partial\rho_3}{\partial h_3}\right\|_{P_s}$
$z_{7,5}$	$\frac{L_1}{2}\left(A_{st}\left.\frac{\partial\rho_1}{\partial h_1}\right\|_{P_s}+A_{sw}\left.\frac{\partial\rho_{w1}}{\partial h_{w1}}\right\|_{P_s}\right)$
$z_{7,6}$	$\frac{A_{sw}}{2}\left(L_1\left.\frac{\partial\rho_{w1}}{\partial h_{w1}}\right\|_{P_s}+L_2\left.\frac{\partial\rho_{w2}}{\partial h_{w2}}\right\|_{P_s}\right)$
$z_{7,7}$	$\frac{A_{sw}}{2}\left(L_2\left.\frac{\partial\rho_{w2}}{\partial h_{w2}}\right\|_{P_s}+L_3\left.\frac{\partial\rho_{w3}}{\partial h_{w3}}\right\|_{P_s}\right)$
$z_{8,1}$	$\rho_c C_{pc} A_p\left(T_{p,1}-T_{p,2}\right)$
$z_{8,8}$	$\rho_c C_{pc} A_p L_1$
$z_{9,9}$	$\rho_c C_{pc} A_p L_2$
$z_{10,1}$	$\rho_c C_{pc} A_p\left(T_{p,2}-T_{p,3}\right)$
$z_{10,2}$	$\rho_c C_{pc} A_p\left(T_{p,2}-T_{p,3}\right)$
$z_{10,10}$	$\rho_c C_{pc} A_p L_3$
$z_{11,1}$	$\rho_t C_{pt} A_t\left(T_{t,1}-T_{t,2}\right)$
$z_{11,11}$	$\rho_t C_{pt} A_t L_1$
$z_{12,12}$	$\rho_t C_{pt} A_t L_2$

Table 7.3 Elements of matrix $Z(\mathbf{x},\mathbf{u})$ (contd.)

Index	Element
$z_{13,1}$	$\rho_t C_{pt} A_t \left(T_{t,2} - T_{t,3}\right)$
$z_{13,2}$	$\rho_t C_{pt} A_t \left(T_{t,2} - T_{t,3}\right)$
$z_{13,13}$	$\rho_t C_{pt} A_t L_3$
$z_{14,1}$	$\rho_t C_{pt} A_{tw} \left(T_{t,w1} - T_{t,w2}\right)$
$z_{14,14}$	$\rho_t C_{pt} A_{tw} L_1$
$z_{15,15}$	$\rho_t C_{pt} A_{tw} L_2$
$z_{16,1}$	$\rho_t C_{pt} A_{tw} \left(T_{t,w2} - T_{t,w3}\right)$
$z_{16,2}$	$\rho_t C_{pt} A_{tw} \left(T_{t,w2} - T_{t,w3}\right)$
$z_{16,16}$	$\rho_t C_{pt} A_{tw} L_3$

Table 7.4 Elements of matrix $F_{\mathbf{x}}(\mathbf{x},\mathbf{u})$

Index	Element
$f_{\mathbf{x},(1,1)}$	$\pi d_s h_{s,1}\left(T_{t,1}-T_{s,1}\right)$
$f_{\mathbf{x},(1,3)}$	$-\pi d_s h_{s,1} L_1 \dfrac{\partial T_{s,1}}{\partial P_s}-\dfrac{\partial h_f}{\partial P_s}\dot{m}^n_{s,wi}$
$f_{\mathbf{x},(1,5)}$	$-\pi d_s h_{s,1} L_1 \dfrac{\partial T_{s,1}}{\partial h^n_{wi}}+\dot{m}^n_{s,wi}$
$f_{\mathbf{x},(1,11)}$	$\pi d_s h_{s,1} L_1$
$f_{\mathbf{x},(2,2)}$	$\pi d_s h_{s,2}\left(T_{t,2}-T_{s,2}\right)$
$f_{\mathbf{x},(2,3)}$	$-\pi d_s h_{s,2} L_2 \dfrac{\partial T_{s,2}}{\partial P_s}+\dfrac{\partial h_f}{\partial P_s}\dot{m}^n_{s,wi}-\dfrac{\partial h_g}{\partial P_s}\dot{m}^n_{s,3}$
$f_{\mathbf{x},(2,12)}$	$\pi d_s h_{s,2} L_2$
$f_{\mathbf{x},(3,1)}$	$-\pi d_s h_{s,3}\left(T_{t,3}-T_{s,3}\right)$
$f_{\mathbf{x},(3,2)}$	$-\pi d_s h_{s,3}\left(T_{t,3}-T_{s,3}\right)$
$f_{\mathbf{x},(3,3)}$	$-\pi d_s h_{s,3} L_3 \dfrac{\partial T_{s,3}}{\partial P_s}+\left(\dfrac{\partial h_g}{\partial P_s}-\dfrac{\partial h^n_3}{\partial P_s}\right)\dot{m}^n_{s,3}$
$f_{\mathbf{x},(3,4)}$	$-\pi d_s h_{s,3} L_3 \dfrac{\partial T_{s,3}}{\partial h^n_3}-\dot{m}^n_{s,3}$
$f_{\mathbf{x},(3,13)}$	$\pi d_s h_{s,3} L_3$
$f_{\mathbf{x},(4,1)}$	$\pi d_{sw} h_{s,w1}\left(T_{t,w1}-T_{s,w1}\right)$
$f_{\mathbf{x},(4,3)}$	$-\pi d_{sw} L_1 h_{s,w1} \dfrac{\partial T_{s,w1}}{\partial P_s}+\left(\dfrac{\partial h^n_{w1}}{\partial P_s}-\dfrac{\partial h^n_{wi}}{\partial P_s}\right)\dot{m}^n_{s,wi}$
$f_{\mathbf{x},(4,5)}$	$-\pi d_{sw} L_1 h_{s,w1} \dfrac{\partial T_{s,w1}}{\partial h^n_{wi}}-\dot{m}^n_{s,wi}$
$f_{\mathbf{x},(4,6)}$	$-\pi d_{sw} L_1 h_{s,w1} \dfrac{\partial T_{s,w1}}{\partial h^n_{w1}}+\dot{m}^n_{s,wi}$
$f_{\mathbf{x},(4,14)}$	$\pi d_{sw} L_1 h_{s,w1}$
$f_{\mathbf{x},(5,2)}$	$\pi d_{sw} h_{s,w2}\left(T_{t,w2}-T_{s,w2}\right)$
$f_{\mathbf{x},(5,3)}$	$-\pi d_{sw} L_2 h_{s,w2} \dfrac{\partial T_{s,w2}}{\partial P_s}+\dfrac{\partial h^n_{w2}}{\partial P_s}\dot{m}^n_{s,w3}-\dfrac{\partial h^n_{w1}}{\partial P_s}\dot{m}^n_{s,wi}$

Table 7.4 Elements of matrix $F_{\mathbf{x}}(\mathbf{x},\mathbf{u})$ (contd.)

Index	Element
$f_{\mathbf{x},(5,6)}$	$-\pi d_{sw} L_2 h_{sw,w2} \dfrac{\partial T_{s,w2}}{\partial h^n_{w1}} - \dot{m}^n_{s,wi}$
$f_{\mathbf{x},(5,7)}$	$-\pi d_{sw} L_2 h_{sw,w2} \dfrac{\partial T_{s,w2}}{\partial h^n_{w2}} + \dot{m}^n_{s,w3}$
$f_{\mathbf{x},(5,15)}$	$\pi d_{sw} L_2 h_{s,w2}$
$f_{\mathbf{x},(6,1)}$	$-\pi d_{sw} h_{s,w3} \left(T_{t,w3} - T_{s,w3}\right)$
$f_{\mathbf{x},(6,2)}$	$-\pi d_{sw} h_{s,w3} \left(T_{t,w3} - T_{s,w3}\right)$
$f_{\mathbf{x},(6,3)}$	$-\pi d_{sw} L_3 h_{s,w3} \dfrac{\partial T_{s,w3}}{\partial P_s} + \left(\dfrac{\partial h^n_{w3}}{\partial P_s} - \dfrac{\partial h^n_{w2}}{\partial P_s} \right) \dot{m}^n_{s,w3}$
$f_{\mathbf{x},(6,7)}$	$-\pi d_{sw} L_3 h_{s,w3} \dfrac{\partial T_{s,w3}}{\partial h^n_{w2}} - \dot{m}^n_{s,w3}$
$f_{\mathbf{x},(6,16)}$	$\pi d_{sw} L_3 h_{s,w3}$
$f_{\mathbf{x},(8,1)}$	$-\pi d_p h_{p,1} \left(T_{p,1} - T_{t,1}\right) - \pi d_{pw} h_{p,1} \left(T_{p,1} - T_{t,w1}\right)$
$f_{\mathbf{x},(8,8)}$	$-\dot{m}_p C_{pc} - \pi d_p h_{p,1} L_1 - \pi d_{pw} h_{p,1} L_1$
$f_{\mathbf{x},(8,9)}$	$\dot{m}_p C_{pc}$
$f_{\mathbf{x},(8,11)}$	$\pi d_p h_{p,1} L_1$
$f_{\mathbf{x},(8,14)}$	$\pi d_{pw} h_{p,1} L_1$
$f_{\mathbf{x},(9,2)}$	$-\pi d_p h_{p,2} \left(T_{p,2} - T_{t,2}\right) - \pi d_{pw} h_{p,2} \left(T_{p,2} - T_{t,w2}\right)$
$f_{\mathbf{x},(9,9)}$	$-\dot{m}_p C_{pc} - \pi d_p h_{p,2} L_2 - \pi d_{pw} h_{p,2} L_2$
$f_{\mathbf{x},(9,10)}$	$\dot{m}_p C_{pc}$
$f_{\mathbf{x},(9,12)}$	$\pi d_p h_{p,2} L_2$
$f_{\mathbf{x},(9,15)}$	$\pi d_{pw} h_{p,2} L_2$
$f_{\mathbf{x},(10,1)}$	$\pi d_p h_{p,3} \left(T_{p,3} - T_{t,3}\right) + \pi d_{pw} h_{p,3} \left(T_{p,3} - T_{t,w3}\right)$
$f_{\mathbf{x},(10,2)}$	$\pi d_p h_{p,3} \left(T_{p,3} - T_{t,3}\right) + \pi d_{pw} h_{p,3} \left(T_{p,3} - T_{t,w3}\right)$
$f_{\mathbf{x},(10,10)}$	$-\dot{m}_p C_{pc} - \pi d_p h_{p,3} L_3 - \pi d_{pw} h_{p,3} L_3$
$f_{\mathbf{x},(10,13)}$	$\pi d_p h_{p,3} L_3$

Table 7.4 Elements of matrix $F_{\mathbf{x}}(\mathbf{x},\mathbf{u})$ (contd.)

Index	Element
$f_{\mathbf{x},(10,16)}$	$\pi d_{pw} h_{p,3} L_3$
$f_{\mathbf{x},(11,1)}$	$-\pi d_p h_{p,1}\left(T_{t,1}-T_{p,1}\right)-\pi d_s h_{s,1}\left(T_{t,1}-T_{s,1}\right)$
$f_{\mathbf{x},(11,3)}$	$\pi d_s h_{s,1} L_1 \dfrac{\partial T_{s,1}}{\partial P_s}$
$f_{\mathbf{x},(11,5)}$	$\pi d_s h_{s,1} L_1 \dfrac{\partial T_{s,1}}{\partial h_{wi}^n}$
$f_{\mathbf{x},(11,8)}$	$\pi d_p h_{p,1} L_1$
$f_{\mathbf{x},(11,11)}$	$-\pi d_p h_{p,1} L_1 - \pi d_s h_{s,1} L_1$
$f_{\mathbf{x},(12,2)}$	$-\pi d_p h_{p,2}\left(T_{t,2}-T_{p,2}\right)-\pi d_s h_{s,2}\left(T_{t,2}-T_{s,2}\right)$
$f_{\mathbf{x},(12,3)}$	$\pi d_s h_{s,2} L_2 \dfrac{\partial T_{s,2}}{\partial P_s}$
$f_{\mathbf{x},(12,9)}$	$\pi d_p h_{p,2} L_2$
$f_{\mathbf{x},(12,12)}$	$-\pi d_p h_{p,2} L_2 - \pi d_s h_{s,2} L_2$
$f_{\mathbf{x},(13,1)}$	$\pi d_p h_{p,3}\left(T_{t,3}-T_{p,3}\right)+\pi d_s h_{s,3}\left(T_{t,3}-T_{s,3}\right)$
$f_{\mathbf{x},(13,2)}$	$\pi d_p h_{p,3}\left(T_{t,3}-T_{p,3}\right)+\pi d_s h_{s,3}\left(T_{t,3}-T_{s,3}\right)$
$f_{\mathbf{x},(13,3)}$	$\pi d_s h_{s,3} L_3 \dfrac{\partial T_{s,3}}{\partial P_s}$
$f_{\mathbf{x},(13,4)}$	$\pi d_s h_{s,3} L_3 \dfrac{\partial T_{s,3}}{\partial h_3^n}$
$f_{\mathbf{x},(13,10)}$	$\pi d_p h_{p,3} L_3$
$f_{\mathbf{x},(13,13)}$	$-\pi d_p h_{p,3} L_3 - \pi d_s h_{s,3} L_3$
$f_{\mathbf{x},(14,1)}$	$-\pi d_{pw} h_{p,1}\left(T_{t,w1}-T_{p,1}\right)-\pi d_{sw} h_{s,w1}\left(T_{t,w1}-T_{s,w1}\right)$
$f_{\mathbf{x},(14,3)}$	$\pi d_{sw} L_1 h_{s,w1} \dfrac{\partial T_{s,w1}}{\partial P_s}$
$f_{\mathbf{x},(14,5)}$	$\pi d_{sw} h_{s,w1} L_1 \dfrac{\partial T_{s,w1}}{\partial h_{wi}^n}$
$f_{\mathbf{x},(14,6)}$	$\pi d_{sw} h_{s,w1} L_1 \dfrac{\partial T_{s,w1}}{\partial h_{w1}^n}$

Table 7.4 Elements of matrix $F_{\mathbf{x}}(\mathbf{x},\mathbf{u})$ (contd.)

Index	Element
$f_{\mathbf{x},(14,8)}$	$\pi d_{pw} h_{p,1} L_1$
$f_{\mathbf{x},(14,14)}$	$-\pi d_{pw} h_{p,1} L_1 - \pi d_{sw} h_{s,w1} L_1$
$f_{\mathbf{x},(15,2)}$	$-\pi d_{pw} h_{p,2} \left(T_{t,w2} - T_{p,2}\right) - \pi d_{sw} h_{s,w2} \left(T_{t,w2} - T_{s,w2}\right)$
$f_{\mathbf{x},(15,3)}$	$\pi d_{sw} L_2 h_{s,w2} \dfrac{\partial T_{s,w2}}{\partial P_s}$
$f_{\mathbf{x},(15,6)}$	$\pi d_{sw} h_{s,w2} L_2 \dfrac{\partial T_{s,w2}}{\partial h_{w1}^n}$
$f_{\mathbf{x},(15,7)}$	$\pi d_{sw} h_{s,w2} L_2 \dfrac{\partial T_{s,w2}}{\partial h_{w2}^n}$
$f_{\mathbf{x},(15,9)}$	$\pi d_{pw} h_{p,2} L_2$
$f_{\mathbf{x},(15,15)}$	$-\pi d_{pw} h_{p,2} L_2 - \pi d_{sw} h_{s,w2} L_2$
$f_{\mathbf{x},(16,1)}$	$\pi d_{pw} h_{p,3} \left(T_{t,w3} - T_{p,3}\right) + \pi d_s h_{s,w3} \left(T_{t,w3} - T_{s,w3}\right)$
$f_{\mathbf{x},(16,2)}$	$\pi d_{pw} h_{p,3} \left(T_{t,w3} - T_{p,3}\right) + \pi d_s h_{s,w3} \left(T_{t,w3} - T_{s,w3}\right)$
$f_{\mathbf{x},(16,3)}$	$\pi d_{sw} L_3 h_{s,w3} \dfrac{\partial T_{s,w3}}{\partial P_s}$
$f_{\mathbf{x},(16,7)}$	$\pi d_{sw} h_{s,w3} L_3 \dfrac{\partial T_{s,w3}}{\partial h_{w2}^n}$
$f_{\mathbf{x},(16,10)}$	$\pi d_{pw} h_{p,3} L_3$
$f_{\mathbf{x},(16,16)}$	$-\pi d_{pw} h_{p,3} L_3 - \pi d_s h_{s,w3} L_3$

Table 7.5 Elements of matrix $F_{\mathbf{u}}(\mathbf{x},\mathbf{u})$

Index	Element
$f_{\mathbf{u},(1,2)}$	$h_{wi}^{n} - h_{f}$
$f_{\mathbf{u},(2,2)}$	h_{f}
$f_{\mathbf{u},(2,3)}$	$-h_{g}$
$f_{\mathbf{u},(4,2)}$	$h_{w1}^{n} - h_{wi}^{n}$
$f_{\mathbf{u},(5,1)}$	h_{w2}^{n}
$f_{\mathbf{u},(5,2)}$	$-h_{w1}^{n}$
$f_{\mathbf{u},(6,1)}$	$h_{w3}^{n} - h_{w2}^{n}$
$f_{\mathbf{u},(6,4)}$	$-\pi d_{sw} L_3 h_{s,w3} \dfrac{\partial T_{s,w3}}{\partial h_{w3}^{n}} + \dot{m}_{s,w3}^{n}$
$f_{\mathbf{u},(7,1)}$	1
$f_{\mathbf{u},(7,3)}$	-1
$f_{\mathbf{u},(8,6)}$	$C_{pc}\left(T_{p,2} - T_{p,1}\right)$
$f_{\mathbf{u},(9,6)}$	$C_{pc}\left(T_{p,3} - T_{p,2}\right)$
$f_{\mathbf{u},(10,5)}$	$\dot{m}_{p} C_{pc}$
$f_{\mathbf{u},(10,6)}$	$C_{pc}\left(T_{p,in} - T_{p,3}\right)$
$f_{\mathbf{u},(16,4)}$	$\pi d_{sw} h_{s,w3} L_3 \dfrac{\partial T_{s,w3}}{\partial h_{w3}^{n}}$

7.1.4 Model implementation for numerical simulation

For the implementation of develop model into MATLAB/Simulink environment (Mathworks, 2017) as introduced in Section 7.1, several additional assumptions are required for a realistic evaluation of load-following operation. This section elaborates such relations applied to the model.

7.1.4.1 Constant pressure operation for URANUS secondary side

Until now, the operation strategies of URANUS under full power operation and load-following operation are not yet established. It leads to a lack of available operating conditions for the simulation. Thus, additional operation conditions is required to be imposed on the secondary side of URANUS reactor system so that the simulation model can estimate the system behavior in a realistic way. In this regard, the secondary side is designated to be operated at a constant pressure for all operation conditions.

7.1.4.2 Steam flow regulation

A steam valve regulates the steam flow rate from the steam generator modules. In a control point of view, the design of steam flow controller is crucial for a system for a stable and efficient operation, which is beyond the scope of this

thesis study. Hence, as an alternative, a simple valve model by means of so-called critical flow approximation (El-Wakil, 1971) is applied to simulate the secondary side conditions, which supposes that the steam flow rate is directly proportional to its upstream pressure, in other words, the steam pressure in the steam generator tube side. In this respect, the total steam flow rate at the outlet of steam generator modules is given by Eqn. (7.78):

$$\dot{m}_{s,3}^{n} = C_L P_s . \tag{7.78}$$

The constant C_L is determined by the values at the nominal full power condition, namely, nominal steam pressure and nominal steam flow rate.

For the simulation of physical behaviors of the steam valve, a simple proportional-integral (PI) gain control model, shown in Eqn. (7.79), is utilized (Kapernick, 2015):

$$G_c(s) = K_p\left(1 + \frac{1}{\tau_I s}\right). \tag{7.79}$$

Accompanied by the constant pressure assumption made in Section 7.1.4.1, the pressure error signal defined by the difference between the current pressure and a pressure setpoint drives a steam valve to be opened or closed. The final form given by Eqns. (7.78) and (7.79) are given by:

$$\frac{d\dot{m}_{s,3}^{n}}{dt} = \frac{C_L}{t_s}\left[\delta P_s + C_{st}\frac{K_c}{P_{s0}}\left(\delta P_s + \frac{\delta P}{t_s}\right)\right], \tag{7.80}$$

where the constants, t_s, C_{st}, K_c, that determines the operational characteristics of the steam valve are $t_s = 1$, $C_{st} = 10$, and $K_c = 5$ (Kapernick, 2015).

7.1.4.3 Model implementation

Figure 7.6 shows the structure of implemented reactor dynamics simulation model. The thermal-hydraulic lumps described by the reactor core model, the hot leg and cold leg models, and the steam generator model, as elaborated through previous sections, are included by separating and connecting each of models with several input and output nodes. This configuration is efficient not only for the implementation but also for a potential model update since one lump can be substituted with other formulations.

Within this model, a system transient is given by an additional input node that describes a change of external load demand from the nominal full power condition. The simulation model would calculate the system response reacting to this load demand change and it leads to the generation of control rod movement requests. As discussed, the error signal of reactor power is defined by the discrepancy between the external power demand and the current power. In addition, how fast the control rods are inserted or withdrawn is proportional to this error signal and this proportionality constant is the loop gain for the closed feedback loop regulating reactor power, as shown in Figure 7.1. In this model, a proper value of 0.01 is applied to the loop gain with which the insertion speed of control rods are given in a realistic range.

In addition, another controllable parameter for URANUS is the feedwater flow rate, as described in Section 7.1. In this model, a simple model with proportional flow rate control is utilized. Similar to the applied concept of steam flow regulation, the detailed design and optimization of feedwater flow controller are out of the thesis scope. Hence, a simple proportionality is applied and the effect and advantage of feedwater flow rate control is elaborated in Section 7.3.1.

For the physical parameters of URANUS, the values under nominal condition estimated in Chapter 4 is extensively utilized. The thermophysical values of LBE is designated by the relation given in the LBE handbook (OECD Nuclear Energy Agency, 2007) while those of water is calculated with the industrial formulations given by the International Association for the Properties of Water and Steam (IAPWS-IF97) (Wagner and Kruse, 1998).

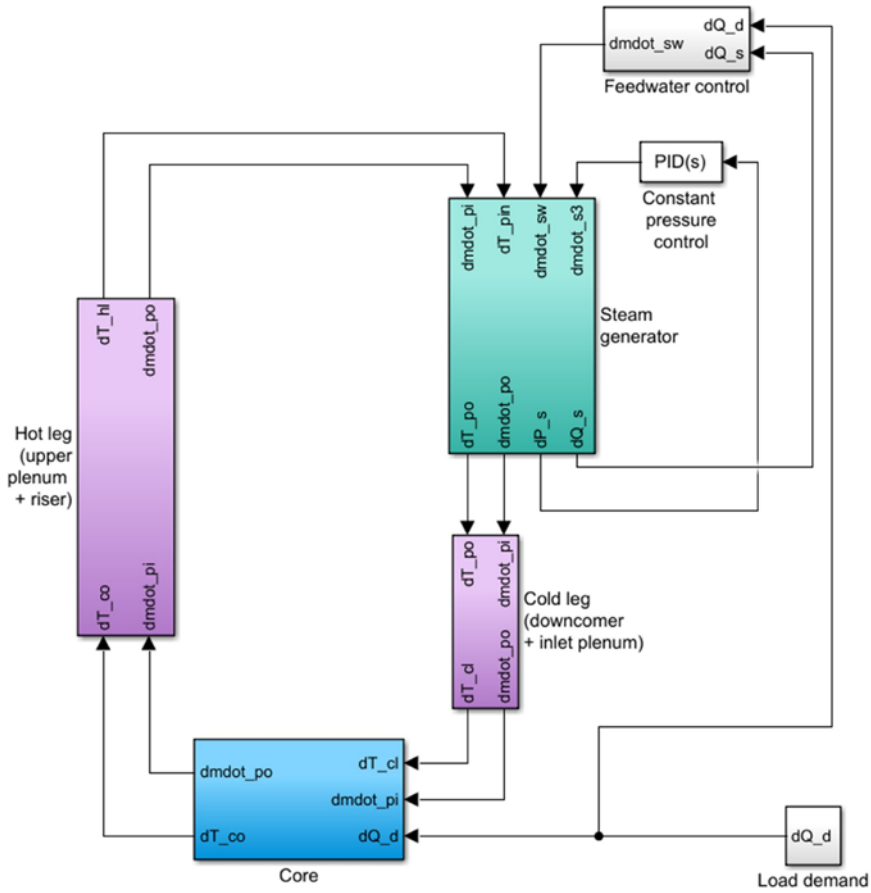

Figure 7.6 Block chain diagram for reactor state-space model implemented to MATLAB/Simulink environment

7.2 Reactor control model validation

Before proceeding into the assessment of load-following capability with the system transient evaluation model developed in the last section, the validation of the model is required. MARS-LBE is to be utilized for the validation of this analytical model as it was already validated for the LBE natural circulation systems with the test results given by HELIOS and PILLAR while its capability of reactor kinetics calculation was verified with SFR experiments throughout other studies.

For the problems used for the validation, two cases are defined: reactor power increase and decrease with a ramp of 5% power change per minute from nominal full power condition (100% power) are compared. Since MARS-LBE and the developed model have different capabilities, as summarized in Table 7.6 and MARS-LBE cannot estimate reactivity change induced from control rod movement, the input file for MARS-LBE is prepared with the reactivity change calculated by the developed model. In this calculation, the reactor power change is induced by load demand change. The calculation results are compared in Figure 7.7 and Figure 7.8. In both figures, the MARS-LBE results are marked with lines and circles while the estimation by the developed model is given with plane curves for the same colors.

The first insets in the figures show reactor power and turbine load changes to follow varying load demand. The turbine load is the same with the amount of heat transferred to the secondary side from primary side. The system transient evaluation model predicts faster core power transients and slower

secondary side heat removal rate saturation compared to the MARS-LBE calculation results. In other words, the developed model estimates the time needed for core power to be saturated to new steady-state values shorter than MARS-LBE does and the transients of core power lags load demand or control rod movements in both results.

Subsequently in the second insets on the figures, the reactivity changes are shown to be have good agreements each other not only on the reactivity insertion given by control rod movements but also on that given by reactivity feedback mechanisms, such as fuel and coolant temperature changes. For the system coolant temperatures as depicted in the third insets, the developed model estimates additional temperature decrease and increase about 2 K in comparison with the MARS-LBE results, respectively, in each problem. Regarding the time-dependent behavior, the developed model predicts that the system would have slower saturation followed by power transient being saturated. This delay is due to a slow power transfer rate change at the steam outlet, as shown in the case of power transients as well.

The primary side mass flow rates by natural circulation is estimated to have 10% larger deviation after saturation with respect to the results given by the developed model in comparison with MARS-LBE results, as shown in the last insets. This deviation is analyzed to come from the nonlinear model used for natural circulation flow rate, given as Eqn. (7.15), which cannot account for friction loss variation with respect to flow rate change. In addition, the model predicts faster saturation of transient.

Therefore, the comparison shows that the developed model is valid on

the reactor dynamics modeling purpose even though there is slight differences on the results compared to MARS-LBE. Meanwhile, the total calculation time for these problems by MARS-LBE is about 30 seconds to 1 minute while the developed model takes only about 1-2 seconds with a personal computer having a general specification. It means that the developed model can estimate actual reactor operation conditions accurately only with a simple formulation.

Table 7.6 Comparison between the developed passive LBE-cooled SMR dynamics model and MARS-LBE

Criteria	MARS-LBE	This model
Main scope	• System thermal-hydraulic analysis to boundary condition change • Safety analysis	• System integral behavior to operational condition change • Stability analysis, controller design and optimization
Basic hydrodynamic formulation	• One-dimensional, two-fluid flow model using two-fluid, six-equation formulation given by mass, momentum, and energy conservation of water and steam • Several additional relations on phase transition between two fluids • Semi-implicit scheme for pressure correction and time advancements	• One-dimensional, single-fluid flow model using two-equation formulation given by mass and energy conservation of LBE • Moving boundary formulation for steam generator Linearized state-space model • Linear ODE solver for stiff system and variable time advancement
Number of calculation nodes	• Total ~400 nodes for URANUS	• ~10 for URANUS
Calculation time	• ~2-3 minutes (depending on the number of calculation nodes)	• ~1-2 seconds
Capability	• Time-domain analysis	• Time-domain analysis • Frequency-domain analysis

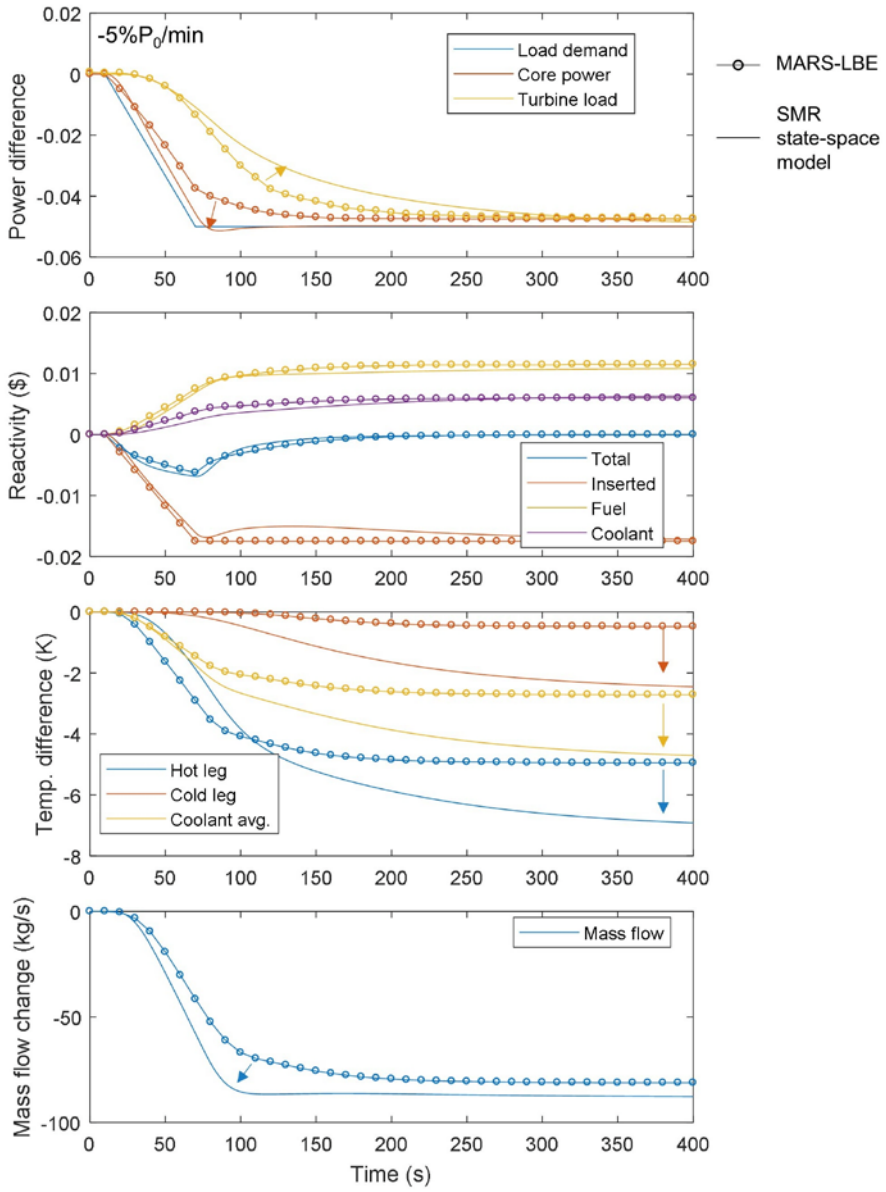

Figure 7.7 Calculation results comparison on the system transient evaluation model for passive LBE-cooled SMR and MARS-LBE for the power ramp rate of -5%P/min from 100% power output

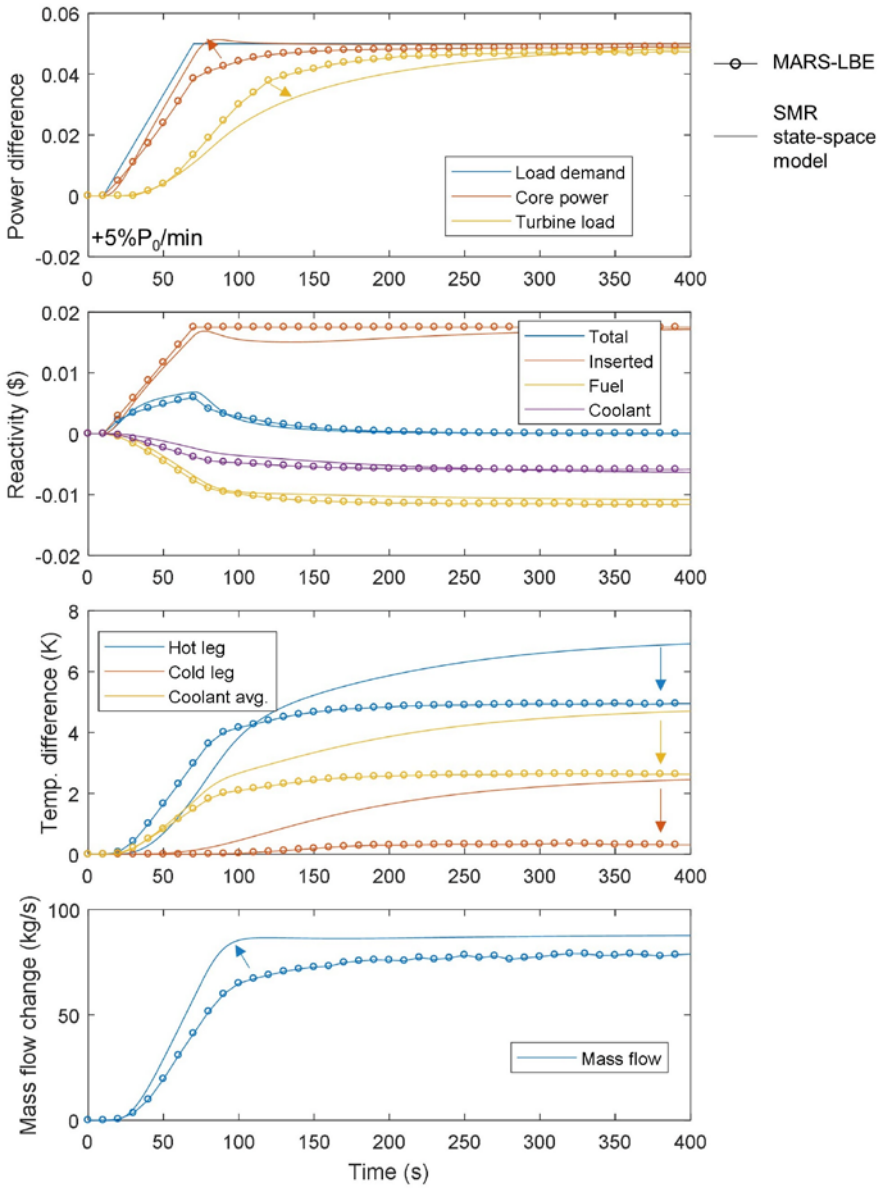

Figure 7.8 Calculation results comparison on the system transient evaluation model for passive LBE-cooled SMR and MARS-LBE for the power ramp rate of +5%P/min from 100% power output

7.3 Assessment of fast load-following capability

In the previous section, the developed analytical reactor dynamics simulation model for LBE-cooled passive SMR was validated through the comparison with MARS-LBE. Since the results showed that the developed model can be concluded to be valid on the reactor dynamics modeling purpose with slight deviations, the fast load-following capability of URANUS, a LBE-cooled passive SMR, will be evaluated with several case studies in the forthcoming sections. The evaluation includes the effect of proportional feedwater control on changing load demand, stability analysis on the reactor power with respect to external load demand, transients under a specific daily load-following operation plan, step response analysis on power recovery in response of the grid demand, and comparison with a load-following strategy in a commercial SMR.

7.3.1 Proportional feedwater control

According to the transient experimental results described in Section 5.2.4.3 and the numerical analysis results given in Section 6.4, it is evident that the characteristics of system responses by the primary and secondary sides to the instantaneous core power change in terms of saturation time would be deviated each other. In other words, the characteristics of secondary side would mostly affect the rate of load or electricity generation change given by external load demand change during load-following operation. Since the physical design of

URANUS is fixed, only controllable parameters are several operational conditions and specifications of the BOP by which the dynamics of whole system can be changed.

As introduced in Section 4.3, the BOP of URANUS is not yet designed in detail. In order to estimate its operation capability during load-following in proper and realistic ways, two boundaries of the secondary side, including the feedwater inlet and the steam outlet, are assumed to be operated with ideal control schemes. An ideal steam valve from which the steam flow rate is designated to be proportional to the steam pressure is applied to the steam outlet. On the other hand, the feedwater inlet condition has been defined by adding a simple, ideal feedwater controller, since the design and optimization of the controllers are out of thesis study. However, this case study can be used to guide the direction of BOP system design by assessing the advantage from the feedwater flow rate control.

The regulation of inlet feedwater flow rate is done by a proportional controller, which controls the water flow rate with respect to the external load demand. In order to evaluate its effect, four cases defined by the external load demand changes with a power ramp rate of ±10%P/min and with and without feedwater flow rate control at the same time are simulated. In the negative power ramp cases, it is assumed that the load demand falls from the nominal full power to 90% reactor power while the positive cases are appointed as power recovery from 90% power to the initial full power.

Figure 7.9 and Figure 7.10 show the simulation results without feedwater flow rate control on decreasing and increasing external load demands,

respectively; meanwhile, Figure 7.11 and Figure 7.12 illustrate the results with controlling feedwater flow rate under the same load demand conditions. The top left insets of both figures depicts external load demand, resultant core power regulated by the control rod movements and primary system reactivity feedback mechanisms, and turbine load calculated by the difference of the multiplications defined by the mass flow rates and enthalpy values at the boundaries. All of those values are expressed in fraction to the nominal full power values. In addition, a shaded region shows the time-dependent difference of the reactor core power and the turbine load. In power decreasing conditions, these discrepancies can be thought as the production of excess steam while those are deficits in steam or required load when the load demand is increasing. The second and third insets on the left hand sides of each of figures are about the primary side transients including temperatures and natural circulation mass flow rates. The top right hand side insets represent the feedwater flow rate at the steam generator inlet and the steam flow rate at the steam boundary. It can be seen that the constant pressure controller works in proper ways as defined.

It can be inferred from the results depicted on the left hand side insets of Figure 7.9 to Figure 7.12 that the primary side responds to the predefined external load demands nearly regardless of the feedwater flow rate control. However, the steam side responses are dramatically changed with the activation of the proportional feedwater flow controller, by comparing Figure 7.11 to Figure 7.9, and Figure 7.10 to Figure 7.12, respectively. The reduction in excess steam production with the proportional feedwater flow control leads to less steam curtailing in decreasing load demand while the steam generator heat

removal slightly differs from the core power with the proportional feedwater flow control with respect to increasing load demand. By referring to the shaded areas, the amount of core-turbine power mismatch can be reduced by 1/3. In addition, the saturation time of steam side, which is defined by the time needed to reach the fractional power difference between the load demand and the turbine load lower than 1%, can be reduced by the feedwater flow control used in this model. It takes about 400 s without the control while only 200 s are required with the proportional feedwater flow control after the reactor core power being saturated. In conclusion, in a passive LBE-cooled SMR, the steam side rather than the primary side needs to be controlled with sophisticated control schemes so that power removal or overcooling to be minimized.

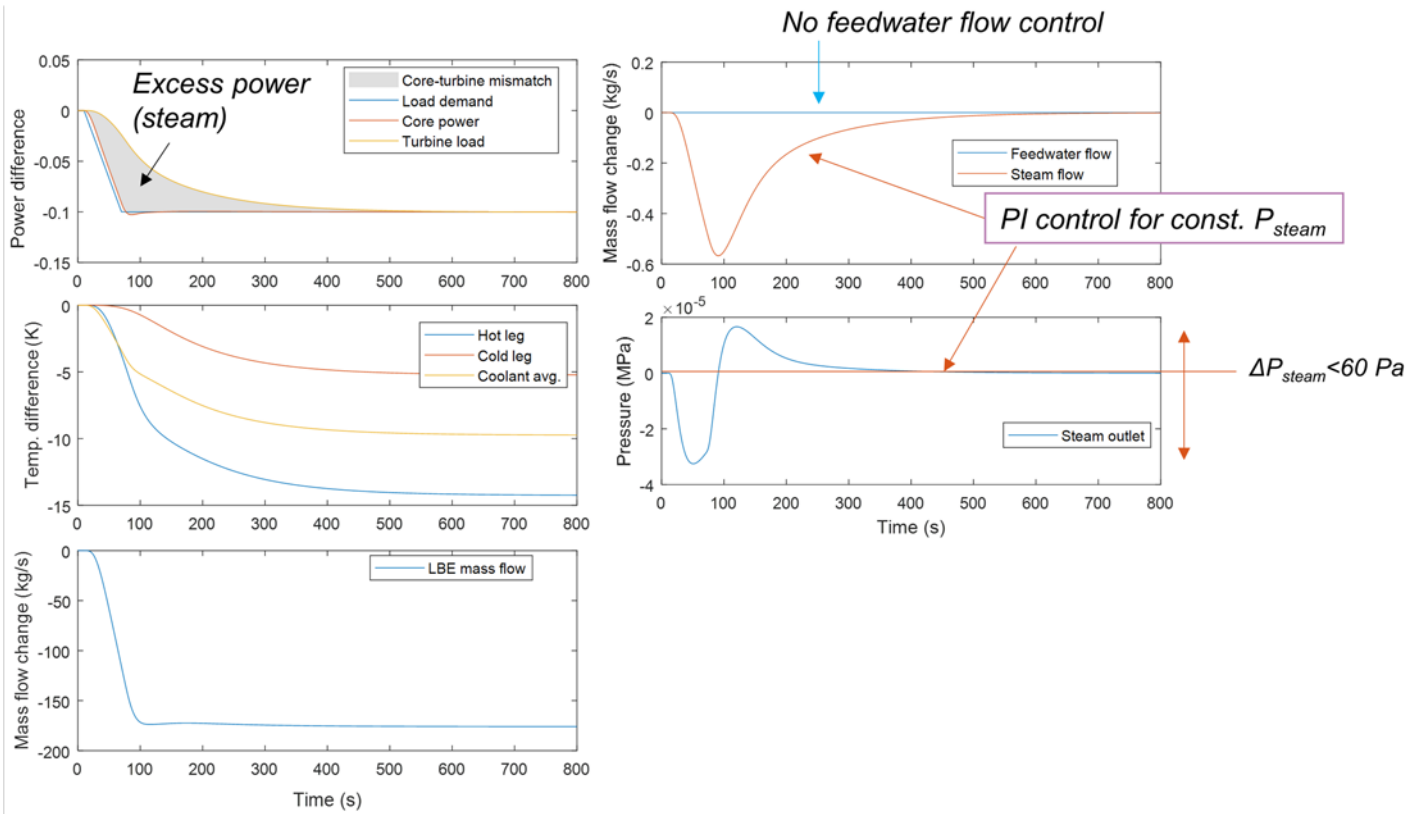

Figure 7.9 Calculation results for the system transients given by a power ramp rate of -10%P/min from 100% power output without feedwater flow rate control

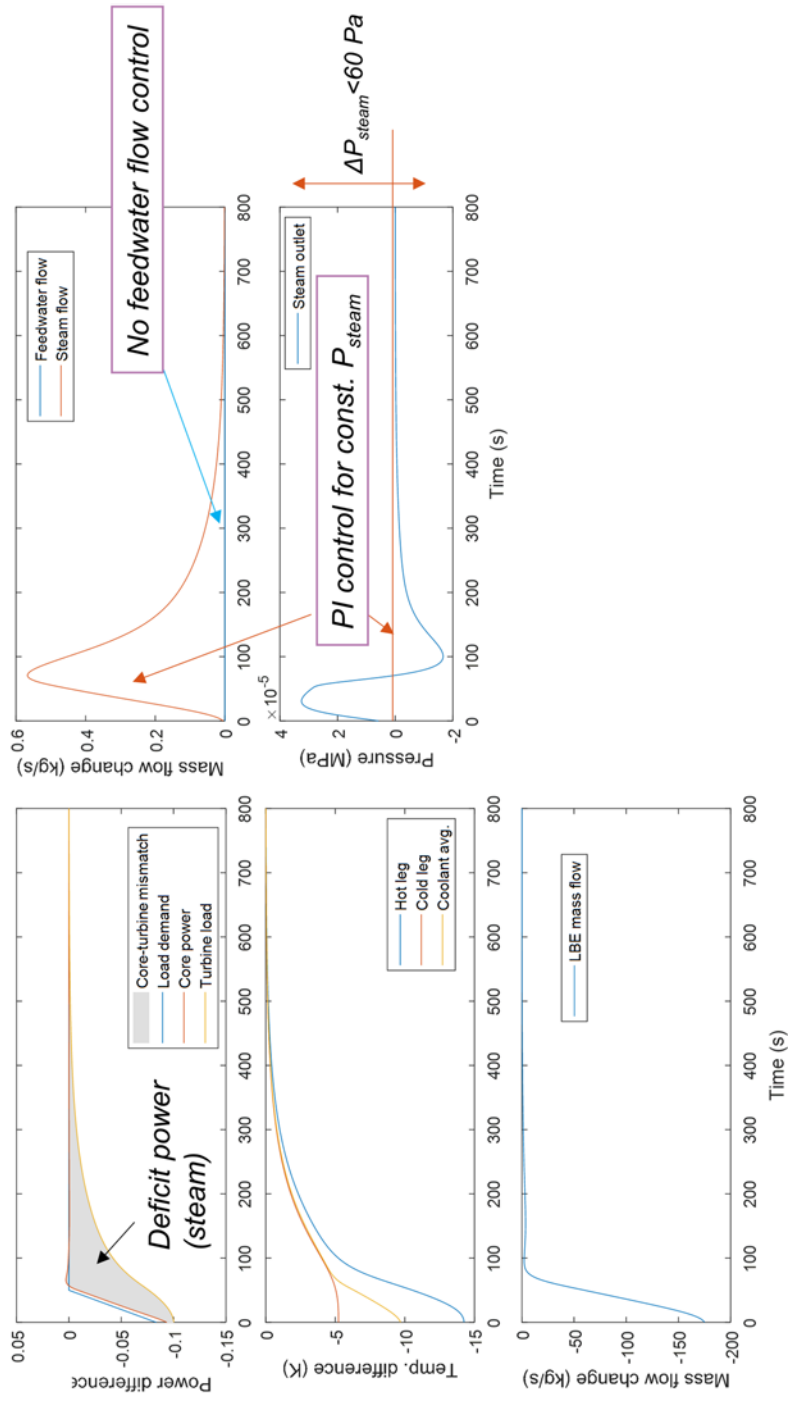

Figure 7.10 Calculation results for the system transients given by a power ramp rate of -10%P/min from 100% power output with feedwater flow rate control

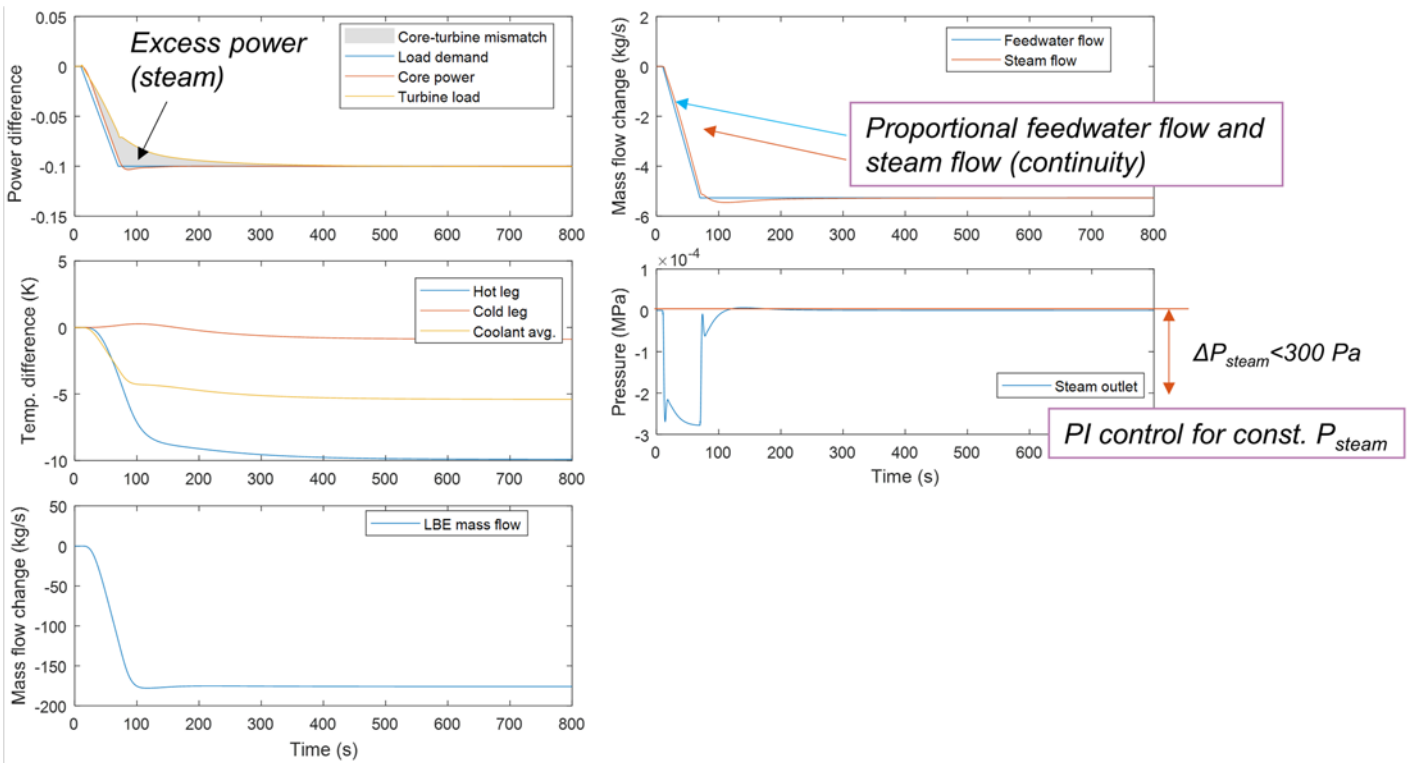

Figure 7.11 Calculation results for the system transients given by a power ramp rate of -10%P/min from 100% power output with feedwater flow rate control

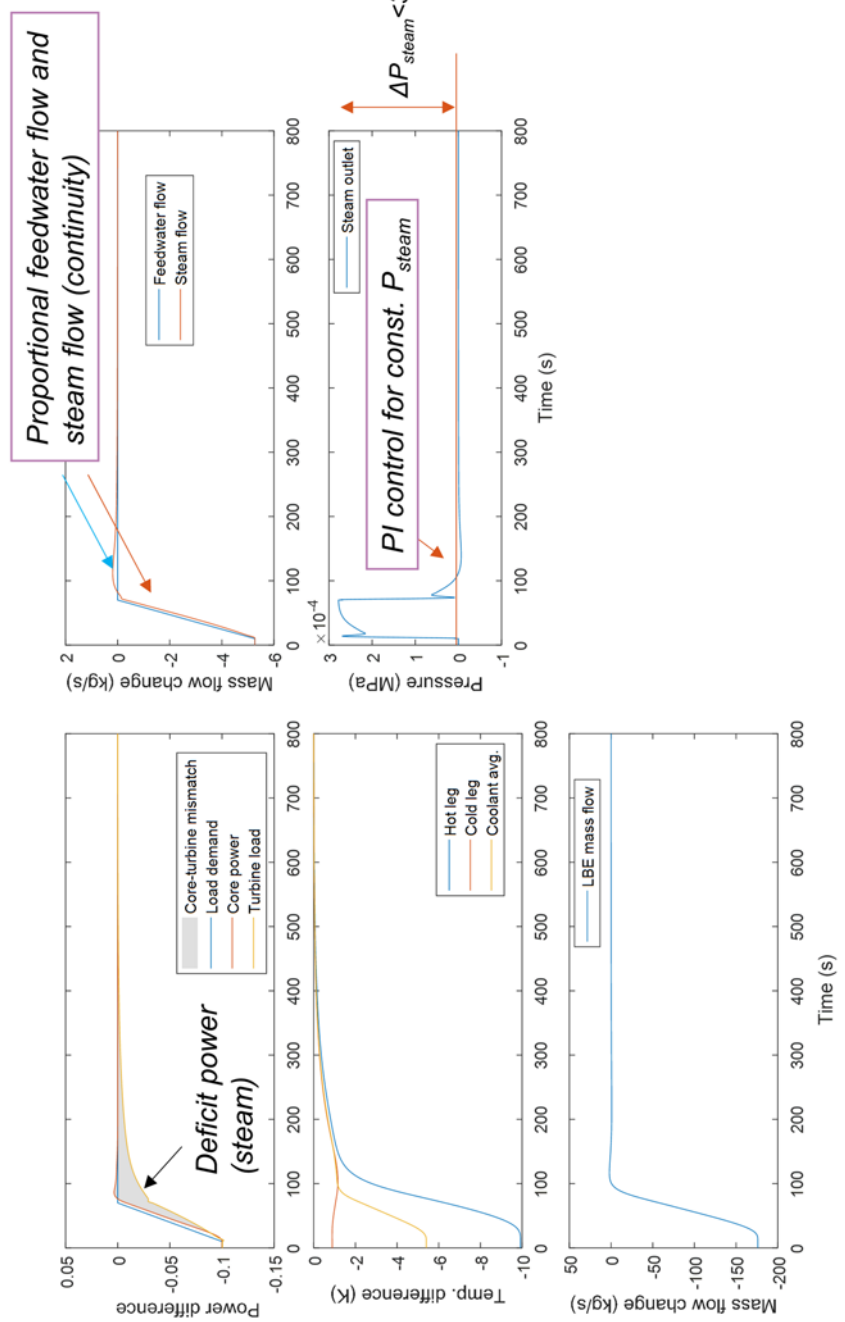

Figure 7.12 Calculation results for the system transients given by a power ramp rate of +10%P/min from 90% power

7.3.2 Stability analysis

In the operation of a system, for example, a powerplant, it is important to maneuver it within a stable range. Hence, the stability boundary should be studied, which depends on the dynamic characteristics of the system. In this regard, a stability analysis on URANUS is conducted in this section using the analytical reactor dynamics simulation model developed in this thesis study. The stability of interest under the load-following operation of this passive system is the dynamic stability of reactor core power in response of the external load demand change, which can be thought as bounded-output (BIBO) condition since it is lying on a bounded range of load demand.

In this section, the stability analysis is one of linear analyses, which make use of transfer functions, and it can be carried out by using the linear analysis tool supported by MATLAB/Simulink environments (Mathworks, 2017). In order to conduct a linear analysis of the implemented system, a user is requested to impose linear analysis points on the graphical user interface, as expressed by a flow diagram such as the block chain diagram of URANUS shown in Figure 7.6. Among several linear analysis points, the open-loop input and the open-loop output are utilized to establish a linear relation in terms of open-loop transfer function in this case.

Two graphical methods of stability analysis, the root locus and Bode diagram are to be used among others. According to the control theory, a dynamic system is BIBO stable if and only if all poles of transfer function have negative real part (Aström and Murray, 2010); in other words, all the poles are

located on the left-hand plane of Gauss plane in the pole-zero map drawn with root locus. Since the root locus illustrates the trajectories of pole locations in the linearized transfer function by varying the open-loop gain, it is confirmed for a system to be stable if the trajectories do not lay on the right hand side of the Gauss plane. Figure 7.13 show the resultant root locus for the transfer function that is linearized by imposing the open-loop input at the external power demand and the open-loop output at the reactor power. It is clearly seen that all the poles are located in the left hand plane of Gauss plane. Hence, the system can be said to be BIBO stable for the entire range of reactor power in response of the external load demand.

The other diagram, the Bode plot, is shown in Figure 7.14. The BIBO stability of a closed-loop is confirmed with an interpretation that the system is BIBO stable if both the phase margin and the gain margin are positive simultaneously (Hahn et al., 2001). The figures shows the phase margin of system response, 141°, is positive while the gain margin is not able to be estimated because phase shift is larger than -180° over all frequency domain. Although it is not defined, the stability of the system response can be evaluated since the phase shift asymptotically reaches -180° at positive infinite frequency and in that condition the gain margin is positive. In conclusion, the reactor core power of URANUS is maneuvered within a stable range by natural circulation under the fast load-following conditions with respect to the external load demand.

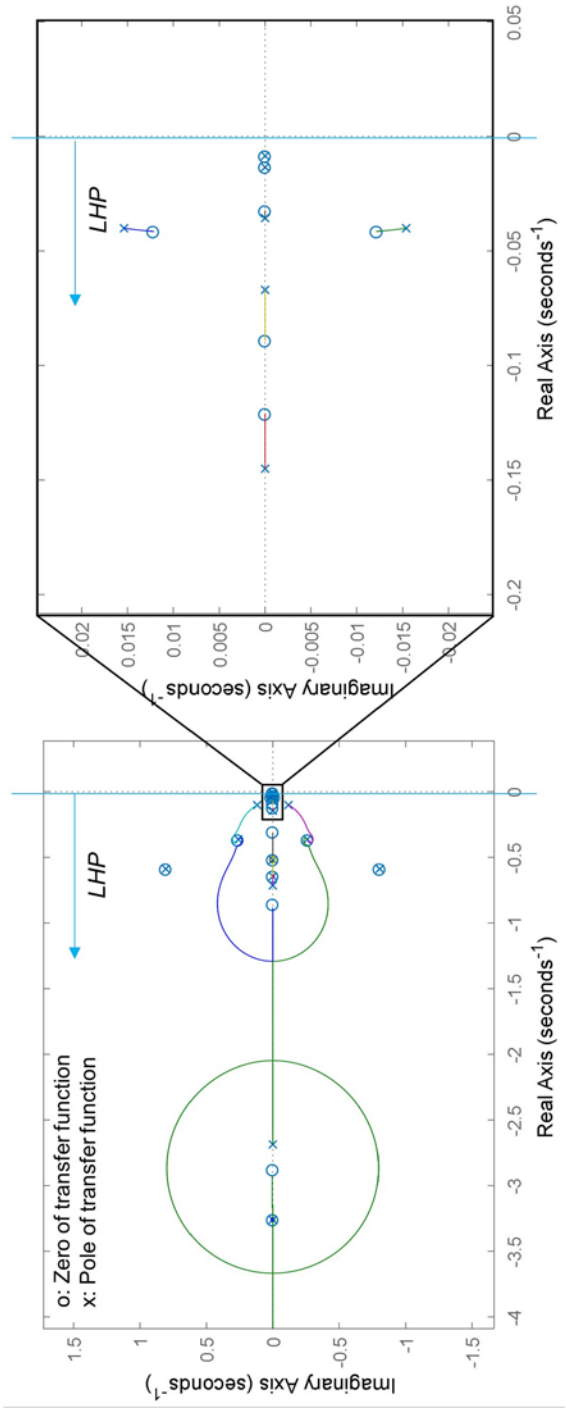

Figure 7.13 Root locus for load demand input to core power output

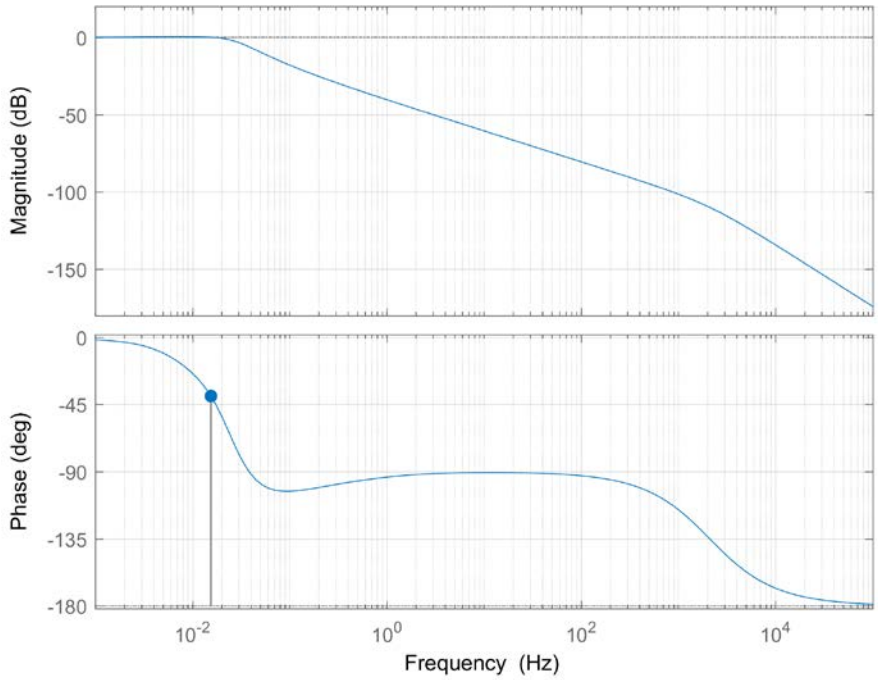

Figure 7.14 Bode diagram for load demand input to core power output

7.3.3 Planned load-following operation

A planned load-following operation is a type of power maneuvering as planned and expected. It is usually done in daily load maneuvering and typically expressed as "100-P-100%P_0, x-y-z-y", where P is given by power fraction in percent with respect to nominal full power and x, y, and z are the time spans between condition changes. In addition, the time spans x and z are the durations that 100% and P% of nominal power are sustained, respectively, while y is the time span necessary to reduce power from 100% to P% or to recover it from P% to 100%.

A scenario of planned load-following operation with a load-following pattern given as 100-60-100%P_0, 12-3-6-3 is simulated using the developed model and compared to MARS-LBE calculation. Since MARS-LBE does not have a capability of directly estimating reactivity change from control rod maneuvering, it is given by the calculation using the developed model. Figure 7.15 depicts the two calculation results simultaneously and the two simulation results show a good agreement even with large power level change from 100% to 60%, vice versa. In addition, for a slow transient, in this case the ramp rate of 13% of full power increase or decrease per hour, stable load-following operation can be achieved with slow mass flow and temperature transient.

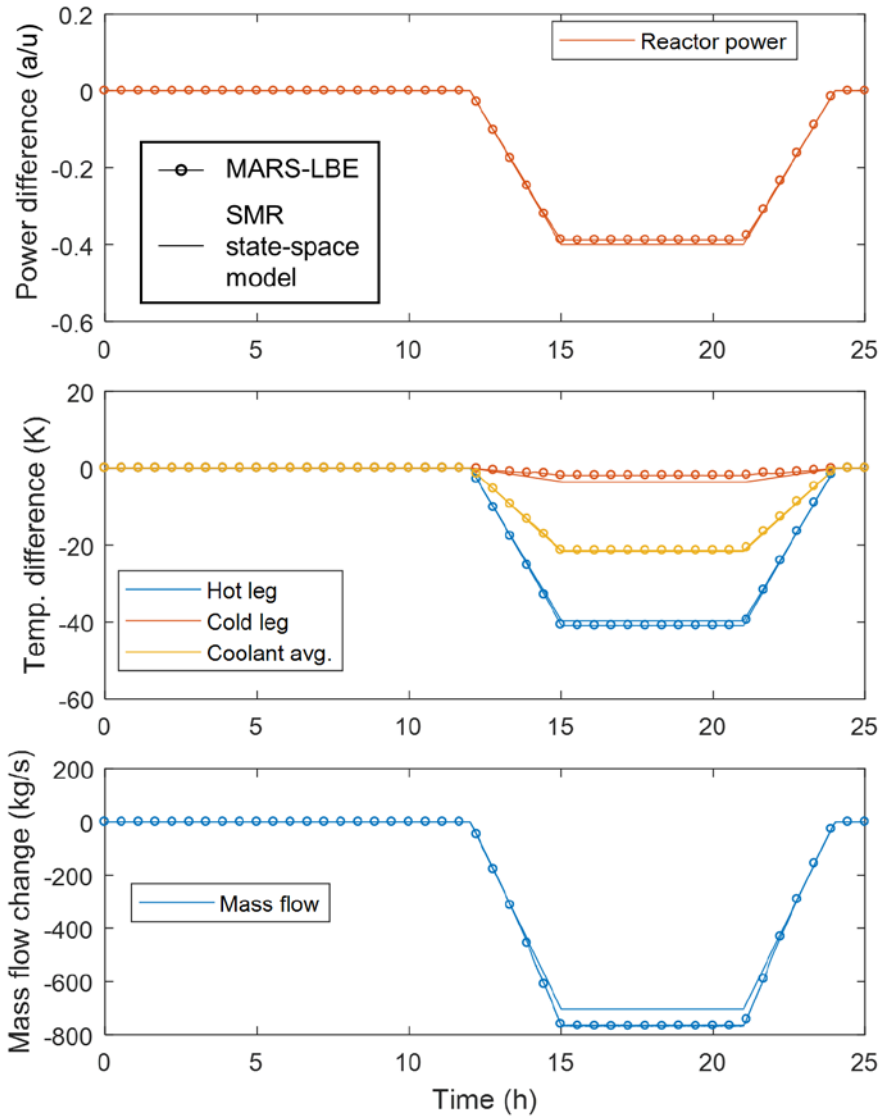

Figure 7.15 Comparison of planned load-following operation simulation results between the analytical model developed in this dissertation (line) and MARS-LBE (circle and line)

7.3.4 Power recovery from low power to full power

In this case study, a specific situation is postulated: URANUS is under low power operation, namely, 50% power of nominal full power, and the electric grid to which URANUS is also connected requires it to recover its core power to the nominal power rating since other powerplants connected to the grid fails, as shown in Figure 7.16. With regard to the grid request to URANUS, an unexpected, rapid request can be expressed in a step jump of core power rating. As utilized in Section 7.3.2, the linear analysis tool presented by MATLAB/Simulink environments (Mathworks, 2017) is also applicable on this type of analysis.

By imposing the open-loop input and output, similar to the procedure conducted in the stability analysis discussed in Section 7.3.2, an equivalent transfer function for the step analysis is established. Figure 7.17 shows the linear analysis results of URANUS. The top inset is calculated by the step response analysis with an open-loop input designated by the external load demand and an open-loop output at reactor core power. The bottom inset depicts the turbine load response with the same input and a different point of open-loop output, the secondary side heat removal.

For the step response analysis, selected terminologies are used; the settling time refers to the time required for a response signal to saturate within a specific range of its steady state value for all future times. In this analysis, the range is designated to be $\pm$2% of the steady state value. Another term, the rise time is defined as the time required for the signal to change from 10% of its

final value to 90% of the final value (Aström and Murray, 2010). According to those definitions, the system response against an input of step power jump can be discussed. The settling times of two systems are 47.9 s for the reactor core power and 232 s for the turbine load, which means the primary side settles first and then the secondary side follows this settlement to a new steady state.

In addition, the rise time of the primary side under step response is evaluated to be 11.4 s, as shown in the upper inset in Figure 7.17. Considering the definition of rise time, it is the time required for the URANUS primary side to change its power rating from 55% of full power to 95% of full power. In this case, the slope in response of step input would be the maximum response rate of the primary system since this step input postulates the most rapid rate of power maneuvering. Hence, the achievable maximum power ramp rate of the primary side of URNAUS in system transients can be estimated as 3.5% of full power per second (3.5%P/s).

This power maneuvering rate is an estimation given in terms of thermal-hydraulic and reactor kinetic aspects of URANUS system regardless of considering material integrity. Among others, the integrity of nuclear fuel is expected to be the most critical limiting factor when it comes to achievable power ramp rates. As a remark, experimental results and code calculation results on the reactor power transient test with a pre-irradiated fuel pin under a power ramp rate of 3%P/s showed that the failure condition of fuel would not be affected by the ramp rate within 1-3%P/s range (Fukano et al., 2009). However, until now, it is not evident whether the integrity of fuel is maintained under low-frequency temperature change expected in the fast load-following

operation. Thus, the estimated value is suggested to be the upper bound of the URANUS primary side.

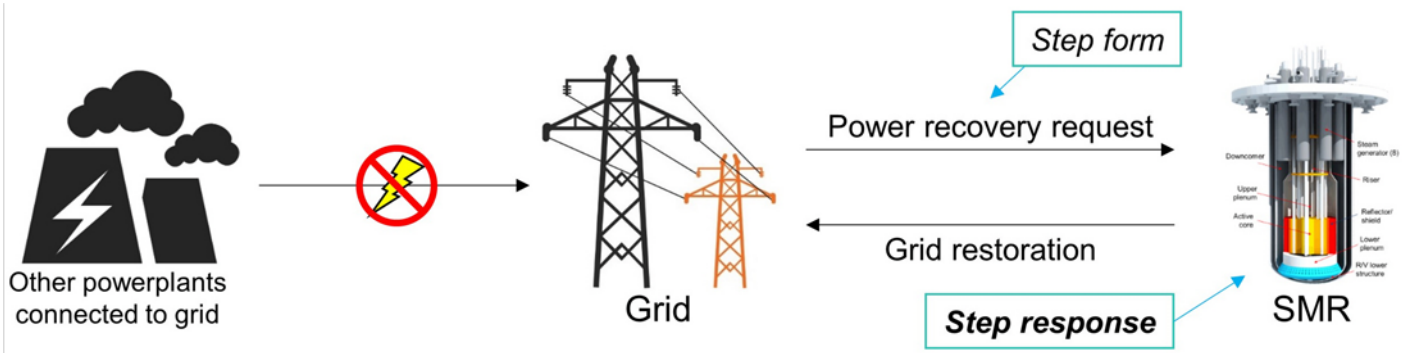

Figure 7.16 Conceptual case on instantaneous power return from low-power condition to nominal full power condition by grid request

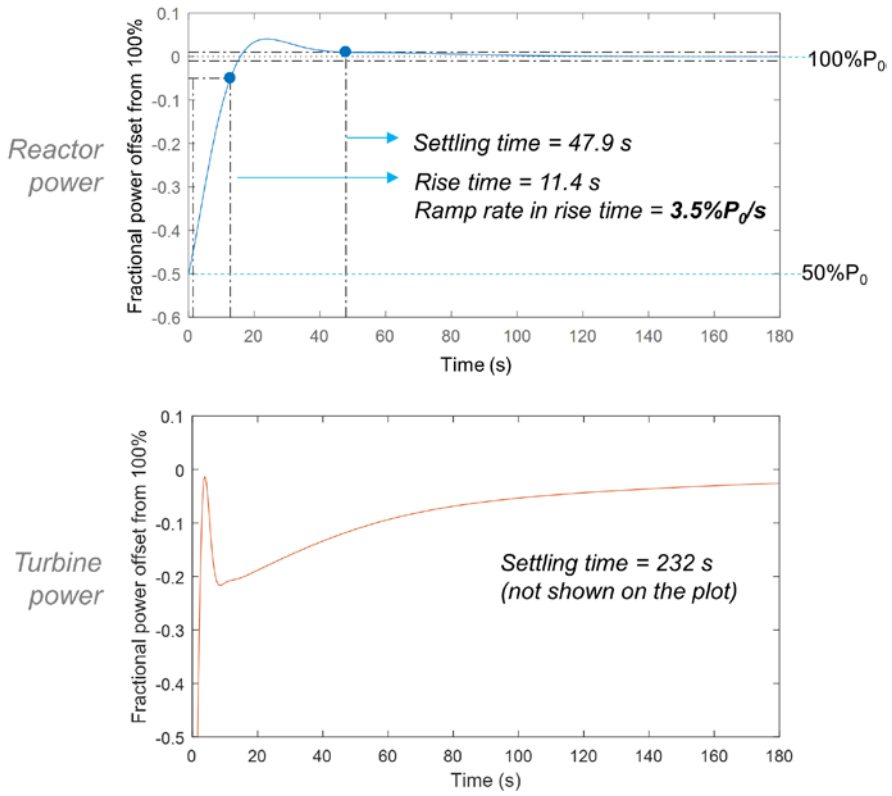

Figure 7.17 Step response analysis results on reactor core power response and turbine load response with respect to power recovery request from 50% to 100%

7.3.5 Comparison with a commercial SMR

This case study compares the load-following strategy suggested by a commercial passive water-cooled SMR, NuScale, named as NuFollow™ (Ingersoll et al., 2015)., NuScale power modules can be utilized in accordance with renewable sources, such as the wind farm, and a preliminary concept of fast load-following operation is given in that literature. The strategy mainly consists of two different ways of electricity generation: load-following operation without reactor core power maneuvering only with turbine bypass and that with both reactor power regulation and turbine bypass in a separate way. As introduced in Section 1.1, water-cooled reactors are not suitable for the fast load-following operation due to material and controlling limitations. In this regard, it seems that NuScale power module cannot follow the fast load demand change given by the wind farm.

However, as seen in the experimental results and evaluated by the analytical reactor dynamics simulation model, URANUS is expected to be able to follow the rapid load requirements given by the wind farm. To compare the fast load-following capability, the same load requirements are applied to URANUS. For the URANUS simulation, 10% extra load demand is added presuming an excess electricity supply to the area since there is no steam (power) deficit in the case of NuFollow™ because it is conceptually operated with steam bypass at all time. Meanwhile, the reactor dynamics model estimates the power transients in both primary and secondary sides from the deviations between the load demand. Hence, when the external load demand increases at

a given time, the steam deficit should occur and it is unrealistic because no electricity supply shortage is allowed.

Figure 7.18 shows the load requirements given by the wind farm and total load demand, and the simulation results with the latter load-following strategy of NuFollow™ (Ingersoll et al., 2015), a combination of reactor power maneuvering and steam curtailing. The case study shows that the fast load-following capability of URANUS contributes to not only the effective maneuvering of the reactor core power with respect to the required power but also the minimization of curtailed steam. In addition, when it comes to the excess steam utilization, the fast reactor power response expected in URANUS might also help where the dumped steam is used by maintaining in a specific range.

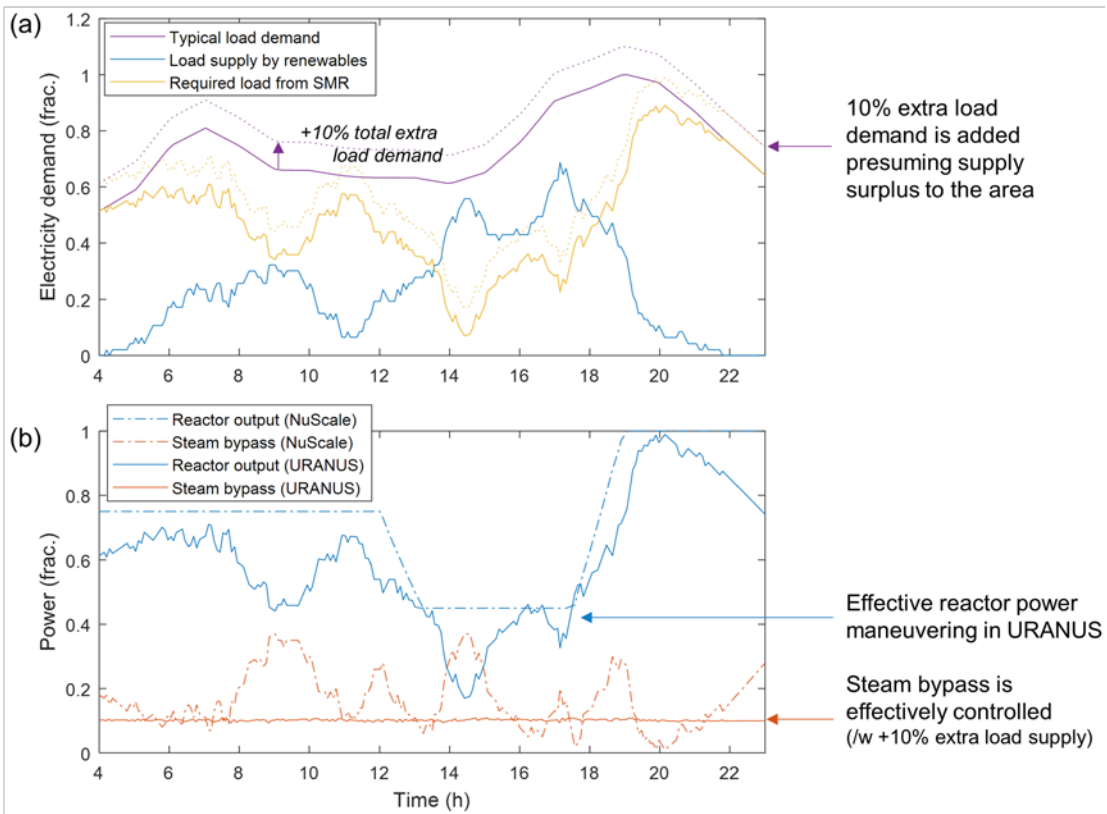

Figure 7.18 Comparison with a commercial passive load-following concept *NuFollow*™ (excerpted from (Ingersoll et al., 2015)). (a) Required load demand and (b) reactor output and steam bypass by NuScale and URANUS

Chapter 8 Conclusions and Future Work

8.1 Conclusions

The objective of this thesis study is to evaluate the fast load-following capability of a passive LBE-cooled SMR in terms of safety requirements and stability. A thorough understanding on the integral system behaviors of a LBE-cooled passive system under transients is necessary and furthermore, a predictive tool for passive system behavior is need to be developed.

To do so, the objective is divided further into three particular objectives as experimental, numerical, and analytical studies. This study has been conducted in three stages as follows: first, a pool-type integral experimental facility has been devised by a hydrodynamic scale reduction method from its prototype SMR design, URANUS, and natural circulation experiments has been carried out in both steady state and transients given by external condition changes. Second, a one-dimensional system thermal-hydraulics code, MARS-LBE, is validated two-fold through the experimental results generated from a loop configuration and the results given by the pool-type facility. Third, an analytical model for one-dimensional, time-dependent passive system transient evaluation has been developed under a commercial numerical software environment, MATLAB/Simulink. This analytical model has been verified with not only experimental results made in the second step

and but also with the one-dimensional system thermal-hydraulics code. Since there is no realization of a LBE-cooled SMR until now, a target reactor URANUS is designed before the three-step approach.

The experimental, numerical, and analytical investigations on the passive LBE-cooled SMR conducted in this thesis study show that the power ramp rate would not be limited by natural circulation, due to its rapid saturation with respect to heat source power transients. In addition, according to the stability analysis core power can be regulated within a stable range with respect to the external load demand change. Hence, the maximum achievable power ramp rate under safe, stable condition is related to nuclear fuel integrity, not the passive nature of reactor system. Furthermore, it is evaluated with an analysis on the step response that the reactor can change its core power rating as fast as 3.5% power per second from 50% of nominal full power to its full power with only considering its thermal-hydraulic and reactor kinetic response.

Since the primary side of a passive LBE-cooled SMR is expected to go through slower transients compared to the primary side under given operational condition changes, it can be concluded that the core power regulation along with feedwater flow rate control is favorable. As a preliminary study the dynamics of the secondary side is simulated with the developed analytical reactor dynamics simulation model and the results showed that the heat balance mismatch between the primary and secondary sides during transients can be minimized with feedwater flow control means, a proportional controller with respect to the external load demand in this case.

8.2 Future work

The evaluation on load-following capability of a passive LBE-cooled SMR shows that it can be operated under stable conditions for all external power demands and the maximum achievable power ramp rate would be 3.5% of full power per second. Beyond this achievement made in this thesis study, several addition studies are suggested as future work for a better understanding on the system integral behaviors and the enhanced performance of URANUS.

The BOP design of URANUS can be further determined. Conceptually, the BOP has been designated to utilize the Rankine cycle and its specific design was not a scope of this thesis study, since the integral behaviors in LBE natural circulation in the primary side was a key question. With the detailed design of BOP side, reactor control parameters can be further defined and a realistic assessment of thermal efficiency can be carried out. In addition, more realistic load demand change can be defined with frequency regulation.

For the experimental investigation, experiments on transients given by feedwater inlet temperature change can be sought. In an actual reactor, a decrease or increase in the steam generator outlet temperature can affect the core inlet temperature, which leads to a positive reactivity insertion by coolant overcooling. In this thesis study, this was excluded because the impact of secondary side temperature change would not be significant compared to the instantaneous flow rate change as shown in the transient experimental results on the secondary side. In this respect, the current PILLAR facility cannot facilitate rapid change of heat exchanger tube side inlet temperature since the

ultimate heat sink for the secondary side is the cooling tower and it shows rather slow transient nature due to relying on air convection. The investigation can be conducted by implementing some additional heaters and chillers on the secondary side to set out water inlet temperature rapidly.

The analytical model can be improved by implementing the capability of burnup-dependent system evaluation and controller optimization. As shown in the case of early French load-following modes having requirements on power ramps at elevated burnup levels, the former contributes to the evaluation of irradiated core. With this capability, the system behaviors at any time can be estimated, as the reactor targets to be operated about 30 years. Although the current model has a capability of stability evaluation, the latter would expand the scope of the analytical model. With optimally designed controllers, the performance of URANUS can be enhanced.

Nomenclature

Since each of chapters describe a number of equations and formulas, which in turn requires the use of numerous parameters accordingly, it is difficult to organize each of the parameters within same notations. Hence, for a better understanding, the relations were formulated with well-known letters on their description and it leads to the overlapping use of some letters. In this respect, this nomenclature section also lists up all the letters by dividing the paragraphs for each of chapters.

Nomenclature for Chapter 5.

a	Flow area (m^2)
A	Nondimensional flow area
Bi	Biot number
C_p	Isobaric heat capacity (J/kg K)
d	Hydraulic diameter (m)
d_{rod}	Diameter of nuclear fuel rod or electrical heater rod (m)
f	Darcy-Weisbach friction factor
F	Friction number
g	Gravitational acceleration constant (m/s^2)
h	Convective heat transfer coefficient (W/m^2 K)
k	Conductive thermal conductivity (W/m K)
K	Form loss coefficient
l	Length of a component (m)
L	Nondimensional length

$\dot{m}$	Mass flow rate (kg/s)
N_{rod}	Number of nuclear fuel rods or electrical heater rods
Nu	Nusselt number
P_0	Core thermal power (W)
Pe	Peclet number
Pr	Prandtl number
$\dot{q}$	Volumetric heat generation rate (W/m3)
Q	Heat source number
Re	Reynolds number
Ri	Richardson number
St	Stanton number
t	Time (s)
T	Temperature (K)
Ti	Time ratio number
u	Area-averaged flow velocity (m/s)
U	Nondimensional flow velocity
y	Transverse distance to flow direction (m)
Y	Nondimensional transverse distance
z	Axial (flow direction) distance (m)
Z	Nondimensional axial distance
Greek	
α	Thermal diffusivity (m^2/s)
β	Thermal coefficient of expansion (K^{-1})
δ	Conduction depth (m)
θ	Nondimensional temperature difference
ξ	Wetted perimeter (m)
ρ	Density (kg/m^3)
τ	Nondimensional time
ψ	Specific parameter
Subscripts	

0	Reference constant value
c	Cold region
h	Hot region
i	Number for *i*-th component
m	Scale model
p	Prototype
r	Representative variable of system
R	Model-to-prototype ratio; $R = m / p$
s	Solid

Nomenclature for Chapter 6.

ΔH	Thermal height center difference (m)
Δp	Pressure loss due to hydraulic resistance (Pa)
ΔT	Temperature difference between the mock-up core inlet and outlet (°C)
A	Flow area (m^2)
A_s	Projected grid cross section (m^2)
A_v	Undisturbed flow area (m^2)
C_p	Heat capacity (J/kg K)
C_v	Modified loss coefficient
d_h	Hydraulic diameter (m)
f	Darcy-Weisbach friction factor
g	Gravitational acceleration (m/s^2)
K	Form loss coefficient
K_{Re}, K_{loc}, K_{fr}	Constants given in (Nippert, 1929)
k	Thermal conductivity (W/m K)
l	Length (m)

$\dot{m}$	Mass flow rate (kg/s)
Nu	Nusselt number
Pe	Peclet number
Pr	Prandtl number
Q	Mock-up core power (W; kW)
Re	Reynolds number
v	Flow velocity (m/s)

Greek

β	Thermal expansion coefficient (K^{-1})
ε	Pipe roughness (m)
μ	Dynamic viscosity (Pa s)
ρ	Density (kg/m^3)

Subscripts

0	Reference
1	Upstream
2	Downstream
i	Component
c	Vena contracta
LBE	Lead-bismuth eutectic
oil	Secondary side thermal oil (Dowtherm© RP)
or	Orifice
w	Water

Nomenclature for Chapter 7.

ΔH	Thermal height center difference (m)
Δp	Pressure loss due to hydraulic resistance, pressure difference

	(Pa)
A	Flow area (m^2)
A_s	Cross-sectional area with respect to direction z (m^2)
C_j	j-th group neutron precursor density (#/cm^3)
C_p	Heat capacity (J/kg K)
C_R	Hydraulic resistance coefficient [ref]
c_m	Constant defined by Eqn. (7.16)
d	Diameter (m)
d_h	Hydraulic diameter (m)
f_f	Power fraction transferred directly to fuel lump
G_{rod}	Reactivity worth per unit length (dk/k/m)
g	Gravitational acceleration (m/s^2)
H	Height (m)
h	Convective heat transfer coefficient (W/m^2 K), fluids enthalpy (J/kg)
k	Thermal conductivity (W/m K)
L	Length of a component (m)
$\dot{m}$	Mass flow rate (kg/s)
N	Number
n	Neutron density (#/cm^3), a constant for the power of Eqn. (7.14)
O	Collection of terms with higher orders
P	Pressure (Pa)
Q	Power (W)
R	Proportionality constant to Eqn. (7.14)
Re	Reynolds number
r	Radius (m)
T	Temperature (K)
t	Thickness (m), time (s)
v_{rod}	Control rod speed (m/s)
z	Length in flow direction (m)

Greek

α	Reactivity constant (pcm/K)
β	Thermal expansion coefficient (K^{-1})
β_{eff}	Effective delayed neutron fraction (dk/k)
β_j	j-th group delayed neutron fraction (dk/k)
γ	Mean void fraction
δ	Deviation between initial value and perturbed value
ε	Pipe roughness (m)
μ_c	Mass flow rate times heat capacity of fluid (W/K)
Λ	Neutron generation time (s)
λ_j	j-th group precursor decay constant (s^{-1})
μ_c	Mass flow rate times heat capacity (W/K)
ρ	Reactivity (in point kinetic equations),
	Fluid density (kg/m^3) (in thermal-hydraulic equations)
ψ	State parameter
Ω	Equivalent heat transfer coefficient (W/K)

Superscript

n	Parameter defined at a boundary node

Subscripts

0	Initial value, nominal value
B	Buoyancy
c	Coolant, core average
ci	Core inlet
cl	Cole leg
clad	cladding
co	Core outlet
core	Core region
f	Nuclear fuel, saturated liquid

g	Gap between fuel pellet and cladding, saturated vapor
hl	Hot leg
i	Index
j	Index
k	Index
loss	Hydraulic loss
p	Primary side
r	Relative value
rod	Control rod or fuel rod
s	Steam generator shell side, secondary side
t	Steam generator tube wall
tube	Steam generator tube bundles
w	Subcooled water region in central feedwater pipe

Vector, matrix notations

$\mathbf{A}$	Matrix
a	Element of the matrix $\mathbf{A}$
$\mathbf{B}$	Matrix
b	Element of the matrix $\mathbf{B}$
$F_{\mathbf{x}}$	Matrix coefficient defined by $F_{\mathbf{x}} = \left[\left. \frac{\partial f}{\partial \mathbf{x}} \right\|_{\mathbf{x}_0, \mathbf{u}_0} \right]$
$F_{\mathbf{u}}$	Matrix coefficient defined by $F_{\mathbf{u}} = \left[\left. \frac{\partial f}{\partial \mathbf{u}} \right\|_{\mathbf{x}_0, \mathbf{u}_0} \right]$
$f(\mathbf{x},\mathbf{u})$	Matrix of $\mathbf{x}$ and $\mathbf{u}$ with a proper dimension
$f_{\mathbf{x}}$	Element of the matrix $F_{\mathbf{x}}$
$f_{\mathbf{u}}$	Element of the matrix $F_{\mathbf{u}}$
$g(\mathbf{x},\mathbf{u})$	Resultant matrix defined by $g(\mathbf{x},\mathbf{u}) = Z^{-1}(\mathbf{x},\mathbf{u})\, f(\mathbf{x},\mathbf{u})$
$\mathbf{u}$	Input vector
$\mathbf{x}$	State vector
$\dot{\mathbf{x}}$	Temporal change of state vector

$Z(\mathbf{x},\mathbf{u})$	Matrix of **x** and **u** with a proper dimension
z	Element of the matrix $Z(\mathbf{x},\mathbf{u})$

Bibliography

Alcouffe, R.E., Baker, R.S., Brinkley, F.W., Marr, D.R., O'Dell, R.D., Walters, W.F., (1995), DANTSYS: A Diffusion Accelerated Neutral Particle Transport Code System. Los Alamos National Laboratory, NM, USA.

Alekseev, A.I., Belyaev, V.V., Goltsov, Y.N., Grechko, G.I., Eremeev, D.V., Pepa, V.N., (2014), Status of Activities on the Reactor Facility for the UNITHERM SNPP, Third International Scientific and Technical Conference “Innovative Designs and Technologies of Nuclear Power” (ISTC NIKIET-2014), NIKIET, Moscow, Russia Federation.

Alemberti, A., (2012), ELFR: The European Lead Fast Reactor. Design, Safety Approach and Safety Characteristics.

ASME, (2005), Test Uncertainty, ASME PTC 19.1-2005 (Revision of ASME PTC 19.1-1998).

Astegiano, J.-C., Achourko, I., Alphonse, P., Aoyama, T., Baque, F., Berte, M., Brachi, R., Cabrillat, M.T., Carbonnier, J.L., Chiarot, D., Gastaldi, O., Giraud, M., Grabon, V., Henslee, S.P., Ibuki, Y., Irie, T., Joulia, E., Lemoine, P., Louvet, J., Martin, L., Mourogov, A., Poncerry, J., Preifer, W., Rajan, M., Ramakrishnan, I., Riou, B., Rodriguez, G., Stanculescu, A., Surendran, C.S., Kumar, K.V.S., Tommasi, J., Vinoche, O., Yu, H., (2004), Operational and decommissioning experience with fast reactors. IAEA, Vienna, Austria.

Aström, K.J., Murray, R.M., (2010), Feedback systems: an introduction for scientists and engineers. Princeton university press.

Ballinger, R.G., Lim, J., (2004), An overview of corrosion issues for the design and operation of high-temperature lead-and lead-bismuth-cooled reactor systems. Nuclear Technology 147, 418-435.

Bandini, G., Casamirra, M., Castiglia, F., Giardina, M., Meloni, P., Polidori, M., (2008a), Analysis of Protected Accidental Transients in the EFIT Reactor With the RELAP5 Thermal-Hydraulic Code. 759-768.

Bandini, G., Meloni, P., Polidori, M., Casamirra, M., Castiglia, F., Giardina, M., (2008b), Decay heat removal and transient analysis in accidental conditions in the EFIT reactor. Science and Technology of Nuclear Installations 2008.

Blue, R., Carelli, M., Delmastro, D., Delpech, M., Hwang, J.-K., Ivanov, E., Kuznetsov, V., Maheshwari, N.K., Sefidvash, F., Shimazu, Y., Sun, Y., Toshinskiy, G., Veshnyakov, K., Wade, D., (2005), Innovative small and medium sized reactors: Design features, safety approaches and R&D trends, Vienna, Austria.

Borgohain, A., Maheshwari, N.K., Vijayan, P.K., (2016a), Natural circulation experiments in a non-uniform diameter lead bismuth loop and validation of LeBENC code. Progress in Nuclear Energy 91, 68-82.

Borgohain, A., Srivastava, A.K., Jana, S.S., Maheshwari, N.K., Kulkarni, R.D., Vijayan, P.K., Tewari, R., Ram, A.M., Jha, S.K., (2016b), Natural circulation studies in a LBE loop for a wide range of temperature. Nuclear Engineering and Design 300, 358-375.

Briggs, L., Hu, W., Su, G., Vezzoni, B., Del Nevo, A., Monti, S., Sui, D., Maas, L., Sarathy, U.P., Petruzzi, A., (2015), EBR-II passive safety demonstration tests benchmark analyses-phase 2, 16th International Topical Meeting on Nuclear Reactor Thermal Hydraulics, NURETH

2015. American Nuclear Society.

Briggs, L., Monti, S., Choi, C., Hu, W., Maas, L., Maschek, W., Merk, B., Mikityuk, K., Mochizuki, H., Morita, K., (2013), Benchmark Analyses of the Shutdown Heat Removal Tests Performed in the EBR-II Reactor, Fast Reactors and Related Fuel Cycles: Safe Technologies and Sustainable Scenarios (FR13).

Carlson, K., Riemke, R., Rouhani, S., Shumway, R., Weaver, W., (1990), RELAP5/MOD3 Code Manual Volume I: Code Structure, System Models and Solution Methods. US NRC NUREG/CR-5535, Washington (DC, USA) June.

Castiglia, F., Giardina, M., Morana, G., De Salve, M., Panella, B., (2012), Analyses of single-and two-phase flow pressure drops in helical pipes using a modified RELAP5 code. Nuclear Engineering and Design 250, 585-591.

Chang, Y., LoPinto, P., Konomura, M., Cahalan, J., Dunn, F., Farmer, M., Krajtl, L., Moisseytsev, A., Momozaki, Y., Sienicki, J., (2005), Small Modular Fast Reactor design description. Argonne National Lab., Argonne, IL (US).

Chen, X.-N., (2015), On LBE natural convection and its water experimental simulation. Progress in Nuclear Energy 78, 372-379.

Cho, J.H., Batta, A., Casamassima, V., Cheng, X., Choi, Y.J., Hwang, I.S., Lim, J., Meloni, P., Nitti, F.S., Dedul, V., Kuznetsov, V., Komlev, O., Jaeger, W., Sedov, A., Kim, J.H., Puspitarini, D., (2011), Benchmarking of thermal hydraulic loop models for Lead-Alloy Cooled Advanced Nuclear Energy System (LACANES), phase-I: Isothermal steady state forced convection. Journal of Nuclear Materials 415, 404-414.

Choi, C., Ha, K., (2016a), Performance test of MARS-LMR code with benchmark analysis of EBR-II SHRT-17. Annals of Nuclear Energy 94, 376-391.

Choi, C., Ha, K.S., (2016b), Assessment calculation of MARS-LMR using EBR-II SHRT-45R. Nuclear Engineering and Design 307, 10-29.

Choi, J.-I., Oh, S.-Y., Song, I.-H., Hah, Y.-J., Kuh, J.-E., Lee, U.-C., (1992), Advanced Load Follow Operation Mode for Korean Standardized Nuclear Power Plants. Journal of the Korean Nuclear Society 24.

Choi, S., Cho, J.-H., Bae, M.-H., Lim, J., Puspitarini, D., Jeun, J.H., Joo, H.-G., Hwang, I.S., (2011a), PASCAR: Long burning small modular reactor based on natural circulation. Nuclear Engineering and Design 241, 1486-1499.

Choi, S., Hwang, I.S., Cho, J.H., Shim, C.B., (2011b), URANUS: Korean lead-bismuth cooled small modular fast reactor activities, ASME 2011 Small Modular Reactors Symposium. ASME, Washington D.C.

Ciampichetti, A., Agostini, P., Benamati, G., Bandini, G., Pellini, D., Forgione, N., Oriolo, F., Ambrosini, W., (2008), LBE–water interaction in sub-critical reactors: First experimental and modelling results. Journal of Nuclear Materials 376, 418-423.

Cinotti, L., (2004), Engineering solutions and thermal-hydraulic issues for a promising safe ADS system, Proc. of the 6 th International Conference on Nuclear Thermal Hydraulics, Operations and Safety (NUTHOS), Atomic Energy Society of Japan, Nara, Japan.

Coccoluto, G., Gaggini, P., Labanti, V., Tarantino, M., Ambrosini, W., Forgione, N., Napoli, A., Oriolo, F., (2011), Heavy liquid metal natural circulation

in a one-dimensional loop. Nuclear Engineering and Design 241, 1301-1309.

Cox, B., (1990), Pellet-clad interaction (PCI) failures of zirconium alloy fuel cladding—a review. Journal of Nuclear Materials 172, 249-292.

Croff, A.G., (1983), ORIGEN2: a versatile computer code for calculating the nuclide compositions and characteristics of nuclear materials. Nuclear Technology 62, 335-352.

De Bruyn, D., Abderrahim, H.A., Baeten, P., Fernandez, R., Engelen, J., Van Den Eynde, G., (2014), The MYRRHA ADS project in Belgium enters the Front End Engineering Phase, International Congress on Advances in Nuclear Power Plants, ICAPP 2014, pp. 646-654.

Dittus, F.W., Boelter, L.M.K., (1930), Heat transfer in automobile radiators of the tubular type.

Dow Chemical Company, (1996), DOWTHER RP Heat Transfer Fluid Product Technical Data.

Dragunov, Y.G., Lemekhov, V., Moiseev, A., Smirnov, V., Yarmolenko, O., Vasyukhno, V., Cherepnin, Y.S., (2016), Detailed design of the BREST-OD-300 reactor facility: development stages and justification, Innovative designs and technologies of nuclear power. IV International scientific and technical conference. Book of abstracts.

Dvoriashin, A.M., Porollo, S., Konobeev, Y.V., Budylkin, N., Mironova, E., Ioltukhovskiy, A., Leontyeva-Smirnova, M., Garner, F.A., (2007), Mechanical properties and microstructure of three Russian ferritic/martensitic steels irradiated in BN-350 reactor to 50dpa at 490° C. Journal of Nuclear Materials 367, 92-96.

Edwards, R.M., Lee, K.Y., Schultz, M., (1990), State feedback assisted classical control: an incremental approach to control modernization of existing and future nuclear reactors and power plants. Nuclear technology 92, 167-185.

Eguchi, Y., Takeda, H., Koga, T., Tanaka, N., Yamamoto, K., (1997), Quantitative prediction of natural circulation in an LMFR with a similarity law and a water test. Nuclear engineering and design 178, 295-307.

El-Wakil, M.M., (1971), Nuclear Heat Transport. International Textbook Co.

Fazio, C., Benamati, G., Martini, C., Palombarini, G., (2001), Compatibility tests on steels in molten lead and lead–bismuth. Journal of nuclear materials 296, 243-248.

Frogheri, M., Alemberti, A., Mansani, L., (2015), The lead fast reactor: demonstrator (ALFRED) and ELFR design, Fast Reactors and Related Fuel Cycles: Safe Technologies and Sustainable Scenarios (FR13). V. 1. Proceedings of an International Conference.

Fukano, Y., Onoda, Y., Sato, I., Charpenel, J., (2009), Fuel Pin Behavior under Slow-Ramp-type Transient-Overpower Conditions in the CABRI-FAST Experiments. Journal of Nuclear Science and Technology 46, 1049-1058.

Garner, F., Toloczko, M., Sencer, B., (2000), Comparison of swelling and irradiation creep behavior of fcc-austenitic and bcc-ferritic/martensitic alloys at high neutron exposure. Journal of Nuclear Materials 276, 123-142.

Grewal, S., Gluekler, E., (1982), Water Simulation of Sodium Reactors. Chemical Engineering Communications 17, 343-360.

Grishchenko, D., Jeltsov, M., Kööp, K., Karbojian, A., Villanueva, W., Kudinov, P., (2015), The TALL-3D facility design and commissioning tests for validation of coupled STH and CFD codes. Nuclear Engineering and Design 290, 144-153.

H. Ait Abderrahim, A. Al Mazouzi, Arien, B., Baeten, P., D. De Bruyn, Maes, D., Malambu, E., Schuurmans, P., Schyn, M., Sobolev, V., G. Van den Eynde, Vandeplassche, D., (2011), MYRRHA Technical Description. . SCK-CEN.

Hahn, J., Edison, T., Edgar, T.F., (2001), A note on stability analysis using bode plots. Chemical Engineering Education 35, 208-211.

He, X., Liu, S., Asada, H., (1995), Modeling of vapor compression cycles for advanced controls in HVAC systems, Proceedings of the American Control Conference, pp. 3664-3668.

Hejzlar, P., Petroski, R., Cheatham, J., Touran, N., Cohen, M., Truong, B.A.O., Latta, R., Werner, M., Burke, T.O.M., Tandy, J.A.Y., Garrett, M., Johnson, B., Ellis, T., McWhirter, J.O.N., Odedra, A.S.H., Schweiger, P.A.T., Adkisson, D., Gilleland, J., (2013), Terrapower, LLC Traveling Wave Reactor Development Program Overview. Nuclear Engineering and Technology 45, 731-744.

Hill, R., Cahalan, J., Khalil, H., Wade, D., (1999), Development of small, fast reactor core design using lead-based coolant, Proceedings of the International Conference on Future Nuclear Systems.

Hong, S.J., Lee, D.Y., (2012), Scaling and Design of Integral Test Facility Simulating 600MWe SFR (Korean version). FNC Technology Co., and Korea Atomic Energy Research Institute

Hosemann, P., Thau, H.T., Johnson, A.L., Maloy, S.A., Li, N., (2008), Corrosion of ODS steels in lead–bismuth eutectic. Journal of Nuclear Materials 373, 246-253.

Hwang, I., Kim, M., Joo, H., (2008a), Development of PASCAR (Proliferation-resistant, Accident-tolerant, Self-sustainable, Capsular, Assured Reactor) design and safety analysis, 10th Information Exchange Meeting on Actinide and Fission Product Partitioning and Transmutation.

Hwang, I.S., Jeong, S.H., Park, B.G., Yang, W.S., Suh, K.Y., Kim, C.H., (2000), The concept of proliferation-resistant, environment-friendly, accident-tolerant, continual and economical reactor (PEACER). Progress in Nuclear Energy 37, 217-222.

Hwang, I.S., Kim, M.H., Joo, H.G., Yoo, B., Kim, M.H., Oh, S.R., Yi, K.W., Han, D.Y., Lim, J., Nam, H.O., Cho, J.H., Lee, K.Y., Bae, M.H., Choi, S., Kim, C.H., (2008b), Development of Transportable Capsule Version of PEACER design. Proc: ICAPP '08, Anaheim, CA, USA.

Hwang, I.S., Lim, J., (2010), Structural developments for lead-bismuth cooled fast reactors, PEACER and PASCAR, 25th KAIF/KNS Annual Conference, Seoul, Korea.

IAEA, (2011), Stress corrosion cracking in light water reactors: good practices and lessons learned, IAEA Nuclear Energy Series.

Idelchik, I.E., (1953), Determination of the resistance coefficients during discharge through orifices. Gidrotekh. Stroit. No. 5., 31-36.

Idelchik, I.E., (1986), Handbook of hydraulic resistance. Washington, DC, Hemisphere Publishing Corp., 1986, 662 p. Translation. 1.

Ikegawa, T., Kawabata, Y., Ishii, Y., Matsuura, M., Hirako, S., Hoshi, T., (2010),

The Plant Feature and Performance of Double MS (Modular Simplified and Medium Small Reactor). Journal of Engineering for Gas Turbines and Power 132, 015001.

Ingersoll, D., Colbert, C., Houghton, Z., Snuggerud, R., (2015), Can nuclear power and renewables be friends?, 2015 International Congress on Advances in Nuclear Power Plants (ICAPP '15), Nice, France.

Ishii, M., Kataoka, I., (1984), Scaling laws for thermal-hydraulic system under single phase and two-phase natural circulation. Nuclear Engineering and Design 81, 411-425.

Ishii, M., Revankar, S.T., Leonardi, T., Dowlati, R., Bertodano, M.L., Babelli, I., Wang, W., Pokharna, H., Ransom, V.H., Viskanta, R., Han, J.T., (1998), The three-level scaling approach with application to the Purdue University Multi-Dimensional Integral Test Assembly (PUMA). Nuclear Engineering and Design 186, 177-211.

Islam, M.R., Gabbar, H.A., (2015), Study of small modular reactors in modern microgrids. International Transactions on Electrical Energy Systems 25, 1943-1951.

Jensen, J.M., Tummescheit, H., (2002), Moving boundary models for dynamic simulations of two-phase flows. Proceedings of the 2nd International Modelica Conference, 235-244.

Jeong, S.H., (2006), Development of an integral test loop, HELIOS and investigation of natural circulation ability for PEACER. Ph.D. Thesis, Seoul National University, Seoul, Korea.

Jeong, S.H., Bahn, C.B., Chang, S.H., Oh, Y.J., Nam, W.C., Ryu, K.H., Nam, H.O., Lim, J., Lee, T.H., Lee, S.G., (2006), Operation Experience of LBE

Loop: HELIOS, 2006 international congress on advances in nuclear power plants-ICAPP'06, Reno, NV, USA.

KAERI, (2006), MARS Code Manual Volume I - Code Structure, System Models and Solution Methods., Daejeon, Korea.

KAERI, (2007), Development of MARS-LMR and Steady-state Calculation for KALIMER-600 (in Korean). Korea Atomic Energy Research Insititute.

Kapernick, J.R., (2015), Dynamic Modeling of a Small Modular Reactor for Control and Monitoring.

Kerlin, T., Katz, E., Thakkar, J., Strange, J., (1976), Theoretical and experimental dynamic analysis of the HB Robinson nuclear plant. Nuclear technology 30, 299-316.

Kerlin, T.W., (1978), Dynamic Analysis and Control of Pressurized Water Reactors, in: Leondes C.T. (Ed.), Control and Dynamic Systems. Academic Press, pp. 103-212.

Khalil, H.K., (1996), Noninear systems. Prentice-Hall, New Jersey 2, 5-1.

Kim, T., Lee, J., Kim, J.H., (2017), Pilgering Process of Functionally Graded Composite Cladding for Liquid Metal Fast Cooled Reactor Application, Global Symposium on Lead and Lead Alloy Cooled Nuclear Energy Science and Technology (GLANST-2017), Seoul, Republic of Korea.

Kimura, A., Kasada, R., Iwata, N., Kishimoto, H., Zhang, C.H., Isselin, J., Dou, P., Lee, J.H., Muthukumar, N., Okuda, T., Inoue, M., Ukai, S., Ohnuki, S., Fujisawa, T., Abe, T.F., (2011), Development of Al added high-Cr ODS steels for fuel cladding of next generation nuclear systems. Journal of Nuclear Materials 417, 176-179.

Klueh, R., Nelson, A., (2007), Ferritic/martensitic steels for next-generation reactors. Journal of Nuclear Materials 371, 37-52.

Lawrence, R., (1983), DIF3D nodal neutronics option for two-and three-dimensional diffusion theory calculations in hexagonal geometry. Argonne National Lab., IL (USA).

Lee, J., Lee, J.H., Kim, J.H., Shin, Y.-H., Hwang, I.S., Ballinger, R.G., (2016), Three-Dimensional Finite Element Analysis of Pilgering Process of Hybrid-layer Cladding for Advanced Small Modular Fast Reactor Application, 2016 International Congress on Advances in Nuclear Power Plants (ICAPP-2016, San Francisco, USA.

Lehto, W.K., Dean, E.M., Fryer, R.M., (1988), Reactor safety implications of pump run-up tests in EBR-II. Nuclear Engineering and Design 110, 47-53.

Li, N., (2008), Lead-alloy coolant technology and materials–technology readiness level evaluation. Progress in Nuclear Energy 50, 140-151.

Lienhard, J.H., (1973), On the commonality of equations for natural convection from immersed bodies. International Journal of Heat and Mass Transfer 16, 2121-2123.

Lim, J., Jeong, S.H., Oh, Y.J., Nam, H.O., Bahn, C.B., Chang, S.H., Nam, W.C., Ryu, K.H., Lee, T.H., Lee, S.G., Lee, N.Y., Hwang, I.S., (2007), Progresses in the operation of large scale LBE loop HELIOS, 2017 International Congress on Advances in Nuclear Power Plants - ICAPP 2007, Nice, France.

Lim, J., Nam, H.O., Hwang, I.S., Kim, J.H., (2010), A study of early corrosion behaviors of FeCrAl alloys in liquid lead–bismuth eutectic environments.

Journal of Nuclear Materials 407, 205-210.

Lokhov, A., (2011), Technical and economic aspects of load following with nuclear power plants. OECD Nuclear Energy Agency, Paris, France.

Ludwig, H., Salnikova, T., Stockman, A., Waas, U., (2011), Load cycling capabilities of german nuclear power plants (NPP). VGB powertech 91, 38.

Ma, W., Bubelis, E., Karbojian, A., Sehgal, B.R., Coddington, P., (2006), Transient experiments from the thermal-hydraulic ADS lead bismuth loop (TALL) and comparative TRAC/AAA analysis. Nuclear Engineering and Design 236, 1422-1444.

Ma, W., Karbojian, A., Sehgal, B.R., (2007), Experimental study on natural circulation and its stability in a heavy liquid metal loop. Nuclear Engineering and Design 237, 1838-1847.

MacFarlane, R.E., (1992), TRANSX 2: A Code for Interfacing MATXS Cross-Section Libraries to Nuclear Transport codes. Los Alamos National Laboratory, NM, USA.

Marcel, C.P., Furci, H.F., Delmastro, D.F., Masson, V.P., (2013), Phenomenology involved in self-pressurized, natural circulation, low thermo-dynamic quality, nuclear reactors: The thermal–hydraulics of the CAREM-25 reactor. Nuclear Engineering and Design 254, 218-227.

Mathworks, (2017), SIMULINK Dynamic System Simulation Language User's Guide.

Mills, K.C., Su, Y., Li, Z., Brooks, R.F., (2004), Equations for the calculation of the thermo-physical properties of stainless steel. ISIJ international 44, 1661-1668.

Mitenkov, F.M., Polunichev, V.I., (1997), Small nuclear heat and power co-generation stations and water desalination complexes on the basis of marine reactor plants. Nuclear Engineering and Design 173, 183-191.

Müller, G., Schumacher, G., Zimmermann, F., (2000), Investigation on oxygen controlled liquid lead corrosion of surface treated steels. Journal of Nuclear Materials 278, 85-95.

Nam, H.O., Lim, J., Han, D.Y., Hwang, I.S., (2008), Dissolved oxygen control and monitoring implementation in the liquid lead–bismuth eutectic loop: HELIOS. Journal of Nuclear Materials 376, 381-385.

Nam, W.C., Lee, H.W., Hwang, I.S., (2007), Fuel design study and optimization for PEACER development. Nuclear Engineering and Design 237, 316-324.

Nippert, H., (1929), Über den Strömungsverlust in gekrümmten Kanälen. VDI-Verlag.

OECD Nuclear Energy Agency, (2007), Handbook on Lead-bismuth Eutectic Alloy and Lead Properties, Materials Compatibility, Thermal-hydraulics and Technologies. OECD Nuclear Energy Agency, Paris, France.

OECD Nuclear Energy Agency, (2012), Benchmarking of thermal-hydraulic loop models for lead-alloy-cooled advanced nuclear energy systems - Phase I: Isothermal forced convection case. OECD Nuclear Energy Agency, Paris, France.

OECD Nuclear Energy Agency, (2014), Technology roadmap update for Generation IV nuclear energy systems - January 2014. OECD Nuclear Energy Agency for the Generation IV International Forum.

OECD Nuclear Energy Agency, (2016a), 2016 GIF Annual Report. OECD

Nuclear Energy Agency for the Generation IV International Forum.

OECD Nuclear Energy Agency, (2016b), Small Modular Reactors: Nuclear Energy Market Potential for Near-term Deployment. OECD Nuclear Energy Agency, Paris, France.

Papukchiev, A., Jeltsov, M., Kööp, K., Kudinov, P., Lerchl, G., (2015), Comparison of different coupling CFD–STH approaches for pre-test analysis of a TALL-3D experiment. Nuclear Engineering and Design 290, 135-143.

Pettit, N., Willatzen, M., Ploug-Sørensen, L., (1998), A general dynamic simulation model for evaporators and condensers in refrigeration. Part II: simulation and control of an evaporator: Modèle général dynamique pour évaporateurs et condenseurs frigorifiques. Partie II: Simulation et régulation d'un évaporateur. International Journal of Refrigeration 21, 404-414.

Popov, S., Carbajo, J., (2000), Thermophysical properties of MOX and UO2 fuels including the effects of irradiation. Oak Ridge National Laboratory.

Rasmussen, B.P., Alleyne, A.G., (2006), Dynamic modeling and advanced control of air conditioning and refrigeration systems. Air Conditioning and Refrigeration Center. College of Engineering. University of Illinois at Urbana-Champaign.

Rehme, K., (1973), Pressure drop correlations for fuel element spacers. Nuclear technology 17, 15-23.

Reyes, J.N., (2011), Overview of NuScaleTechnology, Workshop on Technology Assessment of Small and Medium-sized Reactors (SMRs) for Near Term Deployment, IAEA Headquarters, Vienna, Austria.

Reyes, J.N., Lorenzini, P., (2010), NuScale Power: A modular, scalable approach to commercial nuclear power. Nuclear News 53, 97.

Satyamurthy, P., Biswas, K., (2002), Design of a LBE spallation target for fast-thermal accelerator-driven sub-critical system (ADS), Seventh Information Exchange Meeting on Actinide and Fission Product Partitioning and Transmutation, Jeju, Republic of Korea.

Seban, R.A., Shimazaki, T., (1949), Heat transfer to a fluid flowing turbulently in a smooth pipe with walls at constant temperature. California Univ., Berkeley (USA). Inst. of Engineering Research.

Sekimoto, H., Su'ud, Z., (1995), Design study of lead-and lead-bismuth-cooled small long-life nuclear power reactors using metallic and nitride fuel. Nuclear Technology 109.

Shim, H.-J., Han, B.-S., Jung, J.-S., Park, H.-J., Kim, C.-H., (2012), McCARD: Monte Carlo code for advanced reactor design and analysis. Nuclear Engineering and Technology 44, 161-176.

Shirvan, K., Ballinger, R., (2017), MIT/SNU Lead Bismuth Fast Reactor Project Final Report. Center for Advanced Nuclear Energy Systems, Department of Nuclear Science and Engineering, Massachusetts Institute of Technology.

Short, M.P., Ballinger, R.G., (2012), A Functionally Graded Composite for Service in High-Temperature Lead- and Lead-Bismuth–Cooled Nuclear Reactors—I: Design. Nuclear Technology 177, 366-381.

Sieder, E.N., Tate, G.E., (1936), Heat transfer and pressure drop of liquids in tubes. Industrial & Engineering Chemistry 28, 1429-1435.

Sinha, R., Kakodkar, A., (2006), Design and development of the AHWR—the

Indian thorium fuelled innovative nuclear reactor. Nuclear Engineering and Design 236, 683-700.

Smith, C.F., Halsey, W.G., Brown, N.W., Sienicki, J.J., Moisseytsev, A., Wade, D.C., (2008), SSTAR: The US lead-cooled fast reactor (LFR). Journal of Nuclear Materials 376, 255-259.

Sumner, T., Wei, T., (2012), Benchmark Specifications and Data Requirements for EBR II Shutdown Heat Removal Tests SHRT 17 and SHRT 45R. Nuclear Engineering Division Argonne National Laboratory, ANL-ARC-226-(Rev 1).

Svoboda, V., Wenzl, H., Kaiser, R., Jossen, A., Baring-Gould, I., Manwell, J., Lundsager, P., Bindner, H., Cronin, T., Nørgård, P., Ruddell, A., Perujo, A., Douglas, K., Rodrigues, C., Joyce, A., Tselepis, S., van der Borg, N., Nieuwenhout, F., Wilmot, N., Mattera, F., Sauer, D.U., (2007), Operating conditions of batteries in off-grid renewable energy systems. Solar Energy 81, 1409-1425.

Takahashi, M., Sofue, H., Iguchi, T., Matsumoto, M., Huang, F., Pramono, Y., Matsuzawa, T., Uchida, S., (2005), Study on Pb-Bi natural circulation phenomena. Progress in Nuclear Energy 47, 553-560.

Takahashi, M., Uchida, S., Kasahara, Y., (2008), Design study on reactor structure of Pb–Bi-cooled direct contact boiling water fast reactor (PBWFR). Progress in Nuclear Energy 50, 197-205.

Takaya, S., Furukawa, T., Müller, G., Heinzel, A., Jianu, A., Weisenburger, A., Aoto, K., Inoue, M., Okuda, T., Abe, F., Ohnuki, S., Fujisawa, T., Kimura, A., (2012), Al-containing ODS steels with improved corrosion resistance to liquid lead–bismuth. Journal of Nuclear Materials 428, 125-130.

Takeda, H., Koga, T., Watanabe, O., (1993), Experimental and computational simulation for natural circulation in an LMFBR. Nuclear engineering and design 140, 331-340.

Tarantino, M., Agostini, P., Benamati, G., Coccoluto, G., Gaggini, P., Labanti, V., Venturi, G., Class, A., Liftin, K., Forgione, N., Moreau, V., (2011), Integral Circulation Experiment: Thermal–hydraulic simulator of a heavy liquid metal reactor. Journal of Nuclear Materials 415, 433-448.

Thackeray, M.M., Wolverton, C., Isaacs, E.D., (2012), Electrical energy storage for transportation—approaching the limits of, and going beyond, lithium-ion batteries. Energy & Environmental Science 5, 7854-7863.

Thurgood, M., Kelly, J., Guidotti, T., Kohrt, R., Crowell, K., (1983), COBRA/TRAC-A thermal-hydraulics code for transient analysis of nuclear reactor vessels and primary coolant systems. Pacific Northwest Laboratory, Washington DC, NUREG/CT-3046, PNL-4385 1, 5.

Todreas, N.E., Kazimi, M.S., (2001), Nuclear Systems II: Elements of Thermal Hydraulic Design. Taylor and Francis.

Toppel, B.J., (1983), A User's Guide for the REBUS-3 Fuel Cycle Analysis Capability. Argonne National Laboratory, Illinois, USA.

Trapp, J.A., Ransom, V.H., (1977), RELAP5 Hydrodynamic Model Progress Summary -Abrupt Area Changes and Parallel Branching. . Idaho National Engineering Laboratory.

Tuček, K., Carlsson, J., Wider, H., (2006), Comparison of sodium and lead-cooled fast reactors regarding reactor physics aspects, severe safety and economical issues. Nuclear Engineering and Design 236, 1589-1598.

Van Tichelen, K., Mirelli, F., Greco, M., Viviani, G., (2015), E-SCAPE: A scale

facility for liquid-metal, pool-type reactor thermal hydraulic investigations. Nuclear Engineering and Design 290, 65-77.

Van Tichelen, K., Vanderhaegen, M., Jayaraju, S., Keijers, S., Roelofs, F., (2011), Scaling analysis for the European heavy liquid metal scaled pool facility ESCAPE, The 14th International Topical Meeting on Nuclear Reactor Thermalhydraulics, Toronto, Canada, pp. 25-30.

Wagner, W., Kruse, A., (1998), The industrial standard IAPWS-IF97 for the thermodynamic properties and supplementary equations for other properties. Properties of Water and Steam, Springer 354.

Wallenius, J., Qvist, S., Bortot, S., Mickus, I., Ejenstam, J., Szakalos, P., (2017), SEALER: a small lead-cooled reactor for power production in the Canadian Arctic, International Conference on Fast Reactors and Related Fuel Cycles: Next Generation Nuclear Systems for Sustainable Development (FR17), Yekaterinburg, Russia.

Waltar, A.E., Reynolds, A.B., (1980), Fast Breeder Reactors Pergamon press., New York.

Wedekind, G.L., Bhatt, B.L., Beck, B.T., (1978), A system mean void fraction model for predicting various transient phenomena associated with two-phase evaporating and condensing flows. International Journal of Multiphase Flow 4, 97-114.

Weinberg, D., Suckow, D., MUller, U., Hoffmann, H., (1990), The Transferability to Reactor Conditions of Thermohydraulics Model Investigations of Decay Heat Removal. roc. Int. Fast Reactor Safety Mtg., Snowbird, Utah.

Westinghouse Global Technology Office, (2017), Westinghouse Lead Fast

Reactor. Westinghouse Electric Company.

Willatzen, M., Pettit, N., Ploug-Sørensen, L., (1998), A general dynamic simulation model for evaporators and condensers in refrigeration. part i: moving-boundary formulation of two-phase flows with heat exchange: Modèle général dynamique pour évaporateurs et condenseurs frigorifiques. partic i: Formulation des conditions aux limites variables de flux biphasiques avec échange de chaleur. International Journal of refrigeration 21, 398-403.

Wu, Y., Bai, Y., Song, Y., Huang, Q., Zhao, Z., Hu, L., (2016), Development strategy and conceptual design of China Lead-based Research Reactor. Annals of Nuclear Energy 87, 511-516.

Yoo, B., Koo, G.H., Lee, J.H., Cho, M., (1999), Integrated horizontal and vertical seismic isolation bearing. Google Patents.

Yoo, B., Lee, J.-H., Koo, G.-H., Lee, H.-Y., Kim, J.-B., (2000), Seismic base isolation technologies for Korea advanced liquid metal reactor. Nuclear Engineering and Design 199, 125-142.

Zhang, J., Kapernick, R.J., McClure, P.R., Trapp, T.J., (2013), Lead–bismuth eutectic technology for Hyperion reactor. Journal of Nuclear Materials 441, 644-649.

Zhang, Z., Wu, Z., Sun, Y., Li, F., (2006), Design aspects of the Chinese modular high-temperature gas-cooled reactor HTR-PM. Nuclear Engineering and Design 236, 485-490.

Zigrang, D.J., Sylvester, N.D., (1985), A review of explicit friction factor equations. Journal of energy resources technology 107, 280-283.

Zrodnikov, A.V., Toshinsky, G.I., Komlev, O.G., Dragunov, Y.G., Stepanov,

V.S., Klimov, N.N., Kopytov, I.I., Krushelnitsky, V.N., (2006), Nuclear power development in market conditions with use of multi-purpose modular fast reactors SVBR-75/100. Nuclear Engineering and Design 236, 1490-1502.

초 록

전세계의 원자력 산업은 대형 원자력 발전소에 대한 대중 수용성 감소에 직면하고 있다. 또한 우리 국민의 대다수는 후쿠시마 사고 발생 이후 원자력에 대한 막연한 불안감을 가지고 있다. 이러한 후쿠시마 사고의 영향 외에도 수용할 만한 사용후핵연료 관리 계획이 부재하다는 것은 그러한 대중 수용성 저하에 기여하는 요인이다.

본 논문에서는 태양열 및 풍력을 포함한 재생가능 전력원과 함께 병합되어 작동할 수 있는 안전한 분산 전원으로서 혁신적인 납-비스무스 공융물(LBE) 냉각 피동형 소형모듈화원전(SMR)을 개발했다. 이러한 혁신적 소형모듈화원전의 특징은 원자로 내에 냉각재 순환 펌프를 탑재하지 않는다는 것과 모든 원자로 구성 요소를 단일 원자로용기 내에 포함시킴으로써 고유안전성을 향상시키는 일체형 풀형 설계를 달성한다는 것이다. 이러한 설계 혁신을 통해 납-비스무스 냉각 소형모듈화원전은 격리된 전력 그리드에서 재생가능 전력원의 급격한 변동에 대응할 수 있도록 부하추종 운전 능력을 확보해야 한다. 또한, 가압이 필요 없는 풀형 설계에 의한 피동 안전성을 통해 현재 원자력 발전소의 대부분에서 극도로 낮은 확률로 발생할 수 있는 일차 배관 파단 및 예상치 못한 펌프 실패로 인한 냉각재상실사고와 유량상실사고를 배제할 수 있다.

더욱이, 납-비스무스 냉각재는 미래 원자로의 냉각재로 간주되는 다른 액체 금속인 소듐과 비교해 물이나 공기와 화학적 반응성이 낮고 물과 비교했을 때에는 매우 높은 열전달 특성을 갖고 있기 때문에 원자로의 고유안전성 향상에 기여한다. 납-비스무스는 또한 고속 중성자 스펙트럼을 형성해 핵원료성물질을 핵분열물질로 전환하고 핵연료의 장기 연소를 촉진하여 해당 기간 동안 임계도를 달성

할 수 있도록 한다. 이러한 고속 중성자 스펙트럼은 나아가 효과적으로 초우라늄원소를 저방사성 핵종으로 변환시킬 수 있도록 하여 궁극적으로 핵연료 이용도를 더욱 증가시키고 고준위폐기물의 양을 최소화하는 데에 기여한다.

납-비스무스 냉각 피동형 계통의 과도 상황에서의 계통 통합 거동에 대한 적절한 이해를 위한 예측 도구가 필요하다. 이를 위해 본 연구는 다음과 같이 3단계로 나뉘어 수행되었다. 첫째, 유체역학적 축소 설계에 의해 풀형 일체형 실험 시설이 원형 소형모듈화원전의 설계로부터 고안되었고, 이 설비를 활용해 납-비스무스의 자연 순환 실험을 정상 상태와 외부 운용 조건 변화에 따른 과도 상태에서 수행했다. 둘째, 1차원 열수력 계통 해석 코드를 룹형 설비와 풀형 설비에서 생성된 실험 결과를 통해 검증했다. 셋째, 피동형 계통의 과도 상태 거동 평가를 위한 일차원 시간종속 분석 모델이 개발되었다. 이 분석 모델은 본 연구에서 진행된 납-비스무스 자연순환 실험 결과를 활용해 검증된 1차원 계통 열수력 해석 코드를 통해 검증되었다. 지금까지 납-비스무스 냉각 소형모듈화원전이 실현되지 않았으므로 URANUS를 이러한 3 단계 접근 이전에 설계하여 해당 원자로를 목표로 삼아 축소 실험 설계 및 분석이 진행되었다.

본 논문에서 진행된 피동형 납-비스무스 냉각 소형모듈화원전에 대한 실험, 수치해석 및 분석 결과를 토대로 1차측 냉각재의 자연순환은 원자로 출력 변동 속도를 저해하지 않음을 확인했다. 또한, 개발된 분석 모델을 활용한 안정성 분석 결과, 외부 부하 요구 변화에 대해 URANUS가 노심 출력을 안정된 범위 내에서 조정할 수 있음을 확인했다. 따라서 안전하고 안정적인 범위에서 도달할 수 있는 최대 전력 변화율은 피동형 원자로 계통의 열수력적 및 중성자 동역학적 특성에 의해 결정되지 않고 핵연료의 재료적 건전성에 의해 결정된다고 할 수 있다. 개발된 분석 모델을 활용하여 전출력의 50%

출력 범위에서 운전 중인 URANUS를 최대출력까지 복귀하는 형식의 계단형 입력에 대한 계통 응답 분석을 평가한 결과 URANUS의 노심 출력이 초당 전출력의 3.5%만큼의 출력변동률로 조정될 수 있을 것으로 분석됐다.

이와 더불어 개발된 분석 모델을 통해 예비 연구로서 URANUS 2차측의 동역학적 거동에 대한 시뮬레이션을 수행했다. 이 모델에는 2차측 주급수의 유량 제어 모델이 부여하였으며, 해당 모델로는 외부 부하 요구에 대해 2차측 주급수 유량이 비례하도록 제어하는 비례 제어기를 사용했다. 단순하고 이상적인 유량 제어기를 분석 모델에 적용한 결과 천이상태에서 발생하는 원자로 1차측과 2차측 사이의 열전달 불균형이 그것을 활용하지 않았을 때에 대비하여 약 1/3으로 감소하고 2차측이 새로운 정상상태로 돌입하는 시간이 약 1/2 수준으로 줄어드는 것으로 평가됐다. 상기 결과를 종합할 때, 피동형 납-비스무스 냉각 소형모듈화원전의 2차측은 주어진 운전 상태 변화에 따라 1차측에 비해 느린 과도 상태를 겪을 것으로 예상되므로 빠른 전력망 요구에 대응하기 위해서는 노심 출력 제어뿐만 아니라 주급수 유량 제어가 필요하다는 결론을 도출하였다.

주요어: 납-비스무스 공융물, 자연순환, 소형모듈화원전, 척도 해석, 부하추종 운전

학 번: 2013-21019

공학박사 학위논문

Experiment and Simulation of Load-following Operations of a Lead-cooled Transportable Small Modular Reactor

수송식 납냉각 소형모듈원전의

부하 추종 운전 실험 및 모사 연구

2018년 2월

서울대학교 대학원

에너지시스템공학부

신 용 훈

Experiment and Simulation of Load-following Operations of a Lead-cooled Transportable Small Modular Reactor

지도 교수 황 일 순

이 논문을 공학박사 학위논문으로 제출함

2018 년 1 월

서울대학교 대학원

에너지시스템공학부

신 용 훈

신용훈의 박사 학위논문을 인준함

2018 년 1 월

위 원 장 심 형 진 (인)

부위원장 황 일 순 (인)

위 원 정 호 (인)

위 원 조 형 규 (인)

위 원 김 희 령 (인)

Abstract

Experiment and Simulation of Load-following Operations of a Lead-cooled Transportable Small Modular Reactor

Yong-Hoon Shin

Department of Energy Systems Engineering

The Graduate School

Seoul National University

The nuclear industry of the world faces limited public acceptance for large-scale nuclear power plants. The majority of Korean public tend to be emotional since the outcome of Fukushima accident. In addition to the effects of Fukushima accident, the lack of acceptable management plan for spent nuclear fuel further contributes to this public opposition. In this thesis, , an innovative lead-bismuth eutectic (LBE) cooled small modular reactor (SMR) has been developed as a safe distributed power source that can be operated in hybrid with the renewable electricity sources including solar and wind power. The innovative SMR system features an integral pool-type design achieving enhanced inherent safety by including all the primary reactor components into a single pool while excluding reactor coolant pump. This design innovation leads to an unusual capability for the load-following operation in response to

rapid fluctuations of renewable electricity in an isolated grid system. In addition, the passive safety nature with low-pressure pool-type design provides advantage of the exclusion of loss-of-coolant accident and loss-of-flow accident which is likely happen in most of the current nuclear power plants, even if the likelihood of these accidents are extremely low, from primary piping failure and unexpected pump failure.

Furthermore, the primary coolant, LBE, itself contribute the inherent safety enhancement because it is chemically inert with water and air in contrast with sodium, another liquid metal coolant considered to be the future nuclear system coolant, and a better heat-transfer medium compared to water. LBE also facilitates a long-term burning of nuclear fuel through a hard neutron spectrum that it supports. The hard spectrum leads to the breeding of fissile material from the fertile, and contributes to the criticality that cause sustained over life. In addition, the fast spectrum can help an effective transuranic elements incineration through nuclear conversion as well, which ultimately increases fuel utilization furthermore and minimizes the amount of highly radioactive elements.

For adequate understanding of the integral system behaviors of a LBE-cooled passive system under transients is necessary and furthermore, a predictive tool for passive system behavior is need to be developed. Hence, this study has been conducted in three stages as follows: first, a pool-type integral experimental facility has been devised by hydrodynamic scale reduction from its prototype SMR design and natural circulation experiments has been carried out in both steady state and transients given by external condition changes. Second, a one-dimensional system thermal-hydraulics code is validated two-fold through the experimental results generated from a loop configuration and the results given by the pool-type facility. Third, an analytical model for one-dimensional, time-dependent passive system transient evaluation has been developed. This analytical model has been verified with not only experimental

results made in the second step and but also with one-dimensional system thermal-hydraulics code. Since there is no realization of a LBE-cooled SMR until now, a target reactor URANUS is designed before starting the three-step approach.

The results given by the experimental, numerical, and analytical investigations on the passive LBE-cooled SMR show that passive cooling from natural circulation does not deteriorate the rate of power maneuvering would since the primary side transients are rapidly saturated. In addition, the stability analysis confirms that the reactor core power of URANUS can be regulated within a stable range with respect to the external load demand change. Hence, the maximum achievable power ramp rate under safe, stable condition is related to nuclear fuel integrity, not the passive nature of reactor system. With the analytical simulation model, it is evaluated with an analysis on the step response that the reactor can change its core power rating as fast as 3.5% power per second from 50% of nominal full power to its full power with only considering its thermal-hydraulic and reactor kinetic response.

In addition, as a preliminary study, the dynamics of the secondary side is simulated with the developed analytical reactor dynamics simulation model and the results showed that the heat balance mismatch between the primary and secondary sides during transients can be minimized with feedwater flow control means, a proportional controller with respect to the external load demand in this case. It is concluded that the reactor core power regulation along with feedwater flow rate control is favorable, since the primary side of a passive LBE-cooled SMR is expected to go through slower transients compared to the primary side under given operational condition changes.

Keywords
Lead-bismuth eutectic
Natural circulation
Small modular reactor
Scaling design
Load-following operation

Student Number
2013-21019

Contents

Chapter 1 Introduction 1

1.1 Background 1

1.2 Objective 6

Chapter 2 Literature Review 8

2.1 Lead and LBE-cooled Fast Reactor (LFR) 8

2.2 Passive small modular reactors (SMR) 14

2.3 Experimental studies on LBE natural circulation 18

2.4 Scaling analysis methods for liquid metal experiments 22

Chapter 3 Problem Definition and Research Strategy 26

3.1 Problem definition 26

3.2 Approach 28

3.2.1 SMR reference design definition 30

3.2.2 Experimental setup and tests 30

3.2.3 Numerical validation and modeling 31

3.2.4 Analytical model development and load-following capability assessment 32

Chapter 4 LBE-cooled Passive SMR Design: URANUS 33

4.1 Design goals and requirements 34
4.2 Reactor core design 39
4.2.1 Fuel assembly configurations 39
4.2.2 Fuel rod design 45
4.2.3 Safety control assembly configurations 49
4.2.4 Neutronic analysis 51
4.2.5 Kinetics and reactivity feedback coefficients 56
4.3 Heat transport systems design 62
4.3.1 Primary heat transport system 62
4.3.2 Secondary heat transport system 67
4.3.3 Steady-state thermal-hydraulic analysis 70
4.4 Structure, materials, and components 75
4.4.1 Reactor vessel structure and materials 75
4.4.2 Three-dimensional seismic isolation 77

Chapter 5 Experimental Setup and Test Results 79

5.1 LBE loop natural circulation experiments 80
5.1.1 Experimental setup of LBE loop facility: HELIOS 80
5.1.2 HELIOS experiment procedure and LBE loop natural circulation experimental conditions 89
5.1.3 Experimental results on steady-state LBE loop natural circulation 95
5.2 LBE pool natural circulation experiments 97
5.2.1 Design of LBE pool facility: PILLAR 97
5.2.2 Final design of PILLAR 124
5.2.3 PILLAR experiment procedure and conditions 162

5.2.4 Experiment results and discussion on LBE pool natural circulation 170

Chapter 6 Code Validation and Numerical Analysis 191

6.1 One-dimensional system thermal-hydraulics (STH) code: MARS-LBE 191

6.2 Code validation on thermal-hydraulics with steady-state experimental results 193

6.2.1 Code benchmark with HELIOS loop test results 193

6.2.2 Code benchmark with PILLAR pool test results 210

6.3 Code validation on reactor point kinetics 217

6.4 System thermal-hydraulics modeling on LBE pool transient natural circulation experiments 220

Chapter 7 Load-Following Capability Assessment of Passive LBE-cooled Pool-type SMR 227

7.1 Analytical reactor dynamics simulation model 227

7.1.1 Reactor core model 231

7.1.2 Hot leg and cold leg models 250

7.1.3 Steam generator model 252

7.1.4 Model implementation for numerical simulation 281

7.2 Reactor control model validation 286

7.3 Assessment of fast load-following capability 292

7.3.1 Proportional feedwater control 292
7.3.2 Stability analysis.....300
7.3.3 Planned load-following operation 304
7.3.4 Power recovery from low power to full power.....306
7.3.5 Comparison with a commercial SMR 311

Chapter 8 Conclusions and Future Work..... 314

8.1 Conclusions 314
8.2 Future work..... 316

Nomenclature..... 318

Bibliography 326

초 록 346

List of Tables

Table 4.1 Key design parameters of URANUS 38

Table 4.2 Design parameters of fuel assemblies..... 44

Table 4.3 Design information of fuel rod 48

Table 4.4 Key neutronics parameters of reactor core 55

Table 4.5 Kinetic parameters at beginning of cycle calculated by the deterministic code chain and McCARD 60

Table 4.6 Delayed neutron fractions and precursor decay constants at beginning of cycle calculated by the deterministic code chain and McCARD 61

Table 4.7 Specification of primary and secondary heat transport systems of URANUS 66

Table 4.8 Steady-state system thermal-hydraulic calculation results of URANUS 74

Table 5.1 Thermocouple locations on HELIOS main loop in terms of accumulated length along flow path 88

Table 5.2 Natural circulation test procedure to generate well-defined test results in HELIOS 92

Table 5.3 Test matrix on adiabatic, non-isothermal natural circulation experiments in HELIOS 94

Table 5.4 Adiabatic, non-isothermal, steady-state natural circulation results in HELIOS 96

Table 5.5 PILLAR design requirements and criteria for scaling analysis 101

Table 5.6 Comparison of thermosphysical properties of nuclear fuel, heater rods, and structural materials (Hong and Lee, 2012; Popov and Carbajo, 2000) 117

Table 5.7 PILLAR design specifications for flow area reduction ratio 1:200 122

Table 5.8 Measurement requirements of PILLAR instrumentation system 156

Table 5.9 PILLAR steady-state natural circulation test matrix and case definition 168

Table 5.10 Experimental results on steady-state LBE pool natural circulation in PILLAR 184

Table 6.1 Thermophysical properties of 316 L stainless steel (data retrieved from (Mills et al., 2004; Popov and Carbajo, 2000)) 197

Table 6.2 Correlations used for hydraulic loss coefficient evaluation 198

Table 6.3 MARS-LBE benchmark results for well-defined steady-state experiment results in HELIOS 203

Table 6.4 Node conditions for the original, halved, and trisected models used for sensitivity study 208

Table 7.1 Elements of matrix **A** for linearized state-space formulation 247

Table 7.2 Elements of matrix **B** for linearized state-space formulation 249

Table 7.3 Elements of matrix $Z(\mathbf{x},\mathbf{u})$ 272

Table 7.4 Elements of matrix $F_{\mathbf{x}}(\mathbf{x},\mathbf{u})$ 276

Table 7.5 Elements of matrix $F_{\mathbf{u}}(\mathbf{x},\mathbf{u})$ 280

Table 7.6 Comparison between the developed passive LBE-cooled SMR dynamics model and MARS-LBE 289

List of Figures

Figure 1.1 Material and control limitations in water-cooled reactors for fast and frequent load-following operation 5

Figure 3.1 Thesis research approach 29

Figure 4.1 Radial assembly configuration of active core 42

Figure 4.2 Horizontal view of a single fuel assembly including fuel rods and a central skeletal bar 43

Figure 4.3 Pin-cell model for fuel rod 47

Figure 4.4 Code system used for the neutronic analysis of URANUS core design 53

Figure 4.5 Effective multiplication factor of URANUS core during 20 years of full-power operation 54

Figure 4.6 Schematic diagram of URANUS primary boundary 65

Figure 4.7 Ideal temperature-entropy (T-s) diagram of URANUS..... 69

Figure 4.8 Nodalization of overall heat transport system for steady-state calculation 72

Figure 4.9 Steady-state temperature distributions of fuel centerline, cladding, and coolant bulk at the hottest assembly 73

Figure 4.10 3D seismic base isolation bearing unit, adopted from (Yoo et al., 1999)..... 78

Figure 5.1 (a) System schematic diagram and (b) front-view picture of

HELIOS thermal-hydraulic test loop 83

Figure 5.2 Three-dimensional configuration of HELIOS constituent components and key instrumentation system..... 84

Figure 5.3 (a) Isomeric view (left) and cross-sectional view (right), (b) disassembly view, and (c) photo (white dash) of PILLAR main vessel..... 126

Figure 5.4 Three-dimensional model of PILLAR lower plenum and heater rods assembly in several viewpoints. (a) Isomeric view, (b) cross-sectional view in z-direction, (c) top view, and (d) bottom view..... 130

Figure 5.5 Schematic diagram of PILLAR heater rod..... 131

Figure 5.6 Heater rod and skeletal bar arrangement inside the core region of PILLAR 132

Figure 5.7 Design and axial positions of PILLAR core grid spacers and thermocouple location upon each plate..... 133

Figure 5.8 Three-dimensional model of PILLAR lower vessel and lower barrel assembly in several viewpoints. (a) Isomeric view, (b) cross-sectional view in z-direction, (c) top view, and (d) cross-sectional view in radial direction 136

Figure 5.9 Three-dimensional model of PILLAR dummy rod assembly in several viewpoints. (a) Isomeric view, (b) detail view on the interface with heater rods, and (c) top view..... 137

Figure 5.10 Three-dimensional model of PILLAR middle barrel in several viewpoints. (a) Isomeric view, (b) cross-sectional view

in axial direction, (c) top view, and (d) bolt cover application to middle barrel (left) and middle barrel without the bolt cover (right)..... 139

Figure 5.11 Three-dimensional model of PILLAR upper barrel in several viewpoints. (a) Isomeric view, (b) cross-sectional view in axial direction, (c) top view, and (d) bottom view..... 141

Figure 5.12 Axial position of windows on PILLAR upper barrel and expansion volume for LBE level control with respect to heat exchanger shell side 142

Figure 5.13 Radial position and arrangement of windows on PILLAR upper barrel with respect to heat exchanger and upper vessel 143

Figure 5.14 Three-dimensional model of PILLAR upper vessel in several viewpoints. (a) Isomeric view, (b) cross-sectional view in axial direction, and (c) top (bottom) view 145

Figure 5.15 Three-dimensional model of PILLAR heat exchanger tube side in several viewpoints. (a) Isomeric view, (b) cross-sectional view in axial direction, (c) top view, (d) bottom view, (e) cross-sectional view of lower chamber, and (f) cross-sectional view of upper chambers 148

Figure 5.16 Schematic diagram of lower water chamber and tube arrangements of PILLAR heat exchanger tube side 149

Figure 5.17 Three-dimensional model of PILLAR middle vessel in several viewpoints. (a) Isomeric view, (b) cross-sectional view

in axial direction, and (c) top (bottom) view..... 151

Figure 5.18 Schematic diagram of PILLAR instrumentation system 157

Figure 5.19 Geometrical consideration of thermocouple installation positions on grid spacers 158

Figure 5.20 Axial and radial position of instrumentation probes on the shell side of PILLAR heat exchanger 159

Figure 5.21 Position of instrumentation probes on arbitrary planes A, B, and C in PILLAR heat exchanger on planar cut view 160

Figure 5.22 Position of instrumentation probes on arbitrary planes A, B, and C in PILLAR heat exchanger on axial cut view..... 161

Figure 5.23 Graphical test matrix and case definition on PILLAR transient natural circulation experiments 169

Figure 5.24 PILLAR system integral heat loss evaluation procedure 176

Figure 5.25 Locations of thermocouples for the evaluation of PILLAR system integral heat loss..... 177

Figure 5.26 PILLAR main vessel integral heat loss evaluation test results 178

Figure 5.27 Fitted curve for PILLAR system integral heat loss as a function of temperature difference between surface and ambient temperatures 179

Figure 5.28 PILLAR primary system response to the variation in the amount of heat tracing on the main vessel surface 180

Figure 5.29 PILLAR secondary cooling system (heat exchanger tube side)

response to the variation in the amount of heat tracing on the main vessel surface 181

Figure 5.30 PILLAR transient natural circulation experimental results: instantaneous core power increase (Case No.: T-PINC-210~240/3.5) 187

Figure 5.31 PILLAR transient natural circulation experimental results: instantaneous core power decrease (Case No.: T-PDEC-240~210/3.5) 188

Figure 5.32 PILLAR transient natural circulation experimental results: instantaneous secondary side flow increase (Case No.: T-FINC-240/3.5~4.0) 189

Figure 5.33 PILLAR transient natural circulation experimental results: instantaneous secondary side flow decrease (Case No.: T-FDEC-240/4.0~3.5) 190

Figure 6.1 Nodalization map of HELIOS prepared for MARS-LBE. 196

Figure 6.2 Comparison between measured and calculated mass flow rates as a function of mock-up core power 204

Figure 6.3 Comparison between LBE mass flow rates in HELIOS experiment and MARS-LBE benchmark results..... 205

Figure 6.4 Steady state experiment and benchmark results of HELIOS in cases (a) NC1.0 (9.8 kW power), (b) NC2.0 (15.0 kW power), (c) NC1.0 (27.0 kW power), and (d) NC1.0 (33.6 kW power) 206

Figure 6.5 Comparison of temperature differences between average hot

leg and cold leg temperatures in HELIOS experiment and MARS-LBE benchmark results 207

Figure 6.6 Case study results on the heat exchanger axial node size in (a) the original model with 7 axial nodes, (b) halved model with 14 axial nodes, and (c) trisected model with 21 axial nodes..... 209

Figure 6.7 Nodalization map of PILLAR prepared for MARS-LBE . 212

Figure 6.8 PILLAR heater rod cross-sectional view and equivalent radii for each of constituent material regions 213

Figure 6.9 Comparison between LBE mass flow rates in PILLAR steady-state experiment and MARS-LBE benchmark results 215

Figure 6.10 Comparison of temperature differences between average hot leg and cold leg temperatures in PILLAR steady-state experiment and MARS-LBE benchmark results..... 216

Figure 6.11 Comparison with MARS-LBE modeling results and PILLAR transient natural circulation experimental results: instantaneous core power increase (Case No.: T-PINC-210~240/3.5) 223

Figure 6.12 Comparison with MARS-LBE modeling results and PILLAR transient natural circulation experimental results: instantaneous core power decrease (Case No.: T-PDEC-240~210/3.5) 224

Figure 6.13 Comparison with MARS-LBE modeling results and PILLAR transient natural circulation experimental results: instantaneous secondary side flow rate increase (Case No.: T-

FINC-240/3.5~4.0)..... 225

Figure 6.14 Comparison with MARS-LBE modeling results and PILLAR transient natural circulation experimental results: instantaneous secondary side flow rate decrease (Case No.: T-FDEC-240/4.0~3.5)..... 226

Figure 7.1 Power and steam production regulations in passive SMR by means of control rod movement and feedwater flow control 229

Figure 7.2 Assumptions and approaches for the analytical reactor dynamics simulation model developed in thesis study 230

Figure 7.3 Schematic diagram for core state-space model including both neutronics model and core thermal-hydraulics model 232

Figure 7.4 Schematic diagram for the reactor core model of generic pin-cell model of nuclear fuel..... 240

Figure 7.5 Schematic diagram for steam generator state-space model 255

Figure 7.6 Block chain diagram for reactor state-space model implemented to MATLAB/Simulink environment 285

Figure 7.7 Calculation results comparison on the system transient evaluation model for passive LBE-cooled SMR and MARS-LBE for the power ramp rate of -5%P/min from 100% power output 290

Figure 7.8 Calculation results comparison on the system transient evaluation model for passive LBE-cooled SMR and MARS-LBE for the power ramp rate of +5%P/min from 100% power

output 291

Figure 7.9 Calculation results for the system transients given by a power ramp rate of -10%P/min from 100% power output without feedwater flow rate control 296

Figure 7.10 Calculation results for the system transients given by a power ramp rate of -10%P/min from 100% power output with feedwater flow rate control 297

Figure 7.11 Calculation results for the system transients given by a power ramp rate of -10%P/min from 100% power output with feedwater flow rate control 298

Figure 7.12 Calculation results for the system transients given by a power ramp rate of +10%P/min from 90% power output with feedwater flow rate control 299

Figure 7.13 Root locus for load demand input to core power output . 302

Figure 7.14 Bode diagram for load demand input to core power output 303

Figure 7.15 Comparison of planned load-following operation simulation results between the analytical model developed in this dissertation (line) and MARS-LBE (circle and line) 305

Figure 7.16 Conceptual case on instantaneous power return from low-power condition to nominal full power condition by grid request 309

Figure 7.17 Step response analysis results on reactor core power response and turbine load response with respect to power

recovery request from 50% to 100%..... 310

Figure 7.18 Comparison with a commercial passive load-following concept *NuFollow*™ (excerpted from (Ingersoll et al., 2015)). (a) Required load demand and (b) reactor output and steam bypass by NuScale and URANUS..... 313

Chapter 1 Introduction

1.1 Background

The nuclear industry of the world faces limited public acceptance for large-scale nuclear power plants. The majority of Korean public tend to be emotionally repulsive to nuclear reactors since the outcome of Fukushima accident. In addition to the effects of Fukushima accident, the lack of acceptable management plan for spent nuclear fuel further contributes to this public opposition.

Since Fukushima accident, the paradigm of energy has been changing to expand: the renewable energy sources such as photovoltaic, solar thermal, wind, and so on have been grown and to curtail carbon dioxide. In addition, the resistance to expand power transmission lines results in the deployment of locally distributed power sources will become dominant. This is so-called microgrid which incorporates various types of electricity sources in a small region by increasing electricity utilization with the distributed energy resources (Islam and Gabbar, 2015). Hence, the future energy mix will be likely to be re-established with a high share of renewables.

This energy transition motivates the nuclear industry to develop load-following capacity that supports the microgrid with a significant fraction of renewables. Small modular reactors (SMRs), which are generally defined as

nuclear reactors with power ratings lower than or equal to 300 MWe, receive an increasing attention for continuous and a sustainable nuclear energy utilization. Interests on SMRs are growing and as supporting this, more than 50 SMR designs are under development worldwide (OECD Nuclear Energy Agency, 2016b). Among them, three SMRs including CAREM in Argentina (Marcel et al., 2013), HTR-PM in China (Zhang et al., 2006), and KLT-40s in Russian Federation (Mitenkov and Polunichev, 1997) are under construction and are expected to start their first operations by 2020. In addition, a study on the economics of SMRs states that SMRs that will be built in 2020-2035 could generate up to 21 GWe of the world's electricity based on an optimistic prospect (OECD Nuclear Energy Agency, 2016b).

Not only are the reduced electrical capacity of a single plant, but the enhanced safety and maneuverability of a reactor are required for SMRs to be employed in a microgrid. Fukushima accident suggested that the current active safety systems in nuclear power plants might not be reliably performed during beyond design basis accidents. An outstanding safety can be realized by replacing coolant with lead or lead-bismuth eutectic (LBE) and excluding active components by relying on natural circulation.

Among these promising utilization means, the most competent option is the use as a hybrid power source which incorporates renewable energy sources and SMRs as an integrated power station. Since the electricity generation rate by renewables varies with time in a daily basis and a seasonal basis as well, the installation of energy storage system (ESS) is inevitable. Considering that the market share of renewables will be growing further

worldwide, this innate fluctuation needs to be flattened. In this case, SMR can work like a battery or ESS by changing its electricity generation.

Since the renewables are strongly dependent upon the daily weather of the site, energy storage systems (ESS) should be implemented in a microgrid to compensate for the fluctuation in electricity supply from the sources. Battery-based ESS has been found to be costly and vulnerable to life-shortening under hybrid operation with renewables (Svoboda et al., 2007; Thackeray et al., 2012). SMRs can work as a backup electricity source or the ESS by maneuvering its power output. In this respect, the fast and frequent power maneuvering capability of a nuclear reactor is questioned because most of them are operated under constant and full power conditions or limited power change in a relatively long time span.

Until now, the load-following operation of commercial large-scale nuclear power plants has been developed and sophisticated as seen in French experiences and other practices (Choi et al., 1992; Lokhov, 2011; Ludwig et al., 2011). However, conventional water-cooled reactors are not suitable for the fast and frequent power maneuvering required in the microgrid, which relies a large capacity on the renewables, due to their innate limitations. These can be classified into two categories, material limitations and system control limitation, as summarized in Figure 1.1.

The former includes well-known phenomena in pressurized water reactors such as the pellet-clad interaction (PCI) (Cox, 1990) and stress corrosion cracking (SCC) (IAEA, 2011). A rapid power maneuvering changes the local power and temperature distribution. It leads to pellet fracturing by

which corrosive fission gas such as iodine is no longer able to remain in the pellet structure and contributes to SCC taking place. Furthermore, the pellet goes through a severe deformation called bambooing and the edge of the pellet physically contacts the inner surface of cladding so that PCI can cause cladding failure during fast power ramps. In addition to this, the cladding fatigue failure given by coolant temperature cycle is expected to be present in the cladding.

The latter, the system control limitation, comes from xenon oscillation in principle. Since the reactor power is related to neutron flux, the power maneuvering gives rise to a variation in axial power distribution from the normal operation conditions. Due to the neutron poisoning effect given by xenon, it is required to control its distribution and material balance precisely for a safe and stable operation.

Contrary to the inherent limitations of water-cooled reactors on fast load-following operation and advancement in safety, a passive LBE-cooled SMR can overcome both material failure risks and reactivity non-compliance. In this regard, this thesis mainly focuses on the assessment of fast load-following capability of the system, in terms of passive cooling and stability, with experimental and numerical approaches.

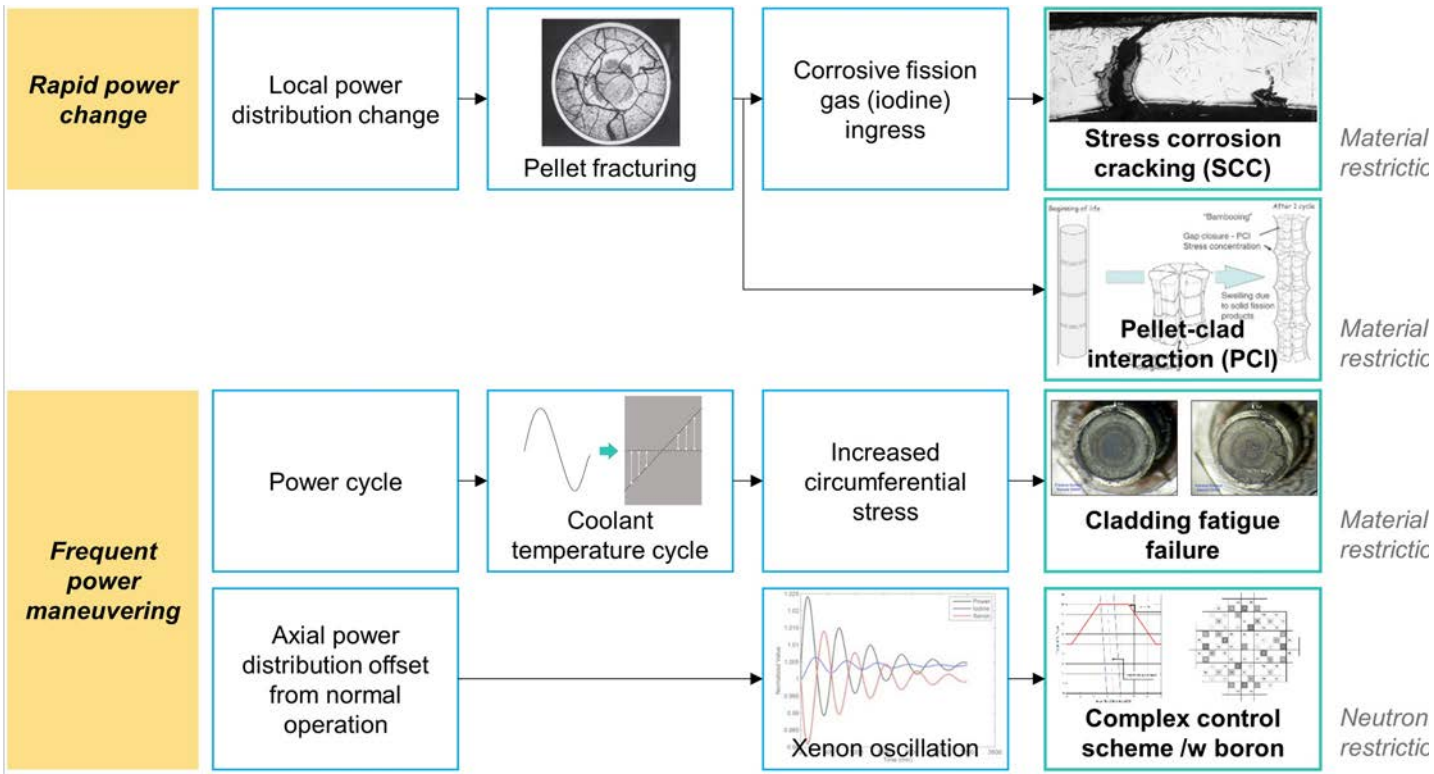

Figure 1.1 Material and control limitations in water-cooled reactors for fast and frequent load-following operation

1.2 Objective

The objective of this thesis study is to evaluate the load-following capability of a passive LBE-cooled pool-type SMR subjected to both safety and stability requirements. To achieve the objective, the thesis study is divided into three separate tasks including experiments, numerical modeling, and analytical studies.

The experimental studies on natural circulation of LBE, both in steady state and transient conditions, are conducted using thermal-hydraulic scaled test loop and pool mockups for a realistic and thorough understanding on the phenomenon. Both steady state and transient test results are utilized for the validation of a numerical system model while the transient results on the system reactions to operational condition maneuvering expected for the load-following operation in an actual passive reactor system are used for the validation of analytical studies.

For the numerical study, a one-dimensional system thermal-hydraulics code named as MARS-LBE that is derived from MARS for a water-cooled reactor is validated for its modeling capability on a passive LBE-cooled reactor. Since water and LBE have significantly different thermophysical properties each other, its thermal-hydraulic simulation results are validated with the steady-state test results produced during the experimental study. Since there is no data from reactor kinetics experiments with lead-cooled systems, the validation in this part is made on the sodium-cooled reactor EBR-II, which are covered extensively by a separate collaboration work.

Finally, the analytical studies resulted in the development of an indigenous analytical formulation which is dedicated to the passive LBE-cooled SMR system, the formulate is used to simulate the system reaction to a variation in external load demand and the stability under that transient. The validity of the simulation results is ensured by the system thermal-hydraulics code that is validated by the numerical model.

Chapter 2 Literature Review

2.1 Lead and LBE-cooled Fast Reactor (LFR)

Lead or lead-alloy cooled fast reactor (LFR) systems are among the six systems selected for joint development by the Generation IV International Forum (GIF) based on their potential to meet the GIF technology goals and have been evaluated as the most promising technology (OECD Nuclear Energy Agency, 2014). The choice of lead and LBE as innovative coolant is motivated by their favorable safety features compared to conventional coolant including water and sodium: chemical inertness that excludes the possibility of heat and pressure load with hydrogen explosion while being compatible with air, carbon dioxide, and water.

The main difference between the heavy liquid metals and other media comes from their significantly higher thermal conductivities (16.6 W/m K for lead at 673 K and 11.8 W/m K for LBE at 573 K) and lower specific heat capacities (~140 J/kg K for lead and ~150 J/kg K for LBE). The former leads to compatible steam generator placement using high heat transfer capability. In addition, their high boiling points (2,021 K for lead, 1,943 K for LBE) enable a system to be free of pressurization and contributes to avoiding the risk of coolant boiling. The kinematic viscosities (0.21E-6 m^2/s for lead at 673 K, 0.18E-6 m^2/s for LBE at 573 K) are considerably smaller than that of air or

water. The higher ratio of inertia force to viscous force leads to good stabilities of coolant flow regime. Small neutron absorption cross-section (0.0060 barn for lead and 0.0015 barn for LBE at 1 MeV), and high atomic mass (207 g/mol for lead and 208 g/mol for LBE), and high retention capability for radionuclides provide additional safety features (OECD Nuclear Energy Agency, 2007).

On the other hand, lead and LBE have some drawbacks in comparison with the conventional coolants as well. One of the issues of lead and LBE is that it is ten times heavier than sodium and water. This presents a challenge to designers of the seismic isolation systems that will be used with these heavy liquid metal reactors. Another drawback connected with LBE, which is not a critical issue to lead, is the accumulated radioactivity, mainly due to the alpha-emitter polonium-210 (^{210}Po), having the half-life of 138 days. ^{210}Po is formed in the process of neutron irradiation on bismuth. Several methods to remove ^{210}Po from lead-polonium compound (PbPo) are introduced such as distillation, hydride stripping, alkaline extraction, rare-earth filtration, and electrodeposition. Lead is considered as a more attractive coolant option than LBE mainly due to its higher availability, lower price and lower amount of induced polonium activity by a factor of 10^4.

LFR systems can have insufficient system lifetime due to the corrosion of structural materials in the primary system. In this regard, FeCrAl and FeCrSi alloys were developed to increase corrosion resistance over lead and LBE in high temperature and strong radiation environments. Austenitic stainless steels experience severe metallic element dissolution while ferritic-martensitic steels suffer from excess oxidation. The studies to improve their

mechanical characteristics were performed by using a FeCrAl or FeCrSi alloy as coating or overlay welding. Thus, FeCrAl or FeCrSi based oxide dispersion strengthened (ODS) steels may solve corrosion and mechanical problems (Hosemann et al., 2008; Kimura et al., 2011; Takaya et al., 2012). In addition, an approach using overlay welding and pilgering techniques to produce corrosion-resistant functionally-graded composite tubes is also under development (Kim et al., 2017; Lee et al., 2016; Short and Ballinger, 2012).

With the efforts to overcome some shortcomings of lead and LBE mentioned above, several LFR concepts have been designed. Among those concepts, GIF has identified three reactor designs as reference systems of LFR in terms of power ratings and the scale of reactor (OECD Nuclear Energy Agency, 2016a). The first one is ELFR which was designed by the European Union to have 600 MWe power rating (Alemberti, 2012). Before the industrial development, a scaled demonstrator called ALFRED was also suggested to demonstrate to achieve safety standards requirements and assess economic competitiveness of the prototypic reactor (Frogheri et al., 2015). A prototype actinide burner, named BREST-OD-300, with the intermediate power rating of 300 MWe was designed by Russian Federation and was designated to be the one of the reference design (Dragunov et al., 2016). SSTAR by the United States is one of the reference designs as well, which has a variable power ranging 10-100 MWe and features a long-life cycle core and the passive cooling of the primary system (Smith et al., 2008). The reactor is distinguished from the use of supercritical carbon dioxide (S-CO_2) Brayton cycle while other two concepts rely on Rankine cycle with superheated steam.

Beyond the GIF reference concepts, several LFR designs have been developed worldwide. A nuclear reactor vendor, Westinghouse, is now developing their own LFR concept while looking at some opportunities in the market and the details are undisclosed at this moment (Westinghouse Global Technology Office, 2017).

Another company, Hydromine, is also developing a compact lead-cooled SMR in cooperation with ENEA, the Italian research center for nuclear and alternative energy (Wallenius et al., 2017). The name of reactor is LFR-AS-200 with 200 MWe power ratings as its name states, while the primary system is arranged in a large single pool.

SEALER is a concept suggested by a Swedish company LeadCold, which targets the deployment in communities and mining sites in the Canadian Arctic (Wallenius et al., 2017). It adopts lead as primary coolant and loads 19.9% enriched uranium oxide fuel. Another feature of this reactor is that it can change its electricity production rate in a range of 3-10 MW while the lifetime of core varies between 10-30 full power years with 90% capacity factor.

G4M also known as Hyperion had been designed in the United States (Zhang et al., 2013). Its single module can produce thermal power of 70 MW, which can be converted to 25 MW per unit. Three applications of the SMR was identified as mining areas, remote communities, and government facilities.

Other than those reactors, a lead-cooled SMR called SVBR-75/100 was designed by Russian Federation (Zrodnikov et al., 2006). With its relatively small power rating within a single module, the reactor can be deployed with several purposes such as renovating old NPP units, supplying heat and

electricity close to urban areas, desalinating seawater in developing countries. SVBR-75/100 features its versatile fuel loading strategy implemented with different types of nuclear fuel based on uranium oxide or mixed oxide (MOX) fuels and nitride or mixed nitride fuels.

Another application of lead and LBE can be found in research activities for accelerator-driven subcritical systems (ADS) that is operated under subcritical conditions by compensating this off-criticality with a high-energy proton accelerator (Satyamurthy and Biswas, 2002). On account of its favorable features, pure lead and/or LBE can be used not only as spallation target for additional neutron generation but also as coolant at the same time. An example of this is EFIT reactor which is a pool-type 100-MWth ADS which uses pure lead as coolant (Cinotti, 2004). Within its design development, some thermal-hydraulic analyses on the system were carried out such as analysis on accidental transients (Bandini et al., 2008a; Bandini et al., 2008b) and pressure drop evaluation for helical tubes in heat exchanger (Castiglia et al., 2012).

Furthermore, SCK-CEN in Belgium has developed MYRRHA which is based on the pool-type ADS concept and utilizes LBE as primary coolant (H. Ait Abderrahim et al., 2011). The design of MYRRHA has progressed and entered into the front end engineering phase (De Bruyn et al., 2014).

China has a plan to develop ADS in three stages by enlarging the magnitudes and incorporating several components in the reactor systems (Wu et al., 2016). In each stage, the magnitudes and proton beam currents of accelerators will be increased so that they support the subcritical cores. As a research facility equipped with a proton accelerator and spallation target,

CLEAR-I is planned to be constructed. After that, a demonstration facility with 100 MWth power ratings, CLEAR-II, will be built. The final stage of Chinese ADS development will be CLEAR-III, a commercial-scale prototype facility having 1,000 MW of thermal power ratings.

2.2 Passive small modular reactors (SMR)

Since the attention to SMR development and its commercialization is increasing, several concepts have been designed with an innovative safety feature by excluding the primary reactor coolant pump in the primary system. An advantage from the exclusion is design simplification that contributes to enabling turnkey-type contracts from vendors by manufacturing whole reactor components in a factory. The other important strength is its enhanced innate safety, which comes from the fact that its passive cooling nature works any conditions as far as temperature difference in coolant along with the height direction is present.

In this respect, a number of SMR concepts that utilizes passive cooling are under development and even under deployment as well. Among them, many of concepts have been designed with a conventional coolant, water. In Argentina, CAREM has been suggested as a passive integral design based on pressurized light water reactor (PWR), which uses light water as coolant and moderator (Marcel et al., 2013). All the primary components are located within the reactor pressure vessel. A notable feature of its reactor system is self-pressurization without adopting a pressurizer, which is achieved by a cold structure in the upper steam dome by means of balance between vapor production and condensation.

NuScale is another PWR-based passive SMR originated from a research done by Oregon State University and the Idaho National Laboratory in the United States (Reyes, 2011; Reyes and Lorenzini, 2010). Thanks to its

integral design, its reactor core is cooled and moderated by the natural circulation of pressurized water, similar to CAREM. NuScale features so-called multi-module concept in a single plant site, which can incorporate up to 12 reactor modules. To enhance the survivability in accident conditions, all the modules are submerged in water inside the reactor building pool so that long-term cooling is viable without any human intervention.

A Russian design, UNITHERM, is also a PWR-based passive SMR which focuses on being used in areas where human access is limited (Alekseev et al., 2014). In this regard, the reactor targets long-term fuel cycle up to 20 years. As water moderates neutrons, it requires a relatively high-enrichment nuclear fuel, about 19.75%, compared to other PWRs while it utilizes CERMET UO_2-ZrO_2 fuel to fulfill its criticality over the target fuel cycle.

Other than PWR-based SMRs, several types of SMRs that exploit light water and heavy water as primary coolant have been presented through common technologies including boiling water reactor (BWR) and pressurized heavy water reactor (PHWR). DMS is a SMR designed by GE-Hitachi and Japan Atomic Power Company and its acronym comes from ‘double MS’, which means modular simplified and medium small (Ikegawa et al., 2010). It utilizes a proven technology based on BWR and features the use of miniaturized, simplified, and standardized equipment while it is constructed in a modular way. A design innovation in this reactor is made through reducing the height of the primary containment vessel about one half (2 m) compared to conventional BWRs (3.7 m). Since its primary flow is given by natural circulation and resultant low flow mass rate, steam and water is separated by only gravity. In

this regard, DMS suggests free surface separation without using steam separators and it contributes to further simplification in reactor component design.

Bahbha Atomic Research Centre, BARC, in India suggested a PHWR-derivative SMR design called AHWR, which stands for the Indian Advanced Heavy Water Reactor (Sinha and Kakodkar, 2006). Since India has an abundant amount of thorium, there have been several domestic studies on the use of thorium-uranium-233 (U-233) fuel cycle. In this purpose, AHWR also aims at the utilization of thorium-based fuel in a large scale. The distinct features of AHWR are reactor system cooling being achieved by light water while neutron moderation is done by heavy water, its geometrical arrangement in terms of using vertical pressure tubes, and the quick replacement of pressure tubes with shop-fabricated coolant channels minimizing effect on other components.

Other than those SMRs using the conventional technologies with light and/or light water, several designs adopting liquid metal coolants have been proposed. It is mainly due to the superiority of heat transfer in liquid metal compared to water, which contributes to enhanced inherent safety with higher temperature distribution in the reactor core and heat flux margin that is expected in low flow rate conditions given by natural circulation. SSTAR, mentioned in Section 2.1 and is one of the reference designs of GIF, is the first SMR concept that relies on natural circulation with lead in the primary side cooling (Smith et al., 2008). Similar to other designs to enhance natural circulation flow rate and reduce hydraulic loss in the core, a large coolant volume fraction is employed.

A Korean design called PASCAR is a LBE-cooled passive SMR with

35 MW of electricity ratings with a single reactor module (Choi et al., 2011a). PASCAR loads metal fuel that is made of uranium and other actinides from spent fuel separated by pyroprocessing. To ensure passive cooling with LBE, the reactor adopts a large flow path and open square lattice between fuel rods allowing cross flow. Its relatively low core power density that finally leads to long-term operation within the given core discharge burnup and low temperature guaranteeing suppressed material degradation.

The Chinese research reactor design based on ADS also introduced in Section 2.1, CLEAR-I can be classified as a passive lead-cooled SMR (Wu et al., 2016). Owing to its low power density along with large expansion coefficient of LBE, passive cooling can be achieved while its safety characteristics are enhanced. In addition, mechanical and chemical damage on structural materials such as corrosion and erosion can be reduced effectively in favor of this low velocity profile.

As a remark, the development of passive SMR is expected to grow further because of its simpler design and better accident tolerance. The up-to-date status of the development can be found further on the IAEA Advanced Reactors Information System (ARIS) website.[1]

[1] The purpose of this remark is some published materials by the IAEA does not recommend to cite their supplement "Advances in Small Modular Reactor Technology Developments (2016)" due to the absence of an official review. The IAEA ARIS website is able to be accessed through: https://aris.iaea.org.

2.3 Experimental studies on LBE natural circulation

Natural circulation enhances the safety of a reactor system through passive cooling and as well as contributes to a simple design by excluding reactor coolant pump from the system. In particular, lead and LBE have an exceptional capability of natural circulation compared to sodium since pressure loss in the core would be reduced by increasing the pitch-to-diameter ratio in fuel bundle (Tuček et al., 2006).

In this regard, the characterization of LBE natural circulation have been made at a large number of laboratories by using loop facilities. An experimental study on LBE natural circulation was performed at TIT in Japan with a water boiling in direct contact with LBE (Takahashi et al., 2005).

Several experiments were carried out in ENEA-Brasimone Research Centre in Italy with NACIE facility for non-isothermal natural circulation given by various heater power ratings and gas-induced circulation by injecting argon bubbles into the loop (Coccoluto et al., 2011; Tarantino et al., 2011). The experiment results were used for the code benchmark of RELAP5/MOD3.3 by implementing the thermophysical properties of LBE.

A large-scale facility TALL at KTH in Sweden was utilized for the characterization of LBE in lead-cooled fast reactors and accelerator-driven systems (Ma et al., 2006; Ma et al., 2007). In KTH studies, various natural circulation phenomena were tested, such as natural circulation capability and stability, start-up from different initial conditions, and accident simulations. Similarly, the experiment results were compared with numerical analyses by

TRAC/AAA and RELAP5 codes.

Experimental studies on the steady-state and transient natural circulation of LBE were also conducted with the HANS facility at BARC in India for a range of core power from 900 W to 5,000 W (Borgohain et al., 2016a). An indigenous code called LeBENC was validated with the test results and the maximum temperature deviation was found to lie within 15% in transient simulations. A new LBE test loop, KTL, was built to investigate natural circulation for a wide temperature range from 200 to 780 °C. The upper limit is significantly higher than the maximum design temperature of most LBE test loops, that is, 550 °C (Borgohain et al., 2016b).

As mentioned above, the thermal-hydraulic behavior of LBE in the one-dimensional loop environments have been studied extensively including those listed. However, when it comes to a pool environment, only limitied studies have been made. The pool behaviors in those systems cannot be approximated one-dimensionally as the main flow is affected by flows in transverse directions to the main flow. Many reactors have hemispherical plenum structures in which the coolant from the downcomer is mixed and redistributed before entering the core. For SMRs that rely on natural circulation as the principal cooling mechanism, the coolant velocity variation in the core is expected to be much greater than those of pump-driven systems. It is because the coolant absorbs different amounts of local power as it flows through subchannels, which in turn generate different buoyancy for flow. Furthermore, if a certain region in the core is restricted for flow or a failure of the steam generator tube causes a void in the core, the perturbations from these three-

dimensional behaviors may propagate to deteriorate the reactor safety.

Understanding of the three-dimensional behaviors in reactor systems is still far beyond the scope of the loop studies. As the first step, many researchers around the world are conducting research into the three-dimensional flow behaviors of LBE under the poo-type reactor configuration.

As aforementioned, in the case of the TALL loop at KTH, the three-dimensional flow simulation region was inserted and converted the original TALL into TALL-3D. An electrical heater was installed outside the three-dimensional flow simulation region of TALL-3D to accelerate the occurrence of thermal stratification in low flow rate conditions to evaluate the effect of the phenomenon on the entire system. In addition, a number of thermocouples are installed in the corresponding area to measure the temperature change over time to measure the data for the verification of three-dimensional CFD codes and the improvement of one-dimensional system analysis code accuracy (Grishchenko et al., 2015; Papukchiev et al., 2015).

At SCK-CEN, the Belgian Nuclear Research Center, a new research reactor is being developed based on fast neutron spectrum to replace their water-cooled research reactor BR-2. For this purpose, MYRRHA is being designed and studied as an LBE-cooled multi-purpose research reactor (H. Ait Abderrahim et al., 2011). To find the effect of the three-dimensional flow inside the MYRRHA reactor pool, E-SCAPE facility, which is a down-scale facility with 1/6 length scale from prototype MYRRHA, is designed. The objectives of the facility is to carry out experiments and tests on the reactor coolant pump since the prototypic reactor uses pumps to circulate the coolant, experiments on

residual heat removal systems after the reactor shutdown, simulation of various accident situations, and data production for the verification of code and one-dimensional system analysis code (Van Tichelen et al., 2015; Van Tichelen et al., 2011).

2.4 Scaling analysis methods for liquid metal experiments

In an engineering point of view, it is unnecessary to make an identical experimental facility with respect to a prototype and thus, a reduction of scale is inevitable. In this regard, several parameters should be selected and designated properly so that the prototype and experimental facility behave equivalently. This procedure is called the scaling design and is started from selecting phenomena of interests and parameters to be conserved.

For decades, several scaling analysis methods have been suggested to apply for real-world experiments. Most of the methods require several considerations on fluid and flow characteristics to determine governing equations according to the conditions of between the prototype and the scale facility. Among them, the scaling methods reviewed for this dissertation are limited to the methods developed for liquid metal fast reactors, as a prototype and a scale facility use LBE as a working fluid.

(Grewal and Gluekler, 1982) suggested a scaling analysis method on natural circulation in SFRs to be tested with water because water and sodium have similar densities utilizing Navier-Stokes equation and several transport equations on heat transfer in the derivation of dimensionless numbers. However, their work did not clearly show how some parameters such as the representative velocity and the representative temperature difference are derived from governing equations, and how a parameter called ‘Euler number’ functions in the scaling analysis. In addition, they simply proposed a possibility in conclusion that an experimental facility with water could simulate thermal-

hydraulic behaviors cast in SFRs if the similarity in main dimensionless numbers is satisfied. (Weinberg et al., 1990) suggested a similar method simulating decay heat removal in SFRs with water like the previous study. In this study, they fixed two main parameters, the representative velocity and representative temperature difference, as core outlet velocity and core inlet-outlet temperature difference, respectively.

Scaling methods on single-phase natural circulation experiments in pool-type SFRs were suggested as well (Eguchi et al., 1997; Takeda et al., 1993). Prototypic reactor in those studies adopted sodium as coolant and the experimental facilities were supposed to be operated with water. It is because water ensures an easy handling due to its visual transparency and material compatibility compared to sodium that is opaque and highly reactive, and above all, it has been studied extensively so that its thermophysical properties are well known. The method features the geometrical similitudes in all directions (horizontal, lateral, and vertical) are equal so that a scale model is to be reduced from a prototype without any distortion in a specific direction. In addition, heat source and heat sink are designated as forms of 'black boxes' which means it is not necessary to conserve geometrical shape between the prototype and model. Internal flow directions in these black boxes are supposed to be unidirectional; in other words, no local flow is available. Furthermore, this study covered the role of Euler number in scaling analysis and the necessity of its conservation, which were not fully shown by former studies, so that previous studies can be supplemented. This methods was also applied to the design of E-SCAPE, a down-scale facility for the MYRRHA reactor developed by SCK-CEN, and

both the prototypic reactor and the scale facility utilize LBE as primary coolant (Van Tichelen et al., 2015).

There was a study on the scaling of pool-type passive LFR to be simulated by water (Chen, 2015). The author suggested not only the scaling analysis method itself but also the methodology to evaluate natural circulation stability in the water model. However, a test facility utilizing this method requires water temperature to be higher than its normal boiling point in a specific condition because many of thermophysical properties of LBE are quite exotic compared to those of water. In this case, the whole facility must include pressurizing means and be designed to ensure high operating pressure.

A scaling analysis method on natural circulation by single-phase and two-phase flows through area-average one-dimensional formulations was studied (Ishii and Kataoka, 1984; Ishii et al., 1998). The nondimensionalization of conservation equations in this method is done by utilizing the steady-state solution of the equations as the representative velocity and representative temperature difference. This method features scaling ratio in length direction (flow traversing direction; z-direction) can be chosen independently and similarity in transient conditions is also conserved because heat transfer between solid heat sources and fluid is also included in governing equations. On the other hand, this method has a limitation in simulating the local phenomena given in the prototype having a large flow area in the scale facility, as it utilizes area-averaged parameters for the set of one-dimensional equations. In this process, such behaviors in traversing directions, perpendicular to the z-direction, are no longer viable. In addition, this method was derived for the

natural circulation of water in single-phase and two-phase conditions. Still, it is applicable to a liquid metal as well, if its thermophysical properties does not vary with temperature.

Chapter 3 Problem Definition and Research Strategy

3.1 Problem definition

As aforementioned in Section 1.2, the objective of this dissertation is to evaluate the load-following capability of URANUS, a passive LBE-cooled pool-type SMR. Since the naturally cooled system is operated without an external momentum source like a reactor coolant pump, primary mass flow rate can be determined by core power and resultant temperature distribution. In this respect, the natural circulation dynamics gives rise to a delayed system reaction. During a system maneuvering in some conditions, its stability might be lost. Therefore, the load-following capability is determined by the stability limits. To achieve the objective, three specific research questions are risen:

1) Question 1: How does a pool-type passive LBE-cooled system react to changes in external operating condition?

2) Question 2: How is the transient integral behaviors of pool-type passive fast reactor system evaluated?

3) Question 3: What is the condition under which a passive LBE-cooled system safely controlled and regulated to follow varying load demand?

To settle the first question, experimental studies on the natural circulation of LBE were conducted with two types of experimental facilities including HELIOS loop and PILLAR pool. Experimental results are given in Chapter 4. Utilizing a loop-type full-height scale facility, several steady-state natural circulation results were generated. After that, a pool-type thermal-hydraulic integral test facility scaled from URANUS was designed and several experiments was conducted using the facility.

The second question was resolved by using the numerical code called MARS-LBE. To do so, the experimental data were utilized in the validation preceded to the numerical modeling. It was concluded that the code calculation showed a good agreement with experimental results and the numerical tool would be able to be used for the design and safety analysis purposes for passive LBE-cooled systems.

Lastly, the third question was cleared by developing an analytical model. The model is dedicated to the passive LBE-cooled system and simulates the system reaction to a variation in external load demand and the stability under that transient. With the model, the passive LBE-cooled SMR can be operated in load-following operation with stable and rapid change of power.

3.2 Approach

The thesis study is prepared with three approaches including experiments, numerical modeling, and analytical simulation. The experimental study deals with steady-state and transient natural circulation in two different geometrical configurations, loop and pool. For the steady-state tests, core power is an independent variable so that sets of natural circulation experiments can be performed. On the other hand, the transient tests are conducted by external operation condition changes in primary side power and heat sink flow rate, which represent the operational condition maneuvering in a reactor system. As a tool for the design and safety analysis of passive LBE-cooled reactor systems, a one-dimensional system thermal-hydraulics code, originally developed for the analyses of water-cooled reactors, was validated. For control design and evaluation purposes, this dissertation seeks to develop an analytical model. With the developed model, the stability of transients given in the passive LBE-cooled SMR in response to load demand and its achievable operation range were evaluated. The research flow and relation between the approaches of this dissertation are depicted in Figure 3.1.

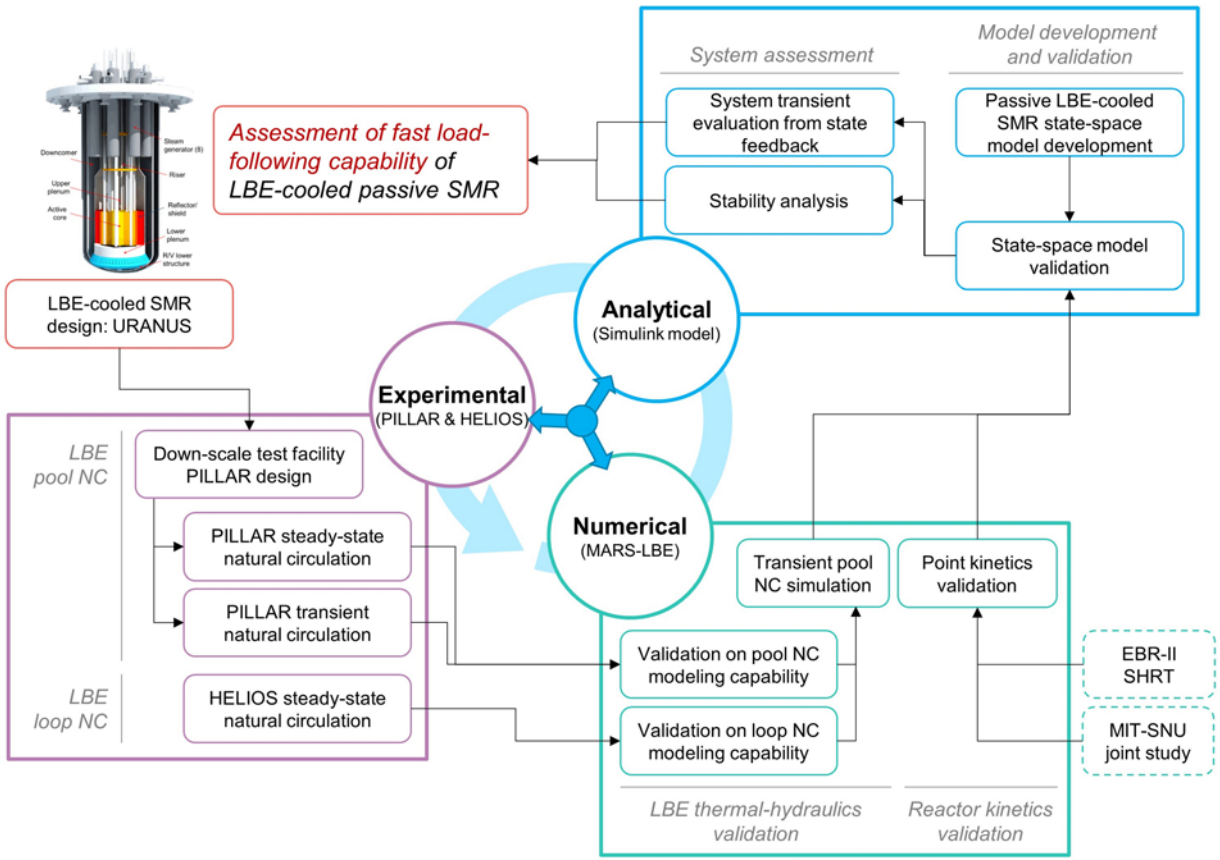

Figure 3.1 Thesis research approach

3.2.1 SMR reference design definition

Until now, no pool-type SMR that utilizes lead or LBE as primary coolant is built or operated. In this regard, a target conceptual design is required and the dissertation begins with the design of a passive LBE-cooled SMR. The activity includes the definition of SMR design criteria and requirements, neutronic core design which enables a long fuel cycle under safety parameters are controlled, system thermal-hydraulics analysis for a normal full-power condition, and conceptualization on the requirements of structural components. The establishment of this physical model is described in detail in Chapter 4

3.2.2 Experimental setup and tests

System integral behaviors given by external condition change in a passive LBE-cooled SMR is studied with experimental campaigns. A thorough understanding on natural circulation is essential since the primary system of the reactor can only be cooled by natural convection.

The experimental campaigns proceed in twofold: firstly, experimental investigation was conducted in a simple geometrical configuration, loop. Several steady-state test results were gathered by changing heat source conditions controlling electrical heaters. Secondly, experiments that are more realistic were carried out with a pool-type test facility. By utilizing the physical model, a pool-type integral test facility dedicated to the evaluation of system

behaviors of the prototypic reactor is designed by scaling analysis. The experimental studies are covered in Chapter 5.

3.2.3 Numerical validation and modeling

As a tool for the design and safety analysis of passive LBE-cooled reactor systems, a one-dimensional system thermal-hydraulics code, originally developed for the analyses of water-cooled reactors, was validated. For a reactor analysis, the code must be validated in two physical aspects: thermal-hydraulics and reactor kinetics. The test results made by two different types of geometrical configuration were utilized for the validation of thermal-hydraulics capability of the code. The code was suitably modified to implement the thermophysical characteristics of LBE. With the steady-state test results in loop and pool configurations, the code was confirmed that it can be used for the analysis of LBE coolant environments. The validated code was utilized for the modeling of transient tests in LBE natural circulation.

The other part, the reactor kinetics, was validated by other studies outside of this dissertation because there have been no experiments on the reactor kinetics of lead-cooled systems. Hence, as liquid metal cooled fast reactors are expected to have similar neutronic behaviors due to its fast neutron spectra, the validation of the code was regarded to be done by sodium-cooled fast reactor experiments. The validation of numerical model is elaborated in Chapter 6.

3.2.4 Analytical model development and load-following capability assessment

When the external load demand differs from a specific condition, the core power should follow it in a load-following operation mode. To do so, the position of control rods are maneuvered to reduce the discrepancy between the core power and load demand. For the assessment of fast load-following capability of a passive LBE-cooled SMR, this dynamic behavior must be included and is not able to be solved in the validated system codes in standalone.

For control design and evaluation purposes, this dissertation seeks to develop an analytical model, which implements the control rod movements and is capable of stability analysis and system behavior simulation at the same time. With the developed model, the stability of transients given in the passive LBE-cooled SMR in response to load demand and its achievable operation range were evaluated. The details in development of analytical model and assessment of load-following capability of the passive LBE-cooled SMR are illustrated in Chapter 7.

Chapter 4 LBE-cooled Passive SMR Design: URANUS[2]

This chapter first conceptualizes a passive LBE-cooled SMR, named as Ubiquitous, Rugged, Accident-forgiving, Nonproliferating, and Ultra-lasting Sustainer (URANUS), with a thermal power rating of 100 MW, for the target conceptual design on the assessment of fast load-following capability. The reactor does not require any fuel refueling nor assembly reconfiguration such as shuffling during its single fuel cycle as long as 20 years. This reactor is a pool-type fast reactor with an array of heterogeneous hexagonal core (Choi et al., 2011b). The coolant is chemically inert and has good neutron characteristics and a high boiling point. To avoid the unexpected common failures of active safety systems, the primary cooling system is operated without reactor coolant pumps. Material corrosion is limited by using corrosion-resistant materials in combination with an oxygen control technique (Ballinger and Lim, 2004; Fazio et al., 2001; Hwang et al., 2000; Li, 2008; Müller et al., 2000; Sekimoto and Su'ud, 1995; Takahashi et al., 2008). The entire reactor containment and its heat transport systems are seismically isolated from the ground through three-dimensional isolators.

---

[2] This chapter has been written based on the following journal paper: Yong-Hoon Shin et al., "Advanced passive design of small modular reactor cooled by heavy liquid metal natural circulation," Progress in Nuclear Energy, 83, 433-442, 2015.

4.1 Design goals and requirements

URANUS is designed to fulfill the philosophies that GIF suggests as described in Section 2.1. Table 4.1 shows the key design parameters of URANUS. These design parameters were estimated based on four design goals for ensuring technical, operational, and economic performances:

1) The reactor module is required to produce 100 MW_{th};
2) The length of one cycle is 20 effective full power years (EFPYs) without fuel refueling or assembly reconfiguration;
3) Geometrical configurations permit full heat removal by only coolant natural circulation by reducing pressure loss; and
4) The diameters of active core and reactor vessel are smaller than 2 m and 4.5 m, respectively, for ensuring land-transportable sizes.

To ensure nonproliferation and nuclear security, several Generation-IV concepts pursue no on-site refueling strategy and adopt cradle-to-grave fuel services, as illustrated in Travelling Wave Reactor that is being designed by Terrapower, LLC (Hejzlar et al., 2013). Since this approach may lead to increase in the frequency and difficulty of fuel transportation from a reactor site to a vendor plant, URANUS aim at a long-burning fuel cycle.

Design constraints were selected for safe and secure operation with sufficient margins without thermal, radiation, material, and structural failures

(Choi et al., 2011a; Nam et al., 2007). The thermal design constraints are:

1) Fuel centerline temperature at the hottest rod should be limited to be lower than the melting temperature of UO_2 fuel, 2,865 °C, with sufficient margin during all operating conditions even in design basis accidents;

2) Peak cladding temperature must not exceed the melting point of HT-9 or T-91 cladding overlaid with Al containing ferrite steels, 1,500 °C, with sufficient safety margin;

3) Inherent negative reactivity feedback has to be secured with sufficient safety margins under all operating conditions to prevent fuels from melting down (Choi et al., 2011a);

4) Reactivity swing has to be less than $1 without burnable poison rods to minimize positive reactivity insertions in the case of control assembly withdrawal without scram (Choi et al., 2011a); and

5) Decay heat can be removed passively on the outermost surface of reactor vessel which uses air cooling in accident conditions (Choi et al., 2011a).

The radiation design constraints are:

1) Peak discharge fuel burnup is required to be as large as possible, but is limited not to exceed an experimentally verified value, 100,000

MWd/MTU (Astegiano et al., 2004); and

2) Fast neutron fluence is limited not to exceed an experimentally verified value to avoid material embrittlement caused by radiation damage and to ensure fuel cladding integrity (Nam et al., 2007). HT-9 or T-91 were observed to has less than 2% swelling up to 200 dpa at around 400-420 °C, higher irradiation resistance than that of austenitic stainless steels (Garner et al., 2000; Klueh and Nelson, 2007).

The material design constraints are:

1) Outlet coolant temperature limit is 450 °C where corrosive reactions between LBE coolant and structural materials are well controlled for long-term full power operation by employing qualified materials and dissolved oxygen controls (Li, 2008);

2) Clad collapse limit from internal fission gas pressure is constrained by American Society of Mechanical Engineers (ASME) Section 3 (Nam et al., 2007);

3) Cumulative fatigue from fuel-clad mechanical interactions and flow-induced vibrations is constrained by ASME Section 3 (Nam et al., 2007); and

4) Total creep strain including both thermal- and irradiation-enhanced creep has to be maintained below creep rupture strain, conservatively set as 1% (Nam et al., 2007).

The structural design constraints are:

1) Radial power peaking factor is required to stay low enough, lower than 1.5, to reduce thermal stress on structures from temperature difference and to secure high margins on fuel melting (Choi et al., 2011a);

2) Reliable seismic isolation has to endure an earthquake of 0.5g zero period acceleration (ZPA) for the Safe Shutdown Earthquakes (SSE) (Yoo et al., 2000); and

3) Containment built underground is needed to assure robust features in support of air defense, explosion proof, and protection from external sabotage actions.

Table 4.1 Key design parameters of URANUS

Design parameter	Value or characteristic
Thermal power	100 MWt
Refueling interval	20 years
Plant design lifetime	60 years
Primary coolant	Lead-bismuth eutectic
Primary heat transport system	Compact pool type
Core configuration	Open hexagonal array
Primary normal cooling mode	Fully natural circulation
Normal decay heat removal	Coolant natural circulation in the primary system combined with water/steam forced circulation in the secondary system
Abnormal decay heat removal	Reactor vessel auxiliary cooling by air
Fuel	UO_2
Cladding	HT-9 or T-91 overlaid with Al containing ferrite steels in functionally graded composite
Steam generators	8 modules of straight shell-tube type
Secondary water/steam cycle	Rankine cycle with superheated steam
Seismic design	Three-dimensional seismic isolators

4.2 Reactor core design

In order to enhance its inherent safety, the reactor coolant pump was excluded from the system so that it resorts natural circulation in both normal and abnormal conditions for a cooling mechanism. Considering the maximization of coolant flow rate, it is required to reduce pressure loss along flow paths and it leads to the enlarged pitch-to-diameter ratio; the wide path of coolant flow reduces pressure loss in the core region. In addition, the core configuration decreases volume power density and discharge burnup compared to conventional fast reactors, and extensively reduces peak excess reactivity and reactivity swing.

4.2.1 Fuel assembly configurations

The reactor core consists of two enrichment zones of fuel assemblies, the three types of reactivity control and shutdown assemblies, and a surrounding LBE reflector zone as shown in Figure 4.1. There are 108 fuel assemblies, 6 primary control assemblies, 6 secondary shutdown assemblies, and 1 ultimate shutdown assembly. The liquid LBE reflectors in which the fluid has almost no flow velocity surround the fuel zones for neutron economy by reflection.

The enrichment of inner core zone is 9.55% while that of outer zone is 17.09%. A large difference in enrichment between inner and outer regions was adopted for three reasons: first, this enrichment zoning is intended to flatten

power distribution to reduce radial power peaking without assembly reconfiguration, providing adequate safety margin and mitigating the effects of thermal gradient. Second, it also helps increase internal breeding by loading enough fertile materials at the center region of core, which in turn loading lower fissile materials on high flux region. Third, it contributes to maintain a radial peaking factor lower than 1.5 from the beginning of cycle (BOC) to the end of cycle (EOC).

The total amount of uranium loaded is nearly 17.8 metric tons. The reactivity swing, which is defined as the difference of maximum and minimum reactivity values over a single fuel loading cycle, is lower than $1. This small reactivity swing reduces the control rod worth and the positive reactivity insertion of a control rod ejection accident (Choi et al., 2011a). The refueling interval could be extended beyond 20 years with material improvements. The determination of refueling interval and plant design lifetime considers cladding corrosion, creep, fatigue and radiation embrittlement (Nam et al., 2007). The specific power density is reduced to achieve a long fuel cycle with a small reactivity swing (Blue et al., 2005; Hill et al., 1999).

A fuel assembly consists of 60 fuel pins and 1 central skeletal bar in a hexagonal lattice with grid plates, as shown in Figure 4.2. The pitch to diameter ratio is 1.35 and the assembly pitch is 166.25 mm. The wide coolant paths between the rods significantly enhance natural circulation by reducing pressure drop, but simultaneously deteriorate neutron economy due to a low fuel volume fraction, which requires more fissile materials to be loaded. Furthermore, the low fuel volume fraction harms breeding performance by softening neutron

spectrum and increasing neutron leakage. In spite of this, it is still sufficient to achieve both neutronics and thermal-hydraulic design goals.

The specifications of fuel assemblies are summarized in Table 4.2. The active core height is 1,800 mm and the active core equivalent diameter is 1,900 mm. The upper fission gas plenum length is 1,300 mm accommodating fission gas released; both low and upper plugs length is 300 mm. Total loaded enriched uranium is 17,812 kg including 6,412 kg for inner core and 11,399 kg for outer core. The total weight of coolant and internal structure including nuclear fuels is less than 750 metric tons. The peak fuel centerline temperature during the normal operation is approximately 760 ^{o}C assuring sufficient margin to the fuel melting point.

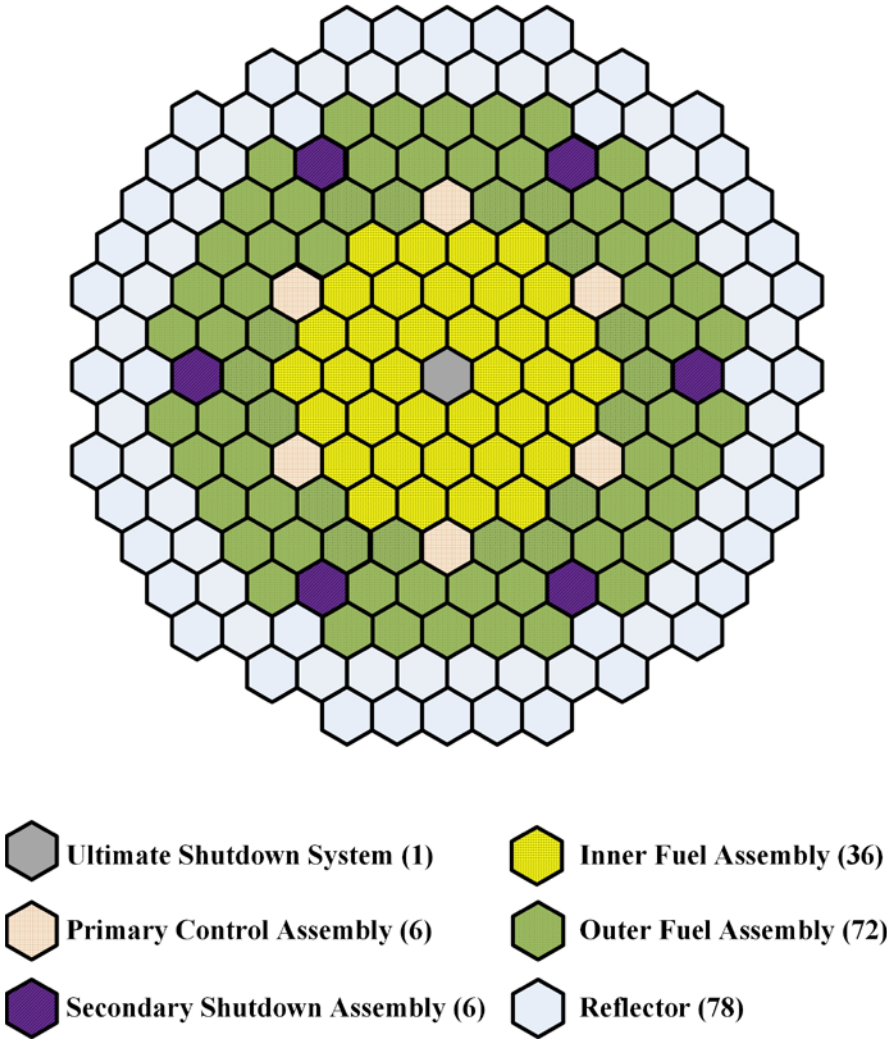

Figure 4.1 Radial assembly configuration of active core

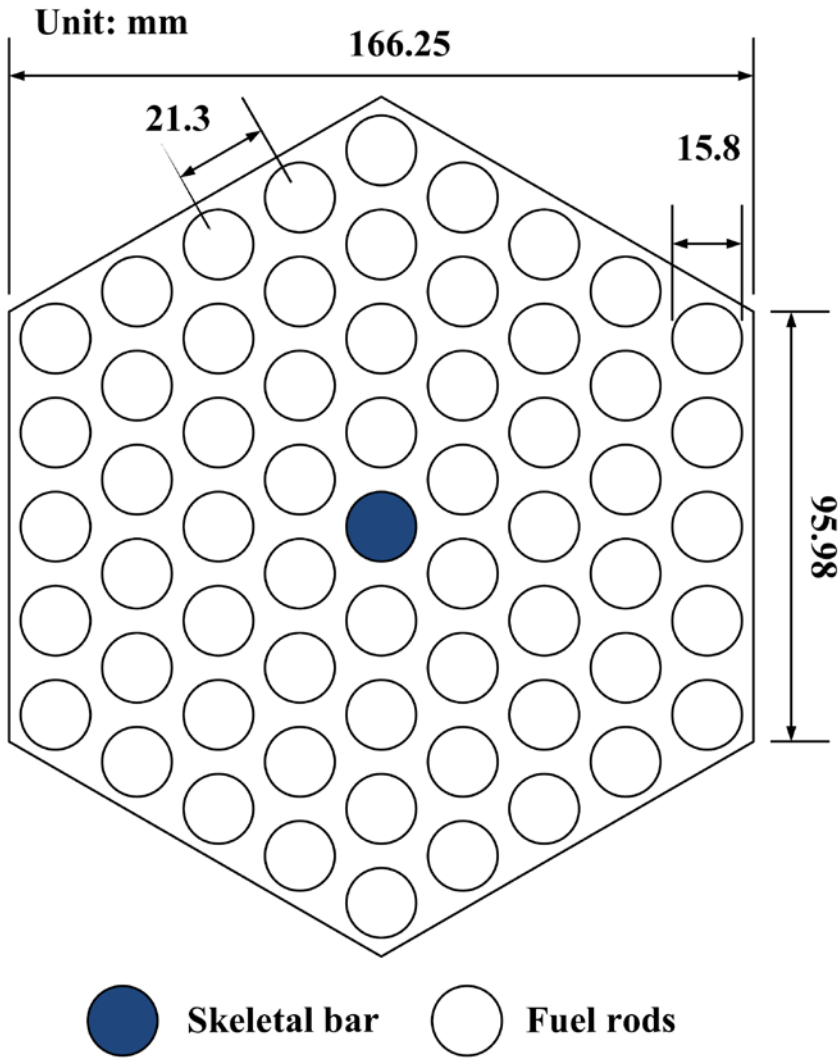

Figure 4.2 Horizontal view of a single fuel assembly including fuel rods and a central skeletal bar

Table 4.2 Design parameters of fuel assemblies

Design parameter	Value
Number of pins per one assembly	61 including 1 skeletal bar
Enrichment	9.55 (wt%) in the inner core
	17.09 (wt%) in the outer core
Pin pitch-to-diameter ratio	1.35
Fuel pin pitch	21.3 (mm)
Fuel pin diameter	15.8 (mm)
Active core height	1,800 (mm)
Equivalent core diameter	1,900 (mm)
Fission gas plenum height	1,300 (mm)
Lower plenum height	300 (mm)

4.2.2 Fuel rod design

Figure 4.3 shows the one-twelfth pin-cell model of a fuel rod. The length of the fuel rod is 3,400 mm including the lower plug, the lower plenum, the UO_2 fuel slug, the upper gas plenum, and the upper plug. Among them, the length of the active core is 1,800 mm as indicated in Table 4.3. The upper fission gas plenum is 1,300 mm long, and the length ratio of the fission gas plenum to the active core is 0.72. This ratio is smaller than the conventional ratio of 2.0 because the low outlet temperature, about 450 °C, limits the ingress of fission gas pressure. The diameter of UO_2 fuel is 14.6 mm and the diameter of fuel rod including cladding is 15.8 mm. This fuel rod has a large fuel diameter for improving natural circulation capability by enlarging coolant flow paths and for loading nuclear materials as much as possible at the same time.

It is known that the oxide thickness of the FeCrAl ferrite steels as a form of Al_2O_3 at 450 °C and 600 °C for 20 years is predicted to be only about 0.5 and 2.5 μm, respectively, so that the alloy can be used for the cladding materials in high temperature LBE environments (Lim et al., 2010). However, Al-containing ferrite steels show significant radiation embrittlement as a result of Al segregation to grain boundaries and Cr-rich α' phase formation at the temperature range of 300-500 °C (Dvoriashin et al., 2007). To achieve appropriate corrosion resistance while keeping desirable mechanical properties, the hybrid fuel cladding tube, HT-9 or T-91 overlaid with Al-containing ferrite steels, was selected (Hwang and Lim, 2010). The thickness of Al-containing ferrite steels is 0.5 mm, forming a thin protective Al oxide layer. This hybrid

approach has been pursued by the MIT based on standard commercial practice with Si-containing alloys (Ballinger and Lim, 2004). A gap is introduced to accommodate fission gas, which is about 0.1 mm thickness between the inner cladding wall and the outer surface of UO_2 rod.

Tag gas capsules are loaded in the fission gas plenum in order to find the location of a failed fuel pin easily. This capsule contains an isotopic blend of inert gases that is unique to that assembly. During the final fabrication, this capsule is punctured into the fission gas plenum and it escapes into the primary coolant in the cladding failure.

Honeycomb-type grid spacers hold each of fuel rods and maintain the hexagonal lattice. Unlike wire wraps, grid spacers have advantages for better structural strength with reduced steel volume, which allows the potential increases of fuel volume and coolant flow area. Furthermore, the use of grid spacers allows the hot channel factor to be lowered by lateral heat conduction and convection.

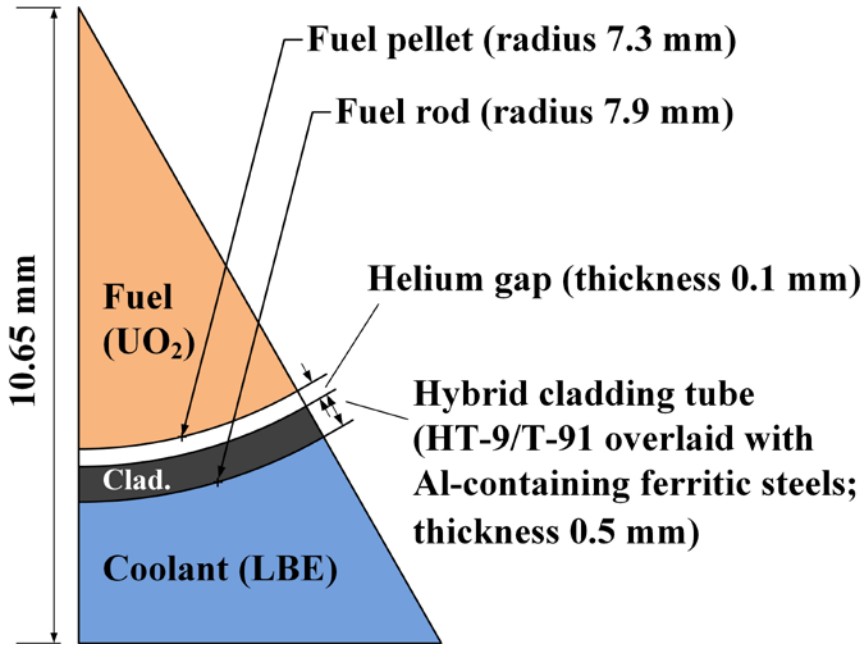

Figure 4.3 Pin-cell model for fuel rod

Table 4.3 Design information of fuel rod

Parameter	Value
Fuel type	UO_2
Enrichment	9.35 (wt%) in the inner core
	17.75 (wt%) in the outer core
UO_2 fuel pellet diameter	14.6 (mm)
Initial gap thickness	0.10 (mm)
Cladding thickness	0.50 (mm)
Cladding material	Al-containing ferrite steels

4.2.3 Safety control assembly configurations

As aforementioned in Section 4.2.1, three independent sets of control systems are employed: the primary control assemblies, secondary shutdown assemblies, and ultimate shutdown system. Both primary and secondary control assemblies are inserted to the active core from the top of the core with the drive mechanisms located at the top of the vessel closure head. The ultimate shutdown system is located at the bottom of reactor vessel. The control and shutdown assemblies consist of a closely packed absorber bundle of natural boron carbide pellets within a duct. The natural boron contains 19.9 at.% of ^{10}B which is a strong neutron absorber.

The primary control system is composed of six assemblies located right outside of inner core assemblies as shown in Figure 4.1. A stepping motor with electro-magnetic holding operates the primary control assemblies. With maneuvering primary control assemblies, reactivity control during normal operation and normal shutdown are achieved. The primary control system is required to shut down the reactor to cold standby conditions from any operation conditions including full-power operation, unprotected transient overpower, and unprotected loss of heat sink conditions. It has sufficient reactivity worth even if one assembly having the largest reactivity worth is not inserted and is able to compensate for the reactivity loss from the fuel burnup and uncertainties in uranium enrichment.

The secondary shutdown system is also consisted of six assemblies located slightly outside compared to the primary control system. The secondary

shutdown system magnetically grasped during the normal condition is passively inserted by gravity when the primary control system is not operated properly and the temperature of holding magnet reaches its Curie point. Similar to the primary system, this secondary shutdown system can shut down the reactor without the insertion of assembly having the highest reactivity worth. The secondary shutdown system is capable of shutting down the reactor at the full power operation condition when the primary control assemblies are suddenly withdrawn.

The ultimate shutdown system is located at the center of the active core. This system works passively without an external trigger signal and a power source. It consists of boron stainless steel balls and is inserted into the core by buoyancy force under the event of core overheating and melting of its fusible stopper. Because it is located at the bottom of reactor vessel, its temperature change is delayed by one primary coolant cycle. Hence, it is an engineering redundancy for the failures of both primary and secondary shutdown systems.

4.2.4 Neutronic analysis

The neutronics analysis of the reactor core was performed by solving nodal diffusion theory methods for a hexagonal geometry option in REBUS-3, a multi-group fuel cycle analysis code (Toppel, 1983). This code can calculate the flux solutions of homogenized nodes or mesh cells using the DIF3D module without thermal-hydraulic feedback effects (Lawrence, 1983). All calculations used a 24 energy-group structure and a TRU burnup chain from Th-232 to Cm-245. Some important long-lived fission products (LLFPs) such as Tc-99, I-129, Sr-90, and Cs-137 were independently treated, while other fission products were not individually considered by classifying them into 4 lumped fission products (LFPs) groups (Hwang et al., 2000).

A cross section library with 80 groups for neutrons and 24 groups for gamma rays based on JEFF3.0, ENDF/B-VI.8, and JENDL3.3 were used as an input of TRANSX-2 producing transport tables in binary cross sections (MacFarlane, 1992). The final cross section for REBUS-3 was weighted by a regional neutron flux calculated by a discrete-ordinates transport code, DANTSYS (Alcouffe et al., 1995). The calculation chain showing data flows and methods used in the codes is described in Figure 4.4.

As can be seen in Figure 4.5, the excess reactivity at BOC is 224 pcm. The excess reactivity continuously decreases down to 135 pcm at the 13^{th} effective full power year (EFPY) and then increases again at EOC. At the initial stage, the breeding ratio is small because the fissile to fertile ratio is relatively large. In addition, the high neutron flux in the outer zone causes high neutron

leakage. After that, the breeding ratio increases as because the fissile to fertile ratio decreases and the neutron flux in the inner zone increases. As listed in Table 4.4, the reactivity swing during 20 years operation is 88.6 pcm, being lower than $1 and satisfying the design parameters listed in Section 4.1.

The average core power density is 19.42 MW/m^3 due to large coolant volume for natural circulation. The average linear heat generation rate is 8.57 kW/m and it is relatively small because the diameter of fuel rods is large, 15.8 mm. The large fuel diameter significantly decreases the ratio of surface area to fuel loading, improving natural circulation capability. The power density is limited to satisfy the outlet coolant temperature. Because of passive natural circulation, the flow rate of LBE coolant is comparatively low, resulting in the small volume density than those of conventional fast reactors. Peak discharge burnup, 40.98 MWd/kg, is smaller than the limit.

Internal conversion continuously increases during 20 years operation. The average conversion ratio is 0.7227, which means that the core internal breeding is properly suppressed in terms of waste management and proliferation resistance while the long-term operation is achieved. Maximum fast fluences, defined as the number of irradiated neutrons over 100 keV on the unit area, for inner and outer core are respectively 1.37E+23 neutrons/cm^2 and 1.54E+23 neutrons/cm^2. In other words, the radiation damage of inner core is 68.7 dpa, and that of outer core is 76.9 dpa.

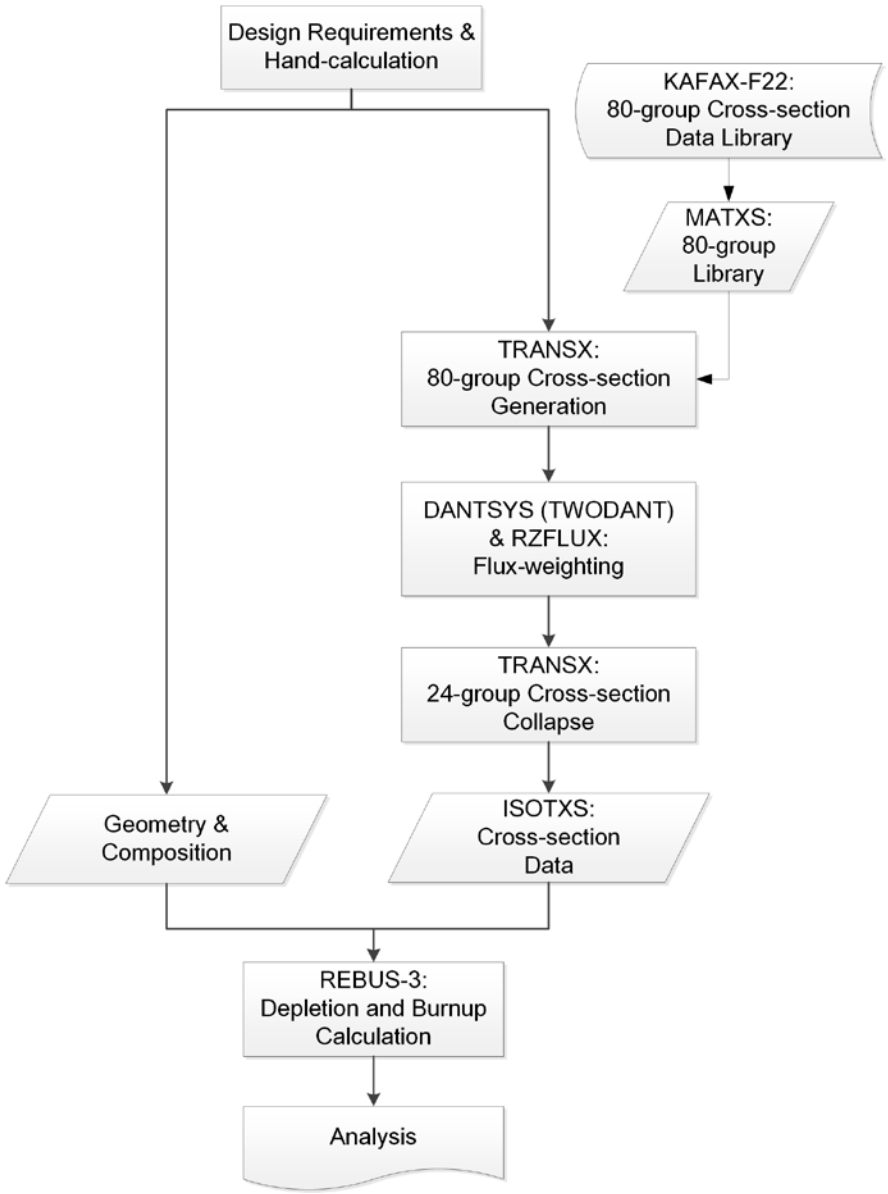

Figure 4.4 Code system used for the neutronic analysis of URANUS core design

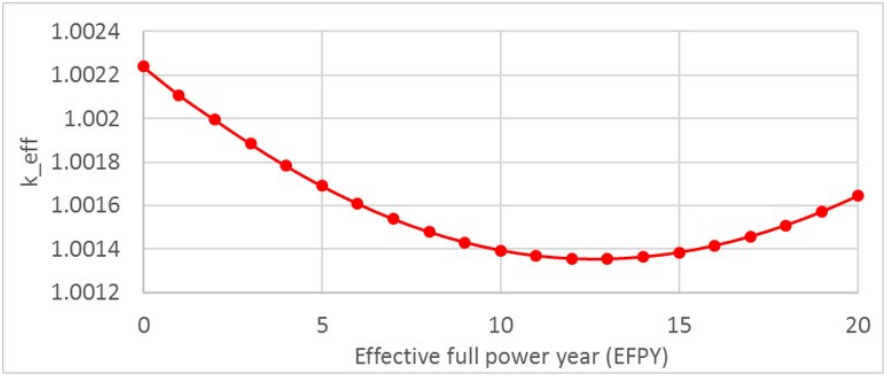

Figure 4.5 Effective multiplication factor of URANUS core during 20 years of full-power operation

Table 4.4 Key neutronics parameters of reactor core

Parameter	Value
Reactivity swing	88.6 pcm
Average effective multiplication factor	1.0016
Excess reactivity at the beginning of cycle	224 pcm
Minimum excess reactivity during cycle	135 pcm (13^{th} effective full power year)
Peak fuel discharge burnup	40.98 (MWd/kg)
Fast neutron fluence	68.7 (dpa) in the inner core
	76.9 (dpa) in the outer core

4.2.5 Kinetics and reactivity feedback coefficients

For the safety analysis and control rod design for normal operation of a nuclear reactor, the values of several kinetic parameters and reactivity feedback coefficients are required. In this section, those values are to be evaluated for BOC using two different code schemes, including the deterministic code system (Alcouffe et al., 1995; MacFarlane, 1992; Toppel, 1983) that has been utilized for the core design and burnup calculation of URANUS as discussed in Section 4.2.4, and a Monte Carlo neutron-photon transport simulation code. For the Monte Carlo analysis, a versatile tool called McCARD (Shim et al., 2012) is used, which features whole-core neutronics calculations, the evaluation of few-group constants, uncertainty propagation calculations, and burnup analysis by incorporating ORIGEN2-type (Croff, 1983) depletion equation solver.

For the analysis of URANUS core, the kinetic parameters to be used include Doppler coefficient, fuel axial expansion coefficient, core radial expansion coefficient, and coolant density coefficient, which are widely used for the fast reactor analyses. Because of the high boiling point of LBE coolant, the coolant void effect is not considered. Although the fuel axial expansion coefficient and the core radial expansion coefficient are usually defined by dimensional change, it is derived with respect to temperature change by converting the dimensional change with linear length expansion relations. Those parameters, denoted by α, are determined as reactivity change $\delta\rho$ given by the temperature change δT of a specific component x, as in Eqn. (4.1):

$$\alpha_x = \frac{\delta\rho}{\delta T_x}, \tag{4.1}$$

where the reactivity change $\delta\rho$ is defined with change in reciprocal effective multiplication factors, $1/k_{eff}$, for two temperature states 1 and 2, respectively, as in Eqn. (4.2):

$$\delta\rho = \frac{1}{k_1} - \frac{1}{k_2}. \tag{4.2}$$

In this case, the subscript 1 means a base design that is determined in Section 4.2.4 while the latter, the subscript 2, refers to a new state that the temperature of a specific component is changed. The multiplication factors in the above equation are evaluated by means of the deterministic code chain and McCARD. The specific components are D for the Doppler coefficient, *l* for the fuel axial coefficient, *R* for the core radial coefficient, and *LBE* for the coolant density coefficient, respectively.

Table 4.5 contains important kinetic parameters at BOC calculated by the deterministic code chain and McCARD including the Doppler coefficient, the fuel axial expansion coefficient, the core radial expansion coefficient, and the coolant density coefficient. For the McCARD calculation for effective multiplication factors, 500,000 particles were used for each cycle under 50 inactive and 100 active cycles while utilizing ENDF/B-VII.1 nuclear cross section library. Two methods show slight different calculation results because it is affected by the use of neutron cross section library. Still, all the coefficients

are negative, which in turn are the reactor core is inherently safe under those temperature-induced reactivity insertion conditions.

The Doppler coefficient produces the largest negative feedback effect when fuel temperature increases. Having a softer neutron spectrum than that of a conventional metal-fueled fast reactor, more neutrons can be captured in the resonance peaks. In addition, a temperature rise results in the axial expansion of fuel rod and the radial expansion of fuel assembly. These expansions reduces the density of fissile materials in the active core, producing negative feedback. At the same time, these expansions can decrease neutron leakage and produce positive feedback (Chang et al., 2005). Since the first effect is stronger, the net effects of axial and radial expansions are negative feedback. The coolant density coefficient is also negative since neutron leakage increases when coolant density decreases.

The effective delayed neutron fraction, β_{eff}, which determines the kinetic response of a reactor core, is also calculated by two methods similar to the evaluation of kinetic parameters. However, the effective delayed neutron fraction is required to be calculated by adjoint flux weighting (Waltar and Reynolds, 1980). While McCARD processes this weighting internally and automatically, it is required for the deterministic method to perform the similar calculation by hand. In addition, McCARD is also capable of the evaluation of point kinetics parameters including the j-th group delayed neutron fractions, β_j, precursor decay constants, λ_j , and neutron generation time, Λ, defined in six-group point kinetics equations.

Table 4.6 summarizes the effective and group delayed neutron

fractions, prompt neutron generation time, and group precursor decay constants at BOC from a literature (Waltar and Reynolds, 1980) and calculated by McCARD. The computational conditions were the same with that of the kinetic parameter evaluation for the base case. Those two results show slightly different but similar values since the values are dependent upon the composition and geometrical distribution of nuclear materials in the core. Nevertheless, the effective delayed neutron fraction is similar to that of ^{235}U, about 680 pcm, because this reactor uses enriched uranium fuels (Waltar and Reynolds, 1980). McCARD evaluates the prompt neutron generation time of URANUS is slightly greater than that of typical fast spectrum reactors, about 4.00E-07 s (Waltar and Reynolds, 1980). Considering this, the reactor transients of URANUS driven by reactivity change are expected to be slower than typical fast reactors.

Table 4.5 Kinetic parameters at beginning of cycle calculated by the deterministic code chain and McCARD

Parameter	Deterministic code chain*	McCARD
Doppler coefficient (α_D)	-0.8735 (pcm/K)	-0.5766 (pcm/K)
Fuel axial expansion coefficient (α_l)	-0.2404 (pcm/K)	-0.2287 (pcm/K)
Core radial expansion coefficient (α_R)	-0.3105 (pcm/K)	-0.4638 (pcm/K)
Coolant density coefficient (α_{LBE})	-0.2874 (pcm/K)	-0.4906 (pcm/K)

* ** Deterministic code chain refers to the calculation system used for the reactor core analysis for URANUS, as defined in Section 4.2.4.*

Table 4.6 Delayed neutron fractions and precursor decay constants at beginning of cycle calculated by the deterministic code chain and McCARD

Parameter	Literature (Waltar and Reynolds, 1980)	McCARD
Effective delayed neutron fraction (β_{eff})*	676.0 pcm	709.4 pcm
Group delayed neutron fraction	β_1 2.184E-04	2.242E-04
	β_2 1.477E-03	1.157E-03
	β_3 1.331E-03	1.147E-03
	β_4 2.673E-03	2.723E-03
	β_5 7.801E-04	1.318E-03
	β_6 2.808E-04	5.257E-04
Neutron generation time (Λ)	4.000E-07 s	5.387E-07 s
Group precursor decay constant	λ_1 1.343E-02 s^{-1}	1.337E-02 s^{-1}
	λ_2 3.069E-02 s^{-1}	3.256E-02 s^{-1}
	λ_3 1.170E-01 s^{-1}	1.211E-01 s^{-1}
	λ_4 3.033E-01 s^{-1}	3.054E-01 s^{-1}
	λ_5 8.637E-01 s^{-1}	8.566E-01 s^{-1}
	λ_6 2.926E+00 s^{-1}	2.878E+00 s^{-1}

** Calculated for URANUS based on the data from (Waltar and Reynolds, 1980).*

4.3 Heat transport systems design

As illustrated in Figure 4.6, the primary system and the steam generator modules are encapsulated within the reactor vessel. Since no pump is included in the primary system, it is cooled by LBE natural circulation in both normal operation and accidental conditions. In the heat transport systems design, the balance of plant (BOP) design is out of consideration in this dissertation because the reactor module is postulated to utilize the most reliable BOP design used in commercial power plants when it is deployed.

4.3.1 Primary heat transport system

The primary heat transport system is located in a double-walled pool-type reactor vessel. The double-walled vessel provides enhanced resistance against the loss of coolant accidents. The reactor vessel is determined to assure its structural integrity under accidental overpressure as well as seismic loads. The pressure of primary system depends on the static pressure of LBE coolant because the primary system does not need a pressurizing mean due to the high boiling point of LBE.

The design parameters of both primary and secondary heat transport systems are summarized in Table 4.7. In the primary system, LBE coolant flows through the reactor system by natural circulation. First, the coolant heated in the core moves upward through the riser region. After that, the coolant flows

outward through the inner barrel windows at the top and passes the steam generator shell. Then, coolant flows downward in the downcomer and gathers at the lower plenum to enter into the active core again by gravity. The temperature difference and vertical distance between the heat source – reactor core – and the heat sink –steam generators – can lead a significant driving force for natural circulation as buoyancy (Choi et al., 2011a).

The core inlet coolant temperature is targeted to around 300 °C which is high enough for maintaining the liquid phase of LBE. The average core outlet coolant temperature is lower than 450 °C, which is low enough for ensuring a slow corrosion rate during the design lifetime of 20 years for fuel-cladding materials and 60 years for the overall system components (Fazio et al., 2001).

Every single assembly is designed to be ductless so that cross-flow among assemblies is allowed to take advantage of a heat transfer mechanism of turbulent mixing. The ductless channels also enhance the inherent safety in postulated accident situations regarding local blockage (Choi et al., 2011a). A large flow area improves natural circulation with reduced pressure drop and produces pressure loss as low as 5 kPa inside the core so that natural circulation performance of primary cooling system is guaranteed and improved (Cho et al., 2011).

If an accident breaks out and the reactivity shutdown systems actuates by the reactor protection system, and residual heat including decay heat can be removed by two passive means such as coolant natural circulation and the reactor vessel auxiliary cooling system (RVACS). RVACS is a passive emergency residual heat removal system using natural circulation of air in an

event of system overheating. The outer surface of the guard vessel is cooled by environmental air, which comes along the cavity to remove the decay heat.

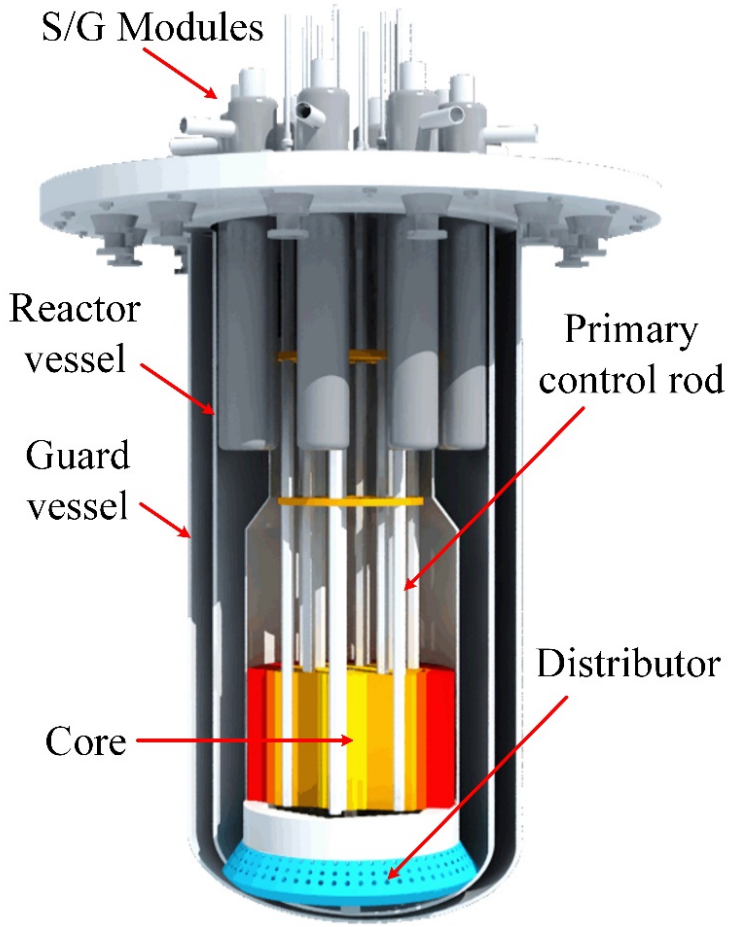

Figure 4.6 Schematic diagram of URANUS primary boundary

Table 4.7 Specification of primary and secondary heat transport systems of URANUS

Design parameter	Value or characteristic
Primary side	
Inner diameter of cylindrical shell	3741 (mm)
Wall thickness of cylindrical shell	50.0 (mm)
Total height, inside	9860 (mm)
Design pressure/temperature	1.0 (MPa) / 700 (°C)
Reactor operating pressure	0.1 (MPa)
Total weight with LBE and internal structure	758 (ton)
Secondary side	
Type	Straight shell-tube
Number of modules	8
Mode of operation	Secondary coolant inside tubes
Material	Functionally Graded Tube (Alloy 690 TT in the water/steam side, Al-containing ferrite steel in the LBE side)
Operating pressure	8.0 (MPa)
Feedwater temperature	252.0 (°C)
Steam outlet temperature	356.0 (°C)
Steam thermal state	Superheated
Steam flow rate	52.68 (kg/s)

4.3.2 Secondary heat transport system

In the secondary system, eight modules of once-through shell-and-tube type steam generators are installed and the tubes are made of functionally graded duplex tubes, Alloy 690TT (Ni-30Cr-10Fe) for the secondary water/steam side and Al-containing ferrite steels for the primary LBE side. The details of secondary heat transport system are elaborated in Table 4.7. The pressurized water at 80 bar is pumped into the steam generators where the water flows downward in the central feedwater pipe and then upward in the tube side while it is heated by the primary coolant flow from the shell side. The downward U-shape flow path of the secondary coolant provides driving force for prolonged natural circulation in the event of the secondary pump failure. The steam flow from the steam generators is collected in steam headers and sent through main steam lines to turbine generators with the flow rate of about 190 metric tons per hour. The main steam lines penetrate two containment vessels heads through double isolation valves that automatically shut in the event of steam generator tube rupture or main steam line break. Feedwater temperature is about 250 °C, while final steam temperature from the steam generators is approximately 360 °C, which ensures superheated state.

Since the detail design of BOP has not been made, the thermal efficiency of the single module of URANUS is only able to be evaluated by assuming ideal Rankine cycle with a single-step turbine generator and a condenser. By using the fluid conditions, the temperature-entropy diagram can be drawn as Figure 4.7 and the thermal efficiency can be estimated to be 39.7% .

In this evaluation, specific assumptions on the condenser is applied; the pressure in the component is given to be 0.005 bar. Considering that the thermal efficiencies of most liquid metal cooled fast reactors lie in a range of 35-45%, the evaluation is reasonable and the additional optimization can be followed after the specific design of BOP is made.

Since LBE has virtually no chemical activities with water or air, steam generator tube rupture accidents can be well managed with the containment. The interaction between LBE and pressurized water was already tested and this experiment confirmed the chemical inertness of LBE coolant (Ciampichetti et al., 2008).

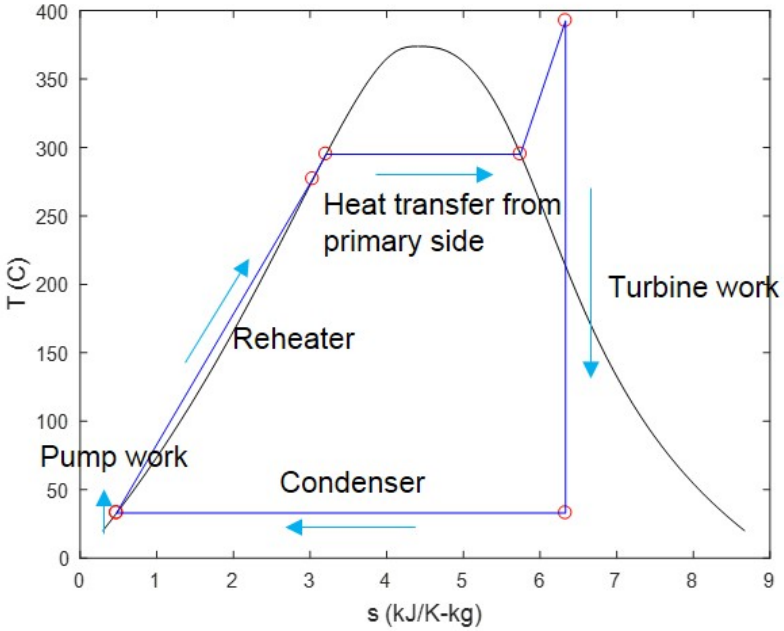

Figure 4.7 Ideal temperature-entropy (T-s) diagram of URANUS

4.3.3 Steady-state thermal-hydraulic analysis

For the thermal-hydraulic analysis under steady-state conditions of URANUS, a system thermal-hydraulics simulation code, named as Multi-dimensional Analysis Reactor System (MARS), was used (KAERI, 2006). A detailed description and code modification is elaborated in Chapter 6.1 with code validation through benchmarking. Figure 4.8 shows a nodalization map of the heat generation and removal systems. To calculate the core region more precisely than other parts, this region, indicated as P100 in Figure 4.8, is divided into 9 sections in the flow direction.

Two variables govern the natural circulation capability of the primary system. The first variable is the pressure loss induced by the hydraulic resistance in the primary system (Idelchik, 1986) while the second one is the thermal center difference defined as height difference between the center of reactor core and the center of steam generators in axial direction. Under the normal condition, the pressure loss and the buoyancy force are balanced as about 10.1 kPa, and thermal center difference is about 4.91 meters. The enhancement of natural circulation requires that hydraulic resistance should be lowered and that thermal center distance is needed to increase.

The temperature distributions of fuel centerline, cladding, and coolants in the hottest fuel assembly under the steady-state conditions is evaluated as shown in Figure 4.9. The peak fuel centerline temperature is near 756 °C having a sufficient margin to the melting point. LBE coolant with the temperature of around 300 °C enters from the inlet plenum and traverses

upward through the core to heat exchanger with the average temperature of 440 °C in the core outlet, as the results of the thermal-hydraulic calculation are summarized in Table 4.8. This temperature increase under the normal condition is within the acceptable range for reducing the corrosion of structural materials and the integrity of fuel rods. The temperature of the cladding at the hottest assembly is maintained below 550 °C.

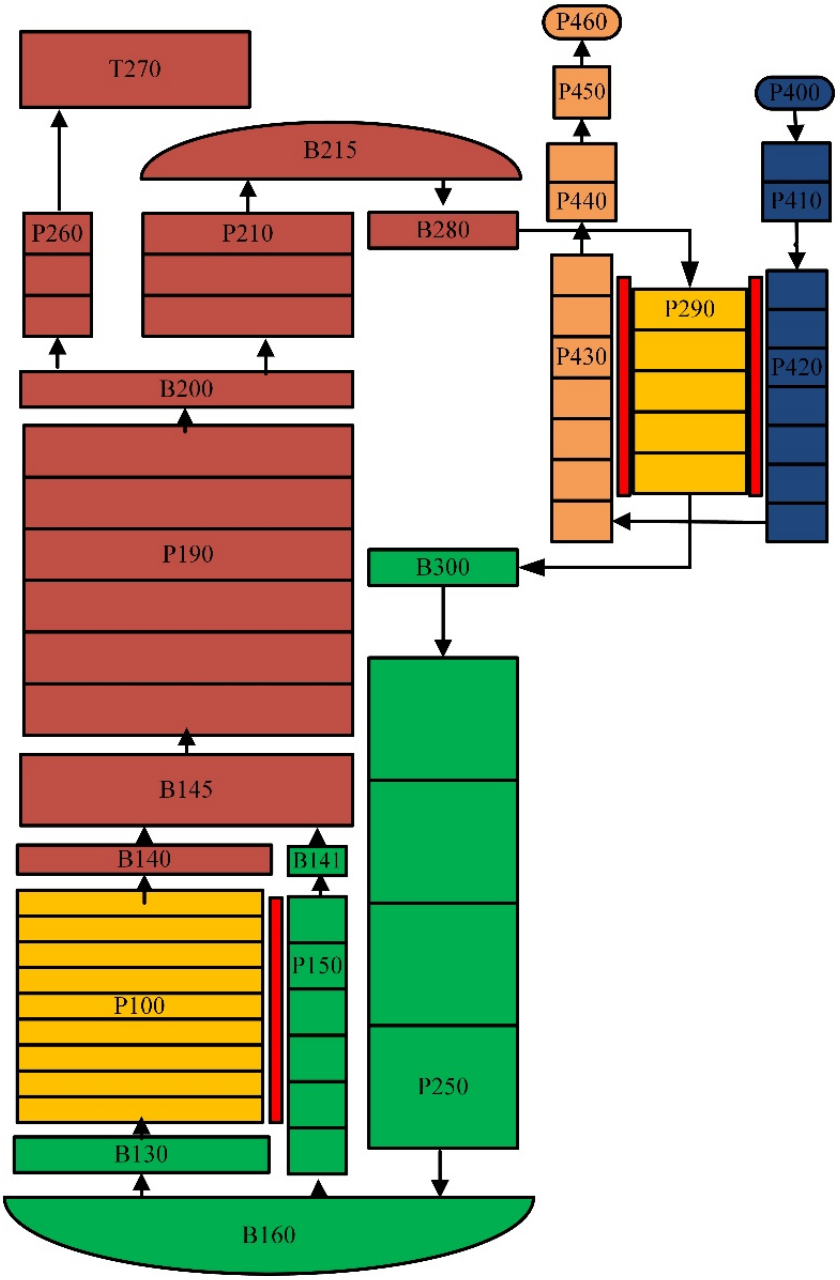

Figure 4.8 Nodalization of overall heat transport system for steady-state calculation

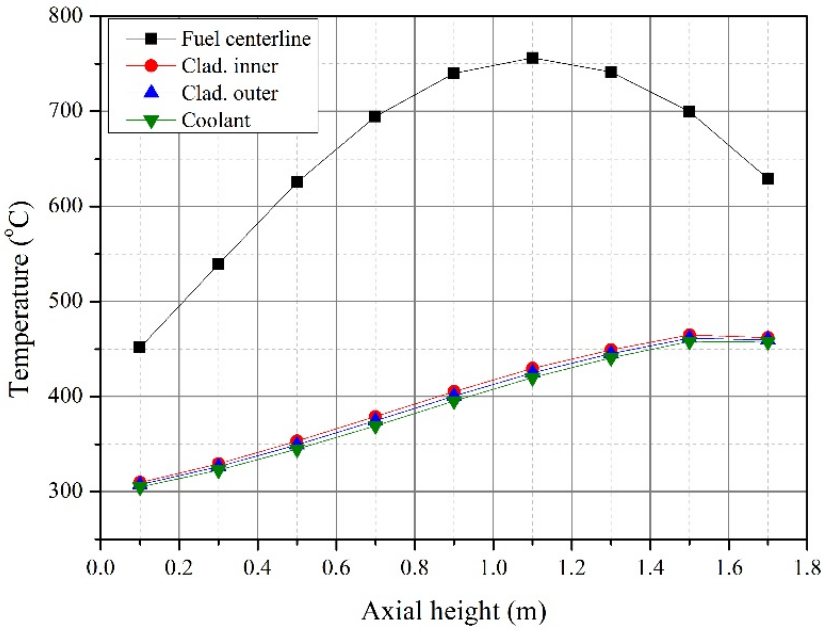

Figure 4.9 Steady-state temperature distributions of fuel centerline, cladding, and coolant bulk at the hottest assembly

Table 4.8 Steady-state system thermal-hydraulic calculation results of URANUS

Parameter	Value
Reactor coolant mass flow rate	4,886 (kg/s)
Core coolant inlet temperature	304.95 (°C)
Core coolant outlet temperature	440.76 (°C)
Peak fuel centerline temperature	756.25 (°C)
Peak cladding temperature	464.96 (°C)

4.4 Structure, materials, and components

The simple primary system design has been adopted to reduce capital cost and fabrication and construction times as well as enhance the quality of components. All reactor internals are replicable and replaceable; enough space is available for in-service inspection. The whole reactor module is separated from land by a three-dimensional isolation system. The double-walled vessels are to reduce the probability of the event of coolant leak and to exclude the outbreak of loss of coolant accident. In order to ensure the integrity of both inner reactor vessel and outer guard vessel, the following design features are applied to the pool-type system:

1) there are no attachments or penetrations in the shells and bottom head of both the reactor vessel and the guard vessel;
2) the vessels have the simple geometries of circular cylinders; and
3) the core support structure is attached to the bottom head of the reactor vessel.

4.4.1 Reactor vessel structure and materials

The double-walled vessels, made of austenitic stainless steels, is about 9.9 m in height and 3.6 m in diameter. The thickness of both vessels is 5 cm. The reactor

vessel and its cover constitute the primary coolant boundary that envelopes and supports the core, reactor internals, coolant, control assemblies, shutdown assemblies, a barrel, steam generators and other components, as shown in Figure 4.6. The reactor vessel hangs from a support ledge, and the head is bolted to this structure with a leak-tight gasket. The core is located on the top of a core support structure hung from the reactor vessel. Assemblies are slotted into positioning holes in the core support structure (Waltar and Reynolds, 1980). The reactor vessel is designed to accommodate high static loads at design temperatures and to minimize the dead load deflections of the reactor cover. It is also important to ensure the uniform radial thermal expansion of the reactor vessel about the vertical center of the entire reactor structure.

The guard vessel provides the secondary containment for the primary LBE coolant in the unlikely event that the reactor vessel has a leak. The gap between the two vessels are decided as wide enough to accommodate electric heating elements for the LBE melting during the initial start-up and the in-service inspection sensors and narrow enough to limit the coolant leak from the reactor vessel down to the acceptable level. The coolant level should be high enough to allow convective cooling from the core to the steam generators. The outer surface of the guard vessel is passively cooled by the RVACS system during accident conditions.

The cover gas control system located above the reactor module controls the oxygen concentration in LBE for the corrosion control. In addition, this system removes toxic gases including Po gas from the primary containment space (Hwang et al., 2008a; Hwang et al., 2008b; Nam et al., 2008).

4.4.2 Three-dimensional seismic isolation

Since LBE is a dense and heavy material, the major challenge in system structural design is to survive a seismic event and provide adequate safe shutdown after earthquake events. The reactor module employs a passive type of seismic isolators in order to achieve this goal (Yoo et al., 2000). The seismic design is based on the earthquake of 0.5g zero-period acceleration for the safe shutdown earthquake. Three-dimensional (3D) isolators are designed to reduce seismic acceleration responses in both vertical and horizontal directions, whereas two-dimensional isolators only work in the horizontal direction. A preliminary design is to float the entire reactor building from land with a 3D seismic isolation system. Figure 4.10 shows the isolation system that combines two-dimensional isolators using horizontal laminated rubber bearing (LRB) with a vertical isolation device, which uses a series of disc (Belleville) springs to provide seismic isolation in all three dimensions.

This system will ensure that the rigid body motion of the reactor building during the earthquake will not affect the reactor building. The space between the intermediate and upper reactor mats is used for the installation, inspection, and maintenance of the isolators. The application of 3D isolators results in the reduction of the horizontal floor acceleration by the reactor vessel, the reactor internals, and other components within the reactor system. Thus, the thickness of reactor vessel cover can be reduced and the relative motions between the control assemblies and the fuel assemblies can be minimized.

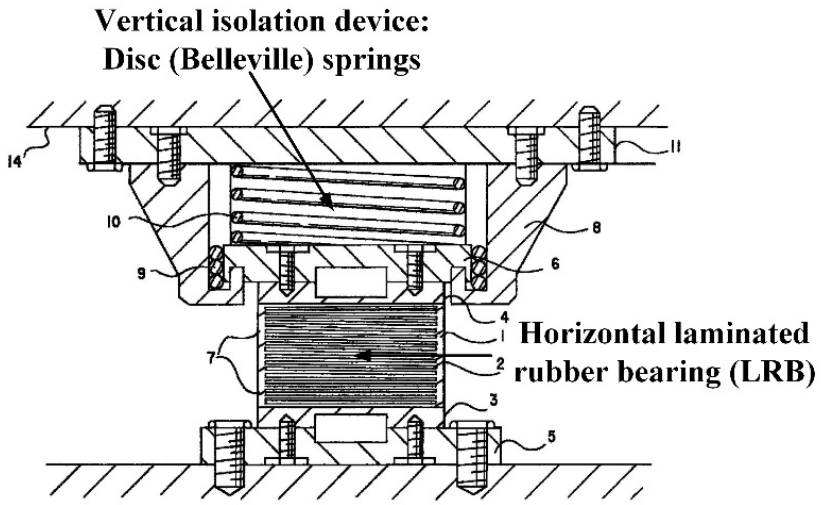

Figure 4.10 3D seismic base isolation bearing unit, adopted from (Yoo et al., 1999)

Chapter 5 Experimental Setup and Test Results

In this chapter, the integral behaviors of passive LBE-cooled systems are investigated experimentally: firstly, the natural circulation tests of LBE in loop configuration is conducted. As a test bed, HELIOS loop is utilized. By changing core power ratings, several sets of natural circulation cases in steady state are produced. In addition to the experimental data generation, system operation practices are also achieved in a rather simple geometry.

Secondly, a pool-type down-scale research facility PILLAR is designed and constructed from a specific reactor concept, URANUS, as designed in Chapter 4. Similar to the HELIOS case, several steady-state natural circulation test results are brought out. Furthermore, since the power level change leads to the variation of natural circulation mass flow rate and temperature distribution in a passive LBE-cooled system, the transient tests are carried out by giving instantaneous changes in the core power rating. In addition to the core power maneuvering, the secondary side condition in terms of mass flow rate is designated to another independent variable to see the effect of heat sink condition change on the primary natural circulation flow and heat transfer rate.

5.1 LBE loop natural circulation experiments[3]

5.1.1 Experimental setup of LBE loop facility: HELIOS

5.1.1.1 Facility descriptions

HELIOS is an integral test facility at SNU (Jeong, 2006) which was originally designed and built to validate the operation capability and safety characteristics of a prototypic LBE-cooled dedicated burner (high-level nuclear waste transmutation reactor), PEACER-300 (Hwang et al., 2000). Scaling ratios for thermal power and height were selected to be 5000:1 and 1:1 on its design, respectively, so that its maximum core power given by electrical heater rods is 60.0 kW and the total height of the facility is about 12 m. In addition to the height conservation, total pressure loss coefficient is conserved to have similar hydraulic loss aspects in natural circulation (Jeong, 2006). With the thermal power reduction and height conservation, flow area reduction is inevitable and therefore friction loss coefficients are dramatically affected by hydraulic diameter change. To accomplish total pressure loss coefficient conservation, some hydrodynamic components in which form loss occurs, such as gate valves,

[3] This section has been written based on the following journal paper: Yong-Hoon Shin et al., "Experimental studies and computational benchmark on heavy liquid metal natural circulation in a full height-scale test loop for small modular reactors," Nuclear Engineering and design, 316, 26-37, 2017.

are installed.

The loop is capable of not only thermal-hydraulic experiments but also materials corrosion tests in LBE flow conditions (Jeong et al., 2006; Lim et al., 2007). Especially, its conservation of height enables it to be used for the investigation of natural circulation capability in SMRs without reactor coolant pumps because its thermal center difference, defined by the distance between the center of heat source (mock-up core) and that of heat sink (heat exchanger) in height direction, is about 7.4 m. Hence, natural circulation experimental data produced with HELIOS can be utilized for the validation of safe operation under natural circulation in the new LBE-cooled SMR concepts as well as in the prototypic reactor. The schematic diagram and picture of the loop are depicted as Figure 5.1.

In HELIOS, two main fluid systems simulate the primary and secondary sides of the prototypic reactor; each system adopts working fluids as LBE and a single-phase, high flashing-point heat transfer oil (Dowtherm© RP), respectively. In virtue of the thermal oil's high boiling point (360 °C) at atmospheric pressure, the secondary side can be operated without any pressurization means.

The primary loop is arranged with mock-up core, expansion tank, mechanical pump, heat exchanger (shell side), and other hydrodynamic elements such as tee-junctions, gate valves, elbows and straight piping with 49.5 mm inner diameter (ANSI SCH 80 2'' pipe) connecting between components. Each component is fabricated from 316L stainless steel. By accepting widely used terminologies on hot leg and cold leg in a nuclear power

plant system, some parts of the primary loop are referred to as hot leg and cold leg. The hot leg is designated as a flow path from mock-up core outlet to heat exchanger inlet; in contrast, the cold leg is assigned to a path from heat exchanger outlet to mockup core inlet. The detailed design and exact dimensions of the components can be found in a report published by the OECD Nuclear Energy Agency (OECD Nuclear Energy Agency, 2012).

For thermal-hydraulic experiments, HELIOS can be operated in two modes, either forced circulation or natural circulation, by selecting flow paths between the heat exchanger and the mockup core; one is connected to the mechanical pump and the other one bypasses it, as shown in Figure 5.1. In natural circulation tests, the pump was bypassed to throughout this thesis study.

Due to a large surface area of the system compared to its volume, the outer surface of HELIOS components is enclosed by local surface heaters and thermal insulation to compensate heat loss to the environment. Hence, these local heaters are actively regulated during most of natural circulation operations as well as in pre-test stages when LBE is being filled up to the top of loop after increasing system temperature above the LBE melting.

The total inventory of LBE is stored in a LBE storage tank located below the loop when the system is not in operation. LBE is melted by heaters on the surface of the tank and is purged with the mixture gas of 4% hydrogen and argon balance to remove dissolved oxygen until operation condition is established.

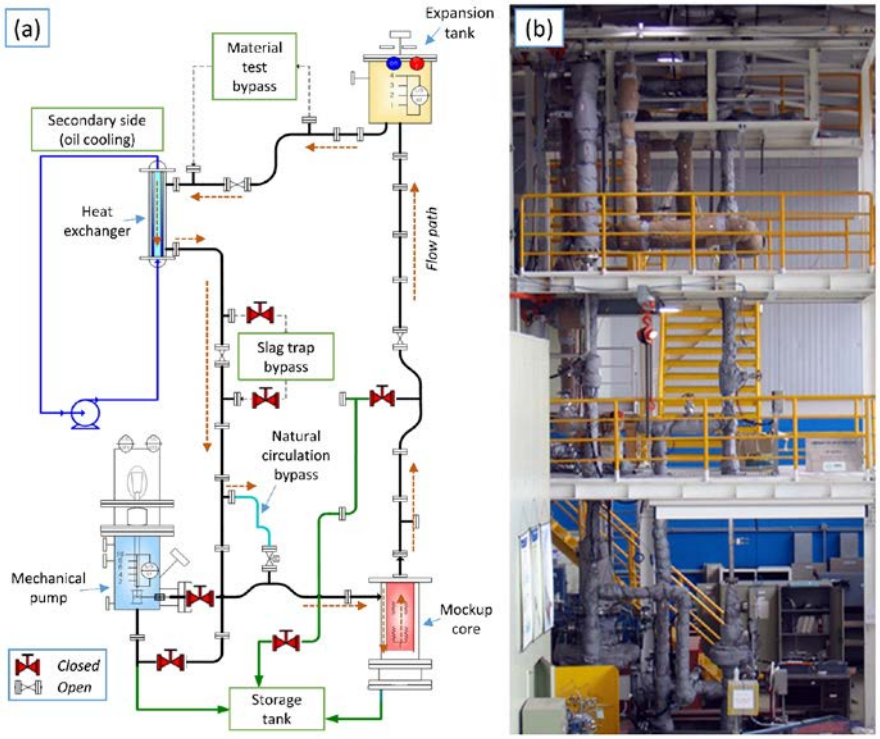

Figure 5.1 (a) System schematic diagram and (b) front-view picture of HELIOS thermal-hydraulic test loop

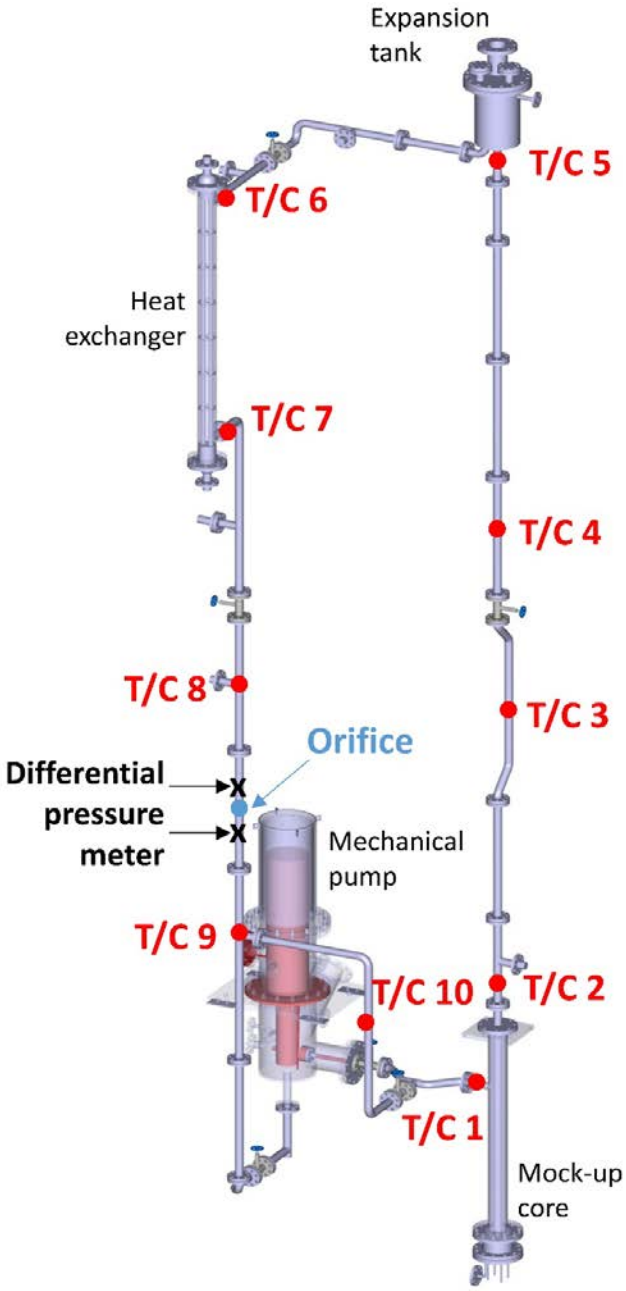

Figure 5.2 Three-dimensional configuration of HELIOS constituent components and key instrumentation system

5.1.1.2 Instrumentation system and uncertainty analysis

In natural circulation experimental campaigns, two thermal-hydraulic parameters of a working fluid are of primary interest: temperature and mass flow rate. For the temperature measurements, Type K thermocouples, which are broadly used in industry and experimental facilities and can be applied to wide temperature range with relatively small error, were selected and installed through the piping for fluid temperature measurement both in primary and secondary fluids in HELIOS. Among various methods to measure mass flow rate of a fluid, pressure drop measurement was used to obtain LBE mass flow rate. For the measurements of secondary side oil flow rate, a turbine flowmeter was used.

The uncertainties in measurements were estimated in terms of the combined standard uncertainty which is the root-mean-square of the systematic standard uncertainty and random standard uncertainty of the mean according to the Performance Test Code (PTC) written by the American Society of Mechanical Engineers (ASME, 2005). For the calculation of systematic standard uncertainty, annually performed calibration data and sensor specification sheets given by manufacturer were used. Expanded uncertainty is reported with a 95% confidence level.

The locations of each Type K thermocouples are depicted as Figure 5.2 and are designated in terms of accumulated length, which is defined by the path length measured from the mock-up core inlet to a certain point, as listed in Table 5.1. The secondary fluid temperatures are measured from the oil inlet and

outlet. The total systematic error of the thermocouples was reported as about ±1.0 K in a temperature range from 200 to 1000 °C by the manufacturer. The maximum expanded uncertainty of measurement by thermocouples in HELIOS was estimated to be ±2.2 K.

In order to make use of increased pressure loss on LBE mass flow rate measurement, an orifice is located in the middle of cold leg and a differential pressure transducer (Rosemount 3051 CD3A) with capillary probes measures the pressure drop over the orifice. The locations of differential pressure measurement are also shown in Figure 5.2. It shows total systematic error in terms of differential pressure as ±0.065% in the full range of 0.8 bar and the maximum expanded uncertainty of measurement by the transducer was estimated to be ±176.8 Pa. The orifice produces pressure loss with sudden area change. The necessity of orifice is due to the fact that the flow rate of natural convection is relatively low compared to that of forced circulation. The pressure drop is proportional to the square of mass flow rate. With the orifice, the small pressure loss can be accurately measured. The conversion equation from measured differential pressure to mass flow rate was produced by calibration test and formulated into a correlation in a previous study (Cho et al., 2011). The error in flow rate measurement has been derived from the correlation and the maximum expanded uncertainty was computed to be ±0.096 kg/s.

A turbine flowmeter (EKFM Industry KT-100-F-F) has been used to measure the secondary side oil flow rate. Its accuracy was given to be ±0.5% of full scale and it is estimated that its maximum expanded uncertainty is ±0.40 L/min. As the flowmeter directly measures volumetric flow rate instead of mass

flow rate, it is required to multiply the oil density at the measurement temperature to obtain mass flow rates. Considering this, the maximum expanded uncertainty of oil mass flow rate measurement was estimated to be ±0.0065 kg/s.

Table 5.1 Thermocouple locations on HELIOS main loop in terms of accumulated length along flow path

T/C No.	Description/position	Accumulated length along flow path (m)
T/C 1	Mock-up core inlet	0.00
T/C 2	Mock-up core outlet	3.72
T/C 3	Hot leg (1)	6.54
T/C 4	Hot leg (2)	9.47
T/C 5	Expansion tank inlet	10.88
T/C 6	Heat exchanger inlet	14.32
T/C 7	Heat exchanger outlet	16.52
T/C 8	Cold leg (1)	19.23
T/C 9	Cold leg (2)	21.42
T/C 10	Cold leg (3); in natural circulation bypass	22.65

5.1.2 HELIOS experiment procedure and LBE loop natural circulation experimental conditions

Non-isothermal LBE natural circulation experiments were performed in HELIOS facility. Well-defined steady-state, adiabatic experiments were conducted and the results were used for the code benchmark of MARS-LBE while some of the results were utilized in an international benchmark program called LACANES (OECD Nuclear Energy Agency, 2012). In order to generate the adiabatic conditions, heat loss through the loop surface was compensated by the local surface heaters.

5.1.2.1 Experiment procedure

HELIOS has to be properly configured to perform natural circulation experiments with the mechanical pump bypassed. To prepare for a steady-state test campaign, the main loop of HELIOS should be filled with LBE, which normally stored in the storage tank when not operated. In the meantime, the local surface heaters on the main loop are activated to maintain temperature at any point over 200-250 °C. After the preheating condition is satisfied, LBE is transferred from the storage tank to the main loop by pressure exerted by the injection of high-purity argon gas or the mixture gas of 4% hydrogen with argon balance. The main loop and the storage tank are isolated after about 1.9 tons of LBE being transferred.

When a hot standby condition is stabilized, all local surface heaters are turned off, and main heater rods in the mock-up core are activated to a specific power rating while the secondary side oil pump is set to a specific flow rate. With these manipulations, natural circulation flow is generated by energy displacements from heat source to heat sink and temperature distribution is also changed until the system reaches first steady state.

Considering the generation of well-defined experimental data for code benchmark, any uncertainties which can affect simulation results must be minimized. In HELIOS, there is no instrumentation system for measuring heat loss, so the uncertainties given by heat loss are inevitable. Furthermore, strictly speaking, ideal adiabatic conditions would not be achievable by nature. Nevertheless, a nearly adiabatic condition can be achieved by compensating heat dissipation to the environment with the surface heaters.

In this regard, heat compensation is made in several steps as follows: firstly, the amount of heat loss over each section defined by a region between two adjacent thermocouples, for example, T/C 1 – T/C 2, T/C 2 – T/C 3, and so on, is estimated from temperature distribution along the main loop with measured mass flow rate at a given state and heat capacity of LBE at a given temperature. Secondly, electric power ratings equivalent to the estimated heat loss over sections are supplied to local surface heaters. Followed by heat addition to the system, temperature transients are expected to take place. The local surface heaters are tuned by trial-and-error until individual temperature measurements in the hot leg and cold leg are respectively in close ranges each other, and the mock-up core power rating and the heat withdrawn by the

secondary side oil are in balance. The total experimental procedures for generating well-defined experiment results are summarized in Table 5.2.

Table 5.2 Natural circulation test procedure to generate well-defined test results in HELIOS

No.	Procedure	Detail	
1	LBE filling to main loop	1.1.	Local surface heaters are turned on to make main loop temperature 200-250 °C.
		1.2.	LBE is transferred to the main loop by Ar (+4% H_2) gas pressure.
		1.3.	Main loop and LBE storage tank are isolated.
2	Natural circulation test start	2.1.	Local surface heaters are turned off and main heater is activated to a given power.
		2.2.	Secondary side flow is generated by oil side pump.
3	First natural circulation steady state with heat loss	3.1.	First equilibrium is reached after temperature and mass flow transients with local surface heater off.
4	Heat compensation to reach adiabatic condition	4.1.	Local surface heaters are turned to compensate heat loss considering temperature drop, mass flow rate, and heat capacity.
		4.2.	System temperature distribution is tuned by trial and error.
5	Final adiabatic steady state with heat compensation	5.1.	Cold leg and hot leg temperatures are close in specific ranges, respectively
		5.2.	Primary and secondary loops are in energy balance.

5.1.2.2 Experiment conditions and test matrix

In non-isothermal natural circulation experiments, the amounts of heat given to and withdrawn from a system are important because natural circulation flow is made by energy transfer in principle. In this context, experimental activities done in HELIOS were classified primarily with the total mock-up core power ratings. Following the experimental procedure, a final steady-state, adiabatic condition can be made after heat compensation on the main loop is achieved and heat balance between the mock-up core power rating and heat transferred to the secondary side oil become consistent. In this study, only those results are utilized for the system code benchmark, even though there had been temperature transients and some fine-tuning processes before reaching the final states.

For the experimental conditions on natural circulation, four different total mock-up core power ratings were selected: 9.8, 15.0, 27.0, and 33.6 kW. Each power rating condition was directly chosen as test numbers from NC1.0 to NC4.0. Other than heat source information, the main LBE loop and secondary side oil conditions in final steady states are listed and illustrated in Table 5.3. In NC1.0 and NC2.0 cases, all four electrical heater rods in the mock-up core were in active, while only three rods were activated in the cases NC3.0 and NC4.0.

Table 5.3 Test matrix on adiabatic, non-isothermal natural circulation experiments in HELIOS

ID	Total mock-up core power (kW)	No. of active heater rods	Avg. oil inlet temperature (°C)	Avg. oil mass flow rate (kg/s)	Total experimental time (hr)
NC1.0	9.8	4	99.65	0.374	80
NC2.0	15.0	4	122.63	0.374	70
NC3.0	27.0	3	155.03	0.382	72
NC4.0	33.6	3	167.60	0.390	48

5.1.3 Experimental results on steady-state LBE loop natural circulation

Non-isothermal natural circulation experiments were performed with four different core power ratings. There was no heat compensation in the beginning of each test case and the system finally reached adiabatic steady state by the trial-and-error approach as described in previous sections. Owing to ambient temperature fluctuation within a day, the whole system reacted to it and temperature distribution along the main loop had periodical change. In other words, a strict 'steady' state could not be achieved due to the temperature change. To overcome this, the system had been maintained and observed without any intervention or manipulation in the last 24 hours out of full test history after reaching adiabatic wall boundary conditions.

The well-defined experimental data were generated from the measurements given in 6-7 hours in which the system showed rather moderate temperature fluctuation out of the 24-hour observation. In those steady state conditions, the individual temperature measurements in the hot leg and cold leg lied in 5-7 °C variation, respectively. In Table 5.4, the experimental data are summarized. The average hot leg temperature is a mean of temperatures measured by T/C-2, 3, 4, 5, and T/C-6, and the average cold leg temperature is defined by averaging measurements from T/C-7, 8, 9, 10, and T/C-1. Also, the average temperature difference means the difference between two average temperatures. Temperature distributions along the loop measured in the experiment cases are described with the code benchmark results in Section 6.2.1.

Table 5.4 Adiabatic, non-isothermal, steady-state natural circulation results in HELIOS

No.	Main loop (LBE side)					Secondary loop (oil side)		
	Total core power (kW)	Hot leg temperature (°C)	Cold leg temperature (°C)	Temperature difference (°C)	LBE mass flow rate (kg/s)	Oil inlet temperature (°C)	Oil outlet temperature (°C)	Oil mass flow rate (kg/s)
NC1.0	9.8	273.84	237.32	36.52	1.80	99.65	114.00	0.374
NC2.0	15.0	315.84	266.83	49.01	2.09	122.63	144.33	0.374
NC3.0	27.0	367.63	300.85	66.78	2.74	155.03	187.52	0.382
NC4.0	33.6	394.43	315.31	79.12	2.83	167.60	204.18	0.390

Note: all of the values given above are average values from measurements in each case.

5.2 LBE pool natural circulation experiments

In contrast with pump-driven systems, the mass flow rate of primary coolant varies with core power rating in passive systems like URANUS. In this situation, a question may arise that the system could be maneuvered properly in power transients because reactor power output changes as control rod moves. In order to investigate the fast load-following capability of a passive pool-type LBE system, a pool-type integral experimental facility was designed and constructed by using thermal-hydraulic scaling analysis. The name of facility is PILLAR, which stands for Pool-type Integral Leading test facility for Lead-Alloy-cooled small modular Reactor. PILLAR features the conservation of height as same as the prototypic reactor URANUS while its radial diameter is reduced with a factor of about 1/14. In this section, a detailed design procedure using thermal-hydraulic scaling method, the area-average method, experimental setup and procedure, and experimental results are elaborated.

5.2.1 Design of LBE pool facility: PILLAR

This section deals with the scaling analysis, design, and specifications of PILLAR. Since there have been many studies on design procedures with scaling analysis, the selection of proper design requires a literature survey. After a suitable method is chosen, some mathematical formulations are to be constructed. Finally, a detail design is achieved in terms of several important

parameters to be conserved.

5.2.1.1 Design requirements and consideration for PILLAR

As reviewed in Chapter 2.4, several scaling analysis methods for the experiment of natural circulation of liquid metal cooled reactors have been suggested and hence, it is required to apply a suitable method to observe the phenomena of interest. The scaling method for PILLAR was determined by considering experimental requirements, budgetary consideration, and physical limitations.

Firstly, the length scale is designated to be unity, in other words, to have same height scale in the prototype and model. It is because the most important behavior to be validated is LBE natural circulation, as it is strongly dependent upon buoyancy force given by height difference. Therefore, the conservation of height and the height difference of heat source and heat sink would be the easiest way not to distort the behavior. Throughout this, the scale model can simulate the natural circulation capability of prototypic reactor without a distortion in the length scale.

Secondly, In this regard, the flow area of downscale facility must be decreased in terms of volume reduction. However, if flow area is too narrow, then it might lead to an unrealistic simulation with a loop configuration. Furthermore, buying new LBE was restricted with a budgetary limit and about 4 metric tons of the retained liquid metal used for HELIOS were to be used.

Thus, the reduction ratio of flow area where volume reduction occurs is able to be chosen to an extent that it can utilize the retained amount of LBE.

Additionally, mean velocity at the core outlet, which is the reference velocity on the scaling analysis, needs to be greater than 10 cm/s so that flow measurement is viable and the thickness of each physical component should be designated with the consideration of design pressure with 20 bar. The requirements and consideration done before the selection of scaling analysis method is summarized in Table 5.5.

Scaling analysis method is decided regarding the limitations and requirements given above. First, the scaling methods suggested by (Grewal and Gluekler, 1982) and (Weinberg et al., 1990) were excluded due to their lack of actual application and insufficient explanations in nondimensionalization. The methods for the geometrical scaling in all directions (Eguchi et al., 1997; Takeda et al., 1993), which were validated through their own SFR facility described in their work and the E-SCAPE facility in the SCK-CEN (Van Tichelen et al., 2015), were ruled out as all the scaling ratios in width, length, and height to be the same and the height scale criterion designated to be unity cannot be met. The method suggested by (Chen, 2015) is not available because it is about the experiments with water replacing LBE.

Hence, the scaling ratios in longitudinal directions (x- and y-directions) need to be differentiated from the height scale (z-direction) to meet the height scale requirements and it leads to the choice of area-average method (Ishii and Kataoka, 1984; Ishii et al., 1998) being the most proper one. As aforementioned, this method can be applicable to liquid metal environments since it had been

applied to the design of HELIOS and STELLA-1 (Hong and Lee, 2012; Jeong, 2006). A shortcoming to this method is that it is impossible to simulate some local phenomena because governing equations are constructed through the area averaging. Therefore, in the design utilizing the area-average method, the local phenomena is limited to that of the facility, not to that of the prototypic reactor.

Table 5.5 PILLAR design requirements and criteria for scaling analysis

Criteria	Facility limitations/requirements
Length scale	1:1
Flow area scale	Limited by the total amount of LBE (< 1/100)
Total LBE mass	< 4.0 ton
Core outlet flow velocity	> 10 cm/s
Design pressure	20 bar (2.0 MPa)

5.2.1.2 Nondimensionalization of governing equations in area-average scaling method

In this section, the governing equations are expressed in nondimensionalized forms by following the area-average method. To do so, the following assumptions are applied:

1) The working fluid is incompressible as its density does not vary with applied pressure or it exists in a system that pressure upon it does not change largely. In addition, the fluid density change is almost linear in a given temperature range so that the buoyancy term in momentum conservation equation is treated by the Boussinesq approximation;
2) The thermophysical properties of working fluid does not change by temperature and is the same in any flow direction, in other words, isotropic; and
3) Heat generated in the solid heat source only conducts in the perpendicular direction to the main flow direction, the transverse direction, and axial heat conduction in the working fluid is neglected.

The area-average method utilizes five equations on mass conservation, momentum conservation, energy conservation in solid and fluid, and boundary condition between fluid and solid media. Furthermore, the Boussinesq approximation is applied to the momentum change term by buoyancy in the

momentum conservation equation and the pressure loss term only consists of momentum loss by friction and form loss. Each term in mass and momentum conservation equations is integrated over flow area and the other equations are given in differential form, as shown in from Eqn. (5.1) to Eqn. (5.5). When it comes to a velocity term (u_i) is included, the term is expressed with the reference velocity (u_r) with Eqn. (5.1). The meaning and use of each of parameters hereafter are defined in Nomenclature.

$$u_i = \frac{a_0}{a_i} u_r \tag{5.1}$$

$$\rho \frac{du_r}{dt} \sum_i \frac{a_0}{a_i} l_i = \rho g \beta \Delta T_0 l_h - \frac{\rho {u_r}^2}{2} \sum_i \left(\frac{l}{d} f + K \right)_i \left(\frac{a_0}{a_i} \right)^2 \tag{5.2}$$

$$\rho C_p \left(\frac{\partial T}{\partial t} + u \frac{\partial T}{\partial z} \right)_i = \frac{4h_i}{d_i} (T_s - T)_i \tag{5.3}$$

$$\left(\rho_s C_{ps} \frac{\partial T_s}{\partial t} \right)_i + \left(k_s \nabla^2 T_s \right)_i - \dot{q}_{si} = 0 \tag{5.4}$$

$$-k_{si} \frac{\partial T_{si}}{\partial y} = h_i (T_s - T)_i \tag{5.5}$$

The following Eqns. (5.7) to (5.11) are in nondimensional forms by defining dimensionless parameter as shown in Eqn. (5.6). In these formulations, each term can be more simplified by designating a specific component in the system as a reference, expressed with the subscript *r*; in this dissertation, the values from the core, which works as heat sources in the prototype and the scale facility, are appointed as reference constants with the subscript 0. In this situation, the

nondimensional area A_r is given by $A_r = a_r/a_0$ and each formula can be simplified further with $A_r = 1$ as a_r and a_0 are to be the same.

$$\begin{array}{llll} U_i = u_i / u_0 & U_r = u_r / u_0 & & \\ L_i = l_i / l_0 & L_h = l_h / l_0 & Y = y/\delta & Z = z / l_0 \\ \tau = tu_0 / l_0 & \theta = \Delta T / \Delta T_0 & & \\ A_i = a_i / a_0 & \nabla^{*2} = \delta^2 \nabla^2 & & \end{array} \tag{5.6}$$

$$U_i = \frac{U_r}{A_i} \tag{5.7}$$

$$\frac{dU_r}{d\tau}\sum_i \frac{L_i}{A_i} = \mathrm{Ri}(\theta_h - \theta_c)L_h - \frac{U_r^{\,2}}{2}\sum_i F_i \frac{1}{A_i^{\,2}} \tag{5.8}$$

$$\frac{\partial \theta_i}{\partial \tau} + \frac{U_r}{A_i}\frac{\partial \theta_i}{\partial Z} = \mathrm{St}_i(\theta_{si} - \theta_i) \tag{5.9}$$

$$\frac{\partial \theta_{si}}{\partial \tau} + \mathrm{Ti}_i \nabla_i^{*2}\theta_{si} - Q_{si} = 0 \tag{5.10}$$

$$\frac{\partial \theta_{si}}{\partial Y_i} = \mathrm{Bi}_i(\theta_{si} - \theta_i) \tag{5.11}$$

Additionally, the hydraulic diameter d_i is related to the flow area a_i and the wetted perimeter ξ_i given as Eqn. (5.12). In addition, the conduction depth δ_i can be defined as the transverse direction area of the solid heat source a_{si} and the wetted perimeter ξ_i as shown in Eqn. (5.13).

$$d_i = \frac{4a_i}{\xi_i} \tag{5.12}$$

$$\delta_i \equiv \frac{a_{si}}{\xi_i} \tag{5.13}$$

The names, physical meanings, and formulae of each of nondimensional parameters shown in the nondimensional equations above are

as follows:

Richardson number	$\mathrm{Ri} \equiv \frac{g\beta\Delta T_0 l_0}{u_0^{\,2}}$	Buoyancy to inertia ratio	(5.14)
Friction number	$F_i \equiv \left(\frac{l}{d} f + K\right)_i$	Friction to inertia ratio	(5.15)
(Modified) Stanton number	$\mathrm{St}_i \equiv \left(\frac{4hl_0}{\rho C_p u_0 d}\right)_i$	Ratio of convective heat transfer from the solid heat source wall to the fluid to convective heat transfer in the flow direction	(5.16)
Time ratio number	$\mathrm{Ti}_i \equiv \left(\frac{\alpha_s}{\delta^2}\frac{l_0}{u_0}\right)_i$	Transport time to conduction time ratio	(5.17)
Biot number	$\mathrm{Bi}_i \equiv \left(\frac{h\delta}{k_s}\right)_i$	Ratio of convective heat transfer from solid heat source wall to the fluid to thermal conductivity in solid heat source	(5.18)
Heat source number	$Q_{si} \equiv \left(\frac{\dot{q}_s l_0}{\rho_s C_{ps} u_0 \Delta T_0}\right)_i$	Ratio of heat source output to energy transfer rate in the flow direction	(5.19)

Accordingly, to obtain the reference temperature difference, ΔT_0, heat generation in the solid heat source and heat transferred to the fluid between the core inlet and outlet are considered as shown in (5.20).

$$\begin{aligned} &\dot{q}_{s0} a_{s0} l_0 = \dot{m} C_p \Delta T_0 = (\rho u_0 a_0) C_p \Delta T_0 \\ &\Rightarrow \Delta T_0 = \frac{\dot{q}_{s0} l_0}{\rho C_p u_0} \frac{a_{s0}}{a_0} \end{aligned} \tag{5.20}$$

Utilizing the reference temperature difference, the core outlet velocity is derived by Eqn. (5.2) at a steady state as in Eqn. (5.21) with vanishing the temporal change term.

$$\rho \frac{du_0}{dt} \sum_i \frac{l_i}{A_i} = 0 = \rho g \beta \Delta T_0 l_h - \frac{\rho u_0^{\,2}}{2} \sum_i \left(\frac{F_i}{A_i} \right)^2$$
$$\Rightarrow 0 = g\beta \frac{\dot{q}_{s0} l_0}{\rho C_p u_0} \frac{a_{s0}}{a_0} l_h - \frac{u_0^{\,2}}{2} \sum_i \left(\frac{F_i}{A_i} \right)^2 \qquad (5.21)$$
$$\Rightarrow u_0 = \left[\beta \frac{\dot{q}_{s0} l_0}{\rho C_p u_0} \frac{a_{s0}}{a_0} l_h \Big/ \frac{1}{2g} \sum_i \left(\frac{F_i}{A_i} \right)^2 \right]^{1/3}$$

5.2.1.3 Similarity requirements in area-average method

In order to make the prototype and model behave in physical equivalence, each term in governing equations must satisfy a criterion given as Eqn. (5.22) with a specific parameter or term expressed by ψ:

$$\psi_R \equiv \frac{\psi_{\text{model}}}{\psi_{\text{prototype}}} = 1. \qquad (5.22)$$

However, not all the ratios of dimensionless numbers can be designated unity and therefore the similitudes of the dimensionless numbers derived from ~~~ should be conserved in which distortion in physical phenomena is minimized as achieved as possible.

Above all, the geometrical similarity is considered. It is the most

fundamental criteria in scaling analysis and defined as dimensionless area ratio given as Eqn. (5.23) and dimensionless length ratio as (5.24) in this method.

$$A_{iR} = \frac{A_{im}}{A_{ip}} = \frac{\left(a_i / a_0\right)_m}{\left(a_i / a_0\right)_p} = 1 \tag{5.23}$$

$$L_{iR} = \frac{\left(l_i / l_0\right)_m}{\left(l_i / l_0\right)_p} = 1 \qquad \left(L_{hR} = \frac{\left(l_h / l_0\right)_m}{\left(l_h / l_0\right)_p} = 1 \right) \tag{5.24}$$

The ideal condition would be the prototype and model are in the geometrical similarity, but it is technically not achievable in most of engineering cases. Hence, in this downscale model, the core, which drives overall behaviors of the system as a heat source, is forced to be in a geometrical similarity while slight geometrical distortions on other components are tolerated. Furthermore, dimensionless length ratio, which include the height difference between the heat source and heat sink, is strictly conserved as unity.

From dynamic similarity, the following Eqn. (5.25) is established:

$$\left(\sum_i F_i / A_i^2 \right)_R = 1. \tag{5.25}$$

If dimensionless areas A_i for all the components are the same between the prototype and the scale model, then this criterion falls in the ratio of gross sum of Friction numbers being unity ($(\sum_i F_i)_R = 1$). In other words, system dynamic behaviors are conserved if the ratios of dimensionless areas in the prototype

and the scale model vary within the kinematic similarity being conserved. Pressure drop criteria are difficult to be matched because total pressure loss in most of downscale models tends to decrease greater than that is needed. Considering the kinematic similarity and the nondimensional area at the same time, the criteria can be met by adding some parts arising pressure drop such as an orifice. As stated, the kinematic similarity criteria can also contribute to mitigate the effect of geometrical similarity distortion.

Successively, the similarity requirements of six nondimensional numbers are considered. As the friction number was already considered by kinematic similarity, the other five nondimensional numbers are covered. In other words, the kinematic similarity which contains the friction number and nondimensional area must be conserved independent of the conservation of other parameters. In order to simplify the equations further, some selected thermophysical properties in both prototype and model are almost the same as shown in Eqn. (5.26).

$$\rho_R = C_{pR} = \beta_R \approx 1 \tag{5.26}$$

Applying this, Eqns. (5.27) to (5.31) are derived from each of nondimensional parameters. If the paramters below become unity then phenomena parametrized by each of terms are conserved in the prototype and the model.

$$\mathrm{Ri}_R = \frac{\Delta T_{0R} l_{0R}}{{u_{0R}}^2} = 1 \tag{5.27}$$

$$\mathrm{St}_{iR} = \frac{h_{iR} l_{0R}}{u_{0R} d_{iR}} = 1 \tag{5.28}$$

$$\mathrm{Bi}_{R} = \frac{h_{iR} \delta_{iR}}{k_{siR}} = 1 \tag{5.29}$$

$$\mathrm{Ti}_{iR} = \frac{\alpha_{s_R} l_{0R}}{{\delta_{iR}}^2 u_{0R}} = 1 \tag{5.30}$$

$$Q_{s0R} = \frac{\dot{q}_{s0R} l_{0R}}{\left(\rho_s C_{ps}\right)_R u_{0R} \Delta T_{0R}} = 1 \tag{5.31}$$

From the heat conservation equation in Eqn. (5.20), the requirements for the thermal output in the prototype and the model can be derived as shown in Eqn. (5.32). This equation suggests that when the ratio of the thermophysical properties of the heat source changes, the flow area scale and the cross-sectional area scale of the solid heat source varies with the heat capacity ratio per unit volume. If the ratio of the heat capacity per unit volume is large, the solid heat source area will be reduced more than the flow area, and in the opposite case, the flow area must be reduced more than the solid heat source area.

$$\begin{aligned} & u_{0R} a_{0R} \Delta T_{0R} = \dot{q}_{s0R} a_{s0R} l_{0R} \\ & \Rightarrow a_{0R} = \dot{q}_{s0R} \frac{l_{0R}}{u_{0R} \Delta T_{0R}} a_{s0R} = \left(\rho_s C_{ps}\right)_R a_{s0R} \end{aligned} \tag{5.32}$$

Meanwhile, the velocity requirement can be independently designated from the similarity in Richardson number given in (5.33):

$$\mathrm{Ri}_{R} = \frac{\Delta T_{0R} l_R}{{u_{0R}}^2} = 1 \Rightarrow u_{0R} = {\Delta T_{0R}}^{1/2} {l_{0R}}^{1/2}. \tag{5.33}$$

Consecutively, Eqns. (5.34) to (5.36) shows the requirements on conduction thickness, the ratio of convective heat transfer coefficients, and hydraulic diameter from the Time ratio number, Biot number, and (Modified) Stanton number. The velocity ratio and thermal conduction thickness are further substituted as obtained in Eqn. (5.33) and (5.34). Through this process, the three parameters are specified as functions of the ratios of thermophysical properties (ρ_s, C_{ps}, k_s, α_s), length scale ratio, or the ratio of temperature difference.

$$\begin{aligned} &\mathrm{Ti}_{iR} = \frac{\alpha_{sR} l_{0R}}{\delta_{iR}^{\ 2} u_{0R}} = 1 \\ &\Rightarrow\ \delta_{iR} = \left(\frac{\alpha_{sR} l_{0R}}{u_{0R}} \right)^{1/2} = \alpha_{sR}^{\ 1/2} l_{0R}^{\ 1/4} \Delta T_{0R}^{\ -1/4} \end{aligned} \tag{5.34}$$

$$\begin{aligned} &\mathrm{Bi}_{iR} = \frac{h_{iR} \delta_{iR}}{k_{siR}} = 1 \\ &\Rightarrow\ h_{iR} = \frac{k_{siR}}{\delta_{iR}} = \left(k_s \rho_s C_{ps} \right)_{iR}^{1/2} l_{0R}^{\ -1/4} \Delta T_{0R}^{\ 1/4} \end{aligned} \tag{5.35}$$

$$\begin{aligned} &\mathrm{St}_{iR} = \frac{h_{iR} l_{0R}}{u_{0R} d_{iR}} = 1 \\ &\Rightarrow\ d_{iR} = \frac{h_{iR} l_{0R}}{u_{0R}} = h_{iR} l_{0R}^{\ 1/2} \Delta T_{0R}^{\ -1/2} \\ &\qquad = \left(k_s \rho_s C_{ps} \right)_{iR}^{1/2} l_{0R}^{\ 1/4} \Delta T_{0R}^{\ -1/4} \end{aligned} \tag{5.36}$$

The equations above are derived for a case that all of each nondimensional parameter are unity, in other words. In this situation, if the similarities of Time ratio number, Biot number, and heat source number are conserved, then that of (modified) Stanton number is automatically obtained, as shown in Eqn. (5.37), by utilizing the hydraulic diameter and the thermal conduction thickness ratios

given in Eqn. (5.12) and (5.13), respectively, and flow area scale and solid heat source area scale as designated by Eqn. (5.33).

$$\begin{aligned}
\mathrm{St}_{iR} &= \frac{h_{iR} l_{0R}}{u_{0R} d_{iR}} = \frac{\alpha_{sR} l_{0R}}{\delta_{iR}{}^2 u_{0R}} \frac{h_{iR} \delta_{iR}}{k_{siR}} \frac{\delta_{iR}{}^2 k_{siR}}{\alpha_{sR} d_{iR} \delta_{iR}} \\
&= \mathrm{Ti}_i \mathrm{Bi}_i \left(\rho_s C_{ps}\right)_R \frac{\delta_{iR}}{d_{iR}} \\
&= \mathrm{Ti}_i \mathrm{Bi}_i \left(\rho_s C_{ps}\right)_R \frac{\alpha_{s0R} / \xi_{0R}}{a_{0R} / \xi_{0R}} \\
&= \mathrm{Ti}_i \mathrm{Bi}_i \frac{\left(\rho_s C_{ps}\right)_R \alpha_{s0R}}{a_{0R}} \\
&= \mathrm{Ti}_i \mathrm{Bi}_i = 1
\end{aligned} \tag{5.37}$$

However, as shown in Eqn. (5.35) for Biot number, the similarity in Biot number is hard to be met between the prototype and the model because it includes convective heat transfer coefficient (Ishii and Kataoka, 1984), which is generally given by the Nusselt number (Nu) in Eqn. (5.38):

$$\mathrm{Nu} = \frac{hd}{k} \Rightarrow h = \frac{\mathrm{Nu} \cdot k}{d}. \tag{5.38}$$

Furthermore, Nu is given as a function of Reynolds number (Re) and Prandtl number (Pr) and is dependent upon the characteristics of fluid, heat transfer condition, flow regime, etc. For LBE in turbulent flow regime, Seban-Shimazaki correlation shown in Eqn. (5.39) is widely used (Seban and Shimazaki, 1949). Hereafter, the fluid is assumed to be turbulent for all time in an engineering point of view, since most of LBE flow has large Re enough to

be turbulent and it will not be laminar in both the prototypic reactor and the scale model.

$$\begin{aligned} \mathrm{Nu} &= f(\mathrm{Re},\mathrm{Pr}) = 5.0 + 0.025\left(\mathrm{RePr}\right)^{0.8} \\ &= 5.0 + 0.025\mathrm{Pe}^{0.8} \end{aligned} \tag{5.39}$$

As the prototype and the scale model utilizes the same working fluid, Pr is almost the same and Nu strongly depends on Re. Furthermore, Re is a function of flow velocity and hydraulic diameter; it is limited to designate the value of convective heat transfer coefficients in the prototype and the scale model with the Biot number and (modified) Stanton number being conserved at the same time. Hence, it is inevitable to have a distortion from the Biot number and (modified) Stanton number and it leads to an impact in terms of the distortion in hydraulic diameter and convective heat transfer coefficient.

Finally, volumetric power density can be derived as shown in Eqn. (5.40) from Eqn. (5.31). Utilizing this and Eqn. (5.20) on heat conservation, the requirement on heat source power is obtained as in Eqn. (5.41). Applying this formula, it can be seen that the ratio of core power outputs is given as a function of the flow area scale, the length scale, and the reduction of the temperature differences as shown in Eqn. (5.40).

$$\begin{aligned} & Q_{s0R} = \frac{\dot{q}_{s0R} l_{0R}}{\rho_{sR} C_{psR} u_{0R} \Delta T_{0R}} = 1 \\ & \Rightarrow \ \dot{q}_{s0R} = \frac{u_{0R} \Delta T_{0R}}{l_{0R}} \left(\rho_s C_{ps}\right)_R = \left(\rho_s C_{ps}\right)_R l_{0R}{}^{-1/2} \Delta T_{0R}{}^{3/2} \end{aligned} \tag{5.40}$$

$$
\begin{aligned}
& P_0 = \dot{q}_{s0} a_{s0} l_0 \\
\Rightarrow\ & P_{0R} = \dot{q}_{s0R} l_{0R} a_{s0R} = \left(\rho_s C_{ps}\right)_R \Delta T_{0R}{}^{3/2} l_{0R}{}^{1/2} a_{s0R} \\
& \quad = a_{0R} l_{0R}{}^{1/2} \Delta T_{0R}{}^{3/2}
\end{aligned}
\tag{5.41}
$$

As explained that the similarity distortion in Biot number and the (modified) Stanton number is inevitable, the similarity of nondimensional numbers parametrizing heat transfer should be conserved by securing the similarity of the Time ratio number and the heat source number. Both nuclear fuel rods in the prototypic reactor and heater rods in the scale facility are produced and operated in cylindrical forms and determined as an appropriated numbers, which can contribute to the similarity of the two nondimensional numbers. Since both the diameter ratio and the thermal conduction thickness ratio are in length dimensions, the diameter ratio between nuclear fuel rods and heater rods can be determined by Eqn. (5.42) from the similairity of the Time ratio number in Eqn. (5.34).

$$
d_{rod,R} = \delta_{0R} = \alpha_{sR}{}^{1/2} l_{0R}{}^{1/4} \Delta T_{0R}{}^{-1/4} \tag{5.42}
$$

From Eqn. (5.32), the relationship between the number of fuel rods and the number of heater rods can be derived as shown in the following Eqn. (5.43):

$$
\begin{aligned}
a_{s0R} &= \frac{a_{0R}}{\left(\rho_s C_{ps}\right)_R} \\
&= \frac{N_{rod,m}}{N_{rod,p}} \frac{\left(\pi/4\right) d_{rod,m}{}^2}{\left(\pi/4\right) d_{rod,p}{}^2} = N_{rod,R} d_{rod,R}{}^2 \\
N_{rod,R} &= \frac{a_{0R}}{\delta_{0R}{}^2 \left(\rho_s C_{ps}\right)_R} = \left(\frac{\Delta T_{0R}{}^{1/4}}{\alpha_{sR}{}^{1/2} l_{0R}{}^{1/4}} \right)^2 \frac{a_{0R}}{\left(\rho_s C_{ps}\right)_{0R}} \\
&= k_{sR}{}^{-1} l_{0R}{}^{-1/2} \Delta T_{0R}{}^{1/2} a_{0R}
\end{aligned}
\quad . \qquad (5.43)
$$

5.2.1.4 Comparison of thermophysical properties of solids

The similarity requirements derived in the former Chapter 5.2.1.3 are shown to be expressed by the ratios of thermophysical properties between the prototype and the scale model. Therefore, it is necessary to compare the solid properties to be used in the prototype and scale model. In the case of the prototype, the solid materials include structural materials and nuclear fuel, while those are comprised of structural materials and the heater rods in the core, which simulate the nuclear fuel. In particular, to maintain the similarity between the time ratio number and the heat source number, it is necessary to confirm the difference in properties between the heater rod and the fuel because the heat source characteristics in the prototype and the scale model must be matched. The physical properties required for the scaling analysis are density (ρ_s), thermal conductivity (k_s), and isobaric heat capacity (C_{ps}). In addition to these properties, the thermal diffusivity (α_s) and the isobaric heat capacity per unit volume ($\rho_s C_{ps}$), which can be calculated as a function of these three properties are identified.

The nuclear fuel adopted for the prototypic reactor is UO_2, as indicated throughout Chapter 4. In reality, its thermophysical properties are affected by neutron irradiation and temperature distribution (Popov and Carbajo, 2000). In this study, it is assumed that it is a fresh fuel, which has not gone through neutron irradiation, and has a small porosity so that its actual density is given in 95% of theoretical density.

Meanwhile, there are various suppliers who produce diverse types of heater rods that simulate the nuclear fuel. In other words, the physical properties would be affected by the selection of the heater rods. Therefore, it was suggested to determine the material properties based on a specific design specification in the scaling analysis and design.

Although there are many candidate structural materials to be used for the scale facility, only selected materials are to be covered in this study (Hong and Lee, 2012). It can be seen from Table 5.6, which summarizes the thermophysical properties of those materials, that some of the metal candidates (stainless steel Type 304 and 316L, nichrome) have similar properties each other so that the structural materials of the prototype and the scale facility are approximated to have almost the same properties. They are also evaluated to have higher thermal conductivity, heat capacity, and thermal diffusivity compared to UO_2 fuel.

The heater rods are comprised of sheath, thermal insulation, heating element, and core constituting the radial center of each rod. Among these elements, the use of ceramic materials such as thermal insulation and the radial core make the heater rods have more similar heat transfer characteristics to UO_2

than metal. However, since the difference in properties is not negligible, it must be considered in the design.

Table 5.6 Comparison of thermosphysical properties of nuclear fuel, heater rods, and structural materials (Hong and Lee, 2012; Popov and Carbajo, 2000)

Material	Property (unit)	Temperature (K)			
		300	400	600	800
SS ANSI 304 (Hong and Lee, 2012)	ρ_s* (kg/m^3)	7900	-	-	-
	C_{ps} (J/kg K)	-	515	557	582
	k_s (W/m K)	-	16.6	19.8	22.6
	$\rho_s C_{ps}$ (J/m^3 K)	-	4.07E+06	4.40E+06	4.60E+06
	α_s (m^2/s)	-	4.08E-06	4.50E-06	4.92E-06
SS ANSI 316L (Hong and Lee, 2012)	ρ_s* (kg/m^3)	8238	-	-	-
	C_{ps} (J/kg K)	-	504	550	576
	k_s (W/m K)	-	15.2	18.3	21.3
	$\rho_s C_{ps}$ (J/m^3 K)	-	4.15E+06	4.53E+06	4.75E+06
	α_s (m2/s)	-	3.66E-06	4.04E-06	4.49E-06
Nichrome (Hong and Lee, 2012)	ρ_s* (kg/m^3)	8400			
	C_{ps} (J/kg K)	-	480	525	545
	k_s (W/m K)	-	14	16	21
	$\rho_s C_{ps}$ (J/m^3 K)	-	4.03E+06	4.41E+06	4.58E+06
	α_s (m^2/s)	-	3.47E-06	3.63E-06	4.59E-06

* *Density at 300 K is used as a reference in calculation of thermal diffusivity and isothermal heat capacity per unit volume.*
*** The physical properties of the heater rods are obtained through individual contact with the manufacturer. Thermal conductivity, thermal capacity per unit volume, thermal diffusivity coefficient are calculated from an arbitrary design and only the physical properties at 800K, operating condition, are considered.*

Table 5.6 Comparison of thermosphysical properties of nuclear fuel, heater rods, and structural materials (Hong and Lee, 2012; Popov and Carbajo, 2000) (contd.)

Material	Property (unit)	Temperature (K)			
		300	400	600	800
Heater rod**	ρ_s* (kg/m^3)	-	-	-	-
	C_{ps} (J/kg K)	-	-	-	-
	k_s (W/m K)	-	-	-	4.70
	$\rho_s C_{ps}$ (J/m^3 K)	-	-	-	3.82E+06
	α_s (m^2/s)	-	-	-	1.23E-06
UO_2 (Popov and Carbajo, 2000)	ρ_s* (kg/m^3)	10413	-	-	-
	C_{ps} (J/kg K)	-	264.3	293.0	305.8
	k_s (W/m K)	-	6.58	5.14	4.17
	$\rho_s C_{ps}$ (J/m^3 K)	-	2.75E+06	3.05E+06	3.18E+06
	α_s (m^2/s)	-	2.39E-06	1.68E-06	1.31E-06

** Density at 300 K is used as a reference in calculation of thermal diffusivity and isothermal heat capacity per unit volume.*
*** The physical properties of the heater rods are obtained through individual contact with the manufacturer. Thermal conductivity, thermal capacity per unit volume, thermal diffusivity coefficient are calculated from an arbitrary design and only the physical properties at 800K, operating condition, are considered.*

5.2.1.5 PILLAR scale design using thermal-hydraulic similarity

This section describes the detail design of PILLAR by using the area-average scaling analysis method. Parameters related to the core power and thermal conditions are designated to be key parameters to the scale design among many parameters, in order to conserve the heat transfer characteristics between the prototype and the scale model as much as possible. Therefore, the thermophysical properties of the fuel rods and electrical heater rods are conserved as similar as possible between the prototype and the model. Other requirements are considered afterwards, independently.

The PILLAR scale design was determined as follows: firstly, the length ratio is chosen to be unity as in the basic design criteria. In addition, the similarities of the Time ratio number and the Biot number is not strictly conserved because it is difficult to be matched between the systems. In this case, most of parameters are rearranged as shown in Eqn. (5.44), but there is no need to have similarity in the parameters that are derived from the Time ratio number as described by Eqn. (5.45):

$$l_{0R}=1 \Rightarrow \begin{cases} \dot{q}_{s0R}=\left(\rho_s C_{ps}\right)_R \Delta T_{0R}{}^{3/2} \\ P_{0R}=a_{0R}\Delta T_{0R}{}^{3/2} \\ N_{rod,R}=k_{sR}{}^{-1}\Delta T_{0R}{}^{1/2}a_{0R} \\ a_{s0R}=N_{rod,R}\alpha_{sR}\Delta T_{0R}{}^{-1/2} \end{cases}, \text{ and} \tag{5.44}$$

$$d_{rod,R}=\alpha_{sR}{}^{1/2}\Delta T_{0R}{}^{-1/4} \text{ (not necessarily be conserved).} \tag{5.45}$$

Secondly, power density ratio and the diameter ratio between nuclear fuel rods and heater rods are designated to be unity so as to match the thermal characteristics of two rods:

$$\begin{aligned} &\dot{q}_{s0R} = \left(\rho_s C_{ps}\right)_R \Delta T_{0R}{}^{3/2} = 1 \\ &\Rightarrow\ \Delta T_{0R} = \left(\rho_s C_{ps}\right)_R^{-2/3} \Rightarrow \begin{cases} P_{0R} = a_{s0R} = \left(\rho_s C_{ps}\right)_R^{-1} a_{0R} \\ N_{rod,R} = k_{sR}{}^{-1}\left(\rho_s C_{ps}\right)_R^{-1/3} a_{0R} \end{cases} . \\ &d_{rod,R} \equiv 1 \end{aligned} \qquad (5.46)$$

Thirdly, for the flow area ratio, it is decided to use an appropriate value (1/200) so that the amount of LBE does not exceed the retaining amount according to the basic requirement. Additional conditions on physical properties, $(\rho_s C_{ps})_R = 1.200$ and $k_{sR} = 1.129$ by referring to Table 5.6, are applied to derive the conditions given in (5.47):

$$\left.\begin{array}{c} l_{0R} = 1 \\ \dot{q}_{s0R} = 1 \\ \Delta T_{0R} = \left(\rho_s C_{ps}\right)_R^{-2/3} \\ P_{0R} = a_{s0R} = \left(\rho_s C_{ps}\right)_R^{-1} a_{0R} \\ N_{rod,R} = k_{sR}{}^{-1}\left(\rho_s C_{ps}\right)_R^{-1/3} a_{0R} \\ d_{rod,R} \equiv 1 \end{array}\right\} \xrightarrow[a_{0R}=1/200,\ k_{sR}=1.129]{\left(\rho_s C_{ps}\right)_R=1.200} \begin{cases} \Delta T_{0R} = 0.8855 \\ P_{0R} = 0.004167 \\ N_{rod,R} = 0.004168 \end{cases} . \qquad (5.47)$$

Finally, using the above relations leads to the establishment of requirements on the PILLAR core power output and number of heater rods as

seen in (5.48). Table 5.7 shows the final design values with this four-step approach.

$$\begin{aligned} P_{0R} = 0.004167 &\xrightarrow{P_{0p}=100000\text{kW}} P_{0m} = 417\text{kW} \\ N_{rod,R} = 0.004168 &\xrightarrow{N_{rod,p}=6480} N_{rod,m} = 27 \end{aligned} \tag{5.48}$$

Table 5.7 PILLAR design specifications for flow area reduction ratio 1:200

Specification	Unit	Prototype (URANUS); p	Scale model (PILLAR); m	Scale; m/p
Core power	kW	100000	417	0.00417
Total amount of LBE	ton	470	2.51	0.00534
Core inlet/outlet temperature difference	°C	153	135	0.886
Core inlet (heat exchanger outlet) temperature	°C	304	304	-
Core outlet (heat exchanger inlet) temperature	°C	457	440	-
Total amount of fuel rod/heater rod	-	6480	27	0.00417
Outer diameter of fuel rod/heater rod	m	0.0158	0.0158	1.00
Total heat transfer area	m^2	578.97	2.41	0.00417
Power given by a single fuel rod/heater rod	kW	15.43	15.43	1.00
Linear power given by a single fuel rod/heater rod	kW/m	8.57	8.57	1.00
Heat flux given by a single fuel rod/heater rod	W/m^2	1.73E+05	1.73E+05	1.00
Core volumetric power density	W/m^3	4.37E+07	4.37E+07	1.00

Table 5.7 PILLAR design specifications for flow area reduction ratio 1:200 (contd.)

Specification	Unit	Prototype (URANUS); p	Scale model (PILLAR); m	Scale; m/p
Effective thermal conductivity of fuel rod/heater rod	W/mK	4.17	4.70	1.13
Effective thermal diffusivity of fuel rod/heater rod	m^2/s	1.31E-06	1.23E-06	0.941
Volumetric heat capacity of fuel rod/heater rod	J/m^3K	3.18E+06	3.82E+06	1.20
LBE average velocity at core outlet	m/s	0.3123	0.2631	0.940
LBE mass flow rate	kg/s	4546.0	21.37	0.00468
Total pressure loss of system	Pa	9743.5	8456.5	0.886

5.2.2 Final design of PILLAR

As described in the previous sections, PILLAR had been designed to be a pool-type experimental facility conserving the axial height of each component while reducing the flow area with a reduction ratio of 1:200 through comprehensive reviews on the scaling analysis methods. In order not to distort the LBE behaviors in the prototype as much as possible, PILLAR was designed to have the pool configuration as well. Considering the geometrical size of the facility, it forms a dual piping structure of outside reactor vessel with inner barrels.

Even if the scale facility has a design of reduction in the flow area, it is inevitable to have a slight distortion to some extent. Originally, the steam generator in URANUS consists of eight independent modules in total; but in PILLAR, it has one single heat exchanger that is comprised of 3 vertically downward feedwater pipes, a chamber, and 21 vertically upward tubes. In addition, the LBE reflector region, which is made up of stagnant LBE so that the coolant itself can be used as a neutron reflector in the actual reactor core, is not considered since it has no importance in the thermal-hydraulic point of view. Furthermore, all components were configured with piping with an ANSI standard profile, i.e. SCH 40, by taking into account the fabrication. As discussed, the area-average method regards each of hydrodynamic regions as the composition of length, (hydraulic) diameter, and flow area. Therefore, if the flow area distortion of components is not large with proper flow areas, the distortion of the entire system's behaviors given by the partial configuration adjustment will not be significant.

In this section, the specifications of components comprising the thermal-hydraulic system of PILLAR are described in the following subsections. Figure 5.3 shows the final design of the facility with an isomeric view, a disassembly view and an actual photograph; the name of each part is also denoted in the isomeric view or in the disassembly view. For a consistency, components that consist of internal structure are designated to be barrels while those that comprise of outer structure are named as vessels.

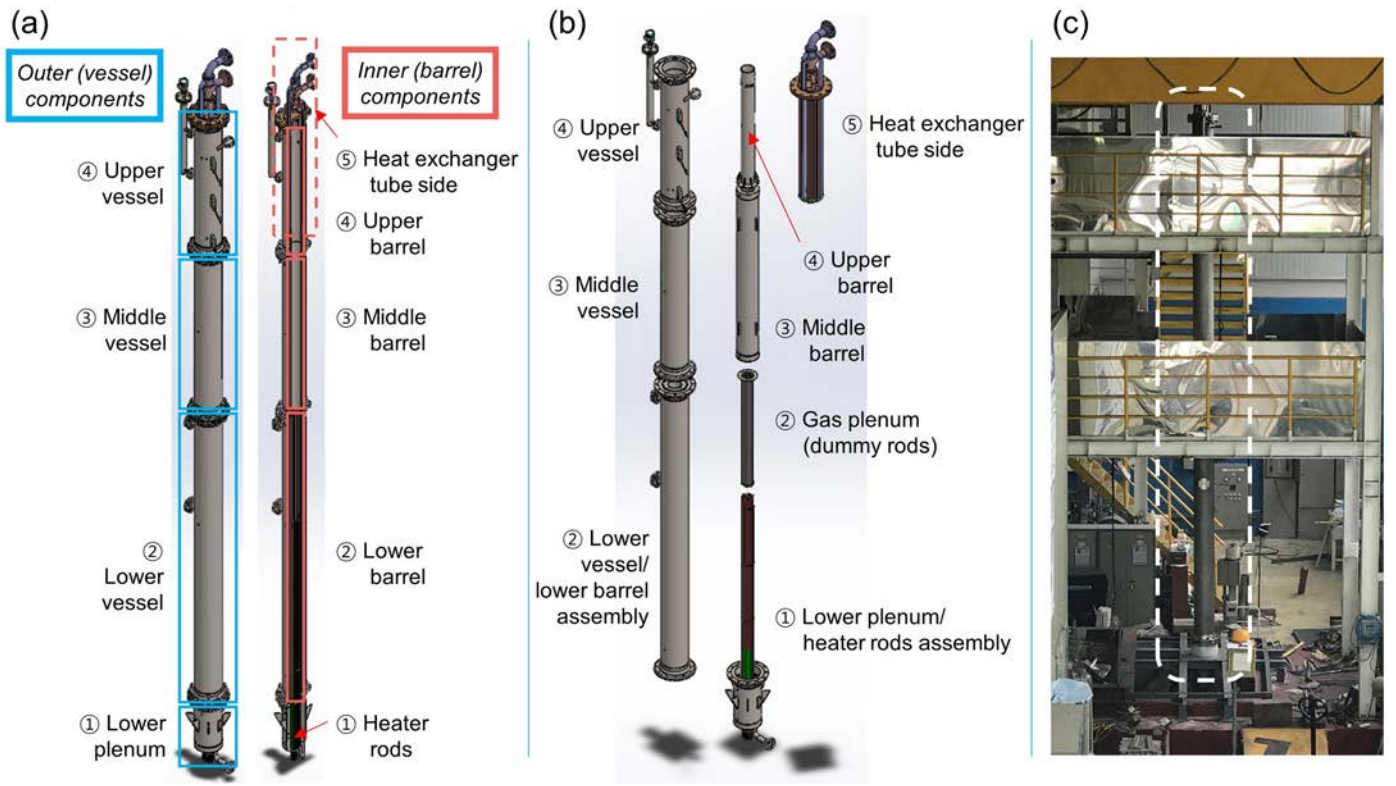

Figure 5.3 (a) Isomeric view (left) and cross-sectional view (right), (b) disassembly view, and (c) photo (white dash) of PILLAR main vessel

5.2.2.1 Lower plenum and heater rods assembly

As indicated in Figure 5.3 (b) the disassembly view of the PILLAR main vessel, the lower plenum and heater rods are combined together as an assembly. Hereafter, all the names of other components are provided by the dissembly view. It consists of the lowest part of the PILLAR main vessel. In the prototypic reactor, the lower plenum is the lowest part of the reactor vessel, which is the region through which LBE came from the downcomer passes before going into the core. It is a large pool and the flow direction changes according to the position, resulting in a local velocity field distribution. The same applies to the lower plenum of PILLAR, while the difference is that the extension of the heater rods penetrates through this region. Figure 5.4 shows the three-dimensional model of the lower plenum and heater rods assembly in several points of views including isomeric, cross-sectional, top, and bottom views.

Unlike nuclear fuel, since the heater rods installed in PILLAR cannot generate heat spontaneously with nuclear reaction, they must have electrical connections at least on one point, such as the top, bottom, or any points on their sides, to provide electrical power. Such connections eventually require multiple power cables, which cannot maintain integrity in high-temperature, about 300 °C, and liquid metal environments. Therefore, a part of the heater rod is extended to the lower end of the vessel to support the rod in the vertical direction while supplying electric power as shown in Figure 5.5. The heating part is as long as 1,800 mm while the non-heating part that is elongated from the end of heating part is about 1,200 mm. At the top of a heater rod, another

non-heating element called end pin is included as a finishing material. In this regard, this extension of non-heating element led to the connection of two elements as a single assembled component joined by welding at each of joints where the heater rods and the vessel meet. This connection is described in the inset (d) in Figure 5.4.

As determined in the final design stage, 27 heater rods were installed in the facility as shown in Figure 5.6. Since the similarity in geometrical arrangement of fuel or heater rods was to be conserved, the heater rods were arranged in a triangular lattice structure while the distance between heater rods was the same with the prototypic reactor as well. They consist of two different voltage ratings, namely with 380 V (rod numbers 7-27 in Figure 5.6) and 460 V (rod numbers 1-6 in Figure 5.6), with the same power rating, 15.5 kW, so that they can be operated under the electrical circumstances of the site where PILLAR is located. Furthermore, the heater rods with voltage rating with 380 V are divided into two groups due to a similar reason on the electrical situations. One group consists of the heater rods Nos. 9, 10, 13, 14, 17, and 18 while the other heater rods with 380 V voltage rating are grouped and controlled as a whole.

In order to prevent the shaking of the rods possibly given by LBE flow, three grid spacers are installed in the axial direction. The design and axial positions of those grids spacers are depicted in Figure 5.7. They were manufactured by electro-discharge machining and wire cutting techniques from a stainless steel plate with 10 mm thickness. Three additional skeletal bars provide a sturdy support among the spacers while the ring on the spacers do not

touch or grab the rods since their inner diameter are slightly larger than the outer diameter of heater rods. In addition, several thermocouples are mounted on the grid plates to measure temperature distribution inside the core region. The detailed information on the temperature measurement is summarized in Section 5.2.2.8.

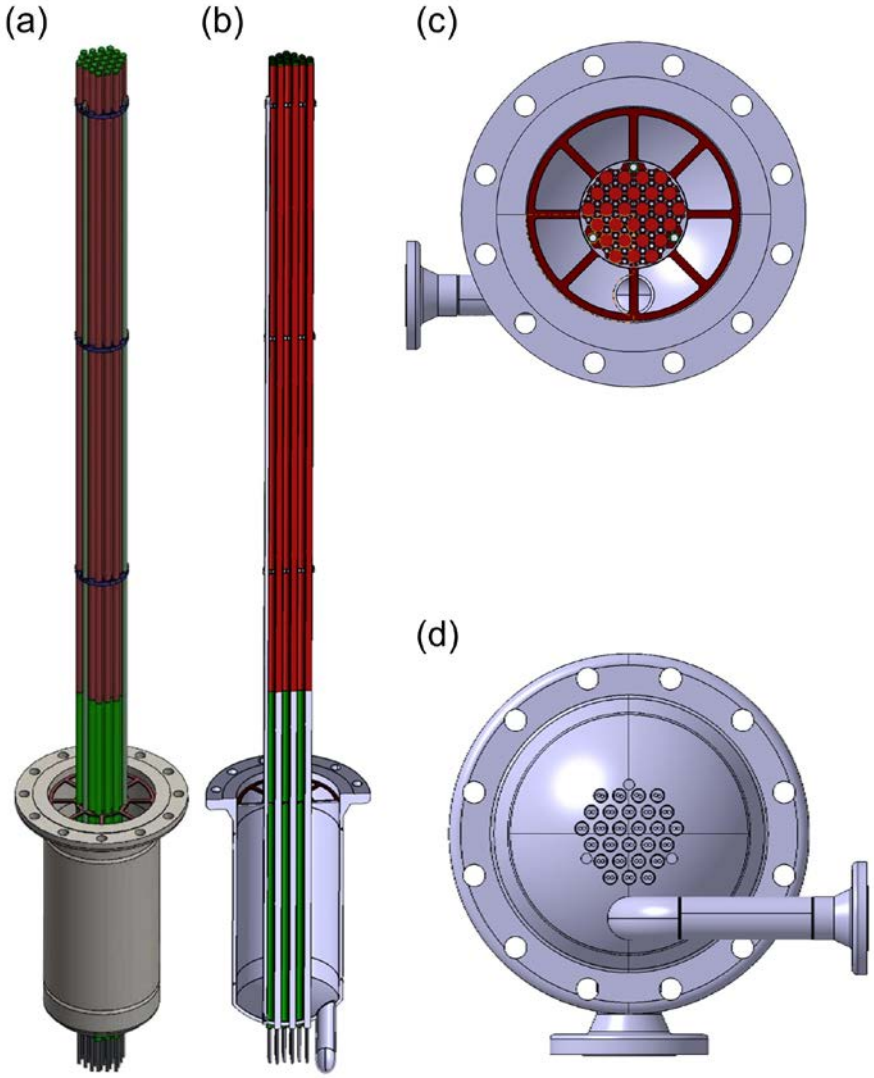

Figure 5.4 Three-dimensional model of PILLAR lower plenum and heater rods assembly in several viewpoints. (a) Isomeric view, (b) cross-sectional view in z-direction, (c) top view, and (d) bottom view

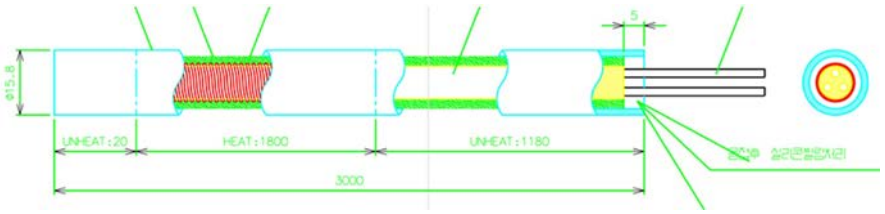

Figure 5.5 Schematic diagram of PILLAR heater rod

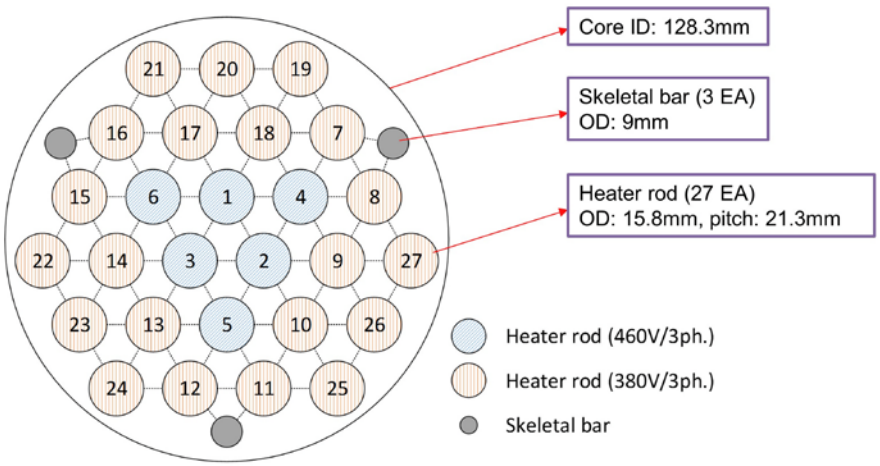

Figure 5.6 Heater rod and skeletal bar arrangement inside the core region of PILLAR

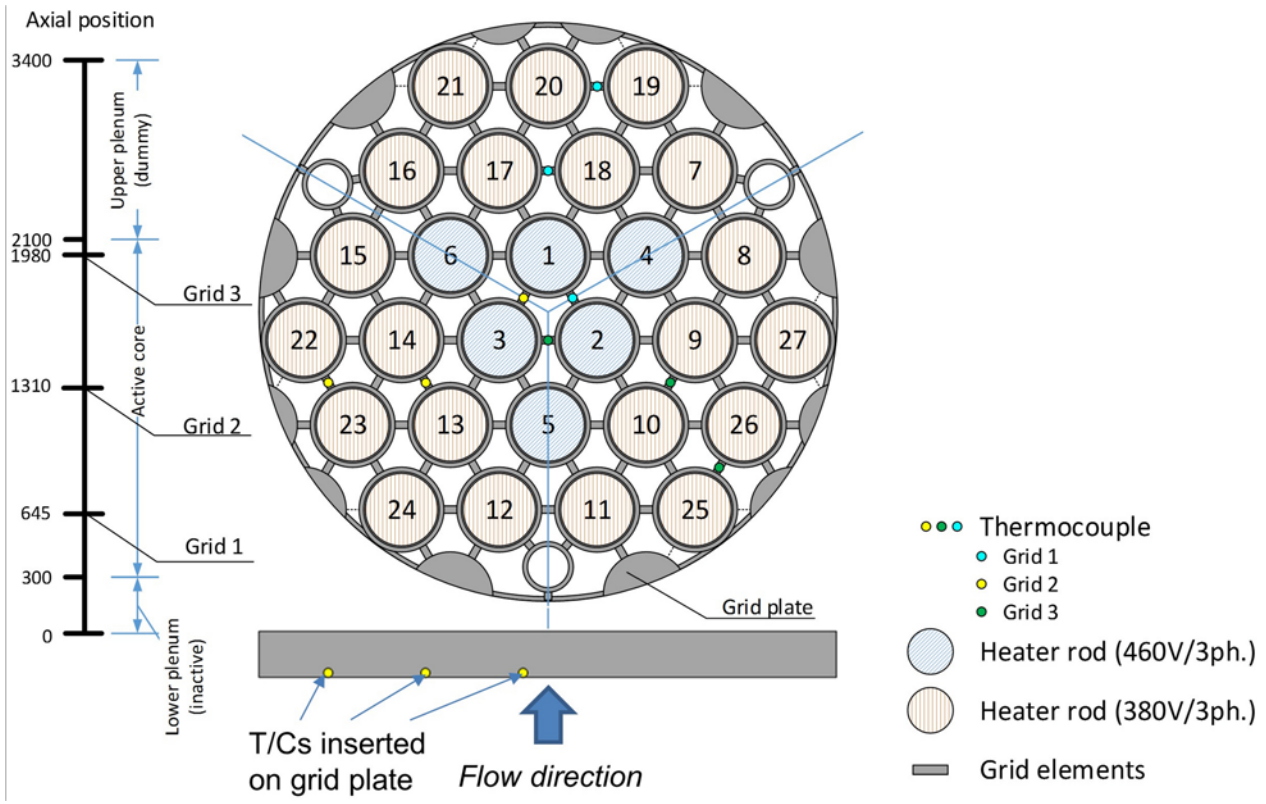

Figure 5.7 Design and axial positions of PILLAR core grid spacers and thermocouple location upon each plate

5.2.2.2 Lower vessel and lower barrel assembly

Since the design of PILLAR is a shell-in-shell configuration, it is difficult to keep an external shell and an internal piping on the concentric axis and to maintain the latter from shaking or moving. Therefore, the lower vessel and lower barrel assembly was designed to include several regions such as lower plenum, core, gas plenum and a lower part of downcomer by constructing concentric configurations. Figure 5.8 shows the three-dimensional model of the lower vessel and lower barrel assembly in various viewpoints with isomeric, cross-sectional, and top views.

In the prototypic reactor, the nuclear fuel rod lies within three regions, the lower plenum, core, and gas plenum. As shown in the previous section, the non-heating element of heater rod supports the rod itself with extrusion through the lower vessel that simulates the lower plenum region. On the other hand, the remaining upper part, gas plenum, needs to have the extension from each of heater rods to conserve the similarity within the region. To do so, another assembly consist of non-heating dummy rods are installed to mimic flow configuration inside the gas plenum as depicted in Figure 5.9. The dummy rods are placed on the top of the assembly and right above the heater rods through the upper plenum region. Since the gas plenum is thought to be an extension of fuel rods, the arrangement of dummy rods are identical to that of heater rods as also shown in the inset (c) in Figure 5.9.

Contrary to URANUS, there are no neutron reflector and/or shielding region in PILLAR, which are placed in the outside of the core in radial direction.

It is expected that LBE flow rate is extremely low in the reflector region while no LBE flow exists inside the shielding region. In this consideration, those parts were excluded in the experimental setup. However, those non-flow region still needs to exist physically for the conservation of geometrical similarity between the prototype and scale facility. Therefore, to eliminate those parts while avoiding geometrical distortion, two inner barrels were included as in a concentric, double-wall structure without filling inside between the barrels. In addition, since the double piping naturally creates an empty space, heat transfer can be effectively suppressed, which contributes to prevent unnecessary heat transfer in the radial direction, leading to a reduction of heat loss through the internal walls.

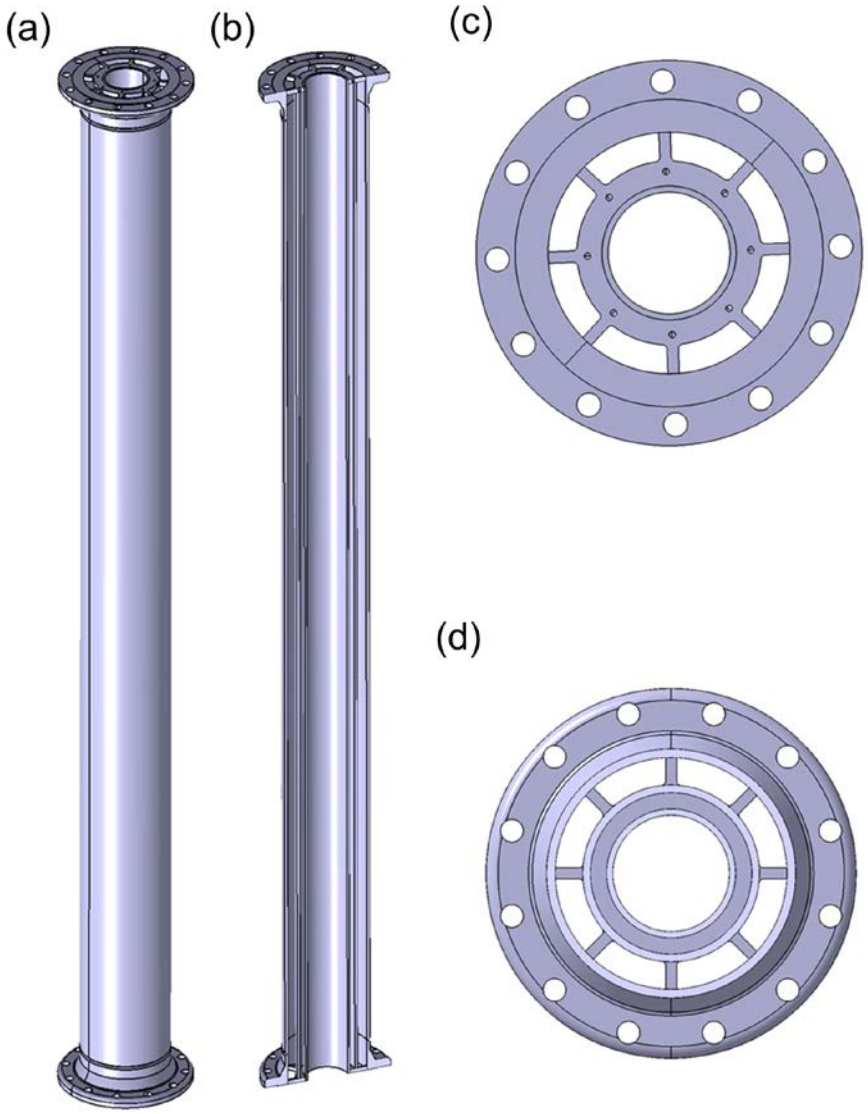

Figure 5.8 Three-dimensional model of PILLAR lower vessel and lower barrel assembly in several viewpoints. (a) Isomeric view, (b) cross-sectional view in z-direction, (c) top view, and (d) cross-sectional view in radial direction

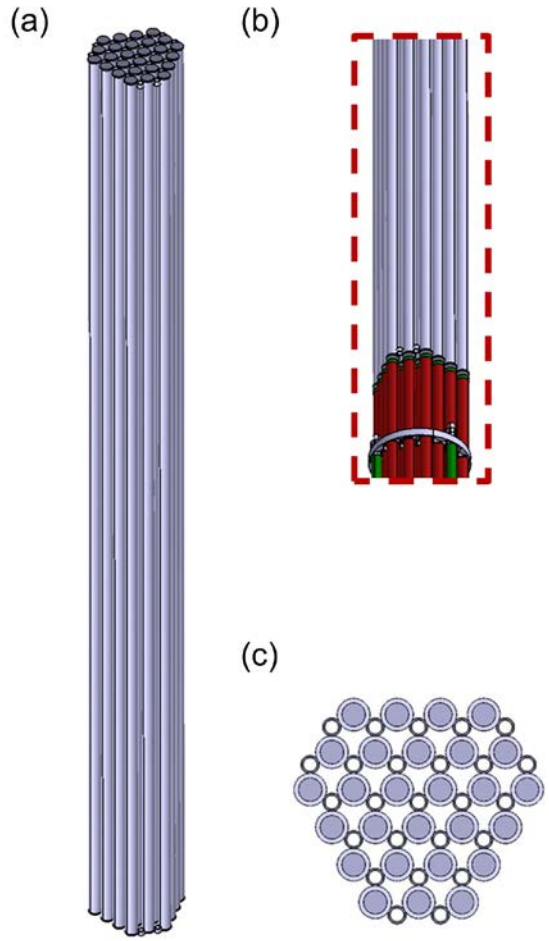

Figure 5.9 Three-dimensional model of PILLAR dummy rod assembly in several viewpoints. (a) Isomeric view, (b) detail view on the interface with heater rods, and (c) top view

5.2.2.3 Middle barrel

The middle barrel is a component dividing two flow regions, the upper part of downcomer and the lower part of riser, which refers to the downstream region of gas plenum and the upstream of heat exchanger, as shown in Figure 5.10. Similar to the lower barrel, the middle barrel also adopts double-wall structure in radial direction. The inset (c) of Figure 5.10 describes eight fins on the surface of the barrel in the radial direction, which provide a firm position to the middle barrel on the concentric axis and out of eccentricity with the outermost shell, the middle vessel. To minimize the unnecessary flow resistance given by flanges and bolts, two bolt covers that surrounds the flanges at both ends of the barrel are provided, as depicted in the inset (d) of Figure 5.10.

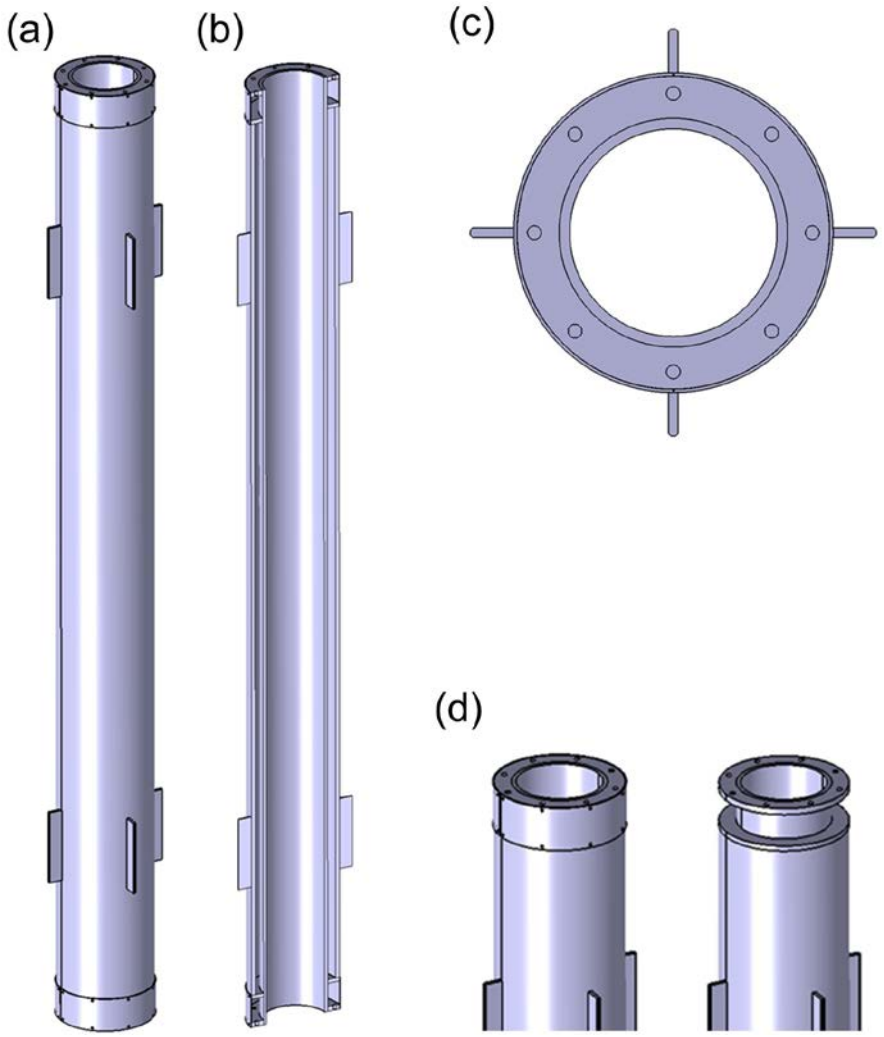

Figure 5.10 Three-dimensional model of PILLAR middle barrel in several viewpoints. (a) Isomeric view, (b) cross-sectional view in axial direction, (c) top view, and (d) bolt cover application to middle barrel (left) and middle barrel without the bolt cover (right)

5.2.2.4 Upper barrel

Figure 5.11 shows the upper barrel that is a component dividing two flow regions, the shell side of heat exchanger and the upper part of riser, similar to the middle barrel. The most distinct feature compared to the middle barrel is that it does not have the double-walled structure to radial direction so that the shell side of heat exchanger have an enough flow area. As shown in Figure 5.12, it also has three windows through which LBE can flow to the shell side while it is connected with the middle barrel with a flange on the bottom. In order to have a margin for the LBE level control, it is elongated for about 300 mm above the windows. In actual experimental situations, an additional piping attached to the upper vessel that has a waveguide radar level sensor controls the free surface level of LBE. Figure 5.13 shows the radial arrangement of those windows. The positions of windows were intended to have an effective heat transfer from LBE to pressurized water through large heat transfer area with several tubes. Detailed descriptions on the heat exchanger and upper vessel are provided in the next chapter.

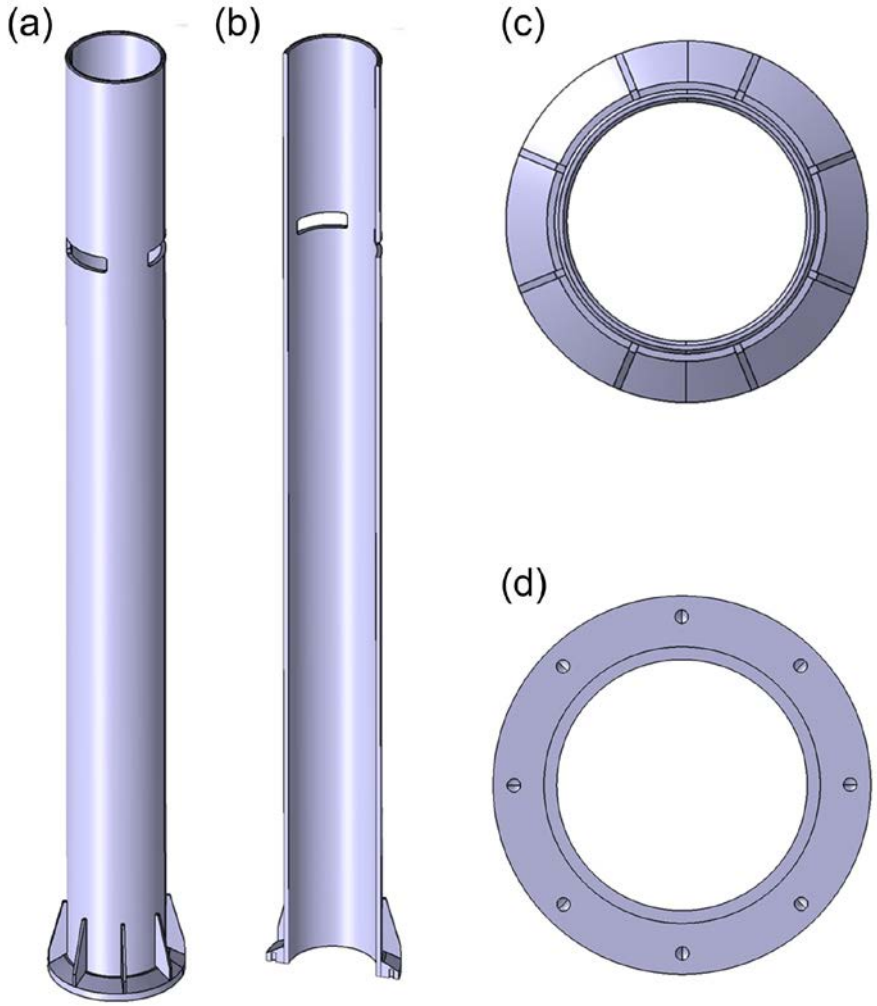

Figure 5.11 Three-dimensional model of PILLAR upper barrel in several viewpoints. (a) Isomeric view, (b) cross-sectional view in axial direction, (c) top view, and (d) bottom view

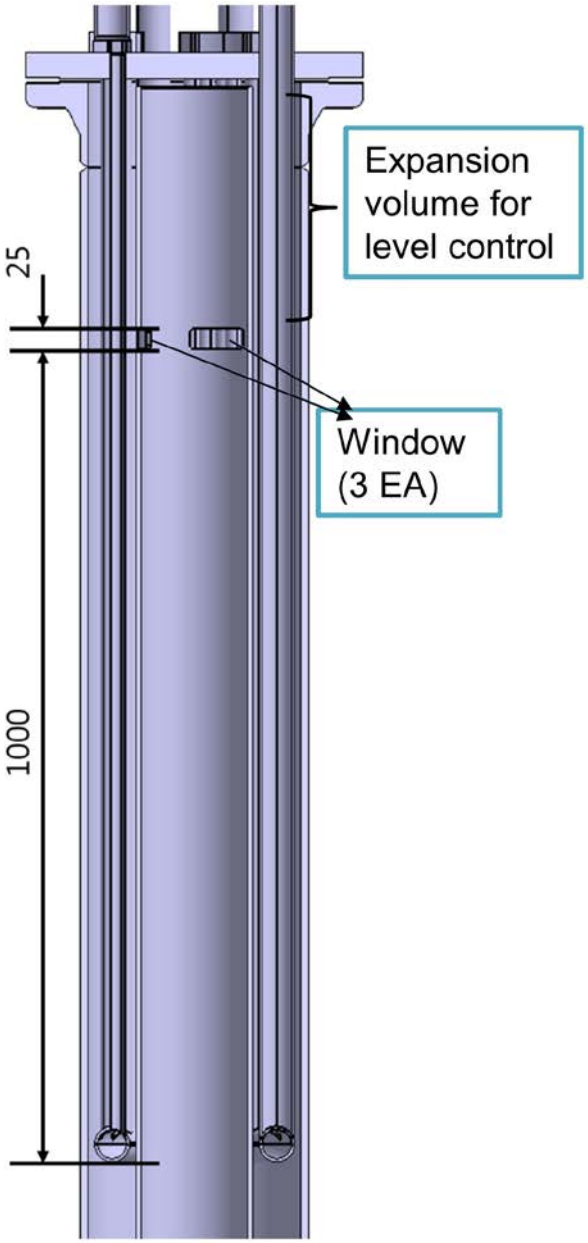

Figure 5.12 Axial position of windows on PILLAR upper barrel and expansion volume for LBE level control with respect to heat exchanger shell side

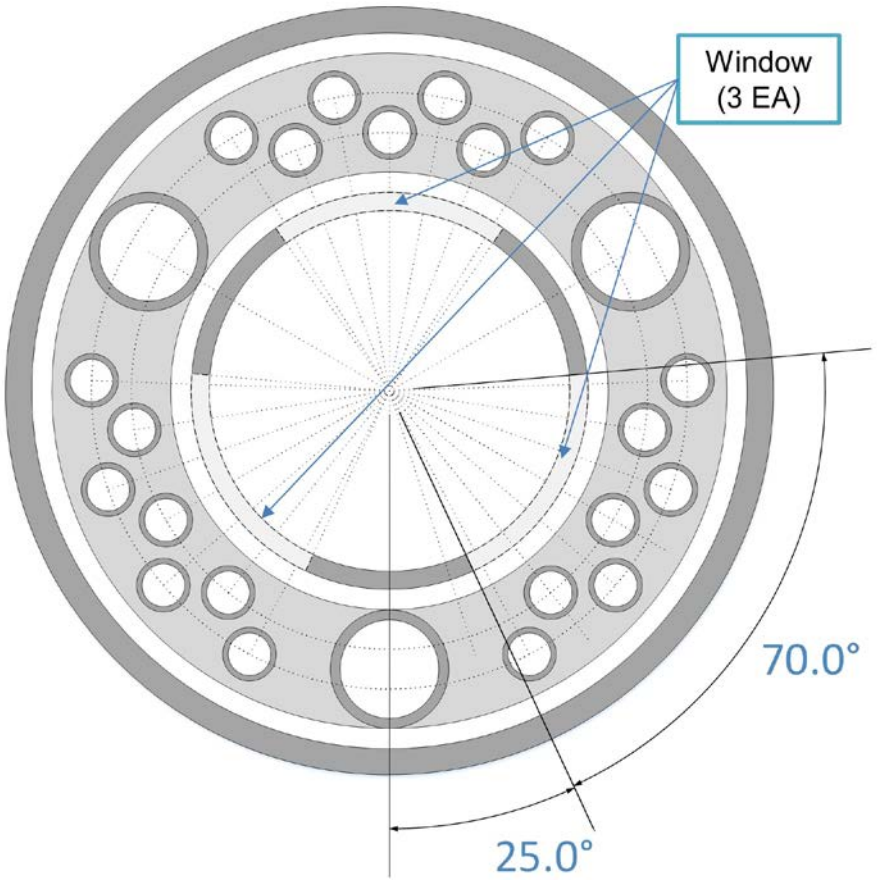

Figure 5.13 Radial position and arrangement of windows on PILLAR upper barrel with respect to heat exchanger and upper vessel

5.2.2.5 Upper vessel

The upper vessel is the outermost shell consisting of the heat exchanger shell side as depicted in Figure 5.14. The heat exchanger tube side is connected with the upper vessel on the top with a flange so that pressure boundary is established while the bottom end is joined with the middle vessel. With the same region for the level control as in the case of upper barrel, this component was elongated about 300 mm. Several instrumental probes are installed through the wall of upper vessel to measure LBE temperature and flow velocity within the shell side of heat exchanger.

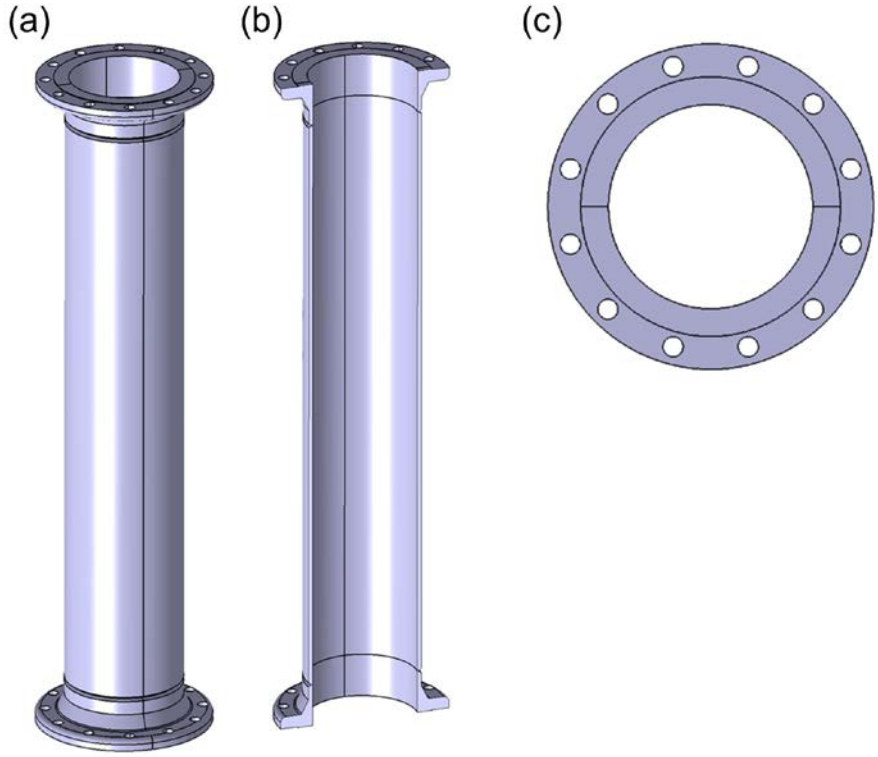

Figure 5.14 Three-dimensional model of PILLAR upper vessel in several viewpoints. (a) Isomeric view, (b) cross-sectional view in axial direction, and (c) top (bottom) view

5.2.2.6 Heat exchanger tube side

The tube side of heat exchanger shown in Figure 5.15 is a key component of PILLAR main vessel, which works as a heat sink that drives LBE natural circulation flow in non-isothermal conditions. It is located inside of the upper vessel within which the shell side of heat exchanger is established with LBE flow and power generated from the core region is transferred to water. As aforementioned, the connection with the upper vessel forms the pressure boundary of PILLAR main vessel and it makes this region to work as a level control system as well. Thus, it is also required that all of the attached tubes were elongated about 300 mm.

The tube side of heat exchanger consists of several tubes for heat transfer from LBE, a top flange, and water chambers connected to the tubes as depicted in the insets (a) and (b) of Figure 5.15. The tubes are categorized by their diameters, which include three downward tubes with a standard dimension with ANSI SCH 40 1-1/4" and 21 upward tubes having 19.05 mm of outer diameter, defined by the direction of water inside those tubes. These tubes are arranged in azimuthal symmetry of 120˚ to prevent distortion that may arise by local flow distribution. A schematic diagram, Figure 5.16, shows the arrangement of those tubes and connection between the lower water chamber. As described in Section 5.2.2.4, the three windows on the upper barrel are arranged so that they ensure an efficient heat transfer at a large area of heat transfer for LBE to face the 21 upward tubes.

Since the cooling of primary side of PILLAR main vessel was

intended to be done with slightly pressurized water, about 8-10 bars, through forced convection given by a centrifugal pump, all the tubes were selected to be withstand that pressure and a pressure test under 25 bars were conducted to confirm the integrity of welding. In a working condition, water enters into the inlet pipe then divided into three downward tubes. After flowing along with those tubes, it is distributed in a lower torus-type chamber, which has the same diameter with the downward tubes as shown in the inset (e) of Figure 5.15, and then flows through the upward tubes. All of water flow is gathered in three upper water chambers connected to seven tubes each as described in the inset (f) of Figure 5.15. Those three-way flows are finally merged in the water outlet and pumped to the ultimate heat sink in the secondary side, the cooling tower.

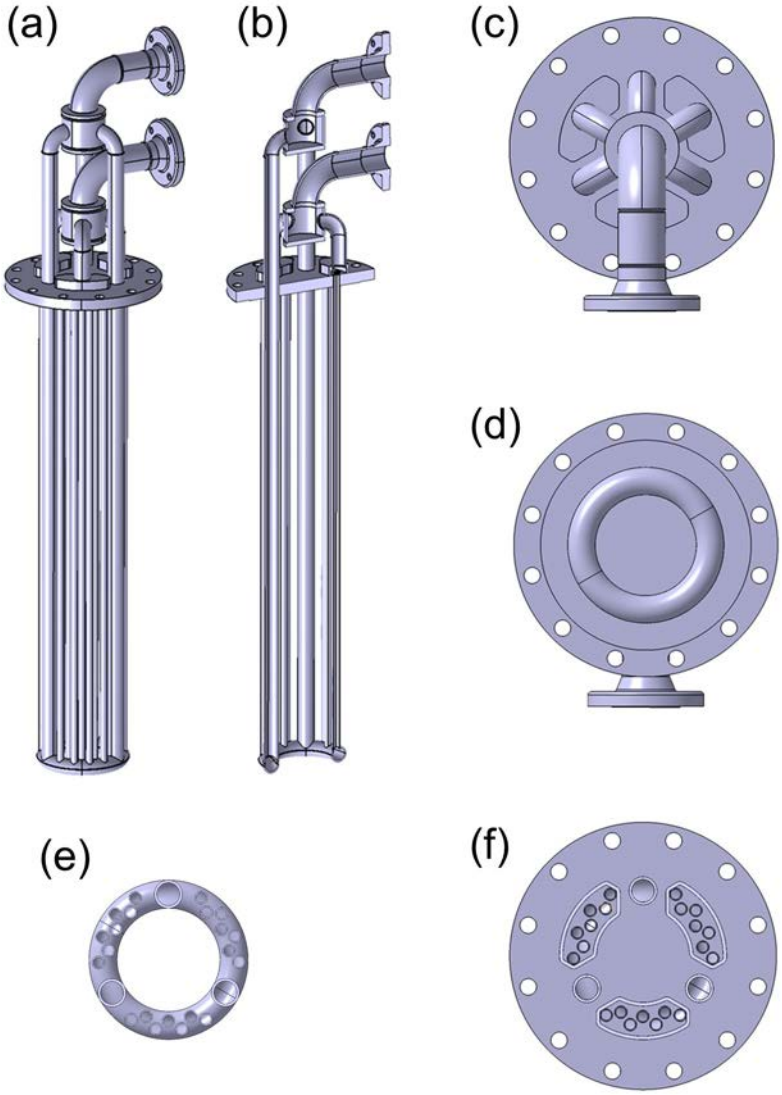

Figure 5.15 Three-dimensional model of PILLAR heat exchanger tube side in several viewpoints. (a) Isomeric view, (b) cross-sectional view in axial direction, (c) top view, (d) bottom view, (e) cross-sectional view of lower chamber, and (f) cross-sectional view of upper chambers

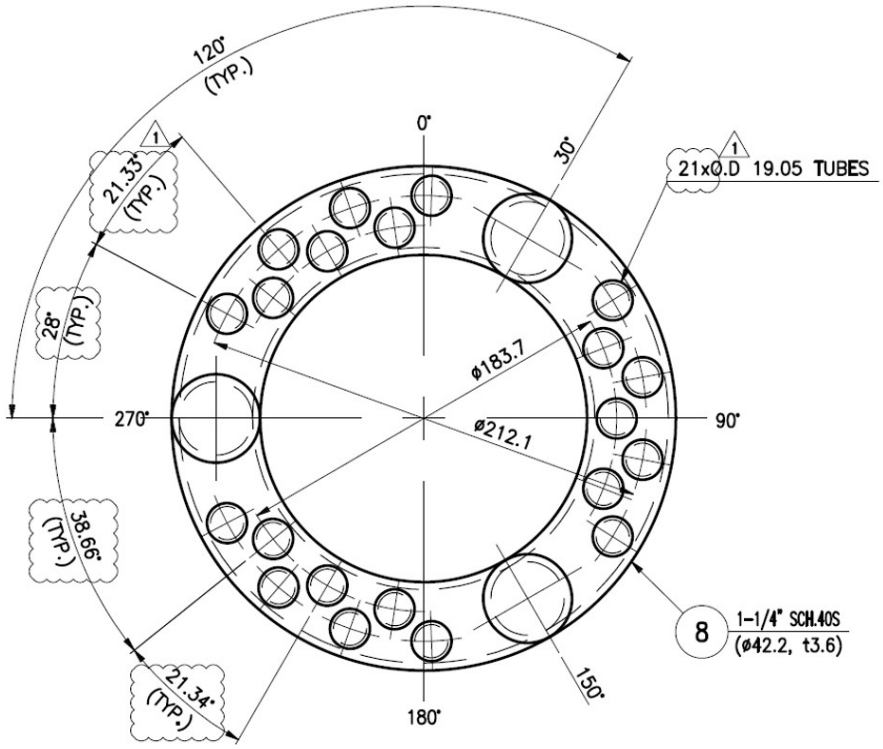

Figure 5.16 Schematic diagram of lower water chamber and tube arrangements of PILLAR heat exchanger tube side

5.2.2.7 Middle vessel

As discussed in Section 5.2.2.2, the downcomer region of PILLAR is divided into two parts, the lower vessel and middle vessel. Figure 5.17 shows the three-dimensional model of the middle vessel in numerous points of view with isomeric, cross-sectional, and top (bottom) views. Through the outer wall of the vessel, several instrumentation probes are installed to measure LBE cold leg temperature in the downcomer.

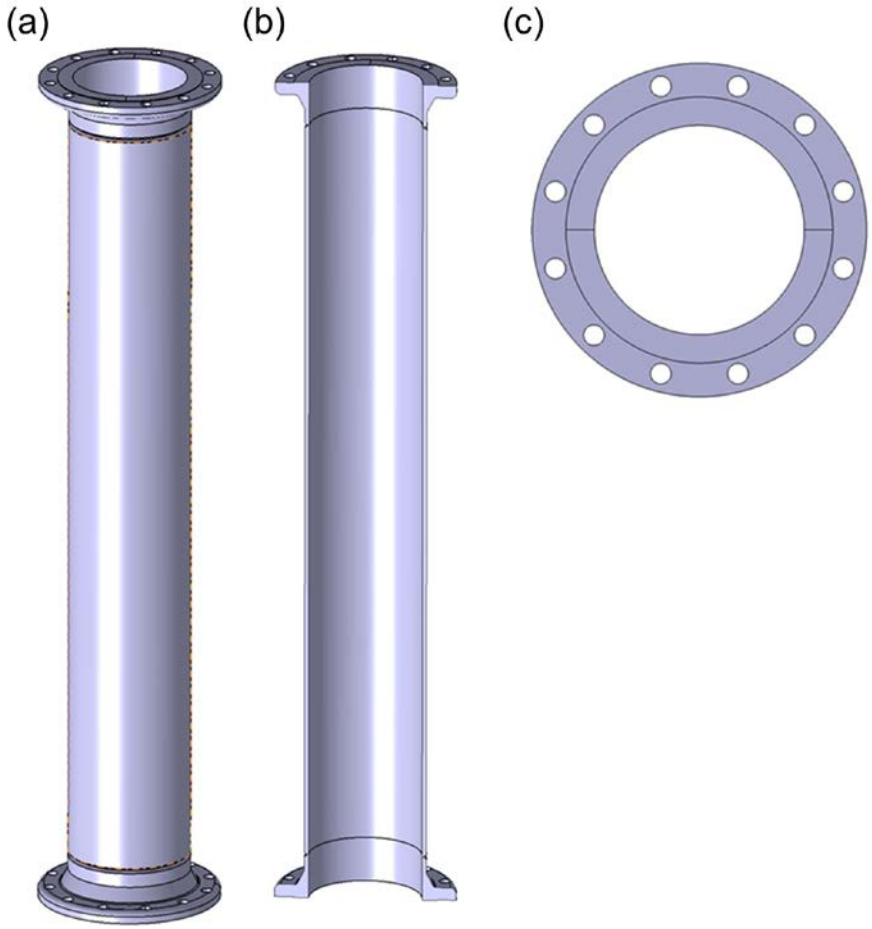

Figure 5.17 Three-dimensional model of PILLAR middle vessel in several viewpoints. (a) Isomeric view, (b) cross-sectional view in axial direction, and (c) top (bottom) view

5.2.2.8 Instrumentation system of PILLAR

PILLAR is designed in the shell-in-shell configuration unlike general loop-type experimental facilities so that there are additional characteristics to be considered for installation and operation of sensors. For example, in the case of downcomer, it is possible to measure the flow by inserting a probe (radially) through or by putting on the sensor the outermost shell, but it is not possible for innermost regions, such as core, upper plenum, and riser. In addition, too many penetrations are not favorable on the viewpoint of assembly and operation because the probes installed through those penetrations interfere with the structure.

For material compatibility, it is not easy to select the material of the lead wire connected to the probes, since LBE temperature is high and chemically reacts with a number of metals. Therefore, it is important to reduce the number of sensors inside the inner shell as much as possible, and to arrange the sensors so that the measurements can be performed only with the limited number of probes. In accordance with this principle, the number of sensors included in the inner shell was determined to be nine Type K thermocouples inside the core region and the remaining sensors are located other than the inner shell region.

Since the heater rods and heat exchanger tubes are installed symmetrically, if the proper position is selected, the flow characteristics can be indirectly grasped without installing sensors to most of parts. Focusing on the measurement of the core and heat exchanger shell side, the instrumentation

system of PILLAR is elaborated. Table 5.8 summarizes the requirements applied to the selection of instrumentation probes and the role of each of sensors. The remaining instrumentation system is not introduced in detail but illustrated on the schematic diagram of the instrumentation system, as shown in Figure 5.18.

As mentioned earlier, the sensors to be included in the internal piping are limited to the core region. This is because the core receives the power from the heater rods, so that the temperature change of the LBE is expected to be the largest. In addition, this region is more important in the thermal-hydraulic point of view as it simulates the actual core in the prototypic reactor. However, there are also limitations in the core region since there are many heater rods that reduces free volume. If the probes are excessively inserted, it may go through some unexpected results by the flow interference from the probes.

To do so, thermocouples were installed, which can easily measure the temperature field inside the core region while their physical dimensions are small enough. However, there is a remaining problem to this configuration because the lead wire connected to the thermocouple is also in contact with the high temperature LBE. Hence, all the thermocouples in the core region were designated to be installed on the three grid spacers, illustrated in Section 5.2.2.1, so that they could remain their positions without disturbing the flow.

Figure 5.7 shows the installation plan and the position of each thermocouple accompanied by the arrangement of the heater rods. The thermocouples were placed on thin plates that connects the support rings in the grid spacers in order not to disturb the flow as much as possible. In addition,

the probes were installed at the bottom of the grid spacers because the flow direction is from bottom to top. Each of grid plates have tiny grooves to accommodate the tips of thermocouples and to prevent them from leaving their positions.

Figure 5.19 illustrates the positioning rationale of the thermocouples. It was done by dividing the region of interest into three zones, depicted by Zones 1, 2, and 3, in the radial direction, and by placing the thermocouples that represent the zone at the center of each zone. Since the arrangements of heater rods have a symmetry in azimuthal direction by 120°, temperature is measured at nearly constant intervals in the radial direction if three thermocouples are placed on each of the grid spacers.

The shell side of PILLAR heat exchanger is located between the inner shell and the external piping through which the flow region is easy to access. In this region, fluid temperature, the outer wall temperature of the heat exchanger tubes, and the LBE flow rate in terms of flow speed are measured. In the case of the LBE temperature measurement, relatively thick thermocouples are installed through the wall to measure it at several positions similar to the core region. The flow rate, in other words, flow speed of LBE is measured with Pitot tubes, which is actually measured by measuring the differential pressure at the locations where the tips of Pitot tubes are located, since the flow velocity is able to be converted from the local pressure measurements. In this case, the pitot tube is also inserted through the outermost pipe, and since it has a curvature perpendicular to the flow direction at the tip portion of the pitot tube, small ducts are attached to a part of the outermost pipe

and each pitot tube is inserted through the ducts. The outer surface temperature of the tube is measured with thin thermocouples that are used in the core region by welding them to the tube surface.

As in the case of the core region, the probes are installed by the azimuthal symmetry. In this regard, only a small part was targeted to have the penetrations so that those would not affect the assembly and/or disassembly process. The axial and radial positions of each of probes are shown in Figure 5.20. Three planes A, B, and C in the axial direction and planes 1, 2, and 3 in the azimuthal direction were arbitrarily chosen to impose different positions. Most of the probes are located on the lines made by those planes and the location is labeled first in the azimuthal direction and then in the axial direction. As depicted in Figure 5.21 and Figure 5.22, three Pitot tubes are on the 1-A, 1-B and 1-C lines while six thermocouples for LBE temperature measurement are on the 2-A, 2-B, 2-C, 3-A, 3-B, and 3-C lines. The number of thermocouples used to measure the temperature outside the tube varies depending on the size of the heat exchanger tube. For the surface temperature measurement on upward pipes, the 1-A and 1-B lines are used while two thermocouples each were installed on the surface of downward tube on plane A and plane B.

Table 5.8 Measurement requirements of PILLAR instrumentation system

System	Type	Parameter to be measured	Precision requirement
Primary system	Type K thermocouple	LBE temperature, environmental temperature	±1 K
	Differential pressure transducer with pitot tube	Local LBE flow velocity/dynamic pressure	±2%
	Pressure transducer	Pressure of pressure boundary above LBE free surface	0.25% (full range)
	Level sensor	LBE free surface level	±2 mm
Secondary system	Type K thermocouple	Water temperature	±1 K
	Electromagnetic flowmeter	Water volumetric flow rate	0.5% (full range)
	Pressure transducer	Water pressure	0.25% (full range)
Auxiliary system	Type K thermocouple	LBE temperature	±1 K
	Pressure transducer	Pressure of pressure boundary in LBE storage tank	0.25% (full range)
	Load cell	LBE mass in LBE storage tank	±10 kg

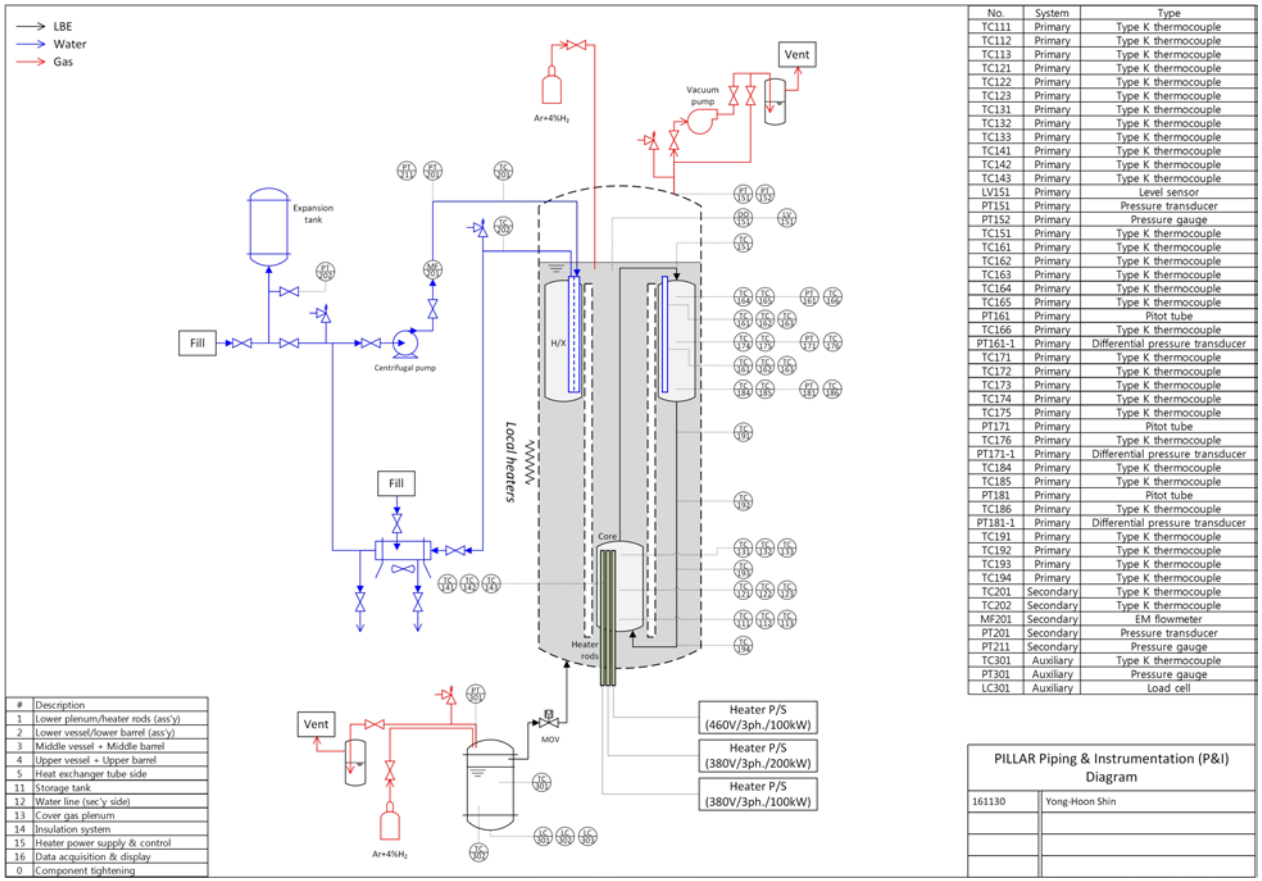

#	Description
1	Lower plenum/heater rods (ass'y)
2	Lower vessel/lower barrel (ass'y)
3	Middle vessel + Middle barrel
4	Upper vessel + Upper barrel
5	Heat exchanger tube side
11	Storage tank
12	Water line (sec'y side)
13	Cover gas plenum
14	Insulation system
15	Heater power supply & control
16	Data acquisition & display
0	Component tightening

No.	System	Type
TC111	Primary	Type K thermocouple
TC112	Primary	Type K thermocouple
TC113	Primary	Type K thermocouple
TC121	Primary	Type K thermocouple
TC122	Primary	Type K thermocouple
TC123	Primary	Type K thermocouple
TC131	Primary	Type K thermocouple
TC132	Primary	Type K thermocouple
TC133	Primary	Type K thermocouple
TC141	Primary	Type K thermocouple
TC142	Primary	Type K thermocouple
TC143	Primary	Type K thermocouple
LV151	Primary	Level sensor
PT151	Primary	Pressure transducer
PT152	Primary	Pressure gauge
TC151	Primary	Type K thermocouple
TC161	Primary	Type K thermocouple
TC162	Primary	Type K thermocouple
TC163	Primary	Type K thermocouple
TC164	Primary	Type K thermocouple
TC165	Primary	Type K thermocouple
PT161	Primary	Pitot tube
TC166	Primary	Type K thermocouple
PT161-1	Primary	Differential pressure transducer
TC171	Primary	Type K thermocouple
TC172	Primary	Type K thermocouple
TC173	Primary	Type K thermocouple
TC174	Primary	Type K thermocouple
TC175	Primary	Type K thermocouple
PT171	Primary	Pitot tube
TC176	Primary	Type K thermocouple
PT171-1	Primary	Differential pressure transducer
TC184	Primary	Type K thermocouple
TC185	Primary	Type K thermocouple
PT181	Primary	Pitot tube
TC186	Primary	Type K thermocouple
PT181-1	Primary	Differential pressure transducer
TC191	Primary	Type K thermocouple
TC192	Primary	Type K thermocouple
TC193	Primary	Type K thermocouple
TC194	Primary	Type K thermocouple
TC201	Secondary	Type K thermocouple
TC202	Secondary	Type K thermocouple
MF201	Secondary	EM flowmeter
PT201	Secondary	Pressure transducer
PT211	Secondary	Pressure gauge
TC301	Auxiliary	Type K thermocouple
PT301	Auxiliary	Pressure gauge
LC301	Auxiliary	Load cell

PILLAR Piping & Instrumentation (P&I) Diagram	
161130	Yong-Hoon Shin

Figure 5.18 Schematic diagram of PILLAR instrumentation system

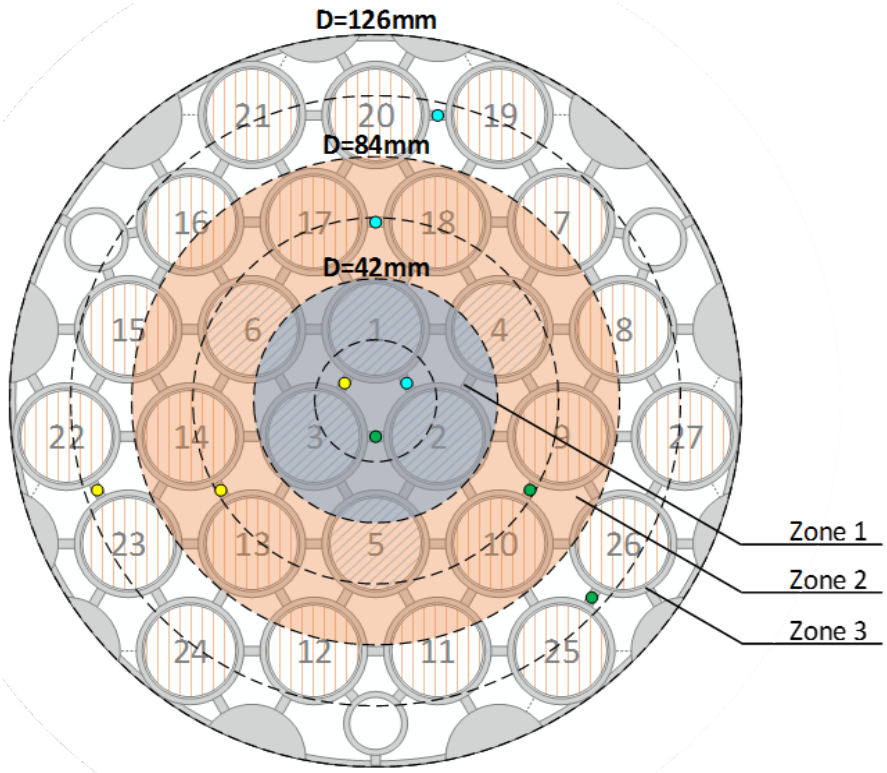

Figure 5.19 Geometrical consideration of thermocouple installation positions on grid spacers

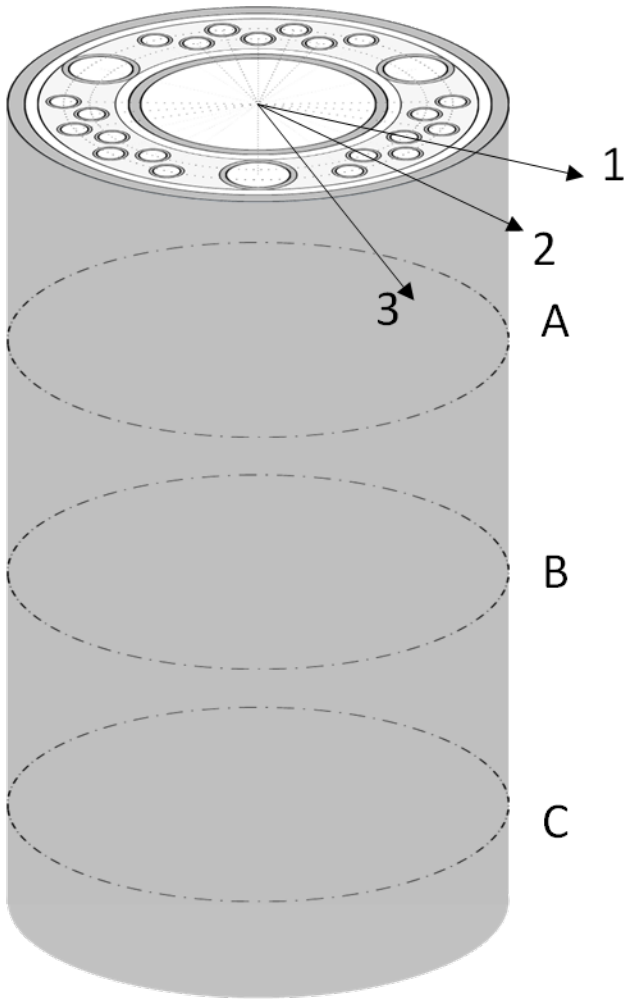

Figure 5.20 Axial and radial position of instrumentation probes on the shell side of PILLAR heat exchanger

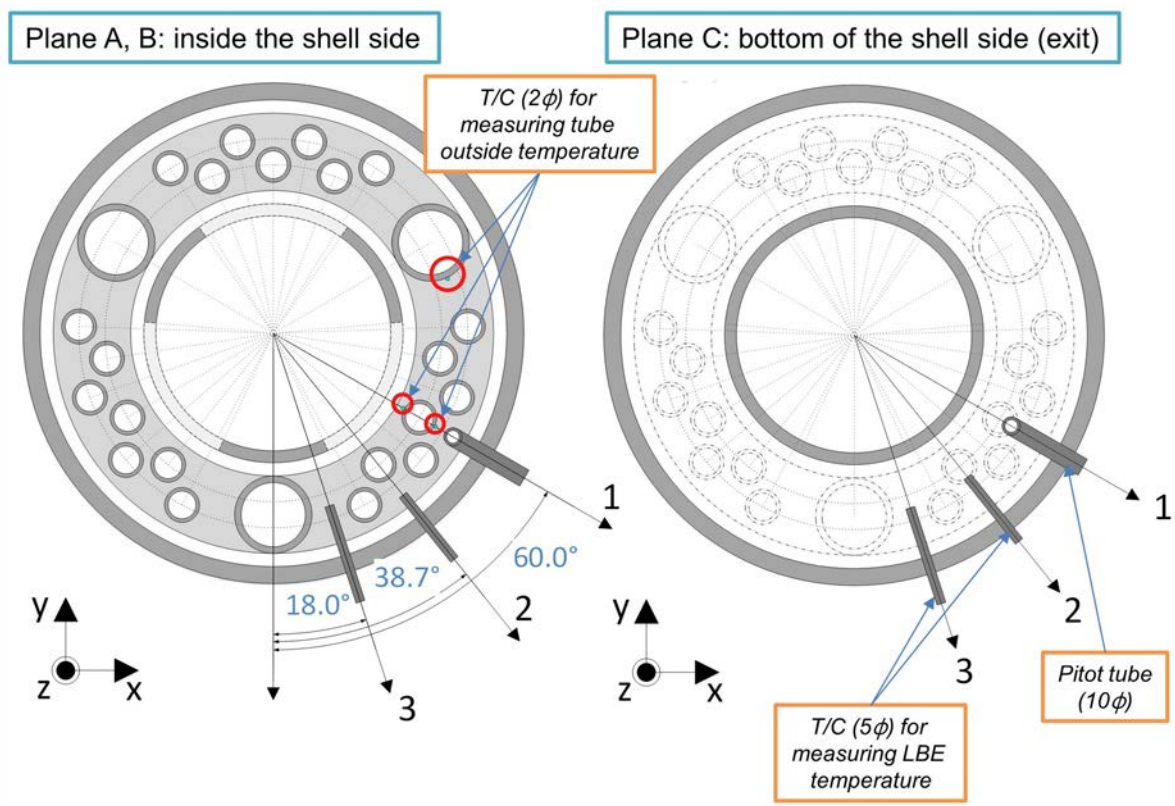

Figure 5.21 Position of instrumentation probes on arbitrary planes A, B, and C in PILLAR heat exchanger on planar cut view

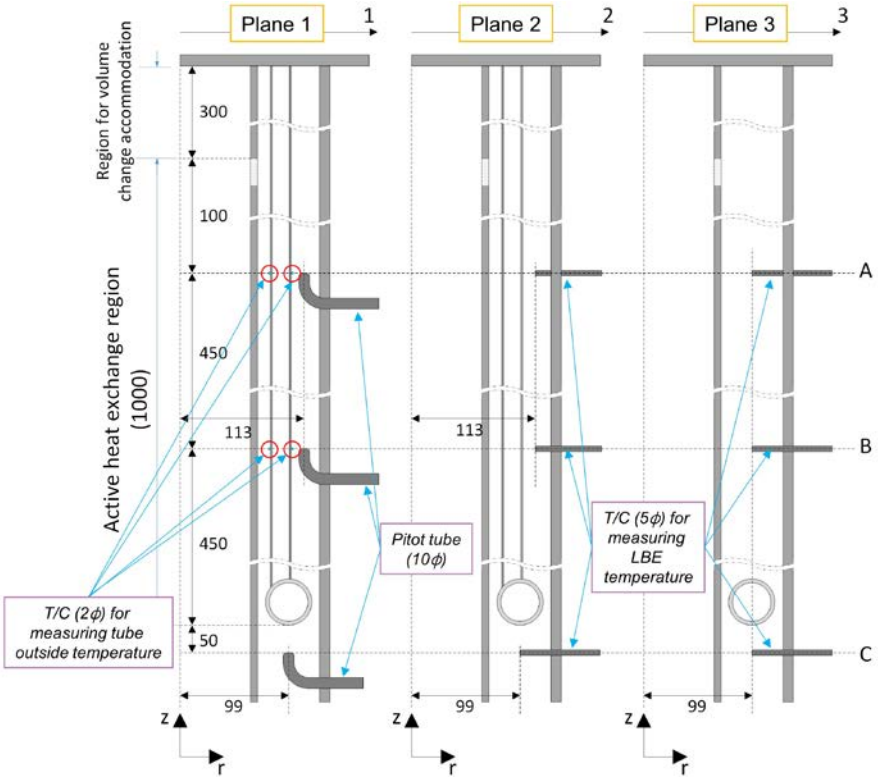

Figure 5.22 Position of instrumentation probes on arbitrary planes A, B, and C in PILLAR heat exchanger on axial cut view

5.2.3 PILLAR experiment procedure and conditions

Both steady state and transient LBE natural circulation experiments were carried out using PILLAR LBE pool integral test facility. Prior to those tests, a pre-conditioning for the new facility and preliminary tests to assess the heat loss of facility was performed. Several sets of the steady-state experiment results were generated for the code benchmark of MARS-LBE by varying the core power rating while trying to keep secondary side conditions as same as possible for all of the sets. The transient experiments were conducted by changing the operation conditions in terms of instantaneous maneuvering in the electrical power supplied to core heater rods and the secondary side pump speed.

5.2.3.1 Pre-conditioning of the facility

As all the components consisting of PILLAR was newly constructed, the conditioning of facility proceeded first. The empty LBE storage was filled with LBE ingots, at least 60% volume of the vessel, as its volume is about 0.5 m^3 and the necessary amount of LBE when running a test is about 0.3 m^3. LBE was prepared with a form of ingot and transferred through an opening, which is usually blocked by a blind flange in normal operation. After that, the heating jackets attached on the surface of the tank were activated to melt the LBE.

The second step for the conditioning was purging hydrogen gas, 4% hydrogen with argon balance, to reduce the amount of oxygen. Even if LBE is

not reactive with oxygen, the surface of LBE ingot might be oxygenated before putting into the storage tank. For a better efficiency, H_2 gas was supplied both on the top of LBE free level and under the level through a submerged feeding line. Since the oxygen content in LBE may change the surface condition of contacting steel, this hydrogen purging can be re-performed between each test campaign when LBE is not on the main vessel to maintain the chemical condition of LBE with respect to oxygen.

The last step is a trial run for the heat exchanger tube side. A centrifugal pump and a glove is two main components comprising the secondary water cooling loop, which controls flow speed and pressure to the fluid, about 6-8 bar. The pump cannot sustain pressure head in a large flow rate if the glove valve is fully opened. Hence, to operate the pump in a desired flow rate range, the openness of glove valve must be controlled. In order to minimize the control effort, only controlling the speed of pump was chosen and the glove valve was to be kept at the same openness by designating it through a trial run. Checking the flow rate and pressure at the same time in the trial run, a conversion curve for inverter frequency, which governs the flow speed, versus flow rate was secured and used for the experimental campaigns.

5.2.3.2 Experimental procedure

A test campaign can proceed when all the LBE in the storage tank is liquefied. The procedure is similar to the first paragraph as described in Section 5.2.3.1.

After LBE is melted, the heating jackets not only on the surface of main vessel and the transfer line between the main vessel and the tank are turned on to make temperature to be higher than 200 ˚C, as in the HELIOS operation procedure. Filling up LBE into the main vessel is the same with the HELIOS as well by exerting gas pressure to the LBE storage tank so that LBE free surface is pushed.

By checking the signals from the sensors, the amount of LBE needed for a test run is finely tuned by trial and error. Especially, the free surface level on the main vessel is of importance in this procedure, while in the HELIOS case it was designated to be higher than the lowest point of expansion vessel. The difference comes from the fact that the level of LBE determines the heat transfer length in the heat exchanger and it must be in a conceivable range expected at the design stage to conduct a precisely controlled experiment. To do so, the final level of LBE is decided by using the signal from the guided wave level sensor (LV151) located in the leveling pipe attached to the shell side of heat exchanger. After the fine tuning is done, the motor-operated valve is closed so that the main vessel and the storage tank are isolated.

Since PILLAR uses pressurized water for the cooling of system, LBE might freeze or water might boil in a certain condition. If LBE is transferred to the main vessel when water is filled in the tube side, the former can happen and the level control no longer is achievable until LBE melts by getting heat from the surface jacket heater. As aforementioned, the LBE level control at the test preparation is of prime importance, so water filling to the secondary side is designated to be preceded by the LBE filling process. In this regard, the freezing of LBE and boiling of water is not avoidable when water is filling up the heat

exchanger tube. For the reliable operation of the centrifugal pump, it is required to fill up the whole system without a cavity. To do so, boiled water needs to be released by opening the valve at the top of the secondary side while water is being purged so that water fills the piping. In this moment, LBE freezing is inevitable. After water fills the whole loop, the secondary side is pressurized and water temperature rises while LBE melts by heat supplied from the heating jacket.

When both LBE is in liquid state and the secondary side is full of pressurized water, a test session can be started by controlling the electrical power supplied to the heater rods in the core region. A certain amount of heat can be supplied to the core and it determines LBE natural circulation flow rate and temperature difference between heat sink and heat source. Before started, all the heating jackets that heat up the surface of main vessel needs to be turned off because during the test campaigns, heat loss to the environment will not be considered, which will be described in Section 5.2.4.1. At the same time, the centrifugal pump for the secondary side is activated by controlling the frequency of inverter as measured and pre-determined by the process delineated in the last section.

These manipulations generate LBE natural circulation flow and temperature distribution through energy transport until the system reaches a new steady state. For a steady state experiment, no other manipulation is made for a few hours so that a set of steady-state experimental data is collected and its quality, in terms of standard deviation when each of parameters are averaged, is maximized. On the other hand, for a transient experiment, any parameter of

interest should be manipulated so that the system reacts to the condition change. In this regard, the transient test begins only after a 'steady state' is maintained over at least two hours so that any interference on reaching the steady state is suppressed as much as possible. When a transient session is started by maneuvering the system, this principle still holds: for two hours, no manipulation is allowed so that the system transients are not interrupted or interfered by the manipulation.

5.2.3.3 Experiment conditions and test matrices

As in the HELIOS experiments, the steady state experiments conducted in PILLAR were defined with the core power ratings. Final steady-state conditions were reached after some manipulations on the system following the experimental procedure. For natural circulation experiments, there are only the limited number of variables to be controlled as the phenomenon is dependent upon the inherent nature of a system such as height difference between heat source and heat sink, the buoyancy of a working fluid given by density difference, and hydraulic resistance, which is affected by the geometrical arrangements of the system. Hence, test conditions that can be controlled directly by maneuvering the facility would only be the electrical power supplied to the core, water flow rate and inlet temperature of the heat exchanger tube side.

For the steady-state natural circulation experiments, seven sets of tests

were performed in terms of different core power ratings: 249, 253, 284, 293, 302, 306, and 315 kW, classified in an ascending order. These conditions were directly designated as test numbers as S-01 to S-07, where the leading 'S' means the test is for steady state and following numbers indicate each case. Besides, the secondary side conditions including water inlet temperature, water mass flow rate, and pressure exerted on it were to made nearly constant to reduce potential uncertainties from boundary condition change so that these results can be utilized for the code validation. Table 5.9 gives the test matrix and the definition of each case.

Unlike the steady state experiments in which the final state is determined distinctively, transient tests needs to be defined by two states, namely, the first state when not manipulated and the final state after the system saturates. Considering the tests are performed by controlling the core power and the secondary side flow rate, the conditions are to be written as in a form of T-VPPP-P1~P2/F1~F2: the leading letter, T, indicates this case is for a transient test. The following V describes which parameter is manipulated and: the letter V is designated to be P for a power transient, while it is F for a secondary side flow transient. PPP is for a condition change such that INC for increasing and DEC for decreasing. The last part consists of the two states given by P1 and F1 as the first condition and P2 and F2 as the final condition. Hence, when just one parameter is manipulated, then it can be expressed like P1/F1~F2 or P1~P2/F1. The power indicators P1 and P2 are given in kW while the flow indicators F1 and F2 are in kg/s. Figure 5.23 shows the definition of each case and test matrix graphically.

Table 5.9 PILLAR steady-state natural circulation test matrix and case definition

Test ID	Core power (kW)	Avg. water inlet temperature (°C)	Avg. water mass flow rate (kg/s)	Avg. water pressure (bar)
S-01	249	102.5	3.30	6.20
S-02	253	100.1	3.26	6.39
S-03	284	102.2	3.31	6.17
S-04	293	102.3	3.32	6.07
S-05	302	102.6	3.31	6.13
S-06	306	101.2	3.23	6.33
S-07	315	102.5	3.32	6.08

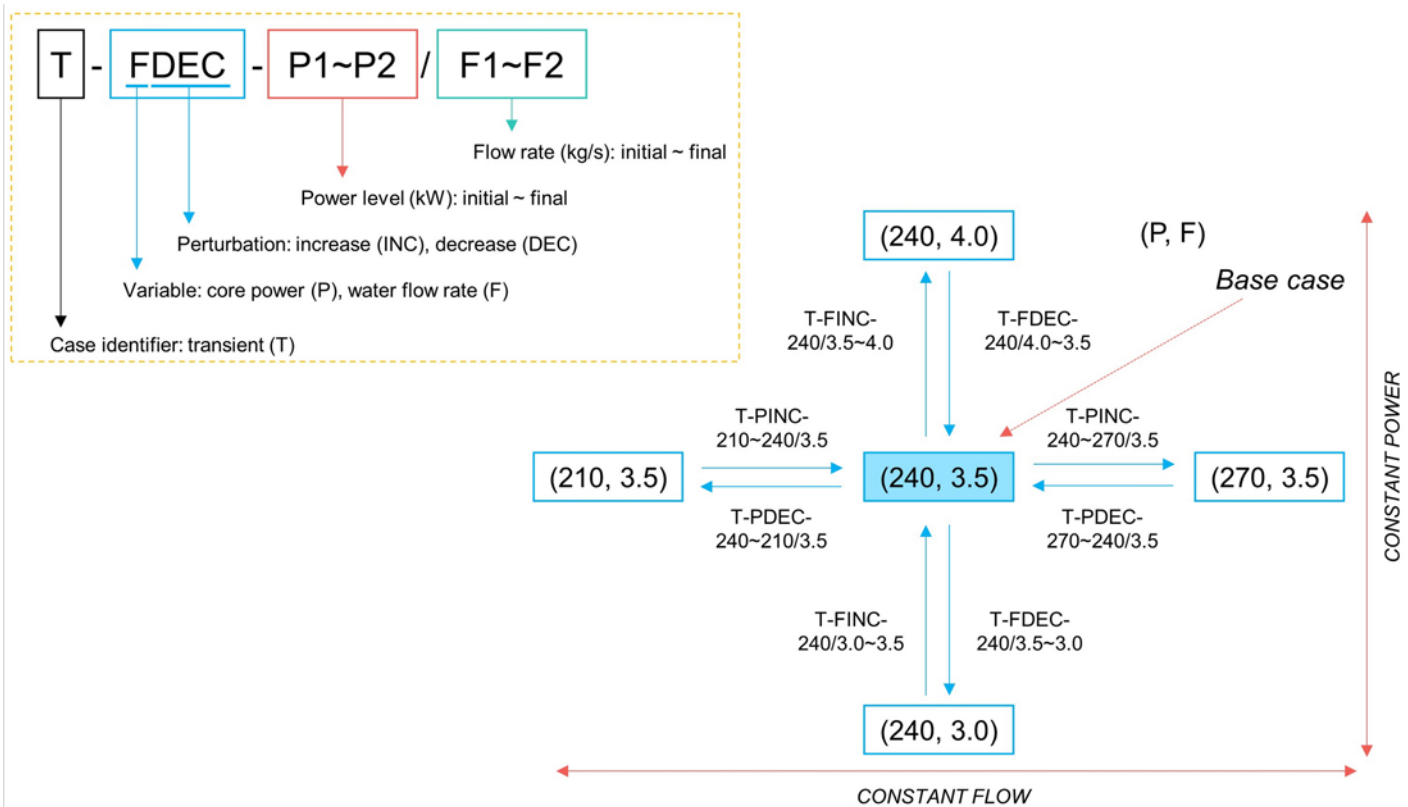

Figure 5.23 Graphical test matrix and case definition on PILLAR transient natural circulation experiments

5.2.4 Experiment results and discussion on LBE pool natural circulation

5.2.4.1 System heat loss evaluation

Prior to starting experiments with the installed PILLAR facility, a trial run and preliminary experiments were conducted to grasp the characteristics of the system. The most important point in the preliminary experiments is to evaluate heat loss, which is crucial in thermal hydraulic experiments, especially in natural circulation in which the behavior of the system depends on the thermal equilibrium between heat source and heat sink. Heat loss to the environment is inherent in the real world; hence, there is no way to prevent. However, if the amount of heat loss is measured, it can be controlled with a corresponding action by compensating for the amount. Therefore, this procedure must precede the actual experimental campaign to increase the reliability of the experimental data.

For this purpose, the heating jacket, a device which incorporates external surface heater to heat up the surface and thermal insulation to prevent heat loss, was operated without filling LBE to the PILLAR main vessel. After the temperature of the whole system was raised, measurements were taken over a few hours. The heating jacket is connected to a proportional-integral-differential (PID) controller to control the heater output so that the system temperature fluctuation can be minimized. In order not to make any uncertainties, the secondary side (H/X tube side) is not filled up with water

during the evaluation procedure because water may contribute to the removal of extra heat further from the system. The above measurements were sustained and repeated for about 2-3 hours to minimize the variation with time.

Through this procedure, the amount of change in the heater output over time can be inversely calculated based on the integrated average of the measurement span. Hence, utilizing the sum of time average of the electric power delivered to each of the heating jackets, which are denoted by subscript i, during the time span from t_0 to $t_0 + \Delta t$, the total amount of heat loss of the system, Q_{loss}, can be defined as in the following Eqn. (5.49). The overall procedure is described in Figure 5.24.

$$Q_{loss} \equiv \sum_i \frac{1}{\Delta t} \int_{t_0}^{t_o + \Delta t} Q_i dt \tag{5.49}$$

In a strict manner, the adiabatic condition cannot be met due to the (laminar) natural convection by surrounding air. When a particular object lying in the air is at a higher temperature than its surroundings, heat loss occurs primarily through natural convection with a slow rate of heat transfer. It is known that this relationship can be expressed as a product of dimensionless numbers, Nusselt number (Nu) and Rayleigh number (Ra) (Lienhard, 1973):

$$\frac{\mathrm{Nu}}{\mathrm{Ra}^{1/4}} = const. \tag{5.50}$$

Each of these parameters have proportional relationships with the convective

heat transfer coefficient and the temperature difference between the fluid surrounding the object, the air in this case, and the wall surface, as shown in Eqn. (5.51):

$$\mathrm{Nu} = \frac{hL}{k},\ \mathrm{Ra} = \frac{g\beta\Delta T\rho^2 C_p L^3}{\mu k} \Rightarrow h \propto \mathrm{Nu},\ \Delta T \propto \mathrm{Ra}\,. \qquad (5.51)$$

With a further manipulation, Eqn. (5.51) can be cast with Q_{loss} and an arbitrary constant c_1 as given in Eqn. (5.52):

$$\begin{aligned} &Q_{loss} = hA\left(T_{surf} - T_\infty\right) = hA\Delta T \\ &Q_{loss} \propto \mathrm{Nu}\Delta T \Leftrightarrow \propto \mathrm{Ra}^{1/4}\Delta T \Leftrightarrow \propto \Delta T^{5/4}\,. \qquad (5.52) \\ &\Rightarrow Q_{loss} = c_1\Delta T^{5/4} \end{aligned}$$

In other words, by knowing the time average of the power variation and the temperature difference between the surrounding air and the system surface, the constant c_1 can be obtained, and it is possible to evaluate the integral heat loss with respect to the change of the system temperature. To do this, the air bulk temperature and the surface temperature of the main vessel of PILLAR should be measured and it was done by installing several thermocouples. The system integral heat loss would be generated through the outside of the heating jacket now that there is no need to remove the heating jacket during the experiment. Therefore, the surface temperature was designated as the surface temperature of the heating jacket measured at a specific point.

In order to select a representative system temperature, the

thermocouples were installed at the center of the device in the axial direction. Three thermocouples were installed, one for measuring the surface temperature and the other for the ambient temperature with a radial offset to allow the measurement of temperature change slightly away from the main vessel surface. The locations of the thermocouple tip was set at the same level with the tip of a thermocouple that measures the internal temperature of the main vessel so that the temperature gradient can be determined qualitatively. The established set of thermocouples for heat loss evaluation is shown in Figure 5.25.

The heat loss evaluation was made using three averages and each utilizes about 2-3 hours of data to reduce the error. The temperature variation and time-average interval in the evaluation are shown in Figure 5.26. One average point that is not visible in the figure is from the data that was measured when the heating jacket was first installed and its first run was conducted. The data were fitted in the form given by Eqn. (5.52); each black dot represents the time-averaged system total heat loss and the red curve in Figure 5.27 presents the fitting, where the function of the fitted curve and R^2 value are given by:

$$\begin{aligned} Q_{loss} &= c_1 \Delta T^{5/4} = 0.09674 \Delta T^{5/4} \\ R^2 &= 0.98815 \end{aligned} . \qquad (5.53)$$

As a result, the heat loss is about 4 kW even when the difference between the outer surface temperature of the heating jacket and the ambient temperature is about 20 ˚C. Considering that the actual experiment campaigns in the following sections were carried out with over 200 kW of core power

ratings, this amount is relatively negligible. In order to make sure of the effect of heat loss and power compensation, a test was conducted by filling the PILLAR main vessel with LBE and providing 250 kW core power for more than 70 hours. Contrary to the heat loss evaluation given earlier, the heat exchanger tube side was active by pumping water into the secondary side to remove the heat from the system. Meanwhile, the PID controller to the heating jackets was allowed to supply electrical power automatically through the temperature measurements. The obtained results are described in Figure 5.28 and Figure 5.29.

In the experiment in approximately 70 hours, after the steady state natural circulation was achieved, a relatively large amount of electrical power was supplied to the external heat tracing over the first 30 hours. It was gradually decreased from 30 hours and about 35 hours from the beginning, about 1/3 to the initial amount was maintained for about 20 hours. From about 55 hours, most PID controllers were turned to be inactive and only one PID controller was active. The amount of heat supplied to the entire system through the heating jackets had changed, but when the temperature variation of the system was observed, it was rather influenced by the fluctuation of the ambient air temperature, as seen in the lower inset of Figure 5.28. As can be seen in Figure 5.29, the amount of heat provided by the primary core is removed in a small error range, regardless of the amount of heat supplied to the heating jacket. Therefore, it is estimated that the heat given by the heating jacket does not have a great influence on the change of the overall system temperature in high core power rating conditions, as previously confirmed that the PILLAR main vessel

has negligible heat loss.

In HELIOS case, about 1/3 of the core output is released to the ambient air when the external surface heater is not operated since the flow traversing length is more than 20 m and the loop has a relatively large surface area compared to its volume. On the other hand, the heat loss of PILLAR can be effectively suppressed mainly due to its three distinct features: firstly, it has small surface area over its volume. Secondly, the components including core, upper plenum, and riser are enclosed by the external components. Lastly, it adopts an improved insulation with its thickness being twice as thick as that of HELIOS (PILLAR: 5cm, HELIOS: 2cm).

The actual test showed that even if the core power rating of 250 kW or more was applied, the difference between the outer surface temperature of the heating jacket and the ambient air temperature was 20 ˚C. Therefore, it was concluded that the heat loss of the entire system is negligible that it will not affect the experimental results. In the experimental conditions, the heating jacket controller is set at a relatively low temperature so that only a small amount of heat loss is compensated.

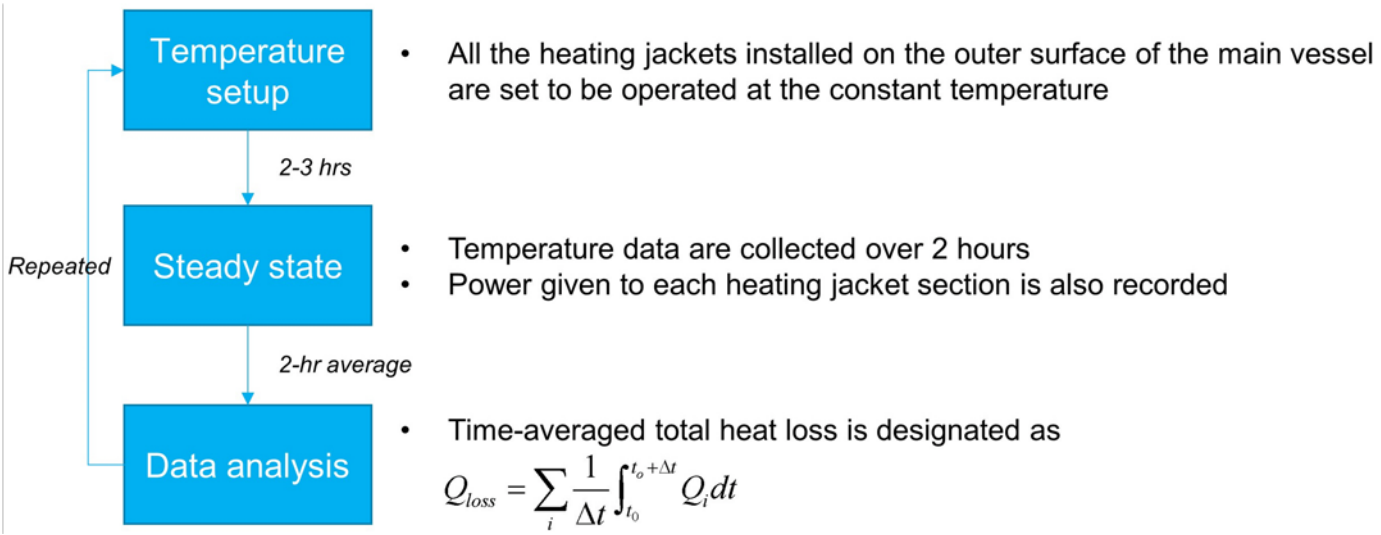

Figure 5.24 PILLAR system integral heat loss evaluation procedure

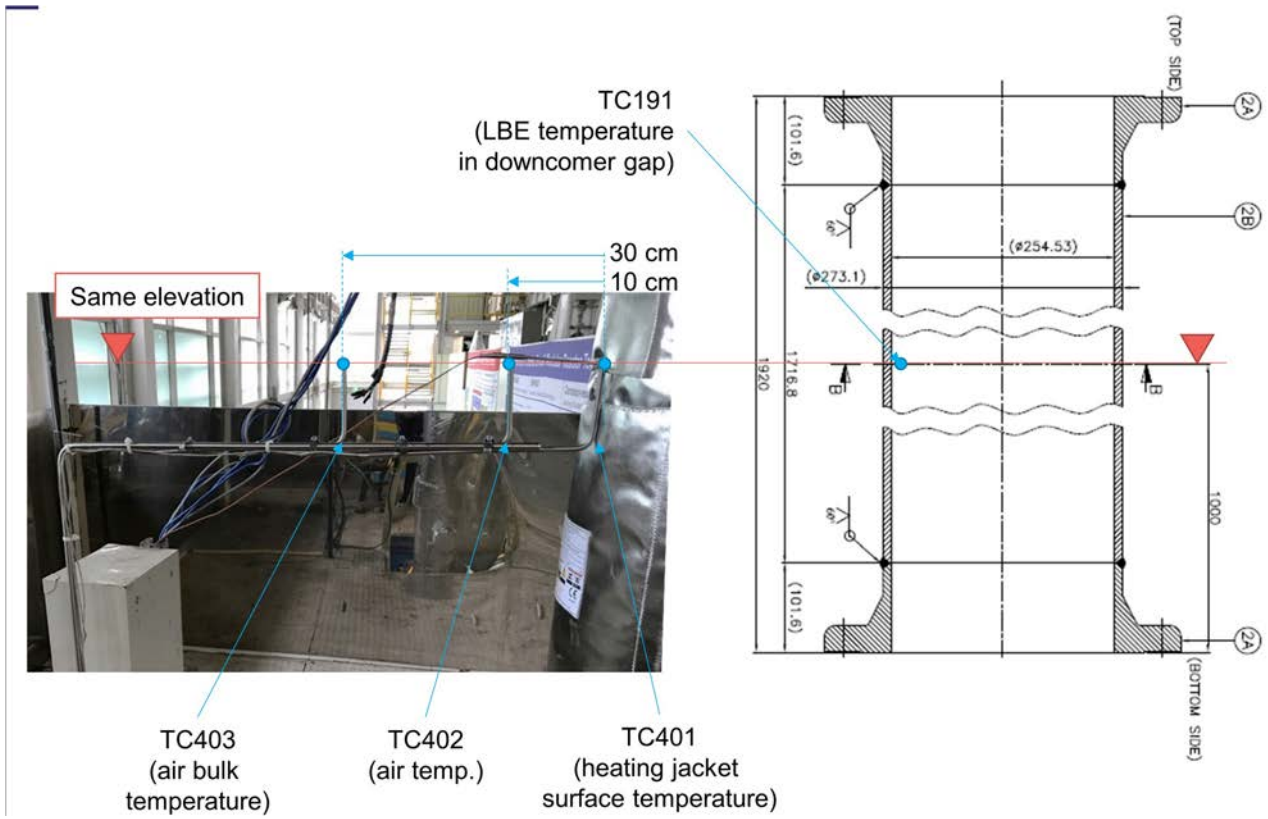

Figure 5.25 Locations of thermocouples for the evaluation of PILLAR system integral heat loss

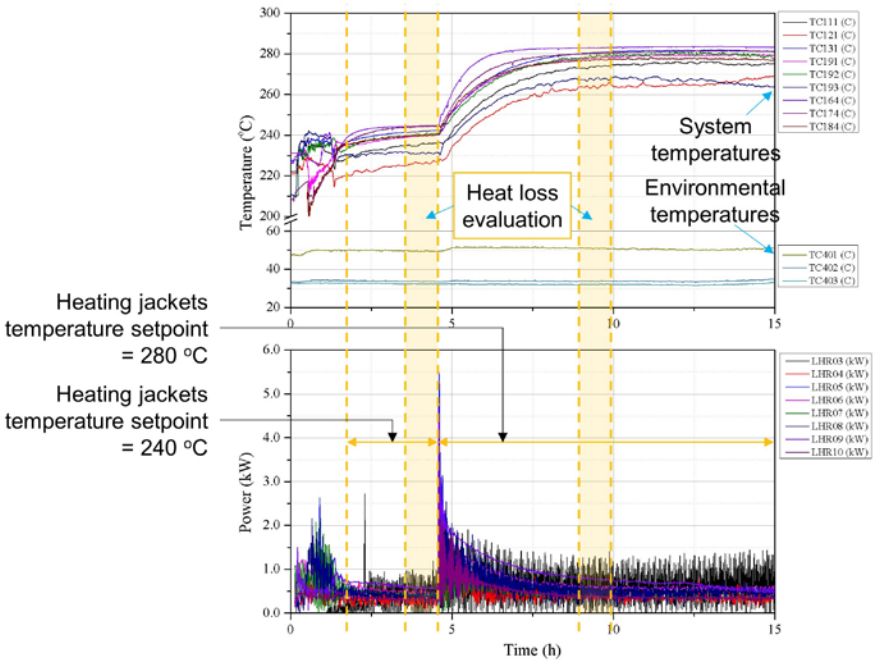

Figure 5.26 PILLAR main vessel integral heat loss evaluation test results

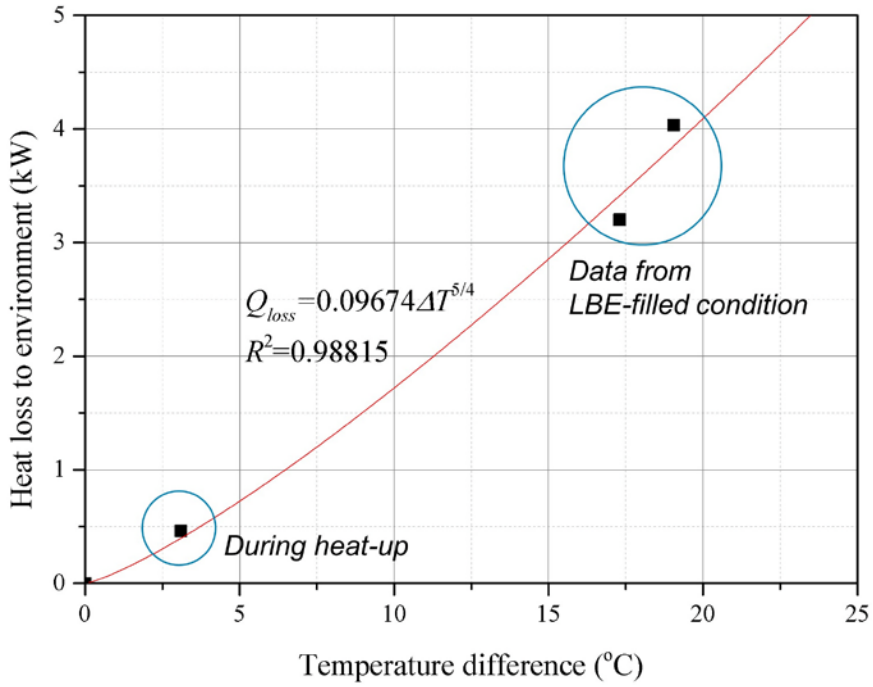

Figure 5.27 Fitted curve for PILLAR system integral heat loss as a function of temperature difference between surface and ambient temperatures

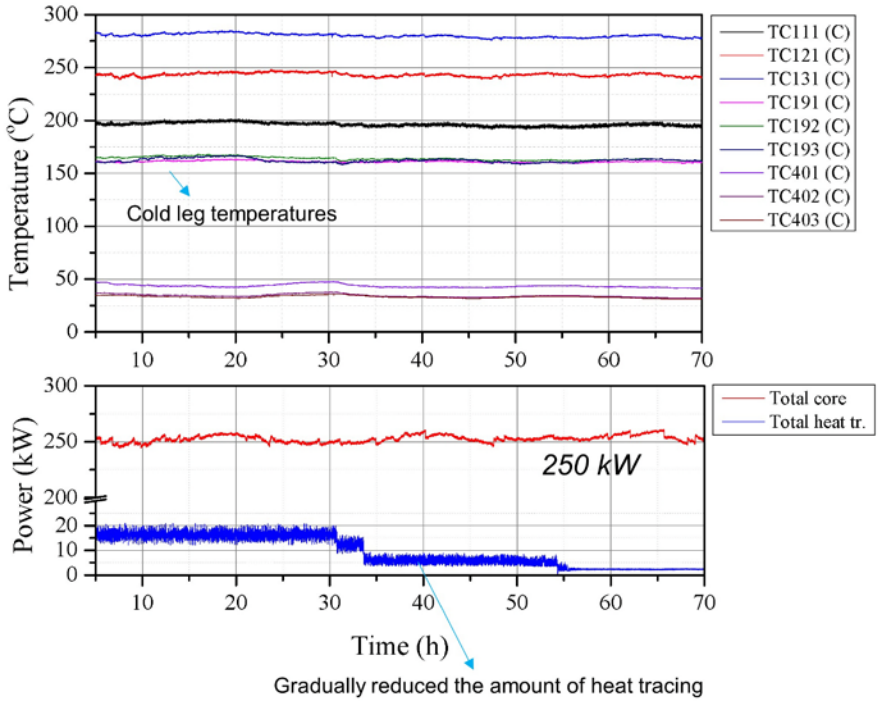

Figure 5.28 PILLAR primary system response to the variation in the amount of heat tracing on the main vessel surface

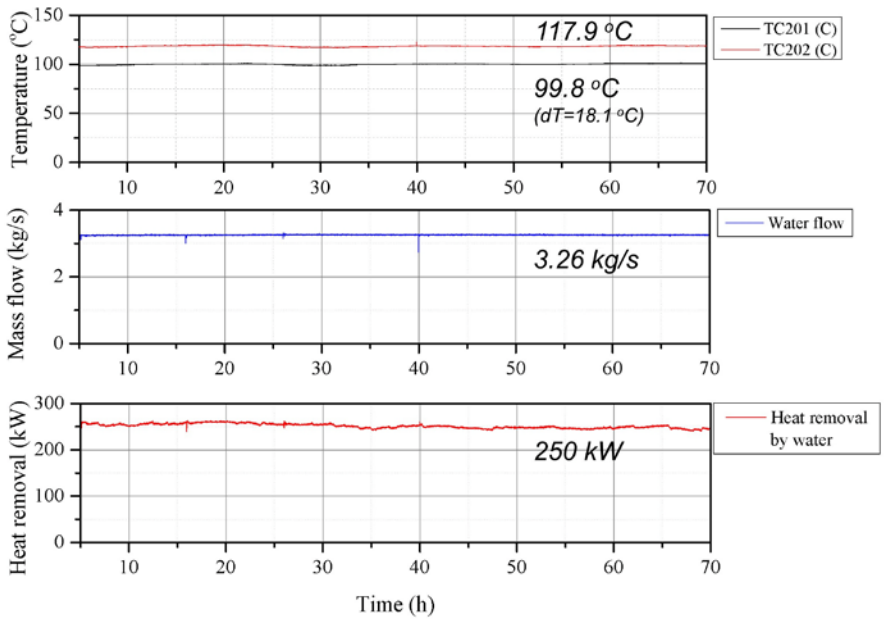

Figure 5.29 PILLAR secondary cooling system (heat exchanger tube side) response to the variation in the amount of heat tracing on the main vessel surface

5.2.4.2 Experimental results and discussion on steady-state LBE pool natural circulation

As defined in Table 5.9, seven LBE steady-state natural circulation experiments were carried out in the pool configuration with PILLAR. Since the main vessel showed negligible heat loss to the environment, no heat compensation was made. Similar to the HELIOS cases, there were slight temperature fluctuations within a day due to the daily temperature change and the system was maintained at least for two hours to minimize the error by following the principle described in Section 5.2.3.2.

Table 5.10 summarizes the steady-state experimental results from S-01 to S-07 cases in terms of temperatures, mass flow rates and pressure in both primary and secondary sides. In all cases, heat balances between primary and secondary side were calculated to be matched within 5% ranges. Considering that there was no heat compensation through the outermost wall of the main vessel, it can be also made certain that the system is equipped with enough insulation so that it loses a negligible amount of heat to the environment.

It is notable that the cold leg temperatures were relatively low compared to the prototypic reactor, about 300 °C. This low cold leg temperature comes from the cooling capability of the heat exchanger; in other words, it is due to a large overall heat transfer coefficient in the heat exchanger. Since temperature difference between heat exchanger and primary coolant is determined by the overall heat transfer coefficient, the secondary side conditions work as boundary conditions in natural circulation. Moreover, at the

same power removal rate, the temperature difference would decrease if the overall heat transfer coefficient increases, vice versa. To elevate the primary side temperature, the secondary water can be heated so that the secondary side inlet temperature would rise, but this approach is limited the pressure exerted upon water and the thickness of each tube in the heat exchanger. Thus, low-power operation is not viable in PILLAR because of the design and cooling capability of heat exchanger. Regarding the experience and the experimental results, the lowest core power would be 200 kW since the cold leg temperature would be about 150 ℃ in this condition. It is recommended to have slight temperature margin between operation condition and LBE freezing condition, 125 ℃, because the system needs to be maneuverable in an exceptional condition during experiments.

Table 5.10 Experimental results on steady-state LBE pool natural circulation in PILLAR

ID	Primary (LBE) side					Secondary (water) side			
	Total core power (kW)	Hot leg temperature (°C)	Cold leg temperature (°C)	Temperature difference (°C)	LBE mass flow rate (kg/s)	Inlet tempe-rature (°C)	Outlet tempe-rature (°C)	Water mass flow rate (kg/s)	Pressure (bar)
S-01	249	163.46	252.53	89.07	18.55	102.5	119.8	3.30	6.20
S-02	253	161.54	251.17	89.63	18.67	100.1	118.2	3.26	6.39
S-03	284	170.74	268.56	97.83	19.25	102.2	122.0	3.31	6.17
S-04	293	172.48	272.74	100.3	19.49	102.3	122.7	3.32	6.07
S-05	302	173.89	276.50	102.6	19.63	102.6	123.6	3.31	6.13
S-06	306	170.60	274.44	103.8	19.70	101.2	122.7	3.23	6.33
S-07	315	176.30	282.82	106.5	19.85	102.5	124.4	3.32	6.08

Note: all of the values given above are average values from measurements in each case.

5.2.4.3 Experimental results and discussion on transient LBE pool natural circulation

Among several experimental sets conducted as defined in the graphical test matrix shown in Figure 5.23, only four cases, T-PINC-210~240/3.5, T-PDEC-240~210/3.5, T-FINC-240/3.5~4.0, and T-FDEC-240/4.0~3.5, are to be presented in this session. It is because each type of tests showed similar aspects in system reactions and therefore, including all the results would be redundant. Each of cases are shown in Figure 5.30 to Figure 5.33, respectively.

For the core power transients tested in T-PINC-210~240/3.5, T-PDEC-240~210/3.5 cases, depicted as Figure 5.30 and Figure 5.31, correspondingly, mass flow rate given by natural circulation saturated within 3 minutes after the core power rating was changed when 12.5% of core power varied from initial conditions. Considering the time needed to be saturated, the primary side tend to saturate to a new steady state faster than secondary side. In addition, water enthalpy at the outlet of secondary side varied so that heat balance to be matched; and it contributed to the much slower saturation. In this condition, heat balance mismatch over the heat exchanger happens until outlet enthalpy increases when a proper control on the secondary side conditions are not given.

As shown in the cases of T-FINC-240/3.5~4.0 and T-FDEC-240/4.0~3.5 with Figure 5.32 and Figure 5.33, respectively, slight overcooling and undercooling were drawn by secondary side flow rate changes while a negligible amount of change happens in core inlet temperature, which is the same with heat exchanger outlet temperature. Since the instantaneous mismatch

in heat balance between the primary and secondary side, the outlet enthalpy also varied similar to the investigation in the power transients so that heat balance were to be matched.

The experimental results with the transient tests can be compared with the actual reactor. Considering that PILLAR does not load nuclear fuel rods but electrical heaters instead, a conceivable difference between the facility and the reactor is the existence of reactivity feedback. For a rapid power transient, it can be achieved in the actual reactor core as well due to a rapid power change expected in the reactor with a steep reactivity insertion. Hence, the power transient tests conducted with PILLAR can be thought to be realistic. Furthermore, the overcooling and/or undercooling expected in the instantaneous change of secondary side flow rate will lead to core inlet temperature change and finally, the reactor core would get a slight amount of reactivity insertion. Meanwhile, similar to the test results, the secondary side of the actual reactor would require more time to be saturated in comparison with the primary side. Overall, the experimental sessions carried out by PILLAR are thought to be represent the behaviors expected in actual passive LBE-cooled systems.

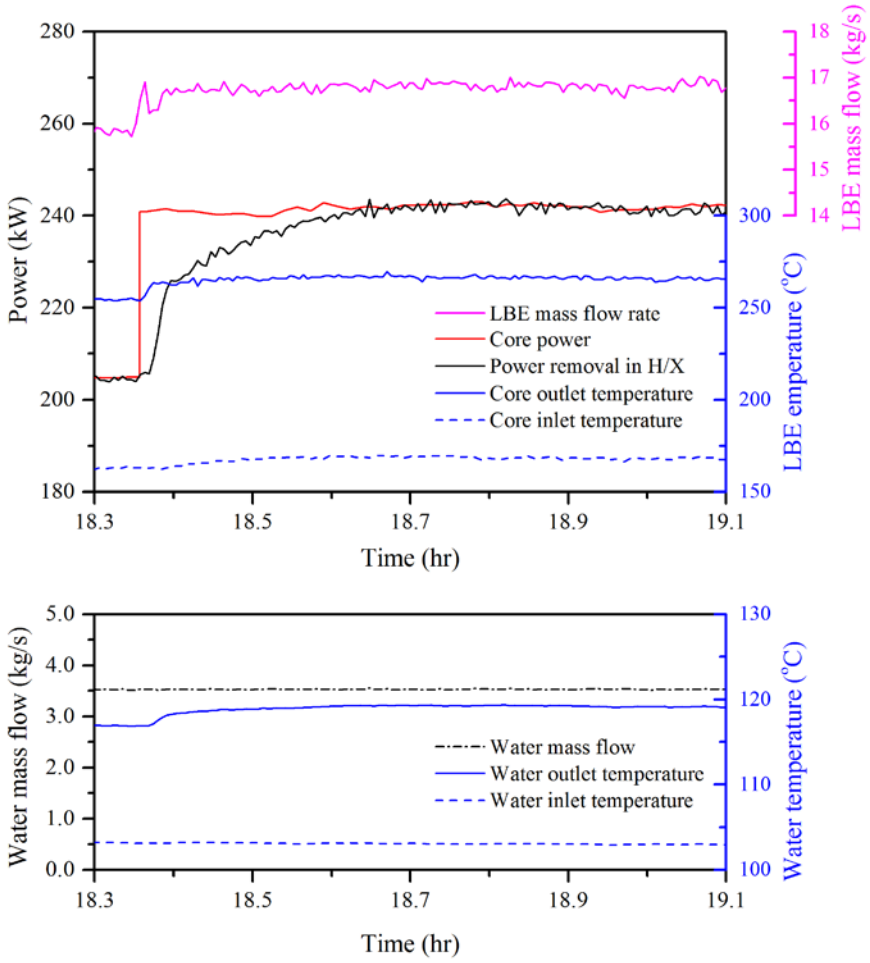

Figure 5.30 PILLAR transient natural circulation experimental results: instantaneous core power increase (Case No.: T-PINC-210~240/3.5)

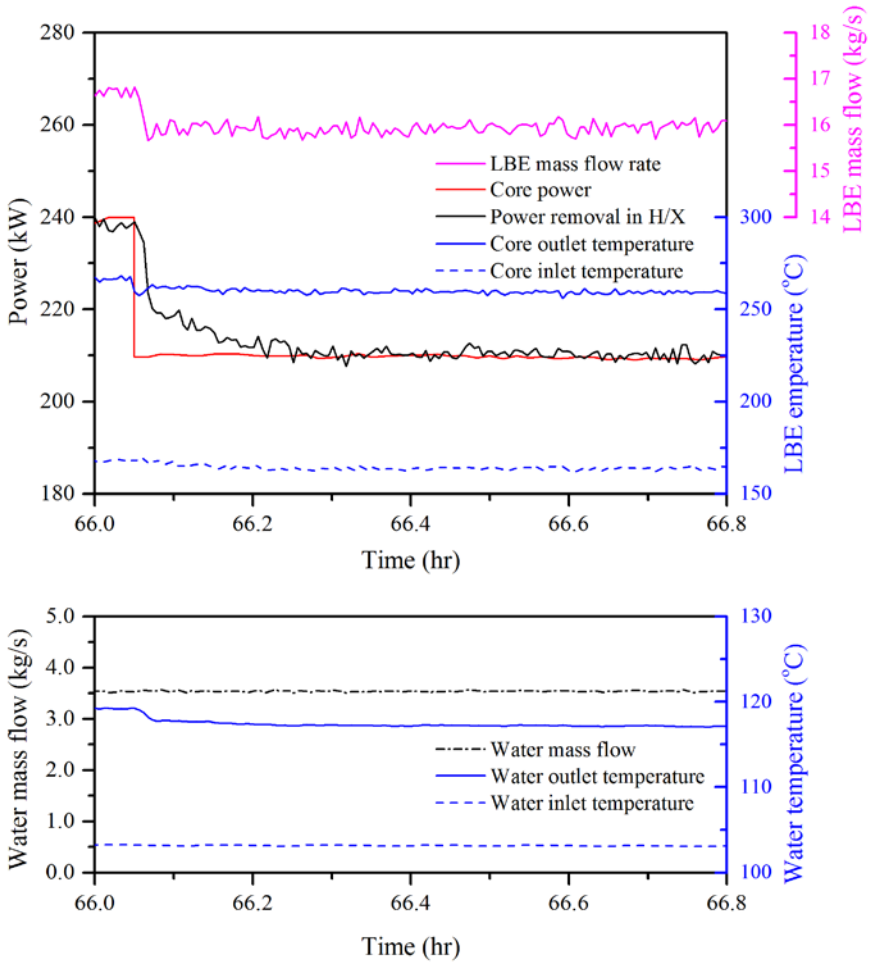

Figure 5.31 PILLAR transient natural circulation experimental results: instantaneous core power decrease (Case No.: T-PDEC-240~210/3.5)

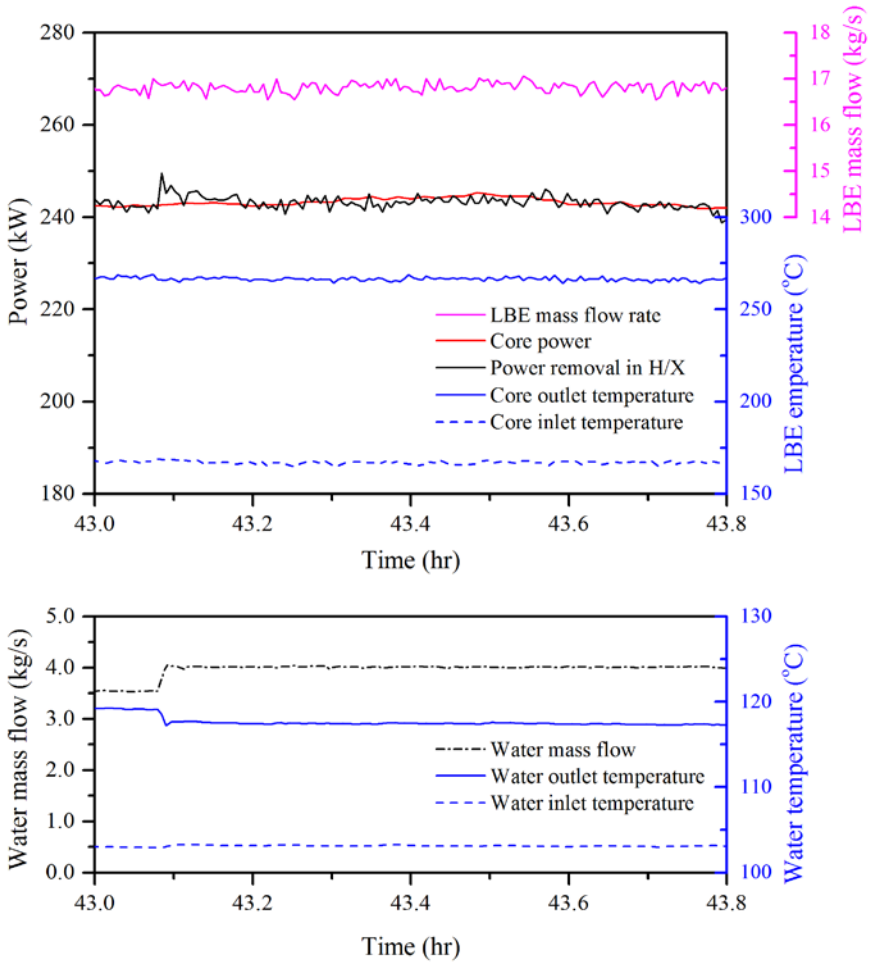

Figure 5.32 PILLAR transient natural circulation experimental results: instantaneous secondary side flow increase (Case No.: T-FINC-240/3.5~4.0)

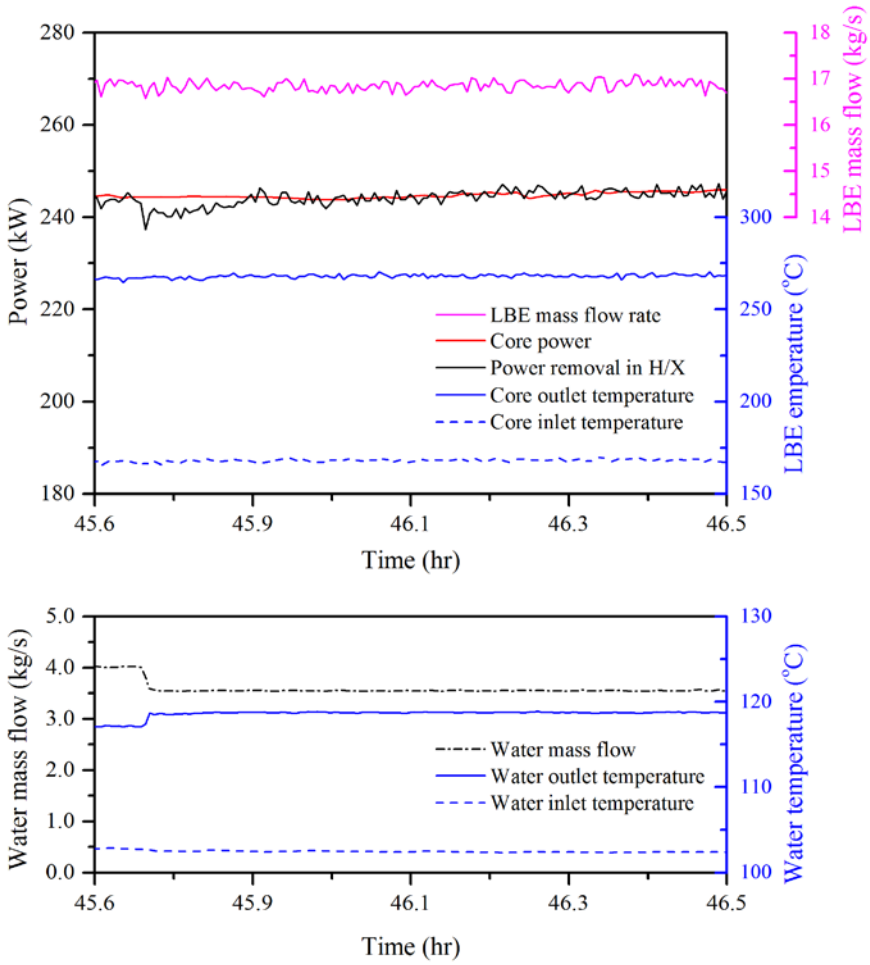

Figure 5.33 PILLAR transient natural circulation experimental results: instantaneous secondary side flow decrease (Case No.: T-FDEC-240/4.0~3.5)

Chapter 6 Code Validation and Numerical Analysis

6.1 One-dimensional system thermal-hydraulics (STH) code: MARS-LBE[4]

MARS is a system safety analysis code based on best-estimate modeling developed by KAERI (Korea Atomic Energy Research Institute) by integrating RELAP5/MOD3 and COBRA-TF which are widely used codes in the thermal-hydraulic analyses for LWR; the integrated code is capable of one-dimensional thermal-hydraulic system analysis and multi-dimensional subchannel analysis where its backbone codes are applicable, respectively (KAERI, 2006). RELAP5 is established on one-dimensional, two-fluid flow model using two-fluid, six-equation formulation given by mass, momentum, and energy conservation of water and steam with several relations on phase transition between two fluids (Carlson et al., 1990). COBRA-TF is a three-field, three-dimensional analysis code and two-phase flow with reflood heat structure

[4] This section has been written based on the following journal paper: Yong-Hoon Shin et al., "Experimental studies and computational benchmark on heavy liquid metal natural circulation in a full height-scale test loop for small modular reactors," Nuclear Engineering and design, 316, 26-37, 2017.

model can be treated with flexible noding schemes (Thurgood et al., 1983). These two codes are coupled implicitly by using dynamic link library techniques in MARS code structure. The code is also capable of other reactor safety calculations such as point kinetics modeling.

MARS has been updated by implementing various fluid properties for instance sodium (Na), helium (He), and carbon dioxide (CO_2) to cope with growing interests on the generation-IV reactor system analysis. In this respect, a group of researchers in SNU has improved the code by modifying some calculation schemes in convective heat transfer suitable for heavy liquid metal and updating LBE thermophysical property table (OECD Nuclear Energy Agency, 2007). The updated code is called MARS-LBE 3.11, which has been originated from MARS 3.1 release.

6.2 Code validation on thermal-hydraulics with steady-state experimental results

6.2.1 Code benchmark with HELIOS loop test results

6.2.1.1 System nodalization and input preparation on HELIOS

For computational modeling, nodalization needs to be preceded by interpreting the system into several calculation nodes with respect to the scope of calculation and the capability of computational code. In this respect, In the input file for MARS-LBE, HELIOS hydrodynamic components are described with several one-dimensional components such as pipes, junctions, time-dependent volumes, and time-dependent junctions to impose unsteady boundary conditions with about 170 hydrodynamic cells, as depicted in Figure 6.1. Considering that the natural circulation experiments were carried out in a loop configuration, one-dimensional calculation schemes used in MARS were sufficient to analyze the global phenomena. In addition, heat structure models are included where heat transfer occurs among solid bodies like heater rods and heat exchanger, and the themophysical properties of constituent material, 316L stainless steel, are provided as listed in Table 6.1 (Mills et al., 2004).

In MARS-LBE, convective heat transfer is treated in a subroutine by calculating convective heat transfer coefficient from Nu, which is generally given by a function of Re (Re = $\rho v_0 d_h/\mu$) and Pr (Pr = $\mu C_p/k$) (or a product of two nondimensional parameters, Pe = $\rho C_p v_0 d_h/k$) of a fluid in a calculation cell.

As convective heat transfer aspects varies considerably with the thermophysical property of a fluid, in other words, the magnitude of Pr, correlations used for Nu is properly chosen accordingly. Seban-Shimazaki correlation (Seban and Shimazaki, 1949) is applied to any heat transfer conditions for LBE:

$$\mathrm{Nu}_{LBE} = 5.0 + 0.025(\mathrm{Re}\,\mathrm{Pr})^{0.8} = 5.0 + 0.025\mathrm{Pe}^{0.8}. \qquad (6.1)$$

Sieder-Tate correlation (Sieder and Tate, 1936) is used for the secondary oil:

$$\mathrm{Nu}_{oil} = 0.027\,\mathrm{Re}^{0.8}\,\mathrm{Pr}^{0.33}\left(\frac{\mu}{\mu_w}\right)^{0.14}, \qquad (6.2)$$

as suggested by the thermal fluid manufacturer (Dow Chemical Company, 1996).

MARS-LBE predicts pressure loss in a component due to friction and flow condition change by following relation:

$$\Delta p_i = \sum_i \frac{\rho_i v_i^2}{2}\left(f\frac{l}{d_h} + K\right)_i \qquad (6.3)$$

In case of the friction loss coefficient ($f(l/d_h)_i$), a user is asked to specify pipe roughness (ε) and an internal subroutine in the code calculates its value in a component. However, form loss coefficient (K_i) should be explicitly provided except the case of using internal sudden area change model. In previous activities (Cho et al., 2011; OECD Nuclear Energy Agency, 2012), all of the

hydraulic loss coefficients in HELIOS were investigated. As a result, the best-practice guidelines for the prediction of the coefficients were suggested. The correlations used in this study are summarized in Table 6.2. Pipe roughness is designated to be 2.53 μm as measured.

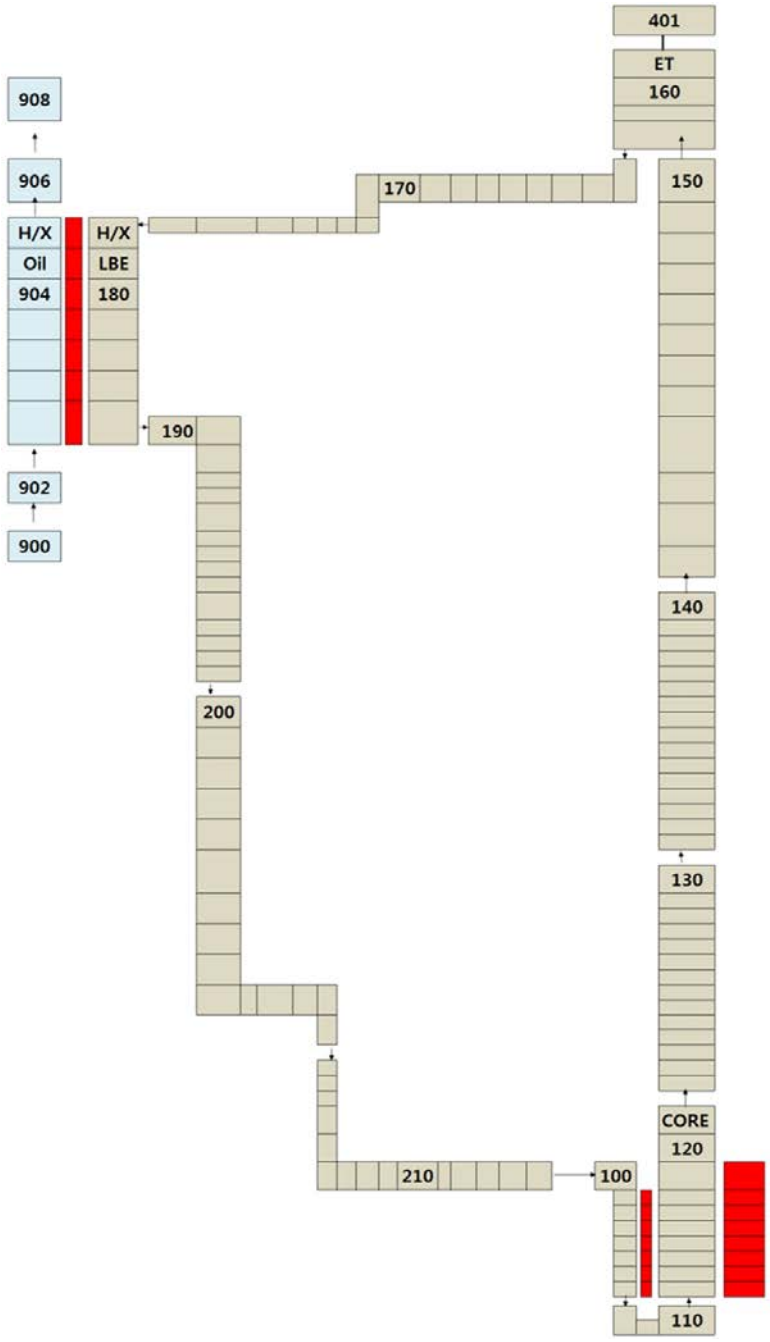

Figure 6.1 Nodalization map of HELIOS prepared for MARS-LBE

Table 6.1 Thermophysical properties of 316 L stainless steel (data retrieved from (Mills et al., 2004; Popov and Carbajo, 2000))

Temperature (°C)	Thermal conductivity (W/m K)	Volumetric heat capacity (10^6 J/m^3 K)
20	14.2	3.78
94	15.3	3.93
205	17.1	4.09
316	18.8	4.21
427	20.5	4.31
538	22.1	4.41
649	23.6	4.50
760	25.1	4.58
871	26.6	4.66
1205	30.7	4.90

Table 6.2 Correlations used for hydraulic loss coefficient evaluation

Hydraulic loss model	Correlation		Note
Wall Friction (Popov and Carbajo, 2000; Zigrang and Sylvester, 1985)	$f = \frac{64}{\mathrm{Re}}$	$0 \le \mathrm{Re} \le 2200$ (Laminar)	Calculated by a subroutine in MARS-LBE, $f_{L,3000}$: value at Re = 2200, $f_{T,3000}$: value at Re = 3000
	$f = \left(3.75 - \frac{8250}{\mathrm{Re}}\right)(f_{T,3000} - f_{L,2200}) + f_{L,2200}$	$2200 < \mathrm{Re} < 3000$ (Transition)	
	$\frac{1}{\sqrt{f}} = -2\log_{10}\left\{\frac{\varepsilon}{3.7d_h} + \frac{2.51}{\mathrm{Re}}\left[1.14 - 2\log_{10}\left(\frac{\varepsilon}{d_h} + \frac{21.25}{\mathrm{Re}^{0.9}}\right)\right]\right\}$	$\mathrm{Re} \ge 3000$ (Turbulent)	
Sudden area change (Trapp and Ransom, 1977)	$K = \left(1 - \frac{A_1}{A_2}\right)^2$	Sudden expansion	Calculated by a subroutine in MARS-LBE
	$K = \left(1 - \frac{A_2}{A_c}\right)^2,\ \frac{A_c}{A_2} = 0.62 + 0.38\left(\frac{A_2}{A_1}\right)^3$	Sudden contraction	
Mock-up core grid spacer (Cho et al., 2011; Rehme, 1973)	$K = C_v\left(\frac{A_s}{A_v}\right)^2,\ C_v = -7.65\log_{10}\mathrm{Re} + 49.0$		Modified drag coefficient suitable for HELIOS core grids
Elbow (Nippert, 1929)	$K = K_{\mathrm{Re}}K_{\mathrm{loc}} + K_{\mathrm{fr}}$		
Orifice (Idelchik, 1953)	$K = \left(1 + 0.707\sqrt{1 - \frac{A_{or}}{A_1}} - \frac{A_{or}}{A_1}\right)^2\left(\frac{A_1}{A_{or}}\right)^2$		$\mathrm{Re} > 10^5$

6.2.1.2 Code benchmark results for HELIOS natural circulation tests

Using the well-defined experimental data generated with HELIOS, MARS-LBE code was benchmarked. The purpose of this benchmark is to validate the capability of MARS-LBE code in a given non-isothermal natural circulation condition by making the code to estimate LBE mass flow rate and LBE temperature distribution in a system. In this respect, boundary conditions such as the mock-up core power rating, secondary side inlet temperature and mass flow rate were designated explicitly as forms of the time-dependent volumes and junctions, heat structures, and property tables in the model.

The code benchmark results for the cases from NC1.0 to NC4.0 are summarized in Table 6.3. Oil side conditions including mass flow rate and inlet temperature are not specified in the table because these parameters were assigned to the boundary conditions since the same values were used in the benchmark. Considering that the measured and calculated temperatures of oil side outlet are within a few degrees deviation, it can be concluded indirectly that the experiments from NC1.0 to NC4.0 were performed in sufficiently adiabatic wall boundary conditions.

The measured LBE mass flow rates and calculated results by MARS-LBE for all cases are compared in Figure 6.2, as a function of mock-up core power rating. The benchmark results show good agreement with measurement within maximum 7% discrepancies as also shown in Figure 6.3. As described, the parameters of interest in natural circulation estimation, mass flow rate and

temperature difference of LBE, show good agreement between experiment and code benchmark results.

Comparisons between experiment and calculation results on LBE temperature distribution and the secondary side temperature distribution for each case are shown in Figure 6.4 (a)-(d). The absolute LBE temperatures along the main loop are benchmarked closely within 1% ranges except the NC1.0 case, as shown in Figure 6.4 (a). In that case, the code benchmark shows about 25 °C temperature underestimation. However, as depicted in Figure 6.5, the temperature differences between measurement and calculation are in a close range, within 7%.

To find the cause of this discrepancy in absolute temperature distribution, the nodalization on the heat exchanger is investigated first with a sensitivity study. In a modeling of a heat exchanger, it is required that the size of calculation nodes should be moderate and fine enough to simulate heat transfer properly within a node since both convective and conductive heat transfer are present and the working fluids flow in the opposite direction. For the sensitivity study, two more numerical cases for each of natural circulation experiments from NC1.0 to NC4.0 are prepared, with the increased number of calculation nodes.

To increase the number of axial nodes, the size of a node is halved and trisected, respectively, which means the total number of calculation nodes in the heat exchanger is doubled and tripled. A comparison on the three models for the sensitivity study is summarized in Table 6.4 in terms of the number of axial nodes and node length-to-diameter ratio (l_i/d_h) defined by the ratio

between node length and hydraulic diameter of a unit node. The sensitivity models were selected in the range of l_i/d_h values being greater than unity below which a calculation model can suffer from numerical instability. The trisected model satisfies this limitation with the ratio being 1.358.

The nodalization of each model is graphically shown in the left hand side of Figure 6.6 (a)-(c): (a) the original, (b) the halved, and (c) the trisected models, respectively. For the sensitivity study, absolute LBE temperature distribution in the heat exchanger is chosen because it is an important parameter of interest in natural circulation as aforementioned. Along with numerical nodalization, the right hand side of Figure 6.6 shows LBE temperature calculation results for each case. The LBE temperatures are reported at the center of each axial node. As a result, all 12 cases including original, halved, and trisected cases for each natural circulation experiment from NC1.0 to NC4.0 shows well-agreed calculation results within 1 °C variation in absolute temperature. It turns out that nodal condition in the original model with seven axial nodes is already sufficient to simulate heat transfer in the heat exchanger properly. In addition, the numerical discrepancy given in the NC1.0 case would not be affected by the node size in the original model.

Another potential cause of this discrepancy can be the correlations that we used for convective heat transfer coefficients because the final temperature distribution over a heat structure model depends on the values of those coefficients in MARS-LBE calculation scheme. If one of the correlations for LBE and secondary oil (or both) is not applicable in terms of flow regime and temperature condition, then it misleads calculation results by nature. Eqn. (6.1)

is recommended to be applicable to a Re range in $0<Re<5\times10^6$, while LBE flow regime in the NC1.0 lies in Re~25,000. Meanwhile, Eqn. (6.2) is suitable for using in sufficiently high turbulent regime (Re>10,000) but oil was under low turbulent regime (Re~6,000). However, this potential cause cannot be confirmed or evaluated due to the absence of heat transfer measurement system in the heat exchanger.

Table 6.3 MARS-LBE benchmark results for well-defined steady-state experiment results in HELIOS

No.	Main loop (LBE side)					Secondary loop (oil side)
	Total core power (kW)	Hot leg temperature (°C)	Cold leg temperature (°C)	Temperature difference (°C)	LBE mass flow rate (kg/s)	Oil outlet temperature (°C)
NC1.0	9.8	247.11	212.64	34.47	1.90	113.43
NC2.0	15.0	314.39	268.74	45.64	2.23	143.09
NC3.0	27.0	369.60	302.43	67.18	2.76	189.10
NC4.0	33.6	397.47	318.00	79.48	2.90	208.03

Note: all of the values given above are average values from measurements in each case.

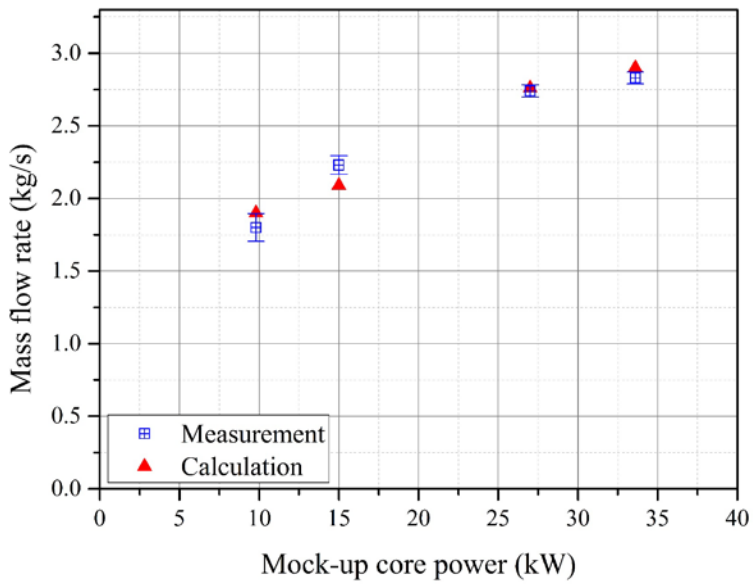

Figure 6.2 Comparison between measured and calculated mass flow rates as a function of mock-up core power

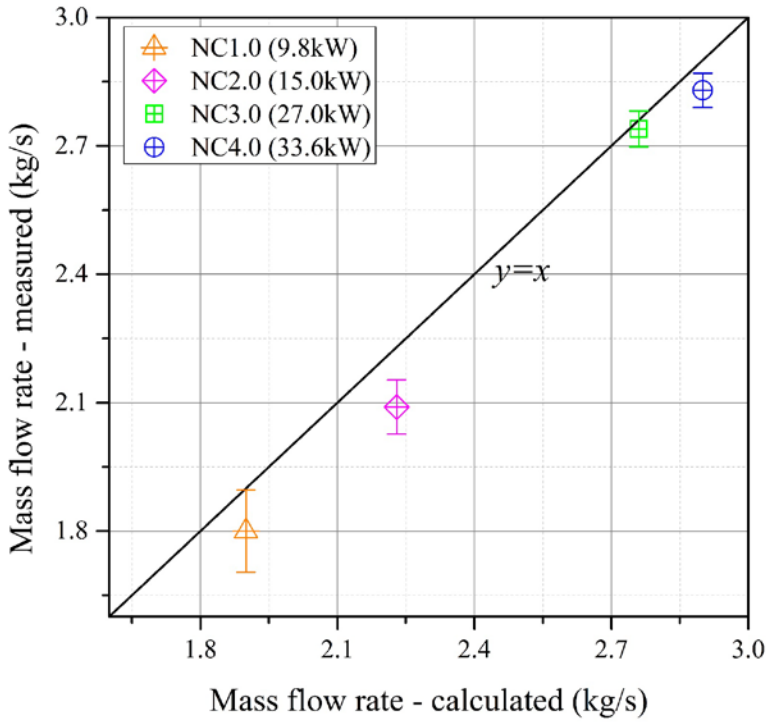

Figure 6.3 Comparison between LBE mass flow rates in HELIOS experiment and MARS-LBE benchmark results

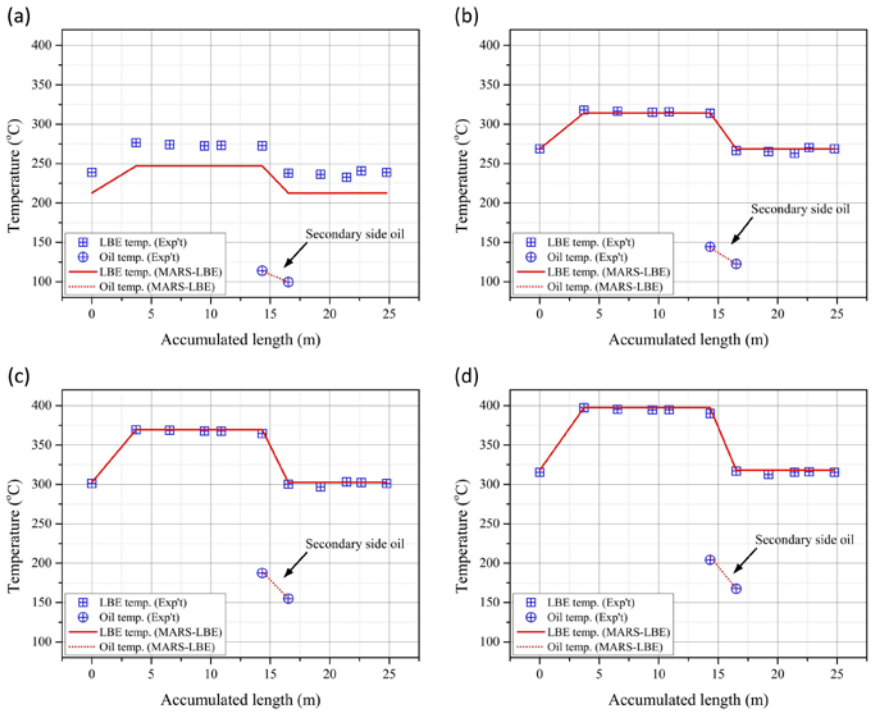

Figure 6.4 Steady state experiment and benchmark results of HELIOS in cases (a) NC1.0 (9.8 kW power), (b) NC2.0 (15.0 kW power), (c) NC1.0 (27.0 kW power), and (d) NC1.0 (33.6 kW power)

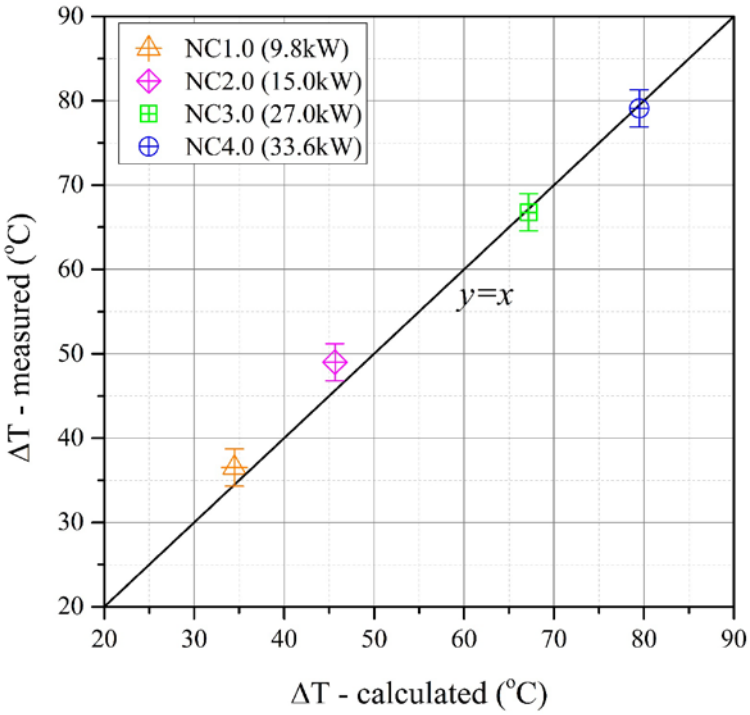

Figure 6.5 Comparison of temperature differences between average hot leg and cold leg temperatures in HELIOS experiment and MARS-LBE benchmark results

Table 6.4 Node conditions for the original, halved, and trisected models used for sensitivity study

Model description	No. of axial nodes	Node length-to-diameter ratio (l_i/d_h)
Original model	7	4.074
Halved	14	2.037
Trisected	21	1.358

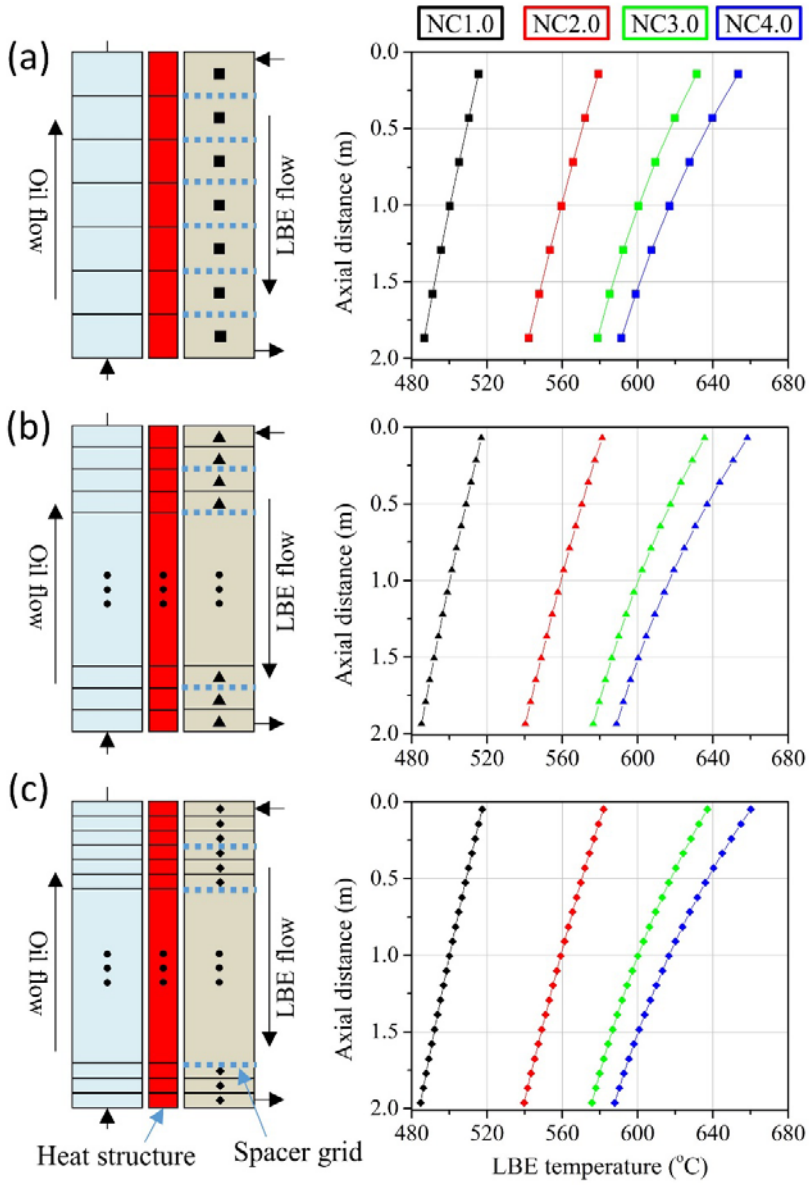

Figure 6.6 Case study results on the heat exchanger axial node size in (a) the original model with 7 axial nodes, (b) halved model with 14 axial nodes, and (c) trisected model with 21 axial nodes

6.2.2 Code benchmark with PILLAR pool test results

6.2.2.1 System nodalization and input preparation on PILLAR

Similar to the HELIOS case, PILLAR is nodalized into several one-dimensional components with about 210 hydrodynamic cells as shown in Figure 6.7. Most of parts are arranged with pipes or annuli, and junctions while the use of the one-dimensional pipe forces to simulate the flow inside the core and upper plenum being averaged over whole flow area.

Several heat structures are designated such as the heater rods, heat exchanger tubes, and the inner shells between downcomer and riser or core regions. Since the themophysical properties of each of heat structures are required to be provided, those of 316L stainless steel for the component wall and heat exchanger tubes are the same with the HELIOS case, as described in Table 6.1. However, the heater rods are comprised of dissimilar materials, as mentioned in Section 5.2.1.4. Furthermore, as depicted in Figure 6.8, there are several lead pins to connect the heating element to electrical lead. For a precise simulation on the effect of thermal inertia, all of the regions are to be included in the modeling while those are interpreted to have equivalent radii by neglecting the lead pins inside the magnesia (MgO) bobbin. The radius of each region is also shown in Figure 6.8 and the thermophysical properties are utilized from Table 5.6.

Differ from the HELIOS case, the convective heat transfer coefficient on water is designated to be the Dittus-Boelter relation (Dittus and Boelter,

1930), a widely used correlation for single- and two-phase water flow in a circular duct, is adopted:

$$\mathrm{Nu}_{water} = 0.023\,\mathrm{Re}^{0.8}\,\mathrm{Pr}^{0.4}, \tag{6.4}$$

where the power of Pr is determined by the state of heat transfer to fluid. In this benchmark, it is given as 0.4 because water is heated so that the primary side LBE is cooled. On the other hand, a value with 0.3 can be used when the fluid is cooled when it flows inside a duct.

For the estimation of hydraulic loss, most of correlations used for HELIOS were taken into account for the PILLAR benchmark. In this respect, the same friction loss correlation is exploited. The roughness of component wall is designated to be 1.0 μm as suggested by manufacturer.

In addition to the system nodalization, the boundary conditions are given by the core power rating exerted to the core through the heat structure for heater rods, and the secondary feedwater conditions including mass flow rate, inlet temperature, and pressure. As the insulation of the system is sufficient to be adiabatic, no heat loss to the environment is modeled.

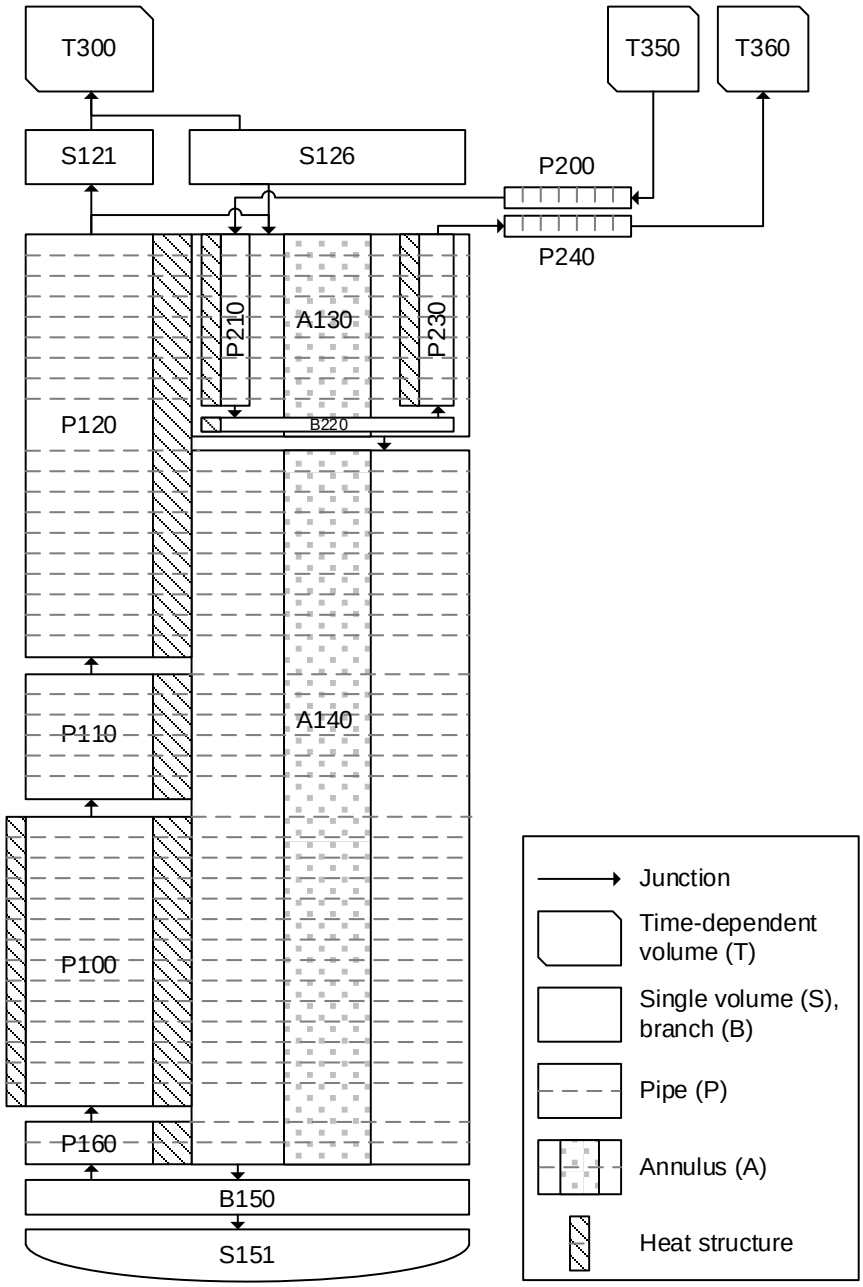

Figure 6.7 Nodalization map of PILLAR prepared for MARS-LBE

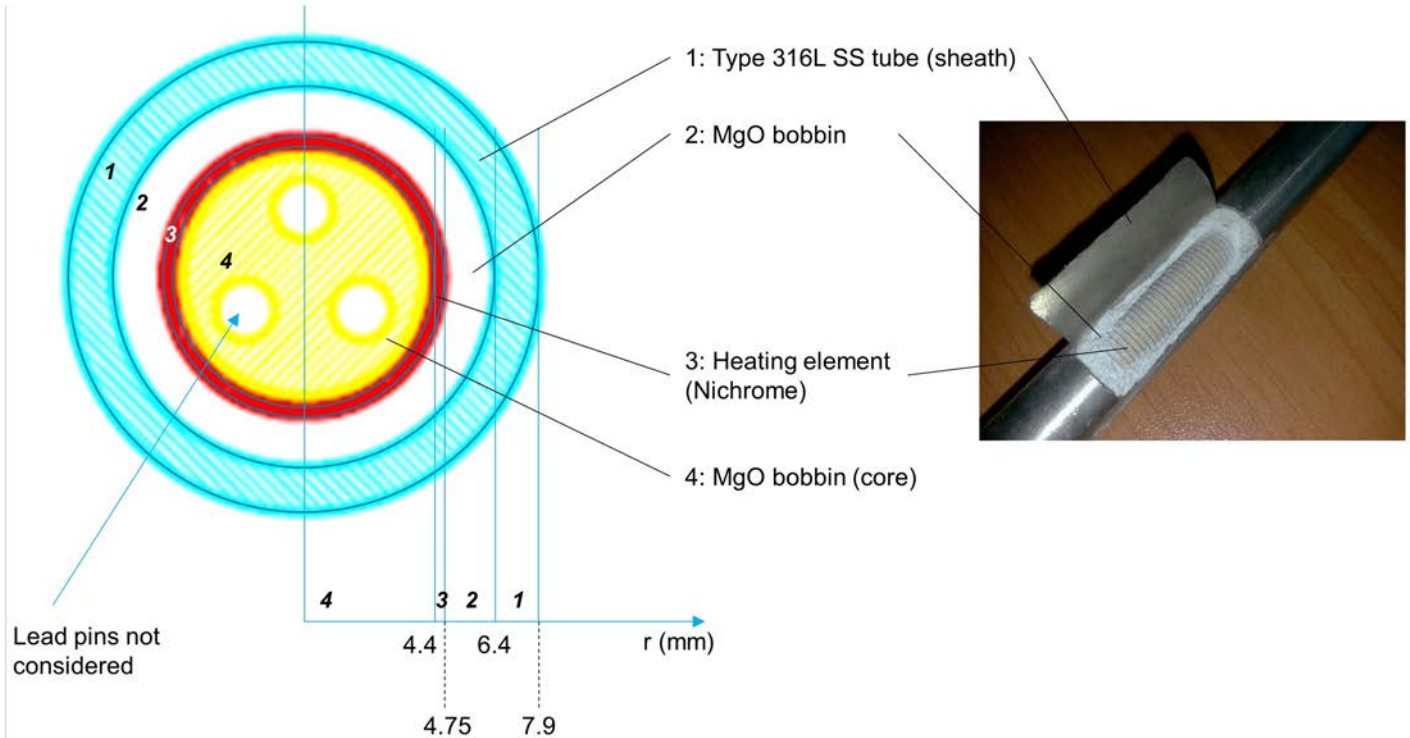

Figure 6.8 PILLAR heater rod cross-sectional view and equivalent radii for each of constituent material regions

6.2.2.2 Code benchmark results for PILLAR natural circulation tests

In this section, the benchmark results of MARS-LBE for LBE natural circulation in pool configuration is described. Through this benchmark, the capability of MARS-LBE on system integral natural circulation behaviors can be validated. The code is made to estimate LBE mass flow rate and temperature difference between the core outlet and inlet within the steady-state natural circulation experimental cases as defined in Section 5.2.4.2. Similar to the benchmark process for HELIOS, boundary conditions such as the core electrical power rating, secondary side conditions including water inlet temperature, mass flow rate, and system pressure were designated with the time-dependent volumes and junctions, and heat structures in the code input file.

Figure 6.9 compares the measured and calculated mass flow rates for all steady-state experimental cases while Figure 6.10 shows the temperature differences between the core inlet and outlet. The benchmark results show that MARS-LBE has a capability on the simulation of LBE natural circulation in pool geometry. As seen in the figures, the measurements and code calculation results lie within maximum ±3% deviations in LBE mass flow rate and the temperature difference, respectively. However, it cannot be confirmed that the code is also capable of simulating some local effects, since the purpose of this benchmark is limited to the integral behavior, mostly on measuring natural circulation flow rate and temperature difference.

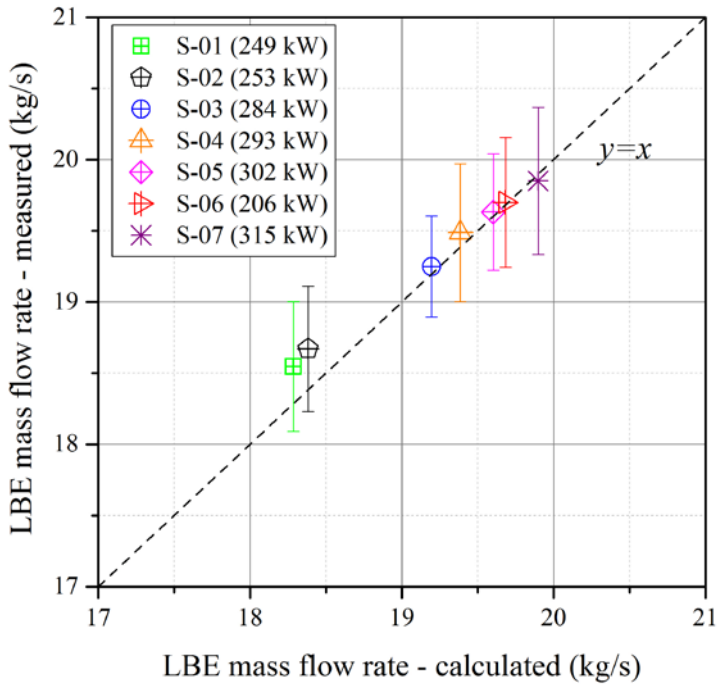

Figure 6.9 Comparison between LBE mass flow rates in PILLAR steady-state experiment and MARS-LBE benchmark results

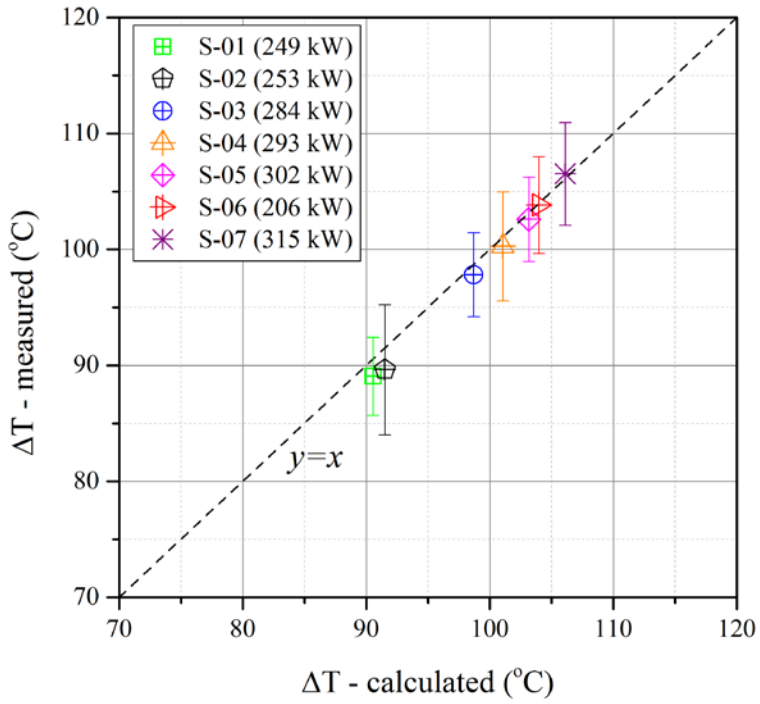

Figure 6.10 Comparison of temperature differences between average hot leg and cold leg temperatures in PILLAR steady-state experiment and MARS-LBE benchmark results

6.3 Code validation on reactor point kinetics

Most of calculation capabilities of MARS-LBE are the same with the original code MARS and one of its variants MARS-LMR, which is prepared for the simulation of liquid metal cooled reactors (KAERI, 2007). The one-dimensional calculation module of MARS can be divided into three main modules including thermal-hydraulics model, reactor kinetics model, and heat structure model. Each of models are related to each other by passing several parameters. Thermal-hydraulics model and heat structure model calculate moderator (coolant) density and fuel temperature, respectively, and the values of those parameters are transferred to the reactor kinetics model. Meanwhile, reactor kinetics model calculates thermal power and passes it to heat structure model. In addition, reactor kinetics model utilizes point kinetics equations for the estimation of neutronic behaviors.

With the validation through the benchmark with LBE natural circulation experimental results as given in Section 6.2, the capability on thermal-hydraulic analysis for LBE systems was ensured. In addition, reactor kinetics module should be validated for the safety analysis of a fast reactor system as well, since MARS was developed for thermal reactors, especially water reactors. However, there has been no experiments for the reactor kinetics of LBE systems so far. Thus, the code cannot be validated in a near term using the experimental data dedicated to LFR.

On the other hand, reactor-scale experiments were conducted with EBR-II (Lehto et al., 1988) in which utilized sodium as primary coolant. As

liquid sodium has more similar thermophysical properties with LBE compared to water and SFR provides fast neutron spectrum, the experimental data have been used for the validation of reactor kinetics module in MARS and MARS-LMR as well. In this respect, the validity of neutron kinetics module in MARS-LBE can be regarded to be confirmed because the backbone code was validated with the sodium experience. This section describes some of the validation work done by other studies.

The International Atomic Energy Agency (IAEA) launched an international benchmark program on the Shutdown Heat Removal Test (SHRT) conducted in EBR-II (Briggs et al., 2015; Briggs et al., 2013). This program designated two different experiments as benchmark targets, SHRT-17 and SHRT-45R, which are loss-of-flow tests with and without scram, respectively. With two experimental results, three main tasks were imposed as system analyses on two test sets and neutronic analysis only on the SHRT-45R test (Sumner and Wei, 2012).

For the former case, SHRT-17, a performance test of MARS was conducted (Choi and Ha, 2016a). The study showed that the calculation results from MARS-LMR and experimental results in transient were in good agreement in overall except the prediction of flow and temperature in a non-fueled subassembly. Another study that dealt with the latter experimental case, SHRT-45R, showed that neutronic and thermal-hydraulic behaviors predicted by MARS-LMR and the measurements were well agreed each other (Choi and Ha, 2016b). Once again, the code had a deviation in the calculation of flow and temperature in the non-fueled subassembly similar to the case of SHRT-17. As

an independent work to the IAEA benchmark program, a code-to-code validation between RELAP-5 and MARS was conducted, by comparing the simulation results on the SHRT-17 data (Shirvan and Ballinger, 2017). The comparison showed consistency in the calculation results from two codes. Considering those activities were reported to be in good agreements with the SFR experiments on simulating reactivity feedback, the reactor kinetics module in MARS-LBE can be concluded to be capable of the prediction of system behaviors under reactivity feedback and sufficient to use the point kinetics equations when it comes to modeling fast neutron reactors.

6.4 System thermal-hydraulics modeling on LBE pool transient natural circulation experiments

As described in Section 6.2, it is identified that the code is capable of the simulation and assessment of thermal-hydraulic behaviors in LBE-cooled systems, especially on natural circulation when it reaches a steady state. However, the validation does not ensure whether MARS-LBE still have the validity on the calculation of time-dependent variation of system parameters. Hence, in this section, the capability of MARS-LBE in transient simulations is verified by comparing the measurements from several sets of transient test results conducted with PILLAR, as described in Section 5.2.4.3.

In order to simulate transient system behaviors with MARS-LBE, several parameters need to be maneuvered within running a problem as simulation time proceeds. MARS-LBE is capable of simulating such cases with a time-dependent component and a control system component (KAERI, 2006). In general, the former directly deals with a specific parameter in the hydrodynamic system by changing its value such as temperature, pressure, mass flow rate, heat flux, and so on. Thus, this model modifies several boundary conditions of the system to make the transient. Several components can also be used as the model described above so that it is a time-dependent component by giving a table that includes temporal change of a given parameter. The latter gives a logical relation as if it is a specific signal to the system. When a system parameter to reach some pre-defined conditions, the control system component can work as a triggering action to a specific component. If this action is defined

by several parameters satisfying each of conditions, then it is required to be constructed with Boolean operations. Due to its versatility, it can be adopted for opening or closing a valve, releasing over-pressure, initiating a certain system transient, and so on.

In this simulation activity, the former elements, time-dependent components, were utilized to impose varying boundary conditions. The conditions were prepared based on the experimental conditions on the core power ratings and secondary side mass flow rates. Other than the component used, those transient results were made from each of steady-state results simulated for the initial conditions. By using the restart option supported by MARS-LBE, it was able to run the transients by initializing system conditions with pre-calculated output data.

Four figures, from Figure 6.11 to Figure 6.14, compare the transient tests conducted with PILLAR and simulation with MARS-LBE. For a better comparison, the test results described in Section 5.2.4.3 with figures from Figure 5.30 to Figure 5.33 are overlapped with the simulation results. The MARS-LBE simulation results, expressed with lines and square marks, and the test results, drawn with bold lines, agree well in all cases including the instantaneous core power and secondary flow rate changes. Some specific behaviors notable in the experiments, such as the time delay for tube side heat transfer saturation, the water outlet temperature variation due to enthalpy change, and the instantaneous tube side heat transfer jump or drop from flow rate changes, are also able to be found in the simulation results. In conclusion, with the benchmarks given in this section, MARS-LBE is capable of simulating

transients in LBE-cooled passive pool-type systems.

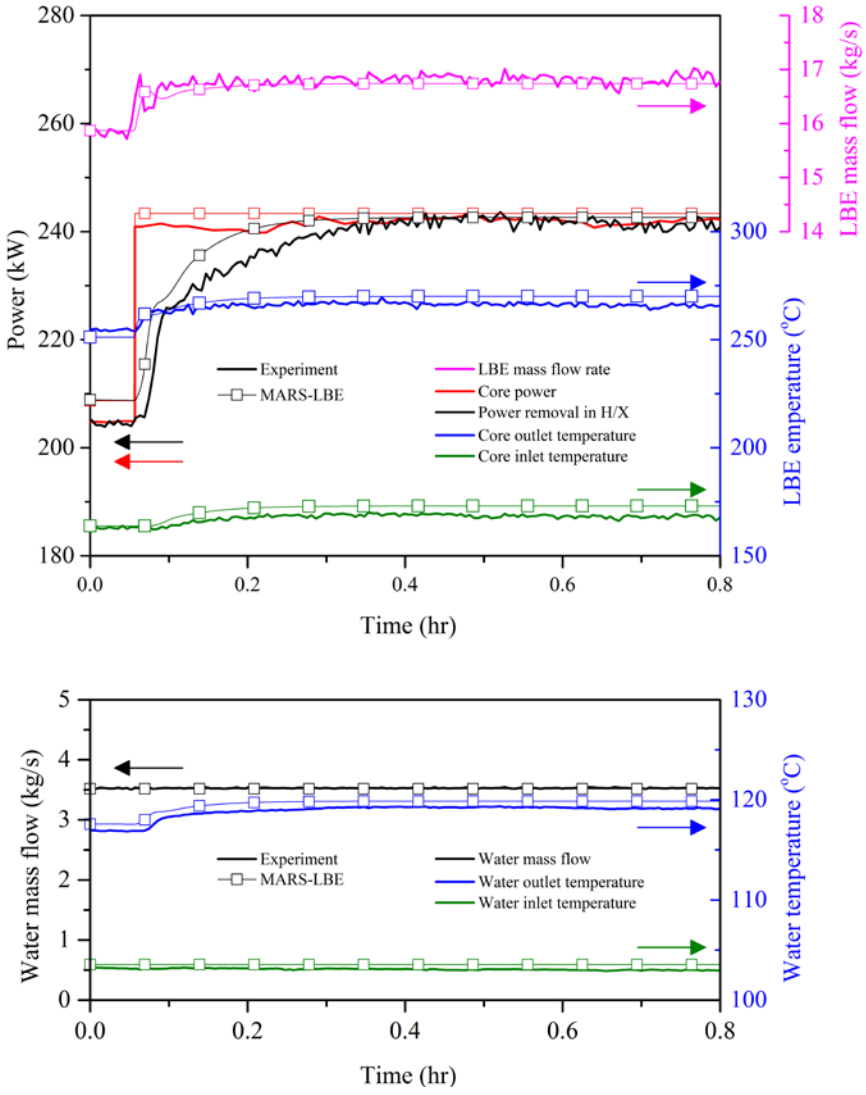

Figure 6.11 Comparison with MARS-LBE modeling results and PILLAR transient natural circulation experimental results: instantaneous core power increase (Case No.: T-PINC-210~240/3.5)

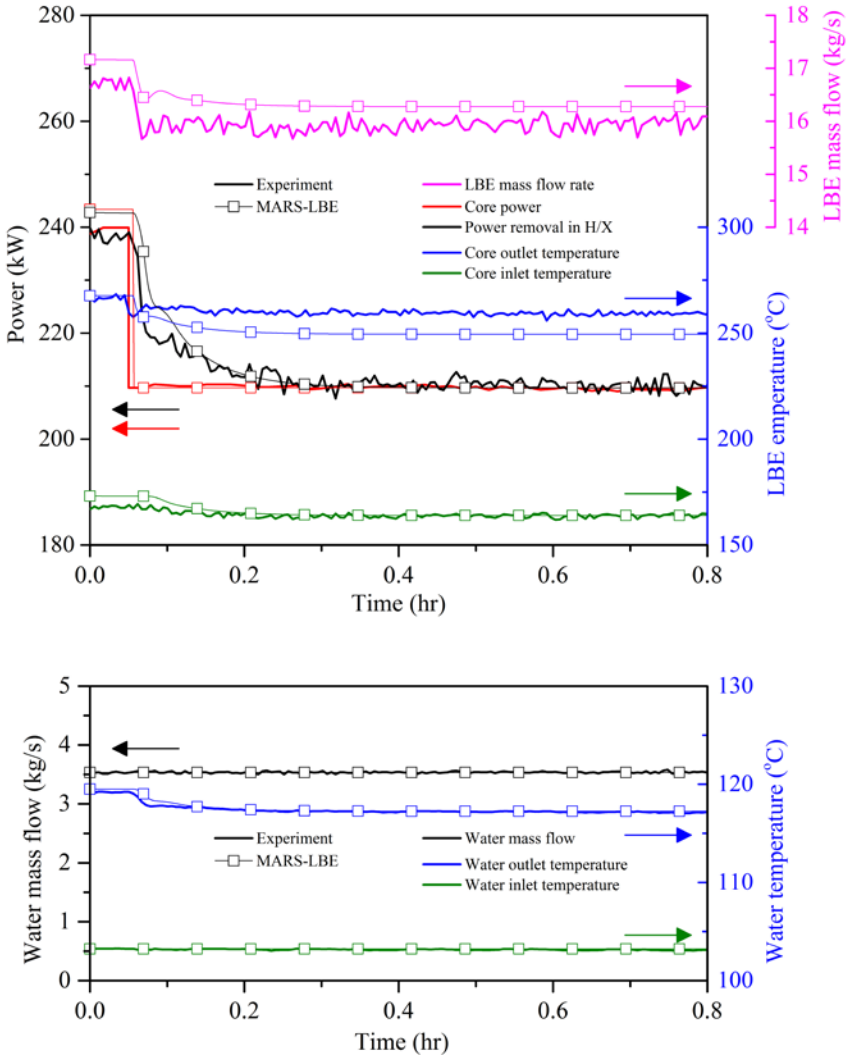

Figure 6.12 Comparison with MARS-LBE modeling results and PILLAR transient natural circulation experimental results: instantaneous core power decrease (Case No.: T-PDEC-240~210/3.5)

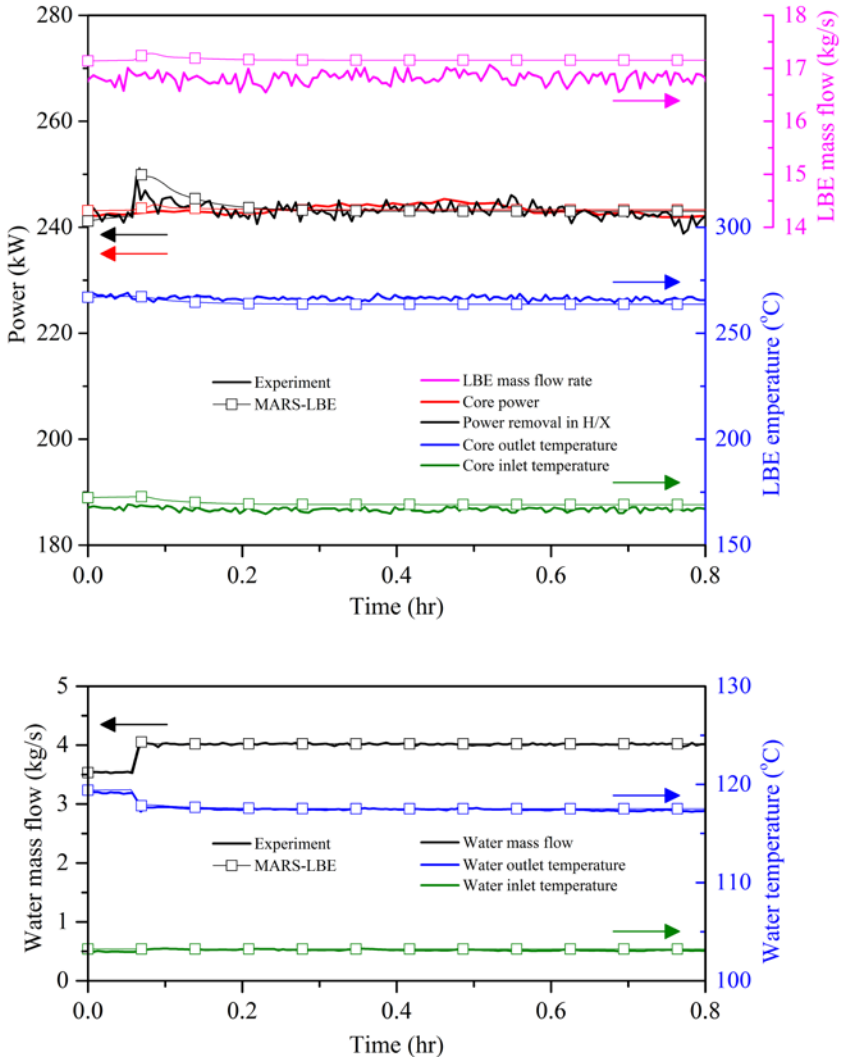

Figure 6.13 Comparison with MARS-LBE modeling results and PILLAR transient natural circulation experimental results: instantaneous secondary side flow rate increase (Case No.: T-FINC-240/3.5~4.0)

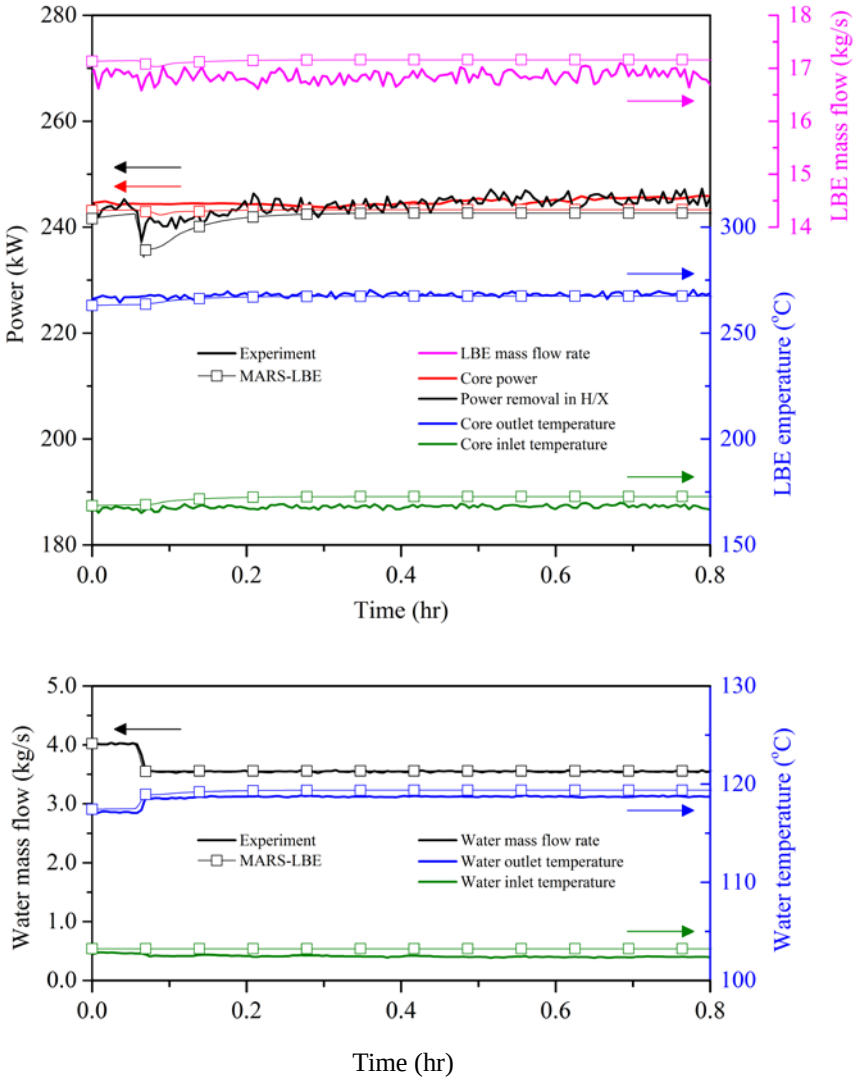

Figure 6.14 Comparison with MARS-LBE modeling results and PILLAR transient natural circulation experimental results: instantaneous secondary side flow rate decrease (Case No.: T-FDEC-240/4.0~3.5)

Chapter 7 Load-Following Capability Assessment of Passive LBE-cooled Pool-type SMR

7.1 Analytical reactor dynamics simulation model

The core power of a passive nuclear system can only be maneuvered by means of control rod movements because there is no reactor coolant pump that can induce the change of temperature condition resulted from flow rate variation so that reactivity feedback comes into action. Considering the maneuverability of the secondary side, another control mechanism can be thought as feedwater flow rate regulation. Reactor power is regulated by the position of control rod while steam production rate is regulated by the amount of feedwater supply and resultant heat removal from the steam generator modules.

In this section, an analytical reactor dynamics simulation model is presented for the purpose of reactor dynamics simulation dedicated to the passive LBE-cooled SMR. The load-following capability of a reactor is assessed and/or evaluated by a simulation considering its dynamic behaviors during maneuvering. Figure 7.1 depicts reactor power and steam production regulations in a passive SMR with control rod movement and feedwater flow control as a schematic diagram. In this formulation, an error signal defined by the discrepancy between a new target state and current state drives the temporal change and the dynamic response of the system. As a simulation target of this

model, URANUS is designated since it is a pool-type passive LBE-cooled SMR, which corresponds to the modeling purpose.

The model is formulated with a lumped parameter approach that nodalizes the whole system into several lumps in which thermophysical properties in a single lump are constant and coolant mass remains constant with respect to coolant temperature change. In this respect, the system of interest, a passive, pool-type, LBE-cooled SMR, is divided into sub-models, reactor core, steam generator, hot leg, and cold leg. As shown in Figure 7.2, a number of assumptions are established for this model, which are discussed in detail through the following sections. The resultant formulations are established in a state-space model that describes time-dependent change of given states in a system. This passive SMR simulation model works along with MATLAB/Simulink R2017a environments that enables relatively short simulation time with high-fidelity solvers and user-friendly graphical interfaces (Mathworks, 2017).

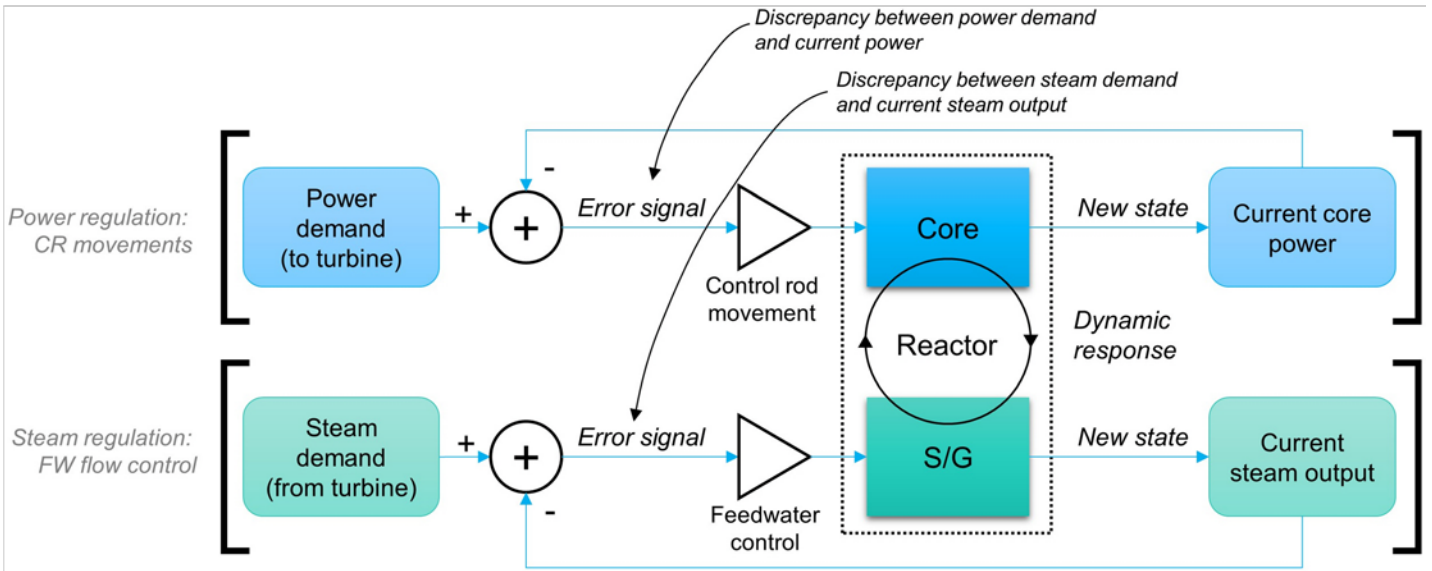

Figure 7.1 Power and steam production regulations in passive SMR by means of control rod movement and feedwater flow control

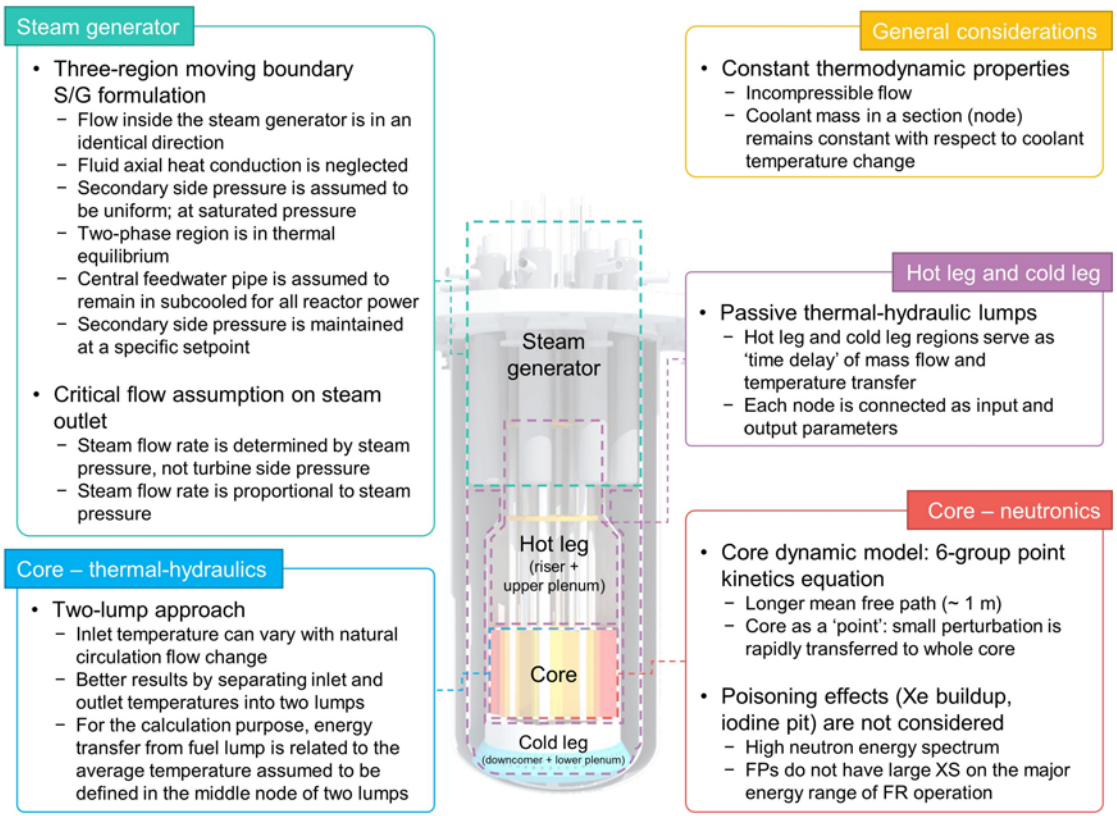

Figure 7.2 Assumptions and approaches for the analytical reactor dynamics simulation model developed in thesis study

7.1.1 Reactor core model

The nonlinear nature of reactor dynamics starts from the reactor core since neutron kinetics is affected by both neutronic and thermal-hydraulic aspects. Considering this, the reactor core model can be comprised of mainly two sub-models: neutronics model that deals with reactivity insertion and feedback and thermal-hydraulics model that is for heat transfer and resultant temperature and mass flow conditions. Within the reactor core model, two sub-models are coupled together by means of reactivity change. Figure 7.3 describes the schematic structure of the reactor core model. The details of each section are elaborated in the following sections.

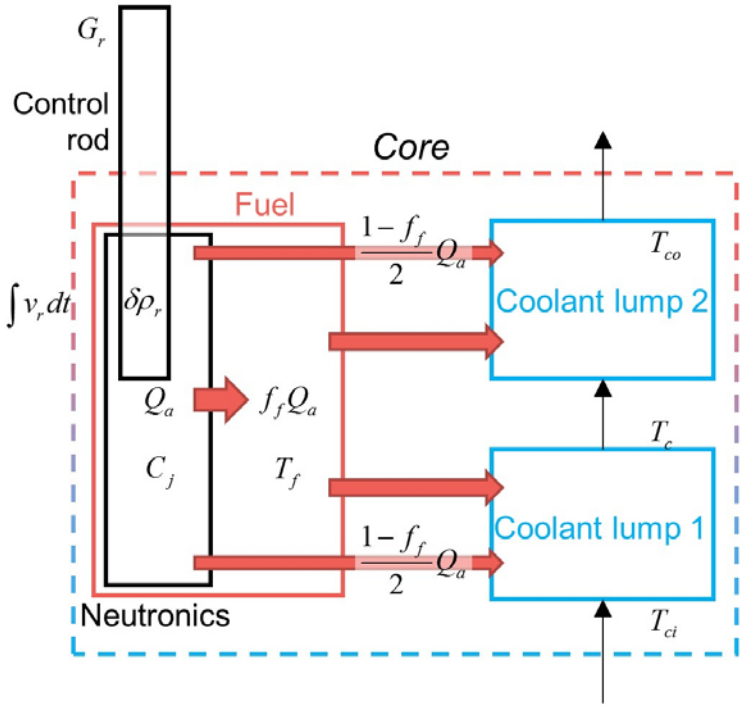

Figure 7.3 Schematic diagram for core state-space model including both neutronics model and core thermal-hydraulics model

7.1.1.1 Neutronics model

For the neutronics model, the point kinetics model is adopted, which utilizes six-group relations and is commonly used among nuclear reactor analyses. The reactor core is treated like a point that has no directional dependence and this assumption is more reasonable for a fast reactor than a thermal reactor due to a longer neutron mean free path in fast neutron spectrum. It is because a small perturbation is rapidly transferred to the entire region in the reactor core by the higher energy spectrum of neutrons (Waltar and Reynolds, 1980). Furthermore, there is no need to consider neutron poisoning effects such as xenon buildup and iodine pit, which exert large negative reactivity insertions, as well. Fission products do not have large neutron absorption cross section on the major energy range of fast reactor operation (Waltar and Reynolds, 1980).

The point kinetics equation used for this model can be formulated with a set of six-group point kinetics equations in terms of the neutron and reactivity balance and delayed neutron precursor densities as shown in Eqns. (7.1) and (7.2):

$$\frac{dn(t)}{dt} = \frac{\rho(t) - \beta_{eff}}{\Lambda} n(t) + \sum_j \lambda_j C_j(t) \quad \text{and} \tag{7.1}$$

$$\frac{dC_j(t)}{dt} = \frac{\beta_j}{\Lambda} n(t) - \lambda_j C_j(t)\,, \tag{7.2}$$

where the effective delayed neutron fraction β_{eff} is expressed with j-th group delayed neutron fractions β_j and precursor decay constants λ_j such that

$\beta_{eff} = \sum_{j=1}^{6} \beta_j$, $\frac{\beta}{\lambda} = \sum_{j=1}^{6} \left(\frac{\beta_j}{\lambda_j} \right)$. Since the temporal terms vanish at the initial condition, t = 0, the following relation can be derived from Eqn. (7.1): $\frac{\beta_j}{\Lambda} n_0 = \lambda_j C_{j0}$. Hence, the equations can be further recast in normalized forms as in Eqns. (7.3) and (7.4):

$$\begin{aligned} \frac{d}{dt} n_r &= \frac{\rho - \beta_{eff}}{\Lambda} n_r + \frac{1}{n_0} \sum_j \lambda_j C_{j0} C_{jr} \\ &= \frac{\rho - \beta_{eff}}{\Lambda} n_r + \sum_j \frac{\beta_j}{\Lambda} C_{jr} \end{aligned}, \tag{7.3}$$

$$\frac{d}{dt} C_{jr} = \frac{\beta_j}{\Lambda} \frac{n_0}{C_{j0}} n_r - \lambda_j C_{jr} = \lambda_j n_r - \lambda_j C_{jr} . \tag{7.4}$$

Since the simulation target is URANUS, the values of kinetic parameters to be used in the model shown in the equations above are also designated to be those calculated in the design stage, as discussed in Section 4.2.

Since the reactor core reacts to total reactivity change as described by the point kinetics equation, the total reactivity change at a specific time, $\delta\rho$, can be given by the sum of reactivity changes induced from control rod movements and several reactivity feedback mechanisms with respect to the temperature change of components as shown in Eqn. (7.5):

$$\delta\rho = \delta\rho_{rod} + \alpha_f \left(T_f - T_{f0} \right) + \alpha_c \left(T_c - T_{c0} \right) . \tag{7.5}$$

In the above equation, the fuel temperature coefficient, α_f, is defined as

$\alpha_f = \alpha_D + \alpha_l$ while the coolant temperature coefficient, α_c, is given by $\alpha_c = \alpha_{LBE} + \alpha_R$ so that the equations can be formulated with fuel and coolant temperature changes within the fuel and coolant lumps depicted in Figure 7.3.

In addition, the rate of external reactivity insertion depends on the rate of rod insertion, i.e. control rod speed, and the reactivity worth of control rods. In general, the reactivity worth of control rods is not the same along the axial direction; in other words, it has an axial profile for more effective and stable regulation of core power. However, this model assumes it constant over the position of control rods. In this regard, the rate of external reactivity insertion is defined as in Eqn. (7.6) with control rod speed and reactivity worth per unit length (Edwards et al., 1990):

$$\frac{d}{dt}\delta\rho_{rod} = G_{rod} v_{rod}\,, \tag{7.6}$$

where the value of reactivity worth per unit length is calculated from a similar design of LBE-cooled passive SMR such that G_{rod} = 4.214E-2 (dk/k)/m (Choi et al., 2011a).

7.1.1.2 Core thermal-hydraulics model

Typically, most of thermal-hydraulic analysis utilizes three transport equations for mass conservation, momentum conservation, and energy balance. In a numerical point of view, the formulations need to be recast since the original

forms are not easy to handle. Hence, the purpose of calculation and the physical aspect of analysis such as the scale of phenomena should be considered. In this regard, the core thermal-hydraulics model and other models for the passive SMR dynamics simulation model developed for this thesis study are defined within the lumped parameter approach so that the model is capable of calculating the transient response of the system.

The core thermal-hydraulics model consists of three lumps that are fuel lump and two coolant lumps. The former treats all the nuclear fuel as a single lump. It is assumed that axial heat transfer in the fuel lump is negligible while core power generated in the fuel lump is transferred to coolant lumps in radial direction. The coolant region is divided into lower and upper coolant lumps, which is called Mann's model named after its developer (Kerlin et al., 1976; Kerlin, 1978). Since core inlet temperature can vary with natural circulation flow change and resultant temperature distribution change in the passive SMR, the most important purpose of this division is to simulate inlet and outlet temperatures independently. The coolant lumps are assumed that fluid flow within each of the lumps are well-mixed, in other words, thermophysical properties in each of the lumps are constant. In addition, this Mann's model features that heat transfer from the fuel lump to coolant is driven by the temperature difference between fuel lump temperature and average coolant temperature, which is defined by the mean value of two coolant lump temperatures.

Applying energy balance relations within and between those lumps, the governing equations of the model can be obtained. In this core thermal-

hydraulics model, heat conduction equation is mainly utilized to relate the fuel lump and coolant lumps accounting for energy balance. As reactor power is proportional to neutron flux or population in the core, it can be expressed with the normalized neutron population and proportional coefficient at the full-power operation condition, as shown in Eqn. (7.7):

$$Q_a(t) = Q_{a0} n_r(t) \quad \cdots \quad Q_{ar}(t) = \frac{Q_{a0} n_r(t)}{Q_{a0}} = n_r(t) \,. \tag{7.7}$$

Heat transfer from fuel to coolant is parametrized by the temperature difference between fuel lump and coolant average temperature, which is defined at the center of each coolant lump. Considering the overall heat transfer coefficient defined by Eqn. (7.8) within a generic pin-cell of nuclear fuel as shown in Figure 7.4, the rate of heat transfer from fuel to coolant is given by Eqn. (7.9):

$$\begin{aligned} \Omega_f = 2\pi N_{rod} H_{rod} \Bigg[& \frac{1}{2k_f} + \frac{1}{r_f h_g} \\ & + \frac{1}{k_{clad}} \ln\left(\frac{r_f + t_g + t_{clad}}{r_f + t_g} \right) + \frac{1}{r_{rod} h_c} \Bigg]^{-1}, \end{aligned} \tag{7.8}$$

$$Q_c(t) = \Omega_f \left(T_f(t) - T_c(t) \right). \tag{7.9}$$

From Eqn. (7.9), the differential form of heat transfer relation can be given as Eqn. (7.10), by assuming that reactor power generated by nuclear reaction is transferred to the fuel lump with a fraction of f_f while the remaining fraction of $(1 - f_f)$ directly heats the coolant:

$$
\begin{aligned}
& f_f Q_a(t) = \left(M_f C_{pf}\right)\frac{d}{dt}T_f + Q_c(t) \\
& \Rightarrow \frac{dT_f}{dt} = \frac{f_f}{\mu_f}Q_{0a}n_r - \frac{\Omega_f}{\mu_f}T_f + \frac{\Omega_f}{\mu_f}T_c
\end{aligned}, \qquad (7.10)
$$

where the total heat capacity of fuel μ_f is given by $\mu_f = M_f C_{pf}$ and the power fraction transferred to the fuel lump f_f is $f_f = 0.98$ (Edwards et al., 1990). It is due to the assumption that coolant mass remains constant to coolant temperature change.

When it comes to heat removal in the two coolant lumps, denoted by node 1 and 2 for lower and upper lumps, respectively, energy balance equation can be formulated as shown in Eqns. (7.11) and (7.12):

$$
\begin{aligned}
& \left(\frac{M_{c,core}}{2}C_{pc}\right)\frac{d}{dt}T_{co} + \dot{m}_p C_{pc}\left(T_{co} - T_c\right) \\
& \qquad = \frac{1}{2}\left[\left(1 - f_f\right)Q_a(t) + Q_c(t)\right] \\
& \Rightarrow \frac{d}{dt}T_{co} = \frac{\left(1 - f_f\right)Q_{0a}}{\mu_{c,core}}n_r + \frac{\Omega_f}{\mu_{c,core}}T_f \\
& \qquad - \frac{\Omega_f}{\mu_{c,core}}T_c + \frac{2C_{pc}}{\mu_{c,core}}\dot{m}_p T_c - \frac{2C_{pc}}{\mu_{c,core}}\dot{m}_p T_{co}
\end{aligned}, \qquad (7.11)
$$

$$
\begin{aligned}
& \left(\frac{M_{c,core}}{2}C_{pc}\frac{d}{dt}\right)T_c + \dot{m}C_{pc}\left(T_c - T_{ci}\right) \\
& \qquad = \frac{1}{2}\left[\left(1 - f_f\right)Q_a(t) + Q_c(t)\right] \\
& \Rightarrow \frac{d}{dt}T_c = \frac{\left(1 - f_f\right)P_{0a}}{\mu_{c,core}}n_r + \frac{\Omega_f}{\mu_{c,core}}T_f - \frac{\Omega_f}{\mu_{c,core}}T_c \\
& \qquad - \frac{2C_{pc}}{\mu_{c,core}}\dot{m}_p T_c + \frac{2C_{pc}}{\mu_{c,core}}\dot{m}_p T_{ci}
\end{aligned}, \qquad (7.12)
$$

where the total heat capacity of coolant within the core region $\mu_{c,core}$ is defined similarly to that of fuel above, such that $\mu_{c,core} = M_{c,core} C_{pc}$. It is noticed that the coolant is directly heated by reactor power generated from nuclear reaction with a fraction of (1 - f_f), as aforementioned.

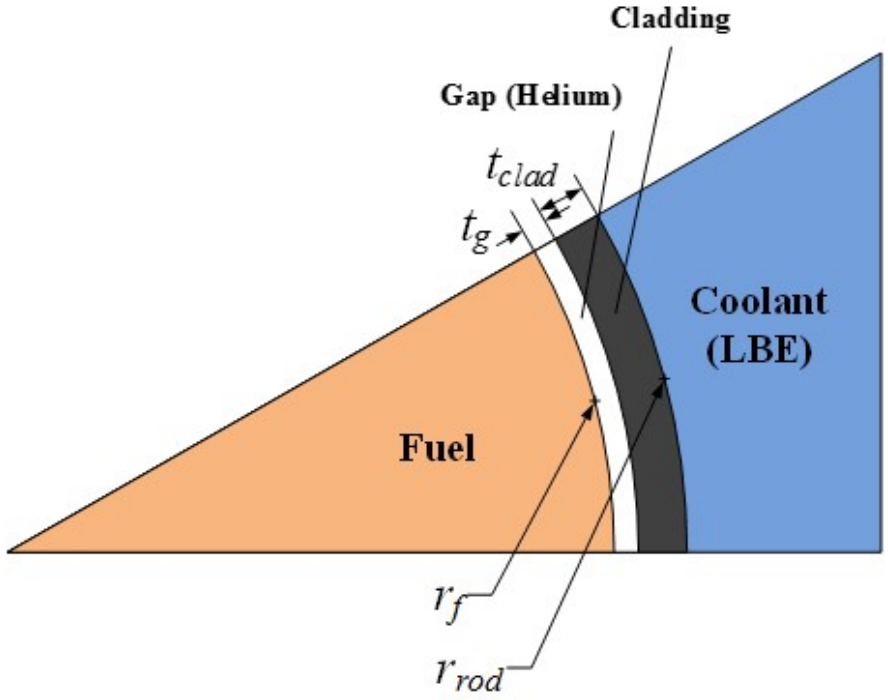

Figure 7.4 Schematic diagram for the reactor core model of generic pin-cell model of nuclear fuel

7.1.1.3 Coolant mass flow rate

In a passive system, coolant mass flow rate given by natural circulation is determined from a balance between buoyancy and hydrodynamic resistance. The buoyancy force is a resultant driving force from the coolant density change caused by coolant temperature gradient along the direction of gravitational force and height difference between the positions where temperature varies. In this regard, the core and steam generator, the heat source and heat sink in a passive SMR, respectively, are the main contributors that generate natural circulation flow. Since the height difference would not remarkably change in most of operating conditions, the temperature difference is a key value that determines natural circulation flow and it can only be regulated by the core power rating. Hence, the mass flow rate varies during load-following operation accompanied by time-dependent power rating change. Meanwhile, the hydrodynamic resistance is dependent upon the configurations and geometries of flow paths, flow speed, flow characteristics, surface conditions, and so on. In general, it is able to be classified with two main categories including friction loss and form loss. In addition, those loss terms are usually nonlinear, which lead to the computation and evaluation of their effects being required to solve it in iterative ways.

In contrast to pump-driven systems, the coolant flow rate is no longer able to be given with a constant value. Due to the existence of the latter, the hydrodynamic resistance, natural circulation flow rate cannot be evaluated with a simple method. The evaluation may need additional computational schemes

with iterations. However, considering the advantage of the lumped parameter approach used in this analytical reactor dynamics simulation model, it is not desirable to implement high-fidelity computational routines for the natural circulation flow rate calculation. In this respect, a simple nonlinear model is applied so that the flow rate is determined independent of other states.

The formulation to evaluate the natural circulation flow rate begins with momentum balance along the flow paths as shown in Eqn. (7.13):

$$\left(\sum_k \frac{L_k}{A_k} \right) \frac{d\dot{m}_p}{dt} = \Delta p_B - \sum_k \Delta p_{loss,k} \ . \tag{7.13}$$

It is noted that the buoyancy head and total pressure drop along the flow paths must be equal to each other in steady-state conditions due to the temporal change of mass flow rate is neglected. To proceed further, a linear relation so-called the Boussinesq approximation, which assumes the fluid density change is linearly given with respect to temperature change, is applied the bouyancy term. As discussed, the sum of pressure drop is usually a nonlinear function of mass flow rate. In this model, an additional assumption is implemented, which describes the total pressure loss is given in a form of Eqn. (7.14) below:

$$\sum_k \Delta p_{loss,k} = C_R \frac{\dot{m}_p^{\ 2}}{2\rho_c}, \tag{7.14}$$

where C_R is the hydraulic resistance coefficient defined by $C_R = R(\dot{m}_p)^{-n}$

(Todreas and Kazimi, 2001). In this relation, *R* is a proportionality constant that can be distinctively determined with the nominal operation condition of the system such that:

$$\sum_k \Delta p_{loss,k} = \frac{R}{2\rho_c}\dot{m}^{2-n} \;\Rightarrow\; R = \frac{2{\rho_c}^2 g\beta\Delta H}{{\dot{m}_0}^{2-n}}\left(T_{co,0} - T_{ci,0}\right). \qquad (7.15)$$

The power *n* is dependent upon flow characteristics. For highly turbulent flow, *n* = 0.2 is to be utilized. Since most of LBE flow expected in URANUS is in turbulent flow regime, this value is used. Accounting for Eqns. (7.14) and (7.15), the momentum balance equation can be further developed as shown in Eqn. (7.16). Since the term $\sum_k \frac{L_k}{A_k}$ is evidently predetermined by the system configurations, it can be given by a constant, c_m.

$$\begin{aligned} &\left(\sum_k \frac{L_k}{A_k}\right)\frac{d\dot{m}_p}{dt} = \rho_c g\beta\Delta H\left(T_{co}(t) - T_{ci}(t)\right) - \frac{R}{2\rho_c}\left\{\dot{m}_p(t)\right\}^{2-n} \\ &\Rightarrow\; \frac{d\dot{m}_p}{dt} = \frac{\rho_c g\beta\Delta H}{c_m}\left(T_{co}(t) - T_{ci}(t)\right) - \frac{1}{c_m}\frac{R}{2\rho_c}\left\{\dot{m}_p(t)\right\}^{2-n} \end{aligned}. \qquad (7.16)$$

For the evaluation of mass flow rate due to natural circulation, the resultant relation above is utilized. It is notable that the dependence of the mass flow rate to the core power is recast with the temperature difference.

7.1.1.4 State-space formulation by linearization

For the establishment of a reactor control model, it is desirable to utilize linearized formulations by designating a state parameter, $\psi(t)$, with an initial value term, ψ_0, and the deviation term, $\delta\psi$, such that $\psi(t) = \psi_0 + \delta\psi$. After replacing all the state parameters with the notation given above and rearranging them with several 1st order terms and 2nd order terms, it can be achieved by leaving only the 1st order terms while neglecting the 2nd order terms, since those terms have negligible impacts (Khalil, 1996).

In this point of view, all the equations established for the reactor core model are to be linearized. First of all, Eqns. (7.17) and (7.18) are rearranged from Eqns. (7.3) and (7.4) with the fact that the initial reactivity is given as $\rho_0 = 0$ and the total reactivity deviation from the initial state is expressed with $\delta\rho = \delta\rho_{rod} + \alpha_f \delta T_f + \frac{\alpha_c}{2}\delta T_{co} + \frac{\alpha_c}{2}\delta T_{ci}$:

$$\frac{d}{dt}\delta n_r = -\frac{\beta_{eff}}{\Lambda}\delta n_r + \sum_j \frac{\beta_j}{\Lambda}\delta C_{ir} + \frac{n_{r0}}{\Lambda}\delta\rho_{rod} + \frac{n_{r0}}{\Lambda}\alpha_f \delta T_f + \frac{n_{r0}}{\Lambda}\frac{\alpha_c}{2}\delta T_{co} + \frac{n_{r0}}{\Lambda}\frac{\alpha_c}{2}\delta T_{ci}, \tag{7.17}$$

$$\frac{d}{dt}\left(\delta C_{jr}\right) = \lambda_j \delta n_r - \lambda_j \delta C_{jr}. \tag{7.18}$$

The time-dependent change of fuel temperature, Eqn. (7.10), can be recast as in Eqn. (7.19):

$$\frac{d}{dt}\delta T_f = \frac{f_f Q_{0a}}{\mu_f}\delta n_r - \frac{\Omega_f}{\mu_f}\delta T_f + \frac{\Omega_f}{\mu_f}\delta T_c . \tag{7.19}$$

The energy balance equations for the lower and upper coolant lumps, Eqns (7.11) and (7.12), are rearranged to be Eqns. (7.20) and (7.21), respectively:

$$\begin{aligned}\frac{d}{dt}\delta T_{co} = {} & \frac{\left(1-f_f\right)Q_{0a}}{\mu_{c,core}}\delta n_r + \frac{\Omega_f}{\mu_{c,core}}\delta T_f - \frac{2\dot{m}_{p0}C_{pc}}{\mu_{c,core}}\delta T_{co} \\ & - \frac{\Omega_f - 2\dot{m}_{p0}C_{pc}}{\mu_{c,core}}\delta T_c - \frac{2C_{pc}}{\mu_{c,core}}\left(T_{co,0} - T_{c0}\right)\delta\dot{m}_p\end{aligned}, \tag{7.20}$$

$$\begin{aligned}\frac{d}{dt}\delta T_c = {} & \frac{\left(1-f_f\right)Q_{0a}}{\mu_{c,core}}\delta n_r + \frac{\Omega_f}{\mu_{c,core}}\delta T_f - \frac{\Omega_f + 2\dot{m}_{p0}C_{pc}}{\mu_{c,core}}\delta T_c \\ & + \frac{2C_{pc}\dot{m}_{p0}}{\mu_{c,core}}\delta T_{ci} - \frac{2C_{pc}}{\mu_{c,core}}\left(T_{c0} - T_{ci,0}\right)\delta\dot{m}_p\end{aligned}. \tag{7.21}$$

The simplified equation for natural circulation mass flow rate, Eqn. (7.16), has a nonlinear term with the power of (2 - *n*), where *n* is determined by coolant flow regime. Eqn. (7.22) shows its binary series expansion and there are resultant higher order terms with respect to $\delta\dot{m}$:

$$\begin{aligned}\left(\dot{m}_{p0} + \delta\dot{m}\right)^{2-n} = {} & \dot{m}_{p0}{}^{2-n} + (2-n)\dot{m}_{p0}{}^{1-n}\delta\dot{m} \\ & + \frac{(2-n)(1-n)}{2}\dot{m}_{p0}{}^{-n}\left(\delta\dot{m}\right)^2 + O\left(\left(\delta\dot{m}\right)^3\right)\end{aligned}. \tag{7.22}$$

Since this linearization process is to neglect the higher order terms above 2nd order, Eqn. (7.16) finally falls into Eqn. (7.23):

$$\frac{d}{dt}\left(\delta \dot{m}_p\right) = \frac{\rho g \beta \Delta H}{c_m}\delta T_{co} - \frac{\rho_c g \beta \Delta H}{c_m}\delta T_{ci} - \frac{R}{2 c_m \rho_c}(2-n)\dot{m}_{p0}^{\,1-n}\delta \dot{m}_p \quad . \tag{7.23}$$

The linearized equations can be used for state-space representation as forms of vector and matrix notations. In general, the temporal change of state vector **x** which represents the states in the system can be expressed with the input vector **u** and coefficient matrices **A** and **B** having appropriate dimensions as in the following relation, Eqn. (7.24):

$$\dot{\mathbf{x}} = \mathbf{A}\mathbf{x} + \mathbf{B}\mathbf{u} \, . \tag{7.24}$$

The resultant state vector x and input vector u is given by Eqns. (7.25) and (7.26), respectively:

$$\mathbf{x} = \left[\delta n_r \quad \delta C_{1r} \quad \delta C_{2r} \quad \delta C_{3r} \quad \delta C_{4r} \quad \delta C_{5r} \quad \delta C_{6r} \quad \delta T_f \quad \delta T_{co} \quad \delta T_c \quad \delta \dot{m}_p \quad \delta \rho_{rod}\right]^T , \text{ and} \tag{7.25}$$

$$\mathbf{u} = \left[\delta T_{cl} \quad \delta \dot{m}_p \quad v_{rod}\right]^T , \tag{7.26}$$

while the elements of coefficient matrices **A** and **B** are summarized in Table 7.1 and Table 7.2. Since those matrices are sparse matrices, non-zero elements are only presented otherwise noted. $a_{i,j}$ and $b_{i,j}$ are the elements of **A** and **B** on the i-th row and the j-th column, respectively.

Table 7.1 Elements of matrix **A** for linearized state-space formulation

Index	Elements	Index	Elements
$a_{1,1}$	$\frac{-\beta_{eff}}{\Lambda}$	$a_{4,4}$	$-\lambda_3$
$a_{1,2}$	$\frac{\beta_1}{\Lambda}$	$a_{5,1}$	λ_4
$a_{1,3}$	$\frac{\beta_2}{\Lambda}$	$a_{5,5}$	$-\lambda_4$
$a_{1,4}$	$\frac{\beta_3}{\Lambda}$	$a_{6,1}$	λ_5
$a_{1,5}$	$\frac{\beta_4}{\Lambda}$	$a_{6,6}$	$-\lambda_5$
$a_{1,6}$	$\frac{\beta_5}{\Lambda}$	$a_{7,1}$	λ_6
$a_{1,7}$	$\frac{\beta_6}{\Lambda}$	$a_{7,7}$	$-\lambda_6$
$a_{1,8}$	$\frac{n_{r0}\alpha_f}{\Lambda}$	$a_{8,1}$	$\frac{f_f Q_{0a}}{\mu_f}$
$a_{1,9}$	$\frac{n_{r0}\alpha_c}{2\Lambda}$	$a_{8,8}$	$\frac{-\Omega_f}{\mu_f}$
$a_{1,12}$	$\frac{n_{r0}}{\Lambda}$	$a_{8,10}$	$\frac{\Omega_f}{\mu_f}$
$a_{2,1}$	λ_1	$a_{9,1}$	$\frac{\left(1-f_f\right)Q_{0a}}{\mu_{c,core}}$
$a_{2,2}$	$-\lambda_1$	$a_{9,8}$	$\frac{\Omega_f}{\mu_{c,core}}$
$a_{3,1}$	λ_2	$a_{9,9}$	$\frac{-2\dot{m}_{p0}C_{pc}}{\mu_{c,core}}$
$a_{3,3}$	$-\lambda_2$	$a_{9,10}$	$\frac{-\Omega_f+2\dot{m}_{p0}C_{pc}}{\mu_{c,core}}$
$a_{4,1}$	λ_3	$a_{9,11}$	$\frac{-2C_{pc}\left(T_{co,0}-T_{c0}\right)}{\mu_{c,core}}$

Table 7.1 Elements of matrix **A** for linearized state-space formulation (contd.)

Index	Elements
$a_{10,1}$	$\frac{\left(1-f_f\right)Q_{0a}}{\mu_{c,core}}$
$a_{10,8}$	$\frac{\Omega_f}{\mu_{c,core}}$
$a_{10,10}$	$\frac{-\Omega_f - 2\dot{m}_{p0}C_{pc}}{\mu_{c,core}}$
$a_{10,11}$	$\frac{-2C_{pc}\left(T_{c0}-T_{ci,0}\right)}{\mu_{c,core}}$
$a_{11,9}$	$\frac{\rho_c g \beta \Delta H}{c_m}$
$a_{11,11}$	$\frac{-(2-n)R\dot{m}_{p0}^{\,1-n}}{2c_m\rho_c}$

Table 7.2 Elements of matrix **B** for linearized state-space formulation

Index	Elements
$b_{1,1}$	$\frac{n_{r0}\alpha_c}{2\Lambda}$
$b_{10,1}$	$\frac{2\dot{m}_{p0}C_{pc}}{\mu_{c,core}}$
$b_{11,1}$	$\frac{-\rho_c g \beta \Delta H}{c_m}$
$b_{12,3}$	G_r

7.1.2 Hot leg and cold leg models

7.1.2.1 Thermal-hydraulic models for hot leg and cold leg

The hot leg and cold leg are physical upstream and downstream components of the core and steam generator, vice versa, as shown in Figure 7.2. Compared to those heat source and sink, there is no heat generation nor heat removal in the hot leg and cold leg and these regions are rather passive components that propagate the change of thermophysical states from a component to the other. Similar to the formulations established for the core thermal-hydraulics sub-model in the reactor core model described in Section 7.1.1.2, energy balance equations can be derived as shown in Eqns. (7.27) and (7.28) for the hot leg and cold leg, respectively:

$$\begin{aligned} &\mu_{c,hl}\frac{d}{dt}T_{hl} = \dot{m}_p C_{pc}\left(T_{co} - T_{hl}\right) \\ &\Rightarrow \frac{dT_{hl}}{dt} = \frac{C_{pc}}{\mu_{c,hl}}\dot{m}_p T_{co} - \frac{C_{pc}}{\mu_{c,hl}}\dot{m}_p T_{hl} \end{aligned}, \tag{7.27}$$

$$\begin{aligned} &\mu_{c,cl}\frac{d}{dt}T_{cl} = \dot{m}_p C_{pc}\left(T_{p1} - T_{cl}\right) \\ &\Rightarrow \frac{dT_{cl}}{dt} = \frac{C_{pc}}{\mu_{c,cl}}\dot{m}_p T_{p1} - \frac{C_{pc}}{\mu_{c,cl}}\dot{m}_p T_{cl} \end{aligned}. \tag{7.28}$$

In the above equations, the total heat capacity of coolant in the hot leg $\mu_{c,hl}$ is given as $M_{c,hl}C_{pc} = \mu_{c,hl}$ while that of coolant in the cold leg $\mu_{c,cl}$ is expressed as $M_{c,cl}C_{pc} = \mu_{c,cl}$, similar to the case in the core thermal-hydraulics sub-model.

Physically, those hot leg and cold leg lumps serve as the time delay of mass flow and temperature transfer. However, this time delay is not constant because the mass flow rate term also depends on the core power rating. With the coolant mass flow rate model implemented in Section 7.1.1.3, the time delay would be influenced.

7.1.2.2 State-space formulation by linearization

In a similar way with the linearization process conducted in Section 7.1.1.4, the hot leg and cold leg models are to be linearized. First, from the energy balance equations for the hot leg as in Eqns. (7.27), the state vector x is given by $\mathbf{x} = \left[\delta T_{hl}\right]$ while the input vector u is designated to be $\mathbf{u} = \left[\delta T_{co} \quad \delta \dot{m}_p\right]^T$. With the same representation shown in Eqn. (7.24), the coefficient matrices **A** and **B** for the hot leg model are:

$$\mathbf{A} = \left[-\frac{\dot{m}_{p0} C_{pc}}{\mu_{c,hl}}\right], \tag{7.29}$$

$$\mathbf{B} = \left[\frac{\dot{m}_{p0} C_{pc}}{\mu_{c,hl}} \quad \frac{C_{pc}\left(T_{co,0} - T_{hl,0}\right)}{\mu_{c,hl}}\right], \tag{7.30}$$

The same approach can be applied to the energy balance equation for the cold leg model, Eqn. (7.28), in which the state vector **x** and input vector **u** are given

by $\mathbf{x} = \left[\delta T_{cl} \right]$ and $\mathbf{u} = \left[\delta T_{po} \quad \delta \dot{m}_p \right]^T$, respectively. The coefficient matrices **A** and **B** for the cold leg model are described in Eqns. (7.31) and (7.32):

$$\mathbf{A} = \left[-\frac{\dot{m}_{p0} C_{pc}}{\mu_{c,cl}} \right], \tag{7.31}$$

$$\mathbf{B} = \left[\frac{\dot{m}_{p0} C_{pc}}{\mu_{c,cl}} \quad \frac{C_{pc} \left(T_{po,0} - T_{cl,0} \right)}{\mu_{c,cl}} \right]. \tag{7.32}$$

7.1.3 Steam generator model

URANUS has eight identical steam generator modules. Each steam generator is a once-through, shell-and-tube type heat exchanger where LBE flows through the shell side while water remove the reactor power with phase transition into superheated steam inside the tube side. Inside the tube side of steam generators, subcooled water comes along central downward feedwater pipes and then distributed in the lower chamber. After that, the fluid flows along the tubes in which most of heat transfer takes place so that counter-current flow with respect to the primary coolant flow is established. As discussed in Section 4.3.2, superheated steam is produced and flows out from the steam generator outlet.

For simplicity, the steam generator model for the reactor dynamics simulation model treats all the modules as a single region by applying the lumped parameter, moving boundary approach (He et al., 1995; Pettit et al.,

1998; Rasmussen and Alleyne, 2006; Willatzen et al., 1998), which utilizes lumped parameter models for each of calculation nodes in a dynamic simulation. This approach is mainly prepared for the prediction of point or position where phase transition occurs in a heat exchanger.

Figure 7.5 shows a simplified moving boundary diagram for steam generator. Since subcooled water transforms into superheated steam as flowing through the tube side, three regions fluid regions such as subcooled, two-phase, and superheated regions are need to be defined. The moving boundaries are designated between those regions. It is assumed that this division into three regions are applied only to the tube bundles, not to the central feedwater pipes as most of heat transfer occurs through the tube bundles, about 95% of total power removal. However, for a consistency of heat transfer relations, the moving boundaries also adopted for the central feedwater pipe region and the tube wall regions comprising of not only the tube bundles but also the feedwater pipes even though there is no phase transition at all. In addition, the lower chamber connecting the central feedwater pipe and tube bundles are not modelled for a simplicity.

Based on the lumped regions as defined and shown in Figure 7.5, the formulations of steam generator model are derived from the partial differential equations, especially on mass conservation and energy balance. By integrating both sides of the equations in terms of flow area, simplified mass conservation equation and energy balance equation can be drawn as shown in Eqns. (7.33) and (7.34), respectively:

$$A_s \frac{\partial \rho}{\partial t} + \frac{\partial \dot{m}_s}{\partial z} = 0\,, \tag{7.33}$$

$$A_s \frac{\partial \left(\rho h - P_s\right)}{\partial t} + \frac{\partial \left(\dot{m}_s h\right)}{\partial z} = \pi d_s h_s N_{tube} \left(T_t - T_s\right). \tag{7.34}$$

As the steam generators have a number of tube bundles, the heat transfer areas between the fluid and the tube surface would proportionally increase. The equations above are further modified by applying an integration rule known as Leibniz's rule as defined in Eqn. (7.35):

$$\begin{aligned} &\int_{a(t)}^{b(t)} \frac{\partial f(z,t)}{\partial t} dz \\ &= \frac{d}{dt}\int_{a(t)}^{b(t)} f(z,t)dz - f(b(t),t)\frac{db(t)}{dt} + f(a(t),t)\frac{da(t)}{dt} \end{aligned}. \tag{7.35}$$

In the following sections, several equations will be described for all the fluid regions by means of Eqn. (7.33) and (7.34), which are suitably recast by the rule given as Eqn. (7.35). The number of equations are dependent upon the number of fluid regions defined moving boundaries that divide the different states of fluids. Since the control volumes are directly related to those moving boundaries, most of sets of equations in each of the fluid regions are given in an almost identical way. However, the formulations in two-phase region should differ from those of other single-phase regions due to additional relations for the mean parameters, such as mean void fraction, being required. It is noted that the derivation and definition of each of those mean parameters are extensively summarized in (Pettit et al., 1998; Rasmussen and Alleyne, 2006) and this thesis will utilize the final forms.

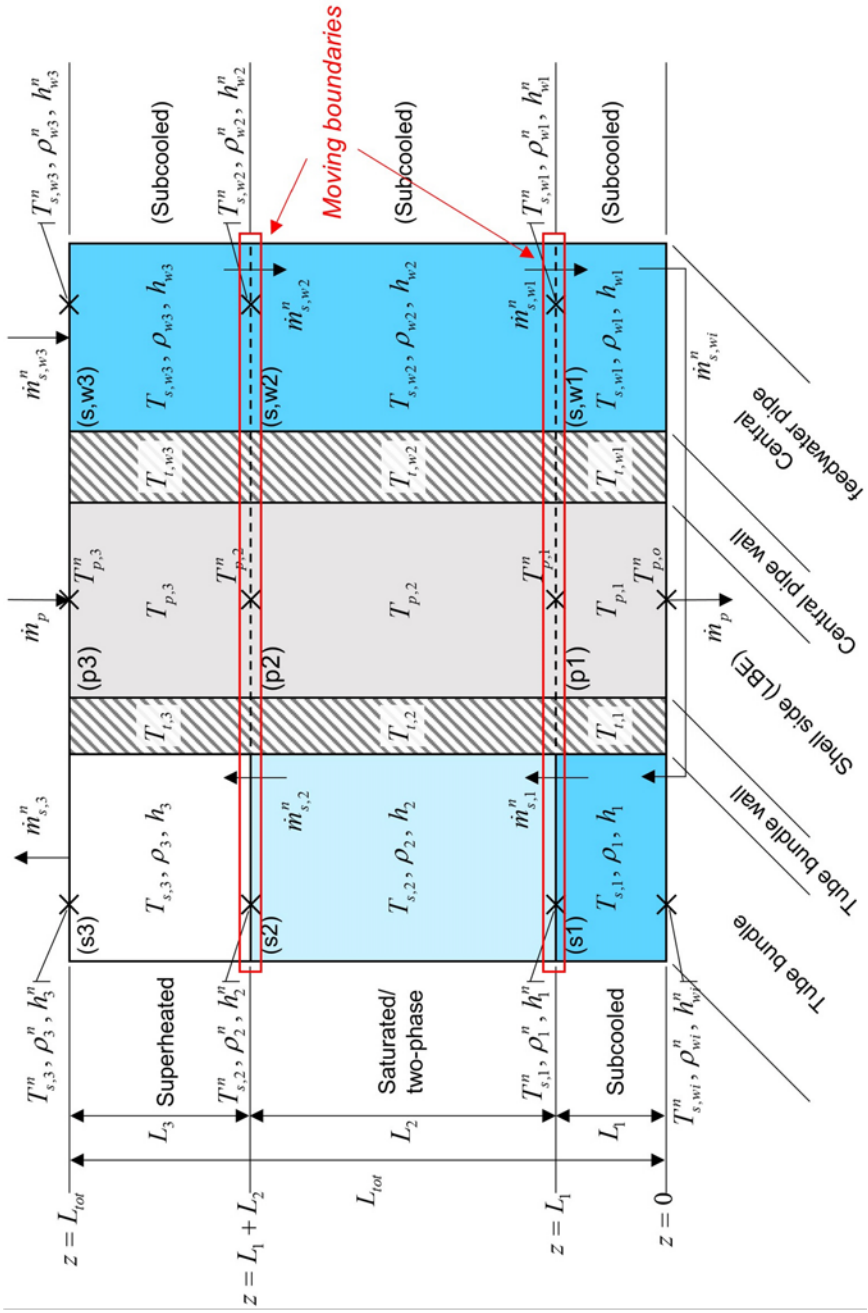

Figure 7.5 Schematic diagram for steam generator state-space model

7.1.3.1 Single phase regions

As shown in Figure 7.5, there are several lumped regions that are filled with single phase fluids, including subcooled water and superheated steam: for example, Regions s1, sw1, sw2, sw3 are for subcooled water while Region s3 is for superheated steam. In those parts, the mean values of fluid density, enthalpy, and volumetric enthalpy, which is defined by the two former parameters, are defined as in Eqns. (7.36) - (7.38), respectively, within the regions between $z = a$ and $z = b$ in which the averaging takes place:

$$\rho_j = \frac{1}{b-a}\int_a^b \rho(z,t)dz = \rho(P_s, h_j)\,, \tag{7.36}$$

$$h_j = \frac{1}{b-a}\int_a^b h(z,t)dz = \frac{h_{j-1}^n + h_j^n}{2}\,, \tag{7.37}$$

$$\rho_j h_j = \frac{1}{b-a}\int_a^b \rho(z,t)h(z,t)dz\,. \tag{7.38}$$

By integrating both sides of Eqns. (7.33) and (7.34) over $z = z_{j-1}$ and $z = z_j$, the following relations, Eqns. (7.39) and (7.40), respectively, can be accounted for the single phase regions:

$$\begin{aligned}
&\int_{z_{j-1}}^{z_j} A_s \frac{\partial \rho}{\partial t}dz + \int_{z_{j-1}}^{z_j} \frac{\partial \dot{m}_s}{\partial z}dz = 0 \\
&\Rightarrow \dot{m}_{s,j-1}^n - \dot{m}_{s,j}^n = A_s L_j \frac{d\rho_j}{dt} + A_s \rho_j \frac{dL_j}{dt} \\
&\qquad\qquad - A_s \rho_j^n \frac{dz_j}{dt} + A_s \rho_{j-1}^n \frac{dz_{j-1}}{dt}
\end{aligned}\,, \tag{7.39}$$

$$
\begin{aligned}
&\int_{z_{j-1}}^{z_j} A_s \frac{\partial\left(\rho h - P_s\right)}{\partial t} dz + \int_{z_{j-1}}^{z_j} \frac{\partial\left(\dot{m}_s h\right)}{\partial z} dz \\
&\quad = \int_{z_{j-1}}^{z_j} \pi d_s h_s N_{tube}\left(T_t - T_s\right) dz \\
&\Rightarrow \pi d_s L_j N_{tube} h_{s,j}\left(T_{t,j} - T_{s,j}\right) + h_{j-1}^n \dot{m}_{s,j-1}^n - h_j^n \dot{m}_{s,j}^n \\
&\quad = -A_s \rho_j^n h_j^n \frac{dz_j}{dt} + A_s \rho_{j-1}^n h_{j-1}^n \frac{dz_{j-1}}{dt} + A_s \rho_j h_j \frac{d\left(z_j - z_{j-1}\right)}{dt} \\
&\qquad - A_s (z_j - z_{j-1}) \frac{dP_s}{dt} + A_s (z_j - z_{j-1}) \frac{d\left(\rho_j h_j\right)}{dt}
\end{aligned}
\qquad (7.40)
$$

For a remark, the direction of integration in the equations above are defined from a direction from bottom to top, the opposite direction to the direction of gravitational force, based on Regions s1 and s3. In the case of the central feedwater pipe regions, including Regions sw1, sw2, and sw3, the direction should be flipped, from top to bottom. In addition, since the equations above uses several thermophysical parameters that are defined on the boundaries and are averaged in the lumped regions at the same time, a careful formulation is required. The parameters with superscript *n* deal with those defined on the boundaries.

From the intermediate forms of mass and energy balance equations as described in Eqns. (7.39) and (7.40), the formulations for each of single phase regions can be further arranged. In the derivation hereafter, several partial derivatives for parameter change with respect to other parameters are utilized, which can be determined by using the so-called steam table, a property table for water and steam. The details on the derivation of those partial derivatives are extensively studied by previous studies (Pettit et al., 1998; Rasmussen and

Alleyne, 2006). Firstly, the final forms for the subcooled region in the tube bundles, Region s1, is given by Eqns. (7.41) and (7.42):

$$\begin{aligned}
&\dot{m}_{s,wi}^{n} - \dot{m}_{s,1}^{n} \\
&= A_{st}\left(\rho_1 - \rho_f\right)\frac{dL_1}{dt} + A_{st}L_1\left(\left.\frac{\partial\rho_1}{\partial P_s}\right|_{h_1} + \frac{1}{2}\left.\frac{\partial\rho_1}{\partial h_1}\right|_{P_s}\frac{\partial h_f}{\partial P_s}\right)\frac{dP_s}{dt}, \\
&\quad + \frac{1}{2}A_{st}L_1\left.\frac{\partial\rho_1}{\partial h_1}\right|_{P_s}\frac{dh_{wi}^{n}}{dt}
\end{aligned} \tag{7.41}$$

$$\begin{aligned}
&h_{s,1}A_{ti,1}\left(T_{t,1} - T_{s,1}\right) + h_{wi}^{n}\dot{m}_{s,wi}^{n} - h_f\dot{m}_{s,1}^{n} \\
&= A_{st}\left(\rho_1 h_1 - \rho_f h_f\right)\frac{dL_1}{dt} \\
&\quad + A_{st}L_1\left[\frac{\rho_1}{2}\frac{\partial h_f}{\partial P_s} + h_1\left(\left.\frac{\partial\rho_1}{\partial P_s}\right|_{h_1} + \frac{1}{2}\left.\frac{\partial\rho_1}{\partial h_1}\right|_{P_s}\frac{\partial h_f}{\partial P_s}\right) - 1\right]\frac{dP_s}{dt}\cdot \\
&\quad + \frac{A_{st}L_1}{2}\left(\rho_1 + h_1\left.\frac{\partial\rho_1}{\partial h_1}\right|_{P_s}\right)\frac{dh_{wi}^{n}}{dt}
\end{aligned} \tag{7.42}$$

Analogously, for the superheated region in tube bundles, Region s3, two following equations are formulated:

$$\begin{aligned}
&\dot{m}_{s,2}^{n} - \dot{m}_{s,3}^{n} \\
&= A_{st}\left(\rho_g - \rho_3\right)\frac{d_1(L_1 + L_2)}{dt} \\
&\quad + A_{st}L_3\left(\left.\frac{\partial\rho_3}{\partial P_s}\right|_{h_3} + \frac{1}{2}\left.\frac{\partial\rho_3}{\partial h_3}\right|_{P_s}\frac{\partial h_g}{\partial P_s}\right)\frac{dP_s}{dt} + \frac{1}{2}A_{st}L_3\left.\frac{\partial\rho_3}{\partial h_3}\right|_{P_s}\frac{dh_3^{n}}{dt}
\end{aligned}, \tag{7.43}$$

$$
\begin{aligned}
&h_{s,3}A_{ti,3}\left(T_{t,3}-T_{s,3}\right)+h_g\dot{m}^n_{s,2}-h^n_3\dot{m}^n_{s,3}\\
&=A_{st}\left(\rho_g h_g-\rho_3 h_3\right)\frac{d\left(L_1+L_2\right)}{dt}\\
&\quad+A_{st}L_3\left[\frac{\rho_3}{2}\frac{\partial h_g}{\partial P_s}+h_3\left(\left.\frac{\partial\rho_3}{\partial P_s}\right|_{h_3}+\frac{1}{2}\left.\frac{\partial\rho_3}{\partial h_3}\right|_{P_s}\frac{\partial h_g}{\partial P_s}\right)-1\right]\frac{dP_s}{dt}\\
&\quad+\frac{A_{st}L_3}{2}\left(\rho_3+h_3\left.\frac{\partial\rho_3}{\partial h_3}\right|_{P_s}\right)\frac{dh^n_3}{dt}
\end{aligned}
\qquad (7.44)
$$

Region sw3, a subcooled region defined in the central feedwater pipes is directly connected to water inlet. The final formulations are:

$$
\begin{aligned}
&\dot{m}^n_{s,w1}-\dot{m}^n_{s,wi}\\
&=A_{sw}\left(\rho_{w1}-\rho^n_{w1}\right)\frac{dL_1}{dt}+A_{sw}L_1\left.\frac{\partial\rho_{w1}}{\partial P_s}\right|_{h_{w1}}\frac{dP_s}{dt}\\
&\quad+\frac{A_{sw}L_1}{2}\left.\frac{\partial\rho_{w1}}{\partial h_{w1}}\right|_{P_s}\frac{dh^n_{wi}}{dt}+\frac{A_{sw}L_1}{2}\left.\frac{\partial\rho_{w1}}{\partial h_{w1}}\right|_{P_s}\frac{dh^n_{w1}}{dt}
\end{aligned}
\qquad (7.45)
$$

$$
\begin{aligned}
&h_{s,w1}A_{twi,1}\left(T_{t,w1}-T_{s,w1}\right)+h^n_{w1}\dot{m}^n_{s,w1}-h^n_{wi}\dot{m}^n_{s,wi}\\
&=A_{sw}\left(\rho_{w1}h_{w1}-\rho^n_{w1}h^n_{w1}\right)\frac{dL_1}{dt}+A_{sw}L_1\left(h_{w1}\left.\frac{\partial\rho_{w1}}{\partial P_s}\right|_{h_{w1}}-1\right)\frac{dP_s}{dt}\\
&\quad+\frac{A_{sw}L_1}{2}\left(\rho_{w1}+h_{w1}\left.\frac{\partial\rho_{w1}}{\partial h_{w1}}\right|_{P_s}\right)\frac{dh^n_{wi}}{dt}\\
&\quad+\frac{A_{sw}L_1}{2}\left(\rho_{w1}+h_{w1}\left.\frac{\partial\rho_{w1}}{\partial h_{w1}}\right|_{P_s}\right)\frac{dh^n_{w1}}{dt}
\end{aligned}
\qquad (7.46)
$$

Region sw2 is also another subcooled region in the central feedwater pipes and the formulations for this region are given by the following Eqns. (7.47) and

(7.48):

$$
\begin{aligned}
&\dot{m}_{s,w2}^{n}-\dot{m}_{s,w1}^{n}\\
&=A_{sw}\left(\rho_{w1}^{n}-\rho_{w2}^{n}\right)\frac{dL_1}{dt}+A_{sw}\left(\rho_{w2}-\rho_{w2}^{n}\right)\frac{dL_2}{dt}\\
&\quad+A_{sw}L_2\left.\frac{\partial\rho_{w2}}{\partial P_s}\right|_{h_{w2}}\frac{dP_s}{dt}+\frac{A_{sw}L_2}{2}\left.\frac{\partial\rho_{w2}}{\partial h_{w2}}\right|_{P_s}\frac{dh_{w1}^{n}}{dt}\,,\\
&\quad+\frac{A_{sw}L_2}{2}\left.\frac{\partial\rho_{w2}}{\partial h_{w2}}\right|_{P_s}\frac{dh_{w2}^{n}}{dt}
\end{aligned}
\tag{7.47}
$$

$$
\begin{aligned}
&h_{s,w2}A_{twi,2}\left(T_{t,w2}-T_{s,w2}\right)+h_{w2}^{n}\dot{m}_{s,w2}^{n}-h_{w1}^{n}\dot{m}_{s,w1}^{n}\\
&=A_{sw}\left(\rho_{w1}^{n}h_{w1}^{n}-\rho_{w2}^{n}h_{w2}^{n}\right)\frac{dL_1}{dt}+A_{sw}\left(\rho_{w2}h_{w2}-\rho_{w2}^{n}h_{w2}^{n}\right)\frac{dL_2}{dt}\\
&\quad+A_{sw}L_2\left(h_{w2}\left.\frac{\partial\rho_{w2}}{\partial P_s}\right|_{h_{w2}}-1\right)\frac{dP_s}{dt}\\
&\quad+\frac{A_{sw}L_2}{2}\left(\rho_{w2}+h_{w2}\left.\frac{\partial\rho_{w2}}{\partial h_{w2}}\right|_{P_s}\right)\frac{dh_{w1}^{n}}{dt}\\
&\quad+\frac{A_{sw}L_2}{2}\left(\rho_{w2}+h_{w2}\left.\frac{\partial\rho_{w2}}{\partial h_{w2}}\right|_{P_s}\right)\frac{dh_{w2}^{n}}{dt}
\end{aligned}
\tag{7.48}
$$

The other subcooled region in the central feedwater pipes is Region sw3, which is assumed to connect the feedwater pipes and tube bundles directly. Eqns. (7.49) and (7.50) describe mass and energy balances within the region:

$$
\begin{aligned}
&\dot{m}_{s,w3}^{n} - \dot{m}_{s,w2}^{n} \\
&= A_{sw}\left(\rho_{w2}^{n} - \rho_{w3}\right)\frac{dL_1}{dt} + A_{sw}\left(\rho_{w2}^{n} - \rho_{w3}\right)\frac{dL_2}{dt} \\
&\quad + A_{sw}L_3\left.\frac{\partial \rho_{w3}}{\partial P_s}\right|_{h_{w3}}\frac{dP_s}{dt} + \frac{1}{2}A_{sw}L_3\left.\frac{\partial \rho_{w3}}{\partial h_{w3}}\right|_{P_s}\frac{dh_{w2}^{n}}{dt}, \\
&\quad + \frac{1}{2}A_{sw}L_3\left.\frac{\partial \rho_{w3}}{\partial h_{w3}}\right|_{P_s}\frac{dh_{w3}^{n}}{dt}
\end{aligned}
\tag{7.49}
$$

$$
\begin{aligned}
&h_{s,w3}A_{twi,3}\left(T_{t,w3} - T_{s,w3}\right) + h_{w3}^{n}\dot{m}_{s,w3}^{n} - h_{w2}^{n}\dot{m}_{s,w2}^{n} \\
&= A_{sw}\left(\rho_{w2}^{n}h_{w2}^{n} - \rho_{w3}h_{w3}\right)\frac{dL_1}{dt} + A_{sw}\left(\rho_{w2}^{n}h_{w2}^{n} - \rho_{w3}h_{w3}\right)\frac{dL_2}{dt} \\
&\quad + A_{sw}L_3\left(h_{w3}\left.\frac{\partial \rho_{w3}}{\partial P_s}\right|_{h_{w3}} - 1\right)\frac{dP_s}{dt} \\
&\quad + \frac{A_{sw}L_3}{2}\left(\rho_{w3} + h_{w3}\left.\frac{\partial \rho_{w3}}{\partial h_{w3}}\right|_{P_s}\right)\frac{dh_{w2}^{n}}{dt} \\
&\quad + \frac{A_{sw}L_3}{2}\left(\rho_{w3} + h_{w3}\left.\frac{\partial \rho_{w3}}{\partial h_{w3}}\right|_{P_s}\right)\frac{dh_{w3}^{n}}{dt}
\end{aligned}
\tag{7.50}
$$

7.1.3.2 Two-phase region

Contrary to the single phase regions described in Section 7.1.3.1, the two-phase region, Region s2, is where phase transition take places. Hence, it is assumed that the thermophysical properties of the working fluid at both ends, the inlet and outlet, are saturated; saturated water at its inlet whilst saturated steam at its outlet. Furthermore, the mean thermophysical properties within the region is defined in terms of the mean void fraction, the volume ratio of vapor to liquid (Rasmussen and Alleyne, 2006; Willatzen et al., 1998). For this assumption

being plausible, it is required that its mean void fraction does not so much change during operation and several experimental results show that this assumption is valid (Wedekind et al., 1978). In this respect, the mean values of fluid density, enthalpy, and volumetric enthalpy are defined in terms of the mean void fraction, γ, of the region and saturated properties as shown in Eqns. (7.51) - (7.53) (Willatzen et al., 1998):

$$\overline{\rho}_2 = \gamma\rho_g + (1-\gamma)\rho_f\,, \tag{7.51}$$

$$\overline{h}_2 = \gamma h_g + (1-\gamma)h_f\,, \tag{7.52}$$

$$\overline{\rho}_2\overline{h}_2 = \gamma\rho_g h_g + (1-\gamma)\rho_f h_f\,. \tag{7.53}$$

For the calculation of the mean void fraction, a correlation given in terms of the ratio of the density of saturated vapor to that of saturated liquid (Jensen and Tummescheit, 2002):

$$\gamma = 1 - \frac{1 + \left(\rho_g/\rho_f\right)^{2/3}\left[(2/3)\ln\left(\rho_g/\rho_f\right) - 1\right]}{\left[\left(\rho_g/\rho_f\right)^{2/3} - 1\right]^2}. \tag{7.54}$$

In analogy with the formulations for the single phase regions, the intermediate forms as described in Eqns. (7.39) and (7.40) are rearranged with the above relations as shown in Eqns. (7.55) and (7.56):

$$
\begin{aligned}
&\dot{m}_{s,1}^{n} - \dot{m}_{s,2}^{n} \\
&= A_{st}\left(\rho_f - \rho_g\right)\frac{dL_1}{dt} + A_{st}\left(1-\gamma\right)\left(\rho_f - \rho_g\right)\frac{dL_2}{dt}, \\
&\quad + A_{st}L_2\left[\gamma\frac{\partial\rho_g}{\partial P_s} + \left(1-\gamma\right)\frac{\partial\rho_f}{\partial P_s}\right]\frac{dP_s}{dt}
\end{aligned}
\tag{7.55}
$$

$$
\begin{aligned}
&h_{s,2}A_{ti,2}\left(T_{t,2} - T_{s,2}\right) + h_f\dot{m}_{s,1}^{n} - h_g\dot{m}_{s,2}^{n} \\
&= A_{st}\left(\rho_f h_f - \rho_g h_g\right)\frac{dL_1}{dt} + A_{st}\left(1-\gamma\right)\left(\rho_f h_f - \rho_g h_g\right)\frac{dL_2}{dt}. \\
&\quad + A_{st}L_2\left[\gamma\frac{\partial(\rho_g h_g)}{\partial P_s} + \left(1-\gamma\right)\frac{\partial(\rho_f h_f)}{\partial P_s} - 1\right]\frac{dP_s}{dt}
\end{aligned}
\tag{7.56}
$$

7.1.3.3 Energy balance equations in constituent walls

As the wall regions including tube bundles and central feedwater pipes work as conductive thermal resistance and there are no fluid flows inside, only energy balance equation is utilized. For this model, the temperature of a wall region, which is defined by the moving boundaries for the two-phase region in the tube bundles, is defined at the center of each lump. In addition, it is assumed that there is no axial conduction among those wall regions. The energy conservation equations for the tube bundles and central feedwater pipes are given as Eqns. (7.57) and (7.58), respectively:

$$
\rho_t C_{pt} A_t \frac{\partial T_t}{\partial t} = -\pi d_p N_{st} h_p\left(T_t - T_p\right) - \pi d_s N_{st} h_s\left(T_t - T_s\right), \tag{7.57}
$$

$$\rho_t C_{pt} A_{tw} \frac{\partial T_{t,w}}{\partial t} = -\pi d_{pw} N_{sw} h_p \left(T_{t,w} - T_p \right) - \pi d_s N_{sw} h_s \left(T_{t,w} - T_{s,w} \right) . \quad (7.58)$$

The above equations require the convective heat transfer coefficients of primary and secondary coolants. For the primary coolant, the Seban-Shimazaki correlation (Seban and Shimazaki, 1949), which already given in Eqn. (6.1), is applied while a widely used correlation for single phase water flows, the Dittus-Boelter correlation (Dittus and Boelter, 1930), is used. Since the two-phase region is also treated as if it is another single-phase flow by means of mean void fraction, the same correlation is utilized to the region.

Considering the boundary conditions given by the fluid regions surrounding those wall regions, the equations above can be further recast. The energy balance equations for the tube bundle wall regions, Region t1, t2, and t3 can indeed be formulated with Eqns. (7.59) - (7.61):

$$\rho_t C_{pt} A_t L_1 \frac{dT_{t,1}}{dt} + \rho_t C_{pt} A_t \left(T_{t,1} - T_{t,2} \right) \frac{dL_1}{dt} = -h_{p,1} A_{to,1} \left(T_{t,1} - T_{p,1} \right) - h_{s,1} A_{ti,1} \left(T_{t,1} - T_{s,1} \right) , \quad (7.59)$$

$$\rho_t C_{pt} A_t L_2 \frac{dT_{t,2}}{dt} = -h_{p,2} A_{to,2} \left(T_{t,2} - T_{p,2} \right) - h_{s,2} A_{ti,2} \left(T_{t,2} - T_{s,2} \right) , \text{ and} \quad (7.60)$$

$$\rho_t C_{pt} A_t L_3 \frac{dT_{t,3}}{dt} + \rho_t C_{pt} A_t \left(T_{t,2} - T_{t,3} \right) \frac{dL_1}{dt} + \rho_t C_{pt} A_t \left(T_{t,2} - T_{t,3} \right) \frac{dL_2}{dt} = -h_{p,3} A_{to,3} \left(T_{t,3} - T_{p,3} \right) - h_{s,3} A_{ti,3} \left(T_{t,3} - T_{s,3} \right) , \quad (7.61)$$

where heat transfer areas between a fluid region and the wall region, including $A_{ti,j}$, $A_{to,j}$, $A_{twi,j}$, and $A_{two,j}$, are respectively defined by $A_{ti,j} = \pi d_s N_{st} L_j$, $A_{to,j} = \pi d_p N_{st} L_j$, $A_{twi,j} = \pi d_{sw} N_{sw} L_j$, and $A_{two,j} = \pi d_{pw} N_{sw} L_j$. Similarly, the central feedwater pipe wall regions, Region tw1, tw2, and tw3 have the following energy balance described with Eqns. (7.62) - (7.64):

$$\begin{aligned} &\rho_t C_{pt} A_{tw} L_1 \frac{dT_{t,w1}}{dt} + \rho_t C_{pt} A_{tw} \left(T_{t,w1} - T_{t,w2}\right) \frac{dL_1}{dt} \\ &= -h_{p,1} A_{two,1} \left(T_{t,w1} - T_{p,1}\right) - h_{s,w1} A_{twi,1} \left(T_{t,w1} - T_{s,w1}\right) \end{aligned} \quad , \tag{7.62}$$

$$\begin{aligned} &\rho_t C_{pt} A_{tw} L_2 \frac{dT_{t,w2}}{dt} \\ &= -h_{p,2} A_{two,2} \left(T_{t,w2} - T_{p,2}\right) - h_{s,w2} A_{twi,2} \left(T_{t,w2} - T_{s,w2}\right) \end{aligned} \quad \text{, and} \tag{7.63}$$

$$\begin{aligned} &\rho_t C_{pt} A_{tw} L_3 \frac{dT_{t,w3}}{dt} + \rho_t C_{pt} A_{tw} \left(T_{t,w2} - T_{t,w3}\right) \frac{dL_1}{dt} \\ &+ \rho_t C_{pt} A_{tw} \left(T_{t,w2} - T_{t,w3}\right) \frac{dL_2}{dt} \\ &= -h_{p,3} A_{two,3} \left(T_{t,w3} - T_{p,3}\right) - h_{s,w3} A_{twi,3} \left(T_{t,w3} - T_{s,w3}\right) \end{aligned} \quad . \tag{7.64}$$

7.1.3.4 Shell side regions

The primary side of a steam generator consists of the shell side. In analogy with other regions, the shell side regions are also divided into three regions according to the moving boundaries given in the tube bundles, which are Region p1, p2 and p3 as depicted in Figure 7.5. Since the phase transition of primary coolant never takes place in URANUS in most of operating and accidental conditions and the mass flow rate relation given in Section 7.1.1.3 accounts for hydraulic

loss for all components, only the energy balance equations are required to describe physical behaviors in the shell side regions. In addition, those regions are related to both the central feedwater pipe regions and the tube bundle regions. Hence, the balance equations are drawn as shown in Eqn. (7.65) by adding those two contributions:

$$\begin{aligned}\rho_c C_{pc} A_p \frac{\partial T_p}{\partial t} = &-\dot{m}_p C_{pc} \frac{\partial T_p}{\partial z} - \pi d_p h_p N_{st} \left(T_p - T_t\right) \\ &- \pi d_{pw} h_p N_{sw} \left(T_p - T_{t,w}\right)\end{aligned} \tag{7.65}$$

By integrating both sides within each of the regions, the above equation can be rearranged as the following equations, Eqns. (7.66), (7.67), and (7.68), for Region p1, p2, and p3, respectively:

$$\begin{aligned}&\rho_c C_{pc} A_p L_1 \frac{dT_{p,1}}{dt} + \rho_c C_{pc} A_p \left(T_{p,1} - T_{p,2}\right) \frac{dL_1}{dt} \\ &= \dot{m}_p C_{pc} \left(T_{p,2} - T_{p,1}\right) - h_{p,1} A_{to,1} \left(T_{p,1} - T_{t,1}\right) \\ &\quad - h_{p,1} A_{two,1} \left(T_{p,1} - T_{t,w1}\right)\end{aligned} \quad , \tag{7.66}$$

$$\begin{aligned}&\rho_c C_{pc} A_p L_2 \frac{dT_{p,2}}{dt} \\ &= \dot{m}_p C_{pc} \left(T_{p,3} - T_{p,2}\right) - h_{p,2} A_{to,2} \left(T_{p,2} - T_{t,2}\right), \\ &\quad - h_{p,2} A_{two,2} \left(T_{p,2} - T_{t,w2}\right)\end{aligned} \tag{7.67}$$

$$\begin{aligned}&\rho_c C_{pc} A_p L_3 \frac{dT_{p,3}}{dt} + \rho_c C_{pc} A_p \left(T_{p,2} - T_{p,3}\right) \frac{dL_1}{dt} \\ &\quad + \rho_c C_{pc} A_p \left(T_{p,2} - T_{p,3}\right) \frac{dL_2}{dt} \\ &= \dot{m}_p C_{pc} \left(T_{p,in} - T_{p,3}\right) - h_{p,3} A_{to,3} \left(T_{p,3} - T_{t,3}\right) \\ &\quad - h_{p,3} A_{two,3} \left(T_{p,3} - T_{t,w3}\right)\end{aligned} \quad , \tag{7.68}$$

7.1.3.5 State-space formulation for steam generator

With the same point of view, the steam generator model has several nonlinear equations and it is appropriate to utilize the linearized forms of those equations for control purposes. Contrary to the case of the reactor core model, the formulations for this model is highly nonlinear. In detail, several number of equations are not easily arranged as a linear summation of temporal term of a state and other terms that are related to the other states so that the state vector is established with the final linear relation, Eqn. (7.24), since the state vector is not linear independent. In this regard, the simple derivation, which is conducted by dividing a state into the initial value and deviation, does not work for the linearization process on constructing state-space formulation of the steam generator model.

In order to overcome this problem, a linear algebraic approach is to be used (Khalil, 1996). A detailed derivation can be found in a previous study (Rasmussen and Alleyne, 2006). This approach begins with the state-space formulation, which is not yet linearized, is given as a form shown in Eqn. (7.69):

$$Z(\mathbf{x},\mathbf{u})\dot{\mathbf{x}} = f(\mathbf{x},\mathbf{u}), \tag{7.69}$$

where $\mathbf{x}$ is the state vector, $\mathbf{u}$ is the input vector, the matrices $Z(\mathbf{x},\mathbf{u})$ and $f(\mathbf{x},\mathbf{u})$ is given by arranging the system of differential equations with vector-matrix formats, respectively, which are derived from the equations for the steam

generator model. If the matrix $Z(\mathbf{x},\mathbf{u})$ is assumed to be invertible, Eqn. (7.69) can be rearranged by adopting a new matrix form $g(\mathbf{x},\mathbf{u})$:

$$\dot{\mathbf{x}} = Z^{-1}(\mathbf{x},\mathbf{u})\, f(\mathbf{x},\mathbf{u}) \equiv g(\mathbf{x},\mathbf{u}) . \tag{7.70}$$

By using the perturbation notation, $\delta\dot{\mathbf{x}} = \mathbf{x} - \mathbf{x}_0$, one would finally get:

$$\delta\dot{\mathbf{x}} = \left[\left.\frac{\partial g}{\partial \mathbf{x}}\right|_{\mathbf{x}_0,\mathbf{u}_0}\right]\delta\mathbf{x} + \left[\left.\frac{\partial g}{\partial \mathbf{u}}\right|_{\mathbf{x}_0,\mathbf{u}_0}\right]\delta\mathbf{u} . \tag{7.71}$$

Then, the matrix differentiation terms in Eqn. (7.71) are expressed as follows:

$$\begin{aligned}\left[\left.\frac{\partial g}{\partial \mathbf{x}}\right|_{\mathbf{x}_0,\mathbf{u}_0}\right] &= \left[Z\big|_{\mathbf{x}_0,\mathbf{u}_0}\right]^{-1}\left[\left.\frac{\partial f}{\partial \mathbf{x}}\right|_{\mathbf{x}_0,\mathbf{u}_0}\right] \\ &\quad - \left[Z\big|_{\mathbf{x}_0,\mathbf{u}_0}\right]^{-2}\left[\left.\frac{\partial Z}{\partial \mathbf{x}}\right|_{\mathbf{x}_0,\mathbf{u}_0}\right]^{-1}\cancel{\left[f_{\mathbf{x}_0,\mathbf{u}_0}\right]} \\ &= \left[Z\big|_{\mathbf{x}_0,\mathbf{u}_0}\right]^{-1}\left[\left.\frac{\partial f}{\partial \mathbf{x}}\right|_{\mathbf{x}_0,\mathbf{u}_0}\right]\end{aligned} \tag{7.72}$$

$$\begin{aligned}\left[\left.\frac{\partial g}{\partial \mathbf{u}}\right|_{\mathbf{x}_0,\mathbf{u}_0}\right] &= \left[Z\big|_{\mathbf{x}_0,\mathbf{u}_0}\right]^{-1}\left[\left.\frac{\partial f}{\partial \mathbf{u}}\right|_{\mathbf{x}_0,\mathbf{u}_0}\right] \\ &\quad - \left[Z\big|_{\mathbf{x}_0,\mathbf{u}_0}\right]^{-2}\left[\left.\frac{\partial Z}{\partial \mathbf{u}}\right|_{\mathbf{x}_0,\mathbf{u}_0}\right]^{-1}\cancel{\left[f_{\mathbf{x}_0,\mathbf{u}_0}\right]} \\ &= \left[Z\big|_{\mathbf{x}_0,\mathbf{u}_0}\right]^{-1}\left[\left.\frac{\partial f}{\partial \mathbf{u}}\right|_{\mathbf{x}_0,\mathbf{u}_0}\right]\end{aligned} \tag{7.73}$$

With the coefficient matrices for the initial values $\mathbf{x}_0$ and $\mathbf{u}_0$, the final linearized form can be drawn as in Eqn. (7.74):

$$\begin{aligned}\dot{\mathbf{x}} &= \left[Z\big|_{\mathbf{x}_0,\mathbf{u}_0} \right]^{-1} \left[\frac{\partial f}{\partial \mathbf{x}}\bigg|_{\mathbf{x}_0,\mathbf{u}_0} \right] \delta\mathbf{x} + \left[Z\big|_{\mathbf{x}_0,\mathbf{u}_0} \right]^{-1} \left[\frac{\partial f}{\partial \mathbf{u}}\bigg|_{\mathbf{x}_0,\mathbf{u}_0} \right] \delta\mathbf{u} \\ &= \left[Z\big|_{\mathbf{x}_0,\mathbf{u}_0} \right]^{-1} F_{\mathbf{x}} \delta\mathbf{x} + \left[Z\big|_{\mathbf{x}_0,\mathbf{u}_0} \right]^{-1} F_{\mathbf{u}} \delta\mathbf{u}\end{aligned}, \qquad (7.74)$$

where the coefficients $F_{\mathbf{x}}$ and $F_{\mathbf{u}}$ are designated to be $F_{\mathbf{x}} = \left[\frac{\partial f}{\partial \mathbf{x}}\bigg|_{\mathbf{x}_0,\mathbf{u}_0} \right]$ and $F_{\mathbf{u}} = \left[\frac{\partial f}{\partial \mathbf{u}}\bigg|_{\mathbf{x}_0,\mathbf{u}_0} \right]$, respectively. In conclusion, the linearization process is about the estimation of the coefficients $F_{\mathbf{x}}$ and $F_{\mathbf{u}}$. The resulting equation above, Eqn. (7.74), is equivalent to the linearized state-space formulation given in Eqn. (7.24) if $\left[Z\big|_{\mathbf{x}_0,\mathbf{u}_0} \right]^{-1} F_{\mathbf{x}}$ and $\left[Z\big|_{\mathbf{x}_0,\mathbf{u}_0} \right]^{-1} F_{\mathbf{u}}$ are designated as $\left[Z\big|_{\mathbf{x}_0,\mathbf{u}_0} \right]^{-1} F_{\mathbf{x}} = \mathbf{A}$ and $\left[Z\big|_{\mathbf{x}_0,\mathbf{u}_0} \right]^{-1} F_{\mathbf{u}} = \mathbf{B}$, respectively.

The resultant 21 differential equations for the steam generator model are required to be rearranged, since they are only expressed with 16 terms related to the temporal changes of states. To do so, Eqns. (7.41), (7.43), (7.45), (7.47), (7.49), and (7.55), which describes mass conservation within the regions, are summed to reduce the number of the differential relations. Meanwhile, the mass flow rate terms given in Eqns. (7.42), (7.44), (7.46), (7.48), (7.50), and (7.56), which represent energy balance within the regions, are replaced with several proper combination of the mass conservation equations above. The derivation of each of relations are quite tedious and is not elaborated in this

section. After this reduction of intermediate terms, the formulation of the linearized state-space model begins with collecting all the states in the steam generator model, the state vector **x** and the input vector **u** are firstly given by Eqns. (7.75) and (7.76), respectively:

$$\mathbf{x} = \begin{bmatrix} L_1 & L_2 & P_s & h_3^n & h_{wi}^n & h_{w1}^n & h_{w2}^n & T_{p,1} \\ T_{p,2} & T_{p,3} & T_{t,1} & T_{t,2} & T_{t,3} & T_{t,w1} & T_{t,w2} & T_{t,w3} \end{bmatrix}^T, \text{ and} \tag{7.75}$$

$$\mathbf{u} = \begin{bmatrix} \dot{m}_{s,w3}^n & \dot{m}_{s,wi}^n & \dot{m}_{s,3}^n & h_{w3}^n & T_{p,in} & \dot{m}_p \end{bmatrix}^T. \tag{7.76}$$

In addition, The matrix $Z(\mathbf{x},\mathbf{u})$ is given by arranging the system of differential equations with vector-matrix format. All of the entries are given in Table 7.3, where $z_{i,j}$ is the i-th row, j-th column entry of $Z(\mathbf{x},\mathbf{u})$. On the right hand side of Eqn. (7.69), $f(\mathbf{x},\mathbf{u})$ is given by the following Eqn. (7.77):

$$f(\mathbf{x},\mathbf{u})=\begin{bmatrix}
h_{s,1}A_{ti,1}\left(T_{t,1}-T_{s,1}\right)+\left(h_{wi}^{n}-h_{f}\right)\dot{m}_{s,wi}^{n}\\
h_{s,2}A_{ti,2}\left(T_{t,2}-T_{s,2}\right)+h_{l}\dot{m}_{s,wi}^{n}-h_{g}\dot{m}_{s,3}^{n}\\
h_{s,3}A_{ti,3}\left(T_{t,3}-T_{s,3}\right)+\left(h_{g}-h_{3}^{n}\right)\dot{m}_{s,3}^{n}\\
h_{s,w1}A_{twi,1}\left(T_{t,w1}-T_{s,w1}\right)+\left(h_{w1}^{n}-h_{wi}^{n}\right)\dot{m}_{s,wi}^{n}\\
h_{s,w2}A_{twi,2}\left(T_{t,w2}-T_{s,w2}\right)+h_{w2}^{n}\dot{m}_{s,w3}^{n}-h_{w1}^{n}\dot{m}_{s,wi}^{n}\\
h_{s,w3}A_{twi,3}\left(T_{t,w3}-T_{s,w3}\right)+\left(h_{w3}^{n}-h_{w2}^{n}\right)\dot{m}_{s,w3}^{n}\\
\dot{m}_{s,w3}^{n}-\dot{m}_{s,3}^{n}\\
\dot{m}_{p}C_{pc}\left(T_{p,2}-T_{p,1}\right)-h_{p,1}A_{to,1}\left(T_{p,1}-T_{t,1}\right)-h_{p,1}A_{two,1}\left(T_{p,1}-T_{t,w1}\right)\\
\dot{m}_{p}C_{pc}\left(T_{p,3}-T_{p,2}\right)-h_{p,2}A_{to,2}\left(T_{p,2}-T_{t,2}\right)-h_{p,2}A_{two,2}\left(T_{p,2}-T_{t,w2}\right)\\
\dot{m}_{p}C_{pc}\left(T_{p,in}-T_{p,3}\right)-h_{p,3}A_{to,3}\left(T_{p,3}-T_{t,3}\right)-h_{p,3}A_{two,3}\left(T_{p,3}-T_{t,w3}\right)\\
-h_{p,1}A_{to,1}\left(T_{t,1}-T_{p,1}\right)-h_{s,2}A_{ti,1}\left(T_{t,1}-T_{s,1}\right)\\
-h_{p,2}A_{to,2}\left(T_{t,2}-T_{p,2}\right)-h_{s,2}A_{ti,2}\left(T_{t,2}-T_{s,2}\right)\\
-h_{p,3}A_{to,3}\left(T_{t,3}-T_{p,3}\right)-h_{s,3}A_{ti,3}\left(T_{t,3}-T_{s,3}\right)\\
-h_{p,1}A_{two,1}\left(T_{t,w1}-T_{p,1}\right)-h_{s,w1}A_{twi,1}\left(T_{t,w1}-T_{s,w1}\right)\\
-h_{p,2}A_{two,2}\left(T_{t,w2}-T_{p,2}\right)-h_{s,w2}A_{twi,2}\left(T_{t,w2}-T_{s,w2}\right)\\
-h_{p,3}A_{two,3}\left(T_{t,w3}-T_{p,3}\right)-h_{s,w3}A_{twi,3}\left(T_{t,w3}-T_{s,w3}\right)
\end{bmatrix}. \tag{7.77}$$

In order to derive the final linearized form as shown in Eqn. (7.74), the coefficients $F_{\mathbf{x}}$ and $F_{\mathbf{u}}$ are need to be addressed. By estimating partial derivatives, all the elements of $F_{\mathbf{x}}$ and $F_{\mathbf{u}}$ are respectively summarized in Table 7.4 and Table 7.5, where $f_{\mathbf{x},(i,j)}$ is i-th row, j-th column entry of $F_{\mathbf{x}}$ while $f_{\mathbf{u},(i,j)}$ is that of $F_{\mathbf{u}}$. Upon the derivation, several partial derivatives are also presented. It is noted that four partial derivatives, $\frac{\partial h_{wi}^{n}}{\partial P_{s}}$, $\frac{\partial h_{w1}^{n}}{\partial P_{s}}$, $\frac{\partial h_{w2}^{n}}{\partial P_{s}}$, and $\frac{\partial h_{w3}^{n}}{\partial P_{s}}$ are neglected since the rates of enthalpy change with respect to saturated pressure would not be significant compared to other terms. The final form can be established by matrix inversion of $Z(\mathbf{x},\mathbf{u})$ in the calculation process.

Table 7.3 Elements of matrix $Z(\mathbf{x},\mathbf{u})$

Index	Element
$z_{1,1}$	$A_{st}\rho_1\left(h_1-h_f\right)$
$z_{1,3}$	$A_{st}L_1\left[\frac{\rho_1}{2}\frac{\partial h_f}{\partial P_s}+\left(h_1-h_f\right)\left(\left.\frac{\partial\rho_1}{\partial P_s}\right\|_{h_1}+\frac{1}{2}\left.\frac{\partial\rho_1}{\partial h_1}\right\|_{P_s}\frac{\partial h_f}{\partial P_s}\right)-1\right]$
$z_{1,5}$	$\frac{1}{2}A_{st}L_1\left[\rho_1+\left(h_1-h_f\right)\left.\frac{\partial\rho_1}{\partial h_1}\right\|_{P_s}\right]$
$z_{2,1}$	$A_{st}\left(\rho_1 h_f-\rho_3 h_g\right)$
$z_{2,2}$	$A_{st}\left[(1-\gamma)\left(\rho_f h_f-\rho_g h_g\right)+\left(\rho_g-\rho_3\right)h_g\right]$
$z_{2,3}$	$A_{st}\left[h_f L_1\left(\left.\frac{\partial\rho_1}{\partial P_s}\right\|_{h_1}+\frac{1}{2}\left.\frac{\partial\rho_1}{\partial h_1}\right\|_{P_s}\frac{\partial h_f}{\partial P_s}\right)+L_2\left[\gamma\frac{\partial(\rho_g h_g)}{\partial P_s}+(1-\gamma)\frac{\partial(\rho_f h_f)}{\partial P_s}-1\right]\right.$ $\left.+h_g L_3\left(\left.\frac{\partial\rho_3}{\partial P_s}\right\|_{h_3}+\frac{1}{2}\left.\frac{\partial\rho_3}{\partial h_3}\right\|_{P_s}\frac{\partial h_g}{\partial P_s}\right)\right]$
$z_{2,4}$	$\frac{1}{2}A_{st}L_3 h_g\left.\frac{\partial\rho_3}{\partial h_3}\right\|_{P_s}$
$z_{2,5}$	$\frac{1}{2}A_{st}L_1 h_f\left.\frac{\partial\rho_1}{\partial h_1}\right\|_{P_s}$
$z_{3,1}$	$A_{st}\rho_3\left(h_g-h_3\right)$
$z_{3,2}$	$A_{st}\rho_3\left(h_g-h_3\right)$
$z_{3,3}$	$A_{st}L_3\left[\frac{\rho_3}{2}\frac{\partial h_g}{\partial P_s}+\left(h_3-h_g\right)\left(\left.\frac{\partial\rho_3}{\partial P_s}\right\|_{h_3}+\frac{1}{2}\left.\frac{\partial\rho_3}{\partial h_3}\right\|_{P_s}\frac{\partial h_g}{\partial P_s}\right)-1\right]$
$z_{3,4}$	$\frac{1}{2}A_{st}L_3\left[\rho_3+\left(h_3-h_g\right)\left.\frac{\partial\rho_3}{\partial h_3}\right\|_{P_s}\right]$
$z_{4,1}$	$A_{sw}\rho_{w1}\left(h_{w1}-h_{w1}^n\right)$
$z_{4,3}$	$A_{sw}L_1\left(\left(h_{w1}-h_{w1}^n\right)\left.\frac{\partial\rho_{w1}}{\partial P_s}\right\|_{h_{w1}}-1\right)$

Table 7.3 Elements of matrix $Z(\mathbf{x},\mathbf{u})$ (contd.)

Index	Element
$z_{4,5}$	$\frac{A_{sw}L_1}{2}\left(\rho_{w1}+\left(h_{w1}-h_{w1}^n\right)\left.\frac{\partial\rho_{w1}}{\partial h_{w1}}\right\|_{P_s}\right)$
$z_{4,6}$	$\frac{A_{sw}L_1}{2}\left(\rho_{w1}+\left(h_{w1}-h_{w1}^n\right)\left.\frac{\partial\rho_{w1}}{\partial h_{w1}}\right\|_{P_s}\right)$
$z_{5,1}$	$A_{sw}\left(\rho_{w1}h_{w1}^n-\rho_{w3}h_{w2}^n\right)$
$z_{5,2}$	$A_{sw}\left(\rho_{w2}h_{w2}-\rho_{w3}h_{w2}^n\right)$
$z_{5,3}$	$A_{sw}\left[L_1 h_{w1}^n\left.\frac{\partial\rho_{w1}}{\partial P_s}\right\|_{h_{w1}}+L_2\left(h_{w2}\left.\frac{\partial\rho_{w2}}{\partial P_s}\right\|_{h_{w2}}-1\right)+L_3 h_{w2}^n\left.\frac{\partial\rho_{w3}}{\partial P_s}\right\|_{h_{w3}}\right]$
$z_{5,5}$	$\frac{A_{sw}L_1}{2}h_{w1}^n\left.\frac{\partial\rho_{w1}}{\partial h_{w1}}\right\|_{P_s}$
$z_{5,6}$	$\frac{A_{sw}}{2}\left[L_1 h_{w1}^n\left.\frac{\partial\rho_{w1}}{\partial h_{w1}}\right\|_{P_s}+L_2\left(\rho_{w2}+h_{w2}\left.\frac{\partial\rho_{w2}}{\partial h_{w2}}\right\|_{P_s}\right)\right]$
$z_{5,7}$	$\frac{A_{sw}}{2}\left[L_2\left(\rho_{w2}+h_{w2}\left.\frac{\partial\rho_{w2}}{\partial h_{w2}}\right\|_{P_s}\right)+L_3 h_{w2}^n\left.\frac{\partial\rho_{w3}}{\partial h_{w3}}\right\|_{P_s}\right]$
$z_{6,1}$	$A_{sw}\rho_{w3}\left(h_{w2}^n-h_{w3}\right)$
$z_{6,2}$	$A_{sw}\rho_{w3}\left(h_{w2}^n-h_{w3}\right)$
$z_{6,3}$	$A_{sw}L_3\left(\left(h_{w3}-h_{w2}^n\right)\left.\frac{\partial\rho_{w3}}{\partial P_s}\right\|_{h_{w3}}-1\right)$
$z_{6,7}$	$\frac{1}{2}A_{sw}L_3\left(\rho_{w3}+\left(h_{w3}-h_{w2}^n\right)\left.\frac{\partial\rho_{w3}}{\partial h_{w3}}\right\|_{P_s}\right)$
$z_{7,1}$	$A_{st}\left(\rho_1-\rho_3\right)+A_{sw}\left(\rho_{w1}-\rho_{w3}\right)$
$z_{7,2}$	$A_{st}\left[(1-\gamma)\left(\rho_f-\rho_g\right)+\left(\rho_g-\rho_3\right)\right]+A_{sw}\left(\rho_{w2}-\rho_{w3}\right)$

Table 7.3 Elements of matrix $Z(\mathbf{x},\mathbf{u})$ (contd.)

Index	Element
$z_{7,3}$	$A_{st}\left[L_1\left(\left.\frac{\partial\rho_1}{\partial P_s}\right\|_{h_1}+\frac{1}{2}\left.\frac{\partial\rho_1}{\partial h_1}\right\|_{P_s}\frac{\partial h_f}{\partial P_s}\right)+L_2\left(\gamma\frac{\partial\rho_g}{\partial P_s}+(1-\gamma)\frac{\partial\rho_f}{\partial P_s}\right)\right.$ $\left.+L_3\left(\left.\frac{\partial\rho_3}{\partial P_s}\right\|_{h_3}+\frac{1}{2}\left.\frac{\partial\rho_3}{\partial h_3}\right\|_{P_s}\frac{\partial h_g}{\partial P_s}\right)\right]$ $+A_{sw}\left[L_1\left.\frac{\partial\rho_{w1}}{\partial P_s}\right\|_{h_{w1}}+L_2\left.\frac{\partial\rho_{w2}}{\partial P_s}\right\|_{h_{w2}}+L_3\left.\frac{\partial\rho_{w3}}{\partial P_s}\right\|_{h_{w3}}\right]$
$z_{7,4}$	$\frac{A_{st}}{2}L_3\left.\frac{\partial\rho_3}{\partial h_3}\right\|_{P_s}$
$z_{7,5}$	$\frac{L_1}{2}\left(A_{st}\left.\frac{\partial\rho_1}{\partial h_1}\right\|_{P_s}+A_{sw}\left.\frac{\partial\rho_{w1}}{\partial h_{w1}}\right\|_{P_s}\right)$
$z_{7,6}$	$\frac{A_{sw}}{2}\left(L_1\left.\frac{\partial\rho_{w1}}{\partial h_{w1}}\right\|_{P_s}+L_2\left.\frac{\partial\rho_{w2}}{\partial h_{w2}}\right\|_{P_s}\right)$
$z_{7,7}$	$\frac{A_{sw}}{2}\left(L_2\left.\frac{\partial\rho_{w2}}{\partial h_{w2}}\right\|_{P_s}+L_3\left.\frac{\partial\rho_{w3}}{\partial h_{w3}}\right\|_{P_s}\right)$
$z_{8,1}$	$\rho_c C_{pc} A_p\left(T_{p,1}-T_{p,2}\right)$
$z_{8,8}$	$\rho_c C_{pc} A_p L_1$
$z_{9,9}$	$\rho_c C_{pc} A_p L_2$
$z_{10,1}$	$\rho_c C_{pc} A_p\left(T_{p,2}-T_{p,3}\right)$
$z_{10,2}$	$\rho_c C_{pc} A_p\left(T_{p,2}-T_{p,3}\right)$
$z_{10,10}$	$\rho_c C_{pc} A_p L_3$
$z_{11,1}$	$\rho_t C_{pt} A_t\left(T_{t,1}-T_{t,2}\right)$
$z_{11,11}$	$\rho_t C_{pt} A_t L_1$
$z_{12,12}$	$\rho_t C_{pt} A_t L_2$

Table 7.3 Elements of matrix $Z(\mathbf{x},\mathbf{u})$ (contd.)

Index	Element
$z_{13,1}$	$\rho_t C_{pt} A_t \left(T_{t,2} - T_{t,3}\right)$
$z_{13,2}$	$\rho_t C_{pt} A_t \left(T_{t,2} - T_{t,3}\right)$
$z_{13,13}$	$\rho_t C_{pt} A_t L_3$
$z_{14,1}$	$\rho_t C_{pt} A_{tw} \left(T_{t,w1} - T_{t,w2}\right)$
$z_{14,14}$	$\rho_t C_{pt} A_{tw} L_1$
$z_{15,15}$	$\rho_t C_{pt} A_{tw} L_2$
$z_{16,1}$	$\rho_t C_{pt} A_{tw} \left(T_{t,w2} - T_{t,w3}\right)$
$z_{16,2}$	$\rho_t C_{pt} A_{tw} \left(T_{t,w2} - T_{t,w3}\right)$
$z_{16,16}$	$\rho_t C_{pt} A_{tw} L_3$

Table 7.4 Elements of matrix $F_{\mathbf{x}}(\mathbf{x},\mathbf{u})$

Index	Element
$f_{\mathbf{x},(1,1)}$	$\pi d_s h_{s,1}\left(T_{t,1}-T_{s,1}\right)$
$f_{\mathbf{x},(1,3)}$	$-\pi d_s h_{s,1} L_1 \dfrac{\partial T_{s,1}}{\partial P_s}-\dfrac{\partial h_f}{\partial P_s}\dot{m}^n_{s,wi}$
$f_{\mathbf{x},(1,5)}$	$-\pi d_s h_{s,1} L_1 \dfrac{\partial T_{s,1}}{\partial h^n_{wi}}+\dot{m}^n_{s,wi}$
$f_{\mathbf{x},(1,11)}$	$\pi d_s h_{s,1} L_1$
$f_{\mathbf{x},(2,2)}$	$\pi d_s h_{s,2}\left(T_{t,2}-T_{s,2}\right)$
$f_{\mathbf{x},(2,3)}$	$-\pi d_s h_{s,2} L_2 \dfrac{\partial T_{s,2}}{\partial P_s}+\dfrac{\partial h_f}{\partial P_s}\dot{m}^n_{s,wi}-\dfrac{\partial h_g}{\partial P_s}\dot{m}^n_{s,3}$
$f_{\mathbf{x},(2,12)}$	$\pi d_s h_{s,2} L_2$
$f_{\mathbf{x},(3,1)}$	$-\pi d_s h_{s,3}\left(T_{t,3}-T_{s,3}\right)$
$f_{\mathbf{x},(3,2)}$	$-\pi d_s h_{s,3}\left(T_{t,3}-T_{s,3}\right)$
$f_{\mathbf{x},(3,3)}$	$-\pi d_s h_{s,3} L_3 \dfrac{\partial T_{s,3}}{\partial P_s}+\left(\dfrac{\partial h_g}{\partial P_s}-\dfrac{\partial h^n_3}{\partial P_s}\right)\dot{m}^n_{s,3}$
$f_{\mathbf{x},(3,4)}$	$-\pi d_s h_{s,3} L_3 \dfrac{\partial T_{s,3}}{\partial h^n_3}-\dot{m}^n_{s,3}$
$f_{\mathbf{x},(3,13)}$	$\pi d_s h_{s,3} L_3$
$f_{\mathbf{x},(4,1)}$	$\pi d_{sw} h_{s,w1}\left(T_{t,w1}-T_{s,w1}\right)$
$f_{\mathbf{x},(4,3)}$	$-\pi d_{sw} L_1 h_{s,w1} \dfrac{\partial T_{s,w1}}{\partial P_s}+\left(\dfrac{\partial h^n_{w1}}{\partial P_s}-\dfrac{\partial h^n_{wi}}{\partial P_s}\right)\dot{m}^n_{s,wi}$
$f_{\mathbf{x},(4,5)}$	$-\pi d_{sw} L_1 h_{s,w1} \dfrac{\partial T_{s,w1}}{\partial h^n_{wi}}-\dot{m}^n_{s,wi}$
$f_{\mathbf{x},(4,6)}$	$-\pi d_{sw} L_1 h_{s,w1} \dfrac{\partial T_{s,w1}}{\partial h^n_{w1}}+\dot{m}^n_{s,wi}$
$f_{\mathbf{x},(4,14)}$	$\pi d_{sw} L_1 h_{s,w1}$
$f_{\mathbf{x},(5,2)}$	$\pi d_{sw} h_{s,w2}\left(T_{t,w2}-T_{s,w2}\right)$
$f_{\mathbf{x},(5,3)}$	$-\pi d_{sw} L_2 h_{s,w2} \dfrac{\partial T_{s,w2}}{\partial P_s}+\dfrac{\partial h^n_{w2}}{\partial P_s}\dot{m}^n_{s,w3}-\dfrac{\partial h^n_{w1}}{\partial P_s}\dot{m}^n_{s,wi}$

Table 7.4 Elements of matrix $F_{\mathbf{x}}(\mathbf{x},\mathbf{u})$ (contd.)

Index	Element
$f_{\mathbf{x},(5,6)}$	$-\pi d_{sw} L_2 h_{sw,w2} \dfrac{\partial T_{s,w2}}{\partial h^n_{w1}} - \dot{m}^n_{s,wi}$
$f_{\mathbf{x},(5,7)}$	$-\pi d_{sw} L_2 h_{sw,w2} \dfrac{\partial T_{s,w2}}{\partial h^n_{w2}} + \dot{m}^n_{s,w3}$
$f_{\mathbf{x},(5,15)}$	$\pi d_{sw} L_2 h_{s,w2}$
$f_{\mathbf{x},(6,1)}$	$-\pi d_{sw} h_{s,w3} \left(T_{t,w3} - T_{s,w3}\right)$
$f_{\mathbf{x},(6,2)}$	$-\pi d_{sw} h_{s,w3} \left(T_{t,w3} - T_{s,w3}\right)$
$f_{\mathbf{x},(6,3)}$	$-\pi d_{sw} L_3 h_{s,w3} \dfrac{\partial T_{s,w3}}{\partial P_s} + \left(\dfrac{\partial h^n_{w3}}{\partial P_s} - \dfrac{\partial h^n_{w2}}{\partial P_s} \right) \dot{m}^n_{s,w3}$
$f_{\mathbf{x},(6,7)}$	$-\pi d_{sw} L_3 h_{s,w3} \dfrac{\partial T_{s,w3}}{\partial h^n_{w2}} - \dot{m}^n_{s,w3}$
$f_{\mathbf{x},(6,16)}$	$\pi d_{sw} L_3 h_{s,w3}$
$f_{\mathbf{x},(8,1)}$	$-\pi d_p h_{p,1} \left(T_{p,1} - T_{t,1}\right) - \pi d_{pw} h_{p,1} \left(T_{p,1} - T_{t,w1}\right)$
$f_{\mathbf{x},(8,8)}$	$-\dot{m}_p C_{pc} - \pi d_p h_{p,1} L_1 - \pi d_{pw} h_{p,1} L_1$
$f_{\mathbf{x},(8,9)}$	$\dot{m}_p C_{pc}$
$f_{\mathbf{x},(8,11)}$	$\pi d_p h_{p,1} L_1$
$f_{\mathbf{x},(8,14)}$	$\pi d_{pw} h_{p,1} L_1$
$f_{\mathbf{x},(9,2)}$	$-\pi d_p h_{p,2} \left(T_{p,2} - T_{t,2}\right) - \pi d_{pw} h_{p,2} \left(T_{p,2} - T_{t,w2}\right)$
$f_{\mathbf{x},(9,9)}$	$-\dot{m}_p C_{pc} - \pi d_p h_{p,2} L_2 - \pi d_{pw} h_{p,2} L_2$
$f_{\mathbf{x},(9,10)}$	$\dot{m}_p C_{pc}$
$f_{\mathbf{x},(9,12)}$	$\pi d_p h_{p,2} L_2$
$f_{\mathbf{x},(9,15)}$	$\pi d_{pw} h_{p,2} L_2$
$f_{\mathbf{x},(10,1)}$	$\pi d_p h_{p,3} \left(T_{p,3} - T_{t,3}\right) + \pi d_{pw} h_{p,3} \left(T_{p,3} - T_{t,w3}\right)$
$f_{\mathbf{x},(10,2)}$	$\pi d_p h_{p,3} \left(T_{p,3} - T_{t,3}\right) + \pi d_{pw} h_{p,3} \left(T_{p,3} - T_{t,w3}\right)$
$f_{\mathbf{x},(10,10)}$	$-\dot{m}_p C_{pc} - \pi d_p h_{p,3} L_3 - \pi d_{pw} h_{p,3} L_3$
$f_{\mathbf{x},(10,13)}$	$\pi d_p h_{p,3} L_3$

Table 7.4 Elements of matrix $F_{\mathbf{x}}(\mathbf{x},\mathbf{u})$ (contd.)

Index	Element
$f_{\mathbf{x},(10,16)}$	$\pi d_{pw} h_{p,3} L_3$
$f_{\mathbf{x},(11,1)}$	$-\pi d_p h_{p,1}\left(T_{t,1}-T_{p,1}\right)-\pi d_s h_{s,1}\left(T_{t,1}-T_{s,1}\right)$
$f_{\mathbf{x},(11,3)}$	$\pi d_s h_{s,1} L_1 \dfrac{\partial T_{s,1}}{\partial P_s}$
$f_{\mathbf{x},(11,5)}$	$\pi d_s h_{s,1} L_1 \dfrac{\partial T_{s,1}}{\partial h_{wi}^n}$
$f_{\mathbf{x},(11,8)}$	$\pi d_p h_{p,1} L_1$
$f_{\mathbf{x},(11,11)}$	$-\pi d_p h_{p,1} L_1 - \pi d_s h_{s,1} L_1$
$f_{\mathbf{x},(12,2)}$	$-\pi d_p h_{p,2}\left(T_{t,2}-T_{p,2}\right)-\pi d_s h_{s,2}\left(T_{t,2}-T_{s,2}\right)$
$f_{\mathbf{x},(12,3)}$	$\pi d_s h_{s,2} L_2 \dfrac{\partial T_{s,2}}{\partial P_s}$
$f_{\mathbf{x},(12,9)}$	$\pi d_p h_{p,2} L_2$
$f_{\mathbf{x},(12,12)}$	$-\pi d_p h_{p,2} L_2 - \pi d_s h_{s,2} L_2$
$f_{\mathbf{x},(13,1)}$	$\pi d_p h_{p,3}\left(T_{t,3}-T_{p,3}\right)+\pi d_s h_{s,3}\left(T_{t,3}-T_{s,3}\right)$
$f_{\mathbf{x},(13,2)}$	$\pi d_p h_{p,3}\left(T_{t,3}-T_{p,3}\right)+\pi d_s h_{s,3}\left(T_{t,3}-T_{s,3}\right)$
$f_{\mathbf{x},(13,3)}$	$\pi d_s h_{s,3} L_3 \dfrac{\partial T_{s,3}}{\partial P_s}$
$f_{\mathbf{x},(13,4)}$	$\pi d_s h_{s,3} L_3 \dfrac{\partial T_{s,3}}{\partial h_3^n}$
$f_{\mathbf{x},(13,10)}$	$\pi d_p h_{p,3} L_3$
$f_{\mathbf{x},(13,13)}$	$-\pi d_p h_{p,3} L_3 - \pi d_s h_{s,3} L_3$
$f_{\mathbf{x},(14,1)}$	$-\pi d_{pw} h_{p,1}\left(T_{t,w1}-T_{p,1}\right)-\pi d_{sw} h_{s,w1}\left(T_{t,w1}-T_{s,w1}\right)$
$f_{\mathbf{x},(14,3)}$	$\pi d_{sw} L_1 h_{s,w1} \dfrac{\partial T_{s,w1}}{\partial P_s}$
$f_{\mathbf{x},(14,5)}$	$\pi d_{sw} h_{s,w1} L_1 \dfrac{\partial T_{s,w1}}{\partial h_{wi}^n}$
$f_{\mathbf{x},(14,6)}$	$\pi d_{sw} h_{s,w1} L_1 \dfrac{\partial T_{s,w1}}{\partial h_{w1}^n}$

Table 7.4 Elements of matrix $F_{\mathbf{x}}(\mathbf{x},\mathbf{u})$ (contd.)

Index	Element
$f_{\mathbf{x},(14,8)}$	$\pi d_{pw} h_{p,1} L_1$
$f_{\mathbf{x},(14,14)}$	$-\pi d_{pw} h_{p,1} L_1 - \pi d_{sw} h_{s,w1} L_1$
$f_{\mathbf{x},(15,2)}$	$-\pi d_{pw} h_{p,2} \left(T_{t,w2} - T_{p,2}\right) - \pi d_{sw} h_{s,w2} \left(T_{t,w2} - T_{s,w2}\right)$
$f_{\mathbf{x},(15,3)}$	$\pi d_{sw} L_2 h_{s,w2} \dfrac{\partial T_{s,w2}}{\partial P_s}$
$f_{\mathbf{x},(15,6)}$	$\pi d_{sw} h_{s,w2} L_2 \dfrac{\partial T_{s,w2}}{\partial h_{w1}^n}$
$f_{\mathbf{x},(15,7)}$	$\pi d_{sw} h_{s,w2} L_2 \dfrac{\partial T_{s,w2}}{\partial h_{w2}^n}$
$f_{\mathbf{x},(15,9)}$	$\pi d_{pw} h_{p,2} L_2$
$f_{\mathbf{x},(15,15)}$	$-\pi d_{pw} h_{p,2} L_2 - \pi d_{sw} h_{s,w2} L_2$
$f_{\mathbf{x},(16,1)}$	$\pi d_{pw} h_{p,3} \left(T_{t,w3} - T_{p,3}\right) + \pi d_s h_{s,w3} \left(T_{t,w3} - T_{s,w3}\right)$
$f_{\mathbf{x},(16,2)}$	$\pi d_{pw} h_{p,3} \left(T_{t,w3} - T_{p,3}\right) + \pi d_s h_{s,w3} \left(T_{t,w3} - T_{s,w3}\right)$
$f_{\mathbf{x},(16,3)}$	$\pi d_{sw} L_3 h_{s,w3} \dfrac{\partial T_{s,w3}}{\partial P_s}$
$f_{\mathbf{x},(16,7)}$	$\pi d_{sw} h_{s,w3} L_3 \dfrac{\partial T_{s,w3}}{\partial h_{w2}^n}$
$f_{\mathbf{x},(16,10)}$	$\pi d_{pw} h_{p,3} L_3$
$f_{\mathbf{x},(16,16)}$	$-\pi d_{pw} h_{p,3} L_3 - \pi d_s h_{s,w3} L_3$

Table 7.5 Elements of matrix $F_{\mathbf{u}}(\mathbf{x},\mathbf{u})$

Index	Element
$f_{\mathbf{u},(1,2)}$	$h_{wi}^{n} - h_{f}$
$f_{\mathbf{u},(2,2)}$	h_{f}
$f_{\mathbf{u},(2,3)}$	$-h_{g}$
$f_{\mathbf{u},(4,2)}$	$h_{w1}^{n} - h_{wi}^{n}$
$f_{\mathbf{u},(5,1)}$	h_{w2}^{n}
$f_{\mathbf{u},(5,2)}$	$-h_{w1}^{n}$
$f_{\mathbf{u},(6,1)}$	$h_{w3}^{n} - h_{w2}^{n}$
$f_{\mathbf{u},(6,4)}$	$-\pi d_{sw} L_3 h_{s,w3} \dfrac{\partial T_{s,w3}}{\partial h_{w3}^{n}} + \dot{m}_{s,w3}^{n}$
$f_{\mathbf{u},(7,1)}$	1
$f_{\mathbf{u},(7,3)}$	-1
$f_{\mathbf{u},(8,6)}$	$C_{pc}\left(T_{p,2} - T_{p,1}\right)$
$f_{\mathbf{u},(9,6)}$	$C_{pc}\left(T_{p,3} - T_{p,2}\right)$
$f_{\mathbf{u},(10,5)}$	$\dot{m}_{p} C_{pc}$
$f_{\mathbf{u},(10,6)}$	$C_{pc}\left(T_{p,in} - T_{p,3}\right)$
$f_{\mathbf{u},(16,4)}$	$\pi d_{sw} h_{s,w3} L_3 \dfrac{\partial T_{s,w3}}{\partial h_{w3}^{n}}$

7.1.4 Model implementation for numerical simulation

For the implementation of develop model into MATLAB/Simulink environment (Mathworks, 2017) as introduced in Section 7.1, several additional assumptions are required for a realistic evaluation of load-following operation. This section elaborates such relations applied to the model.

7.1.4.1 Constant pressure operation for URANUS secondary side

Until now, the operation strategies of URANUS under full power operation and load-following operation are not yet established. It leads to a lack of available operating conditions for the simulation. Thus, additional operation conditions is required to be imposed on the secondary side of URANUS reactor system so that the simulation model can estimate the system behavior in a realistic way. In this regard, the secondary side is designated to be operated at a constant pressure for all operation conditions.

7.1.4.2 Steam flow regulation

A steam valve regulates the steam flow rate from the steam generator modules. In a control point of view, the design of steam flow controller is crucial for a system for a stable and efficient operation, which is beyond the scope of this

thesis study. Hence, as an alternative, a simple valve model by means of so-called critical flow approximation (El-Wakil, 1971) is applied to simulate the secondary side conditions, which supposes that the steam flow rate is directly proportional to its upstream pressure, in other words, the steam pressure in the steam generator tube side. In this respect, the total steam flow rate at the outlet of steam generator modules is given by Eqn. (7.78):

$$\dot{m}_{s,3}^{n} = C_L P_s . \tag{7.78}$$

The constant C_L is determined by the values at the nominal full power condition, namely, nominal steam pressure and nominal steam flow rate.

For the simulation of physical behaviors of the steam valve, a simple proportional-integral (PI) gain control model, shown in Eqn. (7.79), is utilized (Kapernick, 2015):

$$G_c(s) = K_p\left(1 + \frac{1}{\tau_I s}\right). \tag{7.79}$$

Accompanied by the constant pressure assumption made in Section 7.1.4.1, the pressure error signal defined by the difference between the current pressure and a pressure setpoint drives a steam valve to be opened or closed. The final form given by Eqns. (7.78) and (7.79) are given by:

$$\frac{d\dot{m}_{s,3}^{n}}{dt} = \frac{C_L}{t_s}\left[\delta P_s + C_{st}\frac{K_c}{P_{s0}}\left(\delta P_s + \frac{\delta P}{t_s}\right)\right], \tag{7.80}$$

where the constants, t_s, C_{st}, K_c, that determines the operational characteristics of the steam valve are $t_s = 1$, $C_{st} = 10$, and $K_c = 5$ (Kapernick, 2015).

7.1.4.3 Model implementation

Figure 7.6 shows the structure of implemented reactor dynamics simulation model. The thermal-hydraulic lumps described by the reactor core model, the hot leg and cold leg models, and the steam generator model, as elaborated through previous sections, are included by separating and connecting each of models with several input and output nodes. This configuration is efficient not only for the implementation but also for a potential model update since one lump can be substituted with other formulations.

Within this model, a system transient is given by an additional input node that describes a change of external load demand from the nominal full power condition. The simulation model would calculate the system response reacting to this load demand change and it leads to the generation of control rod movement requests. As discussed, the error signal of reactor power is defined by the discrepancy between the external power demand and the current power. In addition, how fast the control rods are inserted or withdrawn is proportional to this error signal and this proportionality constant is the loop gain for the closed feedback loop regulating reactor power, as shown in Figure 7.1. In this model, a proper value of 0.01 is applied to the loop gain with which the insertion speed of control rods are given in a realistic range.

In addition, another controllable parameter for URANUS is the feedwater flow rate, as described in Section 7.1. In this model, a simple model with proportional flow rate control is utilized. Similar to the applied concept of steam flow regulation, the detailed design and optimization of feedwater flow controller are out of the thesis scope. Hence, a simple proportionality is applied and the effect and advantage of feedwater flow rate control is elaborated in Section 7.3.1.

For the physical parameters of URANUS, the values under nominal condition estimated in Chapter 4 is extensively utilized. The thermophysical values of LBE is designated by the relation given in the LBE handbook (OECD Nuclear Energy Agency, 2007) while those of water is calculated with the industrial formulations given by the International Association for the Properties of Water and Steam (IAPWS-IF97) (Wagner and Kruse, 1998).

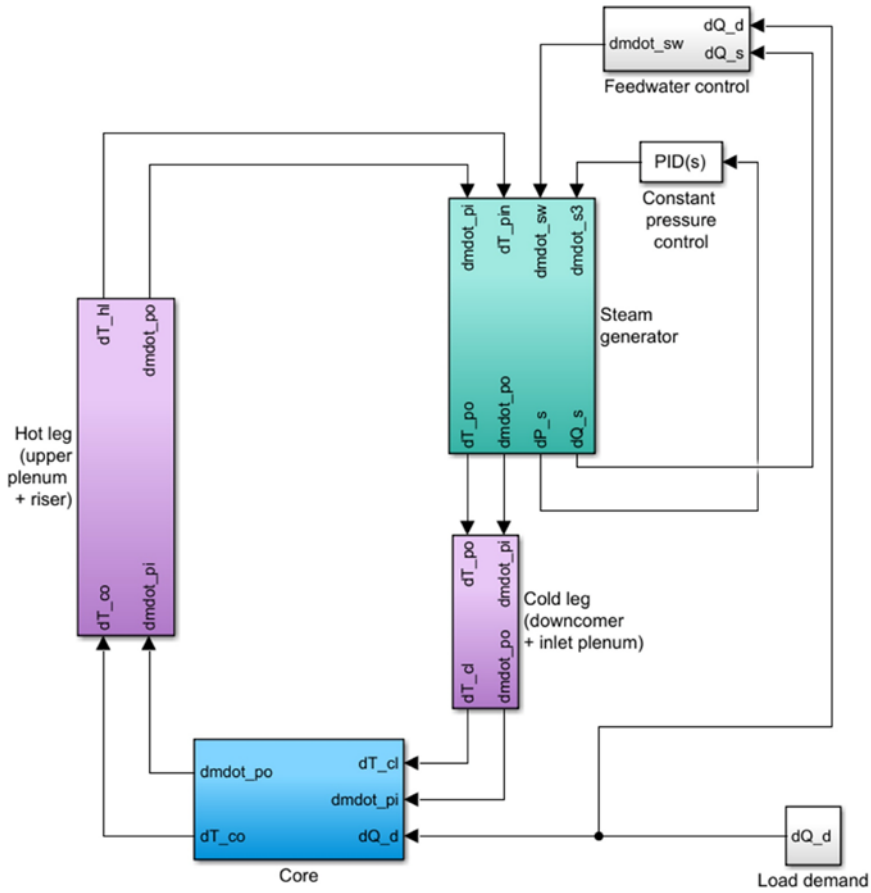

Figure 7.6 Block chain diagram for reactor state-space model implemented to MATLAB/Simulink environment

7.2 Reactor control model validation

Before proceeding into the assessment of load-following capability with the system transient evaluation model developed in the last section, the validation of the model is required. MARS-LBE is to be utilized for the validation of this analytical model as it was already validated for the LBE natural circulation systems with the test results given by HELIOS and PILLAR while its capability of reactor kinetics calculation was verified with SFR experiments throughout other studies.

For the problems used for the validation, two cases are defined: reactor power increase and decrease with a ramp of 5% power change per minute from nominal full power condition (100% power) are compared. Since MARS-LBE and the developed model have different capabilities, as summarized in Table 7.6 and MARS-LBE cannot estimate reactivity change induced from control rod movement, the input file for MARS-LBE is prepared with the reactivity change calculated by the developed model. In this calculation, the reactor power change is induced by load demand change. The calculation results are compared in Figure 7.7 and Figure 7.8. In both figures, the MARS-LBE results are marked with lines and circles while the estimation by the developed model is given with plane curves for the same colors.

The first insets in the figures show reactor power and turbine load changes to follow varying load demand. The turbine load is the same with the amount of heat transferred to the secondary side from primary side. The system transient evaluation model predicts faster core power transients and slower

secondary side heat removal rate saturation compared to the MARS-LBE calculation results. In other words, the developed model estimates the time needed for core power to be saturated to new steady-state values shorter than MARS-LBE does and the transients of core power lags load demand or control rod movements in both results.

Subsequently in the second insets on the figures, the reactivity changes are shown to be have good agreements each other not only on the reactivity insertion given by control rod movements but also on that given by reactivity feedback mechanisms, such as fuel and coolant temperature changes. For the system coolant temperatures as depicted in the third insets, the developed model estimates additional temperature decrease and increase about 2 K in comparison with the MARS-LBE results, respectively, in each problem. Regarding the time-dependent behavior, the developed model predicts that the system would have slower saturation followed by power transient being saturated. This delay is due to a slow power transfer rate change at the steam outlet, as shown in the case of power transients as well.

The primary side mass flow rates by natural circulation is estimated to have 10% larger deviation after saturation with respect to the results given by the developed model in comparison with MARS-LBE results, as shown in the last insets. This deviation is analyzed to come from the nonlinear model used for natural circulation flow rate, given as Eqn. (7.15), which cannot account for friction loss variation with respect to flow rate change. In addition, the model predicts faster saturation of transient.

Therefore, the comparison shows that the developed model is valid on

the reactor dynamics modeling purpose even though there is slight differences on the results compared to MARS-LBE. Meanwhile, the total calculation time for these problems by MARS-LBE is about 30 seconds to 1 minute while the developed model takes only about 1-2 seconds with a personal computer having a general specification. It means that the developed model can estimate actual reactor operation conditions accurately only with a simple formulation.

Table 7.6 Comparison between the developed passive LBE-cooled SMR dynamics model and MARS-LBE

Criteria	MARS-LBE	This model
Main scope	• System thermal-hydraulic analysis to boundary condition change • Safety analysis	• System integral behavior to operational condition change • Stability analysis, controller design and optimization
Basic hydrodynamic formulation	• One-dimensional, two-fluid flow model using two-fluid, six-equation formulation given by mass, momentum, and energy conservation of water and steam • Several additional relations on phase transition between two fluids • Semi-implicit scheme for pressure correction and time advancements	• One-dimensional, single-fluid flow model using two-equation formulation given by mass and energy conservation of LBE • Moving boundary formulation for steam generator Linearized state-space model • Linear ODE solver for stiff system and variable time advancement
Number of calculation nodes	• Total ~400 nodes for URANUS	• ~10 for URANUS
Calculation time	• ~2-3 minutes (depending on the number of calculation nodes)	• ~1-2 seconds
Capability	• Time-domain analysis	• Time-domain analysis • Frequency-domain analysis

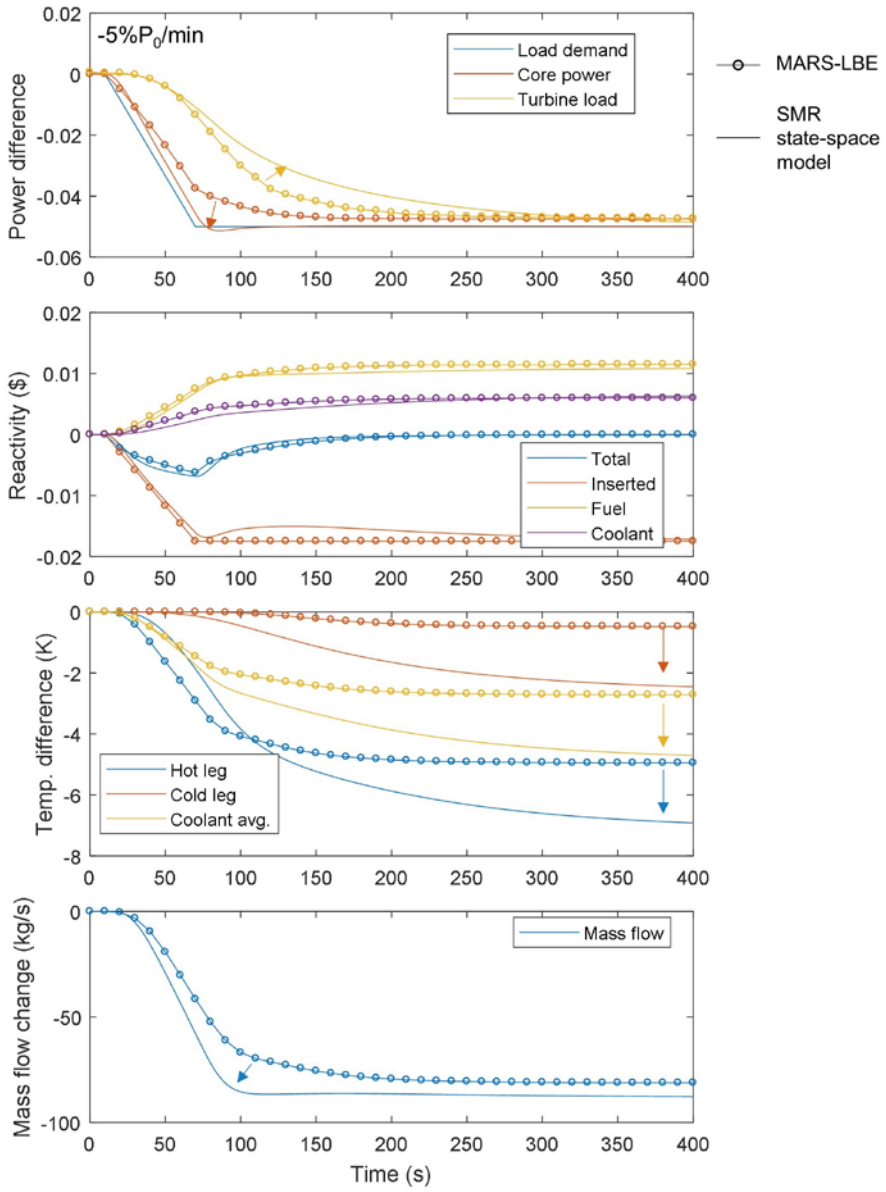

Figure 7.7 Calculation results comparison on the system transient evaluation model for passive LBE-cooled SMR and MARS-LBE for the power ramp rate of -5%P/min from 100% power output

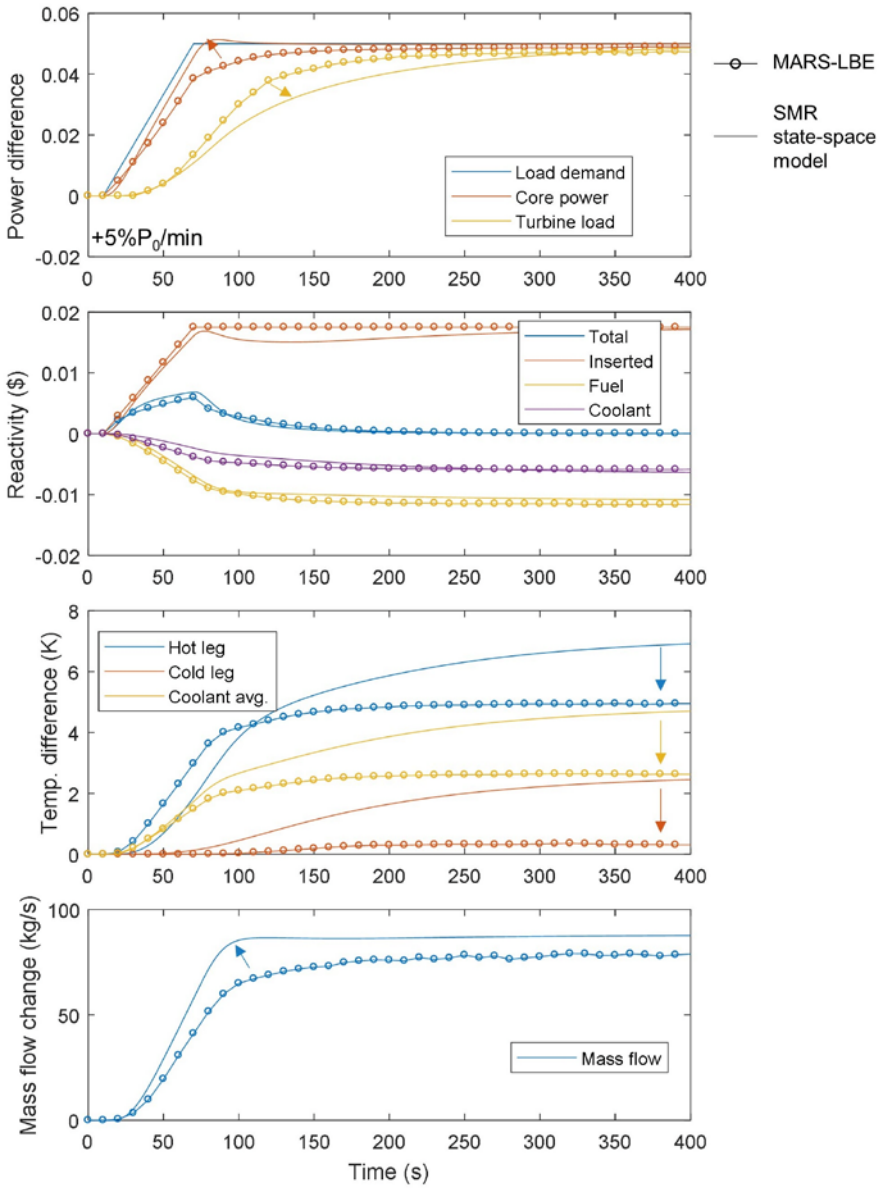

Figure 7.8 Calculation results comparison on the system transient evaluation model for passive LBE-cooled SMR and MARS-LBE for the power ramp rate of +5%P/min from 100% power output

7.3 Assessment of fast load-following capability

In the previous section, the developed analytical reactor dynamics simulation model for LBE-cooled passive SMR was validated through the comparison with MARS-LBE. Since the results showed that the developed model can be concluded to be valid on the reactor dynamics modeling purpose with slight deviations, the fast load-following capability of URANUS, a LBE-cooled passive SMR, will be evaluated with several case studies in the forthcoming sections. The evaluation includes the effect of proportional feedwater control on changing load demand, stability analysis on the reactor power with respect to external load demand, transients under a specific daily load-following operation plan, step response analysis on power recovery in response of the grid demand, and comparison with a load-following strategy in a commercial SMR.

7.3.1 Proportional feedwater control

According to the transient experimental results described in Section 5.2.4.3 and the numerical analysis results given in Section 6.4, it is evident that the characteristics of system responses by the primary and secondary sides to the instantaneous core power change in terms of saturation time would be deviated each other. In other words, the characteristics of secondary side would mostly affect the rate of load or electricity generation change given by external load demand change during load-following operation. Since the physical design of

URANUS is fixed, only controllable parameters are several operational conditions and specifications of the BOP by which the dynamics of whole system can be changed.

As introduced in Section 4.3, the BOP of URANUS is not yet designed in detail. In order to estimate its operation capability during load-following in proper and realistic ways, two boundaries of the secondary side, including the feedwater inlet and the steam outlet, are assumed to be operated with ideal control schemes. An ideal steam valve from which the steam flow rate is designated to be proportional to the steam pressure is applied to the steam outlet. On the other hand, the feedwater inlet condition has been defined by adding a simple, ideal feedwater controller, since the design and optimization of the controllers are out of thesis study. However, this case study can be used to guide the direction of BOP system design by assessing the advantage from the feedwater flow rate control.

The regulation of inlet feedwater flow rate is done by a proportional controller, which controls the water flow rate with respect to the external load demand. In order to evaluate its effect, four cases defined by the external load demand changes with a power ramp rate of ±10%P/min and with and without feedwater flow rate control at the same time are simulated. In the negative power ramp cases, it is assumed that the load demand falls from the nominal full power to 90% reactor power while the positive cases are appointed as power recovery from 90% power to the initial full power.

Figure 7.9 and Figure 7.10 show the simulation results without feedwater flow rate control on decreasing and increasing external load demands,

respectively; meanwhile, Figure 7.11 and Figure 7.12 illustrate the results with controlling feedwater flow rate under the same load demand conditions. The top left insets of both figures depicts external load demand, resultant core power regulated by the control rod movements and primary system reactivity feedback mechanisms, and turbine load calculated by the difference of the multiplications defined by the mass flow rates and enthalpy values at the boundaries. All of those values are expressed in fraction to the nominal full power values. In addition, a shaded region shows the time-dependent difference of the reactor core power and the turbine load. In power decreasing conditions, these discrepancies can be thought as the production of excess steam while those are deficits in steam or required load when the load demand is increasing. The second and third insets on the left hand sides of each of figures are about the primary side transients including temperatures and natural circulation mass flow rates. The top right hand side insets represent the feedwater flow rate at the steam generator inlet and the steam flow rate at the steam boundary. It can be seen that the constant pressure controller works in proper ways as defined.

It can be inferred from the results depicted on the left hand side insets of Figure 7.9 to Figure 7.12 that the primary side responds to the predefined external load demands nearly regardless of the feedwater flow rate control. However, the steam side responses are dramatically changed with the activation of the proportional feedwater flow controller, by comparing Figure 7.11 to Figure 7.9, and Figure 7.10 to Figure 7.12, respectively. The reduction in excess steam production with the proportional feedwater flow control leads to less steam curtailing in decreasing load demand while the steam generator heat

removal slightly differs from the core power with the proportional feedwater flow control with respect to increasing load demand. By referring to the shaded areas, the amount of core-turbine power mismatch can be reduced by 1/3. In addition, the saturation time of steam side, which is defined by the time needed to reach the fractional power difference between the load demand and the turbine load lower than 1%, can be reduced by the feedwater flow control used in this model. It takes about 400 s without the control while only 200 s are required with the proportional feedwater flow control after the reactor core power being saturated. In conclusion, in a passive LBE-cooled SMR, the steam side rather than the primary side needs to be controlled with sophisticated control schemes so that power removal or overcooling to be minimized.

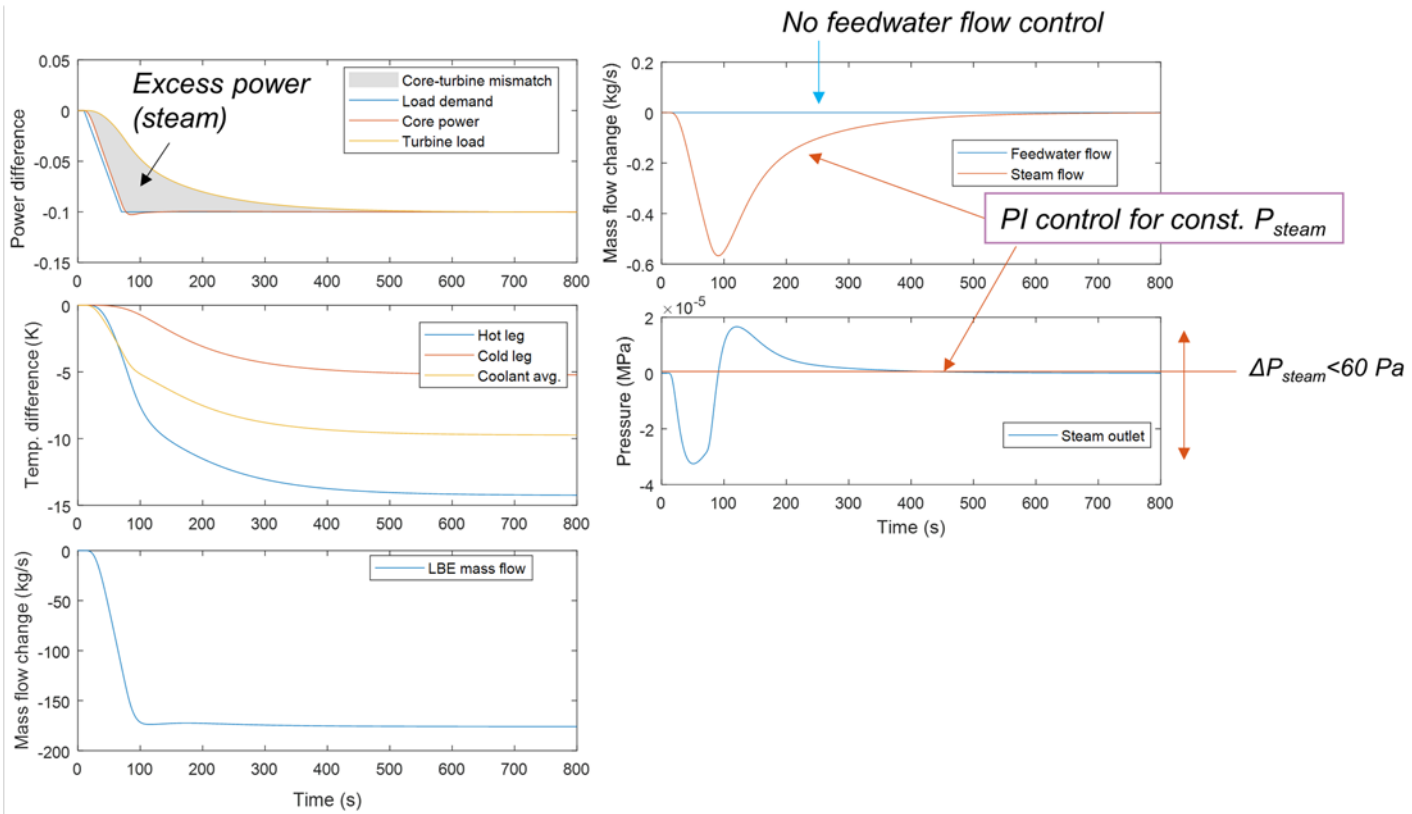

Figure 7.9 Calculation results for the system transients given by a power ramp rate of -10%P/min from 100% power output without feedwater flow rate control

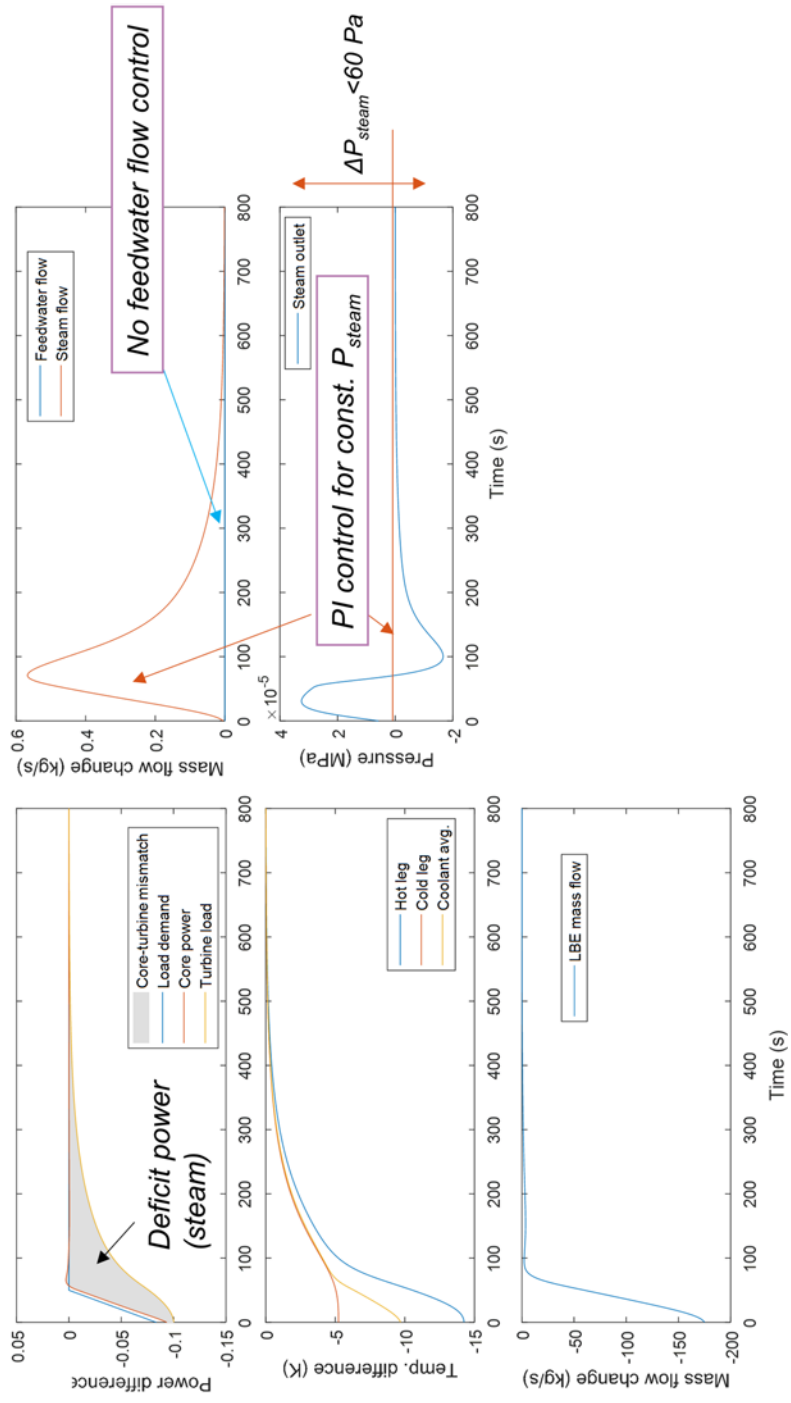

Figure 7.10 Calculation results for the system transients given by a power ramp rate of -10%P/min from 100% power output with feedwater flow rate control

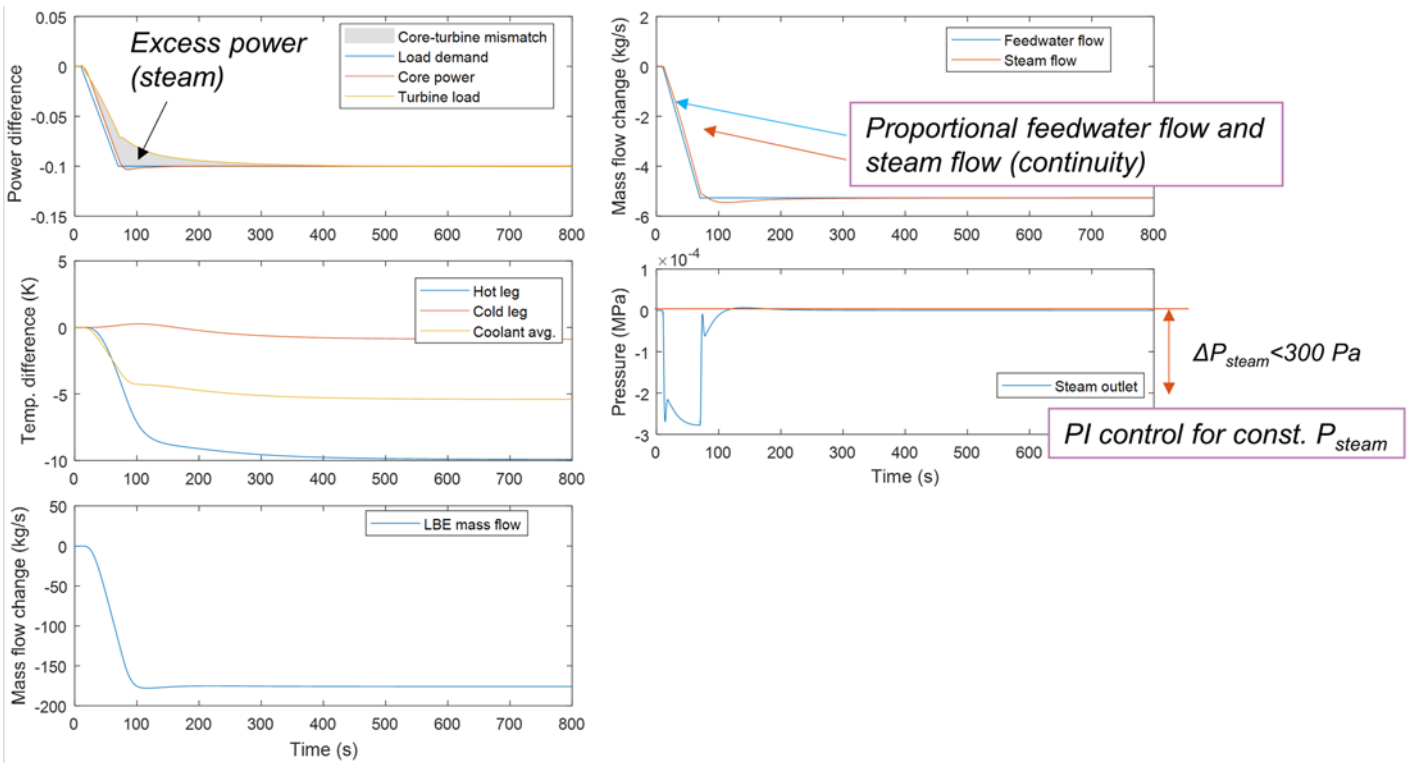

Figure 7.11 Calculation results for the system transients given by a power ramp rate of -10%P/min from 100% power output with feedwater flow rate control

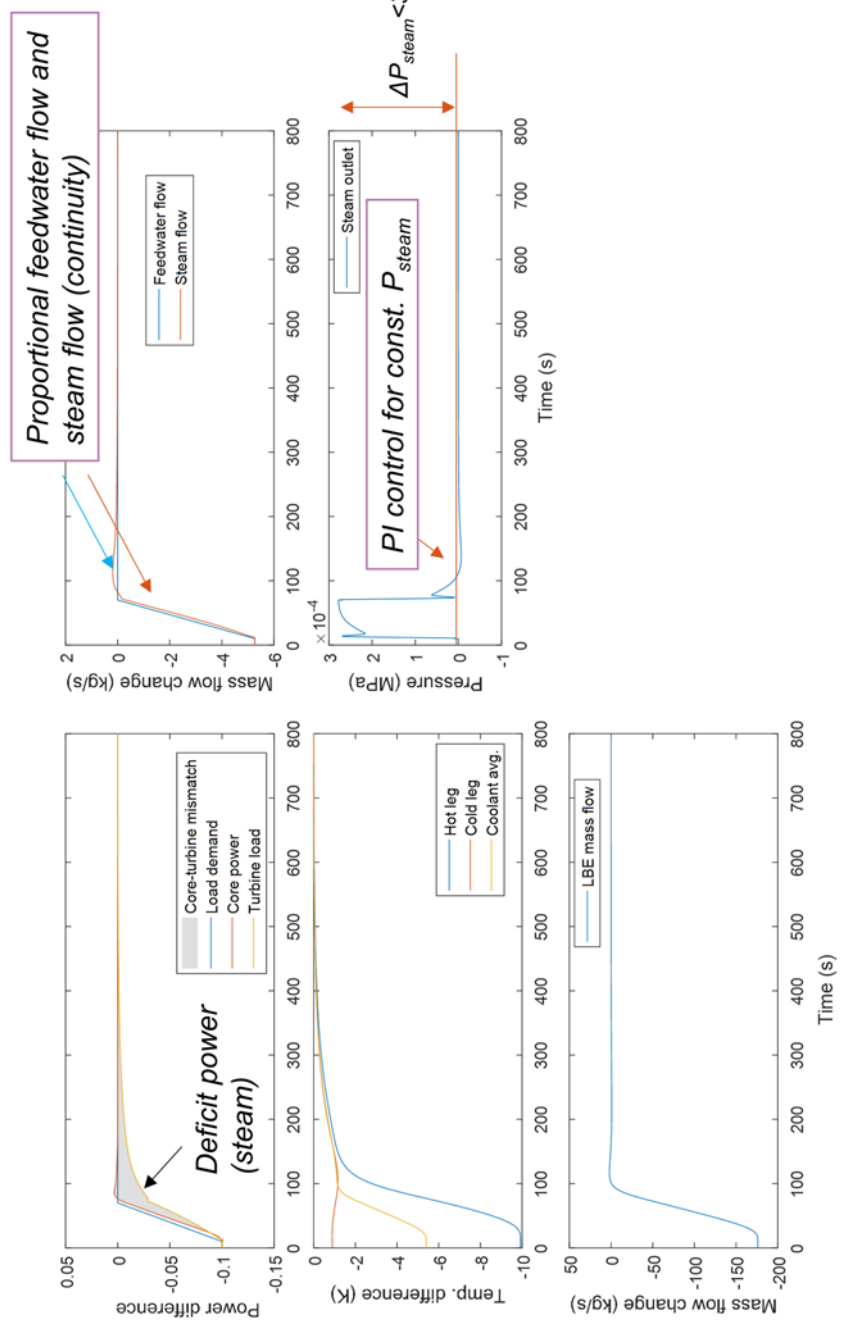

Figure 7.12 Calculation results for the system transients given by a power ramp rate of +10%P/min from 90% power

7.3.2 Stability analysis

In the operation of a system, for example, a powerplant, it is important to maneuver it within a stable range. Hence, the stability boundary should be studied, which depends on the dynamic characteristics of the system. In this regard, a stability analysis on URANUS is conducted in this section using the analytical reactor dynamics simulation model developed in this thesis study. The stability of interest under the load-following operation of this passive system is the dynamic stability of reactor core power in response of the external load demand change, which can be thought as bounded-output (BIBO) condition since it is lying on a bounded range of load demand.

In this section, the stability analysis is one of linear analyses, which make use of transfer functions, and it can be carried out by using the linear analysis tool supported by MATLAB/Simulink environments (Mathworks, 2017). In order to conduct a linear analysis of the implemented system, a user is requested to impose linear analysis points on the graphical user interface, as expressed by a flow diagram such as the block chain diagram of URANUS shown in Figure 7.6. Among several linear analysis points, the open-loop input and the open-loop output are utilized to establish a linear relation in terms of open-loop transfer function in this case.

Two graphical methods of stability analysis, the root locus and Bode diagram are to be used among others. According to the control theory, a dynamic system is BIBO stable if and only if all poles of transfer function have negative real part (Aström and Murray, 2010); in other words, all the poles are

located on the left-hand plane of Gauss plane in the pole-zero map drawn with root locus. Since the root locus illustrates the trajectories of pole locations in the linearized transfer function by varying the open-loop gain, it is confirmed for a system to be stable if the trajectories do not lay on the right hand side of the Gauss plane. Figure 7.13 show the resultant root locus for the transfer function that is linearized by imposing the open-loop input at the external power demand and the open-loop output at the reactor power. It is clearly seen that all the poles are located in the left hand plane of Gauss plane. Hence, the system can be said to be BIBO stable for the entire range of reactor power in response of the external load demand.

The other diagram, the Bode plot, is shown in Figure 7.14. The BIBO stability of a closed-loop is confirmed with an interpretation that the system is BIBO stable if both the phase margin and the gain margin are positive simultaneously (Hahn et al., 2001). The figures shows the phase margin of system response, 141°, is positive while the gain margin is not able to be estimated because phase shift is larger than -180° over all frequency domain. Although it is not defined, the stability of the system response can be evaluated since the phase shift asymptotically reaches -180° at positive infinite frequency and in that condition the gain margin is positive. In conclusion, the reactor core power of URANUS is maneuvered within a stable range by natural circulation under the fast load-following conditions with respect to the external load demand.

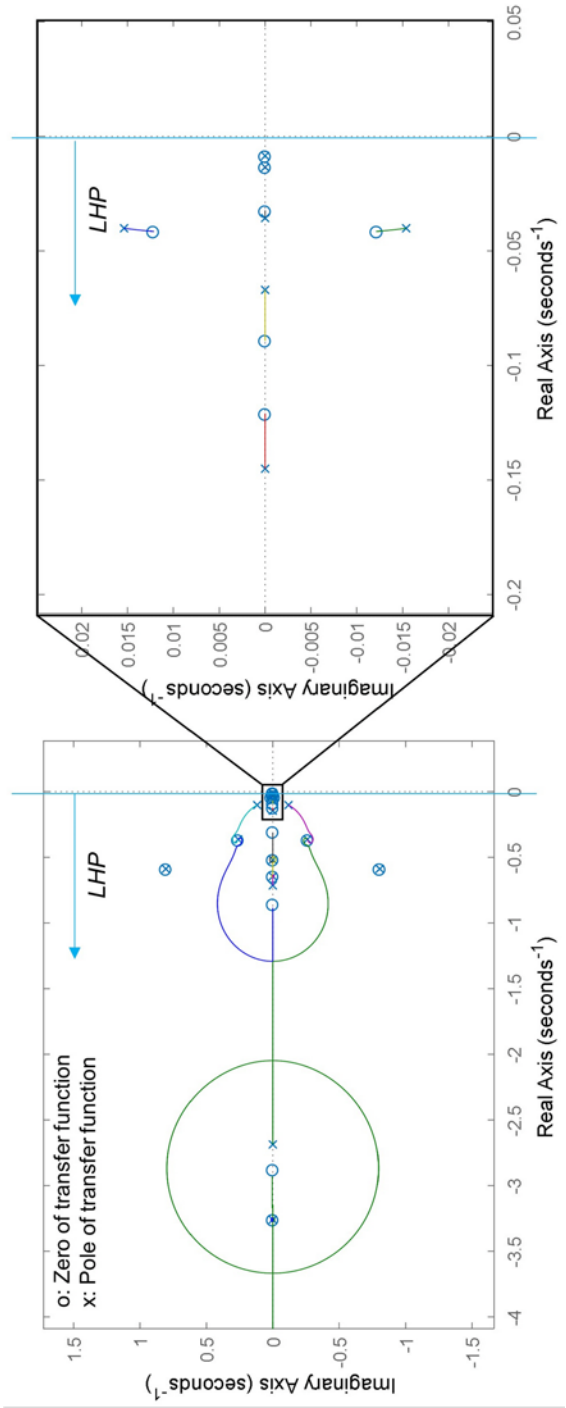

Figure 7.13 Root locus for load demand input to core power output

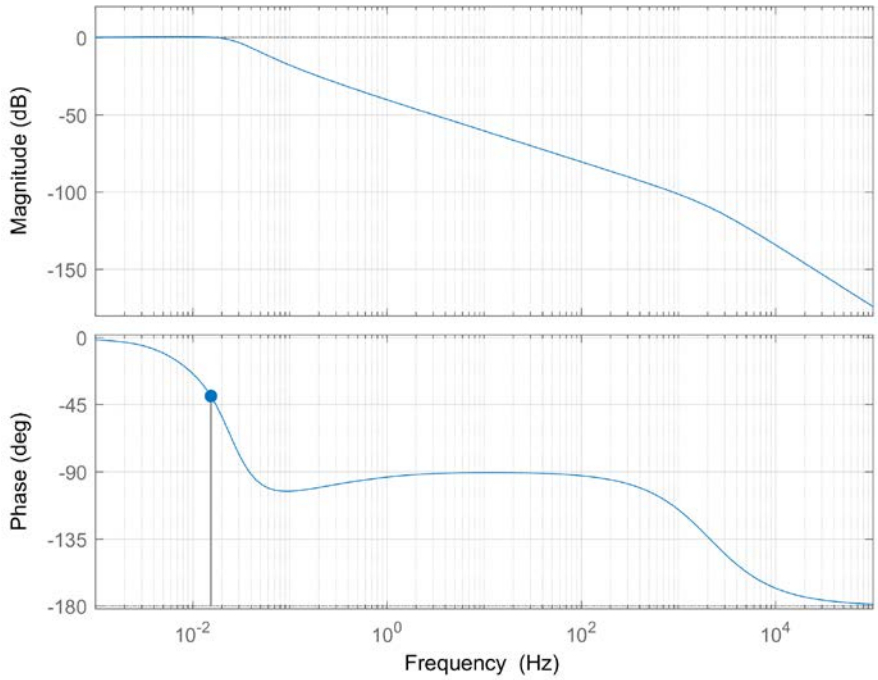

Figure 7.14 Bode diagram for load demand input to core power output

7.3.3 Planned load-following operation

A planned load-following operation is a type of power maneuvering as planned and expected. It is usually done in daily load maneuvering and typically expressed as "100-P-100%P_0, x-y-z-y", where P is given by power fraction in percent with respect to nominal full power and x, y, and z are the time spans between condition changes. In addition, the time spans x and z are the durations that 100% and P% of nominal power are sustained, respectively, while y is the time span necessary to reduce power from 100% to P% or to recover it from P% to 100%.

A scenario of planned load-following operation with a load-following pattern given as 100-60-100%P_0, 12-3-6-3 is simulated using the developed model and compared to MARS-LBE calculation. Since MARS-LBE does not have a capability of directly estimating reactivity change from control rod maneuvering, it is given by the calculation using the developed model. Figure 7.15 depicts the two calculation results simultaneously and the two simulation results show a good agreement even with large power level change from 100% to 60%, vice versa. In addition, for a slow transient, in this case the ramp rate of 13% of full power increase or decrease per hour, stable load-following operation can be achieved with slow mass flow and temperature transient.

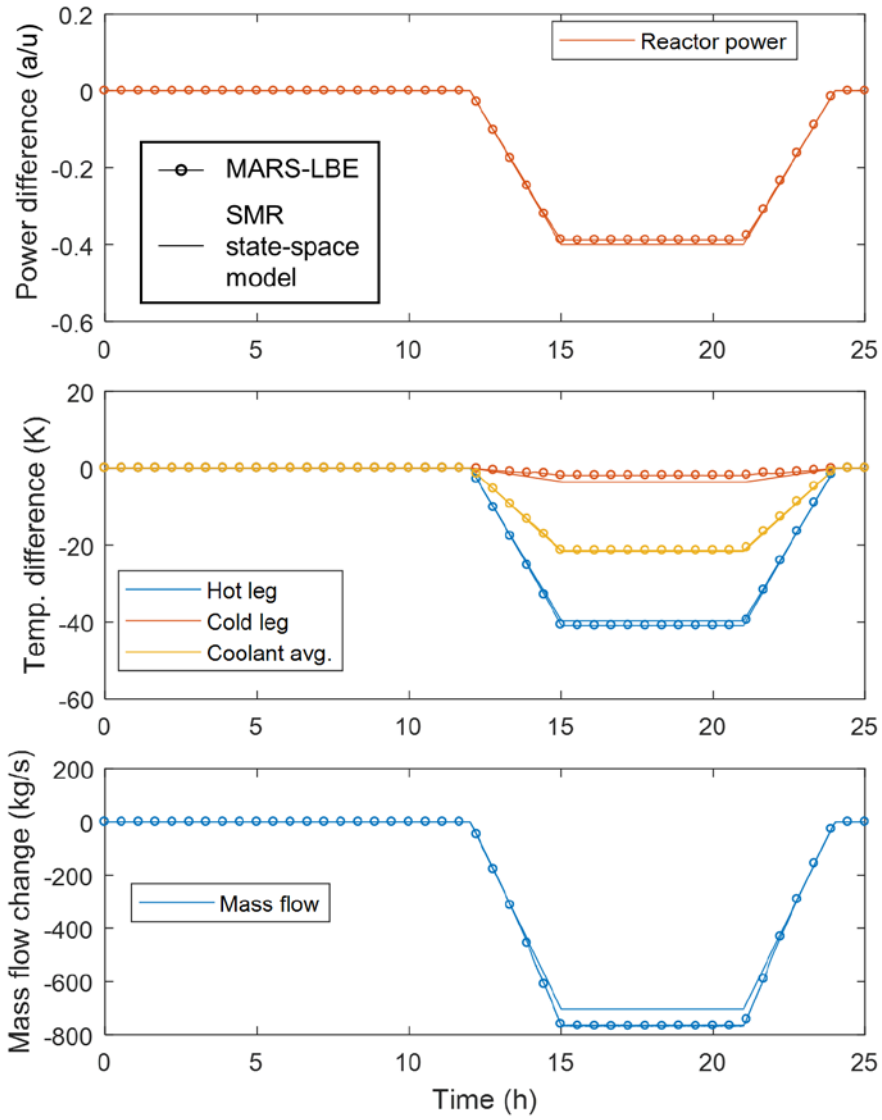

Figure 7.15 Comparison of planned load-following operation simulation results between the analytical model developed in this dissertation (line) and MARS-LBE (circle and line)

7.3.4 Power recovery from low power to full power

In this case study, a specific situation is postulated: URANUS is under low power operation, namely, 50% power of nominal full power, and the electric grid to which URANUS is also connected requires it to recover its core power to the nominal power rating since other powerplants connected to the grid fails, as shown in Figure 7.16. With regard to the grid request to URANUS, an unexpected, rapid request can be expressed in a step jump of core power rating. As utilized in Section 7.3.2, the linear analysis tool presented by MATLAB/Simulink environments (Mathworks, 2017) is also applicable on this type of analysis.

By imposing the open-loop input and output, similar to the procedure conducted in the stability analysis discussed in Section 7.3.2, an equivalent transfer function for the step analysis is established. Figure 7.17 shows the linear analysis results of URANUS. The top inset is calculated by the step response analysis with an open-loop input designated by the external load demand and an open-loop output at reactor core power. The bottom inset depicts the turbine load response with the same input and a different point of open-loop output, the secondary side heat removal.

For the step response analysis, selected terminologies are used; the settling time refers to the time required for a response signal to saturate within a specific range of its steady state value for all future times. In this analysis, the range is designated to be $\pm$2% of the steady state value. Another term, the rise time is defined as the time required for the signal to change from 10% of its

final value to 90% of the final value (Aström and Murray, 2010). According to those definitions, the system response against an input of step power jump can be discussed. The settling times of two systems are 47.9 s for the reactor core power and 232 s for the turbine load, which means the primary side settles first and then the secondary side follows this settlement to a new steady state.

In addition, the rise time of the primary side under step response is evaluated to be 11.4 s, as shown in the upper inset in Figure 7.17. Considering the definition of rise time, it is the time required for the URANUS primary side to change its power rating from 55% of full power to 95% of full power. In this case, the slope in response of step input would be the maximum response rate of the primary system since this step input postulates the most rapid rate of power maneuvering. Hence, the achievable maximum power ramp rate of the primary side of URNAUS in system transients can be estimated as 3.5% of full power per second (3.5%P/s).

This power maneuvering rate is an estimation given in terms of thermal-hydraulic and reactor kinetic aspects of URANUS system regardless of considering material integrity. Among others, the integrity of nuclear fuel is expected to be the most critical limiting factor when it comes to achievable power ramp rates. As a remark, experimental results and code calculation results on the reactor power transient test with a pre-irradiated fuel pin under a power ramp rate of 3%P/s showed that the failure condition of fuel would not be affected by the ramp rate within 1-3%P/s range (Fukano et al., 2009). However, until now, it is not evident whether the integrity of fuel is maintained under low-frequency temperature change expected in the fast load-following

operation. Thus, the estimated value is suggested to be the upper bound of the URANUS primary side.

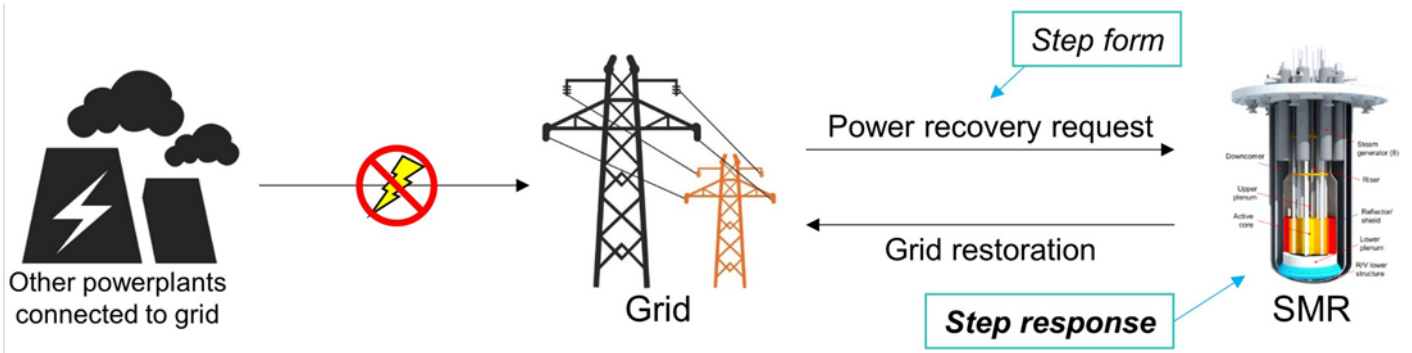

Figure 7.16 Conceptual case on instantaneous power return from low-power condition to nominal full power condition by grid request

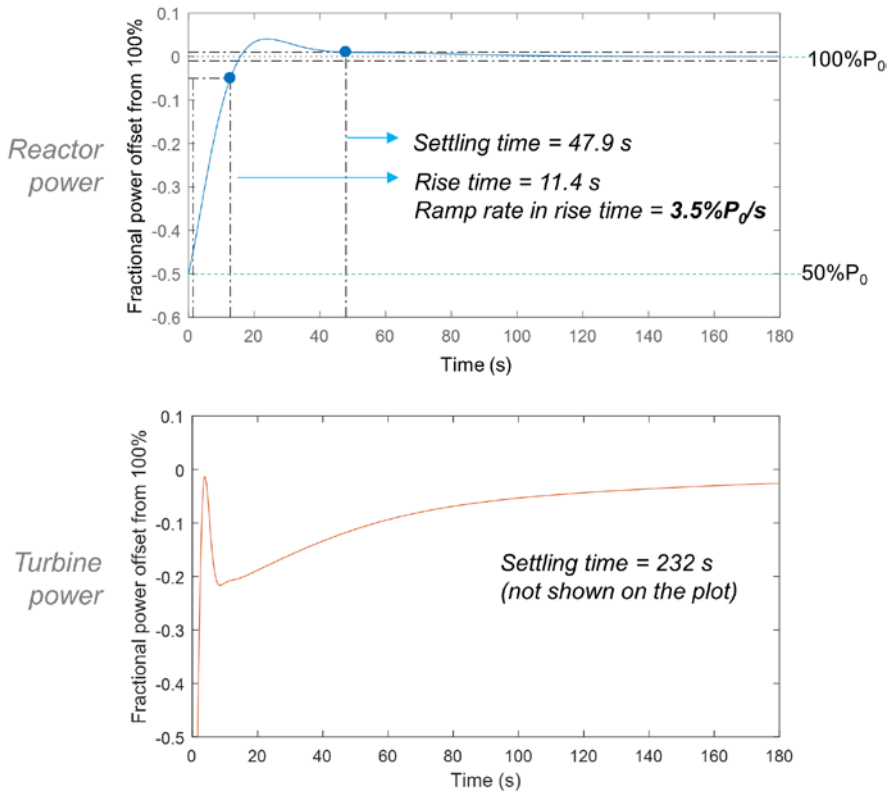

Figure 7.17 Step response analysis results on reactor core power response and turbine load response with respect to power recovery request from 50% to 100%

7.3.5 Comparison with a commercial SMR

This case study compares the load-following strategy suggested by a commercial passive water-cooled SMR, NuScale, named as NuFollow™ (Ingersoll et al., 2015)., NuScale power modules can be utilized in accordance with renewable sources, such as the wind farm, and a preliminary concept of fast load-following operation is given in that literature. The strategy mainly consists of two different ways of electricity generation: load-following operation without reactor core power maneuvering only with turbine bypass and that with both reactor power regulation and turbine bypass in a separate way. As introduced in Section 1.1, water-cooled reactors are not suitable for the fast load-following operation due to material and controlling limitations. In this regard, it seems that NuScale power module cannot follow the fast load demand change given by the wind farm.

However, as seen in the experimental results and evaluated by the analytical reactor dynamics simulation model, URANUS is expected to be able to follow the rapid load requirements given by the wind farm. To compare the fast load-following capability, the same load requirements are applied to URANUS. For the URANUS simulation, 10% extra load demand is added presuming an excess electricity supply to the area since there is no steam (power) deficit in the case of NuFollow™ because it is conceptually operated with steam bypass at all time. Meanwhile, the reactor dynamics model estimates the power transients in both primary and secondary sides from the deviations between the load demand. Hence, when the external load demand increases at

a given time, the steam deficit should occur and it is unrealistic because no electricity supply shortage is allowed.

Figure 7.18 shows the load requirements given by the wind farm and total load demand, and the simulation results with the latter load-following strategy of NuFollow™ (Ingersoll et al., 2015), a combination of reactor power maneuvering and steam curtailing. The case study shows that the fast load-following capability of URANUS contributes to not only the effective maneuvering of the reactor core power with respect to the required power but also the minimization of curtailed steam. In addition, when it comes to the excess steam utilization, the fast reactor power response expected in URANUS might also help where the dumped steam is used by maintaining in a specific range.

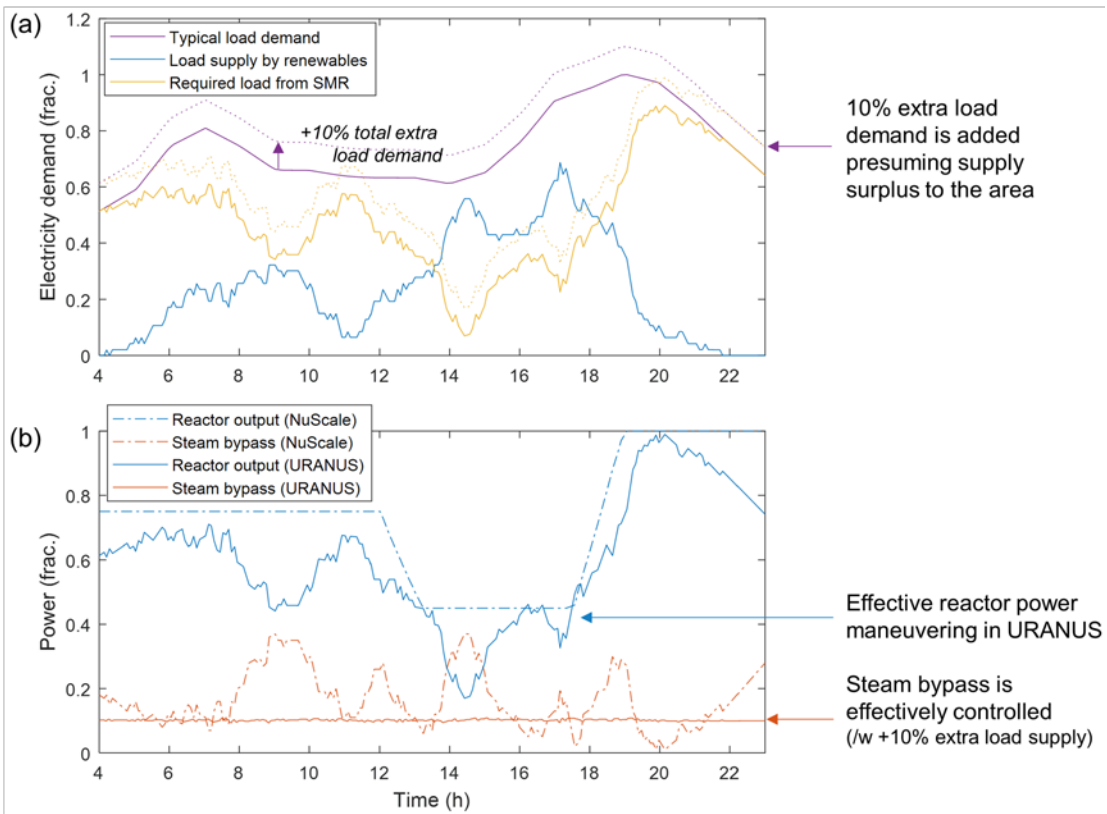

Figure 7.18 Comparison with a commercial passive load-following concept *NuFollow*™ (excerpted from (Ingersoll et al., 2015)). (a) Required load demand and (b) reactor output and steam bypass by NuScale and URANUS

Chapter 8 Conclusions and Future Work

8.1 Conclusions

The objective of this thesis study is to evaluate the fast load-following capability of a passive LBE-cooled SMR in terms of safety requirements and stability. A thorough understanding on the integral system behaviors of a LBE-cooled passive system under transients is necessary and furthermore, a predictive tool for passive system behavior is need to be developed.

To do so, the objective is divided further into three particular objectives as experimental, numerical, and analytical studies. This study has been conducted in three stages as follows: first, a pool-type integral experimental facility has been devised by a hydrodynamic scale reduction method from its prototype SMR design, URANUS, and natural circulation experiments has been carried out in both steady state and transients given by external condition changes. Second, a one-dimensional system thermal-hydraulics code, MARS-LBE, is validated two-fold through the experimental results generated from a loop configuration and the results given by the pool-type facility. Third, an analytical model for one-dimensional, time-dependent passive system transient evaluation has been developed under a commercial numerical software environment, MATLAB/Simulink. This analytical model has been verified with not only experimental results made in the second step

and but also with the one-dimensional system thermal-hydraulics code. Since there is no realization of a LBE-cooled SMR until now, a target reactor URANUS is designed before the three-step approach.

The experimental, numerical, and analytical investigations on the passive LBE-cooled SMR conducted in this thesis study show that the power ramp rate would not be limited by natural circulation, due to its rapid saturation with respect to heat source power transients. In addition, according to the stability analysis core power can be regulated within a stable range with respect to the external load demand change. Hence, the maximum achievable power ramp rate under safe, stable condition is related to nuclear fuel integrity, not the passive nature of reactor system. Furthermore, it is evaluated with an analysis on the step response that the reactor can change its core power rating as fast as 3.5% power per second from 50% of nominal full power to its full power with only considering its thermal-hydraulic and reactor kinetic response.

Since the primary side of a passive LBE-cooled SMR is expected to go through slower transients compared to the primary side under given operational condition changes, it can be concluded that the core power regulation along with feedwater flow rate control is favorable. As a preliminary study the dynamics of the secondary side is simulated with the developed analytical reactor dynamics simulation model and the results showed that the heat balance mismatch between the primary and secondary sides during transients can be minimized with feedwater flow control means, a proportional controller with respect to the external load demand in this case.

8.2 Future work

The evaluation on load-following capability of a passive LBE-cooled SMR shows that it can be operated under stable conditions for all external power demands and the maximum achievable power ramp rate would be 3.5% of full power per second. Beyond this achievement made in this thesis study, several addition studies are suggested as future work for a better understanding on the system integral behaviors and the enhanced performance of URANUS.

The BOP design of URANUS can be further determined. Conceptually, the BOP has been designated to utilize the Rankine cycle and its specific design was not a scope of this thesis study, since the integral behaviors in LBE natural circulation in the primary side was a key question. With the detailed design of BOP side, reactor control parameters can be further defined and a realistic assessment of thermal efficiency can be carried out. In addition, more realistic load demand change can be defined with frequency regulation.

For the experimental investigation, experiments on transients given by feedwater inlet temperature change can be sought. In an actual reactor, a decrease or increase in the steam generator outlet temperature can affect the core inlet temperature, which leads to a positive reactivity insertion by coolant overcooling. In this thesis study, this was excluded because the impact of secondary side temperature change would not be significant compared to the instantaneous flow rate change as shown in the transient experimental results on the secondary side. In this respect, the current PILLAR facility cannot facilitate rapid change of heat exchanger tube side inlet temperature since the

ultimate heat sink for the secondary side is the cooling tower and it shows rather slow transient nature due to relying on air convection. The investigation can be conducted by implementing some additional heaters and chillers on the secondary side to set out water inlet temperature rapidly.

The analytical model can be improved by implementing the capability of burnup-dependent system evaluation and controller optimization. As shown in the case of early French load-following modes having requirements on power ramps at elevated burnup levels, the former contributes to the evaluation of irradiated core. With this capability, the system behaviors at any time can be estimated, as the reactor targets to be operated about 30 years. Although the current model has a capability of stability evaluation, the latter would expand the scope of the analytical model. With optimally designed controllers, the performance of URANUS can be enhanced.

Nomenclature

Since each of chapters describe a number of equations and formulas, which in turn requires the use of numerous parameters accordingly, it is difficult to organize each of the parameters within same notations. Hence, for a better understanding, the relations were formulated with well-known letters on their description and it leads to the overlapping use of some letters. In this respect, this nomenclature section also lists up all the letters by dividing the paragraphs for each of chapters.

Nomenclature for Chapter 5.

a	Flow area (m^2)
A	Nondimensional flow area
Bi	Biot number
C_p	Isobaric heat capacity (J/kg K)
d	Hydraulic diameter (m)
d_{rod}	Diameter of nuclear fuel rod or electrical heater rod (m)
f	Darcy-Weisbach friction factor
F	Friction number
g	Gravitational acceleration constant (m/s^2)
h	Convective heat transfer coefficient (W/m^2 K)
k	Conductive thermal conductivity (W/m K)
K	Form loss coefficient
l	Length of a component (m)
L	Nondimensional length

$\dot{m}$	Mass flow rate (kg/s)
N_{rod}	Number of nuclear fuel rods or electrical heater rods
Nu	Nusselt number
P_0	Core thermal power (W)
Pe	Peclet number
Pr	Prandtl number
$\dot{q}$	Volumetric heat generation rate (W/m3)
Q	Heat source number
Re	Reynolds number
Ri	Richardson number
St	Stanton number
t	Time (s)
T	Temperature (K)
Ti	Time ratio number
u	Area-averaged flow velocity (m/s)
U	Nondimensional flow velocity
y	Transverse distance to flow direction (m)
Y	Nondimensional transverse distance
z	Axial (flow direction) distance (m)
Z	Nondimensional axial distance
Greek	
α	Thermal diffusivity (m^2/s)
β	Thermal coefficient of expansion (K^{-1})
δ	Conduction depth (m)
θ	Nondimensional temperature difference
ξ	Wetted perimeter (m)
ρ	Density (kg/m^3)
τ	Nondimensional time
ψ	Specific parameter
Subscripts	

0	Reference constant value
c	Cold region
h	Hot region
i	Number for *i*-th component
m	Scale model
p	Prototype
r	Representative variable of system
R	Model-to-prototype ratio; $R = m / p$
s	Solid

Nomenclature for Chapter 6.

ΔH	Thermal height center difference (m)
Δp	Pressure loss due to hydraulic resistance (Pa)
ΔT	Temperature difference between the mock-up core inlet and outlet (°C)
A	Flow area (m^2)
A_s	Projected grid cross section (m^2)
A_v	Undisturbed flow area (m^2)
C_p	Heat capacity (J/kg K)
C_v	Modified loss coefficient
d_h	Hydraulic diameter (m)
f	Darcy-Weisbach friction factor
g	Gravitational acceleration (m/s^2)
K	Form loss coefficient
K_{Re}, K_{loc}, K_{fr}	Constants given in (Nippert, 1929)
k	Thermal conductivity (W/m K)
l	Length (m)

$\dot{m}$	Mass flow rate (kg/s)
Nu	Nusselt number
Pe	Peclet number
Pr	Prandtl number
Q	Mock-up core power (W; kW)
Re	Reynolds number
v	Flow velocity (m/s)

Greek

β	Thermal expansion coefficient (K^{-1})
ε	Pipe roughness (m)
μ	Dynamic viscosity (Pa s)
ρ	Density (kg/m^3)

Subscripts

0	Reference
1	Upstream
2	Downstream
i	Component
c	Vena contracta
LBE	Lead-bismuth eutectic
oil	Secondary side thermal oil (Dowtherm© RP)
or	Orifice
w	Water

Nomenclature for Chapter 7.

ΔH	Thermal height center difference (m)
Δp	Pressure loss due to hydraulic resistance, pressure difference

	(Pa)
A	Flow area (m^2)
A_s	Cross-sectional area with respect to direction z (m^2)
C_j	j-th group neutron precursor density (#/cm^3)
C_p	Heat capacity (J/kg K)
C_R	Hydraulic resistance coefficient [ref]
c_m	Constant defined by Eqn. (7.16)
d	Diameter (m)
d_h	Hydraulic diameter (m)
f_f	Power fraction transferred directly to fuel lump
G_{rod}	Reactivity worth per unit length (dk/k/m)
g	Gravitational acceleration (m/s^2)
H	Height (m)
h	Convective heat transfer coefficient (W/m^2 K), fluids enthalpy (J/kg)
k	Thermal conductivity (W/m K)
L	Length of a component (m)
$\dot{m}$	Mass flow rate (kg/s)
N	Number
n	Neutron density (#/cm^3), a constant for the power of Eqn. (7.14)
O	Collection of terms with higher orders
P	Pressure (Pa)
Q	Power (W)
R	Proportionality constant to Eqn. (7.14)
Re	Reynolds number
r	Radius (m)
T	Temperature (K)
t	Thickness (m), time (s)
v_{rod}	Control rod speed (m/s)
z	Length in flow direction (m)

Greek

α	Reactivity constant (pcm/K)
β	Thermal expansion coefficient (K^{-1})
β_{eff}	Effective delayed neutron fraction (dk/k)
β_j	j-th group delayed neutron fraction (dk/k)
γ	Mean void fraction
δ	Deviation between initial value and perturbed value
ε	Pipe roughness (m)
μ_c	Mass flow rate times heat capacity of fluid (W/K)
Λ	Neutron generation time (s)
λ_j	j-th group precursor decay constant (s^{-1})
μ_c	Mass flow rate times heat capacity (W/K)
ρ	Reactivity (in point kinetic equations),
	Fluid density (kg/m^3) (in thermal-hydraulic equations)
ψ	State parameter
Ω	Equivalent heat transfer coefficient (W/K)

Superscript

n	Parameter defined at a boundary node

Subscripts

0	Initial value, nominal value
B	Buoyancy
c	Coolant, core average
ci	Core inlet
cl	Cole leg
clad	cladding
co	Core outlet
core	Core region
f	Nuclear fuel, saturated liquid

g	Gap between fuel pellet and cladding, saturated vapor
hl	Hot leg
i	Index
j	Index
k	Index
loss	Hydraulic loss
p	Primary side
r	Relative value
rod	Control rod or fuel rod
s	Steam generator shell side, secondary side
t	Steam generator tube wall
tube	Steam generator tube bundles
w	Subcooled water region in central feedwater pipe

Vector, matrix notations

$\mathbf{A}$	Matrix
a	Element of the matrix $\mathbf{A}$
$\mathbf{B}$	Matrix
b	Element of the matrix $\mathbf{B}$
$F_{\mathbf{x}}$	Matrix coefficient defined by $F_{\mathbf{x}} = \left[\left. \frac{\partial f}{\partial \mathbf{x}} \right\|_{\mathbf{x}_0, \mathbf{u}_0} \right]$
$F_{\mathbf{u}}$	Matrix coefficient defined by $F_{\mathbf{u}} = \left[\left. \frac{\partial f}{\partial \mathbf{u}} \right\|_{\mathbf{x}_0, \mathbf{u}_0} \right]$
$f(\mathbf{x},\mathbf{u})$	Matrix of $\mathbf{x}$ and $\mathbf{u}$ with a proper dimension
$f_{\mathbf{x}}$	Element of the matrix $F_{\mathbf{x}}$
$f_{\mathbf{u}}$	Element of the matrix $F_{\mathbf{u}}$
$g(\mathbf{x},\mathbf{u})$	Resultant matrix defined by $g(\mathbf{x},\mathbf{u}) = Z^{-1}(\mathbf{x},\mathbf{u})\, f(\mathbf{x},\mathbf{u})$
$\mathbf{u}$	Input vector
$\mathbf{x}$	State vector
$\dot{\mathbf{x}}$	Temporal change of state vector

$Z(\mathbf{x},\mathbf{u})$	Matrix of **x** and **u** with a proper dimension
z	Element of the matrix $Z(\mathbf{x},\mathbf{u})$

Bibliography

Alcouffe, R.E., Baker, R.S., Brinkley, F.W., Marr, D.R., O'Dell, R.D., Walters, W.F., (1995), DANTSYS: A Diffusion Accelerated Neutral Particle Transport Code System. Los Alamos National Laboratory, NM, USA.

Alekseev, A.I., Belyaev, V.V., Goltsov, Y.N., Grechko, G.I., Eremeev, D.V., Pepa, V.N., (2014), Status of Activities on the Reactor Facility for the UNITHERM SNPP, Third International Scientific and Technical Conference “Innovative Designs and Technologies of Nuclear Power” (ISTC NIKIET-2014), NIKIET, Moscow, Russia Federation.

Alemberti, A., (2012), ELFR: The European Lead Fast Reactor. Design, Safety Approach and Safety Characteristics.

ASME, (2005), Test Uncertainty, ASME PTC 19.1-2005 (Revision of ASME PTC 19.1-1998).

Astegiano, J.-C., Achourko, I., Alphonse, P., Aoyama, T., Baque, F., Berte, M., Brachi, R., Cabrillat, M.T., Carbonnier, J.L., Chiarot, D., Gastaldi, O., Giraud, M., Grabon, V., Henslee, S.P., Ibuki, Y., Irie, T., Joulia, E., Lemoine, P., Louvet, J., Martin, L., Mourogov, A., Poncerry, J., Preifer, W., Rajan, M., Ramakrishnan, I., Riou, B., Rodriguez, G., Stanculescu, A., Surendran, C.S., Kumar, K.V.S., Tommasi, J., Vinoche, O., Yu, H., (2004), Operational and decommissioning experience with fast reactors. IAEA, Vienna, Austria.

Aström, K.J., Murray, R.M., (2010), Feedback systems: an introduction for scientists and engineers. Princeton university press.

Ballinger, R.G., Lim, J., (2004), An overview of corrosion issues for the design and operation of high-temperature lead-and lead-bismuth-cooled reactor systems. Nuclear Technology 147, 418-435.

Bandini, G., Casamirra, M., Castiglia, F., Giardina, M., Meloni, P., Polidori, M., (2008a), Analysis of Protected Accidental Transients in the EFIT Reactor With the RELAP5 Thermal-Hydraulic Code. 759-768.

Bandini, G., Meloni, P., Polidori, M., Casamirra, M., Castiglia, F., Giardina, M., (2008b), Decay heat removal and transient analysis in accidental conditions in the EFIT reactor. Science and Technology of Nuclear Installations 2008.

Blue, R., Carelli, M., Delmastro, D., Delpech, M., Hwang, J.-K., Ivanov, E., Kuznetsov, V., Maheshwari, N.K., Sefidvash, F., Shimazu, Y., Sun, Y., Toshinskiy, G., Veshnyakov, K., Wade, D., (2005), Innovative small and medium sized reactors: Design features, safety approaches and R&D trends, Vienna, Austria.

Borgohain, A., Maheshwari, N.K., Vijayan, P.K., (2016a), Natural circulation experiments in a non-uniform diameter lead bismuth loop and validation of LeBENC code. Progress in Nuclear Energy 91, 68-82.

Borgohain, A., Srivastava, A.K., Jana, S.S., Maheshwari, N.K., Kulkarni, R.D., Vijayan, P.K., Tewari, R., Ram, A.M., Jha, S.K., (2016b), Natural circulation studies in a LBE loop for a wide range of temperature. Nuclear Engineering and Design 300, 358-375.

Briggs, L., Hu, W., Su, G., Vezzoni, B., Del Nevo, A., Monti, S., Sui, D., Maas, L., Sarathy, U.P., Petruzzi, A., (2015), EBR-II passive safety demonstration tests benchmark analyses-phase 2, 16th International Topical Meeting on Nuclear Reactor Thermal Hydraulics, NURETH

2015. American Nuclear Society.

Briggs, L., Monti, S., Choi, C., Hu, W., Maas, L., Maschek, W., Merk, B., Mikityuk, K., Mochizuki, H., Morita, K., (2013), Benchmark Analyses of the Shutdown Heat Removal Tests Performed in the EBR-II Reactor, Fast Reactors and Related Fuel Cycles: Safe Technologies and Sustainable Scenarios (FR13).

Carlson, K., Riemke, R., Rouhani, S., Shumway, R., Weaver, W., (1990), RELAP5/MOD3 Code Manual Volume I: Code Structure, System Models and Solution Methods. US NRC NUREG/CR-5535, Washington (DC, USA) June.

Castiglia, F., Giardina, M., Morana, G., De Salve, M., Panella, B., (2012), Analyses of single-and two-phase flow pressure drops in helical pipes using a modified RELAP5 code. Nuclear Engineering and Design 250, 585-591.

Chang, Y., LoPinto, P., Konomura, M., Cahalan, J., Dunn, F., Farmer, M., Krajtl, L., Moisseytsev, A., Momozaki, Y., Sienicki, J., (2005), Small Modular Fast Reactor design description. Argonne National Lab., Argonne, IL (US).

Chen, X.-N., (2015), On LBE natural convection and its water experimental simulation. Progress in Nuclear Energy 78, 372-379.

Cho, J.H., Batta, A., Casamassima, V., Cheng, X., Choi, Y.J., Hwang, I.S., Lim, J., Meloni, P., Nitti, F.S., Dedul, V., Kuznetsov, V., Komlev, O., Jaeger, W., Sedov, A., Kim, J.H., Puspitarini, D., (2011), Benchmarking of thermal hydraulic loop models for Lead-Alloy Cooled Advanced Nuclear Energy System (LACANES), phase-I: Isothermal steady state forced convection. Journal of Nuclear Materials 415, 404-414.

Choi, C., Ha, K., (2016a), Performance test of MARS-LMR code with benchmark analysis of EBR-II SHRT-17. Annals of Nuclear Energy 94, 376-391.

Choi, C., Ha, K.S., (2016b), Assessment calculation of MARS-LMR using EBR-II SHRT-45R. Nuclear Engineering and Design 307, 10-29.

Choi, J.-I., Oh, S.-Y., Song, I.-H., Hah, Y.-J., Kuh, J.-E., Lee, U.-C., (1992), Advanced Load Follow Operation Mode for Korean Standardized Nuclear Power Plants. Journal of the Korean Nuclear Society 24.

Choi, S., Cho, J.-H., Bae, M.-H., Lim, J., Puspitarini, D., Jeun, J.H., Joo, H.-G., Hwang, I.S., (2011a), PASCAR: Long burning small modular reactor based on natural circulation. Nuclear Engineering and Design 241, 1486-1499.

Choi, S., Hwang, I.S., Cho, J.H., Shim, C.B., (2011b), URANUS: Korean lead-bismuth cooled small modular fast reactor activities, ASME 2011 Small Modular Reactors Symposium. ASME, Washington D.C.

Ciampichetti, A., Agostini, P., Benamati, G., Bandini, G., Pellini, D., Forgione, N., Oriolo, F., Ambrosini, W., (2008), LBE–water interaction in sub-critical reactors: First experimental and modelling results. Journal of Nuclear Materials 376, 418-423.

Cinotti, L., (2004), Engineering solutions and thermal-hydraulic issues for a promising safe ADS system, Proc. of the 6 th International Conference on Nuclear Thermal Hydraulics, Operations and Safety (NUTHOS), Atomic Energy Society of Japan, Nara, Japan.

Coccoluto, G., Gaggini, P., Labanti, V., Tarantino, M., Ambrosini, W., Forgione, N., Napoli, A., Oriolo, F., (2011), Heavy liquid metal natural circulation

in a one-dimensional loop. Nuclear Engineering and Design 241, 1301-1309.

Cox, B., (1990), Pellet-clad interaction (PCI) failures of zirconium alloy fuel cladding—a review. Journal of Nuclear Materials 172, 249-292.

Croff, A.G., (1983), ORIGEN2: a versatile computer code for calculating the nuclide compositions and characteristics of nuclear materials. Nuclear Technology 62, 335-352.

De Bruyn, D., Abderrahim, H.A., Baeten, P., Fernandez, R., Engelen, J., Van Den Eynde, G., (2014), The MYRRHA ADS project in Belgium enters the Front End Engineering Phase, International Congress on Advances in Nuclear Power Plants, ICAPP 2014, pp. 646-654.

Dittus, F.W., Boelter, L.M.K., (1930), Heat transfer in automobile radiators of the tubular type.

Dow Chemical Company, (1996), DOWTHER RP Heat Transfer Fluid Product Technical Data.

Dragunov, Y.G., Lemekhov, V., Moiseev, A., Smirnov, V., Yarmolenko, O., Vasyukhno, V., Cherepnin, Y.S., (2016), Detailed design of the BREST-OD-300 reactor facility: development stages and justification, Innovative designs and technologies of nuclear power. IV International scientific and technical conference. Book of abstracts.

Dvoriashin, A.M., Porollo, S., Konobeev, Y.V., Budylkin, N., Mironova, E., Ioltukhovskiy, A., Leontyeva-Smirnova, M., Garner, F.A., (2007), Mechanical properties and microstructure of three Russian ferritic/martensitic steels irradiated in BN-350 reactor to 50dpa at 490° C. Journal of Nuclear Materials 367, 92-96.

Edwards, R.M., Lee, K.Y., Schultz, M., (1990), State feedback assisted classical control: an incremental approach to control modernization of existing and future nuclear reactors and power plants. Nuclear technology 92, 167-185.

Eguchi, Y., Takeda, H., Koga, T., Tanaka, N., Yamamoto, K., (1997), Quantitative prediction of natural circulation in an LMFR with a similarity law and a water test. Nuclear engineering and design 178, 295-307.

El-Wakil, M.M., (1971), Nuclear Heat Transport. International Textbook Co.

Fazio, C., Benamati, G., Martini, C., Palombarini, G., (2001), Compatibility tests on steels in molten lead and lead–bismuth. Journal of nuclear materials 296, 243-248.

Frogheri, M., Alemberti, A., Mansani, L., (2015), The lead fast reactor: demonstrator (ALFRED) and ELFR design, Fast Reactors and Related Fuel Cycles: Safe Technologies and Sustainable Scenarios (FR13). V. 1. Proceedings of an International Conference.

Fukano, Y., Onoda, Y., Sato, I., Charpenel, J., (2009), Fuel Pin Behavior under Slow-Ramp-type Transient-Overpower Conditions in the CABRI-FAST Experiments. Journal of Nuclear Science and Technology 46, 1049-1058.

Garner, F., Toloczko, M., Sencer, B., (2000), Comparison of swelling and irradiation creep behavior of fcc-austenitic and bcc-ferritic/martensitic alloys at high neutron exposure. Journal of Nuclear Materials 276, 123-142.

Grewal, S., Gluekler, E., (1982), Water Simulation of Sodium Reactors. Chemical Engineering Communications 17, 343-360.

Grishchenko, D., Jeltsov, M., Kööp, K., Karbojian, A., Villanueva, W., Kudinov, P., (2015), The TALL-3D facility design and commissioning tests for validation of coupled STH and CFD codes. Nuclear Engineering and Design 290, 144-153.

H. Ait Abderrahim, A. Al Mazouzi, Arien, B., Baeten, P., D. De Bruyn, Maes, D., Malambu, E., Schuurmans, P., Schyn, M., Sobolev, V., G. Van den Eynde, Vandeplassche, D., (2011), MYRRHA Technical Description. . SCK-CEN.

Hahn, J., Edison, T., Edgar, T.F., (2001), A note on stability analysis using bode plots. Chemical Engineering Education 35, 208-211.

He, X., Liu, S., Asada, H., (1995), Modeling of vapor compression cycles for advanced controls in HVAC systems, Proceedings of the American Control Conference, pp. 3664-3668.

Hejzlar, P., Petroski, R., Cheatham, J., Touran, N., Cohen, M., Truong, B.A.O., Latta, R., Werner, M., Burke, T.O.M., Tandy, J.A.Y., Garrett, M., Johnson, B., Ellis, T., McWhirter, J.O.N., Odedra, A.S.H., Schweiger, P.A.T., Adkisson, D., Gilleland, J., (2013), Terrapower, LLC Traveling Wave Reactor Development Program Overview. Nuclear Engineering and Technology 45, 731-744.

Hill, R., Cahalan, J., Khalil, H., Wade, D., (1999), Development of small, fast reactor core design using lead-based coolant, Proceedings of the International Conference on Future Nuclear Systems.

Hong, S.J., Lee, D.Y., (2012), Scaling and Design of Integral Test Facility Simulating 600MWe SFR (Korean version). FNC Technology Co., and Korea Atomic Energy Research Institute

Hosemann, P., Thau, H.T., Johnson, A.L., Maloy, S.A., Li, N., (2008), Corrosion of ODS steels in lead–bismuth eutectic. Journal of Nuclear Materials 373, 246-253.

Hwang, I., Kim, M., Joo, H., (2008a), Development of PASCAR (Proliferation-resistant, Accident-tolerant, Self-sustainable, Capsular, Assured Reactor) design and safety analysis, 10th Information Exchange Meeting on Actinide and Fission Product Partitioning and Transmutation.

Hwang, I.S., Jeong, S.H., Park, B.G., Yang, W.S., Suh, K.Y., Kim, C.H., (2000), The concept of proliferation-resistant, environment-friendly, accident-tolerant, continual and economical reactor (PEACER). Progress in Nuclear Energy 37, 217-222.

Hwang, I.S., Kim, M.H., Joo, H.G., Yoo, B., Kim, M.H., Oh, S.R., Yi, K.W., Han, D.Y., Lim, J., Nam, H.O., Cho, J.H., Lee, K.Y., Bae, M.H., Choi, S., Kim, C.H., (2008b), Development of Transportable Capsule Version of PEACER design. Proc: ICAPP '08, Anaheim, CA, USA.

Hwang, I.S., Lim, J., (2010), Structural developments for lead-bismuth cooled fast reactors, PEACER and PASCAR, 25th KAIF/KNS Annual Conference, Seoul, Korea.

IAEA, (2011), Stress corrosion cracking in light water reactors: good practices and lessons learned, IAEA Nuclear Energy Series.

Idelchik, I.E., (1953), Determination of the resistance coefficients during discharge through orifices. Gidrotekh. Stroit. No. 5., 31-36.

Idelchik, I.E., (1986), Handbook of hydraulic resistance. Washington, DC, Hemisphere Publishing Corp., 1986, 662 p. Translation. 1.

Ikegawa, T., Kawabata, Y., Ishii, Y., Matsuura, M., Hirako, S., Hoshi, T., (2010),

The Plant Feature and Performance of Double MS (Modular Simplified and Medium Small Reactor). Journal of Engineering for Gas Turbines and Power 132, 015001.

Ingersoll, D., Colbert, C., Houghton, Z., Snuggerud, R., (2015), Can nuclear power and renewables be friends?, 2015 International Congress on Advances in Nuclear Power Plants (ICAPP '15), Nice, France.

Ishii, M., Kataoka, I., (1984), Scaling laws for thermal-hydraulic system under single phase and two-phase natural circulation. Nuclear Engineering and Design 81, 411-425.

Ishii, M., Revankar, S.T., Leonardi, T., Dowlati, R., Bertodano, M.L., Babelli, I., Wang, W., Pokharna, H., Ransom, V.H., Viskanta, R., Han, J.T., (1998), The three-level scaling approach with application to the Purdue University Multi-Dimensional Integral Test Assembly (PUMA). Nuclear Engineering and Design 186, 177-211.

Islam, M.R., Gabbar, H.A., (2015), Study of small modular reactors in modern microgrids. International Transactions on Electrical Energy Systems 25, 1943-1951.

Jensen, J.M., Tummescheit, H., (2002), Moving boundary models for dynamic simulations of two-phase flows. Proceedings of the 2nd International Modelica Conference, 235-244.

Jeong, S.H., (2006), Development of an integral test loop, HELIOS and investigation of natural circulation ability for PEACER. Ph.D. Thesis, Seoul National University, Seoul, Korea.

Jeong, S.H., Bahn, C.B., Chang, S.H., Oh, Y.J., Nam, W.C., Ryu, K.H., Nam, H.O., Lim, J., Lee, T.H., Lee, S.G., (2006), Operation Experience of LBE

Loop: HELIOS, 2006 international congress on advances in nuclear power plants-ICAPP'06, Reno, NV, USA.

KAERI, (2006), MARS Code Manual Volume I - Code Structure, System Models and Solution Methods., Daejeon, Korea.

KAERI, (2007), Development of MARS-LMR and Steady-state Calculation for KALIMER-600 (in Korean). Korea Atomic Energy Research Insititute.

Kapernick, J.R., (2015), Dynamic Modeling of a Small Modular Reactor for Control and Monitoring.

Kerlin, T., Katz, E., Thakkar, J., Strange, J., (1976), Theoretical and experimental dynamic analysis of the HB Robinson nuclear plant. Nuclear technology 30, 299-316.

Kerlin, T.W., (1978), Dynamic Analysis and Control of Pressurized Water Reactors, in: Leondes C.T. (Ed.), Control and Dynamic Systems. Academic Press, pp. 103-212.

Khalil, H.K., (1996), Noninear systems. Prentice-Hall, New Jersey 2, 5-1.

Kim, T., Lee, J., Kim, J.H., (2017), Pilgering Process of Functionally Graded Composite Cladding for Liquid Metal Fast Cooled Reactor Application, Global Symposium on Lead and Lead Alloy Cooled Nuclear Energy Science and Technology (GLANST-2017), Seoul, Republic of Korea.

Kimura, A., Kasada, R., Iwata, N., Kishimoto, H., Zhang, C.H., Isselin, J., Dou, P., Lee, J.H., Muthukumar, N., Okuda, T., Inoue, M., Ukai, S., Ohnuki, S., Fujisawa, T., Abe, T.F., (2011), Development of Al added high-Cr ODS steels for fuel cladding of next generation nuclear systems. Journal of Nuclear Materials 417, 176-179.

Klueh, R., Nelson, A., (2007), Ferritic/martensitic steels for next-generation reactors. Journal of Nuclear Materials 371, 37-52.

Lawrence, R., (1983), DIF3D nodal neutronics option for two-and three-dimensional diffusion theory calculations in hexagonal geometry. Argonne National Lab., IL (USA).

Lee, J., Lee, J.H., Kim, J.H., Shin, Y.-H., Hwang, I.S., Ballinger, R.G., (2016), Three-Dimensional Finite Element Analysis of Pilgering Process of Hybrid-layer Cladding for Advanced Small Modular Fast Reactor Application, 2016 International Congress on Advances in Nuclear Power Plants (ICAPP-2016, San Francisco, USA.

Lehto, W.K., Dean, E.M., Fryer, R.M., (1988), Reactor safety implications of pump run-up tests in EBR-II. Nuclear Engineering and Design 110, 47-53.

Li, N., (2008), Lead-alloy coolant technology and materials–technology readiness level evaluation. Progress in Nuclear Energy 50, 140-151.

Lienhard, J.H., (1973), On the commonality of equations for natural convection from immersed bodies. International Journal of Heat and Mass Transfer 16, 2121-2123.

Lim, J., Jeong, S.H., Oh, Y.J., Nam, H.O., Bahn, C.B., Chang, S.H., Nam, W.C., Ryu, K.H., Lee, T.H., Lee, S.G., Lee, N.Y., Hwang, I.S., (2007), Progresses in the operation of large scale LBE loop HELIOS, 2017 International Congress on Advances in Nuclear Power Plants - ICAPP 2007, Nice, France.

Lim, J., Nam, H.O., Hwang, I.S., Kim, J.H., (2010), A study of early corrosion behaviors of FeCrAl alloys in liquid lead–bismuth eutectic environments.

Journal of Nuclear Materials 407, 205-210.

Lokhov, A., (2011), Technical and economic aspects of load following with nuclear power plants. OECD Nuclear Energy Agency, Paris, France.

Ludwig, H., Salnikova, T., Stockman, A., Waas, U., (2011), Load cycling capabilities of german nuclear power plants (NPP). VGB powertech 91, 38.

Ma, W., Bubelis, E., Karbojian, A., Sehgal, B.R., Coddington, P., (2006), Transient experiments from the thermal-hydraulic ADS lead bismuth loop (TALL) and comparative TRAC/AAA analysis. Nuclear Engineering and Design 236, 1422-1444.

Ma, W., Karbojian, A., Sehgal, B.R., (2007), Experimental study on natural circulation and its stability in a heavy liquid metal loop. Nuclear Engineering and Design 237, 1838-1847.

MacFarlane, R.E., (1992), TRANSX 2: A Code for Interfacing MATXS Cross-Section Libraries to Nuclear Transport codes. Los Alamos National Laboratory, NM, USA.

Marcel, C.P., Furci, H.F., Delmastro, D.F., Masson, V.P., (2013), Phenomenology involved in self-pressurized, natural circulation, low thermo-dynamic quality, nuclear reactors: The thermal–hydraulics of the CAREM-25 reactor. Nuclear Engineering and Design 254, 218-227.

Mathworks, (2017), SIMULINK Dynamic System Simulation Language User's Guide.

Mills, K.C., Su, Y., Li, Z., Brooks, R.F., (2004), Equations for the calculation of the thermo-physical properties of stainless steel. ISIJ international 44, 1661-1668.

Mitenkov, F.M., Polunichev, V.I., (1997), Small nuclear heat and power co-generation stations and water desalination complexes on the basis of marine reactor plants. Nuclear Engineering and Design 173, 183-191.

Müller, G., Schumacher, G., Zimmermann, F., (2000), Investigation on oxygen controlled liquid lead corrosion of surface treated steels. Journal of Nuclear Materials 278, 85-95.

Nam, H.O., Lim, J., Han, D.Y., Hwang, I.S., (2008), Dissolved oxygen control and monitoring implementation in the liquid lead–bismuth eutectic loop: HELIOS. Journal of Nuclear Materials 376, 381-385.

Nam, W.C., Lee, H.W., Hwang, I.S., (2007), Fuel design study and optimization for PEACER development. Nuclear Engineering and Design 237, 316-324.

Nippert, H., (1929), Über den Strömungsverlust in gekrümmten Kanälen. VDI-Verlag.

OECD Nuclear Energy Agency, (2007), Handbook on Lead-bismuth Eutectic Alloy and Lead Properties, Materials Compatibility, Thermal-hydraulics and Technologies. OECD Nuclear Energy Agency, Paris, France.

OECD Nuclear Energy Agency, (2012), Benchmarking of thermal-hydraulic loop models for lead-alloy-cooled advanced nuclear energy systems - Phase I: Isothermal forced convection case. OECD Nuclear Energy Agency, Paris, France.

OECD Nuclear Energy Agency, (2014), Technology roadmap update for Generation IV nuclear energy systems - January 2014. OECD Nuclear Energy Agency for the Generation IV International Forum.

OECD Nuclear Energy Agency, (2016a), 2016 GIF Annual Report. OECD

Nuclear Energy Agency for the Generation IV International Forum.

OECD Nuclear Energy Agency, (2016b), Small Modular Reactors: Nuclear Energy Market Potential for Near-term Deployment. OECD Nuclear Energy Agency, Paris, France.

Papukchiev, A., Jeltsov, M., Kööp, K., Kudinov, P., Lerchl, G., (2015), Comparison of different coupling CFD–STH approaches for pre-test analysis of a TALL-3D experiment. Nuclear Engineering and Design 290, 135-143.

Pettit, N., Willatzen, M., Ploug-Sørensen, L., (1998), A general dynamic simulation model for evaporators and condensers in refrigeration. Part II: simulation and control of an evaporator: Modèle général dynamique pour évaporateurs et condenseurs frigorifiques. Partie II: Simulation et régulation d'un évaporateur. International Journal of Refrigeration 21, 404-414.

Popov, S., Carbajo, J., (2000), Thermophysical properties of MOX and UO2 fuels including the effects of irradiation. Oak Ridge National Laboratory.

Rasmussen, B.P., Alleyne, A.G., (2006), Dynamic modeling and advanced control of air conditioning and refrigeration systems. Air Conditioning and Refrigeration Center. College of Engineering. University of Illinois at Urbana-Champaign.

Rehme, K., (1973), Pressure drop correlations for fuel element spacers. Nuclear technology 17, 15-23.

Reyes, J.N., (2011), Overview of NuScaleTechnology, Workshop on Technology Assessment of Small and Medium-sized Reactors (SMRs) for Near Term Deployment, IAEA Headquarters, Vienna, Austria.

Reyes, J.N., Lorenzini, P., (2010), NuScale Power: A modular, scalable approach to commercial nuclear power. Nuclear News 53, 97.

Satyamurthy, P., Biswas, K., (2002), Design of a LBE spallation target for fast-thermal accelerator-driven sub-critical system (ADS), Seventh Information Exchange Meeting on Actinide and Fission Product Partitioning and Transmutation, Jeju, Republic of Korea.

Seban, R.A., Shimazaki, T., (1949), Heat transfer to a fluid flowing turbulently in a smooth pipe with walls at constant temperature. California Univ., Berkeley (USA). Inst. of Engineering Research.

Sekimoto, H., Su'ud, Z., (1995), Design study of lead-and lead-bismuth-cooled small long-life nuclear power reactors using metallic and nitride fuel. Nuclear Technology 109.

Shim, H.-J., Han, B.-S., Jung, J.-S., Park, H.-J., Kim, C.-H., (2012), McCARD: Monte Carlo code for advanced reactor design and analysis. Nuclear Engineering and Technology 44, 161-176.

Shirvan, K., Ballinger, R., (2017), MIT/SNU Lead Bismuth Fast Reactor Project Final Report. Center for Advanced Nuclear Energy Systems, Department of Nuclear Science and Engineering, Massachusetts Institute of Technology.

Short, M.P., Ballinger, R.G., (2012), A Functionally Graded Composite for Service in High-Temperature Lead- and Lead-Bismuth–Cooled Nuclear Reactors—I: Design. Nuclear Technology 177, 366-381.

Sieder, E.N., Tate, G.E., (1936), Heat transfer and pressure drop of liquids in tubes. Industrial & Engineering Chemistry 28, 1429-1435.

Sinha, R., Kakodkar, A., (2006), Design and development of the AHWR—the

Indian thorium fuelled innovative nuclear reactor. Nuclear Engineering and Design 236, 683-700.

Smith, C.F., Halsey, W.G., Brown, N.W., Sienicki, J.J., Moisseytsev, A., Wade, D.C., (2008), SSTAR: The US lead-cooled fast reactor (LFR). Journal of Nuclear Materials 376, 255-259.

Sumner, T., Wei, T., (2012), Benchmark Specifications and Data Requirements for EBR II Shutdown Heat Removal Tests SHRT 17 and SHRT 45R. Nuclear Engineering Division Argonne National Laboratory, ANL-ARC-226-(Rev 1).

Svoboda, V., Wenzl, H., Kaiser, R., Jossen, A., Baring-Gould, I., Manwell, J., Lundsager, P., Bindner, H., Cronin, T., Nørgård, P., Ruddell, A., Perujo, A., Douglas, K., Rodrigues, C., Joyce, A., Tselepis, S., van der Borg, N., Nieuwenhout, F., Wilmot, N., Mattera, F., Sauer, D.U., (2007), Operating conditions of batteries in off-grid renewable energy systems. Solar Energy 81, 1409-1425.

Takahashi, M., Sofue, H., Iguchi, T., Matsumoto, M., Huang, F., Pramono, Y., Matsuzawa, T., Uchida, S., (2005), Study on Pb-Bi natural circulation phenomena. Progress in Nuclear Energy 47, 553-560.

Takahashi, M., Uchida, S., Kasahara, Y., (2008), Design study on reactor structure of Pb–Bi-cooled direct contact boiling water fast reactor (PBWFR). Progress in Nuclear Energy 50, 197-205.

Takaya, S., Furukawa, T., Müller, G., Heinzel, A., Jianu, A., Weisenburger, A., Aoto, K., Inoue, M., Okuda, T., Abe, F., Ohnuki, S., Fujisawa, T., Kimura, A., (2012), Al-containing ODS steels with improved corrosion resistance to liquid lead–bismuth. Journal of Nuclear Materials 428, 125-130.

Takeda, H., Koga, T., Watanabe, O., (1993), Experimental and computational simulation for natural circulation in an LMFBR. Nuclear engineering and design 140, 331-340.

Tarantino, M., Agostini, P., Benamati, G., Coccoluto, G., Gaggini, P., Labanti, V., Venturi, G., Class, A., Liftin, K., Forgione, N., Moreau, V., (2011), Integral Circulation Experiment: Thermal–hydraulic simulator of a heavy liquid metal reactor. Journal of Nuclear Materials 415, 433-448.

Thackeray, M.M., Wolverton, C., Isaacs, E.D., (2012), Electrical energy storage for transportation—approaching the limits of, and going beyond, lithium-ion batteries. Energy & Environmental Science 5, 7854-7863.

Thurgood, M., Kelly, J., Guidotti, T., Kohrt, R., Crowell, K., (1983), COBRA/TRAC-A thermal-hydraulics code for transient analysis of nuclear reactor vessels and primary coolant systems. Pacific Northwest Laboratory, Washington DC, NUREG/CT-3046, PNL-4385 1, 5.

Todreas, N.E., Kazimi, M.S., (2001), Nuclear Systems II: Elements of Thermal Hydraulic Design. Taylor and Francis.

Toppel, B.J., (1983), A User's Guide for the REBUS-3 Fuel Cycle Analysis Capability. Argonne National Laboratory, Illinois, USA.

Trapp, J.A., Ransom, V.H., (1977), RELAP5 Hydrodynamic Model Progress Summary -Abrupt Area Changes and Parallel Branching. . Idaho National Engineering Laboratory.

Tuček, K., Carlsson, J., Wider, H., (2006), Comparison of sodium and lead-cooled fast reactors regarding reactor physics aspects, severe safety and economical issues. Nuclear Engineering and Design 236, 1589-1598.

Van Tichelen, K., Mirelli, F., Greco, M., Viviani, G., (2015), E-SCAPE: A scale

facility for liquid-metal, pool-type reactor thermal hydraulic investigations. Nuclear Engineering and Design 290, 65-77.

Van Tichelen, K., Vanderhaegen, M., Jayaraju, S., Keijers, S., Roelofs, F., (2011), Scaling analysis for the European heavy liquid metal scaled pool facility ESCAPE, The 14th International Topical Meeting on Nuclear Reactor Thermalhydraulics, Toronto, Canada, pp. 25-30.

Wagner, W., Kruse, A., (1998), The industrial standard IAPWS-IF97 for the thermodynamic properties and supplementary equations for other properties. Properties of Water and Steam, Springer 354.

Wallenius, J., Qvist, S., Bortot, S., Mickus, I., Ejenstam, J., Szakalos, P., (2017), SEALER: a small lead-cooled reactor for power production in the Canadian Arctic, International Conference on Fast Reactors and Related Fuel Cycles: Next Generation Nuclear Systems for Sustainable Development (FR17), Yekaterinburg, Russia.

Waltar, A.E., Reynolds, A.B., (1980), Fast Breeder Reactors Pergamon press., New York.

Wedekind, G.L., Bhatt, B.L., Beck, B.T., (1978), A system mean void fraction model for predicting various transient phenomena associated with two-phase evaporating and condensing flows. International Journal of Multiphase Flow 4, 97-114.

Weinberg, D., Suckow, D., MUller, U., Hoffmann, H., (1990), The Transferability to Reactor Conditions of Thermohydraulics Model Investigations of Decay Heat Removal. roc. Int. Fast Reactor Safety Mtg., Snowbird, Utah.

Westinghouse Global Technology Office, (2017), Westinghouse Lead Fast

Reactor. Westinghouse Electric Company.

Willatzen, M., Pettit, N., Ploug-Sørensen, L., (1998), A general dynamic simulation model for evaporators and condensers in refrigeration. part i: moving-boundary formulation of two-phase flows with heat exchange: Modèle général dynamique pour évaporateurs et condenseurs frigorifiques. partic i: Formulation des conditions aux limites variables de flux biphasiques avec échange de chaleur. International Journal of refrigeration 21, 398-403.

Wu, Y., Bai, Y., Song, Y., Huang, Q., Zhao, Z., Hu, L., (2016), Development strategy and conceptual design of China Lead-based Research Reactor. Annals of Nuclear Energy 87, 511-516.

Yoo, B., Koo, G.H., Lee, J.H., Cho, M., (1999), Integrated horizontal and vertical seismic isolation bearing. Google Patents.

Yoo, B., Lee, J.-H., Koo, G.-H., Lee, H.-Y., Kim, J.-B., (2000), Seismic base isolation technologies for Korea advanced liquid metal reactor. Nuclear Engineering and Design 199, 125-142.

Zhang, J., Kapernick, R.J., McClure, P.R., Trapp, T.J., (2013), Lead–bismuth eutectic technology for Hyperion reactor. Journal of Nuclear Materials 441, 644-649.

Zhang, Z., Wu, Z., Sun, Y., Li, F., (2006), Design aspects of the Chinese modular high-temperature gas-cooled reactor HTR-PM. Nuclear Engineering and Design 236, 485-490.

Zigrang, D.J., Sylvester, N.D., (1985), A review of explicit friction factor equations. Journal of energy resources technology 107, 280-283.

Zrodnikov, A.V., Toshinsky, G.I., Komlev, O.G., Dragunov, Y.G., Stepanov,

V.S., Klimov, N.N., Kopytov, I.I., Krushelnitsky, V.N., (2006), Nuclear power development in market conditions with use of multi-purpose modular fast reactors SVBR-75/100. Nuclear Engineering and Design 236, 1490-1502.

초 록

전세계의 원자력 산업은 대형 원자력 발전소에 대한 대중 수용성 감소에 직면하고 있다. 또한 우리 국민의 대다수는 후쿠시마 사고 발생 이후 원자력에 대한 막연한 불안감을 가지고 있다. 이러한 후쿠시마 사고의 영향 외에도 수용할 만한 사용후핵연료 관리 계획이 부재하다는 것은 그러한 대중 수용성 저하에 기여하는 요인이다.

본 논문에서는 태양열 및 풍력을 포함한 재생가능 전력원과 함께 병합되어 작동할 수 있는 안전한 분산 전원으로서 혁신적인 납-비스무스 공융물(LBE) 냉각 피동형 소형모듈화원전(SMR)을 개발했다. 이러한 혁신적 소형모듈화원전의 특징은 원자로 내에 냉각재 순환 펌프를 탑재하지 않는다는 것과 모든 원자로 구성 요소를 단일 원자로용기 내에 포함시킴으로써 고유안전성을 향상시키는 일체형 풀형 설계를 달성한다는 것이다. 이러한 설계 혁신을 통해 납-비스무스 냉각 소형모듈화원전은 격리된 전력 그리드에서 재생가능 전력원의 급격한 변동에 대응할 수 있도록 부하추종 운전 능력을 확보해야 한다. 또한, 가압이 필요 없는 풀형 설계에 의한 피동 안전성을 통해 현재 원자력 발전소의 대부분에서 극도로 낮은 확률로 발생할 수 있는 일차 배관 파단 및 예상치 못한 펌프 실패로 인한 냉각재상실사고와 유량상실사고를 배제할 수 있다.

더욱이, 납-비스무스 냉각재는 미래 원자로의 냉각재로 간주되는 다른 액체 금속인 소듐과 비교해 물이나 공기와 화학적 반응성이 낮고 물과 비교했을 때에는 매우 높은 열전달 특성을 갖고 있기 때문에 원자로의 고유안전성 향상에 기여한다. 납-비스무스는 또한 고속 중성자 스펙트럼을 형성해 핵원료성물질을 핵분열물질로 전환하고 핵연료의 장기 연소를 촉진하여 해당 기간 동안 임계도를 달성

할 수 있도록 한다. 이러한 고속 중성자 스펙트럼은 나아가 효과적으로 초우라늄원소를 저방사성 핵종으로 변환시킬 수 있도록 하여 궁극적으로 핵연료 이용도를 더욱 증가시키고 고준위폐기물의 양을 최소화하는 데에 기여한다.

납-비스무스 냉각 피동형 계통의 과도 상황에서의 계통 통합 거동에 대한 적절한 이해를 위한 예측 도구가 필요하다. 이를 위해 본 연구는 다음과 같이 3단계로 나뉘어 수행되었다. 첫째, 유체역학적 축소 설계에 의해 풀형 일체형 실험 시설이 원형 소형모듈화원전의 설계로부터 고안되었고, 이 설비를 활용해 납-비스무스의 자연 순환 실험을 정상 상태와 외부 운용 조건 변화에 따른 과도 상태에서 수행했다. 둘째, 1차원 열수력 계통 해석 코드를 룹형 설비와 풀형 설비에서 생성된 실험 결과를 통해 검증했다. 셋째, 피동형 계통의 과도 상태 거동 평가를 위한 일차원 시간종속 분석 모델이 개발되었다. 이 분석 모델은 본 연구에서 진행된 납-비스무스 자연순환 실험 결과를 활용해 검증된 1차원 계통 열수력 해석 코드를 통해 검증되었다. 지금까지 납-비스무스 냉각 소형모듈화원전이 실현되지 않았으므로 URANUS를 이러한 3 단계 접근 이전에 설계하여 해당 원자로를 목표로 삼아 축소 실험 설계 및 분석이 진행되었다.

본 논문에서 진행된 피동형 납-비스무스 냉각 소형모듈화원전에 대한 실험, 수치해석 및 분석 결과를 토대로 1차측 냉각재의 자연순환은 원자로 출력 변동 속도를 저해하지 않음을 확인했다. 또한, 개발된 분석 모델을 활용한 안정성 분석 결과, 외부 부하 요구 변화에 대해 URANUS가 노심 출력을 안정된 범위 내에서 조정할 수 있음을 확인했다. 따라서 안전하고 안정적인 범위에서 도달할 수 있는 최대 전력 변화율은 피동형 원자로 계통의 열수력적 및 중성자 동역학적 특성에 의해 결정되지 않고 핵연료의 재료적 건전성에 의해 결정된다고 할 수 있다. 개발된 분석 모델을 활용하여 전출력의 50%

출력 범위에서 운전 중인 URANUS를 최대출력까지 복귀하는 형식의 계단형 입력에 대한 계통 응답 분석을 평가한 결과 URANUS의 노심 출력이 초당 전출력의 3.5%만큼의 출력변동률로 조정될 수 있을 것으로 분석됐다.

이와 더불어 개발된 분석 모델을 통해 예비 연구로서 URANUS 2차측의 동역학적 거동에 대한 시뮬레이션을 수행했다. 이 모델에는 2차측 주급수의 유량 제어 모델이 부여하였으며, 해당 모델로는 외부 부하 요구에 대해 2차측 주급수 유량이 비례하도록 제어하는 비례 제어기를 사용했다. 단순하고 이상적인 유량 제어기를 분석 모델에 적용한 결과 천이상태에서 발생하는 원자로 1차측과 2차측 사이의 열전달 불균형이 그것을 활용하지 않았을 때에 대비하여 약 1/3으로 감소하고 2차측이 새로운 정상상태로 돌입하는 시간이 약 1/2 수준으로 줄어드는 것으로 평가됐다. 상기 결과를 종합할 때, 피동형 납-비스무스 냉각 소형모듈화원전의 2차측은 주어진 운전 상태 변화에 따라 1차측에 비해 느린 과도 상태를 겪을 것으로 예상되므로 빠른 전력망 요구에 대응하기 위해서는 노심 출력 제어뿐만 아니라 주급수 유량 제어가 필요하다는 결론을 도출하였다.

주요어: 납-비스무스 공융물, 자연순환, 소형모듈화원전, 척도 해석, 부하추종 운전

학 번: 2013-21019